

# POWER SOURCES 18

---

## RESEARCH AND DEVELOPMENT IN NON-MECHANICAL ELECTRICAL POWER SOURCES

The 22nd International Power Sources Symposium  
held in Manchester, England, 9–11 April 2001

Edited by  
A. ATTEWELL

Symposium Chairman  
T. KEILY



**DISTRIBUTION STATEMENT A**  
Approved for Public Release  
Distribution Unlimited

THE INTERNATIONAL POWER SOURCES SYMPOSIUM LTD  
Broadway House, The Broadway, Crowborough, East Sussex TN6 1HQ England  
A company registered in England, No. 3202602  
Registered Charity, No. 1056563

20010523 030

---

© 2001 Elsevier Science B.V. All rights reserved.

This journal and the individual contributions contained in it are protected under copyright by Elsevier Science B.V., and the following terms and conditions apply to their use:

**Photocopying**

Single photocopies of single articles may be made for personal use as allowed by national copyright laws. Permission of the Publisher and payment of a fee is required for all other photocopying, including multiple or systematic copying, copying for advertising or promotional purposes, resale, and all forms of document delivery. Special rates are available for educational institutions that wish to make photocopies for non-profit educational classroom use.

Permissions may be sought directly from Elsevier Science Global Rights Department, P.O. Box 800, Oxford OX5 1DX, UK; phone: (+44) 1865 843830, fax: (+44) 1865 853333, e-mail: [permissions@elsevier.co.uk](mailto:permissions@elsevier.co.uk). You may also contact Global Rights directly through Elsevier's homepage (<http://www.elsevier.nl>), by selecting 'Obtaining Permissions'.

In the USA, users may clear permissions and make payments through the Copyright Clearance Center, Inc., 222 Rosewood Drive, Danvers, MA 01923, USA; phone: (+1) (978) 7508400; fax: (+1) (978) 7504744, and in the UK through the Copyright Licensing Agency Rapid Clearance Service (CLARCS), 90 Tottenham Court Road, London, W1P 0LP, UK; phone: (+44) 20 7631 5555; fax: (+44) 20 7631 5500. Other countries may have a local reprographic rights agency for payments.

**Derivative Works**

Subscribers may reproduce tables of contents or prepare lists of articles including abstracts for internal circulation within their institutions. Permission of the publisher is required for resale or distribution outside the institution.

Permission of the publisher is required for all other derivative works, including compilations and translations.

**Electronic Storage or Usage**

Permission of the publisher is required to store or use electronically any material contained in this journal, including any article or part of an article.

Except as outlined above, no part of this publication may be reproduced, stored in a retrieval system or transmitted in any form or by any means, electronic, mechanical, photocopying, recording or otherwise, without prior written permission of the Publisher.

Address permission requests to: Elsevier Science Global Rights Department, at the mail, fax and e-mail addresses noted above.

**Notice**

No responsibility is assumed by the Publisher for any injury and/or damage to persons or property as a matter of products liability, negligence or otherwise, or from any use or operation of any methods, products, instructions or ideas contained in the material herein. Because of rapid advances in the medical sciences, in particular, independent verification of diagnoses and drug dosages should be made.

Although all advertising material is expected to conform to ethical (medical) standards, inclusion in this publication does not constitute a guarantee or endorsement of the quality or value of such product or of the claims made of it by its manufacturer.

☺ The paper used in this publication meets the requirements of ANSI/NISO Z39.48-1992 (Permanence of Paper).

Printed in The Netherlands



# POWER SOURCES 18

Contract R0D9105-CH-00

N68171-01-M-5518

P.I: Lakeman.

Also in this series:

BATTERIES (1963) & BATTERIES 2 (1964)

POWER SOURCES (1967 & 1968)

POWER SOURCES 3 (1971) to POWER SOURCES 17 (1999)

Being the Proceedings of the Third (1962) to the Twenty-first (1999)  
International Power Sources Symposia

## Symposium Board of Trustees

---

Mr. T. Keily	[Chairman]
Mr. G. Ware	[Vice Chairman] Varta Limited
Dr. R.N. Thomas	[Treasurer] SAFT
Dr. G. Archdale	SAFT
Mr. M. Crowther	MC Consultants
Mr. L. Delaney	Hawker Limited
Mr. C.J. Ford	Defence Evaluation Research Agency, Aquila
Mr. D. Goodwin	AEA Technology Battery Systems Limited
Mr. M. Kniveton	British Telecom
Dr. B.L. Lakeman	Defence Evaluation Research Agency, Haslar
Mr. P. Meeds	CMP Batteries Limited
Dr. C.E. Newnham	Ultralife Batteries (UK) Limited
Prof. J. Turner	Transport Research Laboratory
Mr. D. Rice	Hawker Energy Products Limited
Mr. G. Woolf	Batteries International

Associate:

Mr. S. Westwell	Civil Aviation Authority
-----------------	--------------------------

Officers:

Mr. R.D. Bailey	Company Secretary
Mr. A. Attewell	Editor

---

The 22<sup>nd</sup> International Power Sources Symposium and Exhibition was supported by:

AEA Technology Battery Systems Ltd., Batteries International, British Telecom, CMP Batteries, DERA, Hawker Ltd., SAFT, Transport Research Laboratory, Ultralife Batteries (UK) Ltd., Varta Ltd

## Contents

Foreword . . . . .	xi
The Frank Booth Award . . . . .	xiii
The Bourner lecture — do standby batteries need to have a new chemistry? . . . . . G. Karlsson	xv

### Articles

(1) Recent developments and future prospects for lithium rechargeable batteries . . . . . A.G. Ritchie	1
(2) Carbon-carbon composite as anodes for lithium-ion battery systems . . . . . S. Hossain, Y. Saleh, R. Loutfy	5
(3) Optimisation of PVdF-based polymer electrolytes . . . . . N. Muniyandi, N. Kalaiselvi, P. Periyasamy, R. Thirunakaran, B. Ramesh babu, S. Gopukumar, T. Premkumar, N.G. Renganathan, M. Raghavan	14
(4) Investigation of the stability of chlorinated PVC-based polymer electrolytes for lithium batteries . . . . . E.M. Shembel, O.V. Chervakov, L.I. Neduzhko, I.M. Maksyuta, Yu.V. Polischuk, D.E. Reisner, P. Novak, D. Meshri	20
(5) Improving the interfacial resistance in lithium cells with additives . . . . . G. Nagasubramanian, D. Doughty	29
(6) Evolution of power sources for implantable cardioverter defibrillators . . . . . A.M. Crespi, S.K. Somdahl, C.L. Schmidt, P.M. Skarstad	33
(7) Advances in aviation battery systems technology . . . . . J.K. Erbacher	39
(8) Development of true prismatic lithium-ion cells for high rate and low temperature applications . . . . . F. Puglia, R. Gitzendanner, C. Marsh, T. Curran	40
(9) Li-ion battery technology for compact high power sources (CHPS) . . . . . T. Sack, T. Matty	47
(10) Computer simulation of the discharge of metal electrodes in batteries with solid electrolytes . . . . . G.I. Ostapenko, S.N. Antonov	52
(11) Analysis of power limitations at porous supercapacitor electrodes under cyclic voltammetry modulation and dc charge . . . . . W.G. Pell, B.E. Conway	57
(12) Nickel metal hydride batteries for high power applications . . . . . M.L. Soria, J. Chacón, J.C. Hernández, D. Moreno, A. Ojeda	68
(13) Alkaline high power batteries in a bipolar stack design . . . . . D. Ohms, M. Kohlhase, G. Benczúr-Ürmösy, G. Schaedlich, K. Wiesener, J. Harmel	76
(14) The development of hydrogen storage electrode alloys for nickel hydride batteries . . . . . K. Hong	85

The publisher encourages the submission of articles in electronic form thus saving time and avoiding rekeying errors. A leaflet describing our requirements is available from the publisher upon request.

**CONTENTS**  
**Direct**

This journal is part of **ContentsDirect**, the *free* alerting service which sends tables of contents by e-mail for Elsevier Science books and journals. You can register for **ContentsDirect** online at: [www.elsevier.nl/locate/contentsdirect](http://www.elsevier.nl/locate/contentsdirect)

(15) Electrocatalytic characteristics of the metal hydride electrode for advanced Ni/MH batteries . . . . .	90
M. Geng, F. Feng, S.A. Gamboa, P.J. Sebastian, A.J. Matchett, D.O. Northwood	
(16) Performance of valve-regulated lead-acid batteries in real-world stationary applications — utility installations . . . . .	94
P. Butler, J. Dunleavy, M. Farber-DeAnda, P. Moseley	
(17) Latest developments in super high rate lead-acid batteries from India . . . . .	102
A. Bhattacharyya, D. Dasgupta, S. Ghosh	
(18) On the impedance of the gassing reactions in lead-acid batteries. . . . .	106
A. Hammouche, E. Karden, J. Walter, R.W. De Doncker	
(19) Methods for state-of-charge determination and their applications. . . . .	113
S. Piller, M. Perrin, A. Jossen	
(20) Aging in chemically prepared divalent silver oxide electrodes for silver/zinc reserve batteries . . . . .	121
D.F. Smith, C. Brown	
(21) Advanced membranes for alkaline primary and rechargeable alkaline cells with zinc anodes . . . . .	128
H. Lewis, P. Jackson, A. Salkind, T. Danko, R. Bell	
(22) High-rate capability of zinc anodes in alkaline primary cells . . . . .	133
J.-Y. Huot, M. Malservisi	
(23) Future talk . . . . .	140
M. Kniveton	
(24) VARTA micro batteries for wireless telecommunication devices . . . . .	145
D. Ilic, J. Heydecke, M. Kilb, I. Knop, G. Schulz	
(25) Dynamic characterization of small lead-acid cells . . . . .	151
A. Salkind, T. Atwater, P. Singh, S. Nelatury, S. Damodar, C. Fennie Jr., D. Reisner	
(26) Energy sources for the future dismounted soldier, the total integration of the energy consumption within the soldier system . . . . .	160
J.W. Raadschelders, T. Jansen	
(27) Development of an intelligent rechargeable lithium-ion battery and charger system for military applications . . . . .	167
Q. Moore	
(28) Renewable energy systems based on hydrogen for remote applications . . . . .	168
K. Agbossou, R. Chahine, J. Hamelin, F. Laurencelle, A. Anouar, J.-M. St-Arnaud, T.K. Bose	
(29) Solar photovoltaics: an industry of today or tomorrow? . . . . .	173
M. Hammond	
(30) Polymer electrolyte membrane fuel cells for communication applications. . . . .	174
D. Chu, R. Jiang, K. Gardner, R. Jacobs, J. Schmidt, T. Quakenbush, J. Stephens	
(31) Powering the 21st century with Ballard fuel cells . . . . .	179
H. Voss	
(32) Further development of lithium/polycarbon monofluoride envelope cells . . . . .	180
A.G. Ritchie, C.O. Giwa, P.G. Bowles, J. Burgess, E. Eweka, A. Gilmour	
(33) Ultralife's polymer electrolyte rechargeable lithium-ion batteries for use in the mobile electronics industry . . . . .	184
E.A. Cuellar, M.E. Manna, R.D. Wise, A.B. Gavrilov, M.J. Bastian, R.M. Brey, J. DeMatteis	
(34) The development of higher energy density lithium-ion cell designs . . . . .	199
F. Coowar, J.S. Weaving, M. Lee, C.R. Jarvis, W.J. Macklin	
(35) Direct methanol-air fuel cells with membranes plus circulating electrolyte . . . . .	200
K. Kordes, V. Hacker, U. Bachhiesl	
(36) The effect of anode flow characteristics and temperature on the performance of a direct methanol fuel cell. . . . .	204
J.C. Amphlett, B.A. Peppley, E. Halliop, A. Sadiq	
(37) An innovative technique for pore structure analysis of fuel cell and battery components using flow porometry. . . . .	214
A. Jena, K. Gupta	
(38) Possibilities of prevention of formation of poisoning species on direct methanol fuel cell anodes . . . . .	220
R. Manoharan, J. Prabhuram	
(39) In situ X-ray absorption spectroscopy and X-ray diffraction of fuel cell electrocatalysts . . . . .	226
A.E. Russell, S. Maniguet, R.J. Mathew, J. Yao, M.A. Roberts, D. Thompson	
(40) New lightweight bipolar plate system for polymer electrolyte membrane fuel cells . . . . .	233
D.R. Hodgson, B. May, P.L. Adcock, D.P. Davies	
(41) Optimization of the magnesium-solution phase catholyte semi-fuel cell for long duration testing . . . . .	236
M.G. Medeiros, R.R. Bessette, C.M. Deschenes, D.W. Atwater	
(42) Development and characterization of a novel carbon fiber based cathode for semi-fuel cell applications . . . . .	240
R.R. Bessette, M.G. Medeiros, C.J. Patrissi, C.M. Deschenes, C.N. LaFratta	
(43) Multivariate analysis for battery optimisation and testing . . . . .	245
W. Paul Hagan	
(44) Findings of the rechargeable battery study sponsored by NATIBO (North American technology and industrial base organization) . . . . .	246
J.A. Gucinski, M. Slack	
(45) Electrochemical power sources for unmanned underwater vehicles used in deep sea survey operations . . . . .	252
Ø. Hasvold, N. Størkersen	
(46) The thermodynamics of battery safety . . . . .	259
S. Mores, M.R. Ottaway, E. Price	
(47) Safety of lithium batteries in transportation . . . . .	260
M.D. Farrington	

Poster Abstracts . . . . .	266
Author Index . . . . .	272
Subject Index . . . . .	273

AD NUMBER		DATE	<b>DTIC ACCESSION NOTICE</b>  <b>20010523 030</b>
1. REPORT IDENTIFYING INFORMATION			
A. ORIGINATING AGENCY DERA, UK			
B. REPORT TITLE AND/OR NUMBER 22nd International Power Sources Symposium			
C. MONITOR REPORT NUMBER RrD 9105-CH-02			
D. PREPARED UNDER CONTRACT NUMBER N 68171-01-M-5518			<b>REQU</b> 1. Put yr on rev 2. Compl 3. Attach maile 4. Use ui infor 5. Do not for 6
2. DISTRIBUTION STATEMENT APPROVED FOR PUBLIC RELEASE DISTRIBUTION UNLIMITED PROCEEDINGS			<b>DTIC:</b> 1. Assig 2. Retur

DTI OCT 95

DITIONS ARE OBSOLETE

## Foreword

*Power Sources 18* is an edited record of the papers and posters submitted for presentation at the 22nd International Power Sources Symposium that was held at the Crowne Plaza — The Midland Hotel in Manchester, England, during 9–11 April 2001.

Manchester was chosen for the 22nd Symposium following an extensive, country-wide survey by the Board of Trustees who were seeking a venue which met the needs of presenters, delegates and exhibitors with regard to facilities, comfort and accessibility coupled with good value for money.

As in previous years, the call for papers produced an overwhelming response. Forty-eight papers from 14 countries are contained in these Proceedings. This has once again confirmed the variety of work being undertaken into research, development and advancement of battery and fuel cell technology on a worldwide basis.

The number and variety of topics submitted for presentation enabled the Board to organize not only a 3-day programme covering a wide range of electrochemical topics including basic and applied research, development and applications, but also a day-long parallel session concentrating on power sources for communications equipment — ranging from military manpack radios to remote telemetry.

A key event of these symposia is the Bournier Lecture — in memory of our previous secretary, Sheila Bournier — given this time by Gunder Karlsson of Emerson Energy Systems ASB of Sweden. His lecture was entitled: *Do standby batteries need to have a new chemistry?* — a topic with implications for any application where an uninterrupted power supply is critical.

The production of the Symposium Proceedings has always been considered by the Board as one of its prime duties. It also considers that the quality of the publication and its academic content should enhance both the reputation of its contributors and that of the Symposium. As editor since 1993, Austin Attewell has achieved both of these aims with distinction. His international reputation as a battery

expert has given confidence to the Board of Trustees, and to authors that their work would be published to the highest standards. It is therefore, with regret, that the Board has accepted his request to retire as editor, following the publication of *Power Sources 18*.

As a tribute to Austin's outstanding contribution to the advancement of power sources during his career with the U.K. Ministry of Defence at the Royal Aircraft Establishment (later Defence Research Agency) at Farnborough, coupled with his furtherance of the effectiveness of the Symposia, both as an author of several papers and as editor of five volumes of Proceedings, the Board of Trustees have awarded him the Frank M. Booth medal for 2001.

I am pleased to announce the appointment of a new editor in the person of Martin Crowther. Martin is currently a member of the Board of Trustees and is a recognised battery expert — having worked for many years in the U.K. Scientific Civil Service.

As in previous years, I should like to take this opportunity to thank all of the authors who submitted papers and posters for publication. Their efforts not only enhance the reputation of these Symposia but also justify their existence.

I have to report the retirement of several members of the Board since the 21st Symposium in Brighton 2 years ago. These were Dr. B.L. Jones (past Treasurer), Dr. J. Knight and W.R. Young (past Vice Chairman). All three undertook extra responsibilities during their period as Trustees. I should like to express my personal gratitude and that of the other Trustees to them for the support they gave to the Symposia over many years.

I deem it a great privilege to chair the Board of the International Power Sources Symposium. The 22nd meeting in Manchester in 2001 represented the culmination of 2 years of work by my fellow Trustees and professional officers. This effort, in combination with the support of presenters and delegates, ensured the success of this important scientific gathering.

T. Keily (Chairman)



## The Frank M. Booth Award

The Frank M. Booth Award, established in 1970, is named after the founder of these International Symposia. It is presented in recognition of outstanding contributions to the advancement of Power Sources, both technically, and in furthering the effectiveness of the Symposia.

For the 2001 Power Sources Symposium, the Board of Trustees is delighted to announce that they have made the award to Austin Attewell, the retiring Symposium Editor.

**Austin Attewell**



After reading chemistry at London University and service in the Royal Air Force, Austin Attewell joined the UK Scientific Civil Service and for 42 years worked at the Royal Aircraft Establishment, Farnborough. Early in his career with batteries, he began work on thermal and other types of batteries for use in guided weapons. Later, he was involved with primary zinc-air and with the safe usage of lithium primary batteries in military environments. Much of his time was spent in the development of battery hardware, both in-house and extra murally, and in trying to cultivate the correct usage of batteries by the Armed Forces. He organised and supervised several test houses devoted to the evaluation and hazard testing of all types of battery of interest to the British Army and the Royal Air Force.

In later years, as a consultant at the R.A.E., he was involved in specification work and in the creation of a data base containing details of all batteries of interest to the UK military.

Of the delegates at the 2001 Conference, he was the only one who had attended all, except one, of the International Power Sources Symposia since their inception in 1958. He contributed several papers on subjects ranging from thermal batteries to the

safety testing of lithium types, whilst in 1988 he reviewed changes which had occurred in battery technology during the first 30 years of the Symposium's existence. He became editor in 1993, and worked on the production of five volumes of the Proceedings: *Power Sources 14 through 18*.

For several years, he contributed a regular column: *Power Source Voice* to *Batteries International* that, besides presenting his own views of the battery scene, past and present, was used — often blatantly — to publicise forthcoming Power Source Symposia.

Cooperation with those government organisations and manufacturers in North America who were working on weapons' batteries led to an appreciation of the United States as a vacation location and for many years he and his wife have spent several weeks there on annual holiday.

Photography, an interest in all aspects of the British countryside — its landscape, transport and buildings — combined with a lifelong interest in model-making has led him into having a deep involvement with a charitable museum which is involved in an ambitious project to re-create in miniature and with detailed accuracy, a small part of Southern England as it appeared in the inter-war years.

He hopes to be able to attend the next Symposium in 2003, as this will be the occasion to celebrate 50 years of involvement with battery R&D.

Previous recipients of the Award have been:

Dr M. Barak	1960–1970
Dr P. Reasbeck	1960–1970
Mr A.L. Taylor	1960–1970
Mrs J. Burbank	1970
Dr J.F. Laurent	1972
Dr M.I. Gillibrand	1974
Mr D.H. Collins	1976
Prof H.R. Thirsk	1978
Dr P. Ruetschi	1980
Mr M.H.J. Lemmon	1982
Dr J.P. Gabano	1986
Prof F.L. Tye	1986
Mr N.E. Bagshaw	1988
Prof K. Kordesch	1991
Mrs S.M. Bourner	1993
Dr G.J. Donaldson	1995
Dr P.M. Skarstad	1997
Mr S. Goodman	1999
Prof. A.J. Salkind	1999

# The Bournier lecture — do standby batteries need to have a new chemistry?

Gunder Karlsson

*Emerson Energy Systems AB, Dialoggatan 1, Kungens Kurva SE 14182, Sweden*

Received 6 December 2000; accepted 15 December 2000

---

## Abstract

The telecommunication and data communication businesses are experiencing strong growth and so is the demand for batteries for back-up power. The stationary lead-acid battery is the type that dominates these applications. This presentation will give some guidelines for battery scientists who want to apply their technology to back-up power. The opinion of the author is that the advanced batteries that are in the frontline today are poorly adapted to the needs of back-up power for networks. If developers of these advanced batteries are to stand a chance of achieving success in the network power market they must focus on reliability, volumetric energy density and cost. © 2001 Elsevier Science B.V. All rights reserved.

**Keywords:** Standby power supplies; Telecommunications; Lead-acid batteries; Reliability; Cost effectiveness

---

## 1. The market

Data transmission and voice transmission are experiencing strong growth. This is fuelled by the popularity of the Internet and by mobile telephony. Soon Internet and mobile telephony will merge. Voice traffic over the mobile network will become packet-switched (data) instead of line-switched. The mobile network we have today is the so-called 2G (second generation) and will have enhanced data communication. New operators using 3G (third generation) networks will offer even more data transmission over the air interface. The mobile Internet will naturally create a need for more data transmission in the network. When the Internet is more accessible it will of course be used more, and hence, need more capacity. The increased band of 3G mobiles and also that of broadband Internet access will be used, together with new services eating up the bandwidth. Services like TV, video, still pictures and music are popular and they are demanding on the bandwidth.

There is a strong motivation for high availability on the networks. This is for several reasons. A very important one is that of loss of revenue. At transmission centres where traffic is concentrated, loss of service becomes very costly. Today, there are network centres where there are several operators sharing a common installation. These centres are sometimes called Internet hotels and also sometimes referred to as

telehousing. In these premises the company responsible for the infrastructure normally is obligated strictly to provide safe, reliable, electric power. Even on the access side, both at the fixed site and at the radio base station, back-up power is necessary. The traffic at a radio base in a densely populated area is generating revenue, and therefore, back-up power is necessary.

## 2. Reliability

There are several options for back-up power. These options can be ranked in a diagram showing the reliability and volumetric energy density (Fig. 1).

The reliability scale is an important factor for the selection of back-up power. At the lower end of reliability we have motor generator combinations while we have batteries at the higher end of reliability. During my years in telecommunications, I have begun to realise that these two factors are the most important factors for back-up power in the infrastructure of telecom. The batteries we use today are highly reliable. This reliability is not inherent in batteries. It has long been fought for.

Accumulated experience in the production and design of lead-acid batteries has led to the level of reliability that we have at present. A battery consists of a set of cells in series. Every cell has to be highly reliable in order for the battery to have a high reliability. Even with such a mature technology

---

*E-mail address:* arbaseus@algonet.se (G. Karlsson).

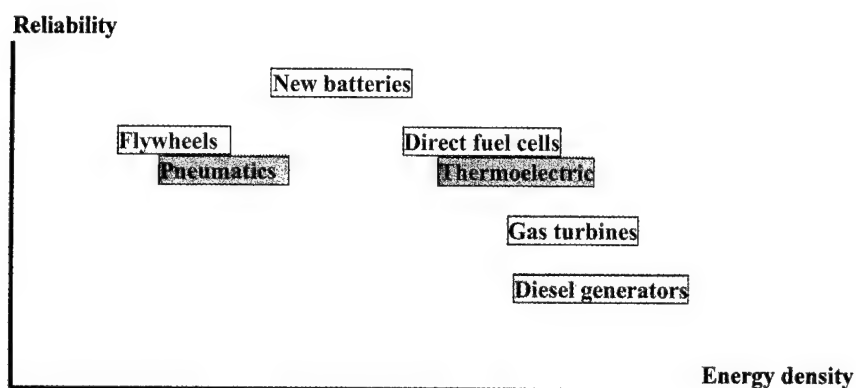


Fig. 1. A ranking of reliability against energy density.

as the lead-acid battery, minor new design features have presented reliability problems. At introduction, the low maintenance flooded and the valve regulated battery designs were plagued by reliabilities lower than the previous, older, technology.

The valve regulated lead-acid battery, which is the most common battery for industrial back-up purposes, has been plagued by problems; some of these failure modes can be found in Table 1.

It has been stated that valve regulated batteries become unreliable very early in life [1,2]. Our experience is that this technology has matured and reliable performance is now achieved. Improvements will continue to be made both in terms of energy density, longevity and production costs. If standardisation can be increased and production more centralised, cost could come down even further.

### 3. Primary versus secondary

Among candidates for back-up power, there are two groups from a systems point of view — electrically refuellable and those that cannot be refuelled electrically. Using terms common among battery scientist the groups are akin to primary and secondary batteries (Table 2).

Because of operational convenience an electrically refuellable battery is always preferred over a back-up power source which needs to be mechanically refuelled. The storage of fuel on site is normally associated with some risk. Storage of fuels is regulated and in some locations a permit is required. This is a concern both for fuel cells and for motor generators. Also the waste product from mechani-

cally refuelled devices can be a problem. For instance, ducting from a diesel generator and from a fuel cell is required.

You need to remove waste heat and moisture. The mechanically refuellable metal/air batteries which have been suggested and promoted as back-up power, create a problem on the waste side rather than the fuel side. The aluminium/air battery has been promoted recently, as a clean back-up source. When end-customers became aware of the waste electrolyte problem the interest in this device soon faded.

### 4. Batteries versus the alternatives

The flywheel has recently caught much attention as a clean back-up power source [3]. The proponents of this technology have stressed its virtues; environmental friendliness, high power density and longevity. Put into a back-up power source perspective reveals that it is less reliable than a battery. This comes from the fact that it uses an electronic power conversion stage for its electrical output. An electric power converter decreases overall reliability. Another drawback of the flywheel is the lack of long term experience. The flywheel is similar to a superconducting coil in many aspects. Both devices are dependent on power electronics for their output of electric power.

The flywheel's measure of performance for gravimetric energy density is ultimate strength divided by density. For those materials with the best index of performance this translates into an ultimate energy density close to that of the lead-acid battery. So the battery fares well in this comparison versus another back-up power source.

Table 1  
Problems with valve regulated lead-acid batteries

Problem	Comment	Cure
Corrosion	The ultimate failure mode	Better alloys, new grid making methods
Top-lead corrosion	An unnecessary failure mode	Proper alloys
PCL	Occurs even for very few cycles	Higher compression, more dense active material, addition of tin
Negative self-discharge	Appears over a 2–4 year span	More lead surface area to positive grid, high overpotential negative

Table 2  
Primary and secondary standby devices

Primary	Secondary
Motor generators	Rechargeable batteries
Thermoelectric generators	SMES
Fuel cells	Flywheels
Metal/air batteries	Reversible fuel cells
Other primary batteries	Pneumatic storage

If we omit metal/air, batteries can be almost completely sealed and be without moving parts — which are very attractive attributes from a reliability point of view. The most desirable features for new batteries are:

1. Higher volumetric energy density.
2. Higher gravimetric energy density.
3. Better endurance at high temperatures.
4. Components that are more environmentally acceptable.

Most of the research for new chemistries has focused on portable batteries and batteries for electric traction. The research on portable batteries is driven by the market and is, to a substantial part, financed by the battery companies. For electric vehicle batteries research is funded mainly by the State. At the present time there is very little research into batteries for stationary applications except for the continuing development of existing lead-acid technology.

## 5. New battery chemistries

We put together last year a diagram showing new battery chemistries (Fig. 2). We found the highest volumetric energy densities in flooded nickel/metal hydride batteries. We found

that the longest working calendar life for full scale batteries was from sodium/nickel chloride batteries. We are aware that most research is spent on lithium batteries in various forms, both in terms of chemistries and in mechanical design.

However, little research has been done so far on calendar life float studies for secondary lithium batteries. The Canadian research into PEO-solid electrolyte batteries proved that this battery did indeed have a long life. The company ARGO-TECH, which uses technology that partly comes from this research is, at present time, the only company that is researching into lithium batteries with the stationary application as main interest.

Each year, a forum for energy related research for telecom is arranged by IEEE: the INTELEC Conference. One of its topics is batteries. There are few presentations about alternate chemistries. In the year 2000, there were the following numbers on various battery systems: lead-acid 29, Ni/Cd 1, Ni/MH 2, Li-ion 1, Li-polymer 2; and this was the year with the most papers on alternate battery chemistries.

## 6. Relations between cost and performance

It is the authors opinion that new chemistries can get substantial market penetration into stationary standby batteries when their cost is in the range of two to four times that of lead-acid batteries. This is the approximate relationship today between industrial nickel/cadmium and lead-acid batteries. The nickel/cadmium battery has the advantage of long life at elevated temperatures. Some customers have been attracted by this feature. The better high temperature endurance enables them to increase the intervals of battery replacement. The alternate solutions, to use compressor

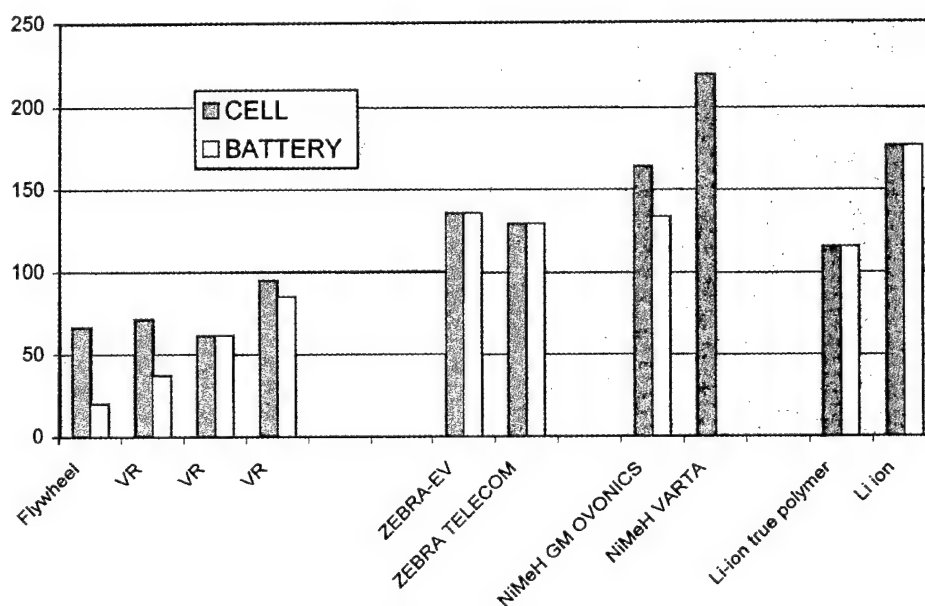


Fig. 2. Volumetric energy densities of a flywheel and of some new chemistries.

driven refrigeration or to use high temperature lead-acid batteries, are less attractive in many applications. Nickel/cadmium batteries will continue to be used in niche applications in telecom where the main advantage is that high temperature endurance is required. However, improved lead-acid batteries, specialised for high temperature, will counteract this. As mentioned previously, the most desirable feature of a new battery is volumetric energy density. In this aspect, the difference is not that great between nickel/cadmium and lead-acid.

To really make a difference, a new chemistry battery has to have a substantial advantage over the best lead-acid battery designs, which have a volumetric energy density of  $100 \text{ Wh dm}^{-3}$ .

## 7. Some basic costs

It is the author's opinion that the cost of battery basically is composed of raw materials cost factor and a necessary surface area factor. The raw materials cost is composed of a cost per ampere-hour of the compound and its relation to the other materials. When using nickel in an aqueous battery with a 1.2 cell voltage and one electron per mole exchange, the unit cost is higher than for a sodium/nickel chloride battery where we get two electrons per mole and 2.5 V. The necessary surface area is not such a definite factor because industrial development can influence this strongly. Battery chemistries which use poorly conducting electrolytes and have low cell voltages need to produce more electrode surfaces for the same performance. The very high power density figure of merit of the lead-acid battery is one of the factors that has contributed to the success of this battery.

Lithium batteries, which have high energy densities, have the draw back that the most efficient materials for the positive electrodes are costly. The really affordable materials that can be used in lithium batteries, such as sulphur polymers and manganese oxides are, as yet, less developed.

## 8. Float charge requirement

Another factor that is very important for a successful battery is the ability to be operated in the float charge mode. Today, back-up power is provided by fully floating configurations. The batteries are connected in parallel with the load and the rectifiers. There is no power electronics between the battery and the load. This is considered as

necessary for high reliability. The various advanced sealed nickel batteries have a disadvantage in this respect, as they do not lend themselves to be operated safely in the float charge mode. The nickel battery which has recently been most successful commercially is a flooded version, which can safely be charged in the float mode. Nickel/metal hydride batteries seem attractive from the volumetric energy density point of view.

## 9. Author's speculation

Nickel metal/hydride batteries have the virtues of high energy density. Their inability to operate safely in float charge mode and in a high temperature environment are problems at present time. If it could be shown that the hydride alloy could survive for a substantial time at elevated temperature, nickel/metal hydride could gain a substantial market share. It might be that flooded design with separate head space for recombination could do the job.

Batteries operating at high and elevated temperatures have been proposed for electric vehicles, but the high temperature is a definite disadvantage for this application. For stationary applications, where the back-up energy is in the range  $>5\text{--}10 \text{ kWh}$ , the drawbacks of high temperature is not so large as in the electric vehicle application. Also the more moderate demand on power density makes batteries based on beta-alumina and on polymers more viable for standby applications.

For lithium batteries, one must keep an eye on the development of production technologies and on the development of non-cobalt positives. If the manufacturing costs for the large amounts of electrode surfaces that are required and their assembly into working units can be brought down substantially, then lithium batteries might have a success in the area of standby power for telecommunications.

For further reading see [4].

## References

- [1] D.O. Feder, T.G. Croda, K.S. Champlin, M.J. Hlavac, in: *Proceedings of the INTELEC Conference*, 1992 (paper 9-5).
- [2] P. Selånger, A.O. Johansson, K. Lundqvist, K. Oberger, L. Humla, in: *Proceedings of the INTELEC Conference*, 1995 (paper 7-3).
- [3] W.E. Stanton, J.R. Saliba, T. Piela, in: *Proceedings of the INTELEC Conference*, 1999 (paper 30-1).
- [4] J. Rouaillrd, C. St Pierre, D. Geoffroy, Y. Choquette, in: *Proceedings of the INTELEC Conference*, 1999 (paper 27-2).

## Recent developments and future prospects for lithium rechargeable batteries<sup>☆</sup>

A.G. Ritchie<sup>\*</sup>

*Defence Evaluation and Research Agency, Haslar, Gosport Hants PO12 2AG, UK*

Received 15 November 2000; accepted 28 November 2000

---

### Abstract

Possible future developments of lithium rechargeable batteries are discussed. Lithium ion liquid electrolyte batteries are now well established, with energy densities of up to around 150 Wh kg<sup>-1</sup>. There are prospects of increases in the energy density to perhaps 200–250 Wh kg<sup>-1</sup> by using new cathode materials (lithium nickel cobalt oxide) and light weight construction. High power cells make it possible for these batteries to find new uses, e.g. in military applications. Some new materials could reduce the cost, which might make lithium rechargeable batteries economic for electric vehicles.

**Keywords:** Lithium ion rechargeable batteries; Lithium oxides

---

### 1. Introduction

Since the introduction of lithium ion batteries by SONY [1], the market for these has grown to around 400 million cells per year [2] for premium consumer applications, such as camcorders, portable telephones and computers. 95% of these batteries are made in Japan [2]. The vast majority of them use the same basic chemistry as announced by SONY, which is a carbon negative electrode into which lithium intercalates and a lithium cobalt oxide, LiCoO<sub>2</sub>, positive electrode. The voltage range is 2.5–4.2 V, with a nominal voltage of 3.6 V. This paper gives a personal assessment of recent developments since the 1999 International Power Sources Symposium and of likely improvements to the lithium ion system. It does not attempt to give an exhaustive review of the subject, as that has been done recently [3], but rather gives the author's opinions of those developments which are significant and have the potential for industrial exploitation. It describes recent developments and new ideas for all aspects of lithium ion batteries: anode, electrolyte, cathode and construction and is not limited to purely chemical aspects.

### 2. Anode development

Existing lithium ion batteries use carbon in various forms, such as graphite, hard carbon and microspheres, as the negative electrode. The use of carbon as a negative defines the lithium ion system, with lithium intercalation into the carbon obviating the use of lithium metal as a negative electrode with the hazards resulting from possible uneven lithium plating and dendrite formation. However, a new electrolyte system has been developed in which, it is reported, lithium can be plated safely [4]. The use of a negative electrode has been avoided completely in the FORTU battery, which is a metal-free system, in which lithium is produced within the battery on charging from the cathode system that uses lithium cobalt oxide [5]. This system uses a sulfur dioxide electrolyte (see below). The advantages of this system arise from the electrolyte, as the cathode is the same as the standard SONY system. However, avoiding the use of an intercalating carbon negative electrode reduces the weight.

Research on tin compounds as negative electrodes to replace the carbon continues, following the announcement by FUJI [6] of lithium ion batteries using this system.

### 3. Electrolyte development

Electrolytes based on organic carbonate mixtures have become the standard for lithium ion batteries. The main

---

<sup>☆</sup>British Crown Copyright © 2001 DERA. Published with the permission of DERA on behalf of the Controller HMSO.

<sup>\*</sup>Tel.: +44-2392-3354-29; fax: +44-2392-3351-2.

E-mail address: agritchie@dera.gov.uk (A.G. Ritchie).



developments recently have been investigations of different mixtures of propylene, ethylene, diethyl, dimethyl and ethyl methyl carbonates to obtain the best low temperature performance. Performance down to about  $-20^{\circ}\text{C}$  is possible with various mixtures of the above compounds. This is adequate for domestic applications. To get lower temperature performance (which is needed for some military applications) with organic electrolyte systems, other organic compounds, such as acetates, need to be added to the carbonate mixtures [7].

An alternative approach to good low temperature performance is to use completely different electrolytes. This is achieved in the FORTU battery. This uses the standard lithium cobalt oxide cathode material, but the electrolyte is liquid sulfur dioxide with lithium tetrachloroaluminate ( $\text{LiAlCl}_4$ ) as the electrolyte salt. This solution has a freezing point below  $-80^{\circ}\text{C}$  and a conductivity at room temperature of about 10 times that of organic electrolytes. Hence, this system has high power capability. The good low temperature performance and high power capability are important for military applications.

Apart from liquid electrolytes, polymer electrolytes are now developing rapidly, particularly those of the gelled electrolyte type. As with the liquid electrolyte cells, production is concentrated in Japan [8]. Performance of liquid and gelled electrolyte cells can be compared for cells of the same construction (envelope or packet cells, see below) made by the same manufacturer (GS-MEL-COTECH) [9]. Performance was remarkably similar. Pure polymer electrolytes have been investigated extensively [10], but still suffer from the problems of low conductivity and poor low temperature performance. Hence, the only application has been for uses in above-ambient temperatures [11].

#### 4. Cathode materials

The standard cathode material remains lithium cobalt oxide,  $\text{LiCoO}_2$ , for the vast majority of lithium ion batteries. Its advantages of reliable performance and long cycle life outweigh its disadvantages of only moderate capacity ( $130\text{ mAh g}^{-1}$ ), high cost of cobalt metal and moderate toxicity. The lithium cobalt nickel oxide ( $\text{LiCo}_{0.2}\text{Ni}_{0.8}\text{O}_2$ ) cathode material was already known at the time of the last International Power Sources Symposium [12]. This material has potential advantages of significantly higher electrochemical capacity ( $180\text{ mAh g}^{-1}$ ) and also should have the advantage of lower cost as 80% of the cobalt in  $\text{LiCoO}_2$  has been replaced by nickel. However, metal prices are volatile and cost advantages cannot be estimated on a long-term basis. The technical problem which has limited its widespread use so far has been the poor capacity retention on cycling, as reported at the last Symposium. However, it has been discovered recently that addition of small amounts of aluminium significantly improves capacity retention

[13,14] so lithium cobalt nickel oxide is likely to replace lithium cobalt oxide.

Lithium manganese oxide spinel ( $\text{LiMn}_2\text{O}_4$ ) continues to attract attention because of the lower price and toxicity advantages of manganese over cobalt. However, notwithstanding large amounts of work, the fundamental problems with this material remain, which are low electrochemical capacity ( $110\text{ mAh g}^{-1}$ ), instability during storage in the charged state and limited cycle life. These may be related to the greater sensitivity of manganese compounds than cobalt ones to hydrolysis by acidic impurities in the electrolyte arising from the lithium hexafluorophosphate electrolyte salt. As major work has failed to eliminate these problems, it seems that they are insuperable, and widespread use of manganese oxide spinel seems unlikely. Another approach has been to try to develop a manganese analogue of the lithium cobalt oxide with the formula  $\text{LiMnO}_2$  [15]. This had been reported before the last Symposium but, although this material showed a high initial capacity, capacity was lost on cycling as the material reverted to the spinel. Another form of  $\text{LiMnO}_2$  has since been made [16]. Possibly this will find application as the lower cost and toxicity of manganese in comparison with cobalt would give it a significant advantage provided that a long cycle life could be obtained and that at least 50% of the manganese could be cycled, as this is roughly the proportion of the cobalt which can be reversibly cycled in lithium cobalt oxide.

Higher voltage cathodes have also been investigated such as  $\text{LiCoMnO}_4$  and related compounds [17]. Application of these is likely to have to await electrolytes which are stable at these high voltages.

An alternative and imaginative cathode system, which was reported at the Symposium back in 1997 [18], was the metal oxide/lithium sulfite system. Various transition metal oxides are being investigated under a European Union CRAFT programme 'LIBEVA'.

Rechargeable lithium/sulfur dioxide liquid cathode batteries have been investigated for many years but have never reached commercial production because of safety concerns. A new approach from Battery Engineering Inc. [19] has been to make a lithium ion/sulfur dioxide rechargeable cell but with a lithium foil negative to act as a source of lithium. On discharge, the lithium reacts to form the normal discharge product for a lithium/sulfur dioxide primary battery, namely lithium dithionite,  $\text{Li}_2\text{S}_2\text{O}_4$ , which can then be cycled as a source of lithium ions. A variant on the rechargeable lithium/sulfur dioxide battery uses a copper chloride cathode, rather than just using the electrolyte as a liquid cathode. This system has been known for many years but has suffered the same safety problems as the lithium/sulfur dioxide rechargeable cell. Recent advances are reported to have avoided these problems [20].

Apart from the major efforts on oxides as cathode materials, some work has been reported on sulfides. These have the advantages of much higher capacity, e.g.  $400\text{ mAh g}^{-1}$  for  $\text{Li}_2\text{FeS}_2$ , cf.  $130\text{ mAh g}^{-1}$  for  $\text{LiCoO}_2$ . However, the



voltages are much less (1.8 V for  $\text{Li}_2\text{FeS}_2$ , 3.6 V (nominal) for  $\text{LiCoO}_2$ ), though the higher electrochemical capacities should more than compensate for this. One factor limiting the use of lithiated transition metal sulfides has been the inconvenient, slow, high temperature solid state syntheses of these materials [21]. New syntheses have been developed which avoid this problem [22].

## 5. Battery construction

Batteries are now widely available in both cylindrical and prismatic formats. Cells are also available using a flat spiral wind construction [23]. To save weight, light-weight packaging can be used and some techniques were reported at the last Symposium [24]. Recently, lithium ion batteries containing either liquid or gelled electrolytes have been announced using light-weight packaging [9]. Energy densities using either electrolyte were similar at about 160–170  $\text{Wh kg}^{-1}$ .

## 6. Battery performance

Energy densities of about 140–150  $\text{Wh kg}^{-1}$  are now available in cells using metal cans, with higher values of 160–170  $\text{Wh kg}^{-1}$  in cells with light-weight packaging [9]. There are prospects for higher energy density batteries.

1. By the use of lithium cobalt nickel oxide cathode material instead of lithium cobalt oxide. This raises Coulombic capacity from around 130 to around 180  $\text{mAh g}^{-1}$ , an increase of nearly 40%.
2. Light weight packaging. This gives an increase of around 20%.
3. Lithium-free batteries (e.g.  $\text{SO}_2$  electrolyte/ $\text{LiCoO}_2$  cathode) for which around 200  $\text{Wh kg}^{-1}$  is claimed.
4. New cathodes, e.g. sulfur compounds.

These improvements, individually or collectively, suggest that further significant increases in energy density for lithium rechargeable batteries are possible, with perhaps 200–250  $\text{Wh kg}^{-1}$  being possible in the foreseeable future. This reflects roughly a doubling of the energy density that was available a few years ago when 100–110  $\text{Wh kg}^{-1}$  was the norm. These energy densities bring the energy density of lithium ion batteries up to seven or eight times that available from lead-acid, which is around 30  $\text{Wh kg}^{-1}$ .

The energy density available from a battery is not the only criterion to judge its performance. Power can be more important. As with any battery, the power available from lithium ion cells depends not only on the chemistry but also on the design. Some lithium ion batteries have been designed specifically for high power [25]. High power cells had power ratings of around 800  $\text{W kg}^{-1}$  (continuous) or 1400  $\text{W kg}^{-1}$  on 18 s pulses. These are high values and

indicate that lithium ion batteries can be high power devices. However, a high power design will affect the energy density, with high power batteries having energy densities of only around 80–100  $\text{Wh kg}^{-1}$ , in contrast to high energy batteries which achieve around 140  $\text{Wh kg}^{-1}$ .

Performance must be judged not only in relation to battery size or weight, but also in relation to cost. Partial replacement of the expensive cobalt in lithium cobalt oxide by nickel should reduce cathode material cost. Manganese compounds would be cheaper still. Sulfur compounds, for either cathode or electrolyte (sulfur dioxide) would further reduce cost.

## 7. New applications for lithium ion batteries

Existing applications for lithium ion batteries are for the premium applications for the consumer market, originally for camcorders, now more widely for portable telephones and computers. Lithium ion batteries for electric vehicles have been extensively investigated, but the cost needs to be reduced significantly. Lithium ion batteries are now being investigated for numerous military applications such as underwater applications [25], aircraft main batteries [26], space [27], and batteries for portable electronic equipment [28].

## 8. Conclusions

Since the introduction of lithium ion batteries nearly 10 years ago, their production has expanded enormously. The performance has improved significantly in the last couple of years, with prospect for further improvements due to different construction and new cathode materials (lithium nickel cobalt oxide). Gelled electrolyte batteries are now coming into production.

## References

- [1] T. Nagaura, K. Tozawa, Lithium ion rechargeable battery, *Progress in Batteries and Solar Cells* 209 (1990) 9.
- [2] C. Pillot, The World-Wide Battery Market and Its Main Applications (1998–2003), *Batteries 2000, Markets and Technologies for Portable Electronic Devices*, Paris, 2000.
- [3] M. Winter, J.O. Besenhard, M.E. Spahr, P. Novak, Insertion electrode materials for rechargeable lithium batteries, *Adv. Mater.* 725 (1998) 10.
- [4] E. Mengeritsky, P. Dan, I. Weissman, A. Zaban, D. Aurbach, *J. Electrochem. Soc.* 2110 (1996) 143.
- [5] G. Hambitzer, V. Döge, I. Stassen, K. Pinkwart, C. Ripp, Characteristics of a new inorganic lithium metal battery system for high energy and high power application, in: *Proceedings of the Conference on 39th Power Sources*, Cherry Hill, USA, 2000, p. 200.
- [6] Y. Idota, M. Nishima, Y. Miyaki, T. Kubota, T. Miyasaka, Nonaqueous secondary battery, *EP* 651,450 (1995).
- [7] S. Herreyre, O. Huchet, S. Barusseau, F. Pertion, J.M. Bodet, Ph. Biensan, New Li ion electrolytes for low temperature applications,

- in: Proceedings of the 10th International Meeting on Lithium Batteries, Lithium 2000, Como, May 2000, Abstract no. 282.
- [8] B.B. Owens, Solid state electrolytes: overview of materials and applications during the last third of the 20th century, *J. Power Sources* 2 (2000) 90.
- [9] T. Tanaka, New Development in Lithium ion Batteries, Batteries 2000, Markets and Technologies for Portable Electronic Devices, Paris, March 2000.
- [10] F.B. Dias, L. Plomp, J.B.J. Veldhuis, Trends in polymer electrolytes for secondary lithium batteries, *J. Power Sources* 169 (2000) 88.
- [11] C. Letourneau, M. Gauthier, A. Belanger, D. Kuller, J. Hoffman, Lithium polymer battery pack design, in: Proceedings of the 14th International Electric Vehicle Symposium and Exposition, EVS14, Orlando, FL, USA, December 1997.
- [12] A.G. Ritchie, C.O. Giwa, J.C. Lee, P. Bowles, A. Gilmour, J. Allan, D.A. Rice, F. Brady, S.C.E. Tsang, Future cathode materials for lithium rechargeable batteries, *J. Power Sources* 98 (1999) 80.
- [13] M. Martikainen, M. Payne, Chemistry of Advanced Rechargeable Batteries, Batteries 2000, Markets and Technologies for Portable Electronic Devices, Paris, March 2000.
- [14] C. Vogler, R. Hemmer, G. Arnold, A. Trepo, M. Wohlfahrt-Mehrens, Lithium nickel oxide  $\text{Li}(\text{Ni}_{0.75}\text{Al}_{0.17}\text{Co}_{0.08})\text{O}_2$  as cathode material for lithium ion batteries, *Ionics* 421 (1999) 5.
- [15] A.R. Armstrong, P. Bruce, *Nature* 381 (1996) 499.
- [16] J.M. Paulsen, C.L. Thomas, J.R. Dahn, Layered Li–Mn-oxide with the O2 structure: a cathode material for Li ion cells which does not convert to spinel, *J. Electrochem. Soc.* 3560 (1999) 146.
- [17] H. Kawai, M. Nagata, H. Tukamoto, A.R. West, High-voltage lithium cathode materials, *J. Power Sources* 67 (1999) 81–82.
- [18] A. Gilmour, A novel rechargeable lithium composite cathode system, *J. Power Sources* 241 (1997) 65.
- [19] A.P. Johnson, M.J. Traub, A rechargeable lithium ion battery with an inorganic electrolyte, in: Proceedings of the 38th Power Sources Conference, Cherry Hill, USA, June 1998, p. 489.
- [20] F.W. Dampier, J.R. Cormier, H.A. Hobbs, A. Srikumar, L.M. Toomey, Rechargeable lithium–copper chloride battery development, in: Proceedings of the Conference on 39th Power Sources, Cherry Hill, USA, June 2000.
- [21] R.A. Sharma, Equilibrium phases between lithium sulfide and iron sulfides, *J. Electrochem. Soc.* 448 (1976) 123.
- [22] A.G. Ritchie, P.G. Bowles, Process for Producing a Lithium Transition Metal Sulfide, International Patent Application PCT/GB00/02179, UK Patent Application 9914041.0.
- [23] R. Doisneau, A Different Type of Lithium ion Battery, Batteries 2000, Markets & Technologies for Portable Electronic Devices, Paris, March 2000.
- [24] A.G. Ritchie, C.O. Giwa, J.C. Lee, P. Bowles, A. Gilmour, J. Allan, Scale-up of lithium rechargeable batteries, *J. Power Sources* 128 (1999) 80.
- [25] G. Chagnon, R. Doisneau, J-P. Descroix, R. Goldsborough, Saft lithium ion technology for underwater applications, Proceedings of the 39th Power Sources Conference, Cherry Hill, USA, June 2000, p. 244.
- [26] J.D. Briscoe, Feasibility of Li ion batteries for the F-16 Aircraft, in: Proceedings of the Conference on 39th Power Sources, Cherry Hill, USA, June 2000, p. 211.
- [27] R. Gitzendammer, C. Marsh, G. Ehrlich, F. Puglia, R. March, S. Vukson, Advancement of lithium ion technology for aerospace applications, in: Proceedings of the Conference on 39th Power Sources, Cherry Hill, USA, June 2000.
- [28] D. Goodwin, D. Gale, R. Neat, W. Macklin, A. Jeffery, The design of smart Li ion batteries for military applications, in: Proceedings of the Conference on 39th Power Sources, Cherry Hill, USA, June 2000, p. 156.

# Carbon–carbon composite as anodes for lithium-ion battery systems

Sohrab Hossain\*, Yousry Saleh, Raouf Loutfy

*LiTech LLC, 7960 S. Kolb Road, Tucson, AZ 85706, USA*

---

## Abstract

Carbon–carbon (C–C) composite has been investigated as an anode for lithium-ion battery systems. The composite electrode delivers high reversible capacity and very low irreversible capacity loss. The test results of lithium-ion cells made with the C–C composite anode show many advantages, such as excellent performance and enhanced safety. The performance improvement is achieved because of strong mechanical integrity (cycle life) and absence of binder (shelf life) in C–C composite. The enhancement in safety comes from high thermal conductivity, fire retardant characteristics and an acceptable ability to overcharge and overdischarge. © 2001 Elsevier Science B.V. All rights reserved.

**Keywords:** Lithium-ion batteries; Carbon–carbon composites

---

## 1. Introduction

The lithium-ion battery is considered to be the rechargeable battery of the future — from portable electronics, to aerospace and to vehicular applications. It provides high specific energy and energy density, excellent cycle life, low self-discharge and does not have memory effects. Because of its advantageous characteristics, lithium-ion batteries are widely used in portable electronic devices and are taking larger market shares each year from its competing technologies of Ni/Cd and Ni/MH. It has been forecast [1] that by the year 2003 most of the mobile consumer electronics will use lithium-ion batteries as their power sources.

However, the state-of-the-art lithium-ion battery system operates within certain voltage limits, beyond which either performance deteriorates and/or safety incidents, such as explosion/fire occur (see Fig. 1). The present lithium-ion battery system is, therefore, an almost zero tolerance technology. As such, overcharge and overdischarge protection circuits and/or devices are used in commercial lithium-ion batteries. For small, relatively low capacity, low voltage batteries, the above measures to protect the battery and users are found to be acceptable. For high capacity, multi-cell high voltage batteries, such as are being considered for use in aerospace and/or vehicular applications, an inherently safe battery chemistry is essential so that, if the battery experiences overcharge and/or overdischarge, there should not be any safety concerns.

The manufacturing of the state-of-the-art lithium-ion batteries demands high cost, sophisticated equipment for the production of cathodes and anodes of uniform loading. The relatively high capital investment and the use of overcharge/overdischarge protection circuits and/or devices are the main contributing factors to the high cost of lithium-ion batteries.

To address the above shortfalls, we have developed an anode based on carbon–carbon (C–C) composite material for lithium-ion batteries. The C–C composite offers many advantages, such as high reversible capacity and low irreversible capacity loss, excellent mechanical strength, good electrical and thermal conductivity, fire retardant characteristics and is reusable. It also offers an overcharge and overdischarge acceptance ability. This paper describes the intercalation/de-intercalation behavior of lithium-ions into the composite material and performance characteristics of lithium-ion cells made with the composite anode.

## 2. Experimental

### 2.1. Preparation of electrodes

#### 2.1.1. The lithium electrode

The 3  $\mu\text{m}$  thick expanded nickel mesh (Delker Corporation) was cut to the size of lithium electrode (25 mm  $\times$  35 mm) with an attached tab (6.3 mm wide and 19 mm long). Both sides of the expanded mesh were cleaned with acetone. The substrates, thus prepared were transferred to a glove box ( $\text{H}_2\text{O} < 1 \text{ ppm}$ ) where 50  $\mu\text{m}$  thick metallic

---

\* Corresponding author. Tel.: +1-520-574-1980.  
E-mail address: shossain@mercorp.com (S. Hossain).

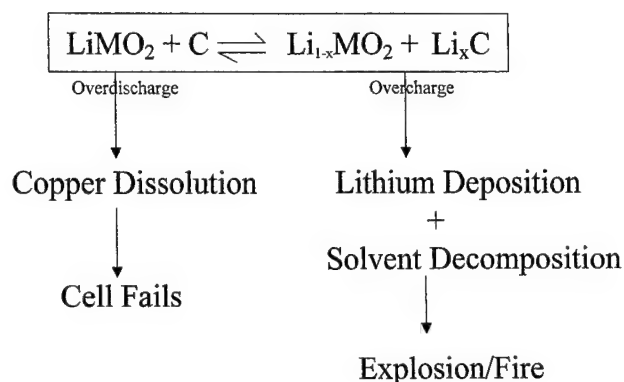


Fig. 1. Voltage limitation of present day lithium-ion battery technology.

lithium (Foote mineral) was press fitted to the substrates. These lithium electrodes were used as counter electrodes for half-cells measurements.

### 2.1.2. The C–C composite electrode

The C–C composite was obtained from MER Corporation. Some of the characteristics of C–C composite are shown in Table 1. The in-plane and cross-sectional views of the C–C composite are shown in Fig. 2(a) and (b), respectively. Fig. 3 shows a comparison of the X-ray diffraction patterns of the C–C composite with graphite. The C–C composite is composed of disordered carbon fiber. The composite plate was cut to the required dimensions (25 mm × 35 mm for half-cells and 50 mm × 62.5 mm to 130 mm × 190 mm for lithium-ion cells) and nickel foil was riveted to one edge of the plates. The resulting C–C electrodes with these nickel tabs were used as working electrodes for half-cells and anodes for lithium-ion cell studies.

Table 1

Characteristics of the C–C composite

Characteristics	Value
Surface area ( $\text{m}^2 \text{g}^{-1}$ )	0.19
Density ( $\text{g ml}^{-1}$ )	1.6
Flexural strength (MPa)	45–50
Tensile strength (MPa)	155–160
Compressive strength (MPa)	45–50
Thermal conductivity ( $\text{W mK}^{-1}$ )	550–650
Coefficient of thermal expansion ( $\text{ppm } ^\circ\text{C}^{-1}$ )	–1.7
Volume resistivity ( $\mu\Omega \text{cm}$ )	250

### 2.1.3. The $\text{LiCoO}_2$ electrode

A slurry of 85%  $\text{LiCoO}_2$  (FMC Corporation), 7% carbon black (Chevron Chemical Corporation), and 8% poly(vinylidene fluoride), PVDF (Aldrich) was prepared in 1-methyl 2-pyrrolidinone, NMP (Aldrich) and coated on a 40  $\mu\text{m}$  thick aluminum substrate. The coated substrate was dried over hot air. It was then cut to the size of the positive electrodes (50 mm × 62.5 mm to 130 mm × 190 mm) with attached tabs for lithium-ion cells. The resulting positive electrodes were pressed, vacuum dried and stored in a desiccator prior to use.

## 3. Development of cells

### 3.1. Half-cells

Half-cells were made according to the following configuration: lithium electrode (Li)/separator (S)/C–C composite electrode (C)/separator (S)/lithium electrode (Li).

The C–C composite electrode was bagged using Celgard 2400 separator. The bagged working electrode was then

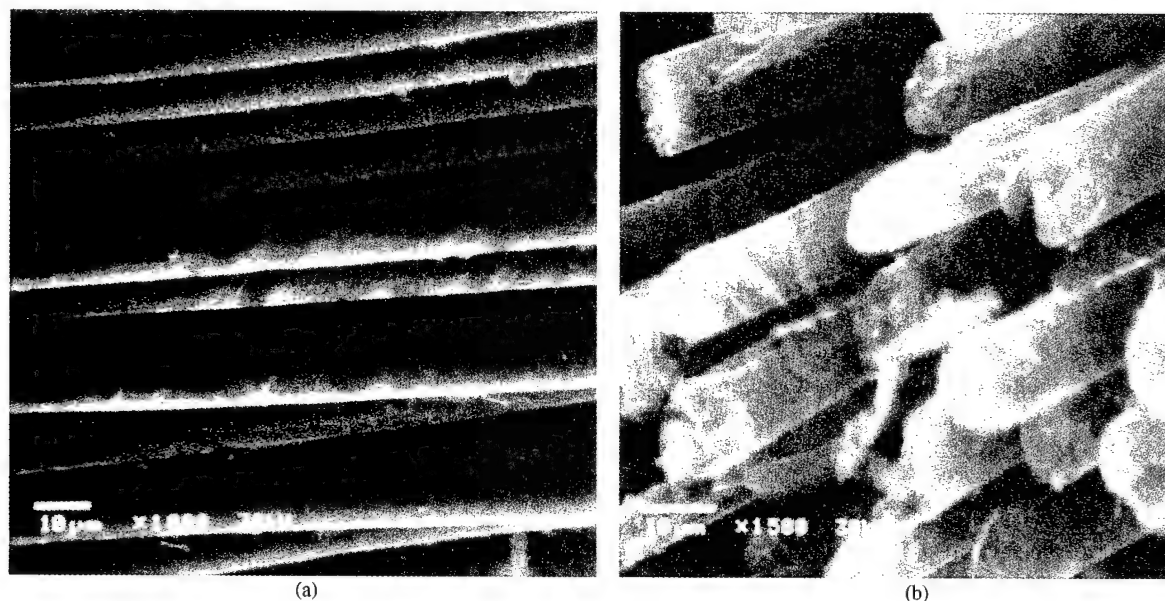


Fig. 2. SEM images of C–C composite (a) in-plane, (b) cross-section.

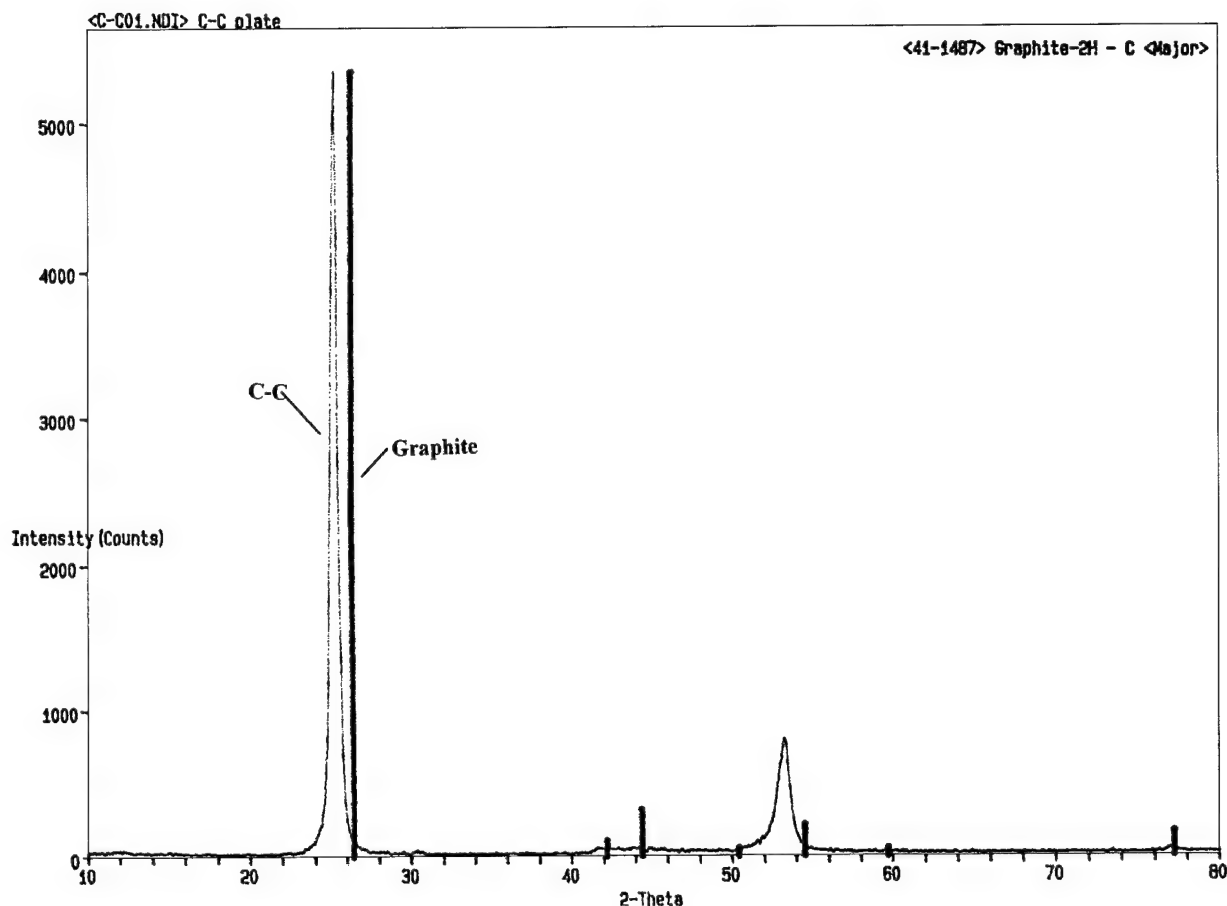


Fig. 3. X-ray diffraction patterns of C-C composite and of graphite.

sandwiched in between two metallic lithium counter electrodes. The electrode stack assembly then wrapped around with a solvent-resistant adhesive tape so that the position of the electrodes remained in place. The two counter electrode tabs were spot-welded together. The resistance between the counter electrodes and the working electrode was measured to insure that the stack was not electronically shorted.

The stack assembly was then placed in between a three-layer white plastic packaging material (Shield Pack Inc.) and sealed along three edges of the stack leaving open the end opposite to the electrode tabs. The sealed stack was then vacuumed and filled with a measured amount of 1 M  $\text{LiPF}_6$  electrolyte in a mixture of ethylene carbonate (EC) and dimethyl carbonate (DMC) (1:1 v/v) obtained from Grant Chemicals. The other end of the cell was then sealed. All these operations were carried out in a glove box ( $\text{H}_2\text{O} < 1 \text{ ppm}$ ). The seal of the plastic bag was checked several times prior to taken out from the glove box for electrochemical measurements.

### 3.2. Complete lithium-ion cells

Prismatic lithium-ion pouch cells were made with two  $\text{LiCoO}_2$  cathodes and a C-C composite anode in 1 M  $\text{LiPF}_6$

electrolyte in EC/DMC (1:1 v/v). Fig. 4 shows the pouch cell design. The cell configuration was as follows: one-sided cathode (C/2)/separator (S)/C-C composite anode (A)/separator (S)/one-sided cathode (C/2).

The fabrication procedure of the lithium-ion pouch cells was the same as that of the half-cells described in clause 3.1. A prototype lithium-ion pouch cell of 1 Ah capacity is shown in Fig. 5.

## 4. Electrochemical measurements

### 4.1. On half-cells

The electrochemical measurements of the half-cells were carried out using an Arbin 24-channel cycler. The half-cells were first discharged at a constant current of  $0.5 \text{ mA cm}^{-2}$  to 0.005 V and then at a constant voltage (0.005 V) until residual current dropped to  $0.05 \text{ mA cm}^{-2}$ . The cells were then charged at a constant current of  $0.5 \text{ mA cm}^{-2}$  to a cut-off voltage of 1.0 V. The half-cells were discharged and charged for several times until a fairly constant value of charge capacity was obtained. The difference between the first discharge capacity and charge capacity provides the

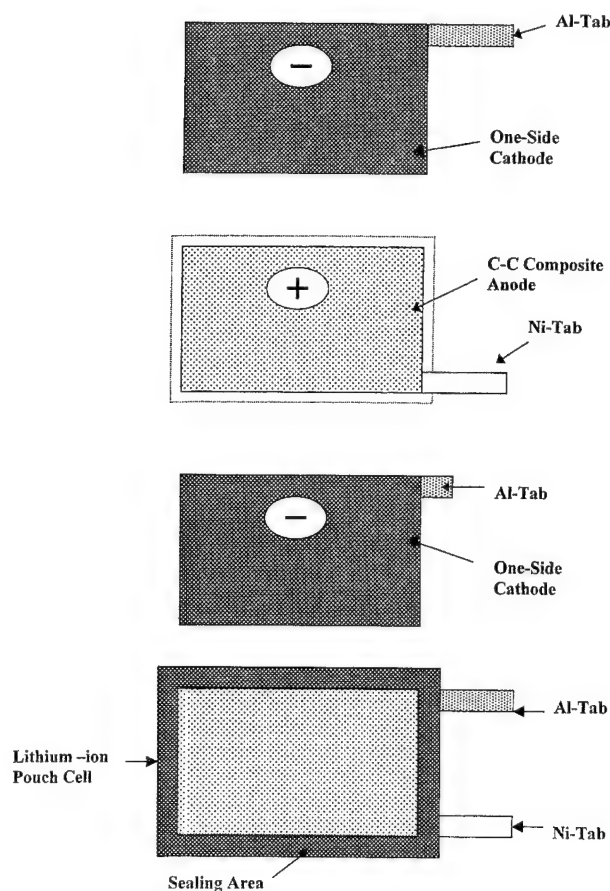


Fig. 4. Schematic diagram of a lithium-ion pouch cell based on C-C composite.

information on irreversible capacity loss of the C-C composite working electrode.

#### 4.2. On lithium-ion cells

The lithium-ion pouch cells were “formed” according to the following procedure: the cells were first charged at a constant current of  $0.5 \text{ mA cm}^{-2}$  to 4.2 V and then at a constant voltage (4.2 V) for a total period of 8 h or until the current dropped to a value of  $0.05 \text{ mA cm}^{-2}$ . The cells were then discharged at a constant current of  $0.5 \text{ mA cm}^{-2}$  to a cut-off voltage of 2.5 V. The charge–discharge process was continued for several (usually 2–5) times until fairly constant values of charge–discharge capacities were obtained. The “formed” cells were then used for performance evaluation. The difference between the first charge capacity and discharge capacity also provides the information on irreversible capacity loss of the lithium-ion cell.

### 5. Results and discussion

Several half-cells, made with C-C composite working electrode and lithium metal counter electrode, were used to investigate the intercalation and de-intercalation behavior of lithium-ions within the composite electrode. Based on the half-cell results, a number of lithium-ion pouch cells were built and their performance characteristics were evaluated. The results are discussed below.

#### 5.1. Intercalation/de-intercalation of lithium ions

Fig. 6 shows a representative plot for the first discharge (intercalation) charge (de-intercalation) characteristics of

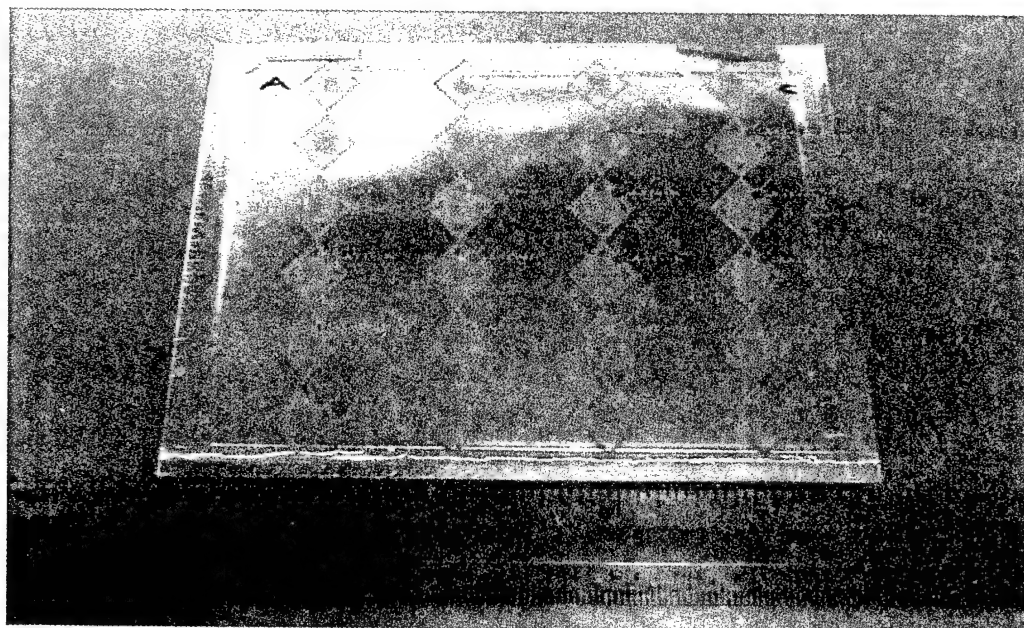


Fig. 5. Prototype 1 Ah lithium-ion pouch cell.



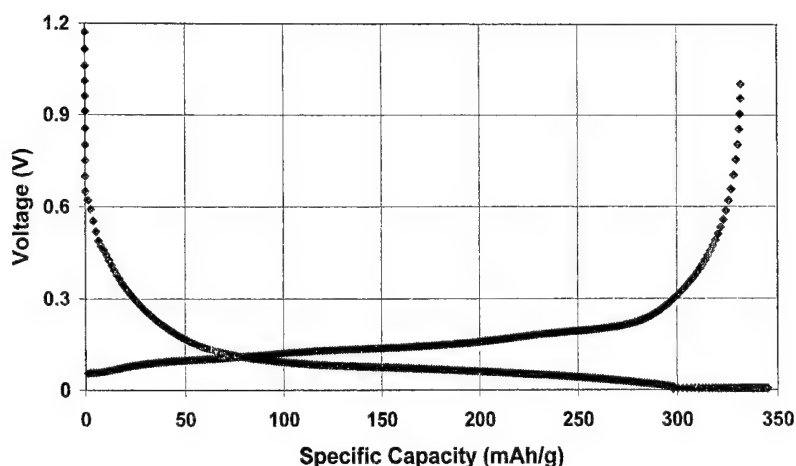


Fig. 6. Discharge-charge behavior of C-C composite at  $0.5 \text{ mA cm}^{-2}$  in  $1 \text{ M LiPF}_6$  electrolyte (EC:DMC 1:1 v/v). Counter electrode: Li.

the C-C composite electrode against the lithium counter electrode. The first discharge and charge capacities due to lithium ions intercalation and de-intercalation correspond to 342 and 332  $\text{mAh g}^{-1}$  of C-C composite, respectively. The irreversible capacity loss is, therefore,  $<3\%$ . This value of irreversible capacity loss is significantly lower than that obtained from the best commercial carbon (MCMB 2528) used by the lithium-ion battery industry. The low irreversible capacity loss is most probably related to the low surface area, absence of binder, carbon black and foreign materials, and little or no surface functional groups within the C-C composite.

The half-cell was cycled for four more times (see Fig. 7) to determine the specific reversible capacity and cycling efficiency of the C-C composite. An average reversible capacity of  $335 \text{ mAh g}^{-1}$  was obtained at  $0.5 \text{ mA cm}^{-2}$  with a Coulombic efficiency of 0.995 for the 2nd cycle, 0.994 for the 3rd cycle, 1.000 for the 4th cycle, and 0.998 for the 5th cycle, respectively. It is noteworthy to mention that the cell made with the C-C composite delivered a Coulom-

bic efficiency of more than 0.99 after completing only one discharge-charge cycle.

### 5.2. Overdischarge

Present state-of-the-art lithium-ion batteries need an over-discharge protection circuit. Overdischarge (discharge below 2.5 V) causes dissolution of the copper that is used as an anode substrate, and degrades cell performance.

One of the most important characteristics of C-C composite based lithium-ion cells is the ability to accept repeated overdischarge without performance deterioration. Fig. 8 represents a plot of repeated overdischarge. The cell was discharged at a constant current of 30 mA to  $-1.0 \text{ V}$ . For the first two cycles, the cell was charged to 4.1 V and for the last two cycles, the charge voltage was 4.2 V. The capacities delivered during overdischarge are 180, 179, 193, and 193 mAh for the cycles 1–4, respectively. In C-C composite based lithium-ion cell, C-C composite is the substrate and the active sites for electrochemical reaction.

### 5.3. Overcharge

Another important feature of C-C composite based lithium-ion battery technology is its tolerance of overcharge. Overcharge is one of the most important safety concerns of present state-of-the-art lithium-ion batteries. Overcharge causes metallic lithium to deposit on the anode, solvent decomposition, sharp rise in temperature, and ultimately thermal run away of the battery. To protect from overcharge, the lithium-ion battery industry uses a number of safety devices, such as overcharge protection circuits, positive temperature coefficient resistors, pressure sensitive rupture disks, temperature sensitive separators, etc.

Fig. 9 shows the voltage and temperature response of a fully charged cell (full capacity is 1 Ah) during overcharge at a constant current of 300 mA for 4 h followed by rest on open-circuit for 1 h. The temperature change recorded was

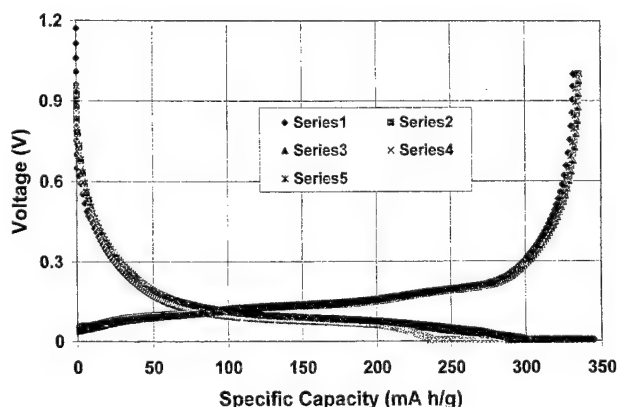


Fig. 7. First five discharge-charge curves of C-C composite at  $0.5 \text{ mA cm}^{-2}$  in  $1 \text{ M LiPF}_6$  electrolyte (EC:DMC 1:1 v/v). Counter electrode: Li.

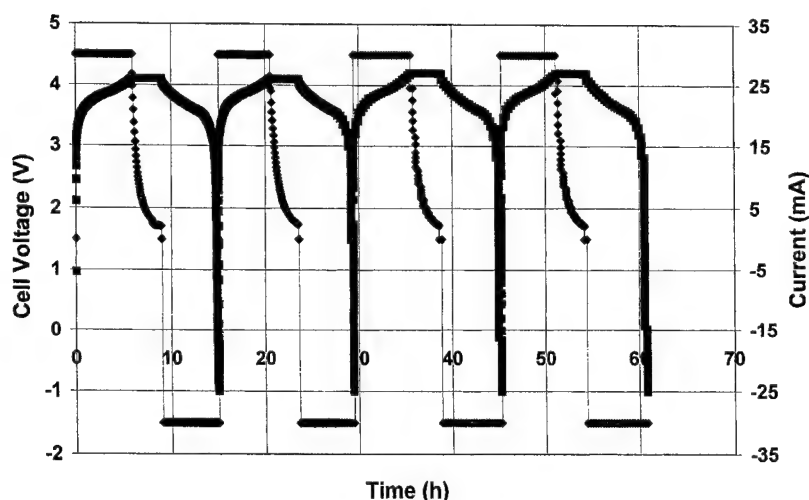


Fig. 8. Charge-overdischarge behavior of a lithium-ion cell based on C-C composite. Cathode:  $\text{LiCoO}_2$ ; electrolyte: 1 M  $\text{LiPF}_6$  in EC/DMC (1:1 v/v).

the outside body temperature of the cell. The voltage of the overcharged cell dropped sharply to about 4.7 V during rest period. During overcharge, the cell voltage went up monotonically to 4.8 V and then at a relatively higher rate to 5.7 V indicating that lithium-ion transfer was the dominant process initially, which was overtaken by the solvent decomposition after 4.8 V. There was an insignificant increase in cell temperature during overcharge.

#### 5.4. Overcharge/overdischarge

Several lithium-ion cells made with the C-C composite anode were repeatedly overcharged and overdischarged. A representative plot is shown in Fig. 10. The cell was overcharged to 4.5 V and overdischarged to  $-1.0$  V. The overcharged capacities were 240, 235, 235, and 235 mAh for

cycles 1–4, respectively. The corresponding overdischarge capacities were 230, 225, 225, and 225 mAh, respectively. The Coulombic efficiency under these overcharge/overdischarge conditions was 0.96.

#### 5.5. Cycle life

The capacity fade of lithium-ion cells on cycling is mostly associated with the increase in impedance of electrodes. During the charge-discharge processes, expansion and contraction of the electrodes occur. The mechanical integrity of the electrodes plays an important role in minimizing the capacity fade.

The cycling behavior of a C-C composite based lithium-ion cell at  $20^\circ\text{C}$  is shown in Fig. 11. The cell was discharged at a constant current of  $C/5$  and charged at the same constant

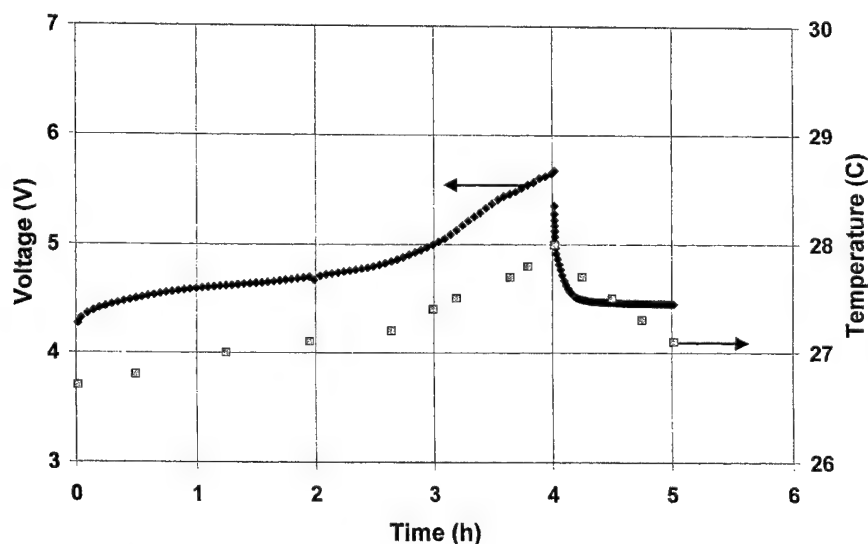


Fig. 9. Voltage and temperature responses during overcharge followed by open-circuit of an 1 Ah lithium-ion cell. Cathode:  $\text{LiCoO}_2$ ; electrolyte: 1 M  $\text{LiPF}_6$  in EC/DMC (1:1 v/v).



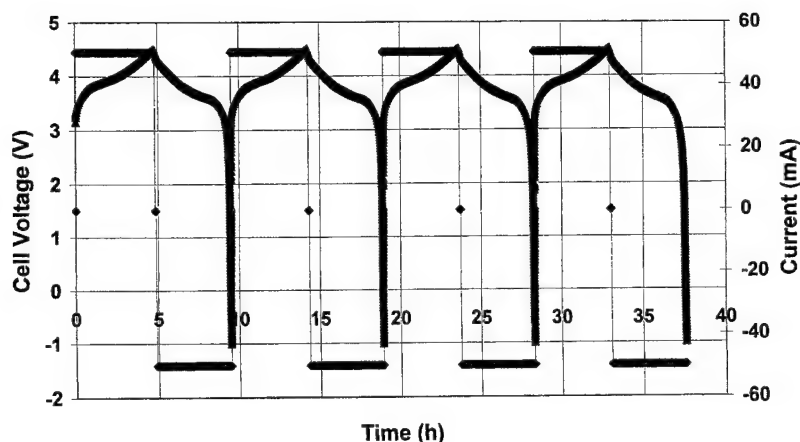


Fig. 10. Repeated overcharge–overdischarge behavior of a lithium-ion cell based on C–C composite. Cathode:  $\text{LiCoO}_2$ ; electrolyte: 1 M  $\text{LiPF}_6$  in EC/DMC (1:1 v/v).

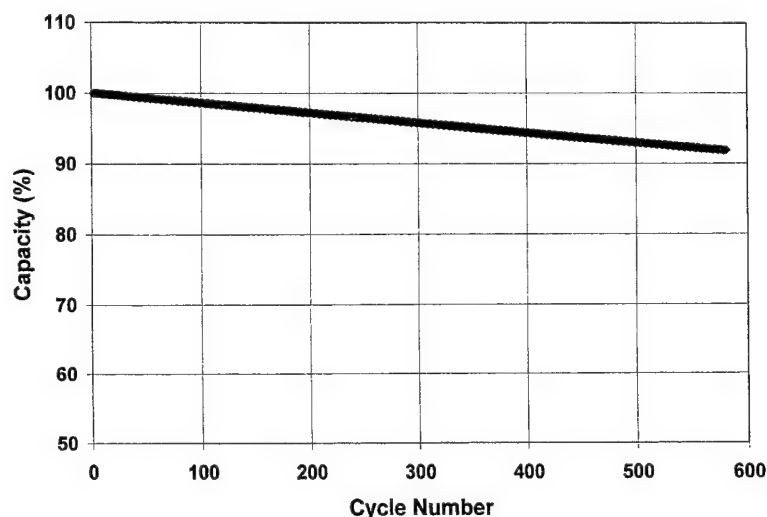


Fig. 11. Cycling behavior at C/5 rate of a lithium-ion cell based on C–C composite. Cathode:  $\text{LiCoO}_2$ ; electrolyte: 1 M  $\text{LiPF}_6$  in EC/DMC (1:1 v/v).

current rate to 4.2 V and then at constant voltage (4.2 V) for 3 h or until the residual current dropped to C/50. The cell delivered over 550 cycles with <10% capacity loss. The high cycle life is associated with the strong mechanical integrity of C–C composite electrode.

#### 5.6. Self-discharge

The self-discharge characteristics of lithium-ion cells, made with C–C composite and also with commercially available MCMB 2528 graphite, were investigated at ambient temperature. After being fully charged, the cells were stored on open-circuit for 1 month (720 h), and the decay of voltage recorded. Fig. 12 compares the voltage decay of two representative cells. A voltage drop of only 10 mV was observed for C–C composite based cell whereas for MCMB 2528 based lithium-ion cell a voltage drop of 60 mV was observed after this 1 month of storage.

The stored cells were then discharged to compare the delivered capacity before and after storage. Fig. 13 shows the discharge characteristics and compares the self-discharge behavior of the cell made with C–C composite. The cell lost about 2% capacity after storage for 1 month. The cell with MCMB 2528 carbon shows about 8% capacity loss after storage for 1 month. The low self-discharge behavior of C–C composite based lithium-ion cell is probably related to the low surface area of C–C composite, absence of binder, carbon black and foreign materials, and relatively little or no surface functional groups.

#### 5.7. Safety and abuse tests

A number of safety and abuse tests have been carried out on fully charged C–C composite based 1 Ah lithium-ion cells. The cells were cycled at least 50 times prior to the safety tests. The test results summarized in Table 2.

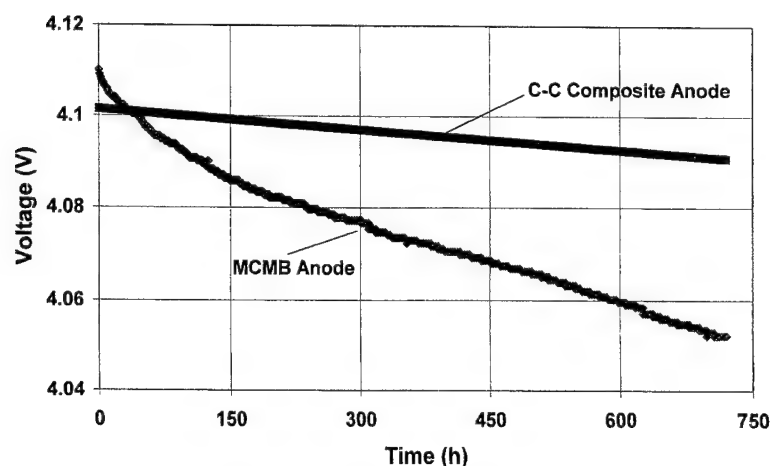


Fig. 12. Voltage decay of lithium-ion cells made with C–C composite and MCMB 2528 graphite stored on open-circuit at ambient temperatures. Cathode:  $\text{LiCoO}_2$ ; electrolyte: 1 M  $\text{LiPF}_6$  in EC/DMC (1:1 v/v).

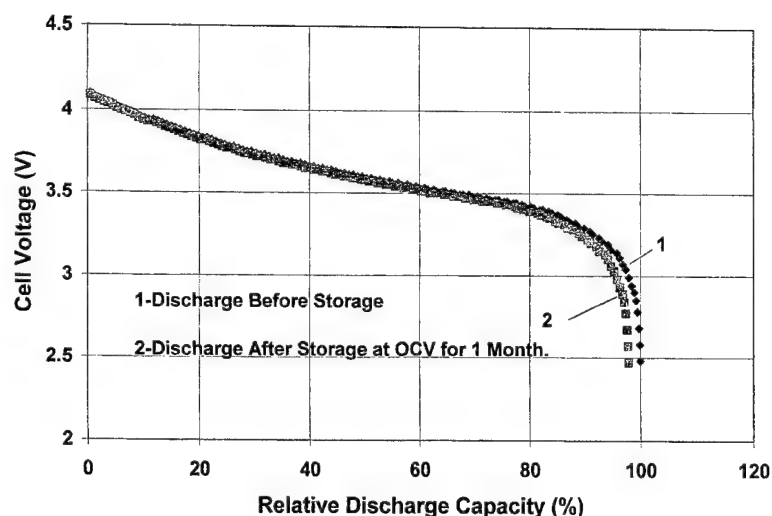


Fig. 13. Discharge behavior at C/4 rate of a lithium-ion cell based on C–C composite before and after storage for 1 month under ambient temperature. Cathode:  $\text{LiCoO}_2$ ; electrolyte: 1 M  $\text{LiPF}_6$  in EC/DMC (1:1 v/v).

The enhanced safety of C–C composite based lithium-ion cells is related to the fact that the composition of anode in a fully charged cell is  $\text{LiC}_{12}$  (substrate is C–C composite which is also available for lithium-ion intercalation). This compound is much less reactive than  $\text{LiC}_6$  that is formed in the conventional graphite based lithium-ion cells. During overcharge, the anode composition of C–C composite based

cell becomes  $\text{LiC}_x$ , where  $x$  is  $<12$ , but  $\geq 6$ . Also, there is no deposition of metallic lithium.

On the other hand, metallic lithium deposits on the graphite or carbon based anode of commercial lithium-ion cells if they are overcharged. So, the use of C–C composite as anodes for lithium-ion batteries allows extension both of performance and safety limit boundaries.

Table 2  
Safety and abuse test results

Test	Results
Overdischarge	No performance degradation
Overcharge	No fumes, fire, or explosion
External short-circuit	No fumes, fire, or explosion
Internal short-circuit (nail penetration)	No fumes, fire, or explosion

## 6. Conclusion

Carbon–carbon (C–C) composite has been investigated as an anode for lithium-ion batteries. The C–C composite offers many advantages, such as:

- High reversible capacity and very low irreversible capacity loss.

- Anode substrate is carbon — no dissolution of substrate during overcharge.
- Substrate and lithium intercalation sites are indistinguishable — can act as lithium-ion sink during overcharge.
- In the charged state, lithium-ions are present as less reactive  $\text{LiC}_{12}$  rather than highly reactive  $\text{LiC}_6$ .
- Strong mechanical integrity provides high cycle life.
- Low self-discharge associated with high compression, low surface area, and absence of binder, carbon black, and foreign materials.

- High thermal conductivity can provide ease of thermal management for high capacity, high voltage batteries.

The C–C composite can, therefore, be considered as a strong candidate for the anodes of lithium-ion batteries.

#### Reference

- [1] Power 2000, San Diego, CA, USA, 24–27 September 2000.

## Optimisation of PVdF-based polymer electrolytes

N. Muniyandi, N. Kalaiselvi, P. Periyasamy, R. Thirunakaran\*, B. Ramesh babu,  
S. Gopukumar, T. Premkumar, N.G. Renganathan, M. Raghavan

*Central Electrochemical Research Institute, Karaikudi 630 006, Tamilnadu, India*

Received 9 January 2001; accepted 12 January 2001

### Abstract

An attempt was made to synthesise PVdF-based polymer electrolytes containing 1:1 EC:PC plasticiser in various salts such as  $\text{LiAsF}_6$ ,  $\text{LiPF}_6$  and  $\text{LiBF}_4$  at different ratios using PVdF as homopolymer. Though, having a high ionic conductivity, certain films were found to be fragile, an indication of poor mechanical strength. Therefore, PVdF-PVC blend polymers were prepared using different ratios of PVdF-PVC as well as with different amounts of plasticiser mixture. Film characterisation was attempted using XRD, DSC, impedance and conductivity measurements. A particular combination of PVdF-PVC in the ratio 25:5 was observed to have high ionic conductivity and good mechanical strength. The electrochemical stability and the stability of lithium-polymer interface of the prepared polymer electrolytes were checked in terms of charge-discharge and impedance studies. Effect of storage time and cyclability are discussed. © 2001 Elsevier Science B.V. All rights reserved.

**Keywords:** Electrolytes/PVdF-PVC polymer; PVdF polymer; Ionic conductivity

### 1. Introduction

With the advent of lithium-ion battery technology [1], aiming for higher output voltages became the next target to be hit in the field of rechargeable lithium batteries.

However, further development of lithium-ion batteries paved the way for the entry of lithium-ion conducting polymer electrolytes in which the conventional non-aqueous electrolyte is immobilised by a polymer matrix [2]. Different polymer matrices and processes are proposed in the literature [3–6]. The concept of gel electrolytes with a high ionic conductivity and mechanical strength came in to existence as early as 1975s [7–9]. In this regard, host polymers for the gel electrolytes, such as poly acrylonitrile [10,11], poly methylmethacrylate [9,10], poly ethylene oxide [12], poly vinylidene fluoride [13] and a co-polymer of vinylidene fluoride with hexa fluoro propylene (PVdF-HFP) [14–17] have been identified as promising cathodes, because they possess high ionic conductivity and good stability.

Of late, PVdF as homopolymer and related co-polymers or blends of PVdF-based polymer electrolytes are gaining popularity, because of their high degree of flexibility, added to other meritorious properties viz. high room temperature conductivity, dimensional stability etc.

In this paper, polymer film electrolytes were made up of PVdF homopolymer and a blend of PVdF-PVC with a range of lithium salts viz.  $\text{LiAsF}_6$ ,  $\text{LiPF}_6$  or  $\text{LiBF}_4$  and using EC + PC as a common plasticiser. Optimisation of these polymer electrolytes were carried out in terms of the amount of polymer, plasticiser and the quantity of lithium salt required to prepare polymer films of sufficient mechanical strength and conductivity.

### 2. Experimental

#### 2.1. Preparation of PVdF gel electrolyte films

A mixture of PVdF (Aldrich, average molecular weight ca. 5,340,000), high purity EC + PC (1:1) and the lithium salt ( $\text{LiBF}_4$  or  $\text{LiPF}_6$  or  $\text{LiAsF}_6$ ) was heated in order to cast the film with the required properties. EC (Merck-Schuchardt) and PC (Fluka AG) were distilled using the usual procedures and kept under an argon atmosphere.

In detail, the calculated amount of a 1:1 mixture of EC + PC and the respective lithium salt such as  $\text{LiBF}_4$  (Merck-Schuchardt),  $\text{LiPF}_6$  (Across Organics) or  $\text{LiAsF}_6$  (Merck-Schuchardt) were weighed individually into a Pyrex bottles. An appropriate amount of PVdF in tetrahydrofuran (THF) was heated to 160–175°C with stirring for 1 h to ensure complete dissolution. To the hot solution, was added

\* Corresponding author.

E-mail address: rthirunakaran@usda.net (R. Thirunakaran).

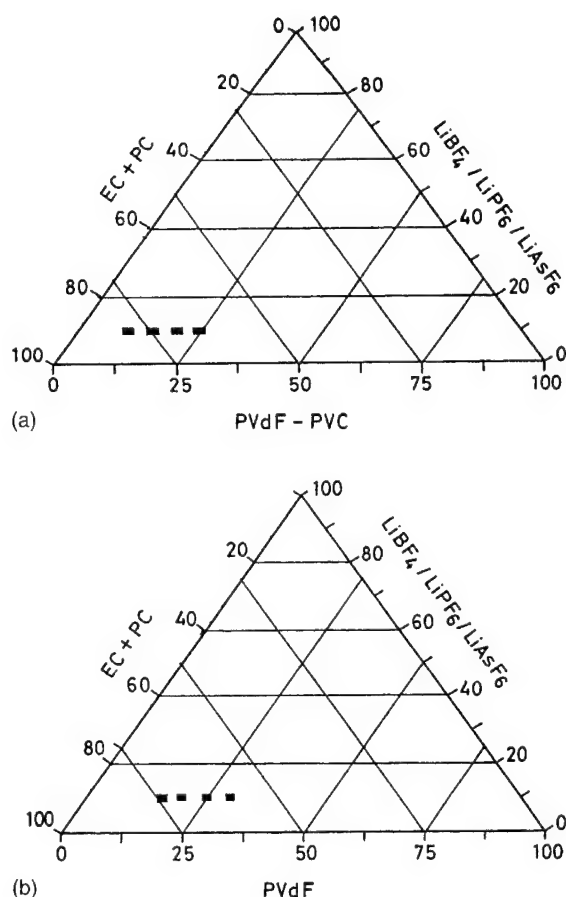


Fig. 1. Composition diagrams of: (a) PVdF-EC + PC-Li salts (lower); (b) PVdF:PVC-EC + PC-Li salts (upper).

the mixture of plasticiser (EC + PC) and the corresponding lithium salt. The solution was further heated with continued stirring to get an homogenous and viscous solution. The resultant viscous solution was poured over glass plates and adjusted for uniform thickness using doctor blades. The cast film was dried in a vacuum oven at 50°C for about 24 h. Solvent free stable films of uniform thickness (100  $\mu\text{m}$ ) were obtained, which were characterised later.

Fig. 1a shows the range of compositions that were prepared.

## 2.2. Preparation of PVdF-PVC blend electrolyte films

A similar procedure was adopted. To the polymer mix of selected ratios of PVdF-PVC, individual lithium salts ( $\text{LiAsF}_6$ ,  $\text{LiPF}_6$  or  $\text{LiBF}_4$ ) were added with 1:1 EC + PC as a common plasticiser. The films were dried in a vacuum oven at 50°C for 24 h and all the films were then found to be stable and solvent free.

Fig. 1b shows the range of compositions that were prepared.

## 2.3. Preparation of composite cathode

High purity  $\text{LiCoO}_2$ , graphite and the gel polymer electrolyte, containing plasticiser and lithium salt, were mixed in

65:10:25 ratio under hot conditions and blended thoroughly. The paste was coated over aluminium foil, the thickness adjusted to 75  $\mu\text{m}$  and dried in a vacuum oven at 110°C for 24 h.

## 2.4. Characterisation studies

The free-standing films were subjected to X-ray diffraction analysis using a Jeol 8030 X-ray diffractometer with a nickel filtered  $\text{Cu K}\alpha$  radiation.

Thermal stabilities of PVdF powder and the resultant PVdF-based polymer electrolytes were studied using differential scanning calorimetry (DSC-SEIKO, TA Station SSC-5000 series). The samples were heated at 300°C from room temperature at a rate of 10°C  $\text{min}^{-1}$ .

Conductivity measurements were made on an electrochemical impedance analyser (EG&G PAAR, model no. 263 A, lock in amplifier, model no. 5210). The conductivity of the polymer films was measured using a two-electrode cell configuration, constructed from a brass body housing, 20 mm in diameter stainless steel electrodes. The electrodes were screwed into the cell, sandwiching the polymer film between them. The fully assembled cell was connected for room temperature conductivity measurements. The impedance spectrum was obtained using test cells fabricated with the polymer films against lithium metal on both the sides. The impedance spectrum was run between the frequency range of 1 Hz–100 kHz at room temperature and the corresponding Nyquist plots were recorded.

Charge-discharge studies were carried out with a test cell containing a Li/polymer electrolyte/composite  $\text{LiCoO}_2$  cathode assembly at room temperature using a constant current of 0.1 mA. The electrochemical interface stability of the polymer electrolytes were measured as a function of impedance over a range of storage periods.

## 3. Results and discussion

The polymer electrolyte films which had been prepared were examined for homogeneity, stability and ease of preparation.

### 3.1. Dimensional stability

The dimensional stabilities observed from the PVdF films are given in Table 1. From the table, it is evident that the higher polymer content is required to get dimensionally stable PVdF films. Though homogeneity was observed invariably for all the ratios, the films with >25% of PVdF were found to be better, based on the stability point of view. Generally, viscosity of the electrolyte depends upon the weight ratio of polymer, plasticiser and the lithium salt [14]. Evidently, the viscosity of the polymer electrolytes involved in the present investigation favours the addition of the lowest possible amount of lithium salt to have the

Table 1  
Dimensional stability of PVdF polymer electrolyte films

Name	PVdF:EC + PC:Li salt	Condition
PVdF (BF <sub>4</sub> )	20:70:10	Fragile
	25:65:10	Fragile
	30:60:10	Stable
	35:55:10	Stable
PVdF (PF <sub>6</sub> )	20:70:10	Fragile
	25:65:10	Fragile
	30:60:10	Stable
	35:55:10	Stable
PVdF (AsF <sub>6</sub> )	20:70:10	Fragile
	25:65:10	Fragile
	30:60:10	Stable
	35:55:10	Stable

optimum viscosity for the formation as well as the free-standing nature of the polymer film.

The amount of lithium salt to be added has been carried out as a separate study and the results will be published elsewhere [18]. Based upon the results of the study, the concentration of lithium salts was fixed as 10% throughout, irrespective of the nature of the salt added and the type of polymer material employed. Subsequently, gel polymer electrolytes containing 30 and 35% polymer along with 10% LiBF<sub>4</sub> or LiPF<sub>6</sub> or LiAsF<sub>6</sub> were identified for good dimensional stability, homogeneity and free standing nature of the film.

A similar analysis was carried out on PVdF–PVC electrolytes, see Table 2. These were also found to be interesting, as all the films cast with 2.5–10% PVC in the blend along with 20–27.5% PVdF were found to be dimensionally stable but the ratio 15:15 (PVdF:PVC) was found to be brittle (Table 2). Thus, the optimisation of polymer electrolytes can be summarised as: an addition of 30–35% PVdF for a homopolymer and an addition of 20–27.5% PVdF with 2.5–10% PVC for PVdF–PVC blend polymer electrolyte is recommended from the dimensional stability standpoint.

Table 2  
Dimensional stability of PVdF–PVC polymer electrolyte films

File name	PVdF	PVC	EC + PC	Li salt	Condition
PVdF–PVC (BF <sub>4</sub> )	15	15	60	10	Brittle
	20	10	60	10	Free-standing
	25	5	60	10	Free-standing
	27.5	2.5	60	10	Free-standing
PVdF–PVC (PF <sub>6</sub> )	15	15	60	10	Brittle
	20	10	60	10	Free-standing
	25	5	60	10	Free-standing
	27.5	2.5	60	10	Free-standing
PVdF–PVC (AsF <sub>6</sub> )	15	15	60	10	Brittle
	20	10	60	10	Free-standing
	25	5	60	10	Free-standing
	27.5	2.5	60	10	Free-standing

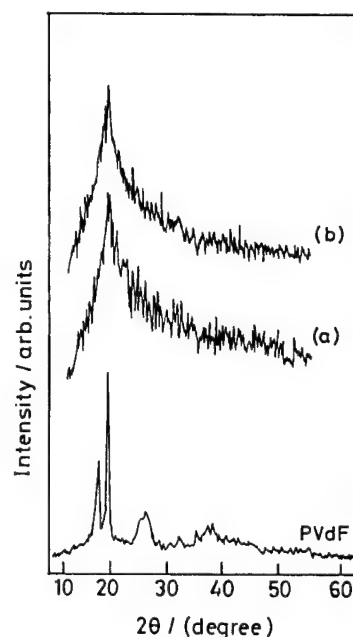


Fig. 2. X-ray diffraction patterns for: (a) 30% PVdF–60% EC + PC–10% LiAsF<sub>6</sub> film; (b) 35% PVdF–55% EC + PC–10% LiAsF<sub>6</sub> film.

### 3.2. X-ray diffraction

X-ray diffraction studies were carried out on the stable films and the results observed are shown in Fig. 2.

XRD patterns of the composition, 30% PVdF, 60% EC + PC, 10% lithium salt and that of 35% PVdF, 55% EC + PC, 10% lithium salt are shown in Fig. 2a and b, respectively.

PVdF, which is highly crystalline by nature, has been modified into the amorphous form in the gel electrolyte, due to the addition of EC + PC and lithium salts. The addition of plasticiser and lithium salt has definitely induced significant disorder into the polymer structure giving a polymer electrolyte of much lower crystallinity [19], which is quite obvious from the broad diffraction peak centred at  $2\theta = 19.8^\circ$ . This is evidence that the polymers apparently undergo structural reorganisation, caused by the swelling process due to the addition of plasticiser and lithium salt.

Similarly, the broad peak centred at  $2\theta = 20.2^\circ$  for PVdF–PVC blend electrolytes (Fig. 3) also confirmed the intimately bound polymer matrix, which has homogeneity and amorphicity, caused mainly by the plasticiser addition. Among the three blended electrolytes, the degree of amorphicity was found to be better for 25:5 and 20:10 ratio of PVdF–PVC than for the 27.5:2.5 ratio.

### 3.3. Differential scanning calorimetry

The DSC data of PVdF and PVdF–PVC blend polymer electrolytes are reproduced in Figs. 4 and 5. An exothermic peak observed between 150–175°C corresponds to the melting point of PVdF. However, the broad exothermic peaks

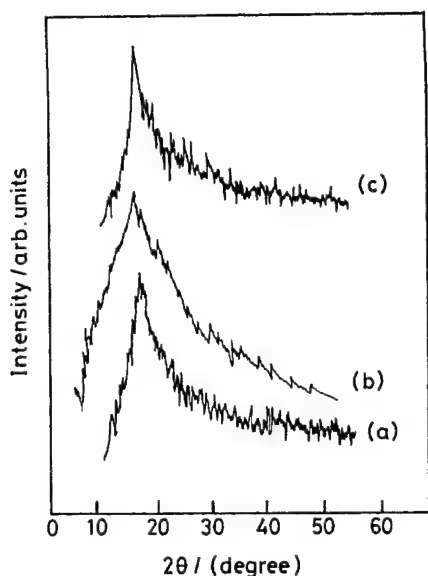


Fig. 3. X-ray diffraction patterns for: (a) 20:10% PVdF:PVC–60% EC + PC–10% LiAsF<sub>6</sub> film; (b) 25:5% PVdF:PVC–60% EC + PC–10% LiAsF<sub>6</sub> film; (c) 27.5:2.5% PVdF:PVC–60% EC + PC–10% LiAsF<sub>6</sub> film.

corresponding to the boiling points of EC and PC are not found in either of the types of polymer electrolytes, an indication that the disappearance of the phase transition of EC + PC is due to the formation of segments of polymer chain (14). Also, the polymer electrolytes exhibited a broad peak at a slightly elevated temperature, which is in favour of the formation of segments of polymer chain with lithium salts resulted from the swelling induced by the addition of

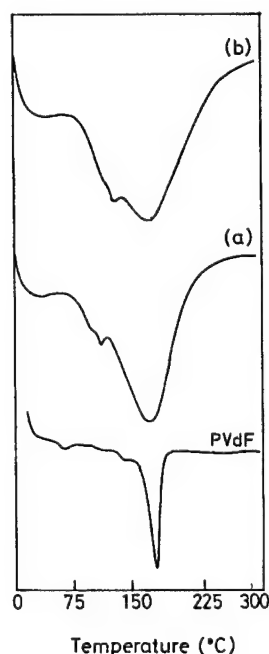


Fig. 4. Differential scanning calorimetry curves of: (a) 30% PVdF–60% EC + PC–10% LiAsF<sub>6</sub> film; (b) 35% PVdF–55% EC + PC–10% LiAsF<sub>6</sub> film.

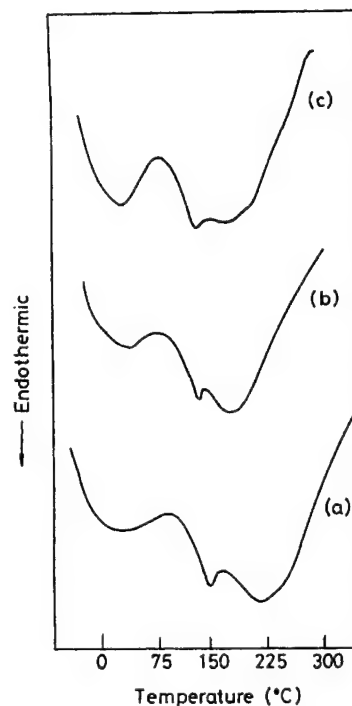


Fig. 5. Differential scanning calorimetry curves of: (a) 20:10% PVdF:PVC–60% EC + PC–10% LiAsF<sub>6</sub> film; (b) 25:5% PVdF:PVC–60% EC + PC–10% LiAsF<sub>6</sub> film; (c) 27.5:2.5% PVdF:PVC–60% EC + PC–10% LiAsF<sub>6</sub> film.

60% EC + PC. Thus, the crystallinity of PVdF has been reduced very much by an optimal addition of 60% EC + PC in both the PVdF and PVdF–PVC blend type of polymer electrolytes.

### 3.4. Electrical conductivity

The conductivity data for the PVdF and the PVdF–PVC electrolytes are summarised in Table 3. Conductivity of the polymer electrolytes, which is determined as a function of weight ratio of polymer to plasticiser, favours the addition of a lesser amount of polymer material. On the other hand, a higher value of the weight ratio increases the mechanical strength, lowers the mobility of charge carriers and results in the reduced conductivity of the polymer electrolytes. Therefore, a combination of a slightly lower amount of polymer and a slightly higher amount of plasticiser are expected to give better results as far as conductivity measurements are concerned. Interestingly, the observed values of conductivity of both PVdF and the blend type PVdF–PVC polymer electrolytes are in good agreement with the expected trend, i.e. among the two stable PVdF polymer electrolyte films, the one due to 30% PVdF with 60% EC + PC showed better conductivity than the film made up of 35% PVdF with 55% EC + PC. However, the other two films viz. 20 and 25% PVdF were not taken in to consideration for conductivity measurements, as they were found to be fragile in nature.

Similarly, among the dimensionally stable PVdF–PVC polymer films, the one with 25:5 ratio of PVdF–PVC with

Table 3

Room temperature conductivity of some PVdF and PVdF-PVC polymer electrolytes<sup>a</sup>

Sample	PVdF	PVC	EC + PC	Li salt	Conductivity (S cm <sup>-1</sup> )
1	30	—	60	10 (LiBF <sub>4</sub> )	0.00034
2	35	—	55	10 (LiBF <sub>4</sub> )	0.00029
3	30	—	60	10 (LiPF <sub>6</sub> )	0.00047
4	35	—	55	10 (LiPF <sub>6</sub> )	0.00040
5	30	—	60	10 (LiAsF <sub>6</sub> )	0.00066
6	35	—	55	10 (LiAsF <sub>6</sub> )	0.00059
1'	20	10	60	10 (LiBF <sub>4</sub> )	0.00028
2'	25	5	60	10 (LiBF <sub>4</sub> )	0.00040
3'	27.5	2.5	60	10 (LiBF <sub>4</sub> )	0.00034
4'	20	10	60	10 (LiPF <sub>6</sub> )	0.00048
5'	25	5	60	10 (LiPF <sub>6</sub> )	0.00060
6'	27.5	2.5	60	10 (LiPF <sub>6</sub> )	0.00056
7'	20	10	60	10 (LiAsF <sub>6</sub> )	0.00062
8'	25	5	60	10 (LiAsF <sub>6</sub> )	0.00086
9'	27.5	2.5	60	10 (LiAsF <sub>6</sub> )	0.00080

<sup>a</sup> Compositions expressed as weight percents.

60% EC + PC was found to exhibit higher conductivity, irrespective of the type of the lithium salt used. Although, addition of increasing amounts of PVC increases the mechanical stability, it reduces the conductivity values. This is quite obvious from the brittle nature of the 15:15 PVdF-PVC film and the lower conductivity values of 20:10 PVdF-PVC with respect to the 27.5:2.5 and 25:5% PVdF-PVC films. However, the conductivity of the polymer electrolyte with 27.5:2.5 PVdF-PVC is slightly less than the conductivity of 25:5 PVdF-PVC electrolyte, which may be correlated to the less amorphicity of the former with respect to the latter. Also, LiAsF<sub>6</sub> was found to exhibit the maximum conductivity rather than LiBF<sub>4</sub> or LiPF<sub>6</sub>, irrespective of the nature of the polymer and the amount of plasticiser used.

### 3.5. Impedance studies

The passivation that occurs at the lithium interface in the gel polymer electrolytes has been studied by monitoring the impedance behaviour of a symmetrical cell that was kept on open circuit for various periods i.e. 24, 72 h and 1 week. A gradual increase in the impedance values was noted (Fig. 6a and b) which is in accordance with the model proposed by Alamgir and Abraham [5]. It is seen from the figures that the  $R_b$  value remains below 5 k $\Omega$ , during the entire period of storage, thus accounts for the prolonged stability of the polymer. However, the increase in  $R_f$  value noted for both the PVdF and PVdF-PVC polymer electrolytes can be correlated to the growth of passivation film formed due to the reaction of lithium with the polymer electrolyte.

### 3.6. Charge-discharge studies

Electrochemical characterisation with charge-discharge studies were performed using a test cell containing lithium

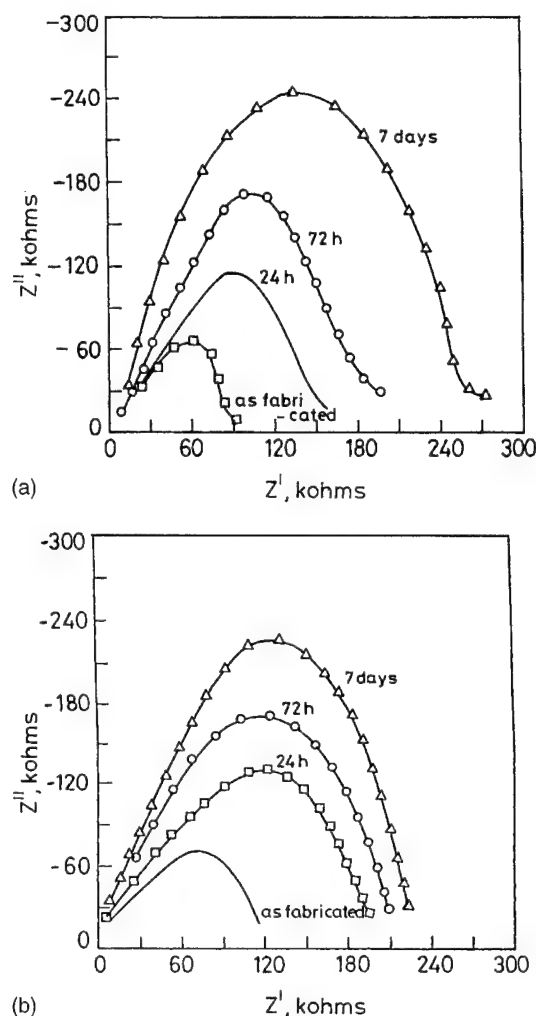


Fig. 6. (a) Impedance changes after storage of Li/PVdF/Li cells; (b) impedance changes after storage of Li/PVdF-PVC/Li cells.

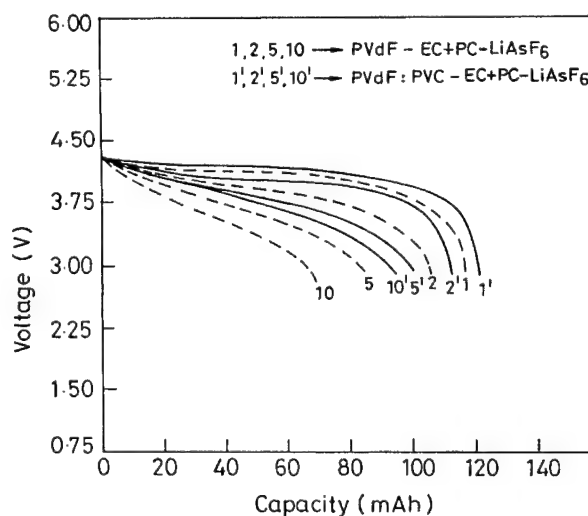


Fig. 7. Discharges from 1st, 2nd, 5th and 10th cycle of a Li/polymer electrolyte/LiCoO<sub>2</sub> cell.



as anode, a composite  $\text{LiCoO}_2$  as cathode and the prepared polymer electrolytes of both types. The charge–discharge efficiency agrees with the better retention of capacity of both PVdF and PVdF–PVC types of polymer electrolytes found during cycling. An efficiency of not less than 60% was observed for PVdF electrolytes and an efficiency of around 70% was maintained by the PVdF–PVC blend type of electrolytes (Fig. 7) after 10 cycles. Similarly, the impedance of the as fabricated cells ( $\text{Li/polymer electrolyte/LiCoO}_2$ ) and the cells after 1, 5 and 10 cycles are shown in Fig. 8a and b.

The decrease in impedance with cycling supports the supposition that the passivating film (formed due to the reaction of lithium with the polymer electrolyte) is being removed and thereby the surface of lithium is subsequently

being renewed. These preliminary observations suggest that PVdF–PVC blend polymer electrolytes seem to be more promising than the homopolymer PVdF electrolytes.

#### 4. Conclusions

Homopolymers-containing PVdF require 30–35% of polymer to get a solvent free film of sufficient stability. Alternatively, a combination of 25% PVdF with 5% PVC along with 20 or 27.5% PVdF with 10 and 2.5% PVC, respectively gave better formation of films. Among the stable films of both the categories, films with 60% EC + PC favoured better conductivity, lower resistance and higher thermal stability. Similarly,  $\text{LiAsF}_6$  gave better results than  $\text{LiBF}_4$  and  $\text{LiPF}_6$ , irrespective of the nature of the polymer and the amount of plasticiser used for casting the films.

A combination of 30% PVdF with 60% EC + PC and 10%  $\text{LiAsF}_6$  and 25:5 (PVdF–PVC) with 60% EC + PC and 10%  $\text{LiAsF}_6$  performed better than the rest of the films.

PVdF–PVC blend polymer electrolytes exhibited improved cycling behaviour rather than the PVdF polymer electrolytes.

#### References

- [1] J.M. Tarascon, D. Guyomard, *Electrochim. Acta* 38 (1993) 1221.
- [2] O. Bohnke, G. Frand, M. Rezzazzi, C. Rousselot, C. Truche, *Solid State Ionics* 66 (1993) 105.
- [3] R. Koksang, I.I. Olsen, D. Shackle, *Solid State Ionics* 66 (1994) 320.
- [4] F. Croce, F. Gerace, G. Dautzenberg, C. Passerini, G.B. Appetecchi, B. Scrosati, *Electrochim. Acta* 39 (1994) 2187.
- [5] M. Alamgir, K.M. Abraham, *J. Power Sources* 54 (1995) 40.
- [6] A.S. Gozdz, C.N. Schmutz, J.M. Tarascon, P.C. Warren, U.S. Patent no. 5418091, May 1995.
- [7] G. Feuillade, P. Perche, *J. Appl. Electro. Chem.* 5 (1975) 63.
- [8] K.M. Abraham, M. Alamgir, *J. Electrochem. Soc.* 137 (1990) 1657.
- [9] G.B. Appetecchi, F. Croce, B. Scrosati, *Electrochim. Acta* 40 (1995) 991.
- [10] S. Kakuda, T. Momma, T. Osaka, G.B. Appetecchi, B. Scrosati, *J. Electrochem. Soc.* 142 (1995) L1.
- [11] T. Osaka, T. Momma, H. Ito, B. Scrosati, *J. Power Sources* 68 (1997) 392.
- [12] T. Osaka, T. Homma, T. Momma, H. Yarimizu, *J. Electroanal. Chem.* 421 (1997) 153.
- [13] F. Boudin, X. Andrieu, C. Jehoulet, I.I. Olsen, *J. Power Sources* 81/82 (1999) 804.
- [14] Z. Jiang, B. Carroll, K.M. Abraham, *Electrochim. Acta* 42 (1992) 2667.
- [15] J.M. Tarascon, C.N. Schmutz, A.S. Gozdz, P.C. Warren, F. Shokoohi, *M R S Fall Meeting Proc.* 595–604 (1994) 369.
- [16] A.S. Gozdz, C.N. Schmutz, J.M. Tarascon, U.S. Patent no. 5, 1994, pp. 296–318.
- [17] J. Fuller, A.C. Breda, R.T. Carlin, *J. Electrochem. Soc.* 144 (1999) L67.
- [18] N. Kalaiselvi, P. Periyasamy, R. Thirunakaran, B. Ramesh babu, N.G. Renganathan, N. Muniyand, *Bull. Mater. Sci.*, in press.
- [19] M. Armand, W. Gorecki, R. Andreani, B. Scrosati, in: *Proceedings of the 2nd International Meeting on Polymer Electrolytes*, Elsevier, New York, 1990, p. 91.

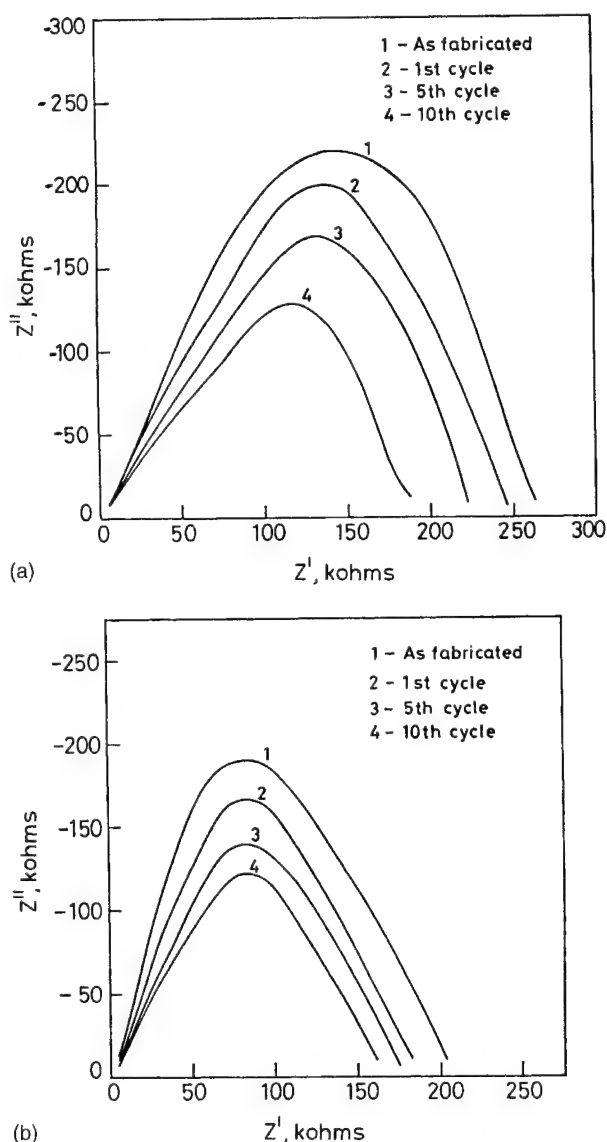


Fig. 8. (a) Variation of impedance with cycle number for a  $\text{Li/PVdF/LiCoO}_2$  cell; (b) variation of impedance with cycle number for a  $\text{Li/PVdF-PVC/LiCoO}_2$  cell.

## Investigation of the stability of chlorinated PVC-based polymer electrolytes for lithium batteries

E.M. Shembel<sup>a,\*</sup>, O.V. Chervakov<sup>a</sup>, L.I. Neduzhko<sup>a</sup>, I.M. Maksyuta<sup>a</sup>,  
Yu.V. Polischuk<sup>a</sup>, D.E. Reisner<sup>b</sup>, P. Novak<sup>c</sup>, D. Meshri<sup>d</sup>

<sup>a</sup>Ukrainian State Chemical Technology University, Gagarin Avenue, 8, Dnepropetrovsk 49005, Ukraine

<sup>b</sup>US Nanocorp., Inc., Farmington, CT, USA

<sup>c</sup>Ener1, LaSpezia, Italy

<sup>d</sup>Advance Research Chemicals, Inc., North Haven, CT, USA

Received 29 January 2001; accepted 30 January 2001

### Abstract

By thermogravimetric analysis, impedance spectroscopy and potentiodynamic cycling, the thermal and electrochemical stability of polymer electrolytes based on PVC and its chlorinated derivatives have been studied. The methods used to modify the properties of these polymeric electrolytes and to provide them with electrochemical stability when used in lithium batteries where the cathode is based on natural, nanostructured, and thermally-sprayed pyrite have been demonstrated. © 2001 Published by Elsevier Science B.V.

**Keywords:** Lithium batteries/polymer electrolyte; Gel polymer electrolytes; Aprotic solvents; Pyrites

### 1. Introduction

Electrolyte systems such as polymer–aprotic solvent–lithium salt have a high conductivity at room temperature ( $\sim 10^{-3}$  to  $10^{-4} \Omega^{-1} \text{cm}^{-1}$ ) [1,2]. Due to the simplicity of preparation and the use of accessible reagents in the systems described, such gel-polymer electrolytes (GPE) are promising for rechargeable lithium batteries.

Investigation of the conductivity of these systems and understanding of its mechanism are of great importance. GPE conductivity depends on lithium ion mobility in the intermolecular space of the polymer matrix of the electrolyte. It is due to a high mobility of the high-molecular compound segments. The mobility is determined both by the character of its chemical structure and the availability of a low-boiling aprotic solvent in GPE. In this case, the solvent also serves as a plasticizing additive. At the same time, one can find the data in some references, concerning a specific interaction between lithium salt and the functional groups of the polymer matrix, e.g. C–O–C in polyethylene oxide, and its structural analogues [3], –CN in polyacrylonitrile [4]

which also makes its contribution to the conductivity of the electrolyte.

An amorphous polymer structure [5] is preferable for good conductivity. This creates an increased interest in the application of amorphous polyacrylonitrile [4], polymethyl-metacrylate [6] or low-crystalline polymers, e.g. polyvinylchloride [7,8].

In spite of the literature data concerning the application of PVC-based GPE [9] in lithium batteries, investigators are interested in thermal and electrochemical stability of the base system [10].

The comparatively low stability of GPE based upon PVC and many other polymers is due to a variety of reasons.

In the process of battery fabrication, chemical and electrochemical reactions are possible within the polymer electrolyte, resulting in the degradation of the electrolyte components. A high chemical activity of metallic lithium [11] and oxidizer (cathode material) [12], favours these reactions.

Salts and various metal compounds occurring accidentally or as specially introduced additives in polymers or in the base materials can have basically different influences on the decomposition process of the polymer materials.  $\text{Li}^+$ ,  $\text{Fe}^{3+}$ ,  $\text{Fe}^{2+}$  ions are known [13,14] to be active dechlorination agents for PVC and its derivatives.

Besides the cation influence, in some cases  $\text{F}^-$ ,  $\text{Cl}^-$ ,  $\text{Br}^-$ ,  $\text{I}^-$ ,  $\text{ClO}_4^-$ ,  $\text{SO}_4^-$  anions and others [14] can accelerate the

\* Corresponding author. Tel.: +380-562-47-03-91;  
fax: +380-562-47-0391.  
E-mail address: shembel@onil.dp.ua (E.M. Shembel).

thermal decomposition of PVC. Destruction by anions and cations depends significantly on the state of the plastic. In aprotic solvents, e.g. DMF, chlorides of alkali metals dissociate with the formation of strongly basic  $\text{Cl}^-$  ions, catalyzing the decomposition process of PVC [15].

Rate of chemical reactions increase with rising temperature. The effect of high temperatures on GPE is possible if an elevated temperature technological process is used for its fabrication, e.g. in drying, when polymer electrolyte is produced from solutions [2], as well as in the case of GPE production by the extrusion method [16], or during battery operation.

In this work, we investigated the influence of lithium salts on the thermal and electrochemical stability of GPE based on chlorinated polyvinylchloride for the Li–FeS<sub>2</sub> battery. The method of PVC chlorination has been developed at our laboratory. Earlier [17] we have shown that PVC chlorination results in amorphization of its structure and increased conductivity of the polymer.

## 2. Experimental

### 2.1. Preparation of polymer electrolytes

Chlorinated polyvinylchloride (Cl-PVC) was obtained under laboratory conditions by heterogeneous chlorination of a PVC suspension in  $\text{CCl}_4$ .

Polymer films were formed on a glass sheet from a solution of the components (polymer, aprotic solvents, lithium salts and additives) in tetrahydrofuran. The films were dried for 24 h at room temperature and then at 48 h in vacuum at 45°C.

$\text{LiClO}_4$  (Iodobrom, Saki, Ukraine),  $\text{LiBF}_4$ ,  $\text{LiPF}_6$  (Advance Research Chemicals, Inc., USA),  $\text{LiCF}_3\text{SO}_3$  (Aldrich), were used as electrolyte salts. PC was obtained from Angarsk Chemical Reagents Plant, Angarsk, Russia.

### 2.2. Thermogravimetric analysis (TGA)

Thermal stability of polymer electrolytes has been investigated on a thermogravimetric analyzer Q-1500 (Hungary), at 5 K min<sup>-1</sup> heating rate with a 200 mg sample. Polymer compositions formed as films from THF by the method described in Section 2.1, were investigated.

### 2.3. IR spectroscopy

IR spectra of the polymer blends were recorded by a spectrophotometer SPECORD 75IR. The investigations were carried out within the wavelength range from 400 to 3800  $\mu\text{m}$ .

### 2.4. Measurements of conductivity

The measurements of the conductivity of GPE films were performed by impedance spectroscopy on the symmetrical

system: Ni–GPE–Ni over the frequency range of 0.08–200 kHz. This was done in an atmosphere of dry argon within a Teflon cell. Ionic conductivity of GPE was calculated from the data for the total resistance  $R_e$  of the electrolyte, measured from the intersection of the high frequency part of the hodograph with the abscissa.

### 2.5. Impedance measurements

Impedance measurements of symmetrical Li–Li cells (in the atmosphere of dry argon in a Teflon cell) or asymmetrical Li–FeS<sub>2</sub> (in 2525 button cells) were carried out with the help of ac bridge P5021 over the frequency range 0.08–200 kHz using a series circuit of the measured values  $R_s$  and  $C_s$ . The hodographs  $1/\omega C_s - R_s$  have the shape of slightly depressed semicircles.

### 2.6. Potentiodynamic measurements

Potentiodynamic cycling was performed in a Teflon cell with three electrodes in the atmosphere of argon. Reference and auxiliary electrodes were made of lithium. For the investigation of the background potentiodynamic characteristics of the polymer electrolyte, a platinum plate served as a working electrode. The electrodes, made from the different samples of pyrite, were used in studying the kinetics of the cathodic reduction of FeS<sub>2</sub>.

Electrode potential sweeps were performed with a potentiostat PI-50-1,1 and programmer PR-8. Scan rate ranged from  $1 \times 10^{-3}$  to  $1 \times 10^{-4}$  V s<sup>-1</sup>. The curves were registered on a two-coordinate recorder PDA-1 within the potential range 0.8–4.8 V in the case of platinum electrode and 1.1–2.8 V with pyrite electrodes.

### 2.7. Preparation of cathode materials

Natural, nanostructured, and thermal-sprayed pyrites (pyrite) were used as cathode materials. Nanostructured and thermally-sprayed pyrite was produced by the unique technology of US Nanocorporation<sup>®</sup>, USA.

Natural pyrite was ball-milled, then sieved. The fraction with a particle size less than 40  $\mu\text{m}$  was used as the active cathode material. Before cathode preparation in mass, the pyrite was washed with boiling water up to neutrality of the washing water, then it was dried at 250°C for 4 h. Natural pyrite, carbon black and graphite in the required mass ratio were thoroughly stirred in a ceramic mortar.

Thirty-three percent by weight of fluoroplastic binder F4D mixed with 1.1 ethanol (96%): distilled water was added to the above composition and mixed in a mortar, then dried at 100°C for 6 h. The cathode mass so prepared was then ready for use. Cathodes based on nanostructured pyrite were prepared similarly.

Thermally-sprayed pyrite was produced by US Nanocorp., USA, using a dc plasma arc gun. Samples of thermally-sprayed pyrite were obtained by plasma spraying of

pyrite onto a stainless steel substrate. The thickness of these electrode films ranged from 83.7–212  $\mu\text{m}$ . The porosity of the films was 50%.

### 2.8. Preparation of a prototype battery

The cathode mass was wetted with heptane and then deposited by a putty knife onto a degreased stainless steel grid-current collector that had been welded to the bottom of the case of a 2525 cell. The assembly was then dried at 100°C for 1 h.

Cell assembly was performed in an atmosphere of dry argon by placing in layers: a cathode, GPE film and metal lithium. The cell was then sealed.

## 3. Results and discussion

### 3.1. Thermal stability

The influence of PC and  $\text{LiClO}_4$  on the thermal stability of chlorinated polyvinylchloride is shown in Fig. 1.

Mass loss in chlorinated polyvinylchloride and in the composition Cl-PVC:PC begins at 105°C. At this temperature, the quantity of the volatile components lost is ~1%.

The following substances can serve as the volatile components:

- Residues of a solvent in the GPE, which is known from the previous work [4] to be partially removed from gelatinous GPE during drying.
- Chemically bound water.

We have carried out a comparative analysis of IR spectra of Cl-PVC films obtained under the normal conditions, given in Section 2.1, and after preliminary thermal treatment at 90°C for 5 h.

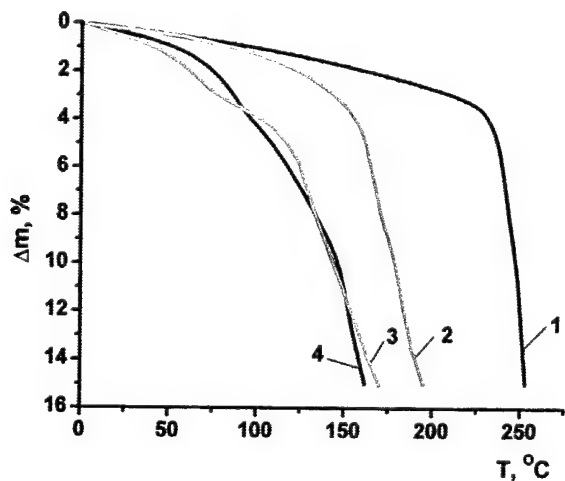


Fig. 1. Mass loss of polymer material samples during thermal oxidation: (1) Cl-PVC; (2) Cl-PVC:PC (1:5); (3) Cl-PVC:PC: $\text{LiClO}_4$  (1:5:0.42); (4) Cl-PVC:PC: $\text{LiClO}_4$ : $\text{FeS}_2$  (1:5:0.42:0.3). Mass ratio of the components are given in brackets.

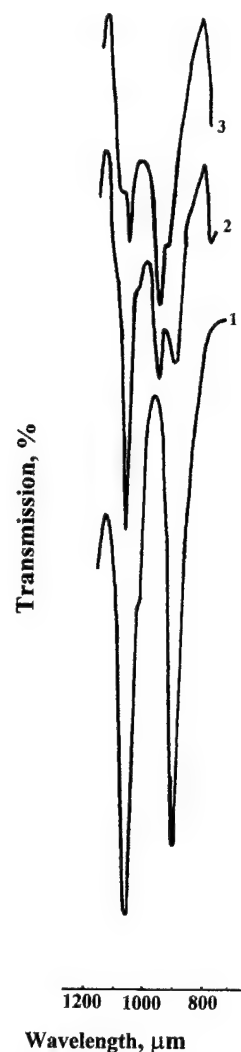


Fig. 2. IR-spectra of THF (1) and Cl-PVC films (2 and 3) obtained from solutions in tetrahydrofuran. Films dried for 24 h at room temperature and 48 h in vacuum at 45°C; (2) for 24 h at room temperature, 48 h in vacuum at 45°C, finally (3) for 5 h at 90°C.

For the thermally treated films, a decrease in the intensity of absorption bands is observed at 1075 and 905  $\mu\text{m}$ . These bands correspond to the asymmetric oscillations of a tetrahydrofuran ring and the oscillations of C–O–C group (Fig. 2). According to the thermogravimetric investigation data, the thermal oxidative destruction of Cl-PVC begins at a temperature higher than 220°C. Therefore, the changes in IR spectra after thermal treatment can correspond only to the process of the forced removal of solvent residue from the Cl-PVC films when heated above the boiling temperature of THF.

In accordance with a weight analysis, we have determined that GPE films dried under the standard conditions contain 7–8% of THF.

The IR spectra of the polymer materials Cl-PVC, Cl-PVC:PC and Cl-PVC:PC: $\text{LiClO}_4$  the presence of a wide maximum at 3400–3450  $\mu\text{m}$ , being a characteristic feature, confirmed the presence of water in the samples.

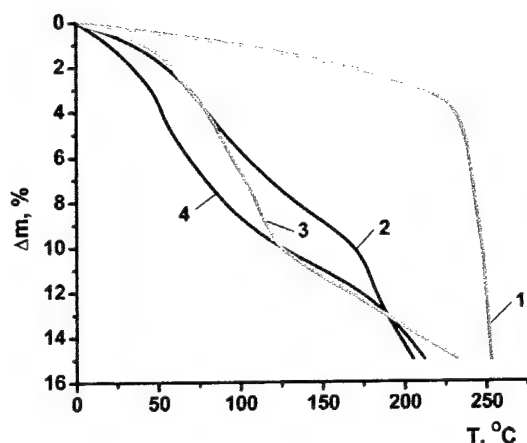


Fig. 3. Effect of the type of lithium salt on the thermal stability of chlorinated polyvinylchloride: (1) CI-PVC; (2) CI-PVC:LiClO<sub>4</sub> (1:0.42); (3) CI-PVC:LiCF<sub>3</sub>SO<sub>3</sub> (1:0.6); (4) CI-PVC:LiBF<sub>4</sub> (1:0.38). Mass ratio of the components are given in brackets.

With increasing temperature, the above samples show different behaviour. With the initial polymer, a 3% mass loss occurs at 220°C, but for its plasticized product it occurs at 145°C. Such behaviour of the plasticized system can be explained by the start of PC decomposition and the evaporation of its decomposition products [18].

Introduction of LiClO<sub>4</sub> into the system, sharply decreases the stability of the polymer composition (Fig. 1, curve 3). This confirms the catalytic effect of this salt on the thermal destruction of CI-PVC.

The presence of natural pyrite in gel-electrolyte does not significantly affect the behaviour of the polymer electrolyte, comprising CI-PVC:PC:LiClO<sub>4</sub>, at temperatures up to 50°C.

In Fig. 3 the influence of the nature of the lithium salt on the thermal stability of CI-PVC is shown. All of them act as a catalyst for the decomposition of CI-PVC. Their effect on CI-PVC decomposition increases in a series of LiCF<sub>3</sub>SO<sub>3</sub> ≈ LiClO<sub>4</sub> < LiBF<sub>4</sub>. In this connection, introdu-

Table 1

Conductivity at 25°C of GPE films based on chlorinated polyvinylchloride

Sample	Electrolyte	Mass ratio	Conductivity <sup>a</sup> $\sigma$ (S cm <sup>-2</sup> )		
			0 days	1 day	5 days
1	CI-PVC:PC:LiClO <sub>4</sub>	1:5:0.42	0.045	0.050	0.060
2	CI-PVC:PC:LiBF <sub>4</sub>	1:5:0.38	0.065	0.065	0.056
3	CI-PVC:PC:LiCF <sub>3</sub> SO <sub>3</sub>	1:5:0.6	0.032	0.032	0.030

<sup>a</sup> Thickness of GPE films is 0.5 mm.

cing stabilizing additives in the polymer electrolyte is very important. The effect of stabilizing additives is discussed later.

### 3.2. Conductivity of polymer electrolytes

In Table 1 the results of the measurements of the conductivity of GPE films at 25°C are presented. Except for the LiClO<sub>4</sub>-based electrolyte where a certain increase in conductivity is observed, it is clear that, after storage for 5 days, conductivity is practically unchanged.

It should be noted that the conductivity of GPE based on chlorinated polyvinylchloride is the same as for the traditional liquid systems [10] and depends on the nature of lithium salts used as solutes. For these electrolytes, conductivity rises in the sequence: LiCF<sub>3</sub>SO<sub>3</sub> ≈ LiClO<sub>4</sub> < LiBF<sub>4</sub>.

### 3.3. Impedance measurements

Analysis of the impedance curves of the symmetrical system Li/GPE/Li shows that for the GPE based on PVC and CI-PVC, hodographs take the forms typical of those from traditional liquid systems (Fig. 4). The CI-PVC-based GPE is characterized by a lower resistance of passivating films on lithium surfaces as compared with PVC. It is evidence of the higher PVC reactivity relative to lithium

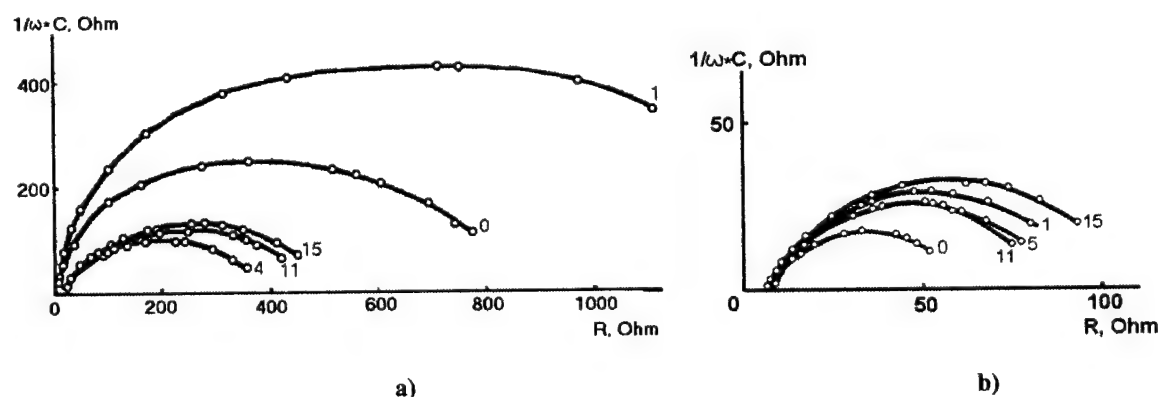


Fig. 4. Impedance characteristics of Li-Li system with GPE: (a) PVC:PC:LiClO<sub>4</sub> (1:5:0.42); (b) CI-PVC:PC:LiClO<sub>4</sub> (1:5:0.42). Numbers by curves indicate ageing time in days.

anodes, than when its chlorinated derivative is used as a polymer matrix.

The results obtained correlate well with the supposition stated earlier [10] about possible lithium passivation by polyvinylchloride in the electrolyte comprising PVC:EC/PC:LiClO<sub>4</sub>.

In [10] the authors consider that the interaction between PVC and lithium in GPE compositions results in the formation of an inorganic surface layer, comprising LiCl. In this case, the resistance of the lithium anode was noted to depend significantly on the nature of the lithium salt nature GPE. GPEs containing LiPF<sub>6</sub> and LiBF<sub>4</sub> showed higher reactivity relative to lithium than ones containing LiClO<sub>4</sub>. The authors explained this fact by the higher reactivity of LiPF<sub>6</sub> and LiBF<sub>4</sub> than LiClO<sub>4</sub> against lithium.

In our opinion, such a significant rise of lithium hydride (LiH) formation can be promoted by the catalytic effect of LiPF<sub>6</sub> and LiBF<sub>4</sub> on the process of PVC dehydrochlorination and, correspondingly, on the formation of LiH. Evidently, presence of the latter gives rise to a high resistance for the system. Note that such an effect is not observed during investigations of liquid systems.

It can be also supposed that halide ions in the Cl-PVC system activate the passivating film on a lithium surface. The effect of halide ions on the properties of the lithium/non-aqueous electrolyte interface has been reported. For example, when PC:LiBr solutions were compared with PC:LiClO<sub>4</sub> ones [19]. Nevertheless, in the case of polymer systems, the influence cannot be so evident and requires additional investigations, in as much as halide derivative-based polymers are widely used in lithium nonaqueous systems. Impedance of the asymmetrical system Li/GPE/FeS<sub>2</sub> is complicated by a possible interaction between the polymer system and the oxidizer — FeS<sub>2</sub>. In [12] we have

shown how the impedance of the nonaqueous system comprising the polymer based on the organosilicone derivatives of polyvinylpyridine changes in of the presence of the different cathode materials MnO<sub>2</sub> and FeS<sub>2</sub>.

In Fig. 5, the impedance of the system Li/GPE/FeS<sub>2</sub>, using as an active substance, the highly reactive nanostructured pyrite from US Nanocorp., is shown. Earlier we mentioned that in the presence of pyrite, data on the thermal decomposition of the polymer system (Fig. 1) was unavailable. However, comparing Figs. 4 and 5, one can see that with pyrite, as compared with the system comprising only Li/GPE/Li, the impedance becomes distorted, and the system resistance increases.

Impedance degradation can have at least two causes. The properties of the film formed on a cathode surface at its interaction with the components of polymer electrolyte change. These result in an increase in the parameters of impedance “semicircles”. The resistance itself also changes with interelectrode spacing, i.e. the specific resistance of the electrolyte changes. This change is reflected by an increase in the length cut-off by the hodograph on an abscissa axis within the high frequency range. The degradation effect is stronger in the PVC-based system (Fig. 5a). When Cl-PVC is used in the asymmetrical system, the resistance value of passivating films on electrode materials and that of GPE in interelectrode spacing are lower as compared with PVC-based system (Fig. 5b).

### 3.4. Potentiodynamic investigations

In Fig. 6 the ground potentiodynamic curve of polymer electrolyte on platinum electrode is shown. The polymer electrolyte based on Cl-PVC is stable enough within the potential range of 0.8–4.5 V.

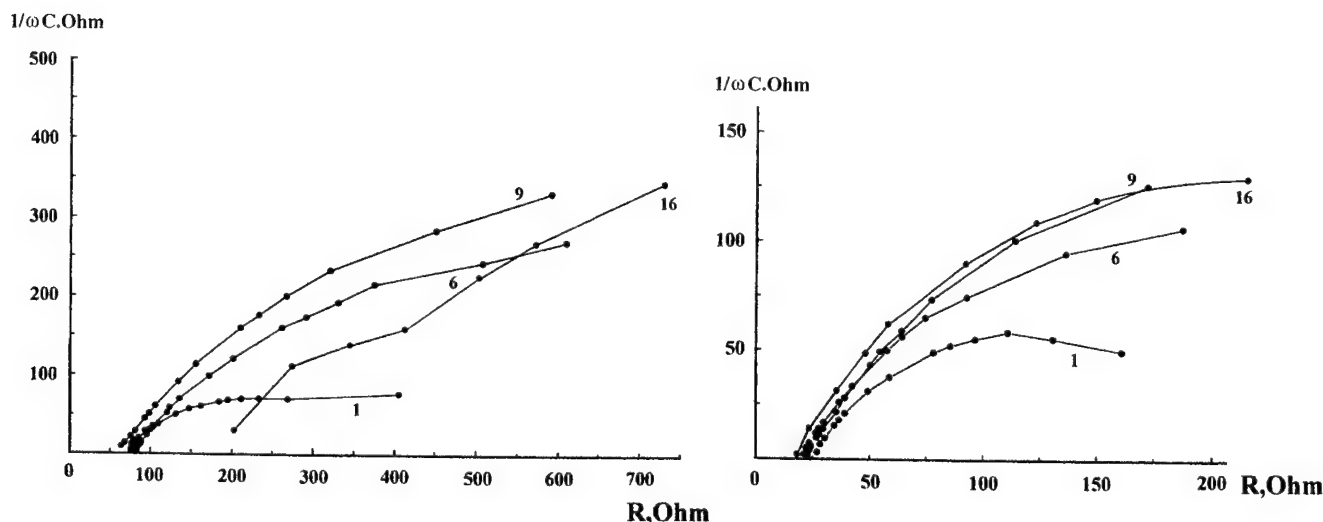


Fig. 5. Impedance hodographs of Li–FeS<sub>2</sub> (US Nanocorp.) system with GPE: (a) PVC:PC:LiClO<sub>4</sub> (1:5:0.42); (b) Cl-PVC:PC:LiClO<sub>4</sub> (1:5:0.42). FeS<sub>2</sub> content in cathode is 70%. Electrode area = 1.45 cm<sup>2</sup>. Numbers by curves indicate ageing time in days.

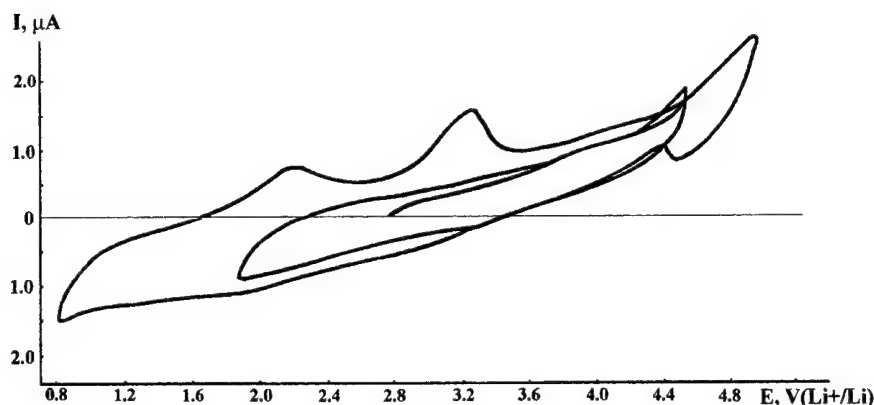


Fig. 6. Background potentiodynamic curve on Pt electrode in polymer electrolyte Cl-PVC:PC:LiClO<sub>4</sub> (1:5:0.42). Electrode area =  $7.8 \times 10^{-3}$  cm<sup>2</sup>.

Thus, the electrolytes developed appear to be promising for rechargeable power sources, with the different operating voltage of: 4.0 V (LiMn<sub>2</sub>O<sub>4</sub>), 3.0 V (MnO<sub>4</sub>), 1.5 V (FeS<sub>2</sub>). As noted above, this work is devoted to Li–FeS<sub>2</sub> system with the operating voltage of 1.5 V.

In Figs. 7–9 the results of the potentiodynamic investigations carried out on the film of thermally sprayed pyrite are

presented. Characteristics obtained in liquid and polymer electrolytes have been compared. In Fig. 7 it is seen that in liquid electrolyte, FeS<sub>2</sub> films are irreversibly reduced cathodically.

The second potentiodynamic curve practically reduces to the background curve observed with inert platinum electrodes.

With a polymer electrolyte, the thermally-sprayed pyrite cycled reversibly (Fig. 8). In the electrolyte containing LiBF<sub>4</sub>, during the first cycles the peak value decreases slightly, and then becomes stable. In the LiPF<sub>6</sub> electrolyte, the current value is less; however, stabilization occurs during the first few cycles.

In the LiCF<sub>3</sub>SO<sub>3</sub>-based electrolyte (Fig. 9), the character of the potentiodynamic curves is different — in the cathodic region, the area occupied by the curve is larger than in anodic one. This could be evidence of the participation of the polymer electrolyte components in the electrochemical process. At the same time, cathode peaks increasing from cycle-to-cycle can be caused by the gradual change in volume of an active cathode. Thus, the potentiodynamic investigations have shown the prospects for application of a new electrochemical system based on the polymer electrolyte and the films of thermal sprayed pyrite as these latter are reversibly cycleable at room temperature.

### 3.5. Prototype batteries

Here are presented the results of galvanostatic cycling of cells with a polymer electrolyte and the cathode based on natural pyrite. We have suggested above the possibility of PVC dechlorination resulting from its interaction with metal lithium. To increase PVC stability we used additives capable of inhibiting its dehydrochlorination.

The cycling results of a system without modifying additive in the electrolyte (Fig. 10) and the electrolyte comprising this additive (Figs. 11 and 12) have been compared.

In the absence of modifying additive, significant capacity loss occurs during the first five cycles (Fig. 10).

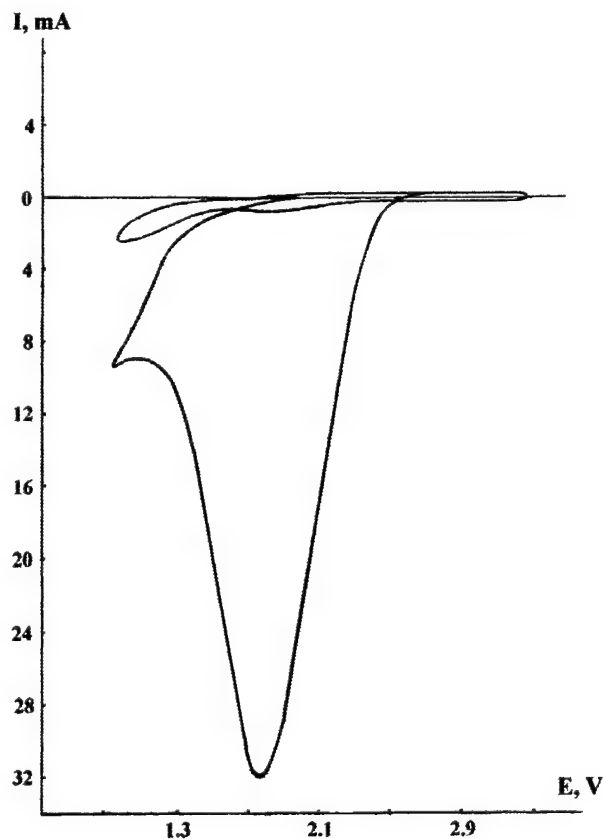


Fig. 7. Cyclic voltammogram of thermally sprayed FeS<sub>2</sub> in a liquid electrolyte: PC:DME (3:1); 1 M LiClO<sub>4</sub>. Scan rate:  $5 \times 10^{-5}$  V s<sup>-1</sup>. FeS<sub>2</sub> area = 8 cm<sup>2</sup>. Thickness of FeS<sub>2</sub> film is 146.7 μm.



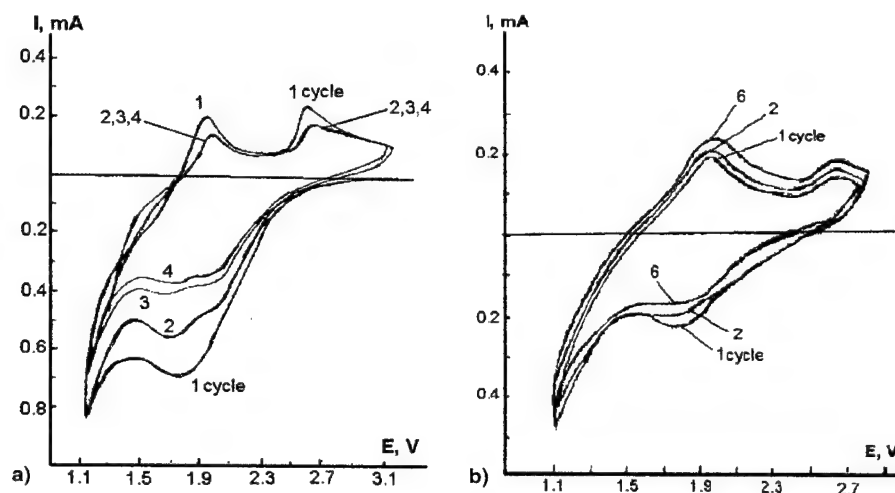


Fig. 8. Cyclic voltammograms of thermally sprayed  $\text{FeS}_2$  in polymer electrolytes: (a) Cl-PVC:PC:LiBF<sub>4</sub> (1:5:0.38); (b) Cl-PVC:PC:LiPF<sub>6</sub> (1:5:0.61).  $\text{FeS}_2$  area is  $8 \text{ cm}^2$ . Scan rate:  $5 \times 10^{-4} \text{ V s}^{-1}$ . Thickness of  $\text{FeS}_2$  film is  $150 \mu\text{m}$  (a) and  $212 \mu\text{m}$  (b).

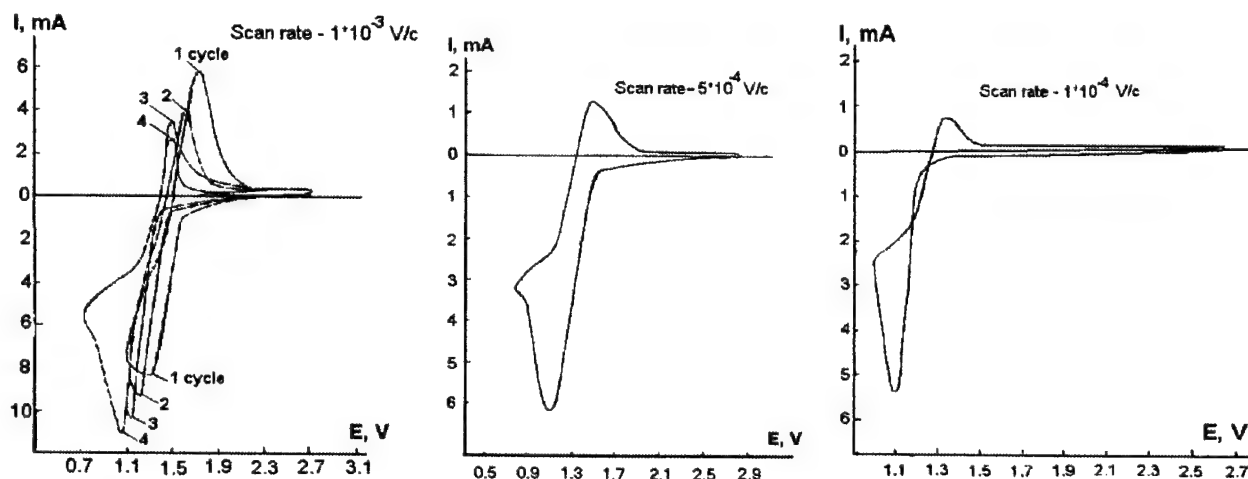


Fig. 9. Cyclic voltammograms of thermally sprayed  $\text{FeS}_2$  in polymer electrolyte Cl-PVC:PC:LiCF<sub>3</sub>SO<sub>3</sub> (1:5:0.6).  $\text{FeS}_2$  area =  $8 \text{ cm}^2$ . Thickness of  $\text{FeS}_2$  film is  $83.7 \mu\text{m}$ .

A quite different situation is observed whilst testing GPE with the same composition (Figs. 11 and 12) but with a modifying additive. After the 50th cycle, the discharge capacity of the system becomes stable at a rather high level.

In the case of a polymer electrolyte based on Cl-PVC, the system is stable enough during cycling even without stabilizing additive (Fig. 13).

The nature of the lithium salt influences the discharge characteristics of the Li- $\text{FeS}_2$  system. The maximum capacity value has been obtained with GPE containing LiCF<sub>3</sub>SO<sub>3</sub>. At the 80th cycle, the discharge capacity was about  $400 \text{ mAh g}^{-1}$ . When LiClO<sub>4</sub> or LiBF<sub>4</sub> was used in the GPE, by the 50th cycle, the discharge capacity was only  $180\text{--}200 \text{ mAh g}^{-1}$ .

The comparatively fast decrease in capacity and the low values for the system comprising GPE with LiBF<sub>4</sub> can be explained by the high reactivity of the salt with lithium [10] and its catalytic ability to decompose polyvinylchloride during the charge/discharge process.

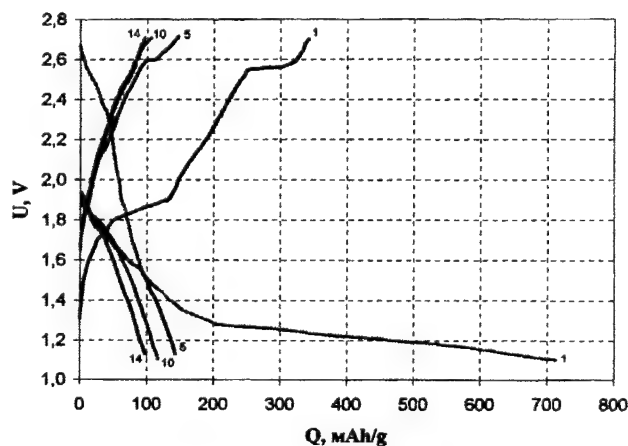


Fig. 10. Change of charge/discharge characteristics of the system Li- $\text{FeS}_2$  with a nonmodified GPE comprising PVC:PC:LiCF<sub>3</sub>SO<sub>3</sub> (1:5:0.3). Content of natural  $\text{FeS}_2$  in cathode is 10% (carbon black, graphite and binding are the remaining components).  $I_{\text{discharge}} = 0.1 \text{ mA}$ ,  $I_{\text{charge}} = 0.02 \text{ mA}$ . Labels on curves correspond to cycle numbers.



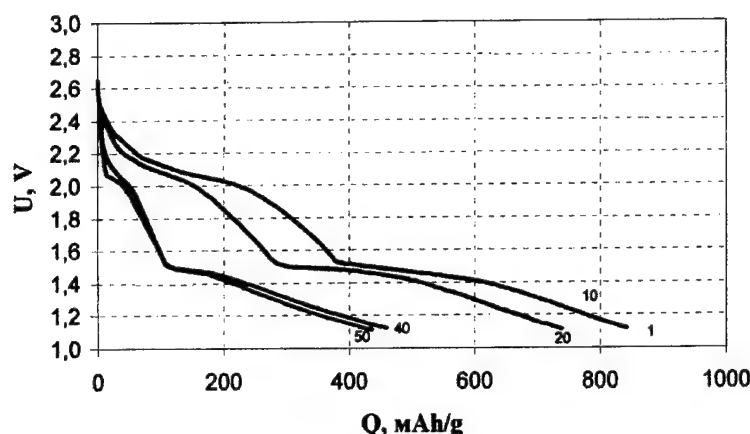


Fig. 11. Discharge characteristics of the system Li-FeS<sub>2</sub> with a GPE comprising PVC:PC:LiCF<sub>3</sub>SO<sub>3</sub> (1:5:0.3) and modifying additive. Content of natural FeS<sub>2</sub> in cathode is 10%.  $I_{\text{discharge}} = 0.1$  mA,  $I_{\text{charge}} = 0.02$  mA. Labels on curves correspond to cycle numbers.

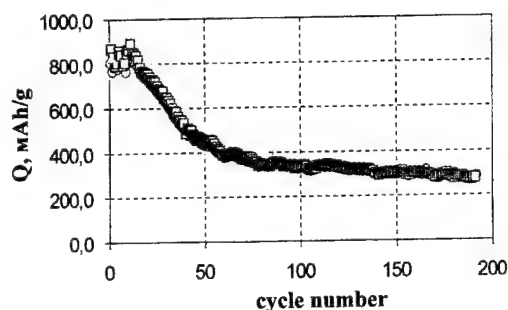


Fig. 12. Change of specific capacity during cycling for the Li-FeS<sub>2</sub> system with a GPE comprising PVC:PC:LiCF<sub>3</sub>SO<sub>3</sub> (1:5:0.3) and modifying additive. Content of natural FeS<sub>2</sub> in cathode is 10%.  $I_{\text{discharge}} = 0.1$  mA,  $I_{\text{charge}} = 0.02$  mA.

In the case of LiClO<sub>4</sub>, such an analogy cannot be drawn. To obtain the data concerning the probable degradation mechanism of GPE based on Cl-PVC and containing LiClO<sub>4</sub> additional investigations are needed.

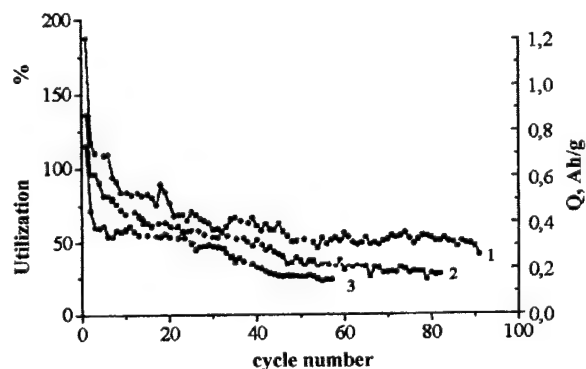


Fig. 13. Influence of the type of salt in the Cl-PVC polymer electrolyte on the discharge characteristics of Li-FeS<sub>2</sub> cells (size 2325): (1) Cl-PVC:PC:LiCF<sub>3</sub>SO<sub>3</sub> (1:5:0.3); (2) Cl-PVC:PC:LiBF<sub>4</sub> (1:5:0.19); (3) Cl-PVC:PC:LiClO<sub>4</sub> (1:5:0.21). Content of natural FeS<sub>2</sub> in cathode is 10%.  $I_{\text{discharge}} = 0.1$  mA,  $I_{\text{charge}} = 0.02$  mA.

#### 4. Conclusions

A gel polymer electrolyte based on chlorinated PVC for use with Li and FeS<sub>2</sub> in secondary cells operating at room temperature has been developed and investigated.

The characteristic feature of this GPE is higher electrochemical stability as compared with polyvinylchloride.

Successful application of polymer electrolytes based on PVC is possible by applying stabilizing additives to increase the electrochemical stability of the electrolyte.

#### References

- [1] G.B. Appetecchi, F. Croce, B. Scrosati, J. Power Sources 66 (1997) 78.
- [2] G.B. Appetecchi, F. Croce, A. De Paolis, B. Scrosati, J. Electroanal. Chem. 463 (1999) 249.
- [3] V.V. Zapol'skikh, V.S. Kolosnitsyn, G.V. Leplyanin, Elektrokhimiya 28 (1992) 995 (in Russian).
- [4] C.R. Yang, J.T. Pern, Y.Y. Wang, C.C. Wan, J. Power Sources 62 (1996) 92.
- [5] P.E. Harvey, J. Power Sources 26 (1989) 23.
- [6] G.B. Appetecchi, F. Croce, B. Scrosati, Electrochim. Acta 40 (1995) 991.
- [7] M. Alamgir, K.M. Abraham, J. Electrochem. Soc. 140 (1993) L96.
- [8] S. Passerini, J.M. Rosolen, B. Scrosati, J. Power Sources 45 (1993) 333.
- [9] M. Alamgir, K.M. Abraham, US Patent no. 5,252,413, 1993.
- [10] G. Pistoia, A. Antonini, G. Wang, J. Power Sources 58 (1996) 143.
- [11] V.P. Verneker, B. Shaha, Polym. Commun. 30 (1989) 92.
- [12] E.M. Shembel, O.V. Chervakov, L.I. Neduzhko, I.M. Maksuta, Elektrokhimiya 36 (2000) 600 (in Russian).
- [13] N.A. Plate, S.L. Davydova, M.A. Yampol'skaya, B.A. Mukhitdinova, V.A. Kargin, Vysokomolekul. Soed. 8 (1966) 1562. (in Russian).
- [14] K.S. Minsker, G.T. Fedoseeva, Destruction and Stability of Polyvinylchloride, Moscow, 1979, p. 83 (in Russian).
- [15] E.Ja. Vaiman, A.B. Pakshver, V.D. Fikhman, Vysokomolekul. Soed., Ser. A 12 (1970) 778 (in Russian).

- [16] Z. Jiang, B. Carroll, K.M. Abraham, in: *Proceedings of the Fall Meeting, San Antonio, TX, USA, 6–11 October 1996*, p. 92.
- [17] E.M. Shembel, O.V. Chervakov, L.I. Neduzhko, A.S. Baskevich, A.G. Ribalka, in: *Proceeding of the 195th Meeting of the Electrochemical Society, Inc., Vol. 99-I, Seattle, USA, 2–6 May 1999*, Abstract 26.
- [18] I.A. Kedrinskiy, V.E. Dmitrenko, Yu.M. Povarov, I.I. Grudiyarov, *Chemical Power Sources with Lithium Electrode*, Krasnoyarsk, 1983, p. 31 (in Russian).
- [19] E.M. Shembel, I.M. Maksuta, O.S. Ksenzek, *Electrokhimia* 8 (1985) 1016 (in Russian).



ELSEVIER

Journal of Power Sources 96 (2001) 29–32

JOURNAL OF  
POWER  
SOURCES

www.elsevier.com/locate/jpowsour

# Improving the interfacial resistance in lithium cells with additives

G. Nagasubramanian\*, D. Doughty

Department 2521 Lithium Battery R&amp;D, Sandia National Laboratories, Albuquerque, NM 87185, USA

Received 30 November 2000; accepted 14 December 2000

## Abstract

Improved interfacial resistance was observed in lithium cells by the use of new additives. The additives, nitrile sucrose and nitrile cellulose and their lithium salts, were evaluated in polyvinylidene difluoride (PVDF) thin-film gelled electrolytes containing a mixture of ethylene carbonate (EC) and diethyl carbonate (DEC). The electrochemical properties of the films with and without the additives were measured as a function of temperature and compared. The interfacial resistance ( $R_{in}$ ) of the films with the additives was significantly lower than that without the additives, especially at sub-ambient temperatures. For example, the  $R_{in}$  at  $-20^{\circ}\text{C}$  for the films with additives was around  $7000\ \Omega\ \text{cm}^2$  and that for the films without the additives was  $>20,000\ \Omega\ \text{cm}^2$ . Results obtained from using the additives in lithium-ion (Li-ion) cells show significant improvements in the low frequency resistance of the cells. © 2001 Published by Elsevier Science B.V.

**Keywords:** Lithium-ion cells; Electrolyte additives; Interfacial resistances

## 1. Introduction

In recent years rechargeable lithium-ion (Li-ion) batteries (also called “rocking chair”, “shuttlecock” or “swing electrode”) containing either organic liquid electrolytes or gelled electrolytes are being extensively investigated as commercial power sources because they offer higher energy per unit weight and volume than nickel-based batteries such as Ni/Cd or Ni/MH [1]. Further, the self-discharge rate of Li-ion batteries is low — about 2% of capacity per month — compared to 15% for Ni/Cd and 25% for Ni/MH. Because of these potential advantages, Li-ion batteries are being investigated for a number of applications including electric vehicle (EV), space, military and commercial. In commercial Li-ion cells, coke or graphite is used as the anode and  $\text{LiCoO}_2$  is used as the cathode. The specific capacity is  $372\ \text{mAh g}^{-1}$  for the anode and  $\sim 140\ \text{mAh g}^{-1}$  for the cathode. New higher capacity metal-based anodes [2] and mixed-oxide cathode materials (for example  $\text{LiNi}_{1-x}\text{Co}_x\text{O}_2$ ) [3] are being developed for use in Li-ion batteries to increase the delivered energy in order to meet the ever increasing power demands of the digital revolution. Further, new low temperature electrolytes [4] and shutdown separators are being investigated for extending the low-temperature performance and safety, respectively, of the batteries. However,

in large part, the impedance behavior, which impacts the electrical performance of Li-ion cells, has been overlooked. No thorough and systematic studies have been reported in the literature on the impedance characteristics of Li-ion cells.

We at Sandia National Laboratories have published several papers on the impedance behavior of Li-ion cells [5–7]. Our studies indicate the following.

1. The ohmic resistance of a Li-ion cell remains low and nearly constant between  $-20$  and  $35^{\circ}\text{C}$ .
2. The total cell impedance increases by an order of magnitude at  $-20^{\circ}\text{C}$ .
3. The increase in cell impedance comes mostly from the cathode–electrolyte interface.

Exploring ways to reduce interfacial resistance ( $R_{in}$ ) is paramount since the much-touted benefits of Li-ion cells over Ni/Cd and Ni/MH will not be realized at sub-ambient temperatures. Our impedance studies underscore the importance of a very low interfacial resistance for high power applications. Especially at sub-ambient temperatures (say  $-20^{\circ}\text{C}$ ) the effect of  $R_{in}$  will be much more pronounced than at elevated temperatures. Even the state-of-the-art non-aqueous electrolytes such as propylene carbonate (PC)/diethyl carbonate (DEC) and ethylene carbonate (EC)/dimethyl carbonate (DMC) which are currently being used in the Li-ion commercial cells, show unacceptable  $R_{in}$  values especially at sub-ambient temperatures. In some instances  $R_{in}$  values as high as  $500\ \Omega\ \text{cm}^2$  have been reported [8].

\* Corresponding author. Tel.: +1-505-844-1684.

E-mail address: gnagasu@sandia.gov (G. Nagasubramanian).

Primarily, the bulk electrolyte resistance and  $R_{in}$  dictate the deliverable power of the battery. Over the years, many different approaches have been successfully made to improve the bulk ionic conductivity of the electrolyte to  $>10^{-3} \text{ S cm}^{-1}$  at room temperature. For example, one of the approaches involves immobilizing organic liquid electrolytes in an electrochemically inactive host polymer (these are called gelled electrolytes), such as polyacrylonitrile (PAN) [8] and polyvinylidene fluoride (PVDF) [9]. This is commendable since it permits the use of thicker electrolyte films without the inherent problems of pin holes and insufficient mechanical stability that are associated with thinner electrolyte films. However, the  $R_{in}$ , which acts in series with the bulk electrolyte resistance, is not optimized, which severely impedes the realizable power. Further, no studies aimed at reducing the  $R_{in}$  have been reported in the literature.

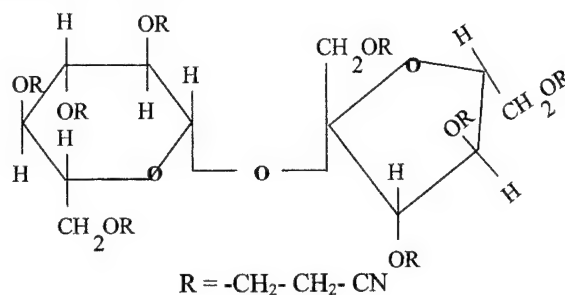
At Sandia National Laboratories we made a systematic attempt to reduce the  $R_{in}$  of the state-of-the-art electrolytes by small quantities of additives. These additives include nitrile sucrose (SUCN) and nitrile cellulose. These are saturated cyclic compounds with functional groups that are known to be stable toward lithium and their lithium salts. These additives are inexpensive, non-hazardous, and stable up to at least 200°C. More importantly they dissolve in common organic solvents. This paper describes the syntheses of lithium salts of the additives, fabrication of thin film PVDF-based gelled electrolytes with and without the additives, and discusses results of electrochemical studies.

## 2. Experimental

### 2.1. Syntheses of the lithium salts of nitrile sucrose and nitrile cellulose

The precursor chemicals were purchased, respectively, from Polysciences, Inc. and from K&K Rare and Fine Chemicals. Only battery grade chemicals were used in this study. These additives have, respectively, six nitrile-groups and eight nitrile-groups per molecule. The salt  $\text{Li}_4\text{SUCN}$  was formed by putting 1.08 g of SUCN into a 100 ml round bottom two-necked flask within a glove box. To this was added 50 ml of tetrahydrofuran (THF) at room temperature and the mixture was stirred well. The flask was tightly sealed and taken out of the glove box, cooled to 0°C in an ice bath and 2.8 ml of *n*-butyl lithium was injected through a septum. The solution was stirred for 2 h, the ice bath was removed and again stirred overnight. The solvent was pumped off leaving behind a bright yellow deposit. The flask was taken into the glove box and the yellow powder collected. The composition of the yellow powder was confirmed to be  $\text{Li}_4\text{SUCN}$ . A similar procedure was employed for the syntheses of other lithium salts and the weights of the chemicals were adjusted appropriately.

Structure of nitrile sucrose (general formula:  $(\text{C}_{12}\text{H}_{14}\text{O}_3) \cdot (\text{OCH}_2\text{CH}_2\text{CN})_8$ ), a viscous liquid at room temperature is given.



### 2.2. Preparation of PVDF-gelled electrolyte

The solvents EC, PC, and DEC were purchased from Mitsubishi Chemicals, Japan and the  $\text{LiPF}_6$  was purchased from Hashimoto, Japan.

EC was mixed with DEC (1/1, v/v) or with PC (1/1, v/v) and  $\text{LiPF}_6$  was added to the solution mixture at room temperature at 1 M concentration. The preparation and the composition of PVDF-based gelled films are given below.

An amount of 1 g of PVDF (2801) was dissolved in about 15 ml of methyl ethyl ketone (MEK) at  $\sim 40^\circ\text{C}$  and the solution was cooled to room temperature before adding 2 g of the electrolyte solution. The mixture was vigorously stirred for a couple of hours before either doctor-blading or pouring the entire solution in a Teflon mold. The MEK was allowed to evaporate slowly overnight. The films were vacuum pumped at  $40^\circ\text{C}$  for a day before making electrochemical measurements, to obtain bulk and interfacial properties. A similar procedure was followed for making PVDF-gelled films containing the additives. About 0.1 g of the additive was added to 10 g of the liquid electrolyte and 2 g of this solution was added to 1 g of PVDF already dissolved in MEK.

In the films that contain the lithium salt of the additive, the concentration of  $\text{Li}^+$  is higher than 1 M. In order to make a meaningful comparison of the electrochemical properties the  $\text{Li}^+$  concentration in other films and electrolytes was adjusted appropriately. Electrochemical measurements were made on these films as well as on the liquid electrolytes. A standard Princeton Applied Research electrochemical ac impedance system described elsewhere was used to measure the electrochemical properties.

## 3. Results and discussion

Before we studied these additives in PVDF-based gelled electrolytes we studied them as additives in liquid electrolytes. In this paper we report our findings on the use of these materials as additives in the following.

1. EC + DEC + 1 M LiPF<sub>6</sub>.
2. PVDF-based gelled electrolyte containing the above organic liquid electrolyte.

Results are only given for nitrile sucrose as the cellulose analog gave almost identical results.

For ac measurements, a symmetrical cell was used. The electrolyte was sandwiched between two smooth, freshly cut, lithium foils. Stainless steel (SS) foil was used as current collector [i.e. SS/Li/Electrolyte/Li/SS]. The cell assembly was vacuum sealed in a polyethylene laminated aluminum bag. For dc measurements, the electrolyte was sandwiched between two well-polished SS foils [i.e. SS/Electrolyte/SS] (blocking contact) and the cell assembly was also vacuum-sealed. For the solution studies, similar electrode assemblies were used but were assembled within airtight glass cells.

### 3.1. Ac results

A small amplitude ac signal of  $V_{p-p} = 1$  mV was used over the frequency regime 60 kHz to 0.1 Hz. From the Nyquist plot, both the ohmic and the interfacial charge transfer resistance of the liquid electrolytes and PVDF-based gelled electrolytes with and without the additives were measured and are given in Table 1.

These data indicate that, while the additive does not affect the bulk conductivity, (this is almost the same) the interfacial resistance is significantly reduced. In the case of the liquid electrolyte, the reduction in  $R_{in}$  is ~33% and in the case of the PVDF-gelled electrolyte the reduction is ~20%. At lower temperatures, the reduction in  $R_{in}$  by the additive is very significant. For example, at  $-20^{\circ}\text{C}$  the  $R_{in}$  for the PVDF-based gelled electrolytes with and without additives are 7092 and 20,340  $\Omega\text{ cm}^2$ , respectively — an improvement of ~66%.

### 3.2. Dc results

A wide potential window is a must for these polymers where they have to be used in conjunction with high voltage cathodes. To evaluate the effect of the additives on the voltage window of the electrolytes we measured the window using dc cyclic voltammetry. The studies were made on PVDF-based gelled films sandwiched between two SS electrodes (blocking contacts). The dc results are given in Table 2.

Table 1  
Conductivity and  $R_{in}$  of the electrolytes with and without additive at room temperature

Electrolyte	$\sigma$ ( $\text{S cm}^{-1}$ )	$R_{in}$ ( $\Omega\text{ cm}^2$ )
EC + PC + LiPF <sub>6</sub>	$2.6 \times 10^{-2}$	189
EC + PC + LiPF <sub>6</sub> + Li <sub>4</sub> SUCN	$2.7 \times 10^{-2}$	125
PVDF + EC + PC + LiPF <sub>6</sub>	$1.7 \times 10^{-3}$	80
PVDF + EC + PC + LiPF <sub>6</sub> + Li <sub>4</sub> SUCN	$1.9 \times 10^{-3}$	60

Table 2

Comparison of dc current flows at 0 and 5 V (vs. Li<sup>+</sup>/Li) for PVDF-gelled films with and without additives at  $-20$ , 25 and  $50^{\circ}\text{C}$

Temperature ( $^{\circ}\text{C}$ )	Without additive ( $\mu\text{A cm}^{-2}$ )		With additive ( $\mu\text{A cm}^{-2}$ )	
	At 0 V	At 5 V	At 0 V	At 5 V
$-20$	1.7	0.87	2.2	1.3
25	10.4	4.5	12.5	5.5
50	29.4	6.9	21.5	6.9

The currents are compared at 0 and 5 V versus Li<sup>+</sup>/Li for three different temperatures, for the two films. The current flowing through the cell at the two extreme potentials for the cells is comparable, which suggests that the additives do not alter the potential window of the electrolyte.

## 4. Impedance studies on 18650 lithium coin cells

We have constructed Li-ion coin cells with and without additives in their electrolyte.

The results from impedance measurements on 18650 Li-ion cells clearly indicate that the interfacial resistance dominates the cell impedance, especially at sub-ambient temperatures. While the ohmic resistance remains nearly constant in this temperature ( $-20$  to  $25^{\circ}\text{C}$ ) range the low frequency resistance, which is mostly the electrode/electrolyte charge transfer resistance, increases by approximately 15 times for the same temperature range.

## 5. Impedance studies on gelled electrolytes

Impedance measurements were made on gelled polymer electrolyte systems. In Table 3 are shown resistance values for the PVDF/EC/PC/LiPF<sub>6</sub> gelled system without the additives. The polymer film was sandwiched between two oxide-free Li electrodes. The low frequency resistance is higher than the ohmic resistance.

Resistance values for films with additives are given in Table 4.

As in results reported earlier in this paper, the performance improvements from the two additives, nitrile sucrose and nitrile cellulose, were similar.

Table 3

The ohmic and low frequency resistances for PVDF-gelled electrolyte without additives

Temperature ( $^{\circ}\text{C}$ )	Ohmic resistance ( $\Omega$ )	Low frequency resistance ( $\Omega$ )
25	0.077	5.24
10	0.359	17.69
0	0.434	49.56
$-10$	0.801	170.5
$-20$	1.220	565

Table 4

Ohmic and low frequency resistances for PVDF-gelled electrolyte with additives

Temperature (°C)	Ohmic resistance ( $\Omega$ )	Low frequency resistance ( $\Omega$ )
25	0.079	3.47
10	0.718	8.75
0	1.041	19.86
–10	1.983	63.5
–20	3.470	197

## 6. Impedance studies on 18650 lithium coin cells

We have constructed Li-ion coin cells with and without additives in their electrolyte.

The results from impedance measurements on 18650 Li-ion cells clearly indicate that the interfacial resistance dominates the cell impedance, especially at sub-ambient temperatures. While the ohmic resistance remains nearly constant in this temperature range (–20 to 25°C) the low frequency resistance, which is mostly the electrode/electrolyte charge transfer resistance, increases by approximately 15 times for the same temperature range.

## 7. Conclusions

We studied the electrochemical properties of EC + PC + LiPF<sub>6</sub> liquid electrolyte and PVDF-based gelled electrolytes with and without additives. We have studied nitrile cellulose and nitrile sucrose and their lithium salts as additives. These additives are off-the-shelf and inexpensive chemicals. They are thermally stable to above the shutdown

temperature of the separators. These additives improved the interfacial properties of the electrolytes contacting metallic lithium and did not affect the bulk properties of the electrolyte. Further, the additives did not alter the voltage window of the electrolytes. The improvement in the interfacial properties by the additives is significant at lower temperatures compared to at room temperature.

## Acknowledgements

Sandia National Laboratories is a multiprogram laboratory operated by Sandia, a Lockheed Martin Company, for the United States Department of Energy under contract DE-AC04-94AL85000.

## References

- [1] D. Anon, *Electronic Product Design* 16 (1995) 2.
- [2] W.I. Cho, S.C. Nam, Y.S. Yoon, B.W. Cho, H.S. Chun, K.S. Yun, in: *Proceedings of the International Symposium on Lithium Batteries*, Electrochemical Society, 1999, Vol. 99-25, p. 203.
- [3] K.K. Lee, K.B. Kim, in: *Proceedings of the International Symposium on Lithium Batteries*, Electrochemical Society, 1999, Vol. 99-25, p. 257.
- [4] M.C. Smart, B.V. Ratnakumar, S. Surampudi, *J. Electrochem. Soc.* 146 (1999) 486.
- [5] G. Nagasubramanian, R.G. Jungst, *J. Power Sources* 72 (1998) 189.
- [6] G. Nagasubramanian, R.G. Jungst, D.H. Doughty, *J. Power Sources* 83 (1999) 193.
- [7] G. Nagasubramanian, *J. Power Sources* 87 (2000) 226, and references therein.
- [8] G. Nagasubramanian, A. Attia, G. Halpert, *J. Appl. Electrochem.* 24 (1994) 298.
- [9] H.S. Choe, J. Giaccai, M. Alamgir, K.M. Abraham, *Electrochem. Acta* 40 (1995) 2289.



ELSEVIER

Journal of Power Sources 96 (2001) 33–38

JOURNAL OF  
POWER  
SOURCES

www.elsevier.com/locate/jpowersour

# Evolution of power sources for implantable cardioverter defibrillators

Ann M. Crespi, Sonja K. Somdahl, Craig L. Schmidt, Paul M. Skarstad\*

Medtronic, Inc., 6700 Shingle Creek Parkway, Minneapolis, MN 55430, USA

Received 18 December 2000; accepted 18 December 2000

## Abstract

The evolution of seven generations of power sources for implantable cardioverter defibrillators (ICD) is presented. The packaging efficiency of the power sources has steadily increased, resulting in smaller, lighter batteries while maintaining the required electrical characteristics. The main areas for improvement were reduction of headspace volume, reduction of separator volume, and a change from a two-cell battery to a single cell. © 2001 Published by Elsevier Science B.V.

**Keywords:** Applications/medical defibrillators; Lithium/silver vanadium oxide batteries

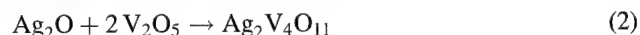
## 1. Introduction

Implantable cardioverter defibrillators (ICDs) are devices that treat very fast, and potentially lethal, cardiac arrhythmias. Implanted in the chest, these devices continuously monitor the heart's electrical signals and sense when the heart is beating dangerously fast. Within about 5–10 s, they deliver one or more electric shocks to return the heart to a normal rhythm. These shocks may range from a few microjoules to very powerful shocks of 25–40 J. The ICD is also capable of delivering continuous low-energy stimuli like a cardiac pacemaker.

The ICD battery must meet stringent requirements. To charge the capacitors that deliver the defibrillation shock, the battery must be capable of delivering about 50 J within about 5–10 s. A high-area electrode design is needed to meet this requirement. The battery must also deliver a continuous low current drain on the order of microamperes, and last for about 5–10 years. The performance of the battery must be highly predictable so that there is adequate warning before it is depleted. Finally, the battery must be very small so the ICD can be as small and comfortable as possible. Typical requirements for batteries for ICDs appear in Table 1.

Lithium/silver vanadium oxide batteries provide the high power, high energy density, and long-term stability required for ICDs and are the only type of battery used in ICDs today. They were invented about 20 years ago, and have continuously improved since then [1–14]. There are two distinct types of silver vanadium oxide (SVO) in use today. DSVO is

synthesized at about 380°C by the decomposition reaction in Eq. (1) [1,2]. CSVO is synthesized at about 500°C by the simple combination reaction shown in Eq. (2) [3].



Lithium/SVO batteries have a distinctive discharge curve with two plateaus, one at 3.24 V and another at 2.6 V. Fig. 1 shows the open-circuit voltage and area-normalized internal resistance of  $\text{Li/Li}_x\text{Ag}_2\text{V}_4\text{O}_{11}$  as a function of  $x$  (using CSVO). Studies have shown that between  $x = 0$  and 2 metallic silver appears in the CSVO cathode [15,16]. The appearance of metallic silver is associated with a decrease in the internal resistance of a Li/CSVO cell, as seen in Fig. 1. In this paper, the composition  $\text{Li}_6\text{Ag}_2\text{V}_4\text{O}_{11}$  will be considered as the fully discharged material. This composition corresponds to reduction of  $\text{Ag}^+$  to  $\text{Ag}^0$  and reduction of  $\text{V}^{5+}$  to  $\text{V}^{4+}$ . In order to maintain low times for charging the output capacitors of an ICD in practical use, batteries are not generally discharged to this degree of lithiation.

Until recently all ICDs were powered by two cells connected in series, doubling the voltage shown in Fig. 1. The circuitry used to power the device and to charge the capacitors has been improved so that many ICDs are now powered by a single cell. This change has greatly reduced the volume of the battery by reducing the volume of encasement material and other inactive components.

Two mechanical configurations have been described previously for Li/SVO batteries used in ICDs, one consisting of a multi-plate cathode and a lithium metal anode wound through the multi-plate cathode in a serpentine manner [6],

\* Corresponding author.

E-mail address: paul.skarstad@medtronic.com (P.M. Skarstad).

Table 1  
Requirements for batteries for implantable cardioverter–defibrillators

Battery requirement	Comments
Power	Must be capable of operating for several years at a background power of 50–100 $\mu$ W. In addition, must be capable of delivering 50–70 J pulses at a power greater than 4–10 W at any time on demand without delay
Energy	Typically about 20 kJ (5.56 Wh)
End-of-service indicator	A measurable battery parameter, such as voltage or resistance which indicates the need to replace the device
Size	Minimum size is required for ease of implant and patient comfort
Predictability	Long-term performance must be readily predictable from short-term data in order to project device longevity accurately
Reliability	The highest possible reliability is required for this life-saving application
Safety	The highest possible level of safety is required to protect the patient and medical personnel as well as manufacturing personnel who handle batteries

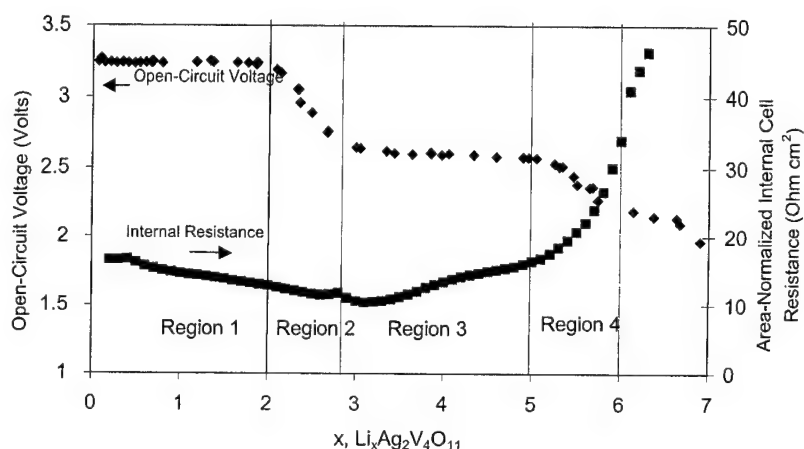


Fig. 1. Open-circuit potential and internal dc resistance of  $\text{Li}_x\text{Ag}_2\text{V}_4\text{O}_{11}$  (Li/CSVO) battery as a function of the extent of lithiation,  $x$ . The discharge curve is divided into four regions, where Region 1 is flat and extends from  $x = 0$  to 2; Region 2 slopes and extends from  $x = 2$  to 3; Region 3 is flat and extends from  $x = 3$  to 5; Region 4 slopes and extends from  $x = 5$  to 6.

the other consisting of a coiled electrode design. The designs described in this paper are all based on the coiled electrode configuration. Single strips of anode and cathode are wound into a flattened coil and inserted into a prismatic case.

A materials balance design model for high-rate, liquid electrolyte primary lithium batteries has been described [17]. This model consists of four equations that define the volumetric constraint, the electrode balance, the electrolyte requirement and the electrode loading. Solving the equations using matrix methods gives the anode and cathode capacities, the volume of electrolyte, and the dimensions of the electrodes. The lithium/CSVO batteries described in this paper, constructed according to this materials balance model, show consistent, predictable performance from design to design, despite wide variation in battery capacity, electrode loading and current density. A predictive model of battery voltage and resistance has been developed for these batteries [18].

### 1.1. Battery construction-general

Batteries were assembled in hermetically sealed stainless steel cans with a lithium metal anode and an electrolyte consisting of 1 M  $\text{LiAsF}_6$  in a 1:1 mixture by volume of

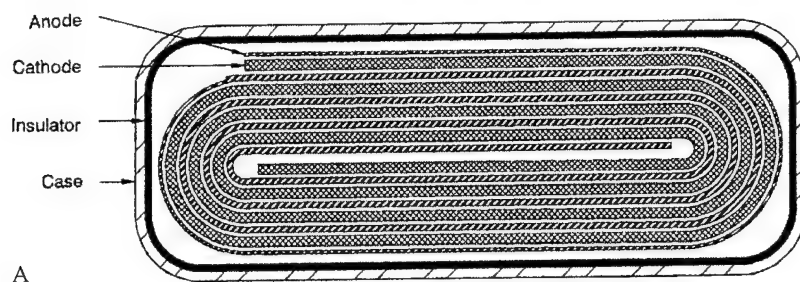
propylene carbonate and 1,2-dimethoxyethane. The shape of the cans was usually a rectangular prism, but in Design VI one end of the cell was given a full radius, resulting in a “mailbox” shape. The cathodes were fabricated by mixing silver vanadium oxide ( $\text{Ag}_2\text{V}_4\text{O}_{11}$ ) with carbon and polytetrafluoroethylene then pressing onto a titanium mesh current collector [6]. The anodes were lithium metal pressed onto a nickel current collector. The anode and cathode were each encased in polypropylene separator, giving two layers of separator between the electrodes. The feedthrough consisted of a niobium wire within Ta23 glass. CSVO was synthesized as described in [1–3]. In all cell designs, the electrodes were wound together in a flattened coil. The designs were all case-negative. The electrode capacities, electrolyte volume, and electrode dimensions for each battery were calculated using the method in [18].

## 2. Design variants and their evolution

### 2.1. General description of design

The design of the ICD batteries is depicted in Fig. 2A and B. Fig. 2A is a cross-sectional view of the battery showing





A



B

Fig. 2. A cross-section view of the coiled electrode configuration (A). An assembly view of a typical battery with the cover and electrode coil partially removed showing the attachments in the headspace (B).

the coiled electrodes. The electrodes are wound into a flattened coil that fits the dimensions of the rectangular prismatic case. The polypropylene separator, which encases both electrodes, is not shown in this figure. Fig. 2B is an assembly view showing the connections of the electrodes to the feedthrough and case. The titanium current collector of the cathode is welded to the niobium feedthrough pin. The feedthrough is insulated with Ta23 glass. The nickel current collector of the anode is welded to the case wall. The case is lined with an insulator, except in areas close to the case-to-cover weld and the weld of the anode current collector to the case. The space between the top of the coil and the inside of the cover is termed the headspace. This volume is used to make connections to the electrodes while keeping features of

opposite polarity insulated from each other. The shapes of the batteries are illustrated in Fig. 3. Characteristics of seven designs are shown in Table 2.

The designs progress chronologically from left to right, showing improvements in volumetric efficiency with time. For medical devices such as the ICD, volumetric efficiency is considered more important than gravimetric efficiency, provided the device does not become unreasonably heavy. Therefore, this discussion will focus on volume rather than mass. The maximum power was calculated by equating the internal resistance of the battery and the resistance of the external load. This power is the instantaneous maximum power. It has been reported that under some conditions concentration polarization will reduce the available the

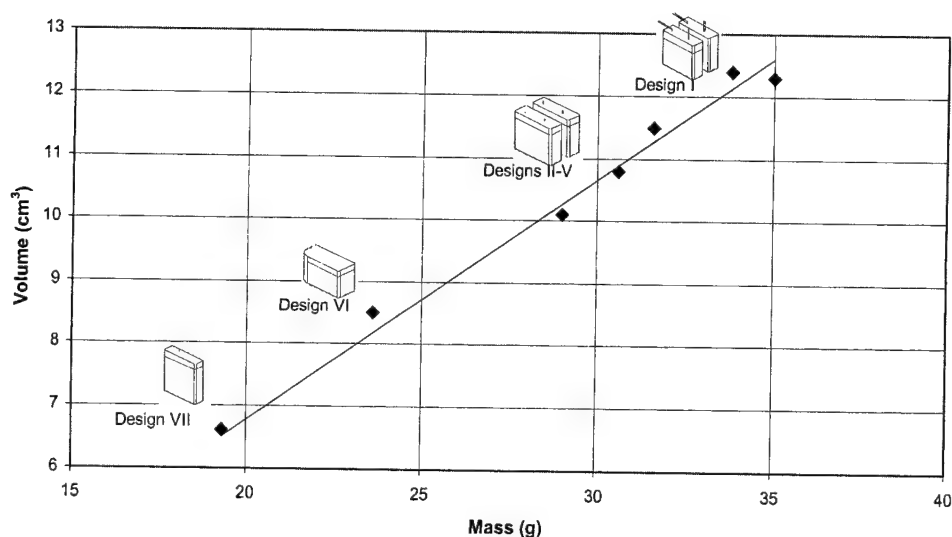


Fig. 3. The relationship between battery volume and mass with drawings of battery shapes. The solid line is a linear regression with an adjusted  $R^2$  of 0.983; intercept:  $-1.0 \text{ cm}^3$ ; slope:  $0.388 \text{ cm}^3 \text{ g}^{-1}$ .

Table 2  
Characteristics of the designs of seven defibrillator batteries<sup>a</sup>

Design	I	II	III	IV	V	VI	VII
External volume per battery ( $\text{cm}^3$ )	12.4	11.5	10.1	12.3	10.8	8.5	6.6
Mass per battery (g)	33.8	31.6	29.0	35.0	30.6	23.6	19.3
Capacity per cell (Ah)	0.93	0.92	0.092	1.15	1.04	1.77	1.35
Maximum power, zero discharge (W)	16.5	16.3	12.3	15.8	10.8	11.6	11.8
Gibbs energy density ( $\text{mWh cm}^{-3}$ or $\text{Wh dm}^{-3}$ )	427	454	515	531	549	590	579
Energy delivered to charge defibrillation capacitors (J)	70	70	58	70	50	65	58
Volumetric efficiency of utilized active components (%)	19.0	20.2	22.9	23.6	24.4	26.2	25.7
Volume of separator (inc. pores) as percentage of total volume (%)	23.1	23.8	21.8	22.6	19.0	21.5	8.5
Headspace (cm)	0.56	0.33	0.33	0.33	0.33	0.31	0.44
Cells per battery	2	2	2	2	2	1	1
Total separator thickness between electrodes (mm)	0.18	0.18	0.18	0.18	0.18	0.18	0.05

<sup>a</sup> Theoretical capacity is defined to a cathode composition of  $\text{Li}_6\text{Ag}_2\text{V}_4\text{O}_{11}$ .

power [19]. However, the effects of concentration polarization are not expected to differ much between battery designs, so the maximum instantaneous power is a valid point of comparison. Full discharge is defined as a cathode composition of  $\text{Li}_6\text{Ag}_2\text{V}_4\text{O}_{11}$ .

## 2.2. Reduction in volume of the headspace

The height of the headspace is measured as the distance between the top of the electrode coil to the inside surface of the cover. Design II was nearly identical to Design I, except the height of the headspace was reduced from 5.6 to 3.3 mm and the overall height of the battery was reduced accordingly. The volume of the battery was reduced by 7%. Design IV has nearly the same external dimensions as Design I, but height of the electrodes was increased to fill more of the headspace. The length of the electrodes was decreased to keep the electrode area nearly the same, and the loading was increased. The Gibbs energy density increased by 24% while

the power was only slightly reduced. Design III was designed for an ICD with lower-energy defibrillation capacitors. It has thicker electrodes with less area, resulting in lower power and higher Gibbs energy density. Design V was designed to charge even lower energy defibrillation capacitors, so it has further reduced power and increased energy density. The height of the headspace was increased slightly in Design VII due to geometric constraints of this particular design.

## 2.3. Progression from two cell to single cell design

For Designs I–V, all of the batteries consisted of two cells in series. After Design V, advances in the ICD circuitry for charging the defibrillation capacitors made it possible to use a single cell rather than two cells in series. The volumetric efficiency increased substantially in Design VI, a single cell battery, because less packaging material is needed for one cell compared to two cells. The electrode area and capacity

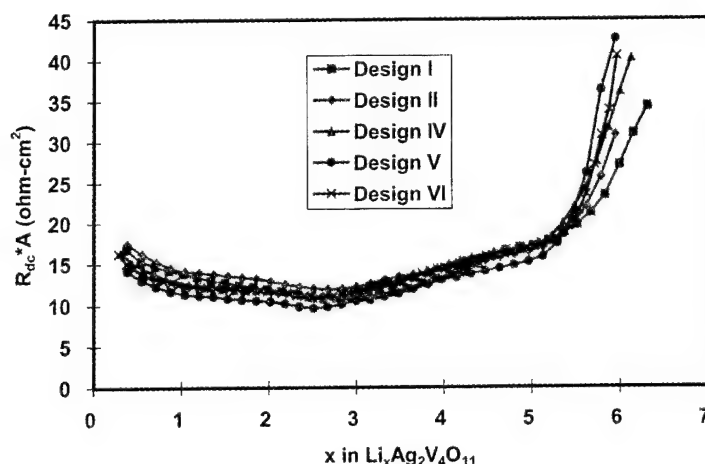


Fig. 4. Area-normalized dc resistance ( $R_{dc}$ ) as a function of degree of cathode lithiation for five of the battery designs. The resistance is calculated from the drop in voltage during a high current pulse using Ohm's law and normalized using the two-sided cathode area. The batteries were discharged on a low current drain for 1 year with a series of four high-current pulses applied every month. The  $R_{dc}$  was calculated using the voltage drop during the fourth pulse in each series. The data points displayed are interpolated for purposes of averaging data.

was increased by about 50% in the single-cell design compared to a two-cell battery.

#### 2.4. Reduction in volume of the separator

In Designs I–V, the separator, including pores, occupied 19–24% of the total volume of the battery (see Table 2). After reducing the volume of the headspace and changing to a single-cell battery it was clear that the volume of separator material must be reduced if the volume of the battery was to be reduced much more. In Design VII, the thickness of the separator was reduced from 0.09 to 0.025 mm per layer. When this change was made, the manufacturing line was moved to a clean room and processes were improved to prevent shorting across the thinner separator by foreign material. Burn-in and acceptance tests were changed to ensure detection of latent short-circuits which may occur when an oxidizable metal particle is present on the cathode. Production batteries were sampled frequently from the line, opened, and is inspected for evidence of foreign materials. The volume occupied by the separator was reduced to about 8% of the total volume of the battery.

### 3. Electrical and mechanical characteristics

The relationship between mass and volume for the battery designs is illustrated in Fig. 3. This graph shows that in spite of the many design changes, there is an excellent correlation between mass and volume. The average gravimetric density of the batteries is  $2.85 \text{ g cm}^{-3}$ . Finally, the electrical characteristics of this family of batteries remain consistent over the full range of designs with wide variation in electrode capacity, electrode loading and pulse-current density. Fig. 4 shows the area-normalized resistance versus degree of lithiation for five of the battery designs. Consistency of

design approach, embodied in the materials balance design model, helps to ensure scaleable battery performance. Despite the many variations in design, battery resistance remains scaleable by electrode area if battery capacity is presented as degree of lithiation.

### 4. Conclusions

Batteries for implantable defibrillators have been continually improved over time, resulting in lower volume, higher energy density, lower charging times and better packaging efficiency. These improvements have resulted in superior performance and smaller volumes for these devices.

### References

- [1] C.C. Liang, M.E. Bolster, R.M. Murphy, US Patent 4,310,609 (1982).
- [2] C.C. Liang, M.E. Bolster, R.M. Murphy, US Patent 4,391,729 (1983).
- [3] A.M. Crespi, US Patent 5,221,453 (1993).
- [4] P.P. Keister, R.T. Mead, B.C. Muffoletto, E.S. Takeuchi, S.J. Ebel, M.A. Zelinsky, J.M. Greenwood, US Patent 4,830,940 (1989).
- [5] P.P. Keister, R.T. Mead, B.C. Muffoletto, E.S. Takeuchi, S.J. Ebel, M.A. Zelinsky, J.M. Greenwood, US Patent 4,964,877 (1990).
- [6] W.G. Howard, R.W. Keim, D.J. Weiss, A.M. Crespi, F.J. Berkowitz, P.M. Skarstad, US Patent 5,439,760 (1995).
- [7] E.S. Takeuchi, M.A. Zelinsky, P. Keister, in: Proceedings of the 32nd Power Sources Symposium, 1986, p. 268.
- [8] P.M. Skarstad, in: Proceedings of the 12th Annual Battery Conference on Applications and Advances IEEE 97Th8226, 1997, p. 151.
- [9] C.F. Holmes, P. Keister, E.S. Takeuchi, Prog. Batt. Solar Cells 6 (1987) 64.
- [10] E.S. Takeuchi, P. Piliero, J. Power Sources 21 (1987) 133.
- [11] W.C. Thiebolt III, E.S. Takeuchi, Abstract 20, p. 29, The Electrochemical Society Extended Abstracts, Vol. 87-2, Honolulu, HI, October 18–23, 1987.

- [12] E.S. Takeuchi, W.C. Thieboldt III, *J. Electrochem. Soc.* 135 (1988) 2691.
- [13] A.M. Crespi, P.M. Skarstad, *J. Power Sources* 43/44 (1993) 119.
- [14] A.M. Crespi, F.J. Berkowitz, R.C. Buchman, M.B. Ebner, W.G. Howard, R.E. Kraska, P.M. Skarstad, in: A. Attewell, T. Keily (Eds.), *Power Sources*, Vol. 15, International Power Sources Committee, Leatherhead, UK, 1995, p. 349.
- [15] A.M. Crespi, P.M. Skarstad, H.W. Zandbergen, *J. Power Sources* 54 (1995) 68.
- [16] K. West, A.M. Crespi, *J. Power Sources* 54 (1995) 334.
- [17] P.M. Skarstad, A.M. Crespi, C.L. Schmidt, D.F. Untereker, in: A. Attewell, T. Keily (Eds.), *Power Sources*, Vol. 14, International Power Sources Committee, Leatherhead, UK, 1993, p. 167.
- [18] A.M. Crespi, C.L. Schmidt, J. Norton, K. Chen, P.M. Skarstad, *J. Electrochem. Soc.*, 148 (2001) A30–A37.
- [19] J.D. Norton, C.L. Schmidt, *Electrochemical Society Proceedings*, Vol. 97-18, (1997, Pennington, N.J.) pp. 389–393.

## Abstract

## Advances in aviation battery systems technology

John K. Erbacher<sup>\*</sup>*Air Force Research Laboratory, AFRL/PRPS, 1950 Fifth Street, Building 18G, Wright-Patterson AFB, OH 45433-7251, USA*

---

**Abstract**

New aircraft battery systems have almost exclusively changed over to a "maintenance-free" concept and older systems in service are transitioning from the vented high maintenance batteries that were prominent 20 years ago. In addition, new chemistries for aviation batteries, such as nickel/metal hydride and lithium-ion are in the development phase with transitions to operational systems projected within the next 3–5 years.

Charger and transformer/rectifier (T/R) electronic units are becoming more sophisticated ("intelligent") to function with the tighter controls needed for the advanced chemistries in development. Statistical data are presented on the transition to a maintenance-free aviation fleet.

Details on current developments of new chemistries and chargers, also T/R units will be presented along with some projections of where aviation battery system technology is heading over the next decade. © 2001 Published by Elsevier Science B.V.

**Keywords:** Applications/aircraft; Lithium ion batteries; Nickel/metal hydride batteries; Chargers/change control

---

---

<sup>\*</sup> Tel.: +1-937-255-7770; fax: +1-937-656-7529.

E-mail address: [john.erbacher@wpafb.af.mil](mailto:john.erbacher@wpafb.af.mil) (J.K. Erbacher).

# Development of true prismatic lithium-ion cells for high rate and low temperature applications

Frank Puglia\*, R. Gitzendanner, C. Marsh, T. Curran

*Lithion Inc., Pawcatuck, CT 06379, USA*

Received 9 January 2001; accepted 11 January 2001

---

## Abstract

Lithium-ion cells are presently being considered for use in a wide range of aerospace applications. Cells for these aerospace applications, such as F-16 and JSF aircraft, are required to operate at rates up to 15 C and at temperatures from  $-40$  to  $71^{\circ}\text{C}$ . To address these requirements, a series of experiments has been undertaken to empirically determine those factors that limit performance. The first experiment compares three different electrode weight loadings and two different anode particle sizes. A chemistry identified from this experiment was able to increase room temperature rate capability by  $>500\%$ . Pulse discharge rates as high as 70 C and continuous discharge rates of 20 C were demonstrated. Furthermore, cell performance of 1 C at  $-40^{\circ}\text{C}$  and 4 C at  $-30^{\circ}\text{C}$  has been demonstrated.

A second experiment evaluated the use of non-solid/electrolyte interface (SEI) forming conductive diluents in the anode. This experiment did not identify any advantages to the conductive diluent at temperatures above  $-20^{\circ}\text{C}$ . However, at a discharge rate of 1 C at  $-40^{\circ}\text{C}$ , the group with the highest level of diluent offers 300% more capacity than the baseline experimental group with no non-SEI forming diluent.

© 2001 Published by Elsevier Science B.V.

**Keywords:** Lithium-ion batteries; Electrolytes/non-aqueous

---

## 1. Introduction

The majority of research performed in the advancement of lithium-ion chemistry has concentrated on improving aspects of performance for commercial applications such as cellular phones and laptop computers. These devices typically operate at moderate temperatures and rates. In such applications, the primary goal has been to maximize capacity through improvements in the specific capacity of the active materials. However, for some applications it is not the capacity of the battery that is the limiting factor. Specifically, for several aerospace applications the driving force in the sizing of a proposed battery has not been the total energy required, but rather the high discharge power. Batteries with 2–20 times the total required energy, and thus, size have been necessary to support the power requirements.

Whenever the discharge rate, and not the actual rated capacity, drives the cell design, those chemistry changes that may reduce capacity, but increase rate capability, are being evaluated.

The first experiment presented in this paper compares anode particles of 6  $\mu\text{m}$  average size to those with an average size of 10  $\mu\text{m}$ . In addition, several other experimental lots that varied the ratio of anode material to cathode material were constructed. A second experiment evaluated the use of very high amounts of silver powder as a conductive diluent in the anode. The specific selection of these first two experiments was based on previous work [1] done by Lithion in the evaluation of candidate chemistries for the MSP01 Mars Lander program. The results presented in this paper are a continuation of the work presented at the San Diego SAE meeting in November 2000 [2].

## 2. Experimental

For both experiments discussed in this paper the cells were constructed using a true prismatic design with a nominal capacity, for the baseline chemistry, of approximately 7 Ah. The baseline chemistry is that which was developed and qualified for the MSP01 Mars Lander battery. In order to minimize experimental variation, all cells within each experiment used cathodes and anodes that came from the same slurry mix. All electrode coating was also per-

---

\* Corresponding author. Tel.: +1-860-599-1100; fax: +1-860-599-3903.  
E-mail address: fjpuglia@yardney.com (F. Puglia).

formed on the same day. For both experiments, all of the cells used the ternary electrolyte, 1 M LiPF<sub>6</sub> in 1:1:1 EC:DMC:DEC, utilized for the Mars 2001 Lander project. All electrical testing on the cells was also performed concurrently, with all cells on the same test system and in the same temperature chamber. The only exception to this was the very high rate cycling for which there were insufficient channels to test all of the cells concurrently.

The first experiment evaluated three different electrode weight loadings. The electrode weight loadings were equally spaced and are referred to as *Medium*, *Low*, and *Very Low*. In addition, two different MCMB particle sizes were evaluated: 6 and 10  $\mu\text{m}$ . This portion of the experiment was fully factorial so all electrode weight loadings were evaluated at both anode particle sizes for a total of six experimental lots. All experimental lots consisted of three individual cells. This first experiment also evaluated the effect of varying the ratio of anode to cathode materials. Specifically, increased ratios of anode to cathode were varied up to approximately twice the baseline ratio. This latter portion of the experiment was added in to evaluate the hypothesis that the anode SEI layer is the limiting factor in low temperature discharge performance. By having “extra” anode, the current density through the anode SEI would be decreased by a factor commensurate with the amount of “extra” anode.

Also based upon previous work performed at Lithion, a second experiment was conducted to evaluate the use of a new type of conductive diluent in the anode. While carbon diluents have been evaluated in the past, these materials still form an SEI layer that somewhat reduces their surface electrical conductivity. Low levels of silver have reportedly [3] been added to the anode by several manufacturers. The major difference is that the quantity of silver used in this experiment was as much as 25,000% higher than levels reported in other manufacturers’ cells. At these levels, some degree of alloying is expected. In this experiment, silver

powder was added to the anode slurry during the mixing operation. Since the performance of carbon diluents is a function of particle size, as well as other aspects, the same was assumed to be true for the silver diluent. Thus, three different silver particle sizes were evaluated. The smallest size was evaluated at three levels while the two larger particle sizes were evaluated only at the central level. A baseline lot, containing no silver, was also constructed. As with the other experiment presented in this paper, three cells per experimental lot were constructed.

### 3. Results and discussion

For reference, some of the initial results, presented previously, are given below. The majority of the discussion concerning the first experiment is centered on Lot 1 through Lot 6. The layout of these lots is given in Table 1. Fig. 1 shows how the cell capacity varied with electrode weight loading. The capacities shown in Fig. 1 are those used to determine the C rate of cells. In most tests, however, the cells were cycled at the same current, regardless of initial capacity. This latter situation more closely resembles the real world requirements to which the cells would be exposed.

Since the cell dimensions were held constant, and not cell capacity or electrode surface area, the lower weight loadings have lower capacity and higher electrode surface area. The capacity drop from the medium weight loading to the low weight loading is approximately 8%. The capacity drop

Table 1  
Experiment layout

	10 $\mu\text{m}$ anode	6 $\mu\text{m}$ anode
Medium loading	Lot 1	Lot 4
Low loading	Lot 2	Lot 5
Very low loading	Lot 3	Lot 6

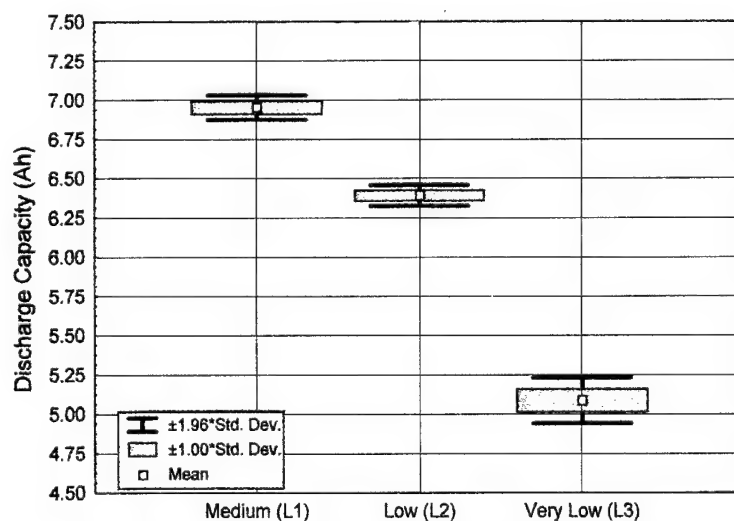


Fig. 1. Capacity at the C/10 discharge rate for the three weight loadings.

Table 2  
Lots 1–6<sup>a</sup>

	Cathode surface area (cm <sup>2</sup> )	Cell mass (g)
Lots 1 and 4	2700	220
Lots 2 and 5	3500	218
Lots 3 and 6	5700	228

<sup>a</sup> Cell masses and surface areas.

from the low weight loading to the very low weight loading is approximately 18%. Both of these values are in excellent agreement with the theoretical capacities based upon equally sized reductions in loading between the lots. The surface areas and cell masses for first six lots, those in which the ratio of anode to cathode material was held constant, are given in Table 2.

A 25°C voltage profile for a discharge rate of 20 A is given in Fig. 2. Since all cells were discharged at the same rate, the 20 A discharge rate corresponds to between 3 and 4 C, depending on the specific lot. The current density is approximately 7 mA cm<sup>-2</sup> for the medium weight loading, 6 mA cm<sup>-2</sup> for the low weight loading, and <4 mA cm<sup>-2</sup> for the very low weight loading. As can be seen in Fig. 2, the lighter weight loadings do not offer any advantage in capacity even up to the 3–4 C discharge rate.

A full statistical analysis of the results at 20 A reveals that the discharge capacity is a strong function of weight loading (*P*-value approaching 0) with the heavier loadings being preferred. However, when either average voltage or energy efficiency is evaluated, the lots with the lighter weight loadings offer statistically significant improvements.

Fig. 3 shows a marginal means plot, with a 95% confidence interval, that shows the lots with the highest weight loadings have a 33% lower energy efficiency. This implies that the lighter weight loading cells would be of interest for very large cells, if heat generation needed to be minimized.

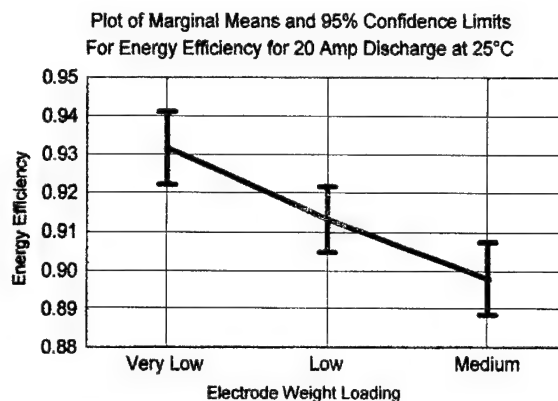


Fig. 3. Energy efficiency for 20 A discharge from the three different weight loadings.

Fig. 4 shows a rate capability plot for the MSP01 Mars Lander cells. This testing was performed at 25°C. This figure shows acceptable performance up to a 5 C discharge rate.

This is well above what is typically obtainable from commercially available cells. In-house testing revealed that

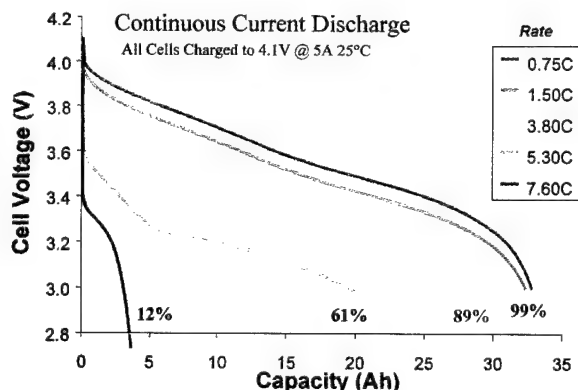


Fig. 4. Discharge capability of baseline chemistry.

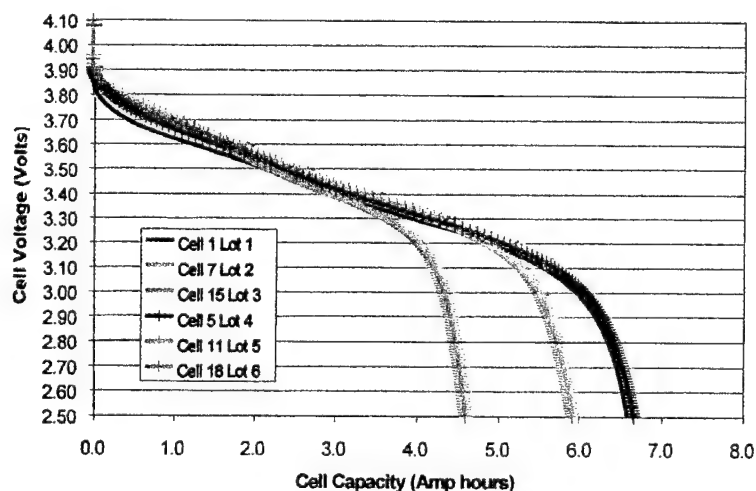


Fig. 2. Voltage profiles for 20 A discharges at 25°C. Highest (Ah): Lots 1 and 4; lowest (Ah): Lots 3 and 6.



the best commercial cells had acceptable performance at discharge rates up to 2.5 C.

Fig. 5 shows the discharge voltage profile for the six lots when subjected to a 50 A continuous discharge between a 7 and 10 C discharge rate, depending on the experimental lot. The current densities are  $18 \text{ mA cm}^{-2}$  for the medium weight loading cells,  $14 \text{ mA cm}^{-2}$  for the low weight loading cells and only  $9 \text{ mA cm}^{-2}$  for the very low weight loading cells. In comparing Figs. 4 and 5, there is excellent agreement between the MSP01 cells and the control cells (Lot 1) constructed with the same chemistry. Both cells show approximately 15% capacity for a 7 C ( $18 \text{ mA cm}^{-2}$ ) load.

Fig. 5 clearly shows that the weight loading is the most significant factor in obtaining high discharge rates at  $25^\circ\text{C}$ . The experimental lots with the  $6 \mu\text{m}$  cells showed only marginally improved performance compared to their  $10 \mu\text{m}$  counterparts. When the Lot 6 cells were subjected

to a  $18 \text{ mA cm}^{-2}$  continuous discharge load, the cells did not perform as would be expected given the performance of the Lot 1 and Lot 4 cells at this current density. Based upon Fig. 5, the anticipated capacity above 2.7 V would be only 15%. The 13 (75 A) and  $18 \text{ mA cm}^{-2}$  (100 A) results are shown in Fig. 6.

The Lot 6 cells, at a discharge current density of  $18 \text{ mA cm}^{-2}$ , or 100 A, delivered in excess of 85% of initial capacity. The true fraction of capacity is somewhat higher since over 200 “other” cycles had occurred after the initial capacity value of 4.9 Ah was determined. A value  $>90\%$  is more appropriate. The comparable continuous discharge current density of  $18 \text{ mA cm}^{-2}$  for the baseline chemistry and the Lot 6 cells clearly shows that the Lot 6 chemistry is not limited to the same current density as the baseline cells. This is a result of the decreased electrode thickness with the lighter weight loadings. A useful comparison tool is to

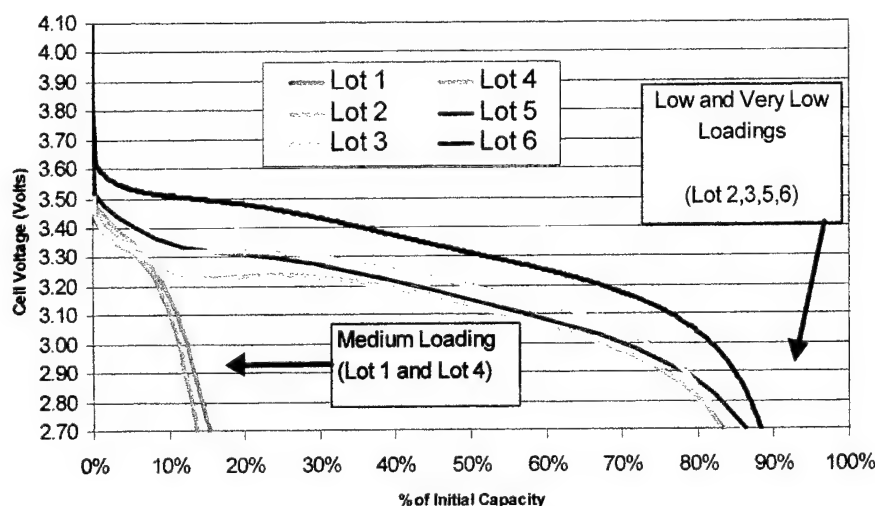


Fig. 5. Voltage profiles for 50 A discharges at  $25^\circ\text{C}$  from the six lots.

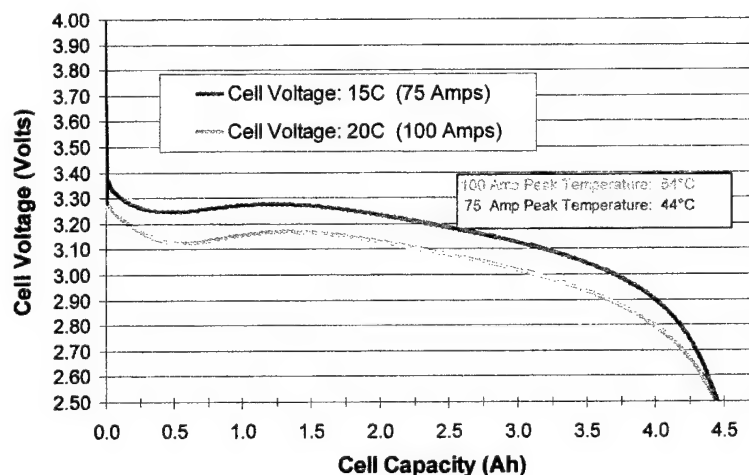


Fig. 6. Voltage profiles for 75 and 100 A continuous discharges.

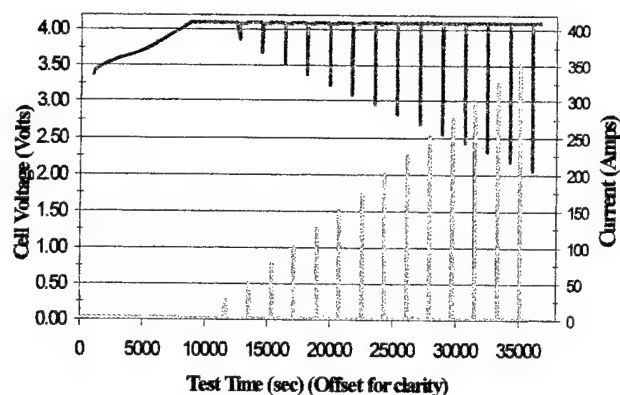


Fig. 7. The 0.100 s discharge pulses at 25°C.

calculate the distance between the center of the cathode coating and the center of the anode coating for each experimental lot. This gives an average distance between the 50% capacity points. The mean diffusion distance for the medium weight loading cells is 2.2 times that of the very low weight loading cells. Thus, because the mean ionic diffusion path is much shorter for the lighter weight loading cells, they are not limited to the same current density. Due to cell construction limitations, continuous discharge testing at rates above 100 A was not viable. Future constructions will incorporate larger terminals and other mechanical improvements aimed at increasing the current carrying capability.

In addition to continuous discharge testing, extensive pulse discharge testing was completed. For brevity, only an analysis of the very low weight loading cells, with the 6  $\mu\text{m}$  anode particles, is presented. Fig. 7 shows the voltage for 0.100 s pulses at various currents.

For clarity on the figure, the voltage is slightly offset in time. The current level in the discharge pulses ranged from 2 (10 A) to 62  $\text{mA cm}^{-2}$  (350 A). These pulses translate into specific energy and energy density values of 3200  $\text{W kg}^{-1}$

and 7200  $\text{W dm}^{-3}$ . If a more gravimetrically and volumetrically efficient cell hardware, such as that for the MSP01 Mars Lander, were used, the same chemistry would easily provide 3700  $\text{W kg}^{-1}$  and 9000  $\text{W dm}^{-3}$ .

The Lot 6 cells were also subjected to a 0.150 s, 150 A pulse at 25°C. During this pulse, the cells were connected to high-speed data recording equipment. Voltage and current data was recorded every 2  $\mu\text{s}$ . By performing this test, the portions of the total polarization attributable to ionic polarization and ohmic polarization can be determined. For this specific pulse, it is estimated that 55% of the polarization is ohmic while 45% is ionic. A summary chart of the results of this test is shown in Fig. 8. Longer duration pulse testing confirmed that the slope of the voltage near the end of the pulse continues to plateau. Thus, for very high rate pulses of even relatively long duration, large improvements are available in both ionic and ohmic related polarization.

Low temperature testing was also conducted on the cells. Both continuous and pulse discharges were evaluated. For brevity, only the continuous discharges are presented in this paper. Fig. 9 shows a discharge voltage profile comparison for a 2.5 A discharge at  $-40^\circ\text{C}$ . These cells were charged at  $-40^\circ\text{C}$ . The figure shows that although the best lot offers twice the capacity of the worst lot, over 80% of the polarization is still present. Of the 20% of the polarization that has been eliminated, only a very small portion is related to the weight loading. Thus, if the electrolyte were responsible for the majority of the polarization, the decrease in bulk ionic current density between the electrodes by a factor of two should have halved the polarization. Instead only a small decrease in polarization is observed suggesting that the electrolyte is not responsible for the main portion of the total polarization at these conditions. This trend exists, to lessening degrees, through the  $-10^\circ\text{C}$  discharge tests that were conducted. However, this trend is the opposite of the result for the 25°C high rate testing. In the very high rate testing at 25°C, the weight loading effect dominated the

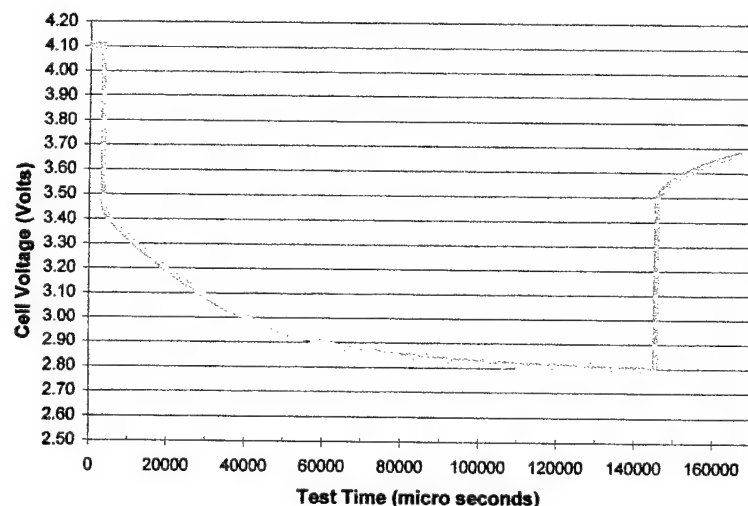


Fig. 8. The 0.150 s, 150 A pulse at 25°C.

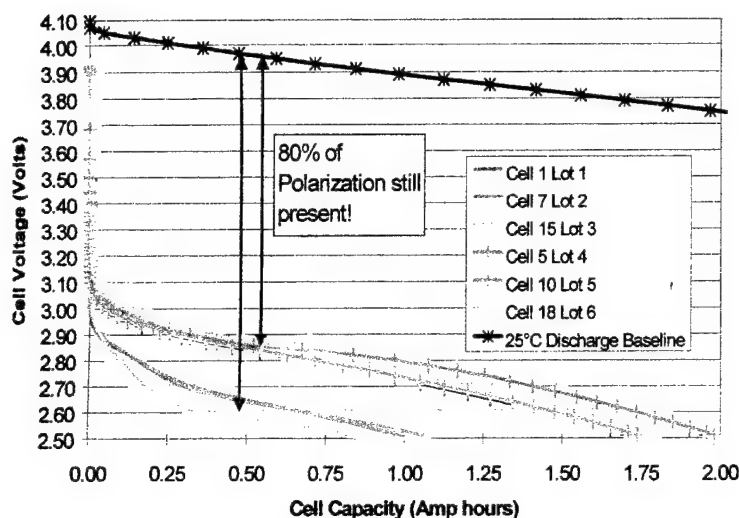


Fig. 9. The 2.5 A discharges at  $-40^{\circ}\text{C}$ , showing better capacities from Lots 4–6.

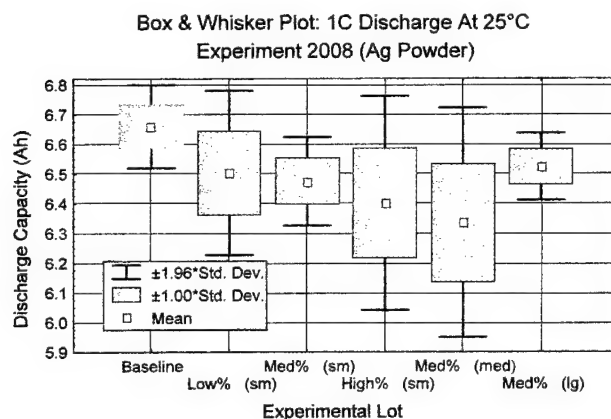


Fig. 10. 1 C discharge capacity at  $25^{\circ}\text{C}$  of cells with anodes containing three different amounts of silver powder in three particle sizes.

polarization. Thus, the rate limiting mechanism is temperature dependant.

A second experiment, to improve high rate and low temperature performance is also underway. As described previously, this experiment involves the doping of the anode with very high amounts of silver. The preliminary results at both 25 and  $-40^{\circ}\text{C}$  are shown in Figs. 10 and 11, respectively. All of these cells are constructed with the medium weight loading and  $10\text{ }\mu\text{m}$  anode particles. The experiment contains a baseline lot with the MSP01 Mars Lander chemistry. This is also the same chemistry as was used in Lot 1 of the previous experiment. Fig. 10 shows that the addition of silver, in large quantities, depresses the  $25^{\circ}\text{C}$  discharge capacity. This may be due to an unfavorable alloying of the lithium with the silver.

In Fig. 10, three levels of silver are compared: Low, Medium and High %. In addition, three silver particle sizes are evaluated: small (sm), medium (med), and large (lg). For clarity, Fig. 11 shows only the results for the first four lots at a rate of 1 C and a temperature of  $-40^{\circ}\text{C}$ .

While the lot with the least amount of silver doping shows a slight depression in performance, the lot with highest amount of silver doping shows three times the capacity of

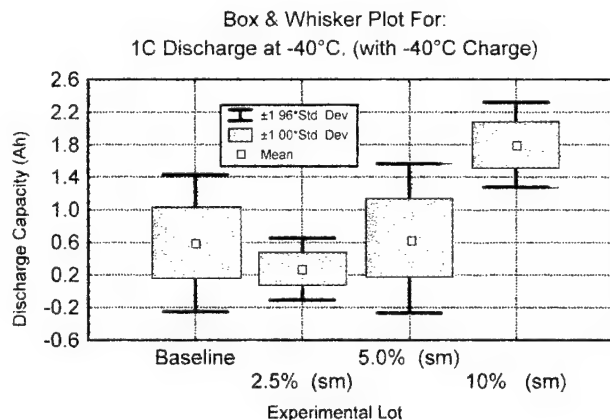


Fig. 11. 1 C discharge capacity at  $-40^{\circ}\text{C}$  of cells with anodes containing three different amounts of silver powder of the small particle size.

the baseline lot. The results of the discharge energy are even more dramatic indicating a slightly higher operating voltage for the silver doped lots.

#### 4. Summary

The results of the two experiments presented in this paper show large improvements in lithium-ion performance at both high rates and low temperatures. The most dramatic improvement is the ability of the Lot 6 cells to deliver over 90% of their capacity, above 2.7 V at a 20 C discharge rate. In addition, discharge rates as high as 4 C at  $-30^{\circ}\text{C}$  have been demonstrated. The first experiment reveals the individual effects from the anode particle size and the weight loading. Thus, it was determined that the rate limiting factor differs at low and high temperature. Furthermore, it was determined that, at low temperature, the majority of the polarization is the result of a variable not captured in these experiments. The

results of the silver doping experiment, while still preliminary, indicate considerable opportunity for this general approach. Future experiments will be aimed at addressing the rate limiting factors not captured in these experiments.

#### Acknowledgements

Special thanks to Steve Vukson and Dick Marsh whose support for USAF PRDA contract F-33615-98-C-2898 allowed this work to take place.

#### References

- [1] C. Marsh, R. Gitzendanner, F. Puglia, J. Byers, in: *Proceedings of the 10th IMLB Conference*, June 2000, p. 351.
- [2] F. Puglia, R. Gitzendanner, C. Marsh, *SAE Power Systems*, San Diego, 2000.
- [3] K. Nishimura, H. Honbo, et al., *J. Power Sources* 68 (1997) 208–211.

# Li-ion battery technology for compact high power sources (CHPS)

Tim Sack, Tom Matty\*

SAFT America Inc., Research & Development Center, 107 Beaver Court, Cockeysville, MD 21030, USA

Received 29 November 2000; accepted 10 December 2000

## Abstract

Li-ion is a relatively new battery technology that has been commercialized within the past 10 years for many consumer products, but especially for portable power. Li-ion operates by using a different principle to other battery technologies. This principle is called intercalation. Recently, work has been undertaken to explore the high power capability of this technology. The results indicate that present products can provide very high rate capability. Investigations are underway to improve this capability in anticipation of needs for defense and other advanced applications that will require compact high power sources (CHPS). © 2001 Elsevier Science B.V. All rights reserved.

**Keywords:** Li-ion batteries; High power; Defense applications

## 1. Introduction

SAFT has been developing and producing Li-ion technologies for more than 6 years. The cells and systems using this technology are now found in a wide variety of applications from undersea to space. Some examples are shown in Figs. 1–4, being the Mars Rover, electric and hybrid vehicles and most recently the DARPA CHPS (Combat Hybrid Power System) vehicle.

High power Li-ion/liquid electrolyte products were originally developed for use in hybrid vehicles. Early in the compact high power sources (CHPS) program the power performance of these cells was evaluated and was found to exceed expectations by significant levels.

## 2. The CHPS system integrated laboratory battery

The initial goal for SAFT in the CHPS program was to deliver a battery system that would support hybrid mobility testing in the CHPS SIL (System Integration Laboratory). During the early phases of the program it was decided to explore the characteristics of cells presently available. This investigation uncovered capabilities that were previously unknown. Some of these results are reported later in this paper. As a result of this investigation a new CHPS cell was designed to maximize both energy and power capabilities which will not only be required for mobility needs but would

also support pulse power applications such as are being considered for the future, including new combat systems.

The characteristics of the CHPS Li-ion battery system are shown in Fig. 5. The packages were developed for hard use in the laboratory, including the need to be stacked. Therefore, the steel case weighs about as much as the internal battery components. It is expected that vehicle applications will allow for more effective packaging.

The design concept delivered a package that is totally sealed to provide both EMI (electromagnetic interference) and thermal isolation. Internal fans and a liquid/air heat exchanger provide a thermal management interface to the system integration laboratory. The heating/cooling liquid is provided via sealed fittings into a metal heat exchanger.

Included in the packs are telemetry and cell management systems that communicate with the SIL management system as shown in Fig. 6. Fiber optic interfaces are used to improve safety and to avoid ground loops and other EMI issues.

Fig. 7 shows the two Li-ion packs installed in the SIL. The packs are mounted on the floor within the notional outline of the vehicle. In the foreground is one of the traction motors. To the right of the packs is the SIL power distribution panel. At the rear, beyond the Li-ion batteries, is a 3.9 m × 1.6 m × 1.6 m rack of 764 commercial Ni/Cd cells. These were used to support SIL operations while the CHPS cells and packs were under development and production.

## 3. High power Li-ion cells

During an earlier phase of the CHPS program an investigation was started at SAFT using 500 A commercial test

\* Corresponding author.

E-mail address: tcmatty@technie.com (T. Matty).



Fig. 1. Mars Rover.

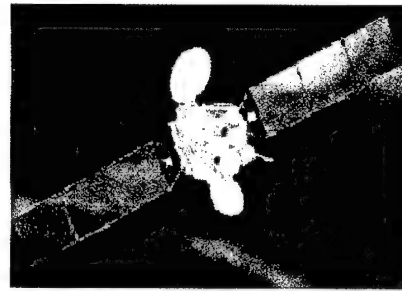


Fig. 3. Li-ion in space applications.



Fig. 2. Hybrid electric vehicle.

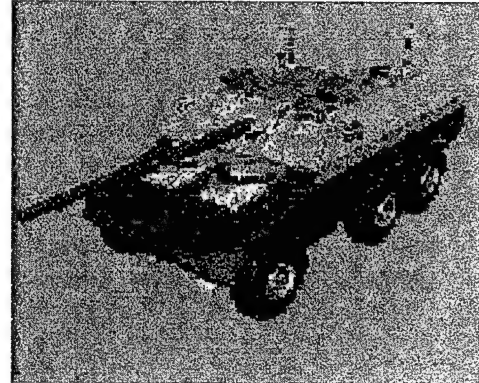


Fig. 4. Notional CHPS military vehicle.

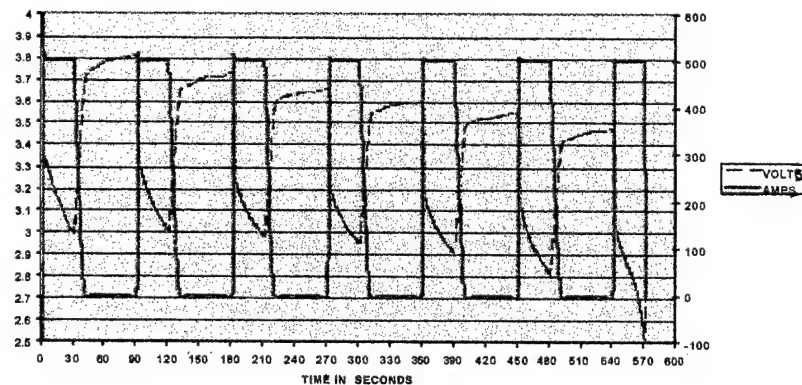


Fig. 5. The CHPS pack of Li-ion cells (two per battery).

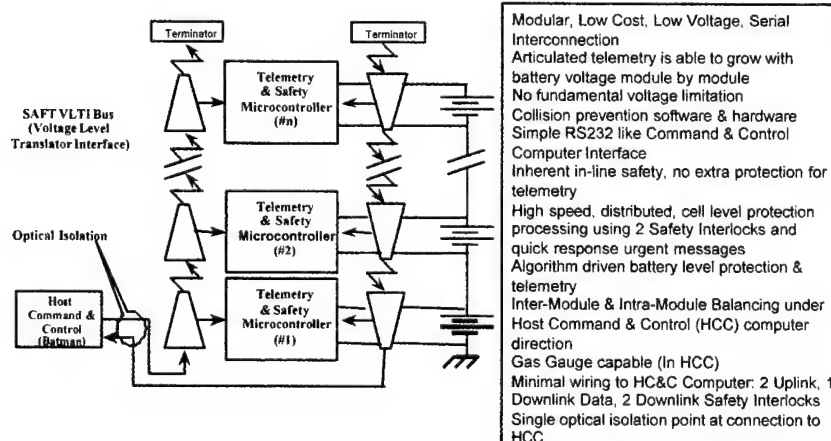


Fig. 6. Telemetry and management system for CHPS pack.

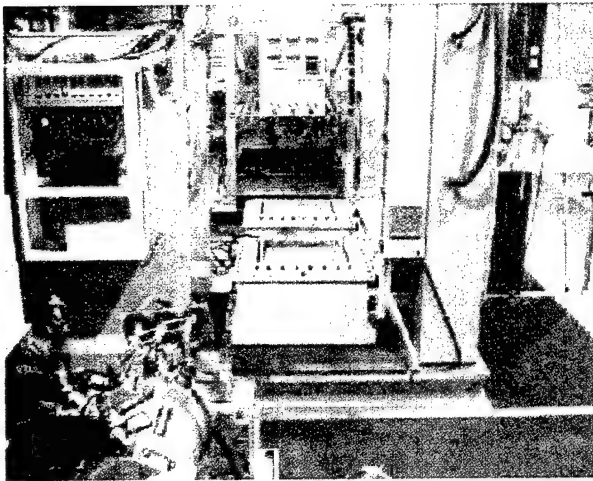


Fig. 7. Two CHPS packs located in the System Integration Laboratory.

equipment to evaluate and characterize the pulse-power performance of the cells. Based on the results of this testing, a new cell was designed to provide both high power as well as high energy. This cell is rated at 30 Ah and has exceptional power delivery capabilities. Fig. 8 shows the discharge of a CHPS cell during a high current pulse test. This discharge pattern, of about 1500 W per 30 s pulse, demonstrates the efficient delivery of high power.

The waveforms show the constant current pulses and the voltages during each pulse.

Each of the 500 A, 30 s, pulses withdraws about 4.1 Ah or about 14% of the stored energy. A total of 29 Ah was withdrawn in seven pulses from this 30 Ah rated cell.

During the evaluation programs, which were conducted to verify tolerance to abuse, it was observed during short circuit tests that cells were able to support a very high current for a significant period without damage. DARPA commissioned the Army Research Laboratory (Aberdeen Proving Grounds) to explore behavior on this high current regime.

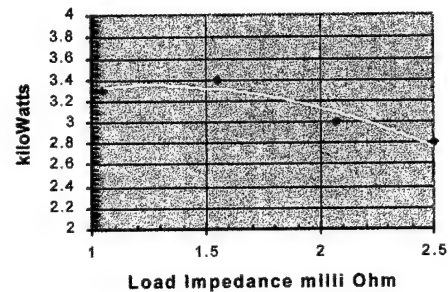


Fig. 9. A 30 Ah CHPS cell. Power output against discharge load.

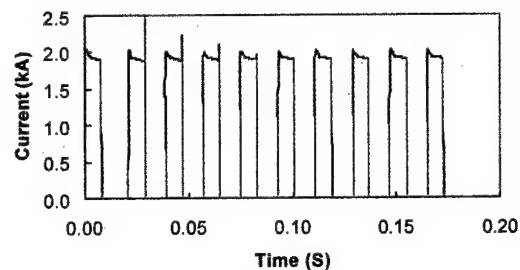


Fig. 10. A 30 Ah CHPS cell (2 kA, 7 ms, repetitive pulse discharges).

The aim of these tests was to determine the peak power that could be drawn repetitively from the cell.

In order to gather the data above 500 A, ARL constructed a test fixture that was capable of operation in excess of 2000 A.

The initial results of these tests are shown in Fig. 9. This plot shows the power withdrawn from a cell while various loads are applied. This test was conducted on a 12 Ah cell. It should be noted that the peak current during this test was about 1200 A or more than the 100 C rate. This figure also shows that the peak power was about 3.4 kW for pulses of about 0.3 s in duration. With a cell mass of 0.68 kg, then the

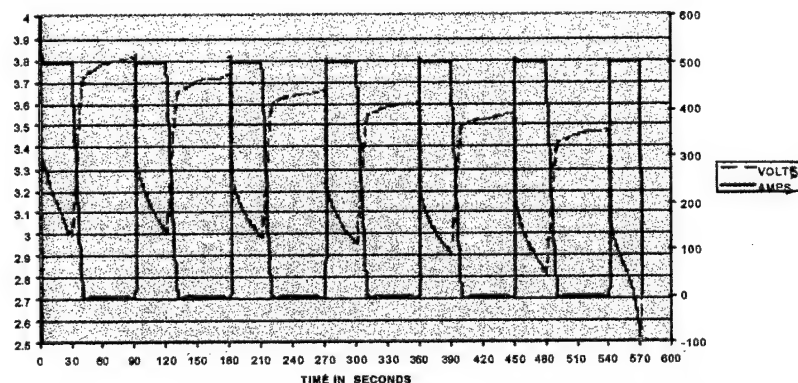


Fig. 8. Repetitive high-power pulse discharging of a 30 Ah CHPS cell at room temperature (500 A for 30 s, repeated seven times with 60 s between pulses; 26.16 Ah withdrawn; final temperature of cell case: 67.8°C).



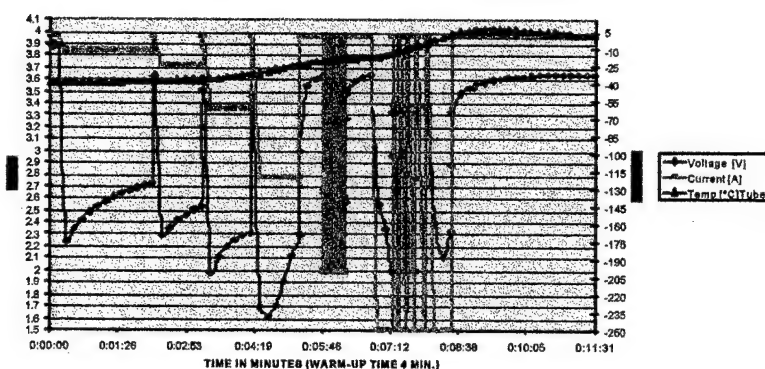


Fig. 11. Performance of a 30 Ah CHPS cell, initially at  $-40^{\circ}\text{C}$ , under increasing loads 12 A, 120 s, then 24 A; 60 A; 120 A; all for 60 s, then 200 and 250 A, each for 30 s; final temperature of cell case:  $+6.9^{\circ}\text{C}$ .

power density is about  $5 \text{ kW g}^{-1}$  for an individual cell, whilst the equivalent specific power is more than  $10 \text{ kW dm}^{-3}$ .

Following these tests, additional work explored the capabilities of the larger 30 Ah CHPS cell that weighs about 1.1 kg and has a volume of  $0.5 \text{ dm}^3$ .

Fig. 10 shows a series of 2000 A pulses being withdrawn using a specific short-duration pulse pattern. These data were gathered using a new ARL test fixture that is capable of operation up to 3000 A and is electronically programmable.

During the evaluation of the CHPS cells, low temperature operation data was also collected. One of these tests is shown in Fig. 11.

This shows the temperature rise of the cell, initially at  $-40^{\circ}\text{C}$ , whilst increasingly higher currents were applied.

After about 4 minutes the cell was nearly capable of delivering full power.

These experiments and data have led to new thoughts regarding the capabilities of other types of solid state power sources (Table 1).

#### 4. Future program

In order to identify possible new applications it was necessary to make some predictions regarding the future of the technology. Table 1 shows the SAFT estimates of the capabilities that are believed to be realistic. These estimates are based on the use of materials and processes that are being developed today for other products.

Table 1  
Current and predicted performances for a battery, volume  $1 \text{ dm}^3$  and weighing 2000 kg

	At present	Near term	Far term
Energy (assuming 80% of usable energy) <sup>a</sup>			
kWh	75	54	50
MJ	270	194	180
Discharge power (MW)			
0.2 s pulse	6.8	13.4	40
2 s pulse	4.2	10.4	30
18 s pulse 2.7	6.7	20	
Applications	HEV power Lasers Targeting Defeating sensors Silent watch	HEV power Lasers Targeting Defeating sensors Defeat light armor Tactical aircraft Missile defense  Electrothermal Cannon (ETC)	HEV power Lasers Targeting Defeating sensors Defeat heavy armor Tactical aircraft Missile defense Long range missiles Theater defense ETC/electromagnetic guns Counter kinetic/high power microwave

<sup>a</sup> Energies available or predicted at indicated pulse-power levels.



## **5. Conclusions**

High power Li-ion is a cornerstone technology for compact high power systems.

It combines the power performance of a flywheel combined with the energy density of a high capacity battery.

Many other applications have shown that it provides long life, low maintenance, and long-term affordability without environmental sensitivities.

This is a young technology, capable of significant increases in performance.

# Computer simulation of the discharge of metal electrodes in batteries with solid electrolytes

Gennady I. Ostapenko<sup>a,\*</sup>, Sergey N. Antonov<sup>b</sup>

<sup>a</sup>*Institute of Radio Engineering and Electronics, Russian Academy of Sciences, Ul'anovsk Division,  
48 Goncharov Str., 432011 Ul'anovsk, Russia*

<sup>b</sup>*Ul'anovsk State Engineering University, 32 Severny Venets Str., 432027 Ul'anovsk, Russia*

Received 14 November 2000; accepted 2 December 2000

---

## Abstract

The computer simulation of the dissolution during discharge of silver electrodes in batteries and other devices with various silver-conducting solid electrolytes was carried out. The model of the pseudo-porous electrode represents small silver spheres, distributed in a solid electrolyte matrix. Various parameters simulated were: diameter of silver particles, silver to electrolyte relationship within the electrode, thickness of the electrode, conductivity of the electrolyte, discharge current and thickness of the separator. Calculated distribution of current in the electrode and the discharge curves at various parameters were obtained. A comparison of the calculated and experimental discharge curves was carried out. The good correspondence of these curves testifies to adequacy of the surveyed model of the dissolution of metal electrode for devices with solid electrolytes. Optimal parameters of the electrode are recommended depending on the use of these devices with solid electrolytes. © 2001 Elsevier Science B.V. All rights reserved.

**Keywords:** Solid electrolyte batteries; Porous electrodes; Computer simulation

---

## 1. Introduction

Batteries and other devices using solid electrolytes can function at zero gravity, under high accelerations and over a wide range of temperature. Such devices have practically unlimited prospects for miniaturization. So, they have excellent prospects for general application in cosmic and military equipment. Usually, one of the electrodes of the solid-state battery is a soluble (during discharge) metal electrode [1]. Frequently, metal electrodes are prepared by the pressing of metal and solid electrolyte powders [2,3]. This is done to lower electrode polarization. In such electrodes, the metal particles are distributed in the solid electrolyte matrix and these electrodes can be viewed as pseudo-porous.

The effective area of the porous electrode is distributed throughout its volume. All parts within the electrode volume are not equally accessible for electrochemical processes, therefore the intensity of the electrode discharge is unequal within the electrode. The theory of porous electrodes gives the current density and potential distribution within the electrode volume or thickness.

In the present work, computer simulation were carried out of electrochemical dissolution of the pseudo-porous silver electrode for the device with the solid electrolyte, depending on the diameter of the silver particles, silver: electrolyte relation in the electrode, thickness of the electrode, conductivity of the electrolyte, discharge current and thickness of the separator.

## 2. Formulation

### 2.1. Description of the electrode model

One of the first major theoretical investigations of the porous electrode was carried out by Stender [4]. Then Coleman [5], Daniel-Bek [6] and Frumkin [7] carried out the quantitative calculations of the current distribution. The problems of the porous electrode simulation by means of electrical elements were surveyed fully by Euler [8–10].

For simplification, the two-phase porous electrode is considered usually as a pseudo-homogeneous medium. This medium has a certain electrical resistance  $R$ , which includes ohmic resistance  $R_\Omega$  and polarization resistance  $R^p$ .

The resistance  $R_\Omega$  is the total electronic resistance of the metal electrode  $R^m$ , ionic resistances in the electrolyte pores

---

\* Corresponding author.

E-mail address: ufire@mv.ru (G.I. Ostapenko).

$R^e$  and in the separator  $R^s$ . The nonlinear resistance  $R^\eta$  is stipulated by polarization phenomenon at the metal/electrolyte interface. Current  $i_n$  at any site in the porous electrode is inversely proportional to the complete resistance  $R_n$  during current flow through this site.

For simulation, the porous electrode is divided conditionally into  $N$  sections, which run connected to an external current source AB, as shown in Fig. 1. The following series of linear equations can be deduced:

$$R_1 = NR^m + R^e + R_1^\eta + R^s$$

$$R_2 = (N-1)R^m + 2R^e + R_2^\eta + R^s$$

$$R_n = (N-n+1)R^m + nR^e + R_n^\eta + R^s$$

$$R_N = R^m + NR^e + R_N^\eta + R^s$$

$$\frac{1}{R} = \sum_{n=1}^{n=N} \frac{1}{R_n}$$

$$\Delta\varphi_{AB} = IR$$

$$I = i_1 + i_2 + \dots + i_n + \dots + i_N$$

where  $\Delta\varphi_{AB}$  is voltage drop between points A and B, i.e. electrode polarization;  $I$  the overall current through the electrode. This set of simultaneous equations was solved by the Gauss method [11].

## 2.2. Operating conditions and physical parameters

The effective conductivity of porous metal and of porous electrolyte can be calculated as the product of conductivity of the material and some coefficient  $K(P)$ , which depends on the porosity of the material (Table 1).

The polarization resistance is calculated as

$$R_n^\eta = \frac{\eta_n}{i_n S_n}$$

where  $S_n$  is the effective area of metal/electrolyte interface in section  $n$ ;  $\eta_n$  an overvoltage in section  $n$  at current flow  $i_n$ . The interrelation  $\eta = f(i)$  is determined from the polarization curve of the metal/electrolyte interface.

The electrode material is represented spherical silver particles, distributed in the solid electrolyte matrix. The

Table 1

Coefficient  $K(P)$  which characterizes conductivity of porous bodies vs. porosity  $P$  [12]

$P$	0.9	0.8	0.7	0.6	0.5	0.4	0.3	0.2	0.1	0.0
$K(P)$	0.008	0.033	0.058	0.14	0.222	0.368	0.515	0.687	0.847	1.000

electrode is a disc with a diameter of 12 mm. The electrode is arbitrarily divided into 20 sections. The polarization curve of the Ag/Ag<sub>4</sub>RbI<sub>5</sub> interface [13] is utilized for the simulation of silver electrodes with other silver-conducting solid electrolytes (Ag<sub>6</sub>WO<sub>4</sub>I<sub>4</sub>), since silver dissolution is reduced by crystallizing effects [13,14] and does not depend on the nature of the solid electrolyte. Tables 2 and 3 show the parameters used in the simulation.

## 2.3. Background of the algorithmic approach

At the moment of current application, the intensity of discharge in the sections is distributed within the electrode thickness according to a primary distribution [18,19], i.e. is caused only by ohmic resistance  $R_\Omega$ . Then there is a redistribution of intensity of discharge owing to the origination of polarization resistance  $R^\eta$  and then occurs a secondary distribution of current.

The calculation of the secondary distribution in each section is carried out without reference to the secondary distribution in subsequent sections, which for the present are not known, since the polarization resistance and current in the sections are interdependent. Therefore, secondary distribution is determined by the method of successive

Table 2

Physical parameters

Parameter	Characteristics
Solid electrolytes	Ionic conductivity (S cm <sup>-1</sup> )
Ag <sub>4</sub> RbI <sub>5</sub>	$2 \times 10^{-1}$ [15]
Ag <sub>6</sub> WO <sub>4</sub> I <sub>4</sub>	$2.3 \times 10^{-2}$ [16]
Density of electrolyte	5 g cm <sup>-3</sup> [17]
Density of silver	10.5 g cm <sup>-3</sup>
Conductivity of silver	$6.25 \times 10^9$ S cm <sup>-1</sup>

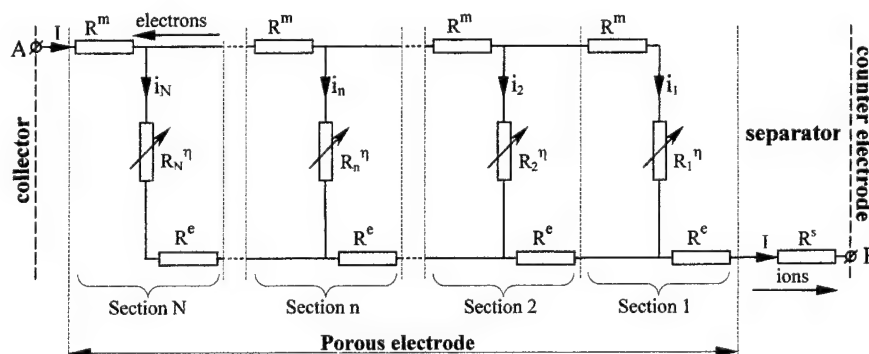


Fig. 1. Equivalent circuit of the porous electrode. Refer text for notations.

Table 3  
Electrode parameters

Electrode number (EN)	Electrode thickness (mm)	Overall current (mA)	Silver to electrolyte (weight ratio)	Electrolyte type	Diameter of silver particles ( $\mu\text{m}$ )	Separator thickness (mm)
1	0.5	10	1:0.5	$\text{Ag}_4\text{RbI}_5$	2.5	0.5
2	0.2	10	1:0.5	$\text{Ag}_4\text{RbI}_5$	2.5	0.5
3	1.0	10	1:0.5	$\text{Ag}_4\text{RbI}_5$	2.5	0.5
4	0.5	5	1:0.5	$\text{Ag}_4\text{RbI}_5$	2.5	0.5
5	0.5	50	1:0.5	$\text{Ag}_4\text{RbI}_5$	2.5	0.5
6	0.5	10	1:0.2	$\text{Ag}_4\text{RbI}_5$	2.5	0.5
7	0.5	10	1:1.0	$\text{Ag}_4\text{RbI}_5$	2.5	0.5
8	0.5	10	1:0.5	$\text{Ag}_6\text{WO}_4\text{I}_4$	2.5	0.5
9	0.5	10	1:0.5	$\text{Ag}_4\text{RbI}_5$	0.5	0.5
10	0.5	10	1:0.5	$\text{Ag}_4\text{RbI}_5$	5.0	0.5
11	0.5	10	1:0.5	$\text{Ag}_4\text{RbI}_5$	2.5	0.1
12	0.5	10	1:0.5	$\text{Ag}_4\text{RbI}_5$	2.5	5.0

approximations. Such an iterative process has a rapid convergence. The calculations stop when the discrepancy of distribution between current and those from previous calculation cycles does not exceed 0.1%.

The metal is dissolved electrochemically at discharge. Therefore metal quantity, the radius and area of metal particles decrease in time. For simplification of the simulation, the calculation of the intensity of discharge in the sections is carried through time intervals  $\Delta t_i = t_i - t_{i-1}$ , which are selected arbitrarily, according to the theoretical electrical capacity of the electrode and the required accuracy. This approach assumes an invariance of currents within sections during the time interval between  $t_i$  and  $t_{i-1}$ . Thus, the calculation of current redistribution with time is reduced to a definition of the stationary secondary current distribution at various instants considering the working area changes of the electrode sections with time.

### 3. Experimental

The solid electrolyte  $\text{Ag}_4\text{RbI}_5$  was prepared by the method described in [15]. Material for the electrodes was prepared by mixing silver and the solid electrolyte powders (the weight ratio  $\text{Ag}:\text{Ag}_4\text{RbI}_5$  was 1:0.5) or silver, the solid electrolyte and carbon (the weight ratio  $\text{Ag}:\text{Ag}_4\text{RbI}_5:\text{C}$  was 1:0.5:0.02). The average diameter of silver particles was about 2.5  $\mu\text{m}$ .

Cells of the type: positive collector, investigated electrode/separator/counter electrode were prepared in dry air atmosphere (dehydrator  $\text{P}_2\text{O}_5$ ) by sequential pressing under a pressure of  $2.2 \times 10^8$  Pa:

- Ni foil (as collector);
- powder of investigated electrode material;
- $\text{Ag}_4\text{RbI}_5$  powder (as separator);
- Ag foil (as counter electrode).

The cell diameter was 12 mm. The separator thickness was 0.5 mm. A silver wire reference electrode of 0.2 mm

diameter was positioned inside the electrolyte. The clamping pressure applied to the cell was approximately  $3 \times 10^6$  Pa.

Before measurements began, the cell was annealed for several hours at 140°C. Polarizations of the cells were made with the P-5848 potentiostat (manufacturer: Gomel Instrument Plant, Russia) at room temperature under a current of 10 mA. The voltage  $\Delta\phi$  was measured between the investigated and the reference electrodes.

### 4. Results and discussion

In Fig. 2 the calculated current distribution within some electrodes is shown. On the ordinate axis, the current flow in the electrode sections is shown. On the abscissa axis the distance from the frontal electrode surface to the interior is shown. The theoretical efficiency is indicated on the curves. Fig. 3 shows the calculated and experimental discharge curves of the electrodes.

As it is shown on Fig. 2, the electrode frontal sections are discharged mainly at the beginning. Then the discharge extends deep into the electrode and at the end, is near the collector.

In Fig. 2a, d and e the dependence of current distribution on overall current quantity  $I$  is shown. As it is shown by these figures, the current distribution depends considerably on  $I$ , while the non-uniformity of distribution increases with increase of  $I$ . The polarization resistance  $R_n^\eta$  decreases with section current  $i_n$  increase. The electrode polarization  $\Delta\phi$  increases (Fig. 3a, d and e) as  $I$  increases.

In Fig. 2a–c the dependence of current distribution on electrode thickness is shown. These figures show that the non-uniformity of current distribution increases with increase of electrode thickness. This is possible to explain by an increase of the electrode ionic resistance. Increase of electrode polarization with decreasing of electrode thickness (Fig. 2a–c) is an interesting effect. However, a thin electrode contains less silver particles than the thick one. Therefore,

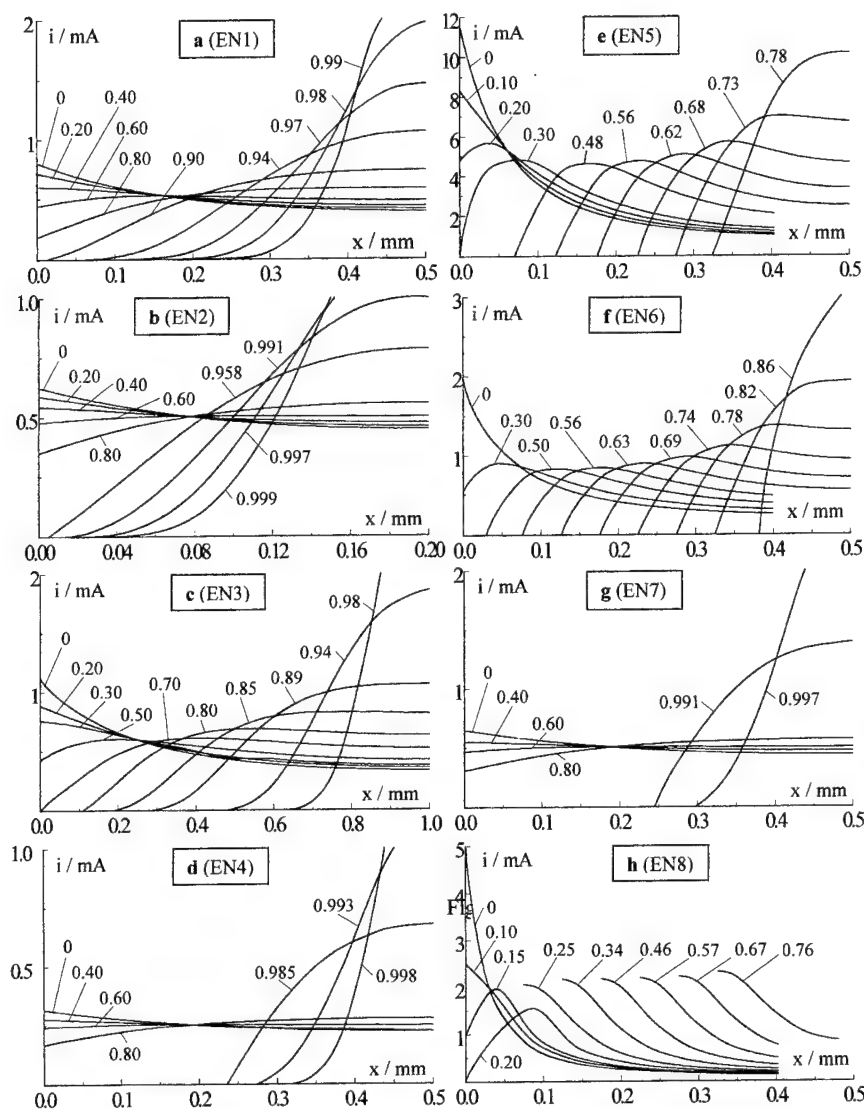


Fig. 2. Calculated current distribution throughout the thickness of the electrode. The electrode numbers (EN) are given in Table 3. The theoretical efficiencies are indicated.

the overall current density  $I/S$  (where  $S$  is the area of all silver particles) in the thin electrode is higher than in the thick one, and the polarization in the thin electrode is higher accordingly.

In Fig. 2a, f and g the dependence of current distribution on the Ag:electrolyte ratio is shown. These figures show that non-uniformity of current distribution and polarization (Fig. 3a, f and g) also decrease with increasing electrolyte

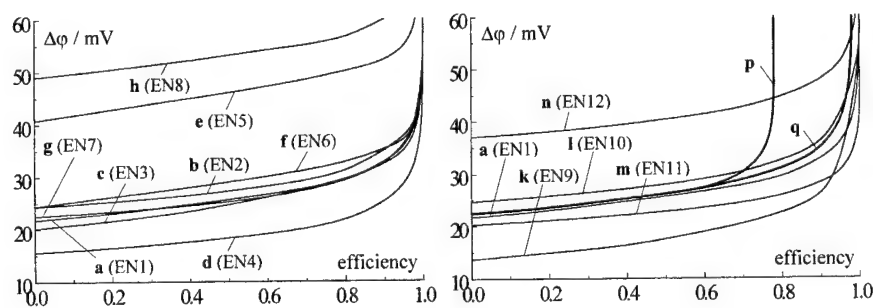


Fig. 3. Discharge curves of the electrodes. The EN for the (a–n) calculated curves are given in Table 3 p and q are the experimental curves. The explanations see in the text.

content in the electrode. It is stipulated by ionic resistance increasing as the electrode porosity decreases.

The use of an electrolyte with lower conductivity causes a sharp increase of current distribution non-uniformity (Fig. 2a and h) and electrode polarization (Fig. 3a and h). This effect is obvious, since in these conditions the ionic resistance of the electrode is increased appreciably.

The variation of the particle diameter does not change the current distribution significantly, but the electrode polarization is increased (Fig. 3a, k and l) with increasing particle diameter. It is possible to explain the last fact by the collapse of the overall area of silver particles, so increasing current density and polarization resistance.

The increase of the separator thickness does not change the current distribution, but causes increasing electrode polarization (Fig. 3a, m and n). This is obvious and does not require explanations. The experimental checking of the current distribution is difficult and was not carried out. However, the adequacy of calculations can be tested by comparison of the calculated and experimental discharge curves.

The calculated (Fig. 3a) and experimental (Fig. 3q) discharge curves of electrodes with identical compositions ( $\text{Ag}:\text{Ag}_4\text{RbI}_5$  is 1:0.5) under a 10 mA overall current practically coincide in polarization, but differ considerably in efficiency (1.0 and 0.78 accordingly). As is visible in Fig. 3p, experimental efficiency increases considerably (up to 0.98) by adding carbon to the electrode material ( $\text{Ag}:\text{Ag}_4\text{RbI}_5:\text{C}$  is 1:0.5:0.02).

Hence, some silver particles in experimental  $\text{Ag} + \text{Ag}_4\text{RbI}_5$  electrode are isolated by electrolyte and have no electronic contact with the collector. In a  $\text{Ag} + \text{Ag}_4\text{RbI}_5 + \text{C}$  electrode, the carbon bridges such particles to give electronic conduction. The good correspondence of the calculated (Fig. 3a) and experimental (Fig. 3p) discharge curves testifies to the adequacy of this model of the soluble metal electrode when applied to devices with solid electrolytes.

The results obtained allow the production of recommendations for the development of metal electrodes in devices with solid electrolytes according to the application of these devices. For example, high current density and low polarization are necessary for powerful primary batteries. Here, it is possible to recommend a thick electrode with high electrolyte content and fine silver powder.

For storage batteries, the counter electrodes of timers and other devices, in which uniform current distribution in the electrode is important, it is possible to recommend a low current density and a high proportion of electrolyte. For example, practically uniform current distribution is observed at 0.4–0.6 efficiencies with EN4 and EN7 electrodes. Therefore, for reversible electrodes, it is possible to recommend an initial discharge of such electrodes up to 0.5

efficiency, then 'discharge-charge' cycles within the limits 0.4–0.6 efficiencies.

## 5. Conclusions

A model of the soluble metal electrode for devices with solid electrolytes was designed. The computer simulation of electrode discharges showed that, to increase the current distribution uniformity in the electrode, it is necessary to reduce the ratio of ionic and polarization resistances in the electrode, i.e. to use high-conductivity electrolytes and metal electrodes with high polarization resistance. The good correspondence of the calculated and experimental discharge curves testifies to the adequacy of this model of the soluble metal electrode for devices with solid electrolytes.

## Acknowledgements

The work is carried out according to the Federal Program "State Support of Integration of the Higher Education and Fundamental Sciences", Russia, Project No. A-0066.

## References

- [1] R.T. Foley, *J. Electrochem. Soc.* 116 (1969) 13C.
- [2] T. Takahashi, O. Yamamoto, *J. Electrochem. Soc.* 117 (1970) 1.
- [3] M. De Rossi, M.L. Berardelli, G. Fonseca, *J. Electrochem. Soc.* 120 (1973) 149.
- [4] V.V. Stender, *Electrochemical Production of Chlorine and Alkali*, Khimteoret, Moscou, 1935 (in Russian).
- [5] J. Coleman, *Trans. Faraday Soc.* 90 (1946) 545.
- [6] V.S. Daniel-Bek, *Zh.Fiz. Khim.* 22 (1948) 697 (in Russian).
- [7] A.N. Frumkin, *Zh.Fiz. Khim.* 23 (1949) 1477 (in Russian).
- [8] K.-J. Euler, *Naturwiss* 45 (1958) 537.
- [9] K.-J. Euler, *Z. Elektrochem.* 63 (1959) 537.
- [10] K.-J. Euler, *J. Appl. Electrochem.* 8 (1978) 49.
- [11] G.A. Korn, T.M. Korn, *Mathematical Handbook for Scientists and Engineers*, McGraw-Hill, New York, 1968.
- [12] V.V. Skorokhod, *Inzh.Fiz.Zh.*, 11 (1959) 51 (in Russian).
- [13] A.M. Kolomoets, G.I. Ostapenko, *Elektrokhimiya* 16 (1980) 379 (in Russian).
- [14] R.D. Armstrong, T. Dickinson, P.M. Willis, *J. Electroanal. Chem.* 57 (1974) 231.
- [15] B.B. Owens, G.R. Argue, *Science* 157 (1967) 308.
- [16] M.De. Rossi, G. Pistoia, B. Scrosati, *J. Electrochem. Soc.* 116 (1969) 1642.
- [17] B.B. Owens, G.R. Argue, *Science* 157 (1967) 310.
- [18] V.I. Layner, N.T. Kudryavtsev, *Principles of Galvanization*, Metallurgizdat, Moscou, 1953 (in Russian).
- [19] J. Newman, *Electrochemical Systems*, Mir, Moscou, 1977 (in Russian).

# Analysis of power limitations at porous supercapacitor electrodes under cyclic voltammetry modulation and dc charge

Wendy G. Pell, Brian E. Conway\*

Chemistry Department, University of Ottawa, 10 Marie Curie Street, Ottawa, Ont., Canada K1N 6N5

Received 28 November 2000; accepted 8 December 2000

## Abstract

A simple capacitor is perceived as being capable of discharge (or recharge) at high rates, limited only by a small equivalent series resistance. However, in the case of electrochemical capacitors, based on high specific area porous electrode materials, power limitations arise due to the complex-distribution of electrolyte internal resistance, coupled with double-layer or pseudo-capacitive elements. The present paper quantitatively examines both numerically and experimentally the effects of internal electrolyte resistance as evaluated by the current-response functions for porous capacitor electrodes, generated in cyclic voltammetry (CV) experiments and for voltage versus time responses in dc charge/discharge regimes. © 2001 Elsevier Science B.V. All rights reserved.

**Keywords:** Electrochemical capacitors; Internal resistance; Cyclic voltammetry; Charge/discharge curves

## 1. Introduction

Electrochemical capacitors are based on utilisation of the distributed interface of conducting materials having large specific areas such as carbon felts, cloths, powders and aerogels [1], and also conducting metal oxides ( $\text{RuO}_2$ ) [2], nitrides [3], or conducting polymers, including chemically or electrochemically generated  $\text{RuO}_2$  deposits on carbon substrates [4,5].

At carbon surfaces, the capacitance arises mainly from electrostatic double-layer charging [6] while, for example, at  $\text{RuO}_2$ , it arises mainly from redox pseudo-capacitance [2,7] coupled with a smaller double-layer capacitance.

It is important to emphasise that electrochemical capacitors cannot functionally substitute for batteries; rather their applications and performance behaviour are *complementary* to those of rechargeable batteries. Elsewhere [8], we have delineated, in some detail, the similarities and differences between batteries and electrochemical capacitors for electrical energy storage and delivery. Primarily, electrochemical capacitors, now often referred to as “supercapacitors” [7], provide high-power performance but at low energy-densities and also with the advantage of large multiple cycle-life of ca. 100,000 cycles to deep depths of discharge, DOD. On the other hand, batteries provide high specific

energy-densities but at relatively low operational power-densities and with limited recyclabilities, especially at appreciable DODs. This complementarity of performance has led to various proposed hybrid applications employing tandem configurations of battery and capacitor modules enabling optimisation of both power and energy-density performance [9].

The relationship between operational power-density ( $P$ ) and simultaneously achievable energy-density ( $E$ ) is commonly represented by so-called Ragone plots [10,11].  $E$  tends to decrease as  $P$  drain is increased. In a capacitor, this effect is mainly due to internal ohmic ( $IR$ ) drop which increases with current ( $I$ ) drain into a load, lowering the voltage. In a battery, it is due to kinetic polarisation effects in addition to  $IR$  drop, together with significant effects arising from concentration gradients developed on charge or discharge. In operation of a capacitor device, for fundamental reasons, the Ragone relations are importantly dependent on state-of-charge [11] (SOC) since the operational voltage ( $V$ ), is directly proportional to charge ( $Q$ ),  $V = Q/C$ , so that both  $P$  and  $E$  are determined by SOC. In battery performance, related effects can arise but are secondary and smaller.

In electrochemical capacitors employing non-aqueous electrolytes, the internal electrolyte resistance is usually appreciably higher than for aqueous solutions but this is compensated by higher operational voltage, which enters “squared” into the energy density.

\* Corresponding author. Tel.: +1-613-562-5481; fax: +1-613-562-5170.

A pure capacitance, such as that of the double-layer [6], can be discharged at high rates, limited only by a (usually small) equivalent series resistance (ESR). However, in the case of electrochemical capacitors based on high-area, porous materials, an unavoidable distributed resistance ( $R$ ) arises (mainly of the electrolyte in the pores) that is coupled in a complex way with the distributed interfacial capacitance elements ( $C$ ), giving rise to a distribution of “ $RC$ ” time-constants and a resultant power spectrum. This situation was treated in mathematical detail by de Levie [12,13] in a series of papers. The important general conclusions, relevant to porous capacitor behaviour, were: (a) that a so-called “penetration effect” (into the porous matrix) applies to any time-dependent electrical signal — current pulse, potential pulse or amplitude voltage (a.v.) modulation — so the charging or discharging response function is time-dependent; and (b) that the overall behaviour under a.v. modulation is a transfer function characterised by a  $-45^\circ$  phase angle of the impedance vector, represented in the complex-plane.

These aspects, treated by de Levie [12] and later by Keiser et al. [14] for pores of various shapes, provide the foundations for consideration of power limitations in the operation of electrochemical capacitor devices based on high-area, porous electrode materials.

Because of the relationship between the response currents,  $I$ , to repetitive linear voltage modulation (cyclic voltammetry (CV)) at sweep rates  $s = \pm dV/dt$ , giving directly the capacitance  $C = I/s$ , CV has become a major procedure for evaluating performance of capacitor devices. It is convenient for determining cycle life, and from analysis of the shapes of the response-current voltammograms as a function of  $s$ , it provides information on internal resistance effects and consequent dissipative losses.

The present paper examines consequences of such effects in quantitative ways, through simulation calculations, especially for cases where the performance characteristics are evaluated by means of CV and dc charging curves. The results of simulation calculations for various conditions applied to voltammetry and dc charging behaviour at porous capacitor electrodes are compared with experimental results obtained at specially fabricated, non-aqueous electrolyte capacitor modules containing sub-optimal electrolyte concentrations in order to enhance internal resistance effects, thus, enabling them to be more quantitatively characterizable.

## 2. Treatment of cyclic voltammetry (CV) and dc charging at porous electrodes

Equations have been developed for potentiostatic and galvanostatic charging transients at porous and tubular electrodes of finite length in the absence of appreciable Faradaic currents, for systems of *constant* electrolyte resistance [15,16]. The case of linear or triangular voltage sweep

(CV) in the presence of significant, but *constant*,  $IR$  drop for porous electrodes was considered in detail by Austin and Gagnon [17].

Effects of internal electrolyte resistance and its changes under certain conditions during charging and discharging of porous capacitor electrodes are examined here for cases of charge/discharge under CV and for dc constant current cycling. The required mathematical equations are developed and their solutions are evaluated with numerical simulations for various conditions.

The assumptions made in the calculations include the following:

1. that the double-layer capacitance,  $C$ , is constant over the voltage window of operation;
2. only capacitive processes occur, i.e. there is no Faradaic charging;
3. only ohmic losses are considered;
4. the electrolyte conductivity is either (1) constant, or (2) a linear function of the local potential at the working electrode.

## 3. Governing equations

The current response,  $I(V_m)$  at a potential  $V_m$ , for a purely capacitive process, involving a constant capacitance,  $C$ , is given by:

$$I(V_m) = C \left( \frac{dV_e}{dt} \right) \quad (1)$$

where  $V_m$  is the measured potential and  $V_e$  the local potential at the capacitive electrode.  $V_e$  differs from  $V_m$  by the “ $IR$ ” loss due to potential dependent passage of response current when the system includes a significant series resistance.

### 3.1. Constant electrolyte resistance

The local electrode potential, during the anodic direction of polarisation of a CV experiment, between the applied potential limits of  $V_1$  and  $V_2$ , assuming the presence of a constant electrolyte series resistance,  $R_0$ , is

$$V_e = V_1 + st - IR_0 \quad (2a)$$

and during the cathodic direction of the CV, between the applied potential limits of  $V_2$  and  $V_1$ , is

$$V_e = V_2 - st - IR_0 \quad (2b)$$

where  $s$  is the applied potential sweep rate,  $dV/dt$ . Differentiating Eqs. (2a) and (2b) with respect to  $t$ , and substituting for  $dV/dt$  in Eq. (1), results in the following first-order differential equation for anodic current  $I_a(V_m)$

$$I_a(V_m) = Cs - R_0C \frac{dI_a}{dt} \quad \text{for } 0 \leq t \leq \frac{(V_2 - V_1)}{s} \quad (3a)$$



and for cathodic current  $I_c(V_e)$

$$I_c(V_m) = -Cs - R_0C \frac{dI_c}{dt} \quad \text{for } \frac{(V_2 - V_1)}{s} \leq t \leq \frac{2(V_2 - V_1)}{s} \quad (3b)$$

The analytical solutions of Eqs. (3a) and (3b), subject to the boundary conditions

$$I_a(t=0) = I_c\left(t = \frac{2(V_2 - V_1)}{s}\right) \quad (4a)$$

and

$$I_a\left(t = \frac{(V_2 - V_1)}{s}\right) = I_c\left(t = \frac{(V_2 - V_1)}{s}\right) \quad (4b)$$

are

$$I_a = sC - \left(\frac{2sC}{1 + \exp((V_1 - V_2)/sR_0C)}\right) \exp\left(-\frac{t}{R_0C}\right) \quad \text{for } 0 \leq t \leq \frac{(V_2 - V_1)}{s} \quad (5a)$$

and

$$I_c = -sC + \left(\frac{2sC}{1 + \exp((V_1 - V_2)/sR_0C)}\right) \times \exp\left(\frac{(V_2 - V_1)/s - t}{R_0C}\right) \quad \text{for } \frac{(V_2 - V_1)}{s} \leq t \leq \frac{2(V_2 - V_1)}{s} \quad (5b)$$

### 3.2. Case for electrolyte being consumed during charging of the capacitor

Consider, next, the case in which, during the course of charging of the capacitive electrode, the electrolyte is “consumed” and, as an approximation, the electrolyte resistance then becomes a linear function of the local electrode potential, thus

$$R = R_0 + rV_e \quad (6)$$

In real, two-electrode, high-area capacitor device this “consumption” of electrolyte from the bulk solution is a measurable effect and arises because of differential cation/anion adsorption between the two electrodes as the their double-layers become charged [18,19].

As a result of Eq. (6), the local potential,  $V_e$ , during the anodic direction of polarisation in a CV experiment, conducted between the applied potential limits of  $V_m = V_1$  and  $V_m = V_2$ , is

$$V_e = V_1 + st - IR_0 - IrV_e \quad \text{or } V_e = (V_1 + st - IR_0)(1 + Ir)^{-1} \quad (7a)$$

while during the cathodic direction of a CV experiment, between the applied potential limits of  $V_2$  and  $V_1$ ,  $V_e$  is

$$V_e = (2V_2 - V_1 - st - IR_0)(1 + Ir)^{-1} \quad (7b)$$

After differentiating Eqs. (7a) and (7b) with respect to  $t$  and substituting into Eq. (1), the following expressions for current as a function of time result:

$$I_a = \frac{Cs(1 + Ir) - C(R_0 + rV_1 + rst)(dI/dt)}{(1 + Ir)^2} \quad \text{for } 0 \leq t \leq \frac{V_2 - V_1}{s} \quad (8a)$$

and

$$I_a = \frac{-Cs(1 + Ir) - C(R_0 + 2rV_2 - rV_1 - rst)(dI/dt)}{(1 + Ir)^2} \quad \text{for } \frac{V_2 - V_1}{s} \leq t \leq \frac{2(V_2 - V_1)}{s} \quad (8b)$$

A numerical solution, subject to the boundary conditions of Eq. (4a) and (4b), may be determined using the Euler–Cauchy method [20], since the change in current with time may be expressed as

$$\frac{dI_a}{dt} = \frac{CsIr + Cs - I - 2I^2r - I^3r^2}{CR_0 + CrV_1 + Crst} \quad \text{for } 0 \leq t \leq \frac{V_2 - V_1}{s} \quad (9a)$$

and

$$\frac{dI_c}{dt} = \frac{-CsIr - Cs - 2I^2r - I^3r^2}{CR_0 + 2CrV_2 - CrV_1 - Crst} \quad \text{for } \frac{V_2 - V_1}{s} \leq t \leq \frac{2(V_2 - V_1)}{s} \quad (9b)$$

with an initial value of  $I_a(t=0)$  being assumed. The numerical solution determined using Eqs. (9a) and (9b), for given  $R_0$  and  $r = 0$  was identical to the analytical solution calculated using Eqs. (5a) and (5b).

### 3.3. Case for electrolyte being consumed during constant current charging of the capacitor

The electrical response during charge/discharge is governed by Eq. (1), but becomes simplified in the case of constant current to:

$$\Delta V_e = \frac{I}{C} \Delta t \quad (10)$$

Given that the measured voltage includes the  $IR$  component, it may be calculated simply as

$$V_m = V_e(1 + Ir) + IR_0 \quad (11)$$

i.e.  $V_m$  is determined both by the intrinsic resistance,  $R_0$ , of the electrolyte medium and its change with polarisation potential expressed by  $r$  in Eq. (6).

## 4. Experimental

### 4.1. Comparisons with behaviour of real capacitor modules

In order to examine the validity of the simulation treatments developed in Section 3, comparisons were made

experimentally with the charge/discharge behaviour of two specially fabricated, non-aqueous porous carbon electrodes, described below. The experimental test procedures employed CV conducted at various sweep-rates and dc charge/discharge cycling at various currents.

The temperature for all experiments was  $25 \pm 1^\circ\text{C}$ . Electrical connections to the modules from the potentiostat were made in a two-electrode configuration, with one of the two capacitor electrodes serving both as a counter and reference (positive terminal).

#### 4.2. Capacitor module fabrication

Type 14–50 (size R6/AA) hardware was used to construct the sealed single-cell electrochemical capacitor modules used in these tests. The porous electrode modules employed 1.0 and 0.40 M tetraethylammonium tetrafluoroborate (TEATFB) in dry propylene carbonate as electrolyte, as described elsewhere [18].

### 5. Results and their interpretations

#### 5.1. Calculated CV responses

##### 5.1.1. Case of constant resistance ( $R_0$ )

In Fig. 1, current responses are conveniently plotted as reduced currents ( $I/(V_m)/sC$ ) as a function of measured potential ( $V_e + IR_0$ ), of a capacitive electrode exposed to electrolytes having various constant electrolyte resistances,  $R_0$ , between 0 and  $50\ \Omega$ , ( $C = 1\ \text{F}$ ,  $s = 20\ \text{mV s}^{-1}$ ,  $V_1 = 0\ \text{V}$ ,  $V_2 = 1\ \text{V}$ ) as previously discussed in some detail [21]. For sufficiently small resistance,  $R_0$ , the current response is essentially that of a pure capacitor (Fig. 1 for  $R_0 \rightarrow 1\ \Omega$ ). Increasing  $R_0$  increases the  $IR_0$  component and, given a sufficiently large  $R_0$ , the overall behaviour of the resistor/capacitor network becomes dominated by the resistive component. Note also, that the form of the CV calculated for the constant resistivity simulation is symmetrical with respect to an in-plane rotation of  $180^\circ$  which renders the  $I_a/sC^{-1}$  versus  $V$  response superimposable with the reverse scan. This indicates that the beginning of discharge behaves identically to the beginning of charge with the exception of reversal in the direction of current.

Examination of the reduced current as a function of the local electrode potential,  $V_e$ , (Fig. 1b) illustrates, given a sufficiently large resistance and resulting  $IR_0$  loss component, how the applied and actual potentials are significantly different so that the actual sweep rate at the working electrode and the effective range of applied potential is far from what the experimenter intended. As well, the local sweep rate,  $dV_e/dt$ , for large  $R_0$ , is not constant, and the  $I/sC^{-1}$  versus  $V_e$  response is not of the expected rectangular form for a purely capacitive device.

Correspondingly, similar behaviour results with increasing capacitance,  $C$ , and/or sweep rate,  $s$ , while maintaining a

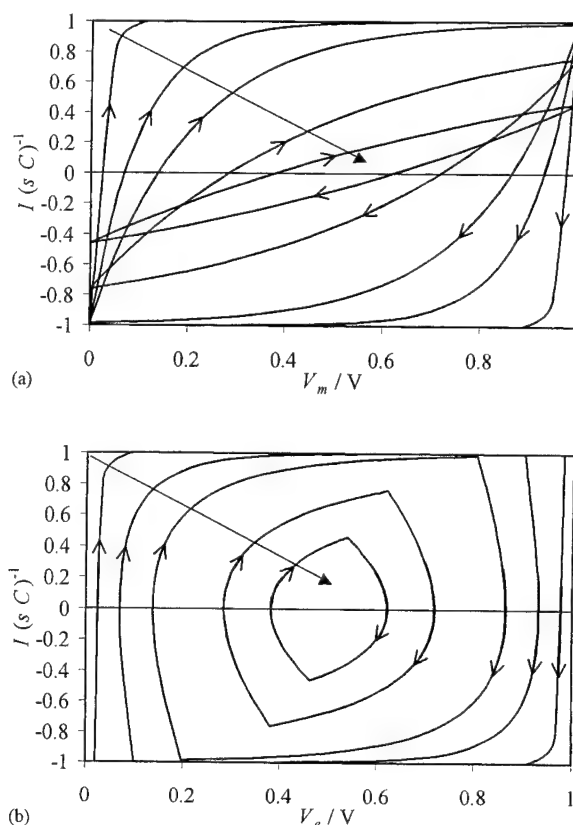


Fig. 1. Calculated cyclic voltammograms expressed as reduced response current ( $I/sC$ ) as a function of (a) measured potential ( $V_e + IR_0$ ) and (b) local working electrode potential ( $V_e$ ) calculated using Eqs. (5a) and (5b) for  $C = 1\ \text{F}$ ,  $V_1 = 0\ \text{V}$ ,  $V_2 = 1\ \text{V}$ ,  $s = 20\ \text{mV s}^{-1}$ . ( $\uparrow$ ) Indicates direction of increasing  $R_0$  (1, 5, 10, 25 and  $50\ \Omega$ ); ( $\rightarrow$ ) direction of voltammetric sweep.

given fixed resistance value. In the former case, an increase in device capacitance,  $C$ , results in an increase in the current  $I$  passed (Eq. (1)), and hence an increase in the  $IR_0$  losses. In the latter case, at low sweep rate,  $I$  is small, so that  $IR_0$  losses are negligible, but as the applied sweep rate is increased, the current increases, so that  $IR_0$  losses become significant. The dependence of “effective” capacitance on sweep rate is of particular importance as it provides an indication of the rate performance of the electrode, i.e. a high sweep rate corresponds to a high rate of charge or discharge of the capacitor electrode, corresponding to greater power levels of operation.

Importantly, these results show that even though the actual capacitance of the working electrode is constant and independent of either  $R_0$  or  $s$ , the “effective” capacitance, which is determined by the  $IR_0$  component, is not constant. Rather, the effective capacitance decreases with increasing  $R_0$  and/or  $s$ , and is typically much less than  $C$ . Thus, less and less of the “theoretical” charge capacity is accessible with increasing  $R_0$  and/or  $s$ , leading to diminution of energy-density and power-density of the device modelled by the above equations.

### 5.1.2. Case where $R$ a linear function of the local working electrode potential

We now examine, in some detail, the results of simulation calculations for a capacitive electrode subject to increasing electrolyte resistivity with increasing state-of-charge, i.e. subject to a resistance component dependent on  $V_e$  as represented by Eq. (6). The effects of the variable resistance on the CV response for three distinct cases are examined: (a) constant  $s$ ,  $C$  and  $r$  (the voltage-dependent component of resistance), and various values of the so-called “fixed” component of the resistance,  $R_0$  (b) constant  $s$ ,  $C$  and  $R_0$ , and various values of the voltage-dependent component of resistance,  $r$ ; and (c) various sweep rates for selected  $C$ ,  $R_0$  and  $r$  values.

Two cases each for  $s = 20 \text{ mV s}^{-1}$ ,  $C = 1 \text{ F}$  and  $R_0 = 1, 5, 10, 25$  and  $50 \Omega$  are considered: the first taking  $r = 1 \Omega \text{ V}^{-1}$  in Eq. (6) and the second  $r = 5 \Omega \text{ V}^{-1}$ . Plots of reduced current as a function of measured potential for  $r = 1 \Omega \text{ V}^{-1}$ , together with that for  $r = 0 \Omega \text{ V}^{-1}$ , for various  $R_0$  values are shown in Fig. 2a. The complementary plot of reduced current as a function of local electrode potential is shown in Fig. 2b.

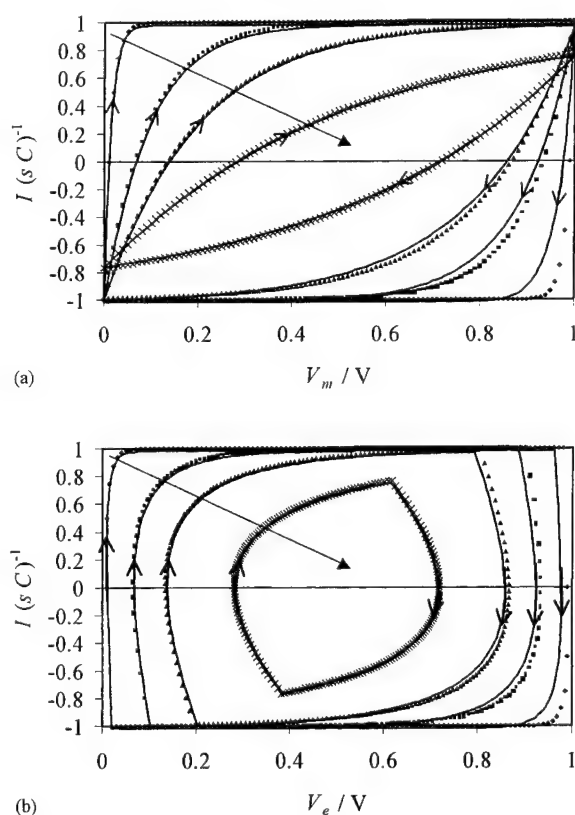


Fig. 2. Calculated cyclic voltammograms expressed as reduced response current ( $I/sC$ ) as a function of (a) measured potential ( $V_e + I(R_0 + rV_e)$ ) and (b) local working electrode potential ( $V_e$ ) calculated using Eqs. (8) and (9) for  $C = 1 \text{ F}$ ,  $V_1 = 0 \text{ V}$ ,  $V_2 = 1 \text{ V}$ ,  $s = 20 \text{ mV s}^{-1}$ . Solid curves  $r = 1 \Omega \text{ V}^{-1}$  and symbols  $r = 0 \Omega \text{ V}^{-1}$ ; (↑) indicates direction of increasing  $R_0$  (1, 5, 10 and 25  $\Omega$ ); (→) direction of voltammetric sweep.

Upon examination of Fig. 2a, it is clear that, for a small  $r$  to  $R_0$  ratio ( $r/R_0 < 1 \text{ V}^{-1}$ ), the anodic scan remains essentially unchanged from that for the  $r = 0 \Omega \text{ V}^{-1}$  case, whereas the cathodic reduced current response is initially more sloping (i.e. resistive). Toward the less positive potential limit of the cathodic scan, the reduced current response is again superimposable upon the response for  $r = 0 \Omega \text{ V}^{-1}$ . Note that the reduced current response for  $r = 1 \Omega \text{ V}^{-1}$  does not exhibit the same symmetry as for the  $r = 0 \Omega \text{ V}^{-1}$  case. From Fig. 2b, it is clear that the  $r$  component further limits the upper voltage window of operation, and thus reduces the power the electrode is capable of delivering.

If  $r$  is comparable to or larger than  $R_0$  (Fig. 3a and b), then both the anodic and cathodic reduced current responses are modified. In this case, the anodic side of the CV has the same general shape as for the case when  $r = 0 \Omega \text{ V}^{-1}$ , but the maximum reduced current,  $I/sC^{-1}$ , achieved is  $< 1$ . Again, the cathodic response at more positive potentials, is more sloping and interestingly, the reduced current at less positive potentials can be greater than 1 (Fig. 3 for  $r = 5 \Omega \text{ V}^{-1}$  and  $R_0 = 1, 5, 10 \Omega$ ). For these cases, the plots of reduced current as a function of local or measured potentials are

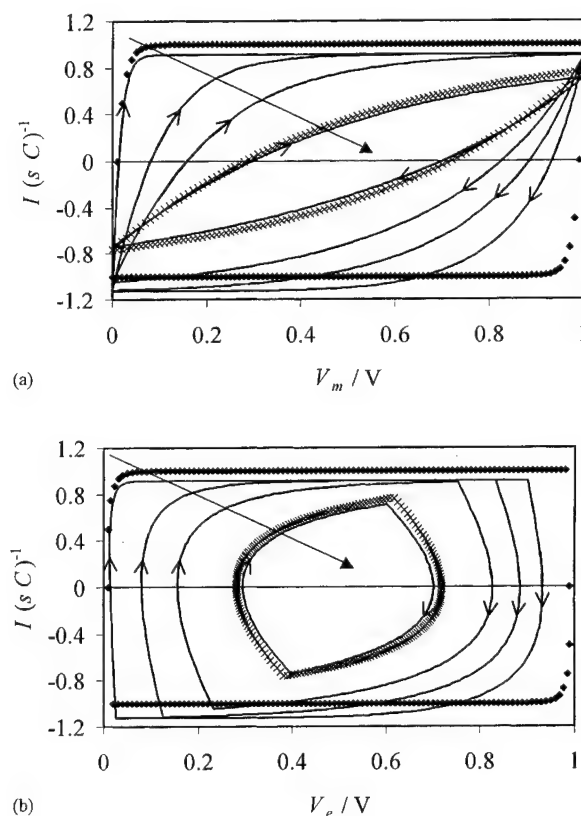


Fig. 3. Calculated cyclic voltammograms expressed as reduced response current ( $I/sC$ ) as a function of (a) measured potential ( $V_e + I(R_0 + rV_e)$ ) and (b) local working electrode potential ( $V_e$ ) calculated using Eqs. (8) and (9) for  $C = 1 \text{ F}$ ,  $V_1 = 0 \text{ V}$ ,  $V_2 = 1 \text{ V}$ ,  $s = 20 \text{ mV s}^{-1}$ . Solid curves  $r = 5 \Omega \text{ V}^{-1}$  and symbols  $r = 0 \Omega \text{ V}^{-1}$ ; (↑) indicates direction of increasing  $R_0$  (1, 5, 10 and 25  $\Omega$ ); (→) direction of voltammetric sweep.

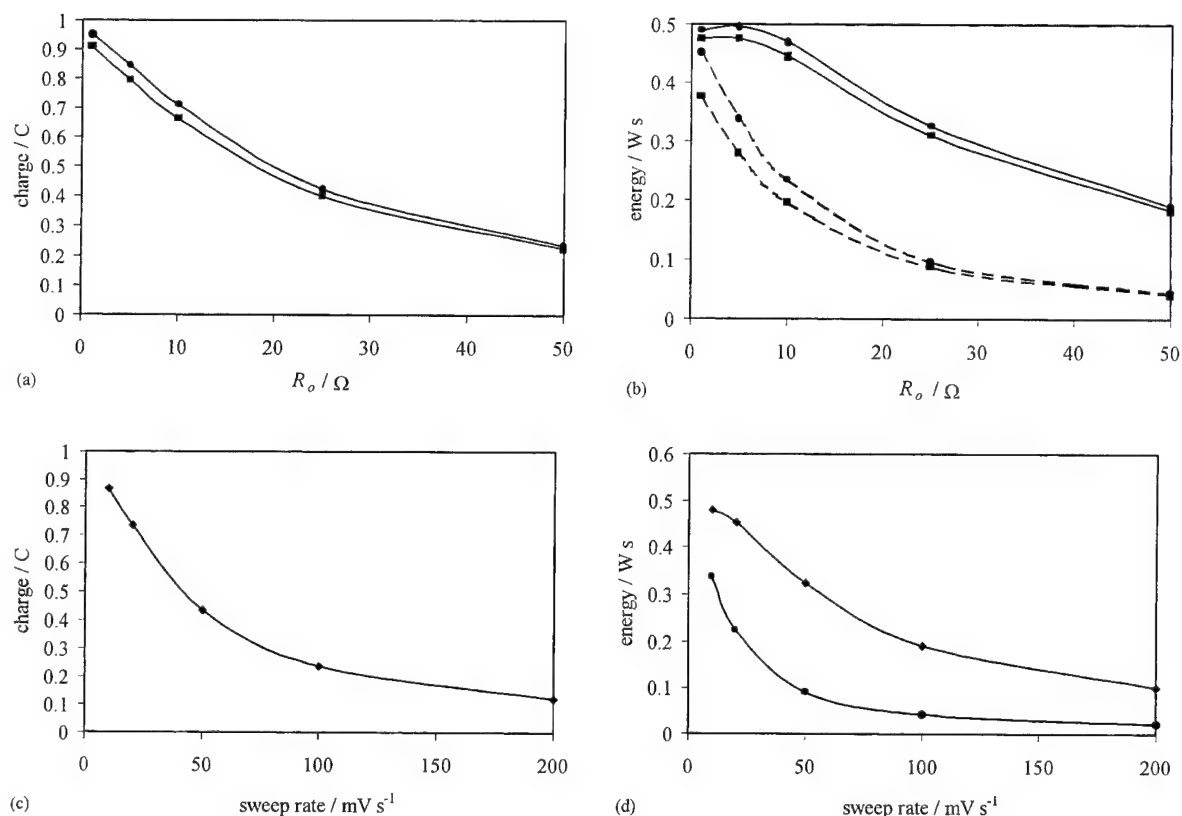


Fig. 4. (a) Charge and (b) energy as a function of  $R_0$ , calculated from the CV's shown in Figs. 2 and 3: (●)  $r = 1$ ; (■)  $r = 5$ ; (—) charge cycle; (---) discharge cycle.

highly asymmetric, indicating that the local electrode sweep rate,  $dV_e/dt$ , can, under certain conditions, be larger than  $s$ .

In Fig. 4a, the charge capacity,  $Q$  in (As) calculated from the CV's shown in Figs. 2 and 3. The charge efficiency determined as  $(Q_{\text{output}}/Q_{\text{input}}) \times 100$  was calculated to be constant and approximately 100% for all values of  $R_0$  and  $r$ . The energy realisable on discharge of the capacitor electrode, especially for cases of large  $R_0$ , will, however, be much less than that involved in charging the same electrode, thus corresponding to serious dissipative losses. This is clearly shown in Fig. 4b in which the energies required for charge and delivered on discharge are plotted as a function of  $R_0$ . The energy efficiency, of course, decreases with increasing  $R_0$ . For  $r/R_0 < 0.5 \text{ V}^{-1}$ , the absolute maximum reduced anodic or cathodic current densities are  $<1$ , and the CVs become more symmetrical.

In Fig. 5a and b, the effect of increasing the ratio of  $r/R_0$  on the reduced current as a function of reduced and local electrode potentials, respectively, is examined for a given constant sweep rate of  $20 \text{ mV s}^{-1}$ , a constant capacitance of  $1 \text{ F}$ , a fixed and significant value of  $R_0 = 10 \Omega$  and  $r/R_0$  values of 0, 0.1, 1, 2, 5 and  $7.5 \text{ V}^{-1}$ . In Fig. 5c, the calculated charge capacity (i.e. charge,  $Q$ ) and the energy required for charge and that delivered on discharge for the CV's shown in Fig. 5a and b.

Again, the CV response is not symmetric about the  $I/sC = 0$  line, and the degree of asymmetry increases with increasing  $r$  value. As  $r$  is increased, the anodic scan becomes more sloping and the maximum anodic current achieved decreases as does the total charge. The cathodic scan response is more complicated. Increasing  $r$ , initially causes the cathodic response to be more sloping, and the maximum reduced current to be  $>1$ , further increase of  $r$  results in an even more sloping CV response, and reduced currents  $<1$ . A plot of the reduced current versus local potential (Fig. 5b) at the working electrode illustrates that increasing  $r$  reduces the potential range over which the working electrode actually cycles.

The effect of reducing the potential range over which the working electrode cycles is shown quantitatively in Fig. 5c in which electrode charge capacity is plotted as a function of  $r$ . In fact,  $Q$  is a linear function of the magnitude of the potential range over which the working electrode actually cycles,  $\Delta V_e$ , as shown in the inset of Fig. 5c. Although the charge capacity decreases with  $r$ , the charge efficiency is independent of  $r$  and approximately 100%. Both the energy required for charge and that delivered on discharge decrease with increase in  $r$  (Fig. 5d), as does the energy efficiency.

Finally, the effect of sweep rate on CV response for a system defined by  $C = 1 \text{ F}$ ,  $R_0 = 5 \Omega$ ,  $r = 10 \Omega \text{ V}^{-1}$  and  $s = 10, 20, 50, 100$  and  $200 \text{ mV s}^{-1}$  is shown in Fig. 6. At

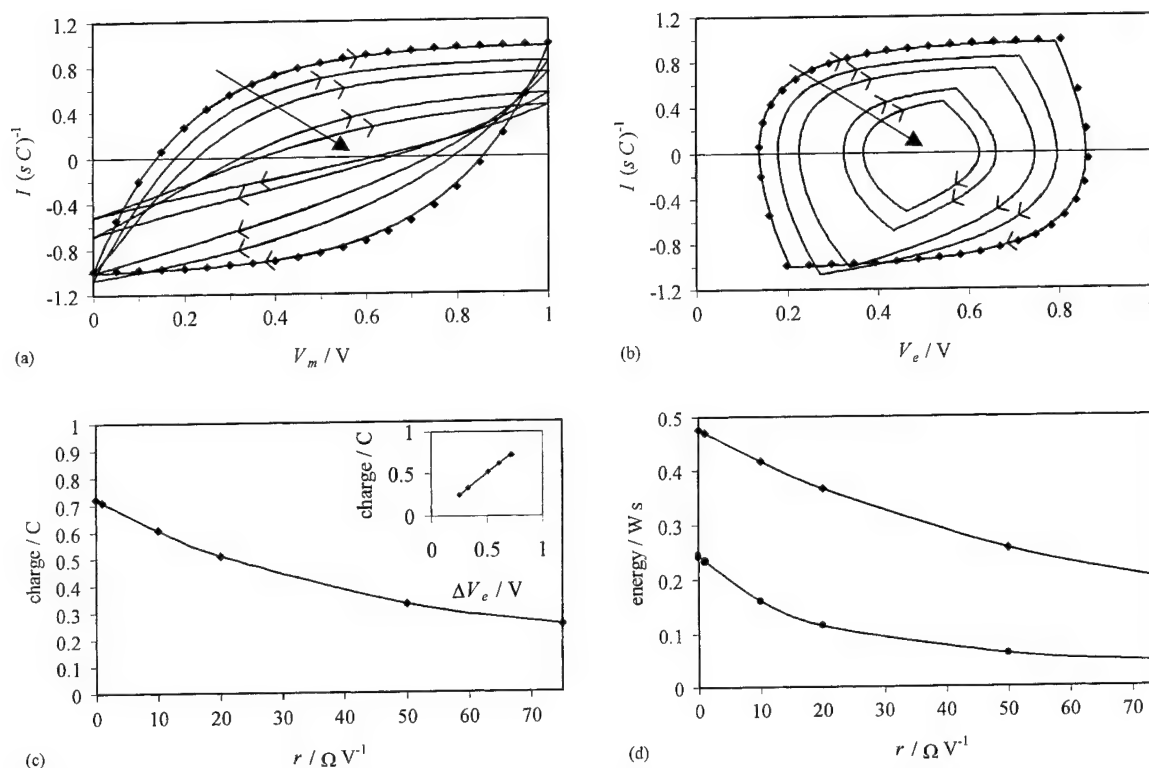


Fig. 5. Calculated cyclic voltammograms expressed as reduced response current ( $I/sC$ ) as a function of (a) measured potential ( $V_e + I(R_0 + rV_e)$ ) and (b) local working electrode potential ( $V_e$ ) calculated using Eqs. (8) and (9) for  $C = 1$  F,  $V_1 = 0$  V,  $V_2 = 1$  V,  $s = 20$  mV s $^{-1}$ ,  $R_0 = 10$   $\Omega$ , symbols  $r = 0$   $\Omega V^{-1}$ . Solid curves  $r = 1, 10, 20, 50$  and  $75$   $\Omega V^{-1}$ ; ( $\nabla$ ) indicates direction of increasing  $r$ ; ( $\rightarrow$ ) direction of voltammetric sweep. (c) Charge and (d) energy as a function of  $r$  calculated from the CV's shown in (a) and (b); ( $\blacklozenge$ ) charge cycle; ( $\bullet$ ) discharge cycle. (c) Charge as a function of  $\Delta V_e$  from CV's shown in (a) and (b).

low sweep rate (10, 20 and 50 mV s $^{-1}$ ), the cathodic current response deviates from the ideal rectangular response much more than does the anodic response. Consider first the anodic scan at low sweep rate; at low potential, the local electrode potential is approximately the same as the measured potential, and the electrolyte resistance is simply  $R_0$ . At higher potential, however, the  $rV_e$  component of the resistance becomes significant resulting in a limiting value for reduced current  $< 1$ . This  $IrV_e$  component then results in a sloping cathodic current response which causes the cathodic response over the full potential range to be far from ideal.

As sweep rate increases,  $IR$  on both anodic and cathodic sweeps increases and both anodic and cathodic responses deviate from the rectangular ideal form, ( $s = 100$  and  $200$  mV s $^{-1}$ ). Further, the voltage range over which the working electrode operates becomes greatly reduced (Fig. 6b), as does the charge capacity of the electrode which falls from 1 C at  $s = 0$  mV s $^{-1}$ , to 0.12 C at  $s = 200$  mV s $^{-1}$ . Again, the charge efficiency independent of  $s$  and 100%.

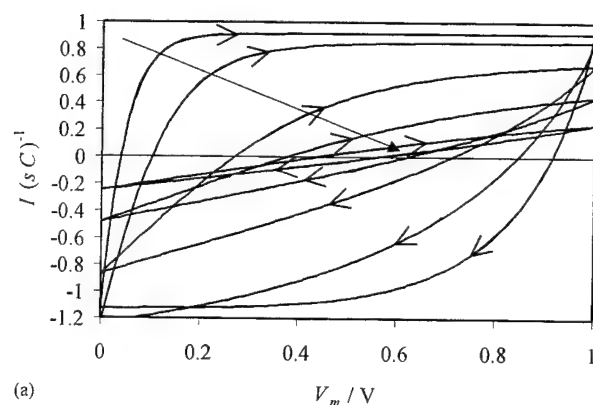
In Fig. 6d, the plot is of energy to charge and the energy recovered on discharge as a function of  $s$ . Both quantities are found to decrease with increase in  $s$  (i.e. decrease with increase in charge/discharge rate), as is the energy efficiency because increase in  $s$  results in an increase in both the  $IR_0$  and  $IrV_e$  losses.

## 5.2. Calculated constant current charge/discharge behaviour

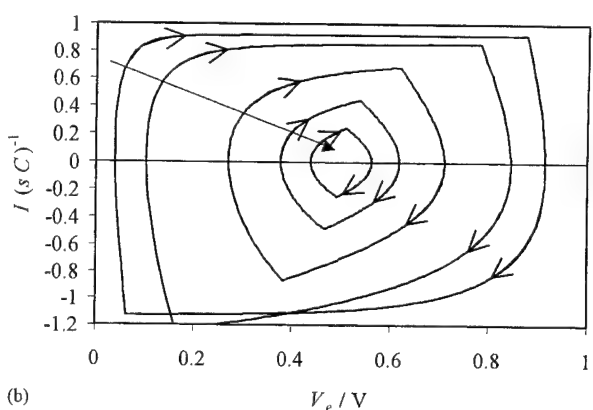
Three cases are considered for a capacitive electrode having a capacitance of 1 F operating within a voltage window of 1 V: (a) constant  $I$ ,  $r$  and various  $R_0$ ; (b) constant  $I$ ,  $R_0$  and various  $r$ ; and (c) constant  $r$ ,  $R_0$  and various constant currents.

### 5.2.1. Case (a)

As  $R_0$  increases the "IR" step which arises at the beginning of charge and discharge increases as seen in the  $V_m$  versus  $t$  plots of Fig. 7a for second and subsequent charge/discharge cycles of an electrode having  $C = 1$  F,  $\Delta V(\text{measured}) = 1$  V,  $I = 10$  mA,  $r = 5$   $\Omega V^{-1}$  and  $R_0 = 0, 1, 5, 10$  and  $25$   $\Omega$ . As a result, the total time of charging to a given voltage limit ( $V_m = V_2$ ) decreases with increased  $R_0$  (therefore, the electrode has less effective charge capacity within a particular voltage window). Also, the average voltage on charge is greater than the average on discharge; as a result, power consumption during charging will be greater than power available on discharge (i.e. watt-hour efficiency will be low, and decrease with increasing  $R_0$ ), a significant practical conclusion. In Fig. 7b, the local electrode potential,  $V_e$ , as a function of time during charge/discharge between measured potential limits of 0 and 1 V.



(a)



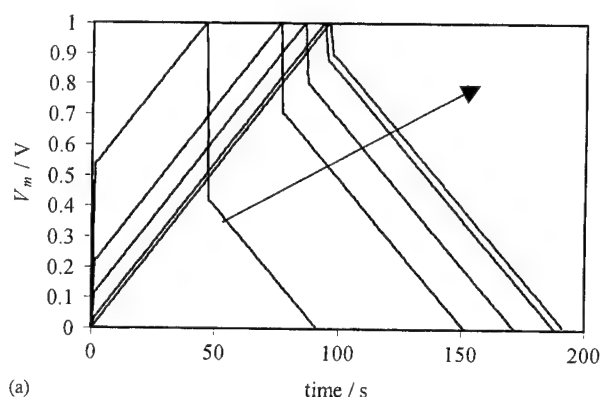
(b)

Fig. 6. Calculated cyclic voltammograms expressed as reduced response current ( $I/(sC)$ ) as a function of (a) measured potential ( $V_e + I(R_0 + rV_e)$ ) and (b) local working electrode potential ( $V_e$ ) calculated using Eqs. (8) and (9) for  $C = 1 \text{ F}$ ,  $V_1 = 0 \text{ V}$ ,  $V_2 = 1 \text{ V}$ ,  $R_0 = 10 \Omega$ ,  $r = 10 \Omega \text{ V}^{-1}$ . (↑) Indicates direction of increasing  $s$ ; (→) direction of voltammetric sweep. (c) Charge and (d) energy calculated from the CV's shown in (a) and (b): (◆) charge cycle; (●) discharge cycle.

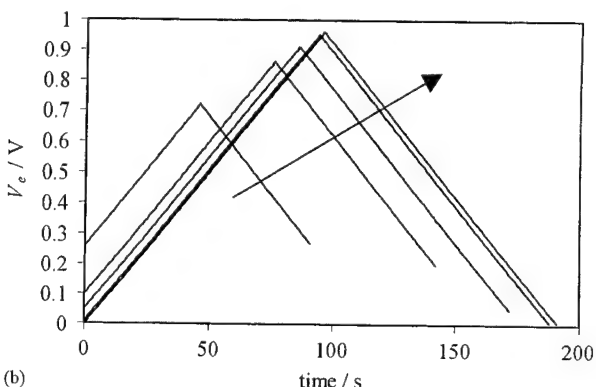
Clearly, the capacitive electrode is cycling within a restricted potential range, which decreases with increasing  $R_0$ . Note also that increasing  $R_0$  both decreases the anodic potential limit and increases the cathodic limit, thus reducing the cycling window at both extremes of potential.

### 5.2.2. Case (b)

Fig. 8a and b plotted the  $V_m$  and  $V_e$  versus  $t$ , respectively, for an electrode defined by  $C = 1 \text{ F}$ ,  $\Delta V(\text{measured}) = 1 \text{ V}$ ,  $I = 10 \text{ mA}$ ,  $R_0 = 10$  and  $r$  of 0, 10, 20, 35, 50 and  $75 \Omega \text{ V}^{-1}$ . The  $IR$  drop on switching from discharge to recharge is determined primarily by  $R_0$  (except in the case of very large  $r/R_0$ ), while that for switching from charge to discharge is due to the combination of  $r$  and  $R_0$  terms. Interestingly, however, the working electrode reversal potential on the second and subsequent charge is determined by the magnitude of  $r$ . Again, increasing  $r$  will lower both watt-hour efficiency (due to higher charging voltage as compared with discharge voltage) and charge storage capacity (as  $r$  increases the local working electrode cycling range decreases).



(a)



(b)

Fig. 7. Calculated voltage profile for second constant current charge/discharge cycle as a function of time using Eq. (11) for  $C = 1 \text{ F}$ ,  $V_1 = 0 \text{ V}$ ,  $V_2 = 1 \text{ V}$ ,  $I = 10 \text{ mA}$ ,  $r = 5 \Omega \text{ V}^{-1}$ : (a) measured potential ( $V_e + I(R_0 + rV_e)$ ) and (b) local working electrode potential ( $V_e$ ). (↑) Indicates direction of decreasing  $R_0$  (25, 10, 5, 1 and  $0 \Omega$ ).

### 5.2.3. Case (c)

The rate effects for a system having  $C = 1 \text{ F}$ ,  $\Delta V(\text{measured}) = 1 \text{ V}$ ,  $R_0 = 5 \Omega$  and  $r = 10 \Omega \text{ V}^{-1}$  and  $I = 10, 20, 30$  and  $40 \text{ mA}$  are shown in Fig. 9a and b for measured and local electrode potentials, respectively, as a function of charge (mAh) for second and subsequent charge/discharges. The effective electrode charge capacity (Ah) and effective capacitance (F) are both rate dependent. Capacity (Ah) decreases with increasing  $I$  (and consequently increasing  $IR$ ). As the current increases the effective capacitance increases, but over a progressively decreasing voltage window. The charging efficiency (Ah) remains relatively constant with increasing  $I$  ( $\geq 90\%$ ). Similar to the results shown in Figs. 7 and 8, increasing rate results in a restriction of the local potential cycling range. Similar trends are shown in the three Figs. 7–9 where it is seen that each of increasing  $R_0$ ,  $r$  and  $I$  results in an increase in the “ $IR$ ” loss component.

## 5.3. Comparison with experimental results for specially prepared non-aqueous carbon electrode supercapacitors

### 5.3.1. Cyclic voltammetry (CV)

The experimentally derived capacitance response voltammograms for specially prepared [18] capacitor devices

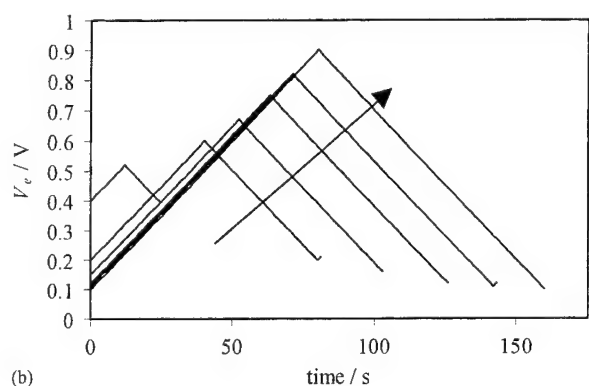
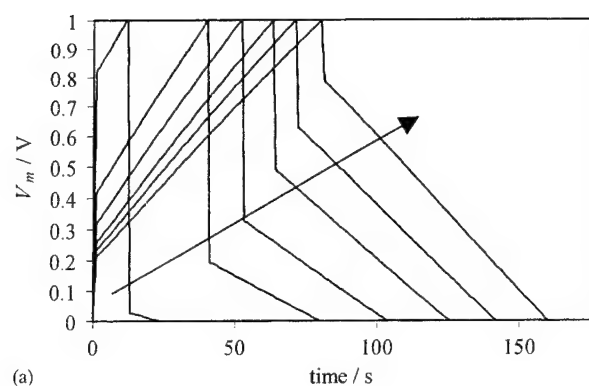


Fig. 8. Calculated voltage profile for second constant current charge/discharge cycle as a function of time using Eq. (11) for  $C = 1 \text{ F}$ ,  $V_1 = 0 \text{ V}$ ,  $V_2 = 1 \text{ V}$ ,  $I = 10 \text{ mA}$ ,  $R_0 = 10 \Omega$ : (a) measured potential ( $V_e + I(R_0 + rV_e)$ ) and (b) local working electrode potential ( $V_e$ ). (†) Indicates direction of decreasing  $r = 0, 10, 20, 35, 50$  and  $75 \text{ V}^{-1}$ .

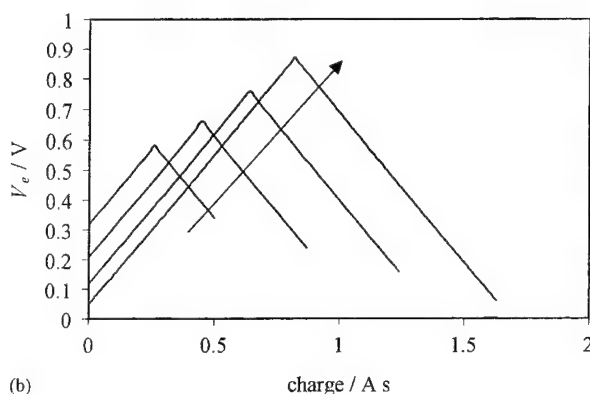
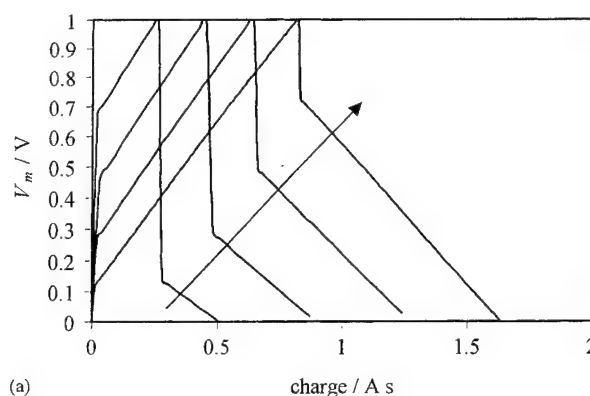


Fig. 9. Calculated voltage profile for second constant current charge/discharge cycle as a function of time using Eq. (11) for  $C = 1 \text{ F}$ ,  $V_1 = 0 \text{ V}$ ,  $V_2 = 1 \text{ V}$ ,  $R_0 = 5 \Omega$ ,  $r = 10 \text{ V}^{-1}$ : (a) measured potential ( $V_e + I(R_0 + rV_e)$ ) and (b) local working electrode potential ( $V_e$ ). (†) Indicates direction of decreasing  $I = 10, 20, 30$  and  $40 \text{ mA}$ .

having 1.0 and 0.4 M TEATFB electrolyte are shown in Fig. 10a and b, respectively, as a function of sweep-rate.

In Fig. 10a, for the 1.0 M electrolyte, the capacitance behaviour approximates to ideal behaviour at the lowest sweep-rate of  $1 \text{ mV s}^{-1}$ , i.e. a voltammogram having an almost rectangular form and mirror-image symmetry of the current responses about the zero-current line is observed. With increasing  $s$  the voltammograms become distorted from the rectangular form expected for an ideal capacitor having constant capacitance, similar to the calculated effects shown in Fig. 1.

The CV response of the module made with 0.4 M electrolyte, shown in Fig. 10b, for  $s = 5, 10, 20, 30$  and  $40 \text{ mV s}^{-1}$ , exhibits behaviour similar to that calculated for the significant resistance models of this study (cf. Fig. 2). Here the capacitance response as a function of voltage is nearly ideal at low sweep rate ( $5 \text{ mV s}^{-1}$ ), while at higher sweep rates, becomes distorted. At high  $s$ , unlike the ideal behaviour, the realised capacitance is both varying with module voltage and increasing with decreasing  $s$ .

### 5.3.2. Constant-current charge/discharge behaviour

The observed constant-current charge/discharge behaviour is plotted in Fig. 11a and b for the respective capacitor

modules discussed in Section 5.3.1, having 1.0 and 0.4 M electrolyte, respectively, as a function of calculated cumulative charge,  $Q$ , in As at constant current charge/discharge rates of 1.33, 1.0, 0.67, 0.33  $\text{A g}^{-1}$  of carbon.

Note, even for the 1.0 M module shown in Fig. 11a, that there is a small, but significant sharp drop in voltage on changing from charging to discharging current and a sharp increase at the start of the charging process. This is not due entirely to a direct ESR effect but is also a characteristic of *redistribution* of charge within the pores. The same characteristic curve was demonstrated in [22] found for a hardware, four-element model RC network, made with relatively small resistive elements. Probe measurements enabled redistribution of charge at each of the capacitor elements in this hardware RC ladder network to be directly observed experimentally [22].

Fig. 11b shows similar plots for the capacitors employing the smaller concentration of electrolyte, 0.4 M. Here the  $IR$  drops are significantly larger than those in Fig. 11a, and even at the lowest rate of charge/discharge of 0.25 A, the charge capacity of the 0.4 M electrolyte module is significantly reduced from that of the 1.0 M module. This further illustrates that in the low concentration electrolyte modules the local electrode potential range is much smaller than the



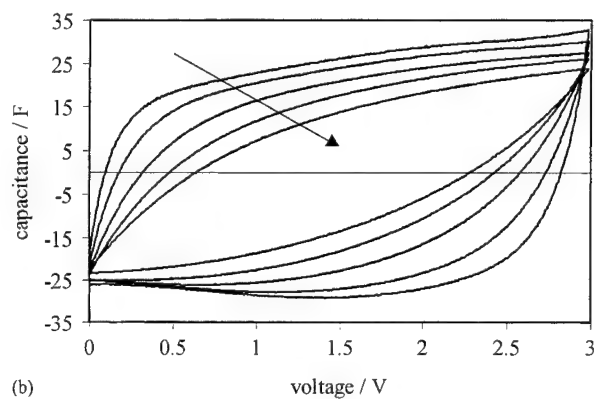
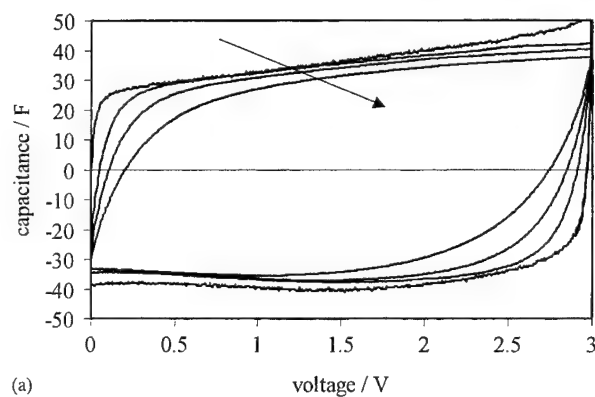


Fig. 10. (a) Cyclic voltammograms, showing the current responses expressed as capacitance, for the 1.0 M TEATFB electrolyte module as a function of voltage over the voltage range 0–3 V at 1, 5, 10 and 20  $\text{mV s}^{-1}$ ; arrow indicates direction of increasing sweep rate; (b) cyclic voltammograms, showing the current responses expressed as capacitance, for the 0.4 M TEATFB electrolyte module as a function of voltage over the voltage range 0–3 V at 5, 10, 20, 30 and 40  $\text{mV s}^{-1}$ . ( $\uparrow$ ) Indicates direction of increasing sweep rate.

measured range. Thus,  $IR$  effects can result in reduced energy- and power-density, and therefore, performance characteristics of practical devices. A rate increase of  $0.33\text{--}1.33 \text{ A g}^{-1}$  of carbon results in a reduction of the charge capacity from 0.99 to 0.72 As (30% reduction) for the 1.0 M electrolyte device, and from 0.61 to 0.21 As (66% reduction) for the 0.4 M electrolyte device. This results from a restriction in the local electrode potential range as previously discussed, and leads to the practically significant reduction in energy storage capacity and energy-density.

These features remain largely unrevealed in constant-current charge/discharge curves for well engineered, practical capacitors having an optimised low resistance of electrolyte, especially in the cases of aqueous electrolyte embodiments.

## 6. Conclusions

Increasing  $s$ ,  $r$ , or  $R_0$  results in a decrease in the overall charge storage capacity of the electrode. The ampere-

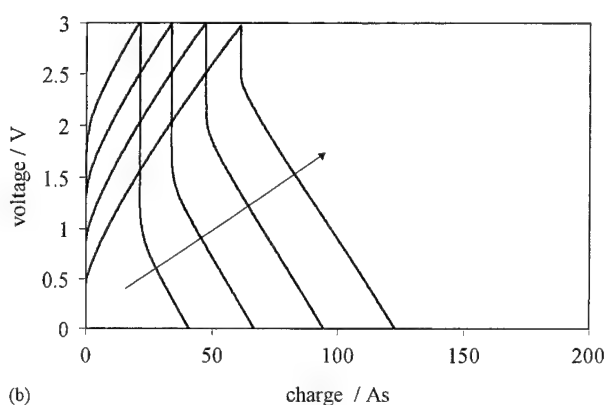
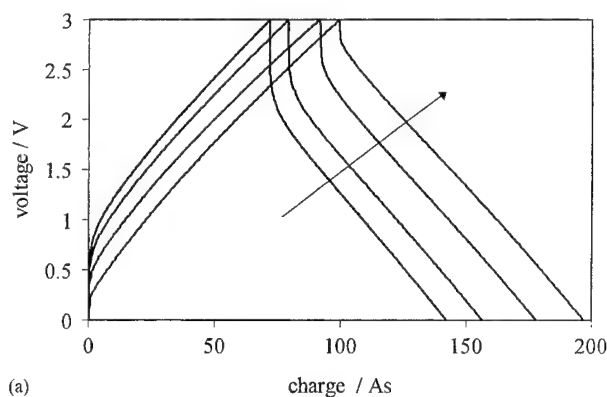


Fig. 11. The voltage response to constant current charging/discharging currents of 1.33, 1.0, 0.67 and  $0.33 \text{ A g}^{-1}$  of carbon, as a function of cumulative calculated charge (As) for a redox engineering 3 V AA electrochemical capacitor: (a) electrolyte concentration 1.0 M, and (b) electrolyte concentration 0.4 M. ( $\uparrow$ ) Indicates the direction of decreasing current density.

hour efficiency remains, however, constant, at 100% for all  $s$ ,  $r$  and  $R_0$  considered (i.e. ampere-hour input = ampere-hour output). The energy efficiency (watt-hour output/watt-hour input) was found to decrease with increasing  $s$ ,  $r$  or  $R_0$ . Any variation in  $s$ ,  $r$  or  $R_0$  which increases the asymmetry of the CV response, results in a decrease in the available energy, and thus a decrease in energy-density an operational energy efficiency. The modelling treatment provides a good computational basis for interpreting the experimental behaviour of selected capacitor test modules.

## Acknowledgements

Grateful acknowledgement is made to the Natural Sciences and Engineering Research Council of Canada for support of this work on a Strategic Grant. Thanks are due to Dr. N. Marincic of Redox Engineering Inc. (Winchester, MA) for preparing the non-aqueous solution capacitor modules.



## References

- [1] B.E. Conway, *J. Electrochem. Soc.* 138 (1991) 1539.
- [2] T.C. Liu, W.G. Pell, B.E. Conway, *Electrochim. Acta* 42 (1997) 3541.
- [3] T.C. Liu, W.G. Pell, B.E. Conway, S. Roberson, *J. Electrochem. Soc.* 145 (1998) 1882.
- [4] Y. Sato, K. Yomogida, T. Nanaumi, K. Kobayakawa, Y. Ohsawa, M. Kawai, *Electrochem. Solid State Lett.* 3 (2000) 113.
- [5] C. Lin, J.A. Ritter, B.N. Popov, *J. Electrochem. Soc.* 146 (1999) 3155.
- [6] D.C. Grahame, *Chem. Rev.* 41 (1947) 441.
- [7] B.E. Conway, *Electrochemical Supercapacitors Scientific Fundamentals and Technological Applications*, Kluwer-Plenum Publication Company, New York, 1999 (Chapter 10).
- [8] B.E. Conway, in: A. Attwell, T. Kelly (Eds.), *Power Sources* 15 (1995) 65.
- [9] J. Miller, in: S. Wolsky, N. Marincic (Eds.), *Proceedings of the 4th International Symposium on Double-Layer Capacitors and Similar Energy Storage Devices*, Florida Educational Seminars, Boca Raton, FL, 1994.
- [10] D. Ragone, in: *Proceedings of the Society Automotive Engineers Conference*, Detroit, MI, USA, May 1968.
- [11] W.G. Pell, B.E. Conway, *J. Power Sources* 63 (1996) 255.
- [12] R. de Levie, *Electrochem. Acta* 8 (1963) 751.
- [13] R. de Levie, *Electrochem. Acta* 9 (1964) 1231.
- [14] H. Keiser, K.D. Beccu, M.A. Gutjahr, *Electrochim. Acta* 21 (1976) 539.
- [15] A.M. Johnson, J. Newman, *J. Electrochem. Soc.* 118 (1971) 510.
- [16] F.A. Posey, T. Morozumi, *J. Electrochem. Soc.* 113 (1966) 176.
- [17] L.G. Austin, E.G. Gagnon, *J. Electrochem. Soc.* 120 (1973) 251.
- [18] W.G. Pell, B.E. Conway, N. Marincic, *J. Electroanal. Chem.* (2000), in press.
- [19] J.P. Zheng, T.R. Jow, *J. Electrochem. Soc.* 144 (1997) 2417.
- [20] F. Kreysig, *Advanced Engineering Mathematics*, 5th Edition, Wiley, New York, 1983 (Chapter 21).
- [21] W.G. Pell, B.E. Conway, *J. Electroanal. Chem.* (2000), in press.
- [22] W.G. Pell, B.E. Conway, W.A. Adams, J. de Oliveira, in: *Proceedings of the 21st International Power Sources*, Vol. 80, Brighton, UK, 1999, p. 134.

# Nickel metal hydride batteries for high power applications

M. Luisa Soria<sup>a,\*</sup>, Joaquín Chacón<sup>b</sup>, J. Carlos Hernández<sup>b</sup>,  
Daniel Moreno<sup>a</sup>, Araceli Ojeda<sup>a</sup>

<sup>a</sup>Tudor Research Laboratory, Exide Technologies, Ctra. N-II, km 42, E-19200 Azuqueca de Henares, Spain

<sup>b</sup>Electro Mercantil Industrial, Exide Technologies, Hierro 38, E-28850 Torrejón de Ardoz, Spain

Received 1 December 2000; accepted 4 December 2000

---

## Abstract

Nickel metal hydride (Ni/MH) is presently the most promising battery system for electric and hybrid vehicle propulsion in the short and mid-term. This paper presents the results obtained in the development of prismatic Ni/MH batteries for high power, mainly hybrid vehicle, applications.

Valve regulated Ni/MH cells rated at 25 and 60 Ah have been designed and assembled using improved positive and negative electrodes. Both types of cells showed excellent high rate discharge capability and fast rechargeability and a satisfactory charge retention when stored and cycle life under deep cycling and hybrid vehicle working conditions. On the other hand, energy and power efficiency ratios were improved in the 60 Ah cells. © 2001 Elsevier Science B.V. All rights reserved.

**Keywords:** Nickel metal hydride batteries; High rate applications; Hybrid vehicles; Electrical testing

---

## 1. Introduction

There is a clear need for clean transportation means, specially in the big cities. Air pollution and the “Green House effect” are environmental problems that can force European legislation into laws similar to the Californian “Clean Air Act” (1988). However, the final acceptance of zero-emission or hybrid vehicles will depend strongly on the final performance of the batteries and on its acquisition price and maintenance costs. Ni/MH is presently the most promising battery system for hybrid vehicle propulsion in the short and mid-term.

During the last decade, the use of Ni/MH batteries [1] has spread quickly for consumer applications, mainly for portable electronic equipment. However, power capability should be improved to answer the increased power demands of the different types of hybrid vehicles (range extender, power assist), and even for the future conventional cars with 42 V electrical systems. The final acceptance of hybrid vehicles will depend on the performance/cost ratio achieved. Also in comparison to the outcome of competing technologies for low and zero-emission vehicles, including the efforts to reduce emissions in conventional gasoline

combustion engines and the development of low emission vehicles using alternative fuels such as natural gas.

This paper presents the results obtained in the development of Ni/MH batteries for high power applications, mainly hybrid vehicles. The work was carried out within a EU funded project [2] aimed at the development of positive electrodes using a novel type of nickel hydroxide characterised by an irregular shaped grain structure and a high tap density.

## 2. Experimental

The development of the positive and negative electrodes for Ni/MH batteries has been reported previously [3,4]. Both types of electrodes were prepared with three dimensional nickel substrates in order to improve the high power capability of the electrodes by means of the conductive network and with additives to decrease the electrode internal resistance.

The nickel hydroxide doped with cobalt and zinc was provided by R.B.C. and was prepared according to a novel electrodialysis process [5], followed by ageing in a KOH solution to promote the  $\beta$ -phase and increase crystallinity. This material is characterised by a high tap density, an irregular shape and a high BET surface area (35–40 m<sup>2</sup> g<sup>-1</sup>). It has been described as a highly defective

---

\* Corresponding author. Tel.: +34-949-263-316; fax: +34-949-262-560.  
E-mail address: soriaml@tudor.es (M.L. Soria).

Table 1  
Characteristics of optimised positive and negative electrodes

	Positive electrodes	Negative electrodes
Substrate type	Ni foam	Ni fibre
Weight ( $\text{g m}^{-2}$ )	500	950
Electroactive material	$\text{Ni(OH)}_2$ doped with Co (1.5%) and Zn (3.5%)	$\text{LaMM}(\text{Ni}_{3.4}\text{Mn}_{0.4}\text{Al}_{0.3}\text{Co}_{0.7})$ 52% La in MM
Additives (%)	Ni powder (15) Co + CoO (5) PTFE (3) Arabic gum (0.7)	Extra-conductive black (3.2) PTFE (1.6) PVA (0.2)
Preparation conditions	Pasting + pressing	Rolling + pressing

material, a fact that is associated with a complex electrochemical behaviour [6,7]. Doping with cobalt and zinc improves the active material efficiency, cycleability and high temperature performance [8,9].

The  $\text{AB}_5$  alloy used for the negative electrodes was supplied by GfE Metalle und Materialien with the standard composition  $\text{LaMM}(\text{Ni}_{3.4}\text{Mn}_{0.4}\text{Al}_{0.3}\text{Co}_{0.7})$  (MM: misch metal) [10]. A mechanical treatment of the alloy was provided by the manufacturer to improve the material power capability [11].

Different additives were used with the aim of improving the performance of the active materials, in terms of conductivity, adequate rheological properties for electrode preparation and to avoid the active material shedding during cycling. The positive and negative electrode preparation conditions were finally optimised according to the materials used and the high power demanding application. Table 1 summarises the characteristics and composition of both types of electrodes.

As shown in the table, the positive active material [12,13] included nickel powder and cobalt compounds to increase conductivity, natural or synthetic polysaccharides to adjust paste rheology thus improving processing conditions and polytetrafluorethylene (PTFE) as binder of the particles, to avoid active material shedding during battery manufacturing and operation. In the negative electrodes, extra-conductive blacks were used to increase conductivity and PTFE and PVA as binders [14–16].

Table 2 shows the capacity ratios of the optimised electrodes used in the assembly of Ni/MH prismatic cells.

Table 2  
Capacity ratios of the optimised positive and negative electrodes

	Positive electrodes	Negative electrodes
Capacity $C/5$ rate		
$\text{mAh g}^{-1}$ active material	275	278
$\text{mAh g}^{-1}$ electrode	157	179
$\text{mAh cm}^{-3}$ electrode	340	677
Capacity $7C$ rate		
$\text{mAh g}^{-1}$ active material	132	180
$\text{mAh g}^{-1}$ electrode	75	116
$\text{mAh cm}^{-3}$ electrode	164	435

Two types of Ni/MH prismatic cells with stacked electrodes have been assembled, with a nominal capacity of 25 and 60 Ah, respectively. Table 3 shows the main features of both types of cells.

All the cell components have been specially designed to achieve the maximum power drain (minimum electrical resistance), with minimum weight and a valve regulated maintenance-free system. Besides the electrodes, the separator and the valve have been studied as key components of the cell to achieve the improved performance and maintenance-free operation. A solution of KOH,  $1.30 \text{ g cm}^{-3}$  with  $20 \text{ g l}^{-1}$  LiOH, was used as electrolyte in the cells, impregnating the electrodes and separator. The incorporation of lithium ions in the nickel lattice combined with the codeposited cobalt, enhances the charge acceptance of the positive electrodes, specially at elevated temperatures, due to the stabilisation of high oxidation states [17].

Table 3  
Ni/MH cell design features and components

Nominal capacity (Ah)	25	60
Cell dimensions ( $\text{mm}^3$ )	$80 \times 34 \times 133$	$114 \times 45 \times 158$
Plate number ( $\pm$ )	12/11	15/14
Plate dimensions ( $\text{mm}^2$ )	$90 \times 70$	$110 \times 105$
Separator	SciMAT 700/14 (grafted polyolefine)	SciMAT 700/14 (grafted polyolefine)
Electrolyte	$\text{KOH } 1.3 \text{ g cm}^{-3} + \text{LiOH } 20 \text{ g l}^{-1}$	$\text{KOH } 1.3 \text{ g cm}^{-3} + \text{LiOH } 20 \text{ g l}^{-1}$
Case and cover	Stainless steel, 0.4 mm thick	Stainless steel, 0.4 mm thick
Cell weight (kg)	0.89	1.95

Table 4  
Electrical testing programme of Ni/MH cells

	Testing conditions
Constant current discharges at different rates	Discharge at the $x$ C rate, being $x = 0.2, 0.5, 1, \dots, 10$ at room temperature
Constant current discharges at different temperatures	Discharge at the 1C rate at room temperature: 0 and 40°C
Power capability	Discharge during 10 s at the 10C rate and at different states of charge: 100, 80, 60, 40 and 20% SOC
Constant current charging at different rates	Charge at the $y$ C rate, being $y = 0.2, 0.5, \dots, 4$ , with a charge factor of 120% at room temperature
Charging efficiency for different states of charge	Recharge the cells at the 1C rate with recharge factors between 50 and 120%
Rapid charge capability	Discharge at the C/2 rate down to 40% SOC
	Recharge between 40 and 80% SOC at the 2C, 5C and 8C rates
Self-discharge	Capacity retention after 48 and 120 h storage at room temperature and 40°C and after 28 days storage at room temperature
Cycle life	Constant current conditions at the C/5 and 1C rates (100% DOD) and according to EUCAR power assist profile
Recombination efficiency	Weight loss during cell overcharge at the C/20 rate

The separator must be characterised by a low internal resistance, to achieve high rate performance (related to thickness and porosity), small pores to avoid short-circuits, high electrolyte absorption, good wettability and chemical stability in alkaline electrolyte even at high temperature. On the other hand, polypropylene non-woven materials grafted with acrylic monomers show enough wettability and ionic exchange capability during battery operation [18].

Valves are quite important elements of the cells, as the internal pressure can rise during overcharge. The functions of the valve are to protect the cell from entering oxygen, to keep  $H_2$  gas in the cell (lower water consumption) and to ensure opening as soon as the internal pressure limit is reached. The valve is designed according to the pressure evolution inside the cell during charge and discharge conditions.

Electrical testing of the Ni/MH cells has been carried out with a computer-controlled cycling equipment (Bitrode LCN-3-100-12) with modules CSM-6-100-12 for testing individual cells. High rate battery discharges have been performed with a Digatron UBT, BTS-500, model HEW 2000-6BTS. Data acquisition was performed with the software available (Bitrode and Digatron) and with a data logger Datataker 505. Temperature measurements were carried out with thermocouples type J.

After cell formation and initial cycling at the C/5 rate (C being the rated capacity of 25 or 60 Ah), the Ni/MH cells were tested according to the conditions mentioned in Table 4.

### 3. Results and discussion

Battery testing conditions were defined according to the nominal capacity of the cells, i.e. 25 and 60 Ah. Previous to all the discharge tests, the cells were charged during 7 h at the C/5 rate. Discharged capacities depend on the testing rates and, at low rates (C/5), the figures obtained are around 110–115% of the nominal capacity.

Figs. 1 and 2 show the constant current discharge curves at different rates, respectively. The results are referred to the nominal capacity (25 or 60 Ah) of the cells. The maximum

battery capacity values obtained were 28.9 and 69.2 Ah at the C/5 rate. After each discharge at the  $x$ C rate, the cells were further discharged at the C/5 rate down to 1.0 V. As shown in the figures, discharge duration depends mainly on the discharge voltage, that means, on the internal resistance of the cell. At the 8C rate, 73% of the real capacity, i.e. 84% of the nominal capacity, is obtained when the 25 Ah cells are discharged down to 0.8 V. The cells rated at 60 Ah deliver 56% of the nominal capacity when discharged at the 10C rate down to 0.6 V. The cell temperature has been measured during the discharges: the 60 Ah cells showed a temperature increases of 6, 10, 14 and 20°C during the discharges at 120, 240, 420 and 600 A, respectively. Heating is mainly due to Joule effect ascribed to the internal resistance of the cells. The metallic container allows for an efficient heat dissipation.

The internal resistance of the cells has been measured both under AC (1 kHz) and DC conditions. The AC resistance of the Ni/MH batteries is 1.6 m $\Omega$  for the 25 Ah cells and 1.2 m $\Omega$  for the 60 Ah cells. The DC resistance has been calculated taking into account the voltage drop of the cells when discharged at two different rates: 1C and 8C for the 25 Ah cells and 1C and 10C for the 60 Ah cells. The values obtained are 1.67 and 1.24 m $\Omega$ , respectively.

In order to establish the temperature influence on the discharge duration, the 60 Ah Ni/MH cells were discharged at 60 A (1C rate) after 18 h storage at three different temperatures: 0, 25 (room temperature) and 40°C. Referred to the capacity obtained at room temperature, the cells showed a 9% decrease in battery capacity at 0°C and a 10% decrease at 40°C.

The power capability of the Ni/MH cells was tested at different SOC: the 60 Ah cells were discharged according to a sequence of current peaks at 600 A at the 100, 80, 60, 40 and 20% SOC, followed by a discharge at 12 A (C/5 rate) to reach the following SOC check point. The discharge curve is represented in Fig. 3. On the other hand, Fig. 4 shows the power values calculated at the different SOC.

Moreover, the AC internal resistance of the Ni/MH cells at the different states of charge has been measured. The values

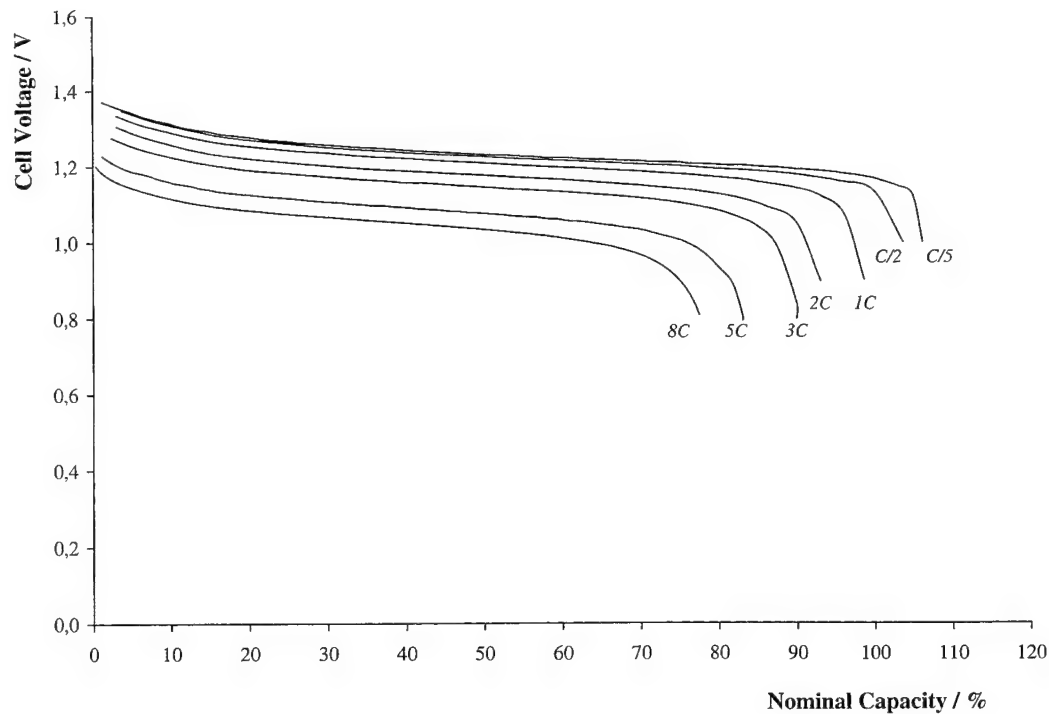


Fig. 1. Constant discharge curves at different rates of Ni/MH cells ( $C = 25$  Ah).

recorded indicate that there is no significant effect of the SOC on the internal resistance as it increased  $0.03 \text{ m}\Omega$  during the discharge.

The rechargeability test included constant current charges at  $C/5$ ,  $C/2$ ,  $1C$ ,  $2C$  and  $4C$ , and the recharge factor

was  $1.2C$  in all cases. After each charge, the cells were discharged at the  $C/5$  rate down to  $1.0 \text{ V}$ . Fig. 5 shows the charge curves of the cells rated  $25 \text{ Ah}$ . The  $60 \text{ Ah}$  cells showed similar charging curves. The temperature increase during the charges of the  $60 \text{ Ah}$  cells was  $5$ ,  $8$ ,  $10$ ,  $13$  and

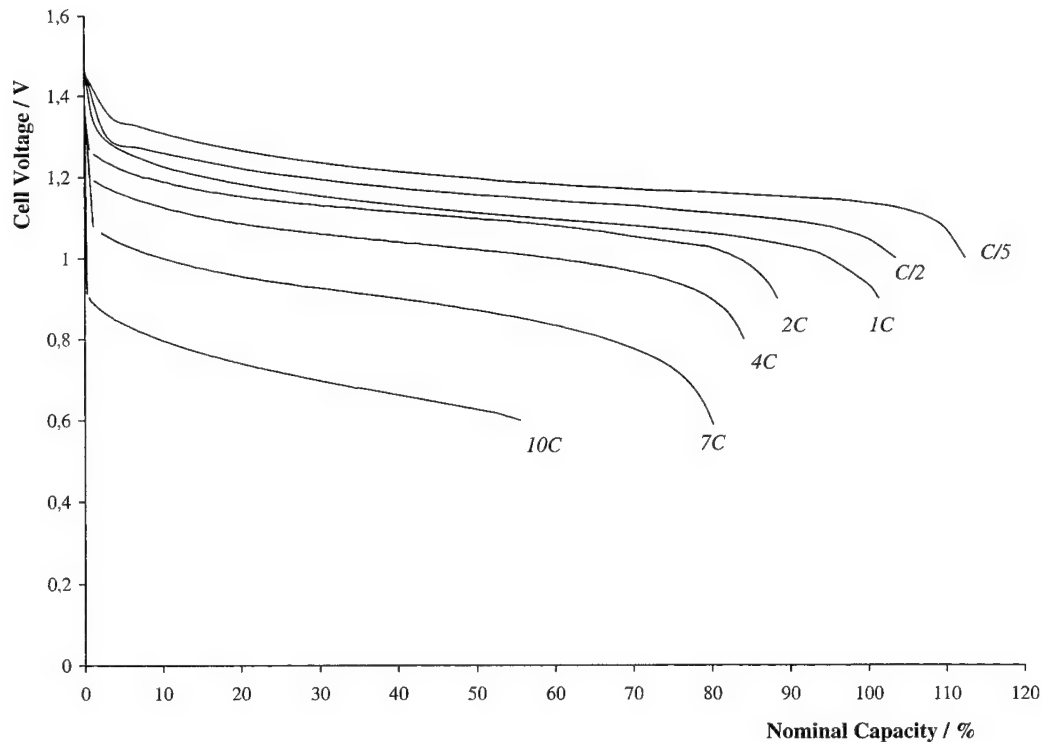


Fig. 2. Constant discharge curves at different rates of Ni/MH cells ( $C = 60$  Ah).

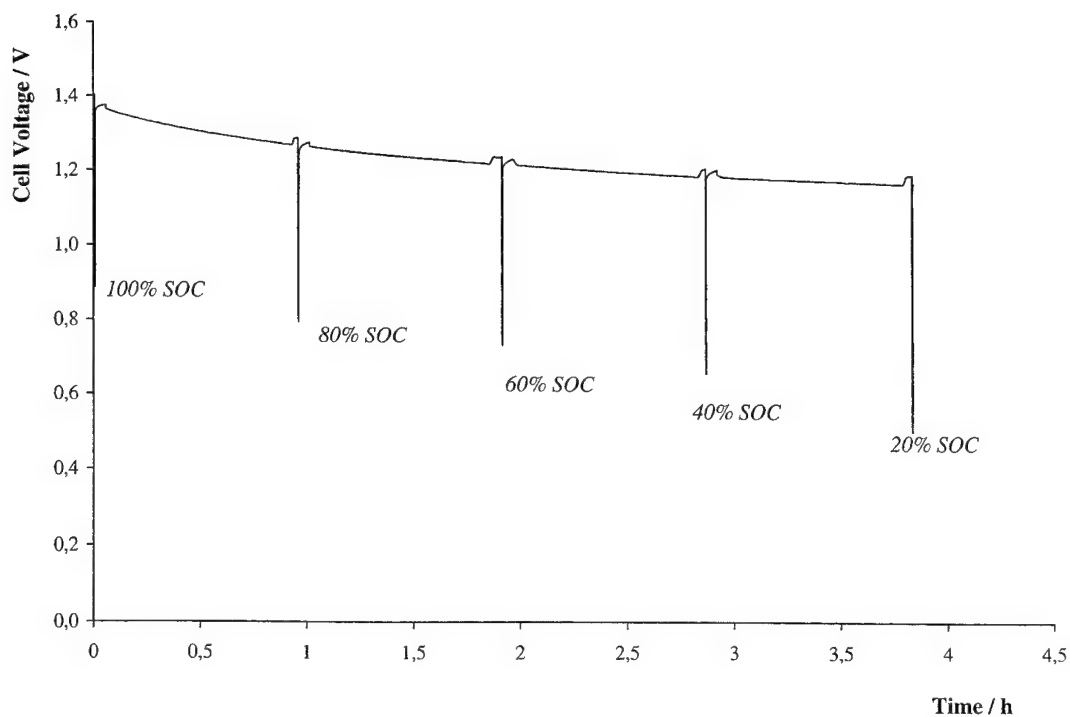


Fig. 3. Power capability discharge test of Ni/MH cells ( $C = 60$  Ah).

25°C for the charges at  $C/5$ ,  $C/2$ ,  $1C$ ,  $2C$  and  $4C$  rates, respectively.

The discharged capacity (at the  $C/5$  rate) obtained after each constant current charge for both types of cells is represented in Fig. 6, where for comparison purposes the

capacity at the  $C/5$  rate of the cells corresponds to a 100% value, according to the following formula:

$$\text{Discharged capacity}(\%) = \frac{\text{Capacity(Ah) at the } yC \text{ rate}}{\text{Capacity at the } C/5 \text{ rate(Ah)}} \times 100$$

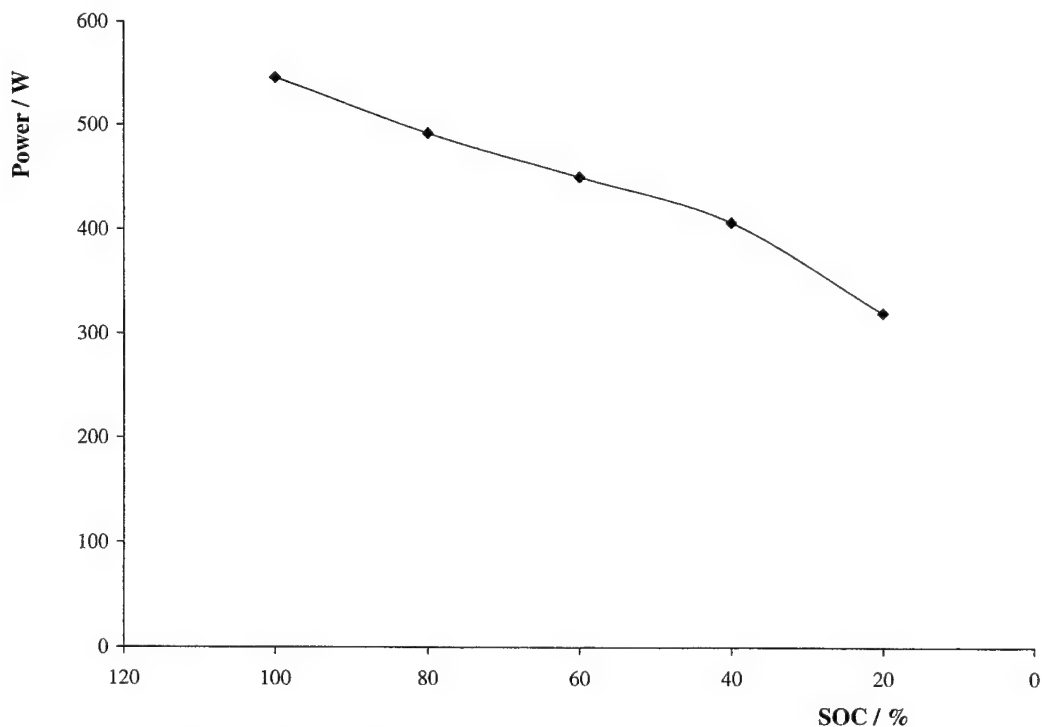


Fig. 4. Power capability of Ni/MH cells at 600 A and at different states of charge ( $C = 60$  Ah).

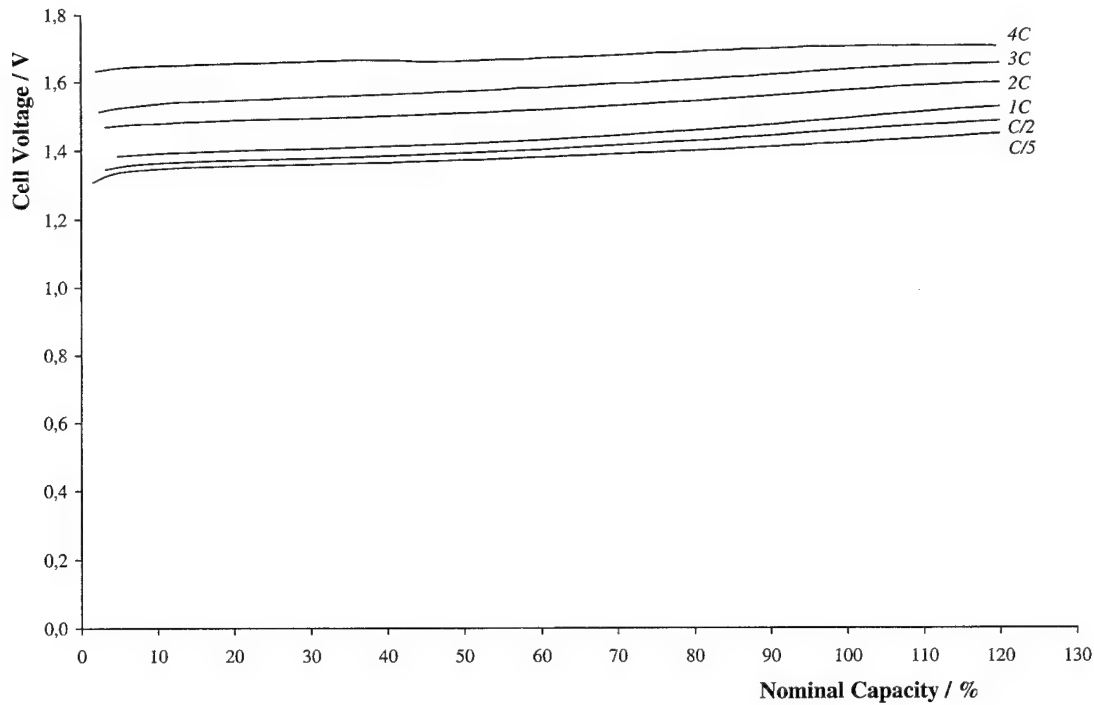


Fig. 5. Constant charge curves at different rates of Ni/MH cells ( $C = 25$  Ah).

The figure clearly shows that in both cases the best charging efficiency is obtained when the cells are recharged at the  $1C$  rate, and that up to  $2C$  rate the values are over 100%.

The charging efficiency for different SOC has also been calculated: charging at the  $1C$  rate the previously discharged

cells and then discharging at the  $C/5$  rate down to 1.0 V. Fig. 7 shows the capacity discharged from the 25 Ah cells, expressed as percentage of the nominal capacity after each partial charge. The charging efficiency obtained for the different charging ratios tested is higher than 95%, and

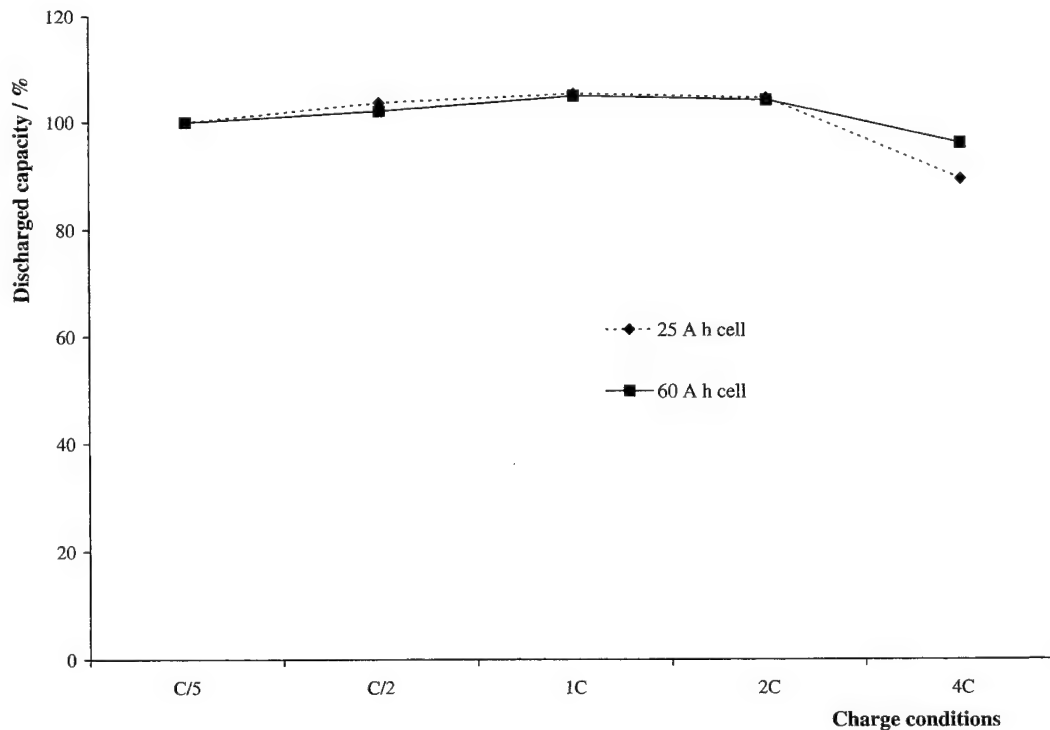


Fig. 6. Discharged capacity after charging at different rates of Ni/MH cells ( $C = 25$  and 60 Ah).

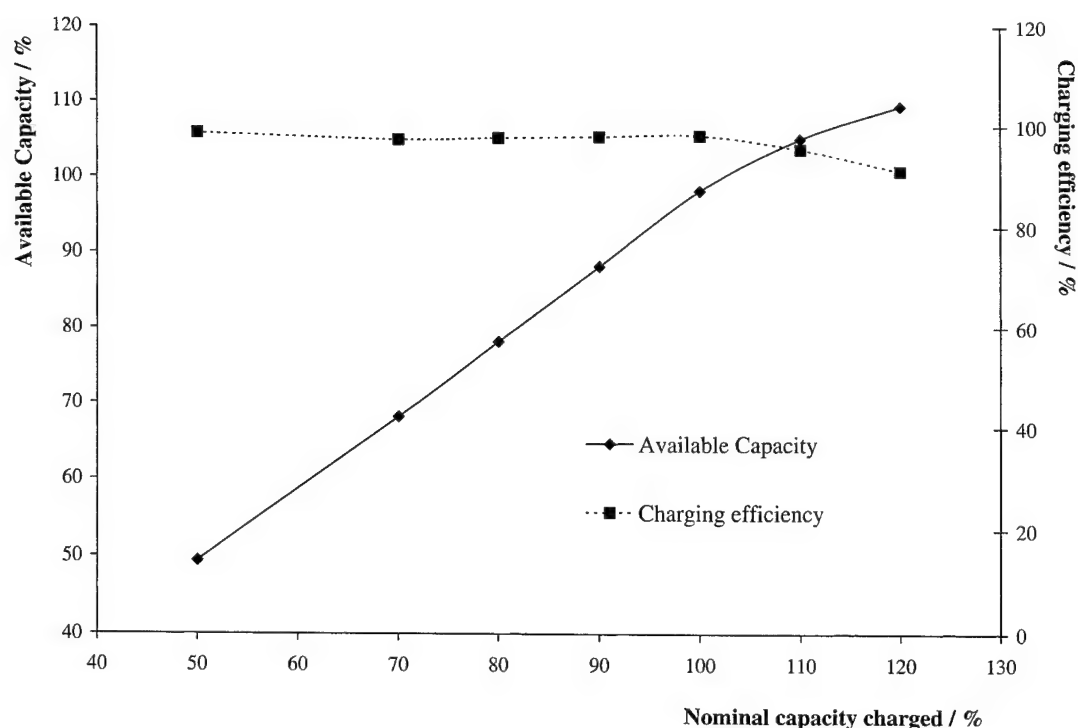


Fig. 7. Charging efficiency of Ni/MH cells at different states of charge ( $C = 25$  Ah).

around 97% up to 90% SOC. The 60 Ah cells show a similar behaviour.

On the other hand, the rapid charge capability of the 60 Ah Ni/MH cells has been determined. The test was performed by charging the cells with a high charge current when between 40 and 80% SOC, and calculating, for three different current values, the coulombic and energy efficiency values. Prior to the test, the 60 Ah cells were discharged by 60% of the useful capacity at the  $C/2$  rate, i.e. down to 40% SOC. Then they were recharged at 120, 300 and 480 A ( $2C$ ,  $5C$  and  $8C$  rates, respectively) up to 80% SOC. The discharge duration at the  $C/2$  rate to 1.0 V was used to calculate the recharge coulombic efficiency, which was higher than 90% for the range 40–80% SOC even at the  $8C$  rate. Also the energy efficiency ratios, which ranged between 74% for the  $2C$  charge and 61% for the  $8C$  charge.

The high efficiency values obtained in the high rate rechargeability tests enable the definition of a quick charge procedure, at least for a few minutes duration and at 80% state of charge, to avoid temperature and internal pressure increases.

The self-discharge test included the measurement of the capacity retained after 48 and 120 h storage at room temperature and at  $40^\circ\text{C}$ . The results obtained are satisfactory, as the 60 Ah Ni/MH cells retained 93 and 90% of the initial capacity after 48 and 120 h at room temperature and 90 and 86% after 48 and 120 h at  $40^\circ\text{C}$ , respectively. On the other hand, the capacity retained by the 25 Ah cells on storage during 28 days at room temperature was 93% of the initial capacity value.

The cycle life performance of the Ni/MH batteries is being tested, both under constant current conditions at the  $C/2$  and  $1C$  rates (100% DOD) and in special tests simulating the hybrid vehicle working conditions (power assist profile of the EUCAR specification). To date the results obtained are satisfactory.

Finally, the recombination efficiency of the valve regulated design has been tested by overcharging the Ni/MH cell at the  $C/20$  rate after a complete charge. The cell has been weighed periodically, and the weight loss figures have been used to calculate the recombination efficiency, considering that if the current were used for the water electrolysis process, each Ah charged would represent a water consumption of 0.3361 g, according to the following formula:

Recombination efficiency (%)

$$= \left( 1 - \frac{\text{Real weight loss}}{\text{Current equivalent water loss}} \right) \times 100$$

Test results show clearly that the recombination efficiency is nearly 100% during the whole test.

#### 4. Conclusions

Valve regulated Ni/MH prismatic cells rated at 25 and 60 Ah have been designed and assembled using high performance electrodes. The cells show excellent high rate discharge capability when on continuous discharges up to the  $10C$  rate, due to the high kinetically active materials



and the optimised design of all the components to give a low value of internal resistance.

The high efficiency values obtained in the high rate rechargeability tests enable the definition of fast charge procedures up to 80% SOC without a significant temperature and internal pressure increase. The Ni/MH cells show also a satisfactory performance under deep discharge cycling and when tested to simulate power-assist hybrid vehicle working conditions. The charge retention when stored, even at high temperature, is good. Also, recombination efficiency is nearly 100%, which allows for a maintenance-free operation.

Work performed up to date on the development of prismatic Ni/MH cells for high power applications encourages further studies in order to optimise energy and power battery ratios ( $\text{Wh kg}^{-1}$  and  $\text{W kg}^{-1}$ ), thus promoting their use for hybrid vehicles and 42 V automotive electrical network systems. However, these applications require the development of battery management systems with algorithms to control continuously the SOC and the state of health (SOH) of the battery. Finally, a battery thermal management can avoid temperature increase during the high rate charging and discharging processes, by means of a forced air draught cooling system.

### Acknowledgements

This work has been partially funded by the European Commission within the framework of the Industrial and Materials Technologies Programme (Brite-EuRam Contract

BRPR-CT97-0515). The authors wish also to thank the project partners R.B.C. (FR) for the samples of doped nickel hydroxide.

### References

- [1] J.J.G. Willems, Philips J. Res. 39 (1984) 1.
- [2] Brite-EuRam III Project BE97-4219, Contract BRPR-CT97-0515.
- [3] M.L. Soria, J. Chacón, J.C. Hernández, in: Proceedings of the International Conference on Advanced Batteries and Accumulators, Brno, CZ, August 2000.
- [4] M.L. Soria, J. Chacón, J.C. Hernández, J. Power Sources (2000), submitted for publication.
- [5] US Patent 5 384 017 and European Patent 0 559 590.
- [6] S. Deabate, F. Fourgeot, F. Henn, J. Power Sources 87 (2000) 125.
- [7] S. Deabate, F. Fourgeot, F. Henn, Ionics 5 (1999) 371.
- [8] P. Oliva, J. Leonardi, J.F. Laurent, C. Delmas, J.J. Braconnier, M. Figlarz, F. Fievet, A. de Guibert, J. Power Sources 8 (1982) 229.
- [9] A.H. Zimmerman, J. Electrochem. Soc. Proc. 94 (27) (1994) 268.
- [10] V. Güther, A. Otto, J. Alloys Comp. 293 (1999) 889.
- [11] A. Otto, V. Güther, J. Alloys Comp. 293 (1999) 734.
- [12] R.D. Armstrong, G.W.D. Briggs, E.A. Charles, J. Appl. Electrochem. 18 (1988) 215.
- [13] B. Aladjov, A. Greenberg, S. Gamburzev, W. Zhang, O. Velez, in: Proceedings of the 37th Power Sources Conference, 1996, p. 402.
- [14] A. Visintin, D. Smith, M. Gamboa-Aldeco, S. Srinivasan, J. Electrochem. Soc. Proc. 97 (18) (1997) 780.
- [15] L. Aymard, C. Lenain, L. Courvoisier, F. Salver-Disma, J.-M. Tarascon, J. Electrochem. Soc. 146 (1999) 2015.
- [16] T. Sakai, A. Takagi, N. Kuriyama, H. Miyamura, H. Ishikawa, Prog. Batteries Solar Cells 9 (1990) 269.
- [17] A.K. Sood, in: D.A. Corrigan, Nickel Hydroxide Electrodes, Vol. 90–94, The Electrochem. Soc. Inc., Pennington, USA, 1990, p. 163.
- [18] J. Cook, Electric and Hybrid Vehicle Tech.'99, 1999, p. 128.

## Alkaline high power batteries in a bipolar stack design

D. Ohms<sup>a,\*</sup>, M. Kohlhasse<sup>a</sup>, G. Benczúr-Ürmösy<sup>a</sup>,  
G. Schaedlich<sup>a</sup>, K. Wiesener<sup>b</sup>, J. Harmel<sup>b</sup>

<sup>a</sup>*Accumulatorenwerke Hoppecke, Bontkirchener Str.2, D-59929 Berlin, Germany*

<sup>b</sup>*Kurt-Schwabe-Institut für Meß- und Sensortechnik e.V. Ziegra-Knobelsdorf, Meinsberg, Germany*

Received 08 January 2001; accepted 09 January 2001

---

### Abstract

For several applications, batteries with a high power/energy ratio are required. In order to meet these requirements, alkaline batteries based on fibre structures and hydrogen storage negative electrodes that are arranged in bipolar stacks, can be used. The bipolar stacks are designed to provide comparatively high voltages, e.g. 12, 36 and even 110 V. These stacks display electrochemical characteristics of a typical battery but are able to provide high power densities. This paper compiles data obtained from such storage units. © 2001 Elsevier Science B.V. All rights reserved.

**Keywords:** Nickel/metal hydride batteries; Bipolar stack designs; Applications/electric vehicles

---

### 1. Introduction

Nickel/metal hydride (Ni/MH) batteries are considered to be a substitute to the widely used nickel/cadmium accumulators. In comparison to nickel/cadmium accumulators a higher energy density can be obtained. For large cells in industrial applications the costs resulting from the use of the expensive hydrogen storage alloys play an important role in the acceptance of such batteries.

Therefore, one way for economic application consists in a special design that enables high power rates but with moderate or even small battery capacities. The aim of our investigations was to increase the power/energy ratio of a Ni/MH battery. Potential fields for applying such bipolar nickel-metal hydride batteries are power equalising, modern net structures for automotive applications and electric hybrid vehicles.

Conventional batteries are made of single cells connected in series. Thus, each cell is equipped with passive material such as cell walls, connectors etc. Looking back to the very beginning of electrochemical energy storage, Volta's pile was designed to obtain high voltages by connecting cells together via bipolar connecting plates [1]. We have tried to use the ideas of such a concept to build an accumulator based on the electrochemical nickel-metal hydride couple. The

advantage of this design is that the cross-section for the electric current collectors is the same size all over the bipolar stack. There is no need for highly conducting support structures in the electrodes. The connecting bipolar plate can be made from an extremely thin metal foil or another electronically conducting material. The bipolar plate has to provide sufficient electronic contact but also has to prevent any electrolytic bridges between adjacent sub-cells (our term for the unit cell in a stack).

In the past, several attempts have been made to realise such a concept of bipolar stacks. Several difficulties involved have so far prevented a wide technical solution. The reasons are as follows:

- Losses of power due to contact resistivity.
- Electrolytic bridges between sub-cells because of spilling or creeping of electrolyte.
- Limited amounts of the electrolyte in the sub-cells.
- Problems with the sealing of adjacent sub-cells.
- Differences of gas pressure in the sub-cells.
- Corrosion of the bipolar plate due to the electrolyte.

It has been shown that electrochemical systems based on simple ion transfer and not involving the electrolyte in the overall cell reaction are favoured for use in bipolar stack designs. As electrolytic resistivity will strongly influence the stack behaviour, we expected that the Ni/MH couple would perform better than cells with non-aqueous electrolytes. At the moment, hydrogen storage alloys of the AB<sub>5</sub> type can

---

\* Corresponding author.

E-mail address: hoppecke.gtg.ohms@online.de (D. Ohms).

provide comparatively low equilibrium pressures at given state-of-charge and temperature. Accumulatorenwerke Hoppecke and Kurt-Schwabe-Institut für Meß- und Sensortechnik e.V. Meinsberg have a joint programme to study the bipolar Ni/MH storage systems, continuing former work [2–5] at Deutsche Automobilgesellschaft mbH.

## 2. Experimental

Fig. 1 displays a scheme of the bipolar arrangement. Bipolar stacks were built using positive electrodes prepared using fibre structure technology at Hoppecke Batterie Systeme GmbH, in a manner rather similar to the conventional production of positive electrodes for FNC batteries. The differences lie in the specific amount of active material related to the electrode size and the smaller thickness of the bipolar electrodes.

Depending upon the demanded power output required, the electrode thickness of bipolar cells can be varied between 1 and 0.5 mm. Most of our stacks are made from 0.7 mm positive electrodes. As all cells are discharge-limited by the positive electrodes, it is necessary to make the electrodes very uniform with respect to their capacity. The laboratory stacks were based on electrode areas of  $72.5 \text{ cm}^2$  giving an electrical capacity of about 1.7 Ah.

Larger stacks with capacities of about 7 Ah are under construction for extended field tests. Non-woven polyamide or poly-hydrocarbons can be used as separators. The bipolar connecting plate is made of nickel. Negative electrodes were prepared in the laboratory using a commercial hydrogen storage alloy and pasted with a binder onto a metallic support. Stacks have been built in plastic as well as metallic containers of appropriate size. The electrolyte is KOH of a

concentration of  $8.5 \text{ mol l}^{-1}$ . The stacks are equipped with sensors for temperature and gas pressure (Fig. 2).

Electrical tests were carried out with DIGATRON battery testing equipment. Some of the experiments were carried out in a climatic chamber so that the temperature of the air around the stack could easily be adjusted to various conditions.

An additional experimental set-up for three bipolar stacks was equipped with a fan to provide constant cooling. The same equipment was used for those experiments in which several bipolar stacks were connected to form units having a higher voltage or higher capacity. Thus, power systems with voltages up to 310 V were built and operated.

## 3. Electrochemistry of Ni/MH batteries

The electrochemistry of the Ni/MH system can be discussed as an ion transfer system with only hydrogen ions being used for the transfer of charges (Fig. 3).

At the negative electrode, an equilibrium between hydrogen stored in the alloy and the gaseous phase in contact to the electrode material is established. Therefore, gas pressure is changing depending on the state of charge of the negative electrode and the temperature. In a stack, the temperature of the sub-cells is never completely uniform, so the hydrogen pressure may differ between individual sub-cells. In order to solve this problem we have designed the stack in such a way that the gas pressure between the sub-cells is equalised.

During overcharging, the oxygen formed at the positive electrode limits the state of charge of the negative. In case of a deep discharge leading to a reversed voltage, the nickel hydroxide electrode may form hydrogen, but this is consumed at the negative. By this mechanism the negative

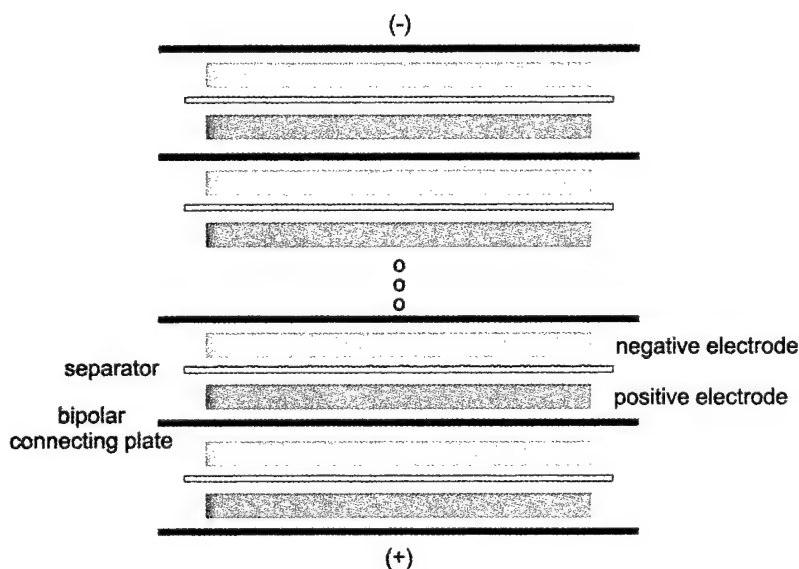


Fig. 1. Schematic diagram of a bipolar arrangement.



Fig. 2. Laboratory bipolar stack. 36 V, 1.7 Ah.

electrode is protected from oxidation as long as the current remains small.

#### 4. Results

##### 4.1. Constant current cycling of bipolar stacks

Apart from the higher voltage, the bipolar stacks display almost the same electrochemical behaviour as conventional Ni/MH cells. A significant difference lies in the arrangement of the electrodes. In conventional cells the electrodes are arranged in such a way that both sides of the electrodes contribute to the overall current. In a bipolar stack only one side of electrode is exposed to the counter electrode. As a consequence, the (geometric) current density of a bipolar electrode is twice that in a comparable conventional cell.

The pressure and voltage response during a typical cycle of a 12 V, 1.7 Ah bipolar stack is given in Fig. 4.

In practice, the internal pressure can be used to terminate the charging process. By doing so, the charging current can be increased. As an example, Fig. 5 demonstrates the voltage curves whilst cycling the stack at the 0.4 C rate of charge and 1 C rate of discharge, but limiting the stack pressure to 1.3 bar.

Of major interest is the behaviour of Ni/MH stacks at lower temperatures. In addition to the electrochemical reaction processes, the gas desorption and the mobility of stored hydrogen are retarded. As a consequence, the performance of Ni/MH cells is limited at these conditions. By optimising the electrode materials it is possible to extend the working range down to  $-20^{\circ}\text{C}$ . In Fig. 6 curves at various temperatures of a bipolar stack discharging at the 1 C rate are given.

##### 4.2. Pulse discharge and stack resistance

In some applications, higher currents are demanded. Normally these currents are demanded only for short time intervals. In Fig. 7 the voltage response of a 12 V bipolar stack is plotted versus time for different regimes of pulsed current. It can be seen that the major part of the voltage decay occurs in the early part of the pulse.

The stack shows a very small internal resistance. The value of the internal resistance is rather constant over a wide range of the state-of-charge (SOC) as seen in Fig. 8. In order to compare cells, the resistivity is normally given related to capacity and for each bipolar cell.

Using a 10 C dc current (17 A for a 1.7 Ah stack) after 1 s of polarisation, a resistance of about  $20\text{ m}\Omega/\text{Ah}$  or about

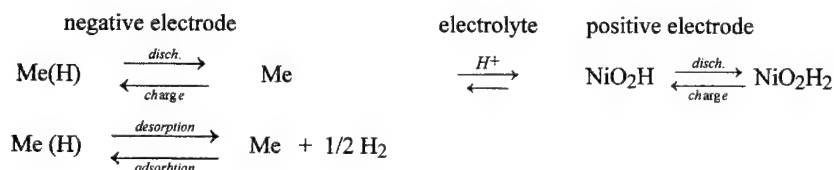


Fig. 3. Electrochemical and chemical reactions in a nickel/metal hydride cell.

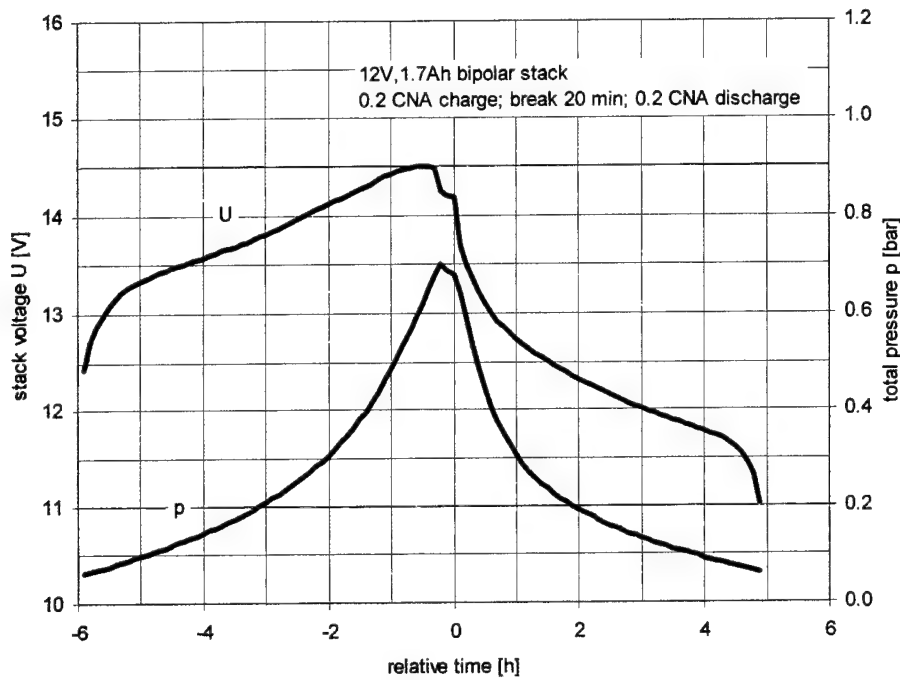


Fig. 4. Pressure and voltage during a typical cycle of a bipolar stack (12 V, 1.7 Ah).

$0.86 \Omega \text{ cm}^2$  per sub-cell can be computed from the voltage drop.

We were able to discharge stacks using current pulses up to the 30 C rate [6,7].

There is a certain change of the internal resistance during continuous cycling. At the beginning, the internal resistance decays slightly. After much cycling with high currents, an increase in resistivity was found after more than 600 cycles. It was caused by a partial (reversible) water loss from the sub-cells (See Fig. 9).

#### 4.3. Electrical cycling and thermal behaviour of bipolar stacks to an hybrid electric vehicle regime

In hybrid automobile applications the bipolar stack would be used to store or deliver energy steadily between the main energy source (internal combustion engine or fuel cell), and the consuming equipment. Using a powerful storage battery can reduce the peak power needed from the main energy supply and can store energy available from braking.

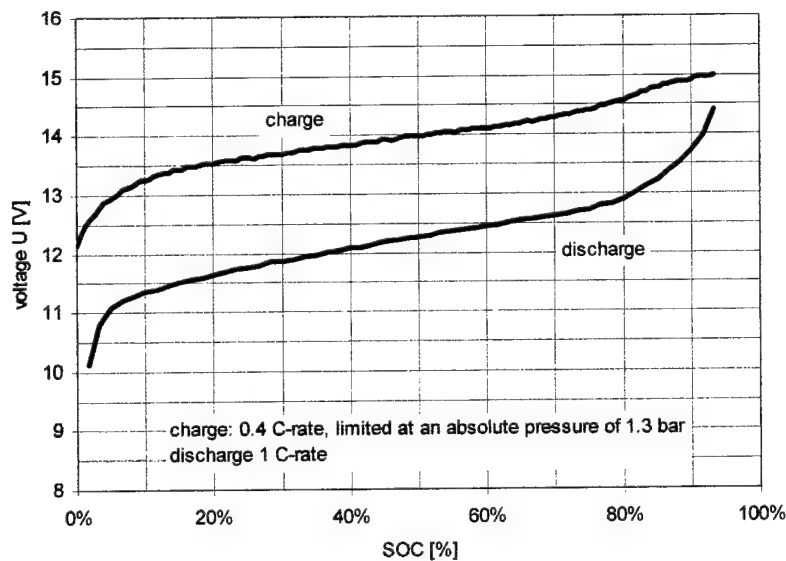


Fig. 5. Voltage of a 12 V, 1.7 Ah bipolar stack during 450 cycles of 0.4 C rate of charge, limited by a stack pressure of 1.3 bar and 1 C discharge.

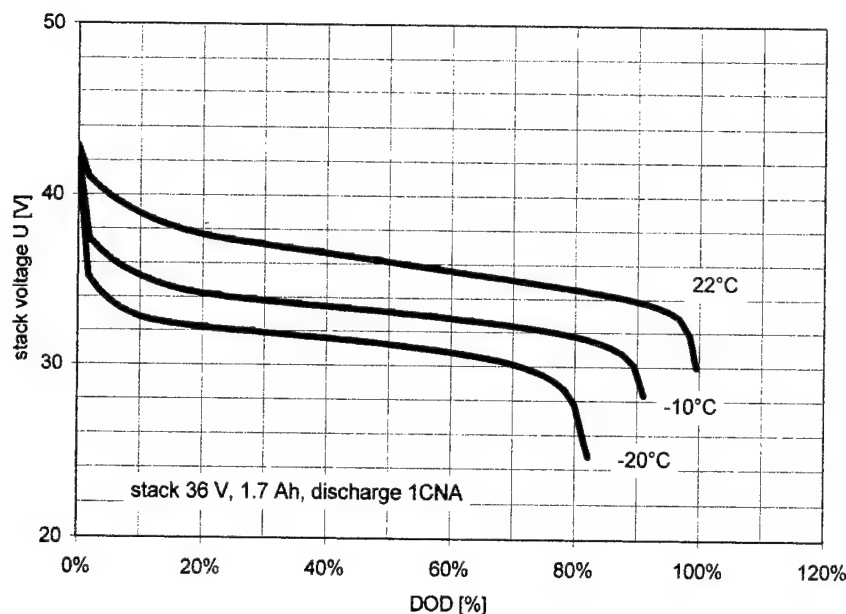


Fig. 6. 36 V, 1.7 Ah bipolar stack discharged at the 1 C rate at various temperatures.

As an example, we have designed a cycling sequence based on a 5 C rate of charge and discharge with a cycle depth of 10% from an initial 60% SOC. There are 5 s intervals between each charge and discharge. The sequence is repeated at least 100 times. This cycling sequence is shown in Fig. 10a.

During the repetitive cycling, a stationary state is achieved (Fig. 10b). The Ah efficiency was determined by measuring the remaining capacity after the cycling programme and it was very close to 98.7%. The energy efficiency amounted to about 90%.

Due to the energy losses while operating the bipolar stack, a temperature raise is observed. In order to provide for continuous operation, a thermal management system is required. In an experimental set-up the stack is exposed to a stream of air. The air originates from the surroundings at a rather constant temperature and flows over the cylindrical wall of the bipolar stack. The internal temperature of the stack was measured at the approximate top of the stack. After an initial period, the temperature becomes constant indicating that the heat produced in the stack is similar to the heat dissipated by the cooling device. Depending upon the

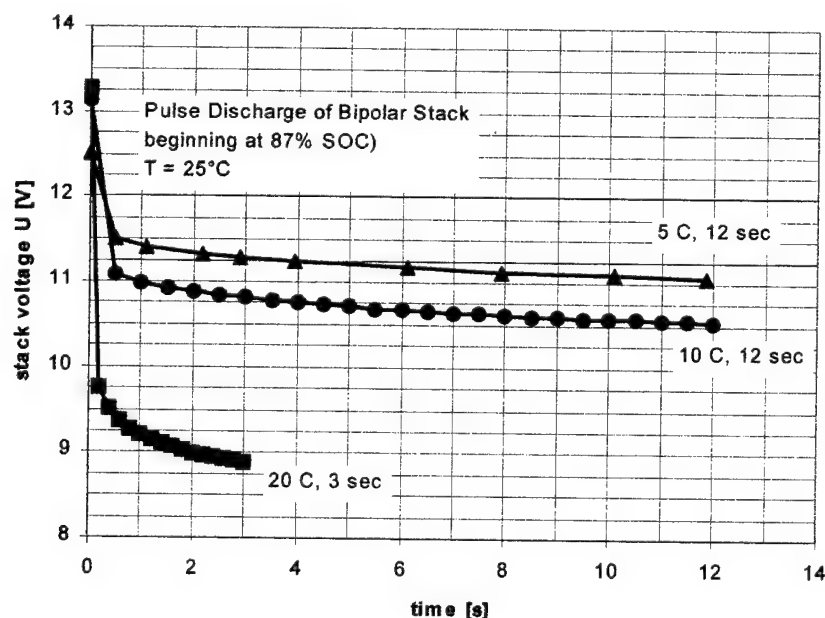


Fig. 7. Selected pulse discharge curves of a 12 V, 1.7 Ah bipolar stack.

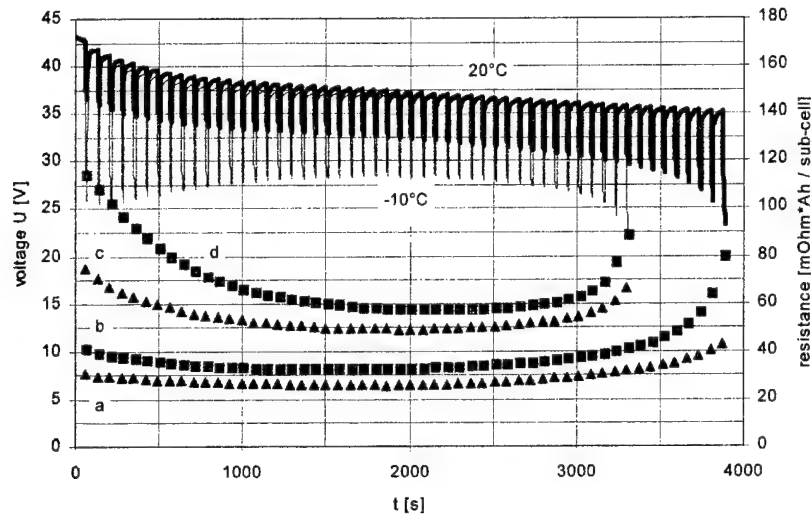


Fig. 8. 5 C Pulse discharges at the 5 C rate for a 36 V, 1.7 Ah bipolar stack at 20°C and at -10°C. Upper curves: voltage response at 20°C and -10°C. Lower curves show resistivity computed from: (a) 1 s polarisation, 20°C; (b) 10 s polarisation, 20°C; (c) 1 s polarisation, -10°C; (d) 10 s polarisation, -10°C.

temperature, the equilibrium pressure in the stack also reaches almost a steady value Fig. 11.

#### 4.4. Self discharge of a bipolar stack

The rate of self-discharge of a bipolar Ni/MH stack is mainly determined by two processes:

1. Decomposition of higher oxides in the positive electrode.
2. Electrolytic bridging across the bipolar plates and the walls between adjacent cells.

As is known from nickel/cadmium accumulators, the rate of self discharge depends upon the state of charge and the temperature.

At the beginning of our studies, electrolytic creepage between sub-cells was not completely eliminated. After improving the design, the self-discharge was reduced to the level found in discrete cell designs.

Fig. 12 gives the residual capacity of a fully charged bipolar stack following various periods on open-circuit at 25°C.

#### 4.5. Changes to the negative electrode during cycling

It was observed that the negative electrode displays some changes during prolonged cycling [8]. After such experiments we have investigated the electrodes by scanning electron microscopy. The SEM photographs (Fig. 13a and b)

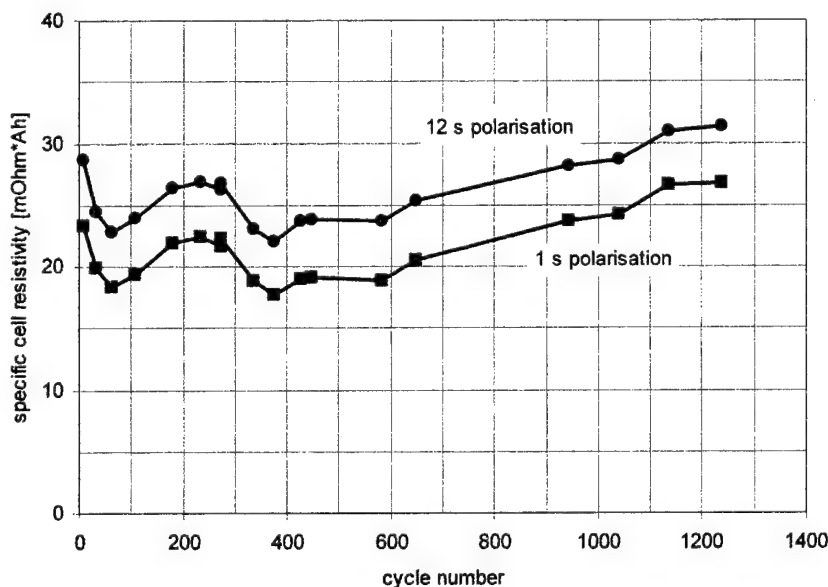


Fig. 9. Long-term specific resistivity of a sub-cell in a 12 V, 1.7 Ah bipolar stack. Data were computed at one and ten seconds into the fifth pulse of a 10 C pulse discharge sequence. Note that early variations are due to different cycling conditions.

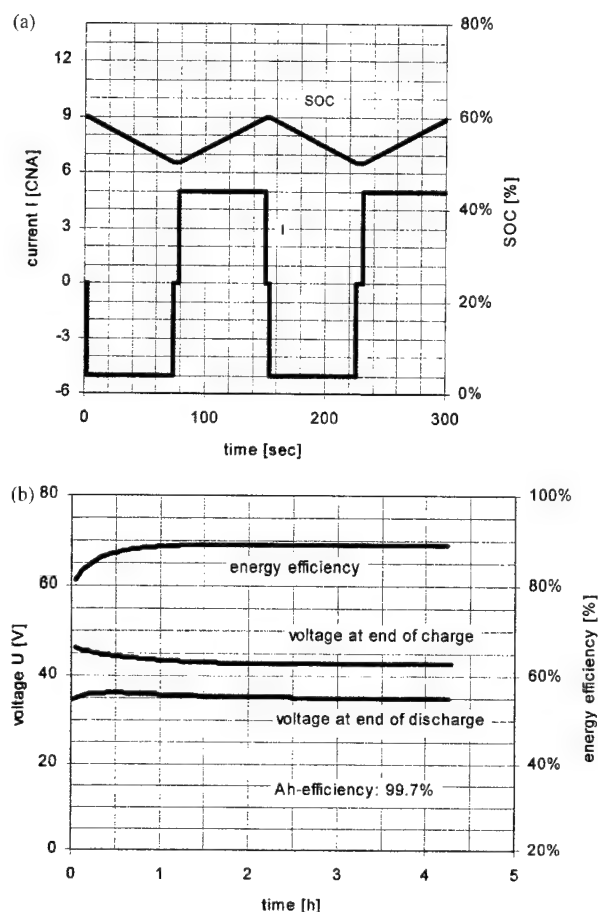


Fig. 10. (a) A 36 V, 1.7 Ah, bipolar stack initially at 60% state-of-charge on a regime representing a hybrid vehicle requirement. Cycling sequence: 5 C charge for 72 s. 5 s open-circuit, 5 C discharge for 72 s. 5 s open-circuit; (b) Hybrid cycles with a 36 V, 1.7 Ah bipolar stack, showing voltages and energy efficiency.

display some changes in the shape of particles of the storage alloy. It is likely that the particle size becomes reduced due to cracks formed as a result of mechanical tensions.

The reason for this could be the change of volume of the alloy during absorption and desorption of hydrogen. The change of particle size does not influence the electric behaviour. Single cell tests give a cycle-life expectancy at 25°C of more than 2000 cycles at 100% DOD.

## 5. Conclusions

Bipolar Ni/MH stacks are an appropriate device for electric power storage. They can operate with relatively high energy efficiencies. Discharges at low temperature are limited by transport processes. The properties of the stack can be tuned by variation in the electrode thickness in such a way that even high power/energy ratios can be obtained. Stacks of higher voltage can be built and operated. A way to overcome the limit of the restricted capacity of individual stacks may be by paralleling. The pressure in the stacks depends upon the state of charge of the negative electrode. For an application in hybrid vehicles, a thermal management system is needed to protect the battery from overheating. It has been shown that excess heat can be removed by an air stream arranged to flow constantly around the stack. The bipolar stack design could be an alternative for power storage in hybrid cars and the new automobile board net structures.

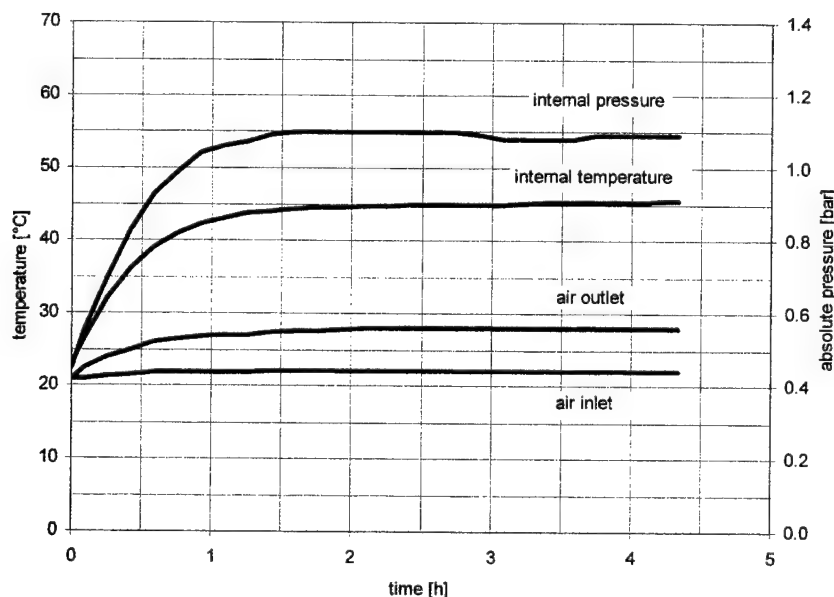


Fig. 11. Temperature and pressure profiles of a 36 V, 1.7 Ah bipolar stack during hybrid cycling in a experimental set-up with air-cooling (power consumption of fan: 0.9 W per stack). Ambient air temperature: 22°C.



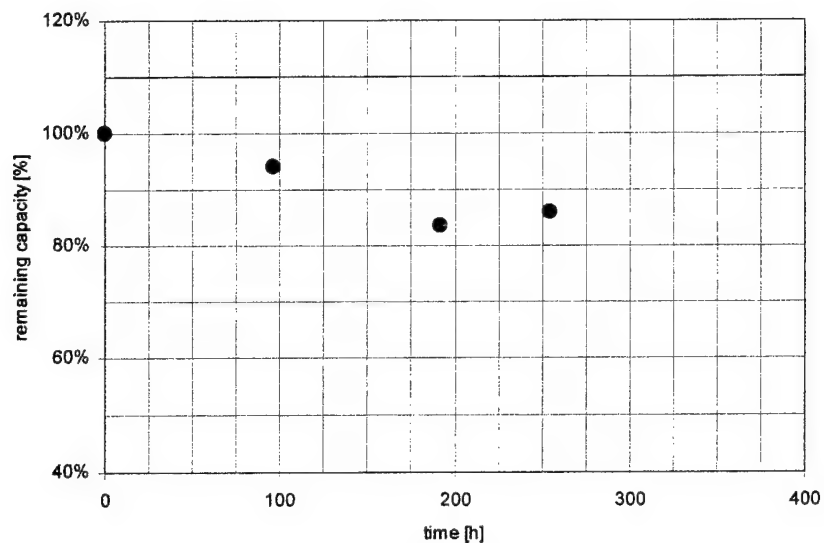


Fig. 12. 36 V, 1.7 Ah bipolar stack: self-discharge behaviour at 25°C.

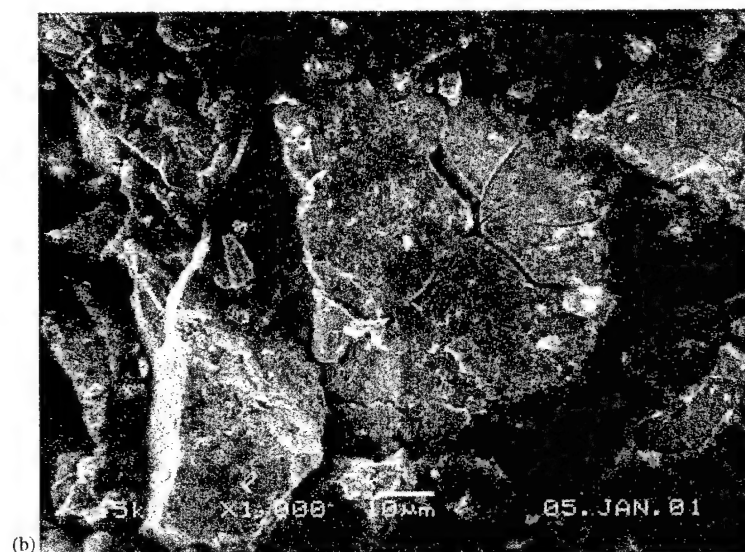
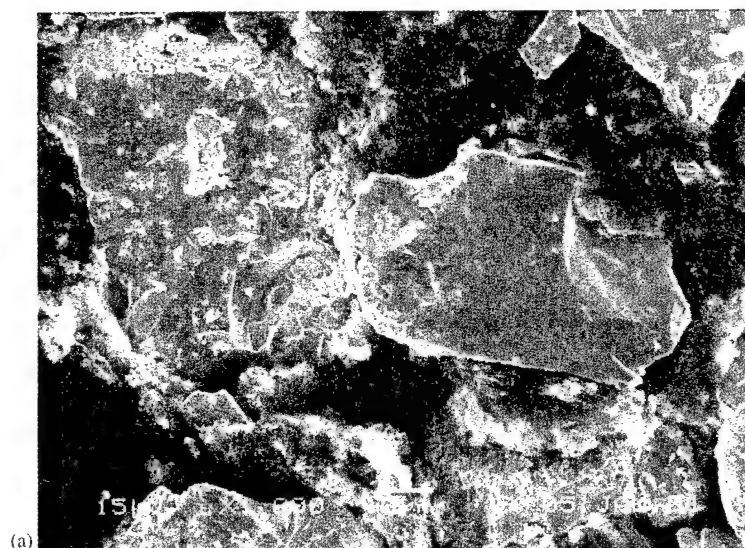


Fig. 13. (a) SEM of a fresh metal hydride electrode; (b) SEM of a metal hydride electrode after cycling.

## Acknowledgements

The authors acknowledge the BMW (Bundesministerium für Wirtschaft, BEO 0329829 5) for financial support of these research activities and Dr. G. Sandstede for contributions and helpful discussion. The authors have to thank the Institute of Chemistry of FH Holzminden for the SEM investigations.

## References

- [1] B.E. Conway, *Can. Chem. News* 1 (2000) 15–17.
- [2] G. Benczúr-Ürmösy, F. Haschka, D. Ohms, K. Wiesener, M. Berthold, in: Jahrestagung der Fachgruppe der GDCh, “Angewandte Elektrochemie”, “Elektrochemische Verfahrenstechnik-Energietechnik, Stoffgewinnung, Bioelektrochemie”, 9–12 October 1996, Monheim, GDCh-Monographie, 9 (1997), GDCh, Frankfurt, Germany, pp. 161–162.
- [3] Research projects BMBF (0329621 A/B and 0329621 C) Final Reports, Bonn, 1998.
- [4] D. Ohms, G. Benczúr-Ürmösy, F. Haschka, W. Wartmann, in: Proceedings of the EVT’95, Paris, 11–13 November 1995.
- [5] K. Wiesener, D. Ohms, G. Benczúr-Ürmösy, M. Berthold, F. Haschka, in: Proceedings of the 6th UECT, 29–30 June 1998, Ulm, Germany; *J. Power Sources* 84 (1999) 248–258.
- [6] D. Ohms, M. Kohlhase, G. Benczúr-Ürmösy, in: Proceedings of the Bunsentagung 2000, 1–3 June 2000, Würzburg, Germany.
- [7] D. Ohms, M. Kohlhase, G. Benczúr-Ürmösy, K. Wiesener, J. Harmel, in: Proceedings of the 7th UECT, 26–27 June 2000, Ulm, Germany; *J. Power Sources*, submitted for publication.
- [8] L. Le Guenne, P. Bernard, in: Proceedings of the 7th UECT, 26–27 June 2000, Ulm, Germany; *J. Power Sources*, submitted for publication.

# The development of hydrogen storage electrode alloys for nickel hydride batteries

Kuochih Hong

*Hong Enterprises Co., 1790 Rollingwoods Drive, Troy, MI 48098, USA*

Received 24 November 2000; accepted 4 December 2000

## Abstract

The development of hydrogen storage electrode alloys in the 1980s resulted in the birth and growth of the rechargeable nickel hydride (Ni/MH) battery. In this paper we describe briefly a semi-empirical electrochemical/thermodynamic approach to develop/screen a hydrogen storage alloy for electrochemical application. More specifically we will discuss the AB<sub>x</sub> Ti/Zr-based alloys. Finally, the current state of the Ni/MH batteries including commercial manufacture processes, cell performance and applications is given. © 2001 Elsevier Science B.V. All rights reserved.

**Keywords:** Metal hydrides; Nickel/metal hydride batteries

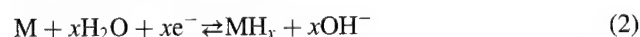
## 1. Introduction

In the 1970s, studies of the hydrogen storage alloys and metal hydride technology were initiated and developed [1,2]. One of the fruits of these studies was their electrochemical applications, more specifically the development of commercial hydrogen storage electrodes and the rechargeable nickel hydride batteries in 1980s [3–13]. The rapid growth of wireless 3C-industries (communication, computer and consumer electronics) helped the mass production of commercial nickel hydride (Ni/MH) batteries. In 1999, the sales of Ni/MH cells were estimated to be about 900 million cells.

In this paper, we will review and discuss the development of high capacity and long-life hydrogen storage electrode materials as used for the commercialization of Ni/MH batteries.

## 2. Metal hydrides for applications in Ni/MH batteries

A hydrogen storage material, M, can form hydride, MH<sub>x</sub>, by the interaction with hydrogen gas and/or electrochemical method as shown in Eqs. (1) and (2):



However, not every hydrogen storage alloy can be charged and discharged electrochemically as given in Eq. (2). As the

active material of a hydrogen storage electrode, a hydrogen storage alloy has two major roles: an electrochemical catalyst for the charge/discharge of hydrogen and a hydrogen storage reservoir/source. Therefore, a good hydrogen storage (hydride) electrode material must meet the following criteria:

1. high reversible hydrogen storage capacity, i.e. >1 wt.%;
2. good electrochemical catalyst for hydrogen charge (reduction/absorption) and discharge (desorption/oxidation);
3. easy activation;
4. excellent corrosion resistance in alkaline electrolyte;
5. suitable hydrogen equilibrium pressure, not higher than 5 bar at 25°C;
6. good charge/absorption and discharge/desorption kinetics and efficiency;
7. long cycle life;
8. small hysteresis in charge/discharge isotherms;
9. low cost.

## 3. The development of commercial hydrogen storage electrode alloys

### 3.1. Three main stages of hydride electrode alloy development

1. The concept of hydrogen storage alloy for electrochemical application began in the 1970s [5–13]. Some

AB- and AB<sub>5</sub>-type hydrogen storage materials were known, such as TiNi, TiFe, LaNi<sub>5</sub> and these were tested. However, these alloys are either difficult to activate, have a short cycle life, and/or low capacity. Therefore, they are not suitable for the commercial application.

2. Later, in the early 1980s, Hong and co-workers [3,4] first studied the Ti/Zr-based AB<sub>2</sub>-type Ti/Zr–V–Ni–M systems. These alloys include the following three families: (a) TiV<sub>2–x</sub>Ni<sub>x</sub>, (b) Ti<sub>1–y</sub>Zr<sub>y</sub>V<sub>2–x</sub>Ni<sub>x</sub> and (c) Ti<sub>1–y</sub>Cr<sub>y</sub>V<sub>2–x</sub>Ni<sub>x</sub> [3,4], which became the basis of Ovonic's Ti/Zr-based AB<sub>2</sub>-type alloys. The capacity of these alloys is up to 450 mAh g<sup>–1</sup> at 25 mA g<sup>–1</sup> current density. Among these three families, the Ti–V–Ni alloys studied have high capacity, but short cycle life. However, the Ti–Zr–V–Ni and Ti–Cr–V–Ni alloys have a long cycle life. The microstructures of these alloys generally are multiphase and crystalline, consisting of a hydrogen storage phase and one or more electrochemical catalytic phases [14]. On the other hand, about the same time as Hong, Willems et al. [15] reported the rare earth-based AB<sub>5</sub>-type Ln–Ni–Co–Mn–Al alloys. These cobalt-containing alloys have less capacity than LaNi<sub>5</sub>, but have a good cycle life. These early 1980s studies in Ti/Zr-based AB<sub>2</sub>-type Ti/Zr–V–Ni–M systems and rare earth-based AB<sub>5</sub>-type Ln–Ni–Co–Mn–Al alloys opened the window for the commercialization of rechargeable nickel hydride batteries.
3. Finally, in late 1980s and early 1990s, Hong [16] and Gamo et al. [17] independently studied AB<sub>x</sub>-type multi-component alloys away from the stoichiometric restriction of AB<sub>2</sub> and AB<sub>5</sub> types. As a result, more new alloys having improved performance including more capacity and/or long cycle life were developed.

### 3.2. A semi-empirical method for developing a hydrogen storage electrode alloy

Hong [16,18–21], based on the thermodynamic and electrochemical studies, presented a semi-empirical method to develop good AB<sub>x</sub>-type multi-component hydrogen storage electrode alloys. In this approach, a potential candidate alloy, A<sub>a</sub>B<sub>b</sub>C<sub>c</sub>... for a rechargeable hydrogen storage electrode has to satisfy three basic conditions:

1. A<sub>a</sub>B<sub>b</sub>C<sub>c</sub>... contains at least 5–85 at.% of Ni, preferably 15–65 at.%;
2. contains at least 10–80 at.% of hydride formers selected from Ti, Zr, and rare earth metals, preferably 15–65 at.%;
3. contains 0.1–15% of two or more modifiers preferably selected from but not limited to the group of V, Nb, Mg, Ca, Hf, Mn, Cr, Co, Mo, Cu, Al, Sn, Bi, Si, Sb, Fe, Zn and Ag;
4. the calculated heat of hydride formation  $H_h$  is between –2.5 and –10.50 kcal mole<sup>–1</sup> H. When the elements A,

B, C, ... are chosen, a set of atomic ratio,  $a, b, c, \dots$  can be obtained by the following equation:

$$H_h = -\frac{aH_h(A) + bH_h(B) + cH_h(C) + \dots}{2(a + b + c + \dots)} + K \quad (3)$$

where  $H_h(A), H_h(B), H_h(C), \dots$  are the heat of formation of hydrides of metals A, B, C, ..., respectively, in the unit of kcal mole<sup>–1</sup> H<sub>2</sub>;  $K$  is a constant depending on the heat of formation ( $H^f$ ) of the alloy, A<sub>a</sub>B<sub>b</sub>C<sub>c</sub>... and the heat of mixing ( $H_h^m$ ) of the hydride AH, BH, CH, ..., as shown in Eq. (4):

$$H_h = -\frac{aH_h(A) + bH_h(B) + cH_h(C) + \dots}{2(a + b + c + \dots)} + H_h^m \quad (4)$$

The values of  $K$  were given as 0.5, –0.2 and –1.5 kcal mole<sup>–1</sup> H for  $a + b + c + \dots$  equal to 2, 3 and 6, respectively [15,20]. For  $a + b + c + \dots$  not equal to 2, 3 and 6, it can be normalized to 3 for Ti/Zr-based alloy and 6 for rare earth-based alloy before calculation. The heats of hydride formation of metals, in kcal mole<sup>–1</sup> H<sub>2</sub>, are given as

$H_h(\text{Mg}) = -17.9$ ,  $H_h(\text{Ti}) = -15.0$ ,  $H_h(\text{V}) = -7.0$ ,  $H_h(\text{Cr}) = -1.81$ ,  $H_h(\text{Mn}) = -2.0$ ,  $H_h(\text{Fe}) = 4.0$ ,  $H_h(\text{Co}) = 3.5$ ;  $H_h(\text{Ni}) = 1.8$ ,  $H_h(\text{Al}) = -1.38$ ,  $H_h(\text{Y}) = -27$ ,  $H_h(\text{Zr}) = -19.5$ ,  $H_h(\text{Nb}) = -9.0$ ,  $H_h(\text{Zr}) = -19.5$ ,  $H_h(\text{Hf}) = -19.5$ ;  $H_h(\text{Pd}) = -4.0$ ,  $H_h(\text{Mo}) = -1.0$ ,  $H_h(\text{Ca}) = -21.0$ ,  $H_h(\text{Si}) = -1.0$ ,  $H_h(\text{C}) = -1.0$ ,  $H_h(\text{Cu}) = 2.0$ ,  $H_h(\text{Ta}) = -10.0$ ;  $H_h(\text{rare earth metals}) = -27.0$ ,  $H_h(\text{Li}) = -21.0$ ,  $H_h(\text{Na}) = -13.4$ ,  $H_h(\text{K}) = -13.7$ ,  $H_h(\text{Rb}) = -12.5$ ,  $H_h(\text{B}) = 2.83$ ;  $H_h(\text{Sn}) = 2.05$ ,  $H_h(\text{Sb}) = 5.5$ ,  $H_h = -20.2$ ,  $H_h(\text{Sc}) = -28.9$ ,  $H_h(\text{Zn}) = -1.2$ ,  $H_h(\text{Ag}) = 1.0$ ,  $H_h(\text{S}) = -1.0$ ,  $H_h(\text{N}) = -0.5$ ;  $H_h(\text{W}) = -0.50$ ,  $H_h(\text{P}) = -0.30$ .

This semi-empirical approach is totally free of any crystal structure restriction and has been found very useful in developing new Ti/Zr transition metal-based and rare earth-based electrode alloys [16,18–26]. Table 1 lists some useful hydrogen storage electrode alloys including both Ti/Zr-based and Mm-based alloys (Mm is the mischmetal, a mixture of rare earth metals).

However, it should be noted that

1. for the Ti/Zr-based alloy the heat of hydride formation is preferably in the range between –4.5 and –8.0 kcal mole<sup>–1</sup> H;
2. for the rare earth-based alloys, the boundary of the heat of hydride formation is between –2.35 and –4.80 kcal mole<sup>–1</sup> H;
3. for high rate applications, the nickel content is no less than 35 at.%, preferably greater than 43 at.% for the Ti/Zr-based alloy and no less than 50 at.% for the rare earth-based alloy. Table 2 shows the comparison of the electrochemical performance between the AB<sub>x</sub> Ti/Zr-based and AB<sub>x</sub> rare earth-based alloys.

Furthermore, based on this approach, we found that a Ti/Zr-based alloy having a calculated heat of hydride formation

Table 1  
The capacity (mAh g<sup>-1</sup> at 100 mA g<sup>-1</sup>) of some AB<sub>x</sub> hydrogen storage electrode alloys

Alloy no.	Composition	C (mAh g <sup>-1</sup> )	H <sub>h</sub> (kcal mole <sup>-1</sup> H)
601	Ti <sub>10</sub> Zr <sub>20</sub> Ni <sub>35</sub> Cr <sub>3.5</sub> Mn <sub>4.5</sub> V <sub>2.5</sub> Al <sub>2.0</sub>	375	-7.10
602	Ti <sub>8</sub> Zr <sub>29</sub> Ni <sub>44</sub> Cr <sub>3.0</sub> Mn <sub>10.0</sub> V <sub>3.0</sub> Mm <sub>2.0</sub>	360	-7.01
603	Ti <sub>24</sub> Zr <sub>17</sub> Ni <sub>41</sub> Cr <sub>2.0</sub> Mn <sub>7.0</sub> V <sub>9.0</sub> Al <sub>0.0</sub>	358	-6.90
604	Ti <sub>12</sub> Zr <sub>27</sub> Ni <sub>48</sub> Cr <sub>1.5</sub> Mn <sub>8.0</sub> V <sub>1.5</sub> Mm <sub>2.0</sub>	354	-6.90
605	Ti <sub>9</sub> Zr <sub>29</sub> Ni <sub>47</sub> Cr <sub>2.0</sub> Mn <sub>10</sub> Nb <sub>2.0</sub> Mm <sub>2.0</sub>	322	-6.86
606	Ti <sub>10</sub> Zr <sub>30</sub> Ni <sub>48</sub> Cr <sub>1.7</sub> Mn <sub>7.0</sub> Nb <sub>3.0</sub> Hf <sub>0.3</sub>	334	-6.80
607	Ti <sub>10</sub> Zr <sub>29</sub> Ni <sub>47</sub> Cr <sub>2.0</sub> Mn <sub>8.0</sub> V <sub>4.0</sub> Al <sub>1.0</sub>	342	-6.70
608	Ti <sub>22</sub> Zr <sub>18</sub> Ni <sub>40</sub> Cr <sub>4.0</sub> Mn <sub>8.0</sub> V <sub>7.0</sub> Al <sub>1.0</sub>	335	-6.65
609	Ti <sub>30</sub> Zr <sub>10</sub> Ni <sub>47</sub> Cr <sub>2.0</sub> Mn <sub>7.0</sub> Nb <sub>3.0</sub>	308	-5.94
610	Mm <sub>17</sub> Ni <sub>61.6</sub> Co <sub>12.5</sub> Mn <sub>6.7</sub> Al <sub>2.2</sub>	285	-4.71
611	Mm <sub>16.8</sub> Ni <sub>59.5</sub> Co <sub>12.4</sub> Mn <sub>6.7</sub> Al <sub>4.5</sub>	280	-4.72
612	Mm <sub>16</sub> Ni <sub>64.9</sub> Co <sub>10.4</sub> Mn <sub>4.8</sub> Al <sub>4.0</sub>	295	-4.44
613	Mm <sub>16.4</sub> Ni <sub>60</sub> Co <sub>14</sub> Mn <sub>4.9</sub> Al <sub>4.7</sub>	275	-4.52
614	Mm <sub>16</sub> Ni <sub>74</sub> Sn <sub>5.0</sub> Mn <sub>4.0</sub> Mo <sub>1.0</sub>	285	-4.53
615	Mm <sub>16</sub> Ni <sub>58</sub> Co <sub>10</sub> Mn <sub>9.4</sub> Al <sub>5.0</sub> Ti <sub>1.0</sub>	295	-4.81

Table 2  
Comparison of the electrochemical performance of AB<sub>x</sub> Ti/Zr-based and AB<sub>x</sub> rare earth-based alloys

Performance	Ti/Zr-based alloy	Rare earth-based alloy
Capacity (mAh g <sup>-1</sup> )	230–430	230–310
Electrode preparation	Dry pressing	Dry or pasting
Pre-assembly activation	Generally required	Not needed
Rate capability	Good/excellent	Excellent
Cycle life	Good/excellent	Good/excellent

more negative than -6.5 kcal mole<sup>-1</sup> H can have an electrochemical capacity of 340–430 mAh g<sup>-1</sup> and that a Ti/Zr-based alloy having a calculated heat of hydride formation between -6.0 and -4.5 kcal mole<sup>-1</sup> H will only have an electrochemical capacity of 230–310 mAh g<sup>-1</sup>, the same range as that of rare earth-based alloys. In later case, the rate capability and working potential of a Ti/Zr alloy is similar to that of a rare earth-based alloy.

#### 4. The Ni/MH<sub>x</sub> battery

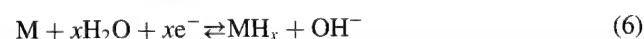
The combination of a hydride electrode with a nickel positive electrode forms a Ni/MH cell. The electrochemical reaction of a Ni/MH cell can be represented by the following half-cell reactions.

##### 4.1. Normal charge reactions (forward reaction is charging, the reverse reaction is discharging)

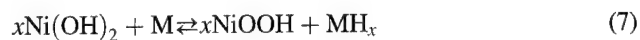
Nickel (positive) electrode:



Hydride (negative) electrode:



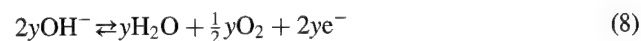
Overall reaction:



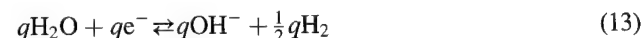
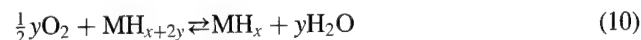
##### 4.2. Over-charge

In the construction of an actual cell especially a sealed cell, the capacity of the hydride negative electrode is higher than that of nickel positive electrode. In this positive-limited cell, oxygen evolution will occur in the positive electrode during over-charge. The oxygen generated will diffuse to the hydride negative electrode to combine the hydrogen to form water as indicated in Eqs. (10) and (11). This is the so-called oxygen recombination in a cell. Therefore, the internal pressure build-up will be eliminated or reduced substantially.

Nickel electrode:



Hydride electrode:

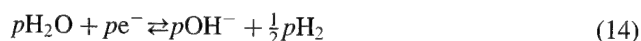


##### 4.3. Over-discharge

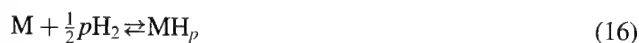
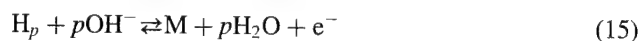
For a positive-limited and negative-pre-charged Ni/MH cell, hydrogen evolution will occur at the nickel electrode during over-discharge. The hydrogen generated at the nickel electrode will diffuse to the hydride electrode and be absorbed by the alloy in the electrode. Thus, the hydride electrode will not be oxidized and no internal pressure is

build-up. These reactions are given in the following equations:

At the nickel electrode:



At the hydride electrode:



During a prolonged and/or in a high current over-discharge, the hydrogen recombination rate at the hydride electrode is generally not fast enough to keep recharging the hydride electrode. Therefore, the electrode will eventually discharge completely and oxygen evolution will occur at the hydride electrode. Consequently the internal pressure of the cell will build-up and the hydride electrode may be partially oxidized and damaged.

## 5. Current status of commercial nickel hydride batteries

### 5.1. The manufacture process [26–29]

The making of nickel hydride batteries mainly includes (1) a negative hydride electrode line, (2) a nickel positive electrode line, (3) a cell assembly line, and (4) a cell formation line. The active material in negative electrodes is hydrogen storage alloy(s). The negative electrode can be made by a wet slurry pasting method or a dry pressing process with or without sintering. The current collector substrate is nickel or nickel plated steel or copper in the form of mesh, perforated foil or expanded sheet. The dry press method with sintering method generally gives a better rate performance. The nickel positive electrode generally is made by a pasting method in which the slurry of the active

material ( $\text{Ni}(\text{OH})_2$  plus additives) is impregnated into the nickel foam/fiber substrate.

### 5.2. Performance

The performance of a nickel hydride cell depends on many factors, including the electrode preparation, active material and its amount, and additives in each electrode, negative/positive capacity ratio, volume and concentration of KOH electrolyte, separator and activation. In general, a well-made Ni/MH cell can show a very good electrochemical properties.

1. High capacity: the capacity of a Ni/MH cell keeps increasing. For example, the capacity of a AAA-sized cell increased from 500 in 1996 to 550, then 600 and now (in 2000) to 750 mAh.
2. High working potential: the discharge capacity above 1.20 V is up to more than 80% of the total at 1C-rate for a AAA size Ni/MH cell, as shown in Fig. 1.
3. Excellent rate capability: a high rate Ni/MH Sc-sized cell can discharge up to 20C-rate, the power is higher than  $500 \text{ W kg}^{-1}$  when fully charged and  $400 \text{ W kg}^{-1}$  nearly fully discharged, equal to or better than a Ni/Cd Sc cell. Fig. 2 shows the discharge curves of a high rate Ni/MH Sc cell.
4. Low self discharge rate: the charge retention after 1 month at ambient temperature is above 80%.
5. Long cycle life: higher than 1000 cycles on a 1C-rate charge–discharge cycle, 100% depth of discharge.

### 5.3. Applications

The applications of Ni/MH cells have been broadened to many areas such as (1) cellular phones, (2) cordless phones, (3) toys, (4) portable computers, (5) CD players, (6) Camcorders, (7) power tools, (8) two-way radios, (9)

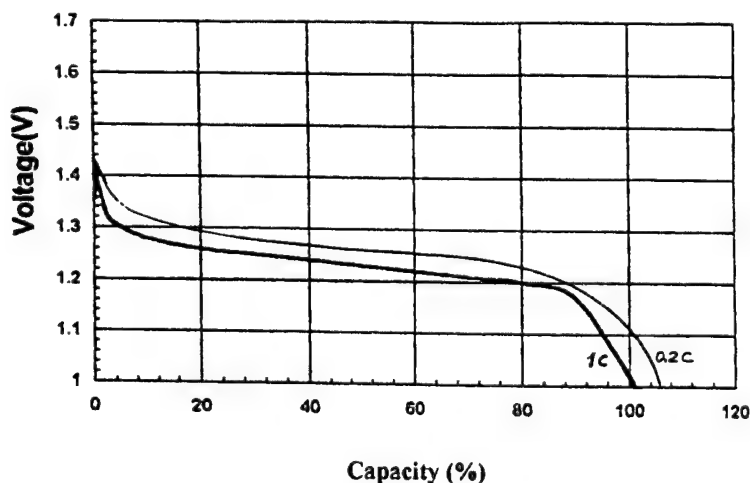


Fig. 1. The typical discharge curves for an AAA-650 mAh cell using a Ti/Zr-based alloy  $\text{Ti}_{10.2}\text{Zr}_{30.0}\text{Ni}_{48.2}\text{Cr}_{2.0}\text{Nb}_{2.8}\text{Mn}_{6.8}$ .

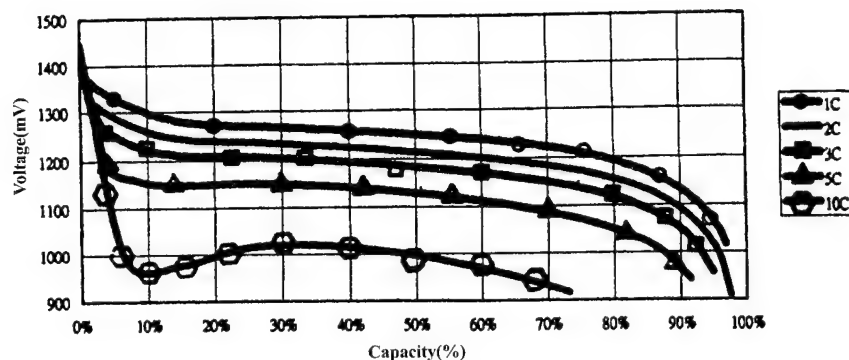


Fig. 2. Typical discharge curves for an EFBC Ni/MH Sc-size cell (1C-rate = 3.0 A).

uninterrupted power sources (UPS), and (10) electric vehicles, especially electric bicycles. Ni/MH batteries will increase the applications into the new portable wireless electronic products. However, Ni/MH batteries are facing very strong competition from lithium batteries in small size cells. It is expected that Ni/MH batteries will focus on areas such as high power and/or high capacity types to penetrate and replace the Ni/Cd battery market.

## 6. Conclusions

Hydrogen storage alloys have been applied successfully to the rechargeable Ni/MH batteries. A semi-empirical electrochemical/thermodynamic method can be used to develop/screen these hydrogen storage electrode alloys. This method is suitable both for the Ti/Zr-based and rare earth metal-based alloys. From the heat of hydride formation calculation, one can obtain a Ti/Zr-based alloy having a useful capacity from 230 up to 450 mAh g<sup>-1</sup>, and rare earth metal-based alloys having a capacity from 230 to about 320 mAh g<sup>-1</sup>. In the same capacity range, a Ti/Zr-based alloy has a similar high rate capability and high working potential as that for a rare earth metal-based alloys. The performance of a Ni/MH cell is excellent, superior to that of a Ni/Cd cell. Therefore, there are many applications for Ni/MH batteries. Ni/MH cells are on the way to replace the market of Ni/Cd cells.

## References

- [1] R.H. Wiswall, J.J. Reilly, Metal hydrides for energy storage, in: Proceedings of the 7th Intersociety Energy Conversion Eng. Conference, San Diego, 1972, p. 1342.
- [2] R. Wiswall, Hydrogen storage in metals, *Hydrogen in Metals II* (1978) 201–242.
- [3] K. Hong, ECD Quarterly Reports, 1981–1985.
- [4] K. Sapru, K. Hong, M. Fetchenko, S. Venkatesan, US Patent 4,51,400 (1985).
- [5] E.W. Justi, et al., *Energy Conversion* 10 (1970) 183–187.
- [6] K.D. Beccu, US Patents 3,669,745 (1972); 3,824,131 (1974).
- [7] J.G. Willems, *Philips J. Res.* 39 (1984) 1.
- [8] J.M.A. Gujalar, H. Buchner, K.D. Beccu, H. Saufferer, in: Proceedings of the 8th International Power Sources Conference, 1973, pp. 79–91.
- [9] G. Bronoel, J. Sarradin, M. Bonnemay, A. Percheron, J.C. Achaed, L. Schlapbach, *Int. J. Hydrogen Energy* 1 (1976) 251–254.
- [10] A. Percheron-Guegan, J.C. Achaed, J. Sarradin, G. Bronoel, in: Proceedings of the International Conference in Hydrides for Energy Storage, 1979, p. 485.
- [11] J. Dunlop, M.W. Earl, G. van Ommering, US Patent 3,959,018 (1976).
- [12] F.G. Will, US Patent 3,874,928 (1975).
- [13] J. Dunlop, J. Stockel, US Patent 4,112,199 (1978).
- [14] K. Hong, in preparation.
- [15] Willems, J. van Beek, J. Buschow, J. Kurt, US Patent 4,487,817 (1984).
- [16] K. Hong, US Patents 4,849,205 (1989); 5,006,328 (1991).
- [17] T. Gamo, Y. Moriwaki, T. Iwaki, US Patent 4,946,446 (1990).
- [18] K. Hong, Taiwan Patent 36351 (1990).
- [19] K. Hong, H. Hong, K. Kong, US Patent 5,552,246 (1996).
- [20] K. Hong, US Patent 5,773,680 (1998).
- [21] K. Hong, H. Hong, K. Kong, US Patent 5,695,530 (1997).
- [22] K. Hong, US Patents 5,536,591 (1996); 5,501,917 (1996); 5,766,799 (1998).
- [23] C.C. Chuang, Master's thesis, Tsing Hua University, Taiwan, 1993.
- [24] Y.L. Po, Master's thesis, Tsing Hua University, Taiwan, 1993.
- [25] T.C. Hsieh, Master's thesis, Tsing Hua University, Taiwan, 1993.
- [26] K. Hong, H. Hong, K. Kong, US Patent 5,541,017 (1996).
- [27] K. Hong, H. Hong, K. Kong, US Patent 5,541,017 (1996).
- [28] K. Hong, H. Hong, K. Kong, US Patent 5,556,719 (1996).
- [29] K. Hong, Abstract no. 557, ECS Meeting, Seattle, 1999.

## Electrocatalytic characteristics of the metal hydride electrode for advanced Ni/MH batteries

M. Geng<sup>a</sup>, F. Feng<sup>a</sup>, S.A. Gamboa<sup>b</sup>, P.J. Sebastian<sup>b</sup>, A.J. Matchett<sup>c</sup>, D.O. Northwood<sup>d,\*</sup>

<sup>a</sup>Mechanical, Automotive & Materials Engineering, University of Windsor, Windsor, Ont., Canada N9B 3P4

<sup>b</sup>Centro de Investigacion en Energia-UNAM 62580 Tomixco, Morelos, Mexico

<sup>c</sup>Chemical Engineering, Tees-side University of Middlesbrough, Middlesbrough TS1 3BA, UK

<sup>d</sup>Faculty of Engineering and Applied Science, Ryerson Polytechnic University, 350 Victoria Street, Toronto, Ont., Canada M5B 2K3

Received 13 November 2000; accepted 28 November 2000

### Abstract

The electrocatalytic characteristics of a metal hydride (MH) electrode for advanced Ni/MH batteries include the hydrogen adsorption/desorption capability at the electrode/electrolyte interface. The hydrogen reactions at the MH electrode/electrolyte interface are also related to factors such as the surface area of the MH alloy powder and the nature of additives and binder materials. The high-rate discharge capability of the negative electrode in a Ni/MH battery is mainly determined by the mass transfer process in the bulk MH alloy powder and the charge transfer process at the interface between the MH alloy powder and the electrolyte. In this study, an AB<sub>5</sub>-type hydrogen-absorbing alloy, Mm (Ni, Co, Al, Mn)<sub>5.02</sub> (where Mm denotes Mischmetal, comprising 43.1 wt.% La, 3.5 wt.% Ce, 13.3 wt.% Pr and 38.9 wt.% Nd), was used as the negative MH electrode material. The MH electrode was charged and discharged for up to 200 cycles. The specific discharge capacity of the alloy electrode decreases from a maximum value of 290–250 mAh g<sup>-1</sup> after 200 charge/discharge cycles. A cyclic voltammetry technique is used to analyze the charge transfer reactions at the electrode/electrolyte interface and the hydrogen surface coverage capacity. © 2001 Elsevier Science B.V. All rights reserved.

**Keywords:** Hydrogen-absorbing alloy; Metal hydride electrode; Hydrogen surface coverage; Cyclic voltammetry

### 1. Introduction

The use of metal hydrides (MH) as active negative electrode material in rechargeable alkaline Ni/MH batteries has been studied for some time. Although Ni/MH batteries have superior specific energy than the other two aqueous electrolyte systems (lead-acid and Ni/Cd batteries), they remain largely inferior to the new rechargeable lithium (Li-ion) batteries. However, lithium batteries are much more expensive to produce [1]. In addition, lithium batteries cannot be operated for a safety reasons without electronic control of each individual cell.

The reaction mechanism of hydrogen in a Ni/MH battery is similar to that of lithium in a Li-ion battery. Both H and Li atoms shuttle between the anode and cathode. We have reported a reaction model for hydrogen which shuttles between the anode and cathode in Ni/MH batteries [2,3]. Based on this shuttling model of hydrogen, Vassal et al. [4]

have developed a rechargeable Ni/MH battery which uses an alkaline solid polymer electrolyte. The reaction processes for hydrogen and lithium in Ni/MH and Li-ion batteries are summarized in Table 1.

Hydrogen diffusion in the MH electrode dominates the high-rate discharge capability of the MH electrode in Ni/MH batteries. We have reported that the MH alloy powder in a Ni/MH battery will be stabilized after about 30 charge/discharge cycles [2]. The microcracking of the MH alloy powder on charge/discharge can lead to an increase in the specific reaction area. This also leads to an improvement in the charge transfer capability at the interface between the MH particles and the electrolyte.

During the discharge process, hydrogen diffuses from the interior of the bulk alloy to the surface of the alloy powder. This is the mass-transfer process. Also, hydrogen combines with OH<sup>-</sup> ion to form H<sub>2</sub>O at the electrode/electrolyte interface. This is the charge-transfer process. The anodic polarization performance of an alloy electrode is related to both the oxidation of the alloy powder (without hydrogen in the alloy) and the hydrogen diffusion from the interior to the surface of the alloy powder (with hydrogen in the alloy).

\* Corresponding author. Tel.: +1-416-979-5102; fax: +1-416-979-5308.  
E-mail address: dnorthwo@acs.ryerson.ca (D.O. Northwood).



Table 1  
Hydrogen and lithium diffusion processes in Ni/MH and Li-ion batteries [5]

Battery	Negative electrode	Electrolyte	Positive electrode
Ni/MH	$\text{MH} \xrightleftharpoons[\text{charge}]{\text{discharge}} \text{M}$	$\text{H}^+$	$\text{NiO}_2\text{H} \xrightleftharpoons[\text{charge}]{\text{discharge}} \text{NiO}_2\text{H}_2$
Li-ion	$\text{C}_6\text{Li} \xrightleftharpoons[\text{charge}]{\text{discharge}} \text{C}_6$	$\text{Li}^+$	$\text{NiO}_2 \xrightleftharpoons[\text{charge}]{\text{discharge}} \text{NiO}_2\text{Li}$

In this paper, we have studied the charge/discharge characteristics of a Mm (Ni, Co, Al, Mn)<sub>5.02</sub> (where Mm denotes Mischmetal, comprising 43.1 wt.% La, 3.5 wt.% Ce, 13.3 wt.% Pr and 38.9 wt.% Nd) alloy electrode. In particular, we have examined the charge transfer reactions at the electrode/electrolyte interface using a cyclic voltammetry technique.

## 2. Experimental

A hydrogen storage alloy of nominal composition Mm (Ni, Co, Al, Mn)<sub>5.02</sub> was prepared by induction melting and rapid cooling. The alloy ingot was mechanically pulverized to obtain a sifted particle size of 45–53  $\mu\text{m}$  (the alloy powder was captured between 325 (45  $\mu\text{m}$ ) and 270 mesh (53  $\mu\text{m}$ ) sieves). The sifted alloy powder was used as the negative electrode material in an experimental cell. The positive electrode in this cell, a sintered  $\text{Ni}(\text{OH})_2/\text{NiOOH}$  plate, was obtained from a commercial supplier.

The set-up of the experimental cells was in a sintered glass apparatus with three compartments. The negative electrode was placed in the central compartment and two  $\text{Ni}(\text{OH})_2/\text{NiOOH}$  electrodes were placed on either side. For the specific capacity and exchange current density measurements, the MH alloy powders were mixed with nickel powder in a weight ratio of 1:1 together with a small amount (3 wt.%) of polytetrafluoroethylene (PTFE) aqueous solution as a binder and then pressed at a pressure of 500 MPa. The capacity of the positive electrode plates was designed to be higher than that of the negative electrode. An amount of 0.1 g of the alloy powder was separately used to make the negative electrode plates for two experimental cells. The electrolyte in the cells was a 6 M KOH aqueous solution [6].

The charge/discharge and polarization tests of the experimental cells were conducted using a Solartron 1285 Potentiostat with CorrWare software for Windows. The testing resolution of the potential, current and time is 0.1 mV, 0.1 mA and 0.1 s, respectively. The charge and discharge regimes were conducted at temperatures ranging from 273 to 335 K. The experimental cells were charged at a current of 100  $\text{mA g}^{-1}$  for 3.2 h. and discharged at a current of 100–600  $\text{mA g}^{-1}$  to an end-of-discharge-potential of  $-0.5$  V versus  $\text{Hg}/\text{HgO}$ . Cycle voltammograms (CVs) were obtained at the scan rates ranging from 100 to 800  $\text{mV s}^{-1}$ . The scanning potential was in the range from  $-1.1$  to 0 V versus  $\text{Hg}/\text{HgO}$ . An interruption of electrode current was

used to compensate for IR potential drop errors. The resistance of the electrolyte between the working electrode and the reference electrode, and the contact resistance are common causes of these errors.

## 3. Results and discussion

The active anode and cathode electrode materials for the rechargeable Ni/MH batteries are the hydrogen-absorbing alloys and nickel hydroxide compounds, respectively. The hydrogen-absorbing alloy, that have been developed in our group for the anode, was based on a  $\text{MmNi}_5$ -based alloy with partial replacement of Ni by Co, Mn and Al. It should be noted that the addition of Mn was used to increase the crystal cell volume, and to achieve an increase in specific capacity and better high-rate dischargeability. Adjustment of the stoichiometric composition of the  $\text{AB}_{5+\delta}$  alloy is used to increase the anti-pulverization capability.

In the KOH aqueous solution, the standard redox potentials of the rare earth elements, Al and Mn range from  $-1.37$  to  $-1.05$  V versus SHE. These metallic elements are easily oxidized to form stable metal oxide compounds at the surface of the alloy powder. These oxides, as passivation phases, are used both to prevent further oxidation of the MH alloy powder, and to increase the charge/discharge cycle lifetime. However, the oxides at the powder surface lead to a decrease in the electrocatalytic activity [6].

Fig. 1 shows the discharge capacity of the Mm (Ni, Co, Al, Mn)<sub>5.02</sub> alloy electrode at different discharge currents. The discharge capacity at a 100  $\text{mA g}^{-1}$  discharge current reaches 290  $\text{mAh g}^{-1}$  during five charge/discharge cycles. The specific discharge capacity at a 600  $\text{mA g}^{-1}$  discharge current reaches a value of 248  $\text{mAh g}^{-1}$ . The MH electrode was charged/discharged over 200 cycles and the specific discharge capacity at a 100  $\text{mA g}^{-1}$  discharge current remains at 250  $\text{mAh g}^{-1}$  at 298 K. Generally, the manufacturing of the electrode, additives and bonding materials

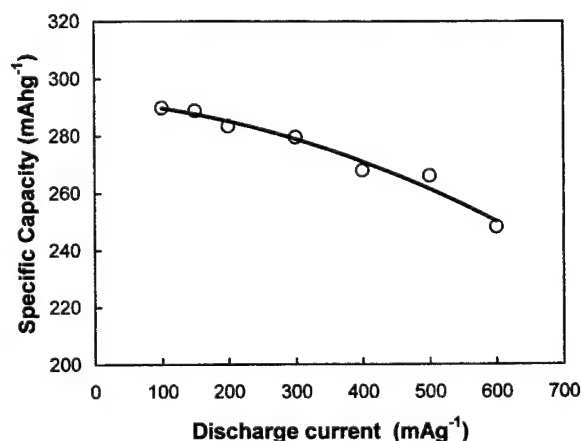


Fig. 1. Variation of specific capacity of Mm (Ni, Co, Al, Mn)<sub>5.02</sub> alloy electrode with discharge current.

slightly influence the specific discharge capacity, especially the high-rate discharge capability, because of the electrode swelling and an increase in the electrode resistance.

Fig. 2 shows the specific discharge capacity versus temperature plot. The discharge capacity was measured at a  $100 \text{ mA g}^{-1}$  discharge current. The specific capacity has a maximum value of  $290 \text{ mAh g}^{-1}$  at  $298 \text{ K}$ . The discharge capacity decreases to  $252 \text{ mAh g}^{-1}$  at  $273 \text{ K}$  and  $246.4 \text{ mAh g}^{-1}$  at  $335 \text{ K}$ . The electrochemical reaction at the surface of the MH alloy powder is controlled by the charge transfer process at the MH electrode/electrolyte interface and the mass transfer process in the bulk MH alloy. A higher temperature leads to both faster charge transfer and mass transfer reactions. However, the higher temperature also leads to a decrease in the hydrogen storage capacity in the MH alloy. The balance of these two factors leads to a maximum specific capacity at  $298 \text{ K}$ .

The equilibrium potential is a measure of the  $\text{H}^+$  activity at the electrode/electrolyte interface. The equilibrium potential of  $\text{Mm}(\text{Ni, Co, Mn, Al})_{5.02}$  alloy as a function of the number of cycles and hydrogen storage capacity is shown in Fig. 3. The equilibrium potential does not change with increasing number of cycles for hydrogen storage capacities  $>60 \text{ mAh g}^{-1}$ . However, at hydrogen storage capacities  $<60 \text{ mAh g}^{-1}$ , the equilibrium potential increases with increasing number of cycles. The instability of the equilibrium potential at a lower hydrogen storage capacity could lead to instability for Ni/MH batteries after a large number of cycles.

The discharge Coulombic capacity ( $Q$ ) of a metal-hydride electrode, obtained electrochemically as a function of the applied overpotential ( $E$ ) in the cycle voltammograms, involves three components, namely:

1. A capacity ( $Q_C$ ) due to the release of the absorbed hydrogen from the interior bulk to the surface of the alloy powder. The hydrogen released from the interior of the alloy powder leads to concentration polarization. Thus, the polarization current density from the con-

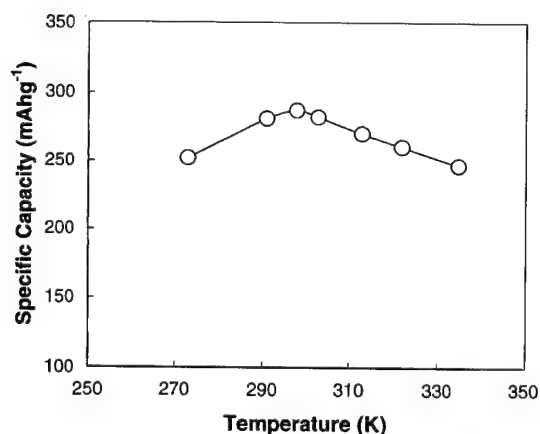


Fig. 2. Variation of specific capacity of  $\text{Mm}(\text{Ni, Co, Al, Mn})_{5.02}$  alloy with temperature.

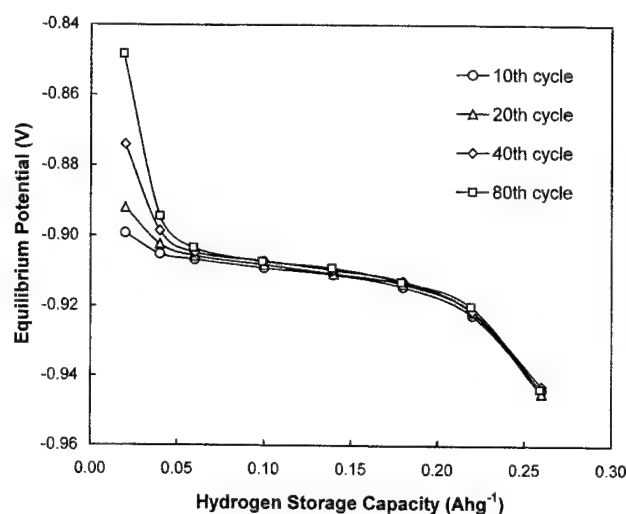


Fig. 3. Equilibrium potential of  $\text{Mm}(\text{Ni, Co, Al, Mn})_{5.02}$  electrode vs. hydrogen storage capacity at varying number of charge/discharge cycles.

centration polarization is dependent on the scan rate for low scan-rate polarization measurements (for example,  $<100 \text{ mV s}^{-1}$  scan rate).

2. A capacity ( $Q_A$ ) due to the activation polarization reaction. The activation polarization current density is strongly dependent on the scan rate for higher scan-rate polarization measurements (for example,  $>200 \text{ mV s}^{-1}$ ).
3. A capacity ( $Q_S$ ) from the hydrogen surface coverage in the alloy powder. This capacity is dependent on both the hydrogen surface coverage and the surface area. Because of a very fast reaction rate, the capacity due to the hydrogen surface coverage is independent of the scan rate.

The Coulombic capacity of the electrode, obtained from the CV technique, can be separated into the scan-rate-dependent activation and concentration capacities ( $Q_A(v)$  and  $Q_C(v)$ ) and the scan-rate-independent capacity ( $Q_S$ ). Thus, the Coulombic capacity ( $Q$ ) can be expressed as follows:

$$Q(v) = Q_C(v) + Q_A(v) + Q_S \quad (1)$$

and

$$Q_S = nF\Gamma \quad (2)$$

where,  $A$  is the reaction surface area of the electrode and  $\Gamma$  the hydrogen surface coverage. The activation-related capacity is inversely proportional to scan rate, which can be approximately expressed as follows:

$$Q(v) = \int_{E_1}^{E_2} i(E) dt = \gamma(E_1, E_2) \frac{1}{v} \quad (3)$$

where  $i(E)$  is the anodic polarization current density and  $\gamma(E_1, E_2)$  is obtained using a equation:  $E = E_1 + vt$ . The Coulombic capacity is calculated from anodic polarization current density in the potential range between  $E_1$  and  $E_2$ .

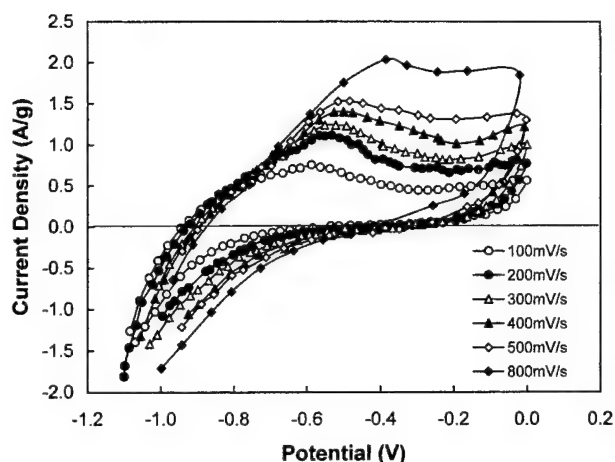


Fig. 4. Cycle voltammograms of a Mm (Ni, Co, Al, Mn)<sub>5.02</sub> alloy electrode at scan rates ranging from 100 to 800 mV s<sup>-1</sup>.

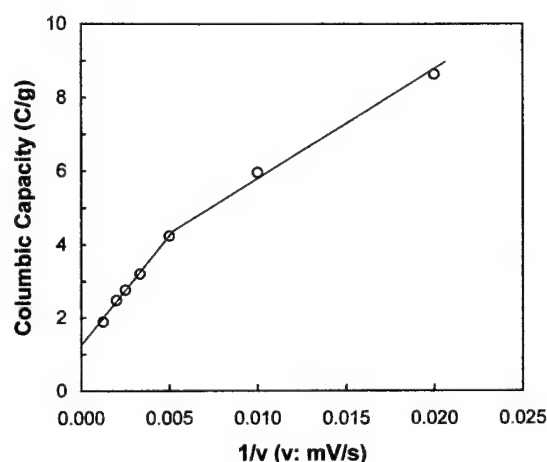


Fig. 5. Coulombic capacity of Mm (Ni, Co, Al, Mn)<sub>5.02</sub> alloy electrode for the anodic polarization process ( $E_2 = 0$  V) vs. the inverse of the scan rate.

Fig. 4 shows cyclic voltammograms at scan rates ranging from 100 to 800 mV s<sup>-1</sup>. The value of peak anodic current density, as seen in Fig. 4, is influenced by the hydrogen release from the interior of the alloy powder at a low scan rate (<200 mV s<sup>-1</sup>) i.e. the concentration polarization current density. The anodic current density mainly results from the activation reaction at high scan rates (>200 mV s<sup>-1</sup>) and hydrogen diffusion from the interior into surface of the alloy powder has only small influence on the anodic current density for high scan-rate polarization. The hydrogen surface coverage capacity can be determined at a sufficiently high scan rate. The Coulombic capacity is plotted in Fig. 5 against the inverse of the scan rate for the anodic polarization

period ( $E_2 = 0$  V). The hydrogen surface coverage capacity,  $Q_s$ , at the surface of the MH electrode, was estimated to be about 1.2 C g<sup>-1</sup> by extrapolation of the Coulombic capacity versus  $1/v$  plot. The value of the hydrogen surface coverage relates to the electrocatalytic characteristics at the electrode/electrolyte interface.

#### 4. Conclusions

The main conclusions from this study are:

1. The discharge capacity of a Mm (Ni, Co, Al, Mn)<sub>5.02</sub> electrode at 298 K remains stable at 250 mAh g<sup>-1</sup> after 200 cycles.
2. The specific discharge capacity of the MH electrode reaches a maximum value at 298 K and the specific capacity decreases to 252 mAh g<sup>-1</sup> at 273 K and 246.4 mAh g<sup>-1</sup> at 335 K.
3. The activation-related capacity, obtained from CVs, is inversely proportional to the scan rate. The Coulombic capacity from hydrogen surface coverage is independent of the scan rate. The hydrogen surface coverage capacity in this electrode, was estimated to be 1.2 C g<sup>-1</sup> by extrapolation of the Coulombic capacity versus  $1/v$  plot.
4. The instability of the equilibrium potential at a lower hydrogen storage capacity could lead to instability in Ni/MH batteries after a large number of cycles.

#### Acknowledgements

Funding for this work is being provided by the Natural Science and Engineering Research Council of Canada through a Research Grant (A4391) awarded to Professor Derek O. Northwood.

#### References

- [1] P. Ruetschi, F. Meli, J. Desilvestro, J. Power Sources 57 (1995) 85.
- [2] M. Geng, J. Han, F. Feng, D.O. Northwood, Int. J. Hydrogen Energy 23 (1998) 1055.
- [3] M. Geng, J. Han, D.O. Northwood, in: Proceeding of the 2nd International Symposium on New Materials for Fuel Cell and Modern Battery Systems, Montreal, Que., Canada, 1997, p. 585.
- [4] N. Vassal, E. Salmon, J.-F. Fauvarque, J. Electrochem. Soc. 146 (1999) 20.
- [5] G. Benczur-Urmossy, D. Ohms, M. Berthold, K. Wiesener, Electrochem. Soc. Proc. (ESC) 97-18 (1997) 812.
- [6] M. Geng, J. Han, F. Feng, D.O. Northwood, J. Electrochem. Soc. 146 (1999) 3591.

## Performance of valve-regulated lead-acid batteries in real-world stationary applications — utility installations

Paul Butler<sup>a,\*</sup>, Jennifer Dunleavy<sup>b</sup>, Mindi Farber-DeAnda<sup>b</sup>, Patrick Moseley<sup>c</sup>

<sup>a</sup>Sandia National Laboratories, MS0613, P.O. Box 5800, Albuquerque, NM 87185-0613, USA

<sup>b</sup>Energetics, Inc., 501 School St. SW, Suite 500, Washington, DC 20024, USA

<sup>c</sup>International Lead Zinc Research Organization, P.O. Box 12036, Research Triangle Park, NC 27709, USA

Received 25 January 2001; accepted 25 January 2001

### Abstract

A multi-phase project to investigate the reliability of valve-regulated lead-acid (VRLA) batteries in the field has been conducted by US industry and government research organizations. The focus of the study has been to characterize the relationships between VRLA technologies, service conditions, performance, and field failures. Two surveys were conducted: one of VRLA end users, and the other of VRLA manufacturers. Data from end users were obtained for over 56,000 telecom and utility installations representing over 740,000 cells. Seven manufacturers participated in the study. Preliminary correlations between utility end-user data, manufacturer information, and battery reliability have been developed and will be reported. Data for telecommunications installations will be reported in a separate publication when completed. © 2001 Published by Elsevier Science B.V.

**Keywords:** Lead-acid batteries/valve regulated; Performance surveys

### 1. Introduction

Valve-regulated lead-acid (VRLA) batteries have been commercially available for more than 20 years and have been enthusiastically embraced by users of uninterruptible power supplies (UPS) because of the anticipated reduction in installation and operating costs, smaller footprint, lighter weight, and fewer environmental concerns. However, as with any evolving technology, users have encountered varying degrees of performance reliability. Manufacturers and end users postulate that the premature failures experienced at some field installations may be due to temperature and charging sensitivities, manufacturing quality control, or compatibility issues with particular applications. Proprietary concerns and inadequate data acquisition systems have reduced the amount of performance and life-cycle data that is publicly available. This has limited the ability to evaluate premature capacity loss, which has been reported for VRLA batteries in some cases after as few as 2 years of service.

The International Lead Zinc Research Organization (ILZRO), Sandia National Laboratories (for the U.S. Department of Energy, Energy Storage Systems Program) and the Advanced Lead-Acid Battery Consortium (ALABC) have

sponsored a multi-phase project to investigate these issues. The focus of this study is to characterize the relationship between VRLA technologies, service conditions, and failure modes. These organizations are impartial regarding VRLA battery choice, and their sponsorship of this effort has created an unbiased forum for evaluating VRLA product characteristics, operating conditions, field performance, and service life.

This study consists of three phases.

- Confidential survey of manufacturers of VRLA cells for stationary applications.
- Confidential survey of VRLA end users with stationary applications, primarily in the electric utility and telecommunications business sectors.
- Analysis of the two surveys to characterize the VRLA population and identify parameters of design, manufacturing, and operation that may affect VRLA performance and reliability.

As of 1 December 2000, 16 utilities and eight telecommunications firms completed surveys. These responses represent over 56,000 installations with over 740,000 cells. Many respondents completed surveys representing hundreds or thousands of installations. This was particularly true among surveyed telecom end users, who typically provided responses for over 6000 installations, while the typical utility respondent represented 13 installations (Table 1).

\* Corresponding author. Tel.: +1-505-844-7874.

E-mail address: pbutle@sandia.gov (P. Butler).

Table 1  
General profile of the end users that were surveyed

Application	Installations	Cells	Ah
Utility	215	15522	105040
Telecom	55992	725988	3558100
Total	56207	741510	3663140

These installations use cells produced by seven manufacturers.

In order to investigate the particular nature of the VRLA market, the two sectors had to be treated separately. The telecom market dwarfs the utility VRLA market in the USA and combined analysis would not reveal relevant information for utility operators. In addition, fundamental differences in configuration, age, operation, monitoring, and rate of failure all support distinct analyses for the two sectors. The present paper deals with the utility results; the telecom results will be described separately.

Electric utility companies use VRLA batteries as UPS systems to provide back-up power for switchgear equipment and other critical loads. Switchgear enables utilities to bypass a localized outage (e.g. failed transformer or downed cable) and to provide power to other parts of the grid. Critical loads include computer centers, banks, and other financial institutions, air traffic control centers, hospitals, critical manufacturing processes, various government agencies, and stock exchanges.

A battery provides a virtually instantaneous power source, and is sized to bridge the gap between loss of utility power and start-up of an alternate power source such as a generator. Where an alternate power source is not available, the battery is sized to allow for an orderly shutdown of critical loads. VRLA batteries are also used to support photovoltaic (PV) or other renewable energy installations in remote, grid-independent applications. In such cases, the battery is sized to provide a few days of demand.

This paper focuses on characterizing utility VRLA installations, considering:

- operating environment: geographic distribution, indoor/outdoor, temperature controlled;
- cell type: AGM/gelled electrolyte, monobloc/module, voltage;

- monitoring regime: frequency and choice of voltage, temperature, current, and/or internal ohmic measurements;
- float voltage and maximum ambient temperature;
- year installed, date first cell replaced, and contributing factors.

The procedure employed for data collection and analysis is described in Section 2.

## 2. Procedure

The survey of manufacturers identified differences in VRLA design and manufacturer quality control. Each manufacturer was asked to respond to questions describing a specific cell's physical, electrical, and performance characteristics (Table 2).

The survey of end users was designed to facilitate responses from operators of multiple installations. For instance, one utility provided survey responses for 75 installations. Similar installations were bundled according to age of installation, manufacturer and model, voltage class, and other information specific to the application. The survey of end users attempted to reveal installation and operating procedures that may have contributed to the apparent success or failure of the VRLA cells. Each end user was asked to respond to questions describing from whom they purchased their cells, a description of their VRLA installation, and operating and monitoring regimes (Table 3).

Every effort was made to conceal the identity of participants, yet survey response was initially less than desired. End users identified 76 different VRLA cell models, far more than the number in completed manufacturer surveys. Manufacturers tended to complete surveys for new product lines, whereas end users more often identified older models, no longer produced or sold. To fill in the gaps, the authors performed research on the Internet to verify model numbers and obtain product literature. Only a subset of the survey questions could be answered with the information obtained from the web.

Two linked, password-protected Access databases were created for the VRLA battery end users and manufacturers. Manufacturer's name, cell model, and end-user name are numerically coded to conceal identities. The collected and estimated data are provided as metric measurements.

Table 2  
Question categories in the survey of VRLA manufacturers

Physical characteristics	Electrical characteristics	Performance characteristics
Exterior dimensions	Cell Ah capacity	Application
Electrolyte	Internal resistance	Recommended float voltage
Separator material	Monthly self-discharge	Premature failures
Case and post-seals	Specific energy	Cause of premature failures
Plate geometry		
Recommended operating temperature		

Table 3

Question categories in the survey of VRLA end users

Battery identification	Installation description	Operation/monitoring
Type of application	Make/model of cells	Float voltage
Seller/installer	Installation size (number of cells, modules, Ah capacity)	Year first cell replaced
Receipt of installation/operating instructions	Year installed	Total cells replaced
Unusual failures	Location	Parameters monitored and frequency
Root cause of failure	Temperature and control	

Queries have been developed to interrogate the databases, with analysis performed in Excel.

None of the surveyed end users documented VRLA battery operation and maintenance at the level needed for exact numerical responses. A respondent's recall often resulted in date ranges instead of a specific year for installation or first cell replacement. Multiple-survey respondents typically provided ranges, resulting in use of the midpoint value for the installations. For instance, one utility respondent installed three substation batteries in 1996–1998; the authors set the year as 1997 for all three installations. Midpoints were also used for float voltage, e.g. 2.25 V where 2.24–2.26 V was provided.

Linking the manufacturer and end-user surveys required identifying the model used in each installation. In some cases, respondents could not remember the exact model number and could not easily visit the site (e.g. remote and unmanned, underground, or pole-mounted facilities). Sleuthing was required to determine the appropriate model, cells per module, Ah capacity (at the 8 h rate to 1.75 V per cell), and other parameters for calculations. Survey respondents occasionally provided incomplete model numbers, contradicting model number and Ah capacity, or general guidelines for dividing a bundle of installations by make and model. The measures taken to overcome the shortcomings in the gathered data are believed to have been adequate to

protect the validity of the conclusions drawn from the data set.

### 3. Results

Utility VRLA end users responding to the survey operate 215 installations, distributed across 13 States of the USA. To conceal end-user identity, survey results are reported for four regions: northeast, midwest, south, and west. The geographic distribution of the survey sample is skewed towards the midwest and west regions. This characteristic is biased by the random nature of the survey. The VRLA cells installed in the northeast appear to be smaller in capacity than those installed elsewhere in the country.

By comparison, the south is less represented in the survey sample. While the use of VRLA cells is not promoted in very hot climates, a good portion of the south is still reasonably temperate and opportunities for VRLA applications abound. More installations are known in the south, but potential respondents were unwilling to participate. A regional map of the USA with the number of cells and estimated Ah represented by surveyed utility end users is shown in Fig. 1.

Location and temperature control define the operating environment of VRLA installations. Utility VRLA install-

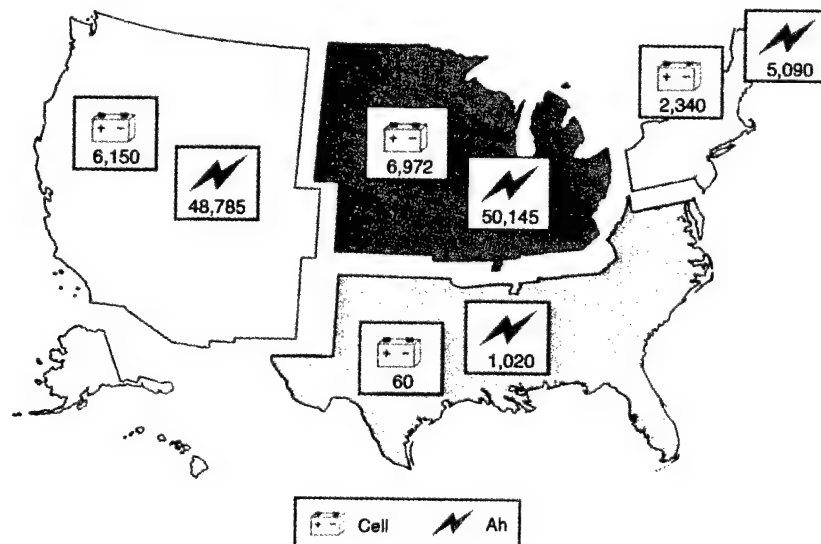


Fig. 1. Geographical distribution of utility VRLA cells and their total energy output.



ations are primarily indoor facilities; almost 90% of the surveyed installations are indoors. Not surprisingly, maximum temperature exposure is not high for the surveyed utility respondents. In fact, none of the 215 installations is operated above 40°C. Manufacturers by and large do not require temperature control. Nonetheless, almost half of the utility installations were temperature-controlled, typically by a fan or small air conditioning unit.

The manufacturer chooses a particular cell configuration to meet the customer's needs, which in turn, impacts surface area, air circulation, and stack and rack design. Utility installations are comprised of single cells, modules of three–eight cells connected in series or parallel, or monoblocs of up to six cells within a single container. Modules are the configuration of choice for the surveyed utility installations. Use of monobloc designs is also popular. A key advantage of the monobloc is a smaller battery footprint. The key disadvantage is that failure of a single cell within the block results in the replacement of the entire container and its cells.

A key determinant of cell chemistry is the mode of electrolyte immobilization. Early in this survey, the authors assumed that both gel and AGM materials would be well represented in the survey. After all, gelled-electrolyte technology has been available since the early 1960s and AGM cells have been marketed only since 1972 [1]. Gel cells experience less electrolyte stratification than AGM cells, particularly under deep cycle conditions, and typically require less overcharge to reach full state of charge. AGM cells have high-rate discharge capacities that make them suitable for UPS and standby applications where charging periods are predictable and regulated [1]. Acid stratification impacts the permitted height of the container (or jar). Gel cells can be twice as tall as AGM cells, which are limited to about 380 mm (15 in.) in height, when in an upright position.

Utility respondents indicated that only four installations used gelled electrolyte in their 476 cells, with the remaining 211 installations employing AGM. As expected, most (64%) of the surveyed utility installations operate at 125 V for substations and industrial customer sites (see Fig. 2). This group accounts for 83% of the cells employed by the surveyed utilities. A third of the installations operate at 48 V, and these are employed in a wide variety of applications.

In order to get a complete picture of the status of a VRLA battery, it is important to take account of its state of health. VRLA batteries are often closely packed in module racks or designed as monoblocs, making the measurement of individual cell voltages difficult. In addition, the spread of individual cell voltages during float service exceeds that of conventional flooded batteries, especially when the battery is new, making float voltage measurements less meaningful [2].

Monitoring temperature is important in VRLA batteries, because they are more sensitive to heat than flooded lead-acid batteries, and increased temperature can result in water loss and thermal runaway.

Since, conventional discharge tests are time consuming and expensive, many end users have taken to monitoring battery health in terms of voltage, current, temperature, and internal ohmic measurements (internal resistance, conductance, impedance). Because not all regimes are ideal for every installation, end users must decide for themselves which parameters are most effective in identifying their battery's state of health. There has been much talk of late regarding simply tracking ohmic measurements to detect faults that impact on a battery's capacity [3]. These readings measure impedance, which will increase due to loss of electrolyte or corrosion of the conducting components [2]. None of the surveyed utility participants measure internal ohmic readings alone.

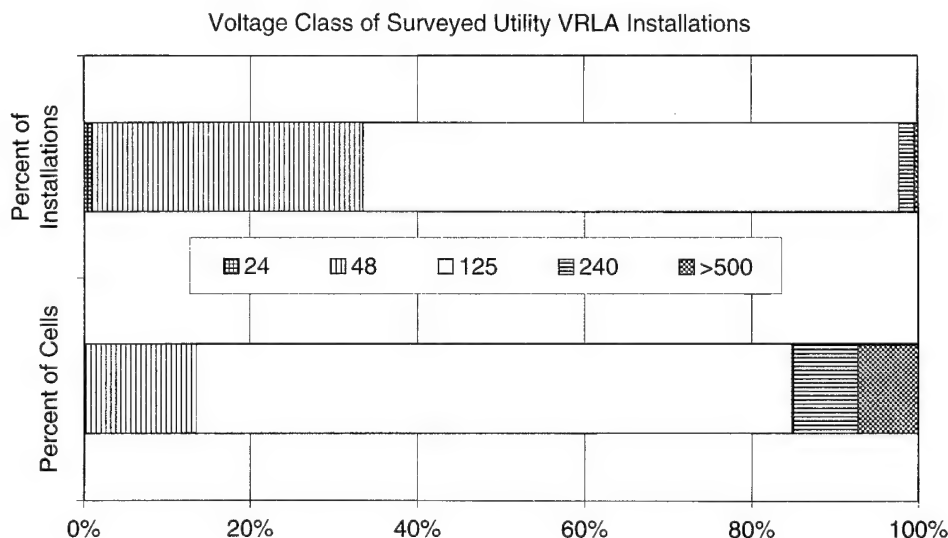


Fig. 2. Voltage of utility VRLA installations and the cell groups surveyed.

Table 4  
Parameters monitored by utility installations

Installations	Cells	Parameters			
		Voltage	Temperature	Current	Ohmic measurements
38	3990	×	×	×	
21	653	×	×		×
6	720	×	×		
81	6660	×		×	×
29	1313	×			×
40	2186	×			
215 (total)	15522 (total)				

There were six different sets of parameter combinations used by utility respondents (Table 4). Two-thirds of the participating utility installations included monitoring three parameters in their regime. None of the end users monitored all parameters. Voltage, current, and internal ohmic measurements were the favored combination, monitored at 43% of all surveyed cells. None of the utility respondents indicated visually checking their cells for cover, case, and post-integrity.

Every utility installation surveyed measured voltage, 84% of the installations monitored it at the cell level, thus impacting 88% of all surveyed utility cells. For only 31% of the installations was the battery room's ambient temperature monitored. Internal ohmic measurements were taken on 55% of all cells, and although only two regimes included monitoring current, 69% of all surveyed cells are impacted by this measurement.

Not only must companies monitor their cells, they must do it consistently to assess battery health accurately. Only 7% of cells surveyed were monitored on a daily basis, and voltage, current, and ambient temperature were checked. While a quarter of the utility VRLA cells are monitored monthly, over half of the cells are monitored semi-annually for voltage, current, and internal ohmic measurements.

The life of the lead-acid battery is dependent on the choice of positive plate geometry, positive grid alloy and thickness, processing parameters, electrolyte, and other design variables. Each battery manufacturer sets operational limits for warranties, e.g. involving ambient temperature, float voltage, normal and equalization charges, depth of discharge, etc. When operating conditions fall outside specified limits, customers are given guidelines for compensating the difference to maintain the design life of the product.

A fully charged cell in a standby condition has a predictable voltage determined by its chemistry and temperature. Overcharging cells can lead to them drying out. In order to prevent this, the recommended float voltage for the majority of VRLA cells surveyed is 2.26 V per cell. If the cells are exposed to ambient temperatures above 25°C, manufacturers recommend temperature compensation to reduce unwanted aging effects.

- Too high a float voltage will lead to accelerated corrosion and water loss.

- Too low a float voltage will lead to self-discharge and, potentially, sulfation of the negative plates.

Some manufacturers suggest reducing the float voltage by 2.5–3.25 mV for each degree above 25°C. The float voltage for VRLA cells operated at 35°C would then be reduced to 2.24 V. As seen in Table 5, most of the utilities surveyed float their VRLA cells at 2.24–2.25 V. However, there are 22 installations that float their 2600 cells above 2.28 V.

Other manufacturers do not insist on temperature compensation between 5 and 35°C. Temperature-compensated float voltages are required for outdoor installations, where the range of operating temperatures can be large [2]. Without temperature control, many indoor installations may also need temperature-compensated float voltage.

The survey of end users focused on VRLA cell performance and premature failure. However, the survey was somewhat handicapped in obtaining this information because of the following reasons.

- VRLA cell replacements and unusual experiences are not well documented by utility operators. Rather, the survey had to depend on respondent recall, which is both subjective and inexact.
- VRLA cells are typically installed at remote, unmanned locations. If the owner/operator does not have a data acquisition system with remote access or a regular monitoring program to track cell health, he can only guess as to when the cells first failed.

Table 5  
Maximum temperatures and float voltages found in the surveyed utility installations

Float voltage per cell	Maximum temperature		Unknown	Total
	20–30°C	30–40°C		
<2.24		1		1
2.24–2.25	83	30	26	139
2.26–2.27	23	29		52
2.28–2.29	1			1
>2.29	3	18		21
Unknown			1	1
Total	110	78	27	215



Table 6  
Age of first cell when replaced within the utility installations surveyed

Year installed	<1 year	1–3 years	4–5 years	>6 years	None replaced	Total
1980–1985					10	10
1986–1989		2				2
1990–1993		61	30	3	14	108
1994–1996		42	6		8	56
1997–2000	4	3			32	39
Total	4	108	36	3	64	215

- The age at which the first cell was replaced is used as a proxy for premature cell failure. The age of the second and third cell replacements would also be of great interest and could be considered for subsequent surveys.

Despite these shortcomings, it is believed that the major conclusions of the analysis are reasonable. Cell failures within the first year of operation are typically due to manufacturing defects, usually covered by the warranty. Given the negative publicity surrounding VRLA performance, the authors expected to find a large number of failures within the first year. However, only four utility installations had their first cells replaced within the first year. The range of ages for first cell replacement naturally broke at 1–3 years, 4–5 years, and more than 6 years. The remaining category is “None Replaced”, the most desirable condition for end users.

Having no cells replaced could easily indicate that the battery was recently installed, e.g. since 1997. For older installations, having no cells replaced means the battery has performed as expected. This could be due to any number of conditions, e.g. the end user’s preventive maintenance program, a particular product’s technical superiority, very little use, or no method of checking the capacity of the cells. To provide a more complete appreciation of the age of the installation at first cell replacement, the year installed is included (particularly for those installations with none replaced). The year installed parameter has been grouped for analysis purposes: 1980–1985, 1986–1989, 1990–1993, 1994–1996, and 1997–2000.

Half of the utility respondents had their first cell replaced within 3 years of installation (Table 6). Another 36 installations replaced their first cells after the fourth or fifth year. Three installations waited for 6 years. One interesting feature of this table is the number of installations where no cells were replaced. Half of the 64 installations where no cell has been replaced were installed prior to 1997. One operator reported that he has never replaced any cells at 10 facilities installed prior to 1985. This skews the analysis into suggesting that older models performed better than newer designs. This may not be a reliable conclusion, however, since only 12 of the 215 surveyed utility installations were delivered prior to 1990. Considerable

changes in VRLA cell design have occurred during the past decade.

Unfortunately, this survey cannot test the impact of those design improvements. Subsequent survey efforts should increase the number of respondents with installations dating back before 1985 in order to permit a more complete appraisal of the performance of earlier VRLA cell designs.

Batteries installed between 1990 and 1996 constitute the largest portion of utility installations surveyed. These limited data suggest that there is a 56% probability that a VRLA battery installed by utilities between 1990 and 1993 will

Table 7  
Profiles of the 125 and 48 V surveyed utility installations

Description	125 V installations	48 V installations
Year installed		
1980–1985	1	9
1986–1989	2	0
1990–1993	75	32
1994–1996	42	9
1997–2000	18	20
Maximum temperature		
20–30°C	74	35
30–40°C	55	18
Unknown	9	17
Outdoor configuration		
Monobloc	1	2
Module	8	11
Indoor configuration		
Cell	6	0
Monobloc	13	25
Module	110	32
Temperature controlled		
Controlled	85	24
Not controlled	53	46
Float voltage		
<2.25 V	105	33
>2.25 V	33	37
Parameters monitored		
Voltage	23	17
Voltage, ohmic	12	15
Voltage, ohmic, temperature	4	17
Voltage, ohmic, current	81	0
Voltage, current, temperature	12	21
Voltage, temperature	6	0

Table 8  
Probability of first cell replacements within the 125 and 48 V surveyed utility installations

Age of installation	125 V batteries installed (%)				48 V batteries installed (%)			
	1990–1993		1994–1996		1990–1993		1994–1996	
	<2.25 V	>2.25 V	<2.25 V	>2.25 V	<2.25 V	>2.25 V	<2.25 V	>2.25 V
1–3 years	46		82	25	100	100	100	25
4–5 years	49		16					
>6 years	2	14						
None replaced	3	86	3	75				75

experience its first cell failure within the first 3 years of operation. The odds increase to 75% for batteries installed by utilities between 1994 and 1996. Examining the possible reasons for this situation, the authors investigated 125 and 48 V installations separately. Recall that almost two-thirds of the surveyed utility installations operate at 125 V and another one-third operate at 48 V (Fig. 2). Analysis of these two voltage classes helps to quantify differences in operation and monitoring that these two types of installations experience. Table 7 profiles the two groups.

Over 85% of the 125 V batteries surveyed were installed in 1990–1996. The 125 V batteries are mostly modules installed indoors, with over 61% temperature-controlled even though not required by the manufacturer. The float voltage is below 2.25 V for three-quarters of the cases and almost 60% of the installations monitor voltage, current, and internal ohmic measurements.

By contrast, over 58% of the 48 V batteries surveyed were installed in 1990–1996. The 48 V batteries are either modules or monoblocs, primarily located indoors. These units are typically not temperature-controlled. Slightly over half of the 48 V installations float their cells above 2.25 V. Owners of 48 V batteries monitor either voltage, voltage and ohmic measurements, voltage, ohmic and temperature, or voltage, current and temperature.

Do certain operational characteristics increase or decrease the probability of early first cell replacements? Table 8 examines the year installed, age of installation at first cell replacement, and float voltage of the 125 and 48 V batteries in an attempt to tackle this question. The 125 V batteries installed in 1990–1993 and floated below 2.25 V had a 46% chance of experiencing their first cell replacement within 3 years. Another 50% experienced the first cell replacement by fifth year. The batteries in this voltage category that were floated above 2.25 V lasted longer than 6 years or had never had cells replaced.

For 125 V batteries installed between 1994 and 1996 and floated below 2.25 V, the probability of early cell failure worsened, with 82% of the installations replacing their first cell within the first 3 years of operation. The likelihood of no cell replacements was slightly less for the 125 V batteries installed between 1994 and 1996 and floated above 2.25 V compared to those installed between 1990 and 1993.

On the other hand, over half of the 125 V batteries installed between 1990 and 1993 operated beyond 3 years before replacing their first cell. It is possible that the operators monitored these installations more closely than the 24 and 48 V facilities, since these were more likely to be located on utility property.

The 48 V batteries installed between 1990 and 1996 and floated below 2.25 V universally experienced first cell replacements within 3 years. The 48 V batteries installed in 1990–1993 and floated above 2.25 V also experienced first cell replacements within 3 years. This situation improved slightly for the 48 V batteries installed in 1994–1996, with 75% yet to replace any cells.

A tentative conclusion for both categories (125 and 48 V) would be that the greatest concentration of first cell replacements occurs for the batteries that have float voltages below 2.25 V. This would be consistent with a failure mechanism involving self-discharge, aggravated by the difficulties of maintaining all of the cells in a long string at a sufficiently high voltage.

#### 4. Conclusions

Even though the surveys are still in the process of being analyzed, a number of important conclusions are worthy of note.

- A significant number of the VRLA cells covered by the surveys are lasting for 5 or more years. The 28% of the utility installations have cells lasting more than 5 years, with another 15% installed in the past 3 years without any cell replacements.
- There is a large spread in the range of life expectancy for utility VRLA cells, from 1 to 16 years.
- In some cases, it appears that adjusting float voltage may enhance battery life. Inadequate float voltage may be an important life-limiting factor for VRLA cells in float duty.
- A vigorous monitoring program does not appear to extend the life of VRLA cells without an equally proactive cell maintenance program. Every installation measured voltage and 81% of the utility installations measured one or two more parameters regularly.

Further analyses of the data and feedback from manufacturers are needed before drawing additional conclusions.

### **Acknowledgements**

The authors gratefully acknowledge financial support for this project from Sandia National Laboratory/DOE, from the International Lead Zinc Research Organization, from the Advanced Lead-Acid Battery Consortium, and from Hollingsworth and Vose.

### **References**

- [1] R.H. Newnham, Advantages and disadvantages of valve-regulated, lead-acid batteries, *J. Power Sources* 52 (1994) 149–153.
- [2] D. Berndt, *Maintenance-Free Batteries*, Research Studies Press Ltd., Taunton, UK, 1993.
- [3] M. Hlavac, D. Feder, VRLA battery monitoring using conductance technology, in: *Proceedings of the 17th Intelec*, The Hague, The Netherlands, October 1995, pp. 285–291.

# Latest developments in super high rate lead-acid batteries from India

Amal Bhattacharyya\*, Dipak Dasgupta, Subhabrata Ghosh

*Exide Industries Ltd., R&D Centre, 217, Nazrul Islam Avenue, Calcutta 700059, India*

Received 11 January 2001

---

## Abstract

The application of lead-acid batteries for automobile applications has to meet stringent specification guidelines. Design engineers are more concerned to meet the high rate discharge (HRD) performance of a battery, particularly for automobile applications. The required HRD is to be tested to the full satisfaction of the ultimate user. This paper gives a review on lead-acid batteries manufactured in India with special focus on their HRD performance.

Basically, there is a cut-off voltage (which is 7.20 V for a 12 V battery system) down to which the battery shall be able satisfactorily to deliver current to the starting mechanism of a vehicle at the low critical temperature of  $-18^{\circ}\text{C}$ .

For determination of HRD performance under simulated conditions a high rate discharge tester is used to draw a constant discharge current from the battery, kept and conditioned in a cold chamber. It uses a built-in data acquisition system for logging of current and voltage values at an interval of 5 s. © 2001 Elsevier Science B.V. All rights reserved.

**Keywords:** Lead-acid batteries; Testing/high-rate; Applications/automobiles

---

## 1. Introduction

India is now producing super high rate lead-acid batteries to meet global standards. These batteries are achieving the stringent International requirements of battery performance in sub-zero as well as in high ambient temperatures.

The rate of discharge of a lead-acid battery (or any other storage type) is usually expressed in terms of current flow (amperes) and the duration (hour/minute) obtained to a certain cut-off voltage. The quantity of electricity, which can be delivered during discharge of the battery at a constant current to the cut-off voltage, is the capacity of the battery.

The capacity obtained from a lead-acid battery is strongly dependent upon the rate of discharge. Increasing the rate from nominal to a high rate value results in voltage depression, shortening of the discharge time and a discharge characteristic having a slope of steeper gradient (as against that of a nominal rate). During rapid discharge, the electrochemical reactions take place mainly on the surface of the plates, because of the limited time available for adequate diffusion of acid into the pores of the active material. Moreover, the reaction product ( $\text{PbSO}_4$ ) tends to block the pores, a process that further restricts the even percolation

of acid throughout the volume of the plates and so the capacity is severely reduced at high rate discharge [1].

Tables 1 and 2 summarise the performance of a 12 V, 100 Ah battery and show that the final voltage and the available capacity is depressed at high rates.

For this reason, various International as well as Indian standards have been introduced in order to compare the performances of different batteries. Attempts have also been made throughout Europe to unify the requirements through a battery section of the International Electrotechnical Commission (IEC) using SAE and BS specifications.

Japanese Industrial Standards have drawn up specification JIS D5301 for batteries compatible for SLI (starting, lighting and ignition) applications, which is different from other International standards in some respects.

As indicated by the SAE/BSI specifications, the primary function of the SLI battery is to provide power to crank the engine during starting [2]. With the increase in the compression ratio of internal combustion engines, this duty has become more and more difficult especially at sub-zero temperature owing to the increased viscosity of the engine oil. Therefore, SAE/BSI standards declared SLI performance as the current, in amperes, delivered at a temperature around  $-17.8^{\circ}\text{C}$  ( $0^{\circ}\text{F}$ ) for not less than 30 s to a voltage, not less than 1.2 V per cell or 7.2 V for a 12 V battery. This value is referred to as CCA (cold cranking ampere) of the battery.

---

\* Corresponding author.

E-mail address: amal@md.exide.co.in (A. Bhattacharyya).

Table 1  
Voltage limits at normal temperature, 25°C

Discharge rate	Final voltage (V)
20 h to 1 h	10.50
30 min to 1 min	8.00

Table 2  
Capacity at normal temperature of 25°C, expressed as % of 20 h rate

Discharge rate	Capacity (Ah)	Current (A)	% Capacity
20 h	100	5.0	100
10 h	89.5	8.95	89
5 h	78	15.6	76
3 h	70	23.3	68
1 h	53	53.0	51
30 min	45.8	91.5	43
20 min	42.3	127.0	39
10 min	34.6	208.0	30
5 min	27.2	327.0	22
3 min	20.5	410.0	16
1 min	8.8	528.0	6

The corresponding IEC requirement, also at  $-18^{\circ}\text{C}$ , is a minimum duration of 1 min to not less than 1.4 V per cell or 8.4 V for a 12 V battery. The current delivered under SAE condition is greater than that specified by IEC by a factor of 1.6–1.8. The German DIN specification also has the cold start test at  $-18^{\circ}\text{C}$  down to a cut-off of 1 V per cell, i.e. 6 V for 12 V battery with a minimum duration of 150 s. A 30 s voltage with a minimum requirement of 9 V is also mentioned.

To cater for the lowest temperature met in USA or elsewhere, the SAE specification includes a second low temperature requirement, i.e. current in amperes delivered at  $-29^{\circ}\text{C}$  ( $-20^{\circ}\text{F}$ ) for not less than 90 s to a voltage of 1 V per cell or 6 V for 12 V battery. The IEC adopted the duration at  $-29^{\circ}\text{C}$  as 1 min and 8.4 V minimum for 12 V battery in the CCA test.

The JIS differs more. JIS D5301 specifies temperature of  $-15^{\circ}\text{C}$  and currents of 150, 300 and 500 A, to a voltage of 6 V for 12 V battery for a period of 1.4–4.3 min depending upon the size of the battery. Certain minimum voltages of 7.1–8.9 V after 5 s and 7.6–8.2 V after 30 s are also mentioned, depending on the battery size.

However, in India, the ambient being quite on the high side, performance of the battery at sub-zero temperature is not a dominant factor. Indian standards (IS), therefore, concentrate on specifying the performance of an SLI battery at  $27^{\circ}\text{C}$ . The current requirement in IS is 3 times the  $C_{20}$  rate for normal type batteries and 4.5 times of  $C_{20}$  rate for heavy duty type batteries down to 1.33 V per cell. Gulf countries normally follow IS condition as the atmospheric environment is more or less similar to that in India.

The high rate discharge performance obtained from the above-mentioned specifications is determined by several factors such as:

1. Materials/components used
2. Construction/design
3. Method of production/processes
4. Maintenance and life of the battery
5. Temperature

## 2. Battery materials

Raw material, like lead, should be 100% pure. Impurities cause depression of over voltage and resist a full recharge after a discharge, leading to sulphation and drop in HRD performance within a short period.

For active material or paste, the oxide used should be tetragonal in character. Above 1% ortho-rhombic oxide leads to scaling during formation that hinders HRD performance to some extent.

Various types of separators have been developed for various International and Indian battery types.

The resistance values in Table 3 show that the batteries with microporous thin polyethylene type and also LEWK glass mat type separators give better performance in comparison with PVC to obtain a good high initial voltage (IV), i.e. at 5 or 30 s on HRD.

## 3. Battery construction

### 3.1. Grids

In a lead-acid battery, the grid is not only for holding the active material, it also acts as a good conductor of current. Traditional rectilinear grid structures with a lug at one corner perform the structural function well, but are not so efficient from the conductivity point of view. Ohmic losses in the current collecting grid are inversely related to HRD performances. In terms of % utilisation in current conduction, different types of grid are described in Table 4.

From above discussion, it is evident that a radial grid with the lug at the centre is the best design so far as HRD performance character is concerned.

### 3.2. Plate pitch

The batteries required for engine cranking are designed with minimum plate pitch. Low internal resistance depends on the number of plates per element. Plates of the same

Table 3  
Types of separator

Type of separator	Resistance of surface area ( $\Omega\text{ cm}^{-2}$ )
Sintered poly vinyl chloride (PVC) sheet	0.32
Poly ethylene (PE) envelope	0.075
Bonded glass mat (LEWK)	0.09

Table 4  
Relative merits of various grid designs

Type of grid	Utilisation
Rectilinear grid with lug on one corner	10% of grid area
Radial grid with lug on one corner	19% of grid area
Radial grid with lug at centre	34% of grid area

polarity in a group are in parallel and act as a parallel resistance. Higher the number of plates, greater will be the deliverable current from a given contact volume of electrolyte and smaller will be the internal resistance. Thus, larger numbers of thin plates per element in a given volume increases the surface area and delivers more current from a battery, thereby showing better HRD performance.

### 3.3. Electrolyte

At the time of discharge, positive and negative plates, as per the double sulphate theory, consume equal amounts of  $\text{H}_2\text{SO}_4$ . During discharge, sulphate ions migrate towards the negative and hydrogen ions towards positive. A good part of these hydrogen ions reacts to form  $\text{H}_2\text{O}$  at positive electrode. So, near the positive plate, there is always a dilution caused by this water. Thus, the volume of acid required is 1.6 times higher in positive plates than in negative plates for complete reaction.

Therefore, separator design is such that near to the positive plate more space is given for quick discharge, such that vigorous gassing and formation of water can easily take place in this excess space.

### 3.4. Group bars

Group bar thickness has also to be designed properly for optimum high current discharge.

### 3.5. Assembly design

In some cases, reverse ratio assembly design is made so that end plate is positive instead of negative to improve the initial voltage during high rate discharge.

## 4. Manufacturing processes

### 4.1. Grid alloys

High antimony (Sb) increases electrical resistances and lowers CCA/HRD performance. Lowering of Sb to 1.6% improves the CCA value to a large extent.

Superiority of Pb–Ca alloy over Pb–Sb alloy is due to low electrical resistivity, being very close to that of pure lead. As a result, CCA is maximum for this alloy. Ca alloy has also other advantages including maintenance-free characteristics. Presence of Sn above 0.1% increases conductivity and reduces oxidation loss.

### 4.2. Grid quality

No breaks in radial/vertical wires are allowed. No weakness in lug or frame is acceptable. These factors reduce conductivity.

### 4.3. Paste

High paste density (above  $4.2 \text{ g ml}^{-1}$ ) in the positive plate causes degradation of HRD performance. Paste densities in the order of  $3.8\text{--}4.0 \text{ g ml}^{-1}$  for positive plates improve plate porosity and decreases internal resistance (IR) and thereby helps HRD performance.

Carbon black used in negative plates increases conductivity to some extent and improves cold performances.

Vanisperse is the lignin sulphonate used in negative plates for improving cold performance. It contains 50% humic acid, has ion exchange properties and retains hydrogen ions around negative plates. Some conducting fibres that adhere to pastes are used today for better HRD performances.

Residual Pb below 3% is ideal, so that formation will be satisfactory and internal resistance will be less.

### 4.4. Terminal posts

The quality of terminal building is advancing day by day, to avoid any incipient cracks or shrinkage or holes that lead to failure during HRD. A cold forging system has been applied to terminal post building, resulting in significant improvement in strength of terminals and their current carrying capacity and longer life.

BCI type terminals, however, ensure firm contact with connecting bolts. They reduce heating and voltage drop at the connection/contact surface.

### 4.5. Miscellaneous factors

Apart from other factors, it should be mentioned here that the processes of pasting and formation of plates are affected by high temperature. So, a temperature controlled method for chilling improves the process for production of good plates, particularly in India where the environmental temperature is high.

Drying of positive plates should not be above  $80\text{--}90^\circ\text{C}$  so that the positive plate will not be passivated and give poor HRD performance.

For SLI systems with more and more usage, the life and HRD performance decreases and to maintain longer life and better performance, the following points must be avoided:

1. Overcharging
2. Undercharging
3. High ambient temperature
4. Keeping idle for a long period
5. Addition of concentrated acid when topping-up

6. Abuse, allowing impurities inside the battery
7. Hammering on terminals

## 5. Model analysis

The generic representation of a battery circuit is shown in Fig. 1. The metallic internal resistance which includes the terminal posts, straps, grids and grid-paste is  $R_m$ ,  $R_e$  the resistance of the electrochemical path, comprising electrolyte and separator and depends on acid concentration, separator resistance, presence of impurities and temperature,  $C_p$  the capacitance of the parallel plates. This is shunted by a non-linear resistance contributed by the contact resistance of plate and electrolyte ( $R_l$ ).

Overcharge current results in water loss which reduces electrolyte volume and increases electrolyte concentration. Higher concentrations, due to volume loss or addition of acid from outside, leads to rapid sulphation of negative plates. Undercharging leading to sulphation of plates and may cause similar situations. Overheating, improper topping up and overcharging may lead to plate corrosion. Loss of active material in contact with electrolyte increases the value of  $R_l$ .

Hammering, or hammering after wrong fixing of terminal cables (negative clip to positive and vice versa) may create fine cracks leading to an increase of the  $R_m$  value.

At sub-zero temperatures, the viscosity of electrolyte increases and diffusion of electrolyte in plates become more difficult. In other words,  $R_e$  and  $R_l$  are increased. The viscosity has found to increase 2-fold from  $+30^\circ\text{C}$  to  $0^\circ\text{C}$  and about 8 times at  $-30^\circ\text{C}$ . The internal resistance of  $\text{H}_2\text{SO}_4$  ( $R_e$ ) increases 3.5–3.8 times at  $-18^\circ\text{C}$  and 2.8–3 times at  $-15^\circ\text{C}$  depending upon the acid concentration.

However, the value of  $C_p$  which is responsible for good HRD, is perfectly maintained by selecting a correct alter-

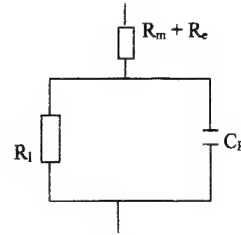


Fig. 1. The battery circuit.

nator voltage to keep the battery always in a completely charged condition at the respective ambient. So, the HRD performance for starting a car will always then be satisfactory irrespective of a cold atmosphere.

## 6. Conclusion

In India, a wide portfolio of automotive and industrial batteries are manufactured to cope up with various requirements and different geographical characteristics. As such, batteries are designed for high temperature zones like SE Asia, Sri Lanka, etc. and also very low ambient zones found in parts of Europe, USA and the Scandinavian countries. Quality and technical up-grading are the focus areas to survive the globalisation of economy. New paradigm is, therefore, is the motto of the battery manufacturers of India.

## References

- [1] G.W. Vinal, Storage Batteries, Wiley, New York.
- [2] T. Denton, Automobile Electrical & Electronic Systems, Edward Arnold.

# On the impedance of the gassing reactions in lead-acid batteries

Abderrezak Hammouche\*, Eckhard Karden, Jörg Walter, Rik W. De Doncker

*Institute for Power Electronics and Electrical Drives, Aachen University of Technology, Jägerstrasse 17-19, D-52066 Aachen, Germany*

Received 29 November 2000; accepted 16 December 2000

## Abstract

Oxygen and hydrogen evolution reactions in flooded lead-acid batteries during float charging were studied by galvanostatic steady-state polarization and impedance spectroscopy techniques. Given the very low relaxation frequencies of such processes (between 2 and 0.05 mHz), impedance measurements needed to be extended to the ultra-low frequency domain. Investigation of their dynamic behavior provided a complete description of the porous character of the active zone. The steps involved in the reaction mechanisms are also discussed. © 2001 Elsevier Science B.V. All rights reserved.

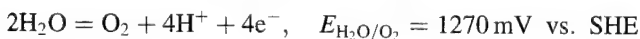
**Keywords:** Lead-acid batteries/flooded; Polarization; Gas evolution reactions

## 1. Introduction

The purpose of float charging is to maintain a battery in a full state of charge and to return it to that state after it has undergone a discharge. This is accomplished by applying a voltage slightly higher than the open-circuit voltage of the fully-charged battery, to compensate for unavoidable gradual self-discharge.

Lead-acid batteries are especially suited for float charging, because they can be recharged completely at float voltage and retain full capacity when charged continuously at a fairly low float voltage of about 100–150 mV per cell above open-circuit.

In lead-acid batteries, completion of charge is followed by “gassing”, that is to say oxygen evolution at the positive plate and that of hydrogen at the negative one



The generation of such gases can never be completely suppressed because hydrogen evolution starts above the equilibrium potential of the negative (Pb/PbSO<sub>4</sub>) electrode, and oxygen evolution below the equilibrium potential of the positive (PbSO<sub>4</sub>/PbO<sub>2</sub>) electrode. In order to prevent water loss caused by gassing, many attempts were made either by hindering such processes by the use of lead–calcium and

low-antimony grids (which, unfortunately, are not without side effects) or better, by recombining, chemically and/or electrochemically, the hydrogen and oxygen gases given off during overcharging.

Another relevant reaction in such conditions is corrosion of lead in the current-collector, which reduces the lead dioxide, taking place at the rest potential without any outside current.

Knowing the high time constants of the processes occurring in the lead-acid battery (many tens of hours are usually needed to allow the dc signals relax), Karden and co-workers [1,2] developed in the last few years a specialized impedance spectroscopy to investigate the dynamic behavior of such systems in the microhertz frequency range, taking into account all the specific requirements of industrial batteries. Applied to a set of 100 Ah lead-acid cells, it showed good reproducibility and consistency of the results.

Because of the limited understanding of gas evolution mechanisms and the resulting uncontrolled life expectancy of lead-acid batteries, further studies are needed. Lead and lead dioxide plates present a rather poor catalytic activity towards, respectively, hydrogen and oxygen evolution [3,4]. It can then be expected that their time constants will be very high. Consequently, the method of ultra-low frequency impedance spectroscopy is especially suitable for investigation of such processes.

The purpose of this study is to analyze the electrochemical processes occurring at both plates in a flooded lead-acid battery when in the overcharge region, by dc polarization and ultra-low frequency impedance spectroscopy.

\* Corresponding author. Tel.: +49-241-80-69-45; fax: +49-241-67-505.  
E-mail address: hm@isea.rwth-aachen.de (A. Hammouche).



## 2. Experimental

All experiments were performed with a flooded 4GroE100 cell, made by Hoppecke, with a nominal  $C_{10}$  capacity of 100 Ah. The electrolyte was a sulfuric acid solution with a density of  $1.22 \text{ kg l}^{-1}$ . The temperature of measurements,  $23^\circ\text{C}$ , was constant to within  $1^\circ\text{C}$ .

Impedance measurements were performed during float operation after charging the cell with a high charge coefficient and after several days of float operation at a fixed voltage of 2.23 V. In fact, this voltage value, which corresponds to the minimum rate of grid corrosion, is usually recommended for float operation. The impedances of the full cell and of both half-cells were successively measured galvanostatically with dc currents ranging from 40 to 270 mA, after stabilization during 30 h for each dc current. Laboratory instrumentation, used for the present experiments, has been developed at ISEA for high-precision impedance measurements of industrial batteries [2].

The ac current amplitude was automatically chosen for each frequency so that the optimum ac voltage response was always equal to 3 mV (which is well below the thermal energy " $RT/F = 25 \text{ mV}$ " at room temperature and more than two orders of magnitude below the dc overvoltages). Also, the upper ac current value was limited to 2/3 of the dc current value, to keep the net current  $[I(t) = I_{\text{dc}} + I_{\text{ac}} \sin(\omega t)]$  always within the charging regime and so prevent occurrence of the battery discharging during the negative half-period of the ac signal.

The frequency range was 3 kHz–38  $\mu\text{Hz}$  with eight frequencies per decade for the cell and the positive plate. Each spectrum required a measuring time of almost 4 days (the measurement of  $Z$  at 38  $\mu\text{Hz}$  alone lasts  $3/38 \times 10^6 \text{ s}$ ,  $\approx 22 \text{ h}$ ). Knowing that very slow dynamics exist in the battery, it would be desirable to go even further, but adding one frequency decade makes the measuring time 10 times as long. The time required for a single experiment would then be counted in months rather than days. However, the frequency range for the negative plate was taken down to only 150  $\mu\text{Hz}$  as this covered mostly its whole relaxation frequency range, as can be seen on the experimental data. The initial parts of the spectra (down to 1 mHz) were usually repeated after the first spectrum to check if the experimental conditions were stationary. These measurements were always in good agreement with each other.

Unfortunately, our test bench does not yet allow for multi-channel voltage measurement. Therefore, we measured the cell impedance and the electrode impedances in subsequent experiments. Anyway, the sum of both half-cell impedances turns out to be always very close to the cell impedance, though all three quantities were measured in different experiments, each of which lasting several days.

The experimental data were fitted to the relevant equations using the least-square fit, built-in with Excel, to optimize the parameters. In the case of impedance diagrams, the real and the imaginary components were fitted at the

same time through minimizing the sum of the "weighted" squares of the difference between the measured ( $Z_{\text{m}}(\omega)$ ) and the simulated ( $Z_{\text{s}}(\omega)$ ) data sets

$$S = \sum_{i=1}^n w_i [(Z'_{\text{m}} - Z'_{\text{s}})^2 + (Z''_{\text{m}} - Z''_{\text{s}})^2]$$

Only one weight factor,  $w_i$ , was used as both data sets are not independent of each other. It is equal to the inverse of the square of the modulus of the impedance,  $w_i = 1/(Z'_{\text{m}}{}^2 + Z''_{\text{m}}{}^2)$ , letting each measurement contribute equally to the sum of squares.

We used a mercury/mercurous sulfate reference electrode (RE), of standard design, in the same sulfuric acid concentration as the cell electrolyte, to measure the electrode potentials separately and avoid liquid junction potential error. Its thermodynamic potential, in the  $1.22 \text{ kg l}^{-1}$   $\text{H}_2\text{SO}_4$  solution at  $23^\circ\text{C}$ , is estimated to be 606.5 mV versus SHE [5]. The RE tip was located in the midpoint between the two current collecting tabs and 20 mm above the top of the plates.

## 3. Results and discussion

### 3.1. Current and potential distribution near the tabs

According to Newman's reports on half-cell investigations on lead-acid batteries [6], RE measurements are most meaningful when the exact position of RE is specified. Actually, distribution of current lines and equipotential surfaces in lead-acid batteries is deeply affected by the limited electrical conductivity of the plate's grid. A non-homogeneous current and potential distribution entails a heterogeneous utilization of the plates and so a loss in capacity.

Orientation of current lines can be inferred from the variations of the ohmic resistance measured between a working and a reference electrode, this latter being located in different positions in the cell. Since, the diameter of the RE used was too large to be inserted into the limited space between the plates, where heterogeneity of current and potential is expected to be more pronounced, impedance measurements were performed in the present study only for positions in the free solution above the plates, near the tabs (Fig. 1).

No significant effect was observed in the impedance of the electrodes whatever the position of RE, but the ohmic resistance between either tab and RE was sensitive when RE was moved horizontally in the  $x$  direction (i.e. parallel to the plates), for different values of  $y$  and  $z$ . As RE came near one tab, the respective ohmic resistance decreased while that corresponding to the opposite tab increased (Fig. 2). The sum of these partial resistances was, however, very close to the one measured for the complete cell.

It can readily be inferred from this observation that the current lines in this region are rather oriented towards the

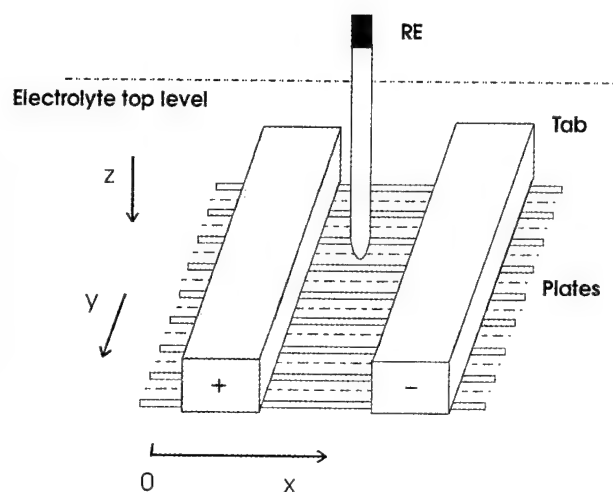


Fig. 1. Location of the reference electrode for half-cell measurements.

tabs, suggesting that these take part to some extent in the electrode processes. This statement is confirmed by observation of some gas bubbles given off from the surface of the tabs, in float charge conditions. Since, gassing reactions give rise to additional water loss, it is desirable to suppress them. This may be achieved, for instance, by covering the tabs with an insulating substance.

In the subsequent measurements, RE was definitely placed in the midpoint between the two current collecting tabs and 20 mm above the top of the plates.

### 3.2. Polarization curves (dc)

From a fundamental point of view, float charging of a fully-charged battery seems to be the only experimental situation in which the electrochemical processes can be regarded as stationary. The only change in the chemical compositions within the cell is caused by the gassing reactions which consume water, but do not significantly change the electrolyte concentration on time scales out to many days. Besides, the gas bubbles cause some convection which

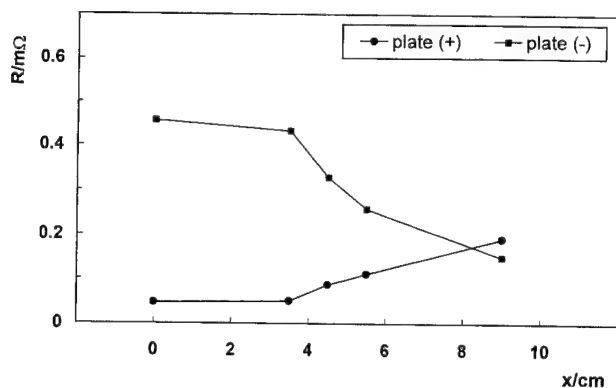


Fig. 2. Variation of ohmic resistance of the half-cells as a function of location of the reference electrode.

makes it plausible that the electrolyte concentration is almost constant all over the cell.

Most of the float current flows through the gassing reactions during overcharge, while only a very small fraction of the total current is consumed by the parallel side reactions. It is, thus, expected that both the dc current/voltage and the impedance characteristics of the electrodes are essentially determined by the gassing reactions.

At open circuit and on overcharge in the lead-acid battery, the overvoltages for oxygen and hydrogen evolution are large ( $\eta_{O_2} > +434$  mV and  $\eta_{H_2} < -359$  mV). If these electrochemical processes are under activation control, their kinetics exhibits a Tafel behavior, i.e. a linear potential-log current relationship of the form

$$\eta = U_T \log \left( \frac{I}{I_0} \right) \quad (1)$$

where  $\eta = U - U_0$ , the overpotential of each reaction; and  $I_0$ , the exchange current which is a parameter depending on the concentration of reacting species. The temperature and the transfer coefficient  $\alpha$ , give  $U_T = 2.3RT/\alpha nF$  which defines the Tafel slope.

If this law is valid for both half-cell reactions and no parallel reactions occur, a similar law holds for the whole cell voltage

$$\begin{aligned} U &= U_{0(O_2/H_2)} + \eta_{O_2} + \eta_{H_2} \\ &= U_{0(O_2/H_2)} + U_{T,H_2} \log \left( \frac{I_{0,O_2}}{I_{0,H_2}} \right) \\ &\quad + (U_{T,O_2} + U_{T,H_2}) \log \left( \frac{I}{I_{0,O_2}} \right) \\ &= \text{Cste} + U_{T,\text{cell}} \log \left( \frac{I}{I_{0,O_2}} \right) \end{aligned}$$

This equation also shows that the Tafel slope for the complete cell is given by adding up the Tafel slopes of the electrode reactions.

The dc cell and half-cell polarization curves were plotted considering the proper currents involved in the main reactions, obtained by subtracting the currents corresponding to the side reactions. Cathodic currents were corrected for that corresponding to oxygen reduction at the negative plate; its value, independent on overvoltage, was estimated to  $-2.5$  mA [7]. Anodic currents were corrected for that corresponding to grid corrosion, which depends on the positive plate overvoltage, showing its minimum at  $\eta \sim +80$  mV [7].

Fig. 3 depicts the Tafel plots for the whole cell and the individual electrodes. These slopes are, respectively, 215.3, 127.8 and 81.4 mV per current decade for the cell, the negative and the positive plates. The Tafel slope for the cell is slightly greater than the sum of the slopes for the electrodes. This is related to the fact that the raw float current used for the calculations concerning the cell, includes the contribution of the secondary reactions. Their

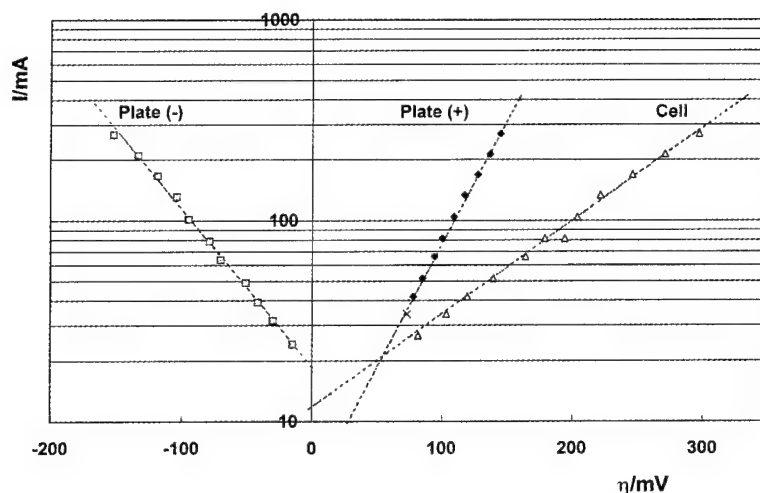


Fig. 3. Float current vs. electrode and cell overvoltages.

effect is somewhat more influential in the low current-overpotential values.

The law, mentioned above, was empirically well defined in a Varta technical report [8]. The overcharging voltage of a lead-acid battery increases by 200 mV per current decade, at room temperature. This increase is shared between the electrode potentials: 120 mV for the negative electrode, and 80 mV for the positive electrode, per current decade. The slight discrepancy shows that these kinetic parameters are dependent on cell design and materials, methods of manufacture and cell age.

### 3.3. Impedance measurements

#### 3.3.1. Negative plates

A typical impedance diagram under non-zero dc current is shown in Fig. 4. It is mainly composed of a single depressed

semicircle. This semicircle can be viewed as approximately equivalent to the response of a simple parallel RC circuit, describing a CPE element. The  $R_{ct}$  value measured at the limit of low frequencies corresponds to the slope of the steady-state  $I(\eta)$  curve at the corresponding polarization. The agreement between these two values indicates that the recorded diagrams describe the full cell response: there are no other semicircles at lower frequencies.

According to the present results, investigation of the ultra-low frequency domain is necessary since the frequency of the maximum of such semicircles decreases to about 100  $\mu$ Hz, for the low values of float current. This seems to be logical with regards to the poor catalytic activity of lead towards hydrogen evolution, characterized by a very low exchange current density ranging between  $10^{-8}$  A  $\text{cm}^{-2}$  [3] and  $10^{-11}$  A  $\text{cm}^{-2}$  [4]. Actually, for batteries with a large electrode surface area, the double-layer electrode

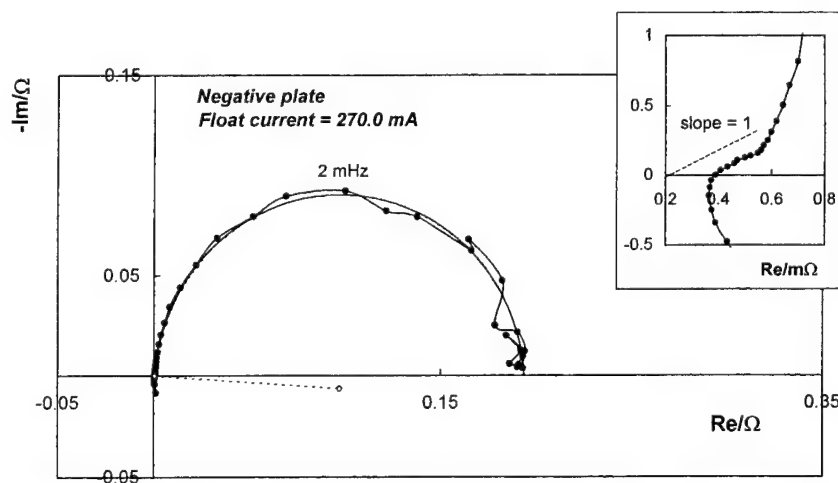


Fig. 4. Typical impedance diagram obtained for the negative plate, under an overcharge current of 270.0 mA. The magnification in the top right part of the figure concerns the high frequency region of the impedance diagram.

capacitance is very large while the charge transfer resistance is not small enough. Consequently, the relaxation frequency, given by the quantity  $(2\pi R_{ct}C_{dl})^{-1}$ , will go down to the millihertz range. Moreover, if the reaction mechanism involves additional steps like adsorption of electroactive species and/or diffusion processes, the relevant relaxation frequencies will be even lower. Similar experiments reported in the literature were restricted to more than 1 mHz [9], showing only the high frequency branch of the impedance diagram, which appeared more or less vertical. Accordingly, the explanation based on a quasi-blocking character, reported for the electrodes investigated, does not describe actually their electrochemical behavior.

A more careful analysis of the experimental diagrams at high frequencies reveals a straight line in the capacitive quadrant (see the magnified part of the diagram in Fig. 4). Even after correcting for the likely influence of the inductance of the wiring and the intrinsic inductance of the measuring cell (generally ranging between 20 and 200 nH) on the cell impedance in this frequency region [10], the slope of such a line always keeps a value close to unity. This impedance segment is characteristic of the infinite pore behavior of porous electrodes in the high frequency region, where the penetration depth of the alternating signal does not reach the bottom of the pore, when  $Z$  identifies to a simple parallel  $RC$  circuit [11]. This result indicates that the hydrogen evolution reaction takes place at the internal surface of the electrode pores.

According to the general features of the impedance spectra, the polarization resistance  $R_{ct}$  characterizes a charge transfer reaction. This quantity corresponds to the slope,  $dU/dI = U_T/I$ , of the stationary dc curve  $\eta = f(I)$  obtained by differentiating Eq. (1). As can be deduced from the recorded spectra, the variations of  $R_{ct}$  with overpotential also obey an exponential law. Accordingly, the product of this resistance times the dc current does not vary with the electrode overpotential. It defines the Tafel slope of the electrode and it is approximately equal to 131.9 mV per

decade, showing a good agreement with the data obtained from dc polarization measurements.

The electrode capacitance, estimated as a fitting parameter, has a value decreasing from approximately 70 to 50 F when the electrode potential decreases from  $-380$  to  $-520$  mV versus SHE. This capacitance corresponds to the electrode double layer ( $C_{dl}$ ). Its large order of magnitude confirms that not only the external surface of the plate is active, but that the internal pore zones are involved in the electrode process as well. Based on a unit surface capacitance of  $18 \text{ mF cm}^{-2}$ , given in the literature for the lead electrode [12], the mean active surface can be estimated to about  $300 \text{ m}^2$ , which is consistent with the rough estimation deduced from morphology parameters.

It is worthy of note that the decrease of the electrode capacitance is expected as the potential decreases in the explored range. This fact can be related to the decrease of the specific adsorption of mainly  $\text{SO}_4^{2-}$  anions as the potential approaches that of zero charge, lying at  $-620$  mV versus SHE for the lead electrode [13].

### 3.3.2. Positive plates

The general shape of the impedance diagrams obtained for the positive plate is shown in Fig. 5. Two capacitive loops can be distinguished, respectively, around 4 and 0.1 mHz. The order of magnitude of such relaxation frequencies confirms once again the importance of investigating the ultra-low frequency domain. The resistive component associated with both of these loops decreases as the float current increases, but the low frequency loop, being greater, masks completely the higher frequency one under low values of float current.

The mean value of the Tafel slope deduced from these impedance data is 74.3 mV per decade. It represents the sum of 7 and 67.3 mV per decade of Tafel slopes determined for the high and low-frequency loops, respectively. This value is somewhat smaller than the one obtained from the dc polarization data.

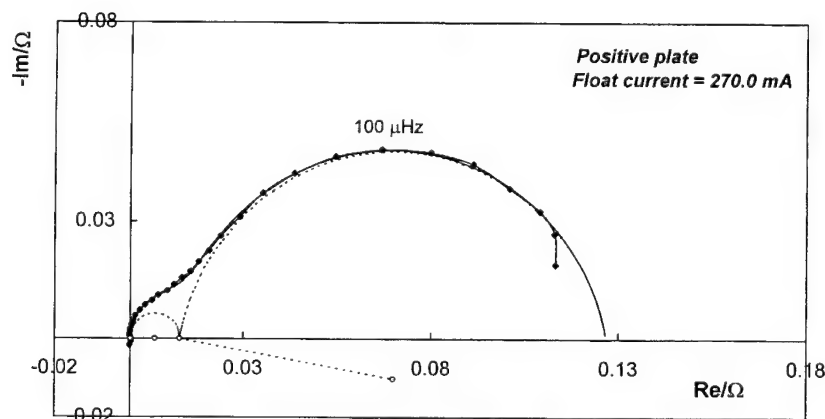
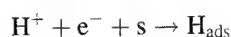


Fig. 5. Typical impedance diagram obtained for the positive plate, under an overcharges current of 270.0 mA.

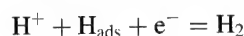
### 3.4. Mechanisms of hydrogen and oxygen evolution

#### 3.4.1. Hydrogen electrode reaction

On the most of soft metals in groups 5B and 6B of the periodic table, such as Pb, Bi, Cd, In, Sn and Hg, the hydrogen electrode reaction takes place according to the following two-step mechanism, consisting of a rate determining charge transfer step:



followed by a fast ion–atom recombination



The latter step is in a quasi-equilibrium state. The coverage  $\theta$  by adsorbed hydrogen atoms must be very low, since none was ever detected, even at the highest overpotentials measured [3]. The rate of the overall reaction is equal to twice that of the first step and is given by

$$I = I_0 \exp\left(\frac{-\alpha n F \eta}{RT}\right) \quad (2)$$

where  $I_0 = 2Fk_1(\text{H}^+)(1 - \theta) \exp(-\alpha n F U_{\text{eq}}/RT)$  is the exchange current of the overall reaction, where  $k_1$  is the constant rate of the first step,  $\text{H}^+$  the activity of protons, and  $U_{\text{eq}}$  the equilibrium potential.

Eq. (2) is applicable at high overpotentials, where the reverse reaction can be ignored. Also, it is assumed that mass transport limitation is negligible, which is true in view of the high sulfuric acid concentration. This equation can be written in a logarithmic form as

$$\eta = U_T \log(I) + b$$

where  $U_T = 2.3RT/\alpha n F$  and  $b = -U_T \log(I_0)$ .

The experimental results corresponding to hydrogen evolution on the negative plate fit this equation. The mean Tafel slope of 130 mV per decade corresponds to a transfer coefficient of 0.45, close to the value (0.5) which is characteristic of this family of metals [3]. Moreover, the exchange current density, deduced by extrapolation of the Tafel curve to  $\eta_{\text{H}_2/\text{H}^+} = 0$  mV, and based on the actual surface area ( $S_{\text{Pb}} = 300 \text{ m}^2$ ), yields a value of  $3.10^{-11} \text{ A cm}^{-2}$ , which is in the range of the values determined for this family of materials [3].

The electrode impedance exhibits a simple form, resulting from the parallel combination of the double layer capacitance and the Faradaic impedance which corresponds, for the aforementioned mechanism, to the transfer charge resistance

$$Z = \frac{R_{\text{ct}}}{1 + (j\omega R_{\text{ct}} C_{\text{dl}})^\phi}$$

where  $R_{\text{ct}} = (U_T/2.3I_0) \exp(\alpha n F \eta/RT)$  and  $\phi$  the empirical exponent reflecting heterogeneity effects of the electrode material. The complex-plane representation of this impedance gives rise to a more or less depressed semicircle identical to that measured experimentally. Its size decreases

exponentially, in accordance with the above formula, as the overpotential becomes more cathodic, but the product of the term  $R_{\text{ct}}$  times the dc current equals the constant value  $U_T$ .

#### 3.4.2. Oxygen electrode reaction

In contrast to hydrogen evolution, there is no common concept about the mechanism of the elementary reactions that proceed during oxygen evolution on the  $\text{PbO}_2$  electrode. According to the results of early investigations, evolution of oxygen in acid media is considered to come from discharge of water molecules to form adsorbed OH radicals. These radicals are oxidized to yield adsorbed oxygen atoms, which combine subsequently to produce oxygen molecules [14,15]. The first step is supposed to be rate determining and would then be responsible for the large capacitive loop observed at low frequencies on the impedance diagram.

The origin of the high frequency loop is not obvious. It would not be related with an electrochemical step in view of its weak sensitivity to electrode polarization (7 mV per decade). On the other hand, ascription of such a loop to relaxation of charge carriers in a thin layer occurring on top of the electrode surface, like the hydrated amorphous  $\text{PbO}_2/\text{PbO}(\text{OH})_2$  layer with mixed protonic–electronic conduction properties as reported by Pavlov and coworkers [16,17], is also questionable. Such a relaxation process is expected to happen in the hundreds of Hertz frequency range, which is five orders of magnitude larger than the highest relaxation frequency observed in the present measurements. The positive electrode behavior deserves further investigation to elucidate the relevant mechanism.

### 4. Conclusions

As a result of this work we have shown the following:

- Relaxation of the gassing processes in the lead-acid battery occur at frequencies ranging between 2 and 0.05 mHz, strongly justifying the exploration of the ultra-low frequency domain to observe the whole dynamic response of the system under study.
- Gassing reactions take place in the internal surface areas of the electrode pores under the experimental conditions reported.
- Hydrogen evolution on lead electrodes follows the mechanism, found with most soft metals, consisting of a rate determining charge transfer step followed by fast ion–atom recombination. The dc polarization curves and impedance parameters are in good agreement, presenting a mean Tafel slope of 130 mV per decade.
- According to the impedance results, oxygen evolution involves a mechanism that includes at least two steps of comparable kinetics for the larger float current values. In contrast to the step associated with the low frequency loop, which is sensitive to the electrode potential (Tafel slope = 67 mV per decade), the step corresponding to the

high frequency one has low sensitivity (slope = 7 mV per decade). The corresponding mechanism deserves further investigation.

### Acknowledgements

One of the authors (A.H.) is grateful to the Alexander von Humboldt Foundation for making cooperation possible. The authors would like to thank S. Buller for valuable discussions.

### References

- [1] P. Mauracher, E. Karden, J. Power Sources 67 (1997) 69.
- [2] E. Karden, S. Buller, R.W. De Doncker, J. Power Sources 85 (2000) 72.
- [3] E. Gileadi, Electrode Kinetics for Chemists, Chemical Engineers, and Materials Scientists, VCH Publishers, New York, 1993.
- [4] S. Trasatti, J. Electroanal. Chem. 111 (1980) 125.
- [5] H. Bode, Lead-acid Batteries, Wiley, New York, 1977 (R.J. Brodd, K.V. Kordesch, Trans.).
- [6] J. Newman, W. Tiedemann, J. Electrochem. Soc. 140 (1993) 1961.
- [7] D. Berndt, R. Bräutigam, U. Teutsch, Temperature compensation of float voltage — the special situation of VRLA batteries, in: Proceedings of the 17th INTELEC Conference, The Hague, The Netherlands, 1995, p. 1.
- [8] Bleiakumulatoren, Herausgegeben von der Varta Batterie AG, 1986.
- [9] N. Yahchouchi, Mesure de l'impédance d'un accumulateur tubulaire au plomb: application à la détermination de la capacité électrique, Doctorate Thesis, University of Paris VI, Paris, 1981.
- [10] M. Keddam, Z. Stoyanov, H. Takenouti, J. Appl. Electrochem. 7 (1977) 539.
- [11] R. de Levie, in: R. Delahay (Ed.) Advances in Electrochemistry and Electrochemical Engineering, Vol. VI, 1967, p. 329.
- [12] B.N. Kabanov, S. Jofa, Acta Physicochim. (USSR) 10 (1939) 617.
- [13] A.N. Frumkin, J. Electrochem. Soc. 107 (1960) 461.
- [14] J.P. Hoare, The Electrochemistry of Oxygen, Interscience, New York, 1968.
- [15] A.I. Krasil'shchikov, Z. Fiz. Khim. 37 (1963) 531.
- [16] D. Pavlov, I. Balkanov, J. Electrochem. Soc. 139 (1992) 1830.
- [17] D. Pavlov, B. Monahov, J. Electrochem. Soc. 143 (1996) 3616.



ELSEVIER

Journal of Power Sources 96 (2001) 113–120

JOURNAL OF  
**POWER  
SOURCES**

www.elsevier.com/locate/jpowsour

# Methods for state-of-charge determination and their applications

Sabine Piller\*, Marion Perrin, Andreas Jossen

*Center for Solar Energy and Hydrogen Research (ZSW), Division 3: Electrochemical Energy Storage and Energy Conversion,  
Helmholtzstr. 8, 89081 Ulm, Germany*

Received 8 January 2001; accepted 10 January 2001

## Abstract

State-of-charge (SOC) determination becomes an increasingly important issue in all the applications that include a battery. Former operation strategies made use of voltage limits only to protect the battery against deep discharge and overcharge. Currently, battery operation is changing to what could rather be called battery management than simply protection. For this improved battery control, the battery SOC is a key factor.

Much research work has been done in recent years to improve SOC determination. Operational conditions differ for batteries in, for example, photovoltaic applications, (hybrid)-electric vehicles or telecommunications. Hence, a given method for SOC calculation will be more suitable for a certain application than for another. The authors introduce commonly used methods for SOC determination and establish a relationship between the advantages of the different methods and the most common applications. As a main illustration, the analysis of Kalman filter technique for lead-acid battery SOC determination are presented and some results for other calculation methods as well. © 2001 Elsevier Science B.V. All rights reserved.

**Keywords:** Lead-acid batteries; State-of-charge

## 1. Introduction

Most of us use a mobile phone, a laptop computer, perhaps a cordless shaver, maybe even an electric car for the luckiest of us. All these devices are now part of our daily life and bring a big contribution to our mobility and our freedom (even if this point is more questionable).

But besides the comfort that is gained by all these devices that use the electrical energy delivered by an accumulator, a new source of stress has appeared: will I be able to shave this morning, will the battery last until I have written the last page of my paper? In most systems that use a battery, an important point is the knowledge of the state-of-charge (SOC) of the battery or more simply: how long do I have until my device stops working?

In addition to the immediate displaying of the SOC to the user, the knowledge of the remaining battery capacity is of importance for its management. Namely, many systems are sensitive to deep discharge or overcharge because these states of extremely high or too low SOC can lead to irreversible damage in the battery.

Given the importance of knowing the SOC of a battery, another question arises: how to measure it? And before measuring the SOC, we need to know what it actually is. In a recent paper [1] the different definitions for the capacity and SOC were summarised. According to this paper, we will make reference to the SOC as: the ratio between the difference of the rated capacity and the net amount of charge discharged from a battery since the last full SOC on the one hand, and the rated capacity on the other hand. Due to this definition, the full SOC is reached when (according to DIN 43539), the battery current is not changing during 2 h at a constant charge voltage and constant temperature.

This definition leaves behind the problem of battery ageing. In fact, the capacity that can be delivered by a battery may change in the course of its life due to problems like the loss of charge acceptance of the active material on either of the electrodes, changes in the physical properties of the electrolyte or corrosion of the current conductors. In this paper, we will also not deal with the state-of-health (SOH) of batteries, which is another topic of actual research.

The paper summarises different techniques that exist for determining the SOC of a battery. Additionally, the most suitable field of application for each method is presented. The main focus is put on the lead-acid system.

\* Corresponding author. Tel.: +49-731-9530-201;

fax: +49-731-9530-666.

E-mail address: sabine.piller@zsw-bw.de (S. Piller).



## 2. Methods for determining the state-of-charge

The determination of the SOC of a battery may be a problem of more or less complexity depending on the battery type and on the application in which the battery is used. Since this paper will focus on lead-acid accumulators, the SOC determination methods are described explicitly for this type of battery system, but apply partially also for the other electrochemical systems.

### 2.1. Discharge test

The most reliable test for the determination of the SOC of a battery — i.e. its remaining capacity — is a discharge test under controlled conditions. But such a test, which usually includes a consecutive recharge, is too time consuming to be considered for most applications. As a second drawback during testing the system function is interrupted.

### 2.2. Ampere hour counting (including loss calculation)

This is the most common technique for calculating the SOC. Since the charge and discharge are directly related to the supplied or withdrawn current, the idea of balancing the battery current is evident. If a starting point (SOC<sub>0</sub>) is given, the value of the current integral (Eq. (1)) is a direct indicator for the SOC.

$$\text{SOC} = \text{SOC}_0 + \frac{1}{C_N} \int_{t_0}^t (I_{\text{batt}} - I_{\text{loss}}) d\tau \quad (1)$$

where  $C_N$  is the rated capacity,  $I_{\text{batt}}$  the battery current, and  $I_{\text{loss}}$  is the current consumed by the loss reactions.

Two main complications arise with this method: firstly, incorrect current measurement could add up to a large error and accurate current measurement is expensive. Secondly, not all current supplied to the battery is consumed by charging and the corresponding losses have to be taken into account. The first point can be overcome by investing money in measuring equipment, while for the second one, many different approaches have been developed. As an example, two loss calculations will be presented below. The errors can be kept low if points for re-calibration are reached, e.g. the SOC is set to one if a full charge is detected or open circuit voltage measurement (see below) is used to correct the SOC value.

The most simple loss estimation method is to apply a constant charge factor to the battery at each recharge, i.e. a constant loss is assumed and this loss is additionally returned to the battery. Such a method is only suitable for systems that are not too sensitive to overcharge. In Ni/MH batteries, for example, a value of 1.3 is often used to assure full charge of the battery. Ni/MH batteries are not as sensitive to overcharge as are lead-acid or especially Li-based batteries. With lead-acid batteries, a charge factor of 1.05–1.2 is used, depending on the battery type. Additionally, this method implies that the charging operation is controlled.

A current-loss calculation approach for photovoltaic (PV) applications was developed by Jossen [2]. The Butler–Volmer equation is used to calculate the major losses during charging, i.e. the gassing current. Since in PV applications the currents are small, the Butler–Volmer equation could be modified and normalised to become finally that shown in Eq. (2)

$$I_{\text{loss}} = I_0 \exp\left(\frac{U_{\text{batt}} - U_N}{K_1} - K_2 \frac{T - T_N}{T T_N}\right),$$

$$I_0 = I_0 \exp\left(\frac{U_N}{K_1} - \frac{K_2}{T_N}\right) \quad (2)$$

where  $I_{\text{loss}}$  is the current consumed by the loss reactions;  $K_0$ ,  $K_1$ ,  $K_2$  are the constants;  $U_{\text{batt}}$  and  $U_N$  are the battery and rated battery voltage;  $T$  and  $T_N$  are the battery temperature and temperature under standard conditions.

As mentioned above, the errors for this method can be kept low if points for re-calibration can be identified. Since in PV applications the time for recharge is limited by the length of daylight, full charge is seldom achieved. Concerning this problem, in the same publication [2] a so-called remaining charge current technique for re-calibration is presented which allows re-calibrations if the SOC is above 90%. For more details see [3].

The same loss calculation was used in a SOC algorithm published on [4]. This algorithm was developed only for PV applications, i.e. currents in the range of  $I_{10}$ , and measurement intervals of about 1 min or more. It is not designed for online use because ‘future’ data is necessary to calculate the SOC. The reference data for the linear model [5] and the Kalman filter [6] approach (both described below) was generated with this programme.

Another procedure based on Ah counting is reported in [7]. This publication focuses on discharges during the operation of electric vehicles. Three empirical gauge functions are established concerning the problems of temperature influence, maximum deviation from the nominal capacity and SOC dependence on discharge rate.

Ah counting is the most common method applied to most systems and applications. Indeed, the method is easy and reliable as long as the current measurement is accurate and enough re-calibration points are available. For example, for EV application, the method can take benefit of the regular full recharges under controlled conditions. In that field of application, the technique finds a limit in the case of high temperature effects and/or high current variations but it can be applied to all the battery systems used for the EV application. (i.e. lead-acid, Ni/Cd, Ni/MH, Zebra and lithium systems).

In the same way, because of its simplicity, Ah counting is used in most consumer applications.

### 2.3. Measurement of the electrolytes physical properties

In a lead-acid battery, the electrolyte takes part in the reactions during charge and discharge. The linear



relationship between the change of acid density and the SOC can be used to determine the latter. This method is feasible only with vented lead-acid batteries, while methods for density measurement within VRLA batteries are not yet available. Possible applications are, therefore, in stationary batteries with liquid electrolyte. The density is measured directly or indirectly by ion-concentration, conductivity, refractive index, viscosity, ultrasonics, etc. A detailed description of the different methods is given, for example, in [8].

Problems related to this technique are the occurrence of acid stratification, water loss and the long term stability of the sensors. The first two can be avoided by electrolyte circulation and automatic water refill systems. Additionally, the measurement of the physical properties of the acid cannot be done in the pores of the electrodes where the acid is actually either consumed or produced. This means that during high current processes, slow electrolyte diffusion is a source of errors for this technique.

#### 2.4. Open circuit voltage

Similar to the acid density measurements described in Section 2.3, the open circuit voltage relates in a linear manner to the SOC. Fig. 1 shows this linear dependence as obtained from four 12 V, 52 Ah (C/5) VRLA batteries of the Optima type when tested at the University of Ulm.

In applications where relatively long rest periods are common, this method is promising. Since the rest periods will only occur from time to time, the open circuit voltage measurement is usually combined with other techniques [9] to ensure a continuous indication of SOC. In such a combination, the open circuit voltage measurement can be utilised to adjust the other technique(s). The difference in the open

circuit voltage for a fully charged and a flooded lead-acid cell is about 100 mV. Especially in VRLA batteries long times (several hours) are needed to reach a steady state and this can cause problems. A second point to mention is the question of what is meant by *rest period*. Often a minimal current flow is required for monitoring devices: clocks, etc. In such a case, the open circuit voltage is never reached. Finally, like with all methods which use directly or indirectly the monitoring of acid concentration, acid stratification can generate inaccurate results.

#### 2.5. Heuristic interpretation of measurement curves

The following gives a brief, non-comprehensive, selection of techniques that use the electrical discharge/charge characteristics to calculate the SOC. Some methods were developed to get data on the SOC by interpreting only parts of the discharge curves. The chosen parts are understood to be significant for the battery SOC.

##### 2.5.1. Coup de fouet

In [10] the so-called *coup de fouet* region is used to calculate not exactly the SOC but the capacity that can be delivered after a full recharge for a discharge at a given current and temperature. The *coup de fouet* is the short voltage drop at the beginning of discharge following a full charge of a lead-acid battery. Two parameters are established, which are shown to have a linear relationship to the deliverable capacity: firstly the trough voltage, i.e. the minimum voltage during the occurrence of *coup de fouet* and secondly the plateau voltage, i.e. the maximum voltage reached during voltage recovery at the end of the *coup de fouet*. For one cell type it has been shown that the linear

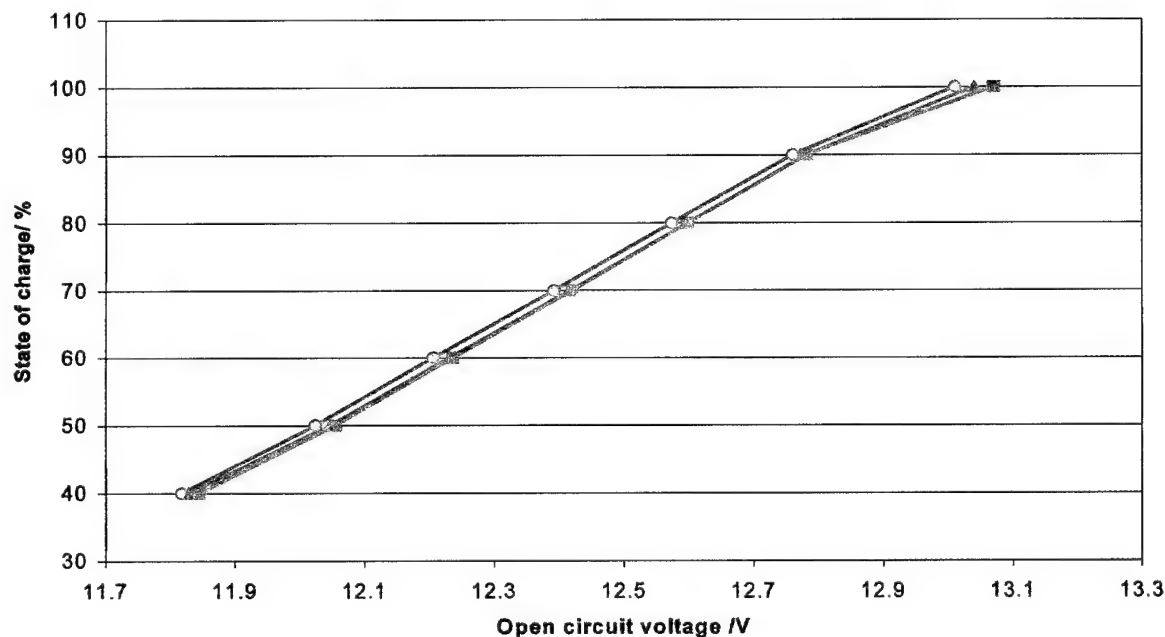


Fig. 1. Dependence of the state-of-charge on the open circuit voltage from four VRLA batteries of the same type.

equation determined by regression stays within an error limit of 12.5% for high discharge-current variations and temperature changes. Since the *coup de fouet* region occurs only after a full charge, this method can be used if a full charge is frequently reached during operations. For static discharge-currents this method is advantageous, because it gives an estimation of the actual available capacity, which depends on the discharge-current and temperature. The authors suggest this technique for batteries in telecommunication installations.

### 2.5.2. Linear model

In [5] a linear relationship (Eq. (3)) was established between the variation of SOC, the intermediate electrical measurements on the battery and the previous SOC value.

$$\begin{aligned}\Delta Q(i) &= \beta_0 + \beta_1 U(i) + \beta_2 I(i) + \beta_3 Q(i-1), \\ Q(i) &= Q(i-1) + \Delta Q(i)\end{aligned}\quad (3)$$

where  $Q(i)$  is the state-of-charge,  $\Delta Q(i)$  the SOC-difference,  $U$  the voltage and  $I$  is the current measurements.

The factors  $\beta_0, \dots, \beta_3$  are determined from reference data by least-mean-square calculations. The model was developed for PV applications, i.e. for low currents and slow SOC changes, and is characterised by high robustness in relation to measurement errors and wrong initial conditions, as shown in Fig. 2.

It is important to note that the  $\beta$ -factors do not describe physical parameters.

The linear model can be applied to various battery types and to batteries at different stages in their lives. However, best results are achieved if reference data from the same battery type is used to calculate the  $\beta$ -factors.

### 2.5.3. Artificial neural network

The utilisation of artificial neural networks for SOC determination is presented in [5,11,12]. Since artificial neural networks establish a relationship between input/output data of any kind, this method can be utilised for all battery systems and for all applications, providing that training data for the net is available. In [5], an artificial neural network is presented which is trained before use, whereas in [11,12] adaptable artificial neural networks are used. If an adaptable artificial neural network is applied, other methods for SOC determination are used to provide training data at selected states of operation. Errors depend strongly on the training data and the training method. Since the training methods usually minimise functions that lead to an evenly distributed error, the error is usually no function of the SOC. However, in Fig. 3 (taken from [5]) error extremes occur at high SOC, because the net was trained with data obtained from a battery with slightly larger capacity and better electrolyte circulation. But the SOC curves of a battery of the same type as the one corresponding to the training data show smaller and evenly distributed errors.

### 2.6. Impedance spectroscopy

Much research work has been carried out on impedance spectroscopy. This method is a common measurement technique to investigate electrochemical processes and has been studied for all battery systems not only for SOC but also for SOH determination. A review of impedance measurements for determination of the SOC for lead-acid and nickel/cadmium batteries is given in [13]. Fig. 4 shows a Nyquist diagram of the complex impedance of a lead-acid battery (OPzS 150) during discharge.

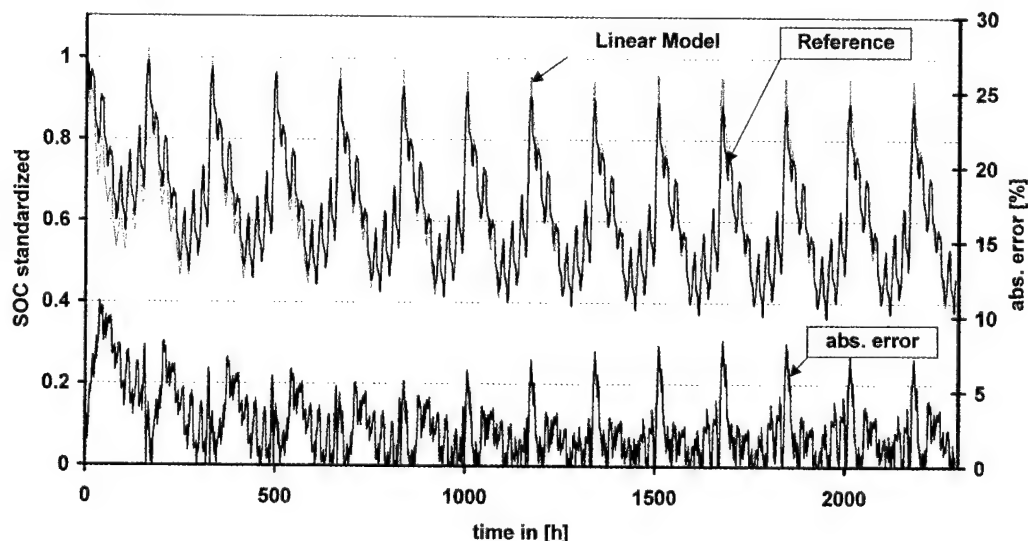


Fig. 2. SOC curves of the linear model, showing the reference and the error between the two curves.

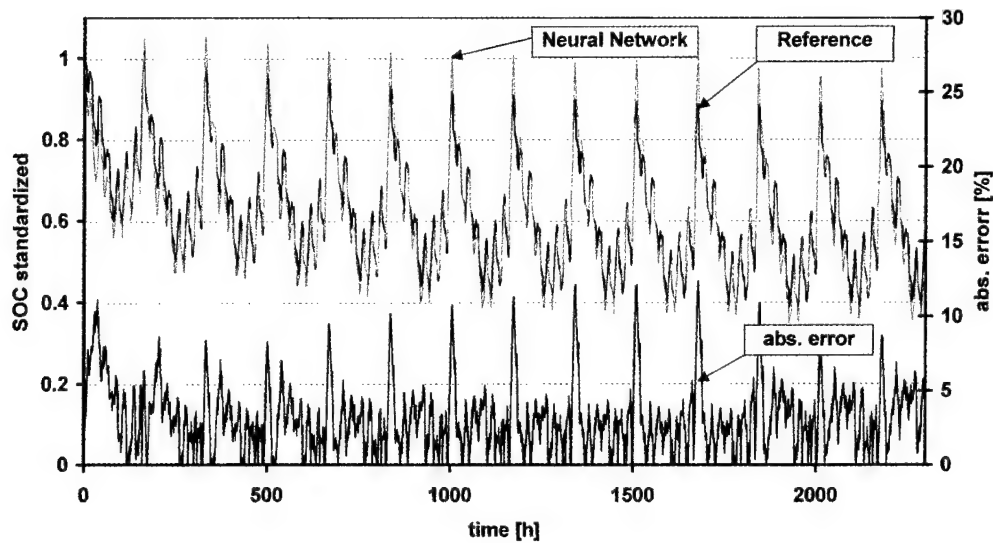


Fig. 3. SOC curves of back-propagation artificial neural network, showing the reference and the error between the two curves.

A combination of impedance spectroscopy with fuzzy logic methodology is presented in [14]. Two battery systems were investigated, a lithium/sulphur dioxide and a nickel/metal hydride system. A fuzzy model was used to establish a relationship between battery model parameters derived from impedance spectroscopy measurements and the SOC. For the lithium/sulphur dioxide cells the imaginary component of the impedance at three different frequencies was used as input for the SOC calculation and an accuracy of  $\pm 5\%$  was achieved, for the nickel/metal hydride cells the C2 capacitance (also derived from impedance measurement) and the

cycle number was the input and for the available reference points of 0, 25 and 100% an error below 10% was achieved.

Impedance curves are strongly influenced by temperature effects. Therefore, the best utilisation of this method is with batteries in temperature controlled environment, e.g. large stationary battery installations.

Surprisingly, in spite of the quantity of papers written on the subject, impedance spectroscopy is seldom implemented for practical SOC determination and it stays still a subject of debate. In a review [13], Huet concluded that the temperature influence is so high that practical application

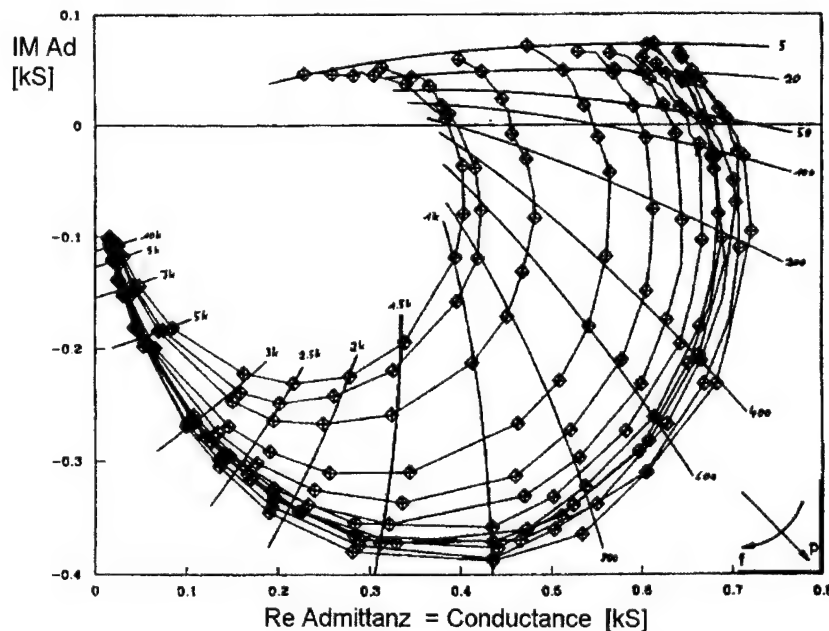


Fig. 4. Impedance measurements from a lead-acid battery (OPzS 150) during discharge (from [8]).

of impedance spectroscopy can only be made in ranges of high frequencies. This technique seems to be more suitable for lead-acid systems than for nickel/cadmium and is more promising for the determination of SOH rather than for the precise measurement of SOC.

Another review on this subject is given in [17]. Besides conventional systems (i.e. lead-acid, nickel/cadmium, nickel/metal hydride), initial measurements on lithium-ion batteries are presented. For this system, impedance spectroscopy seems to be a possible method for SOC determination.

In fact, conductance measurements at a given frequency are performed on batteries for quality control and provide information about state-of-health. They can also be used for SOC evaluation provided they are taken within a convenient frequencies range (e.g. in Fig. 4, the SOC varies only at low frequencies).

### 2.7. Internal resistance

Related to the impedance spectroscopy is the calculation of the internal resistance of the battery, i.e. the voltage drop

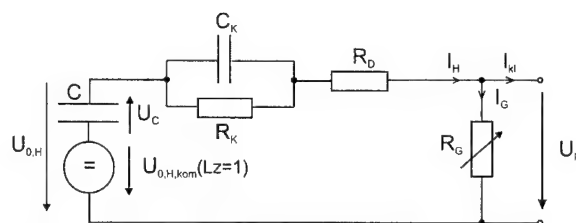


Fig. 5. Battery model for SOC determination in PV applications.

divided by the current change during the same (short) time interval. The value of the resistance depends heavily upon the chosen time interval. For a time interval smaller than 10 ms, only Ohmic effects are measured. If the interval is extended, other effects such as transfer reactions or acid diffusion are involved and the resistance becomes complex. In this case it would be better to use the previously described impedance spectroscopy instead of the voltage current ratio.

For lead-acid batteries the change in the internal (Ohmic) resistance between full SOC and SOC = 0 is only some mΩ per cell. This kind of measurement is more useful for

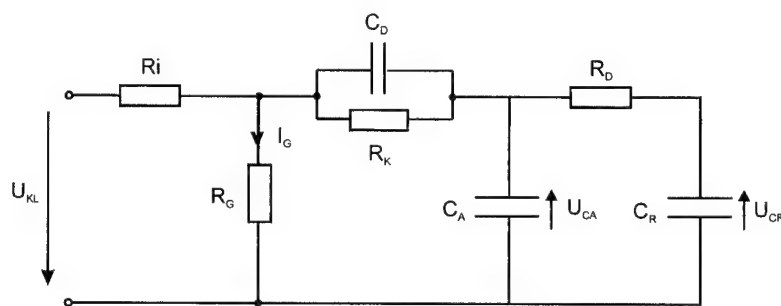


Fig. 6. Battery model for dynamic applications such as HEV and EV.

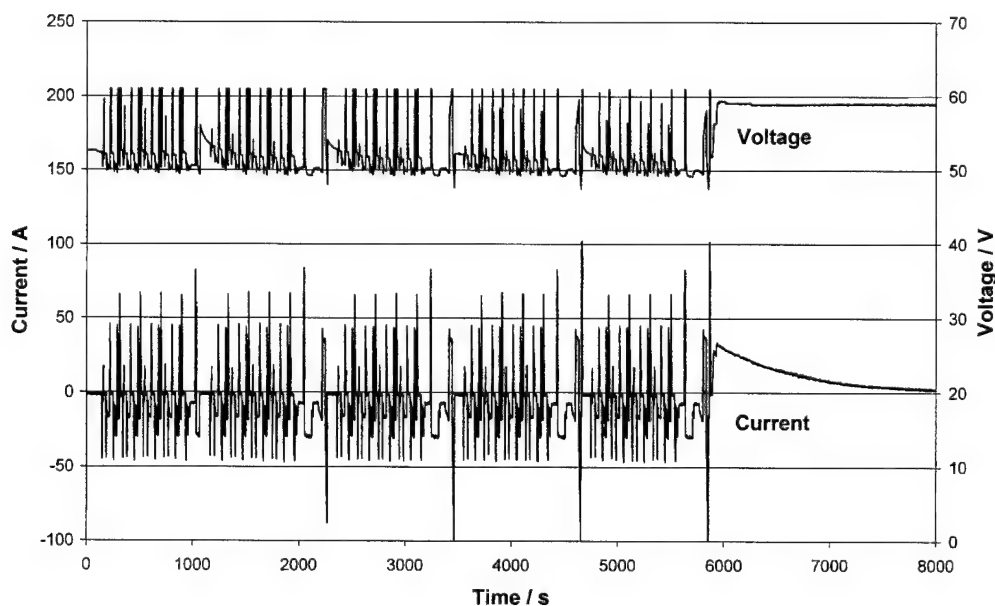


Fig. 7. Current and voltage curves measured on four 12 V lead-acid battery blocks used for Kalman filter SOC determination (simulated hybrid vehicle cycle).

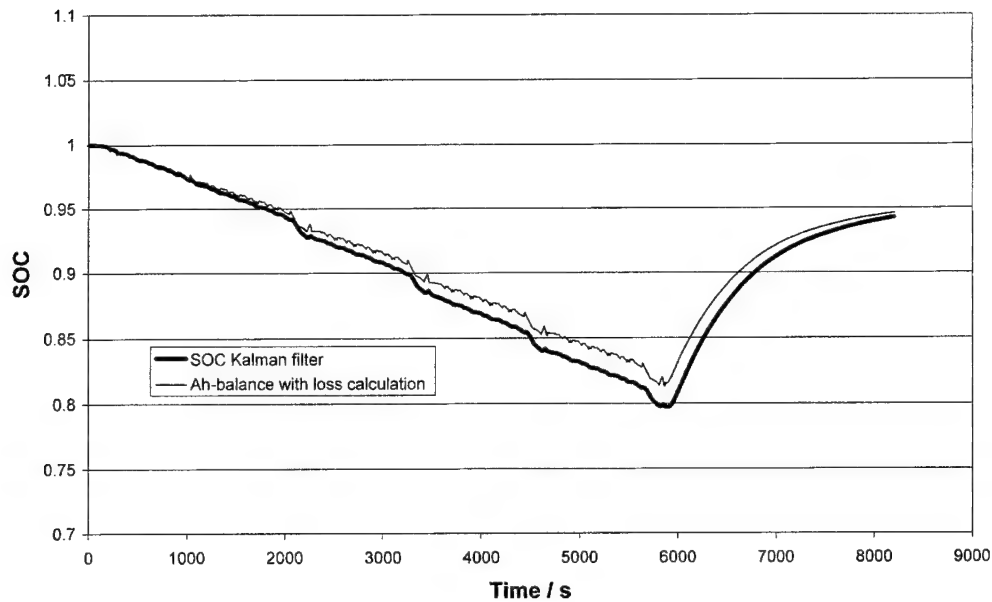


Fig. 8. SOC curve calculated by the Kalman filter technique compared with Ah balance with loss calculation.

providing statements on the state-of-health of the batteries. It can also provide some information about the SOC provided the battery is not fully charged [18].

## 2.8. Kalman filters

A Kalman filter is an algorithm to estimate the inner states of any dynamic system. In our case, the battery is the

dynamic system and one of the inner states is the SOC. The estimation is based on a model of the dynamic system. At the ZSW, Kalman filters with two models are specially investigated. The first is a model based on [15], which is seen as appropriate for PV applications and the second one is a more dynamical model, being a simplification of the battery model in [16]. The models are shown in Figs. 5 and 6.

Technique	Field of application	Advantages	Drawbacks
Discharge test	All battery systems Used for capacity determination in the beginning of life	Easy and accurate, independent of SOH.	Offline, time intensive, modifies the battery state, loss of energy
Ah balance	All battery systems, most applications (consumer, PV, EV).	Online, easy, accurate if enough re-calibration points are available and with good current measurement.	Needs a model for the losses. Sensitive to parasite reactions. Cost intensive for accurate current measurement Needs regular re-calibration points
Physical properties of electrolyte (density, concentration, colour)	Lead, possibly Zn/Br and Va	Online Gives information about SOH	Error if acid stratification. Low dynamic. Problem of stability of sensors in electrolyte. Sensitive to temperature and impurities.
Open circuit voltage	Lead, Lithium, Zn/Br and Va	Online, cheap	Low dynamic, error if acid stratification and needs long rest time (current = 0) for lead system. Problem of parasite reaction (e.g. Sb poisoning by lead)
Linear model	Lead PV, possibility for other battery systems ? (not tried yet)	Online, easy	Needs reference data for fitting parameters
Artificial neural network	All battery systems	Online	Needs training data of a similar battery
Impedance spectroscopy	All systems	Gives information about SOH and quality. Possibility of online measurement.	Temperature sensitive, cost intensive.
D.C. Internal resistance	Lead, Ni/Cd	Gives information about SOH, cheap. Possibility of online measurement. Easy	Good accuracy, but only for low SOC
Kalman filter	All battery systems, PV, dynamic applications (e.g. HEV)	Online. Dynamic	Needs large computing capacity. Needs a suitable battery model. Problem of determining initial parameters

Fig. 9. Summary of the different techniques for determination of state-of-charge, presented with their field of application, advantages and drawbacks.

The results for the SOC determination from the Kalman filter using the first model (Fig. 5) were presented in [5]. It was shown that the errors could be kept below 10% for data of a 12 V, 125 Ah flooded lead-acid battery, which was cycled on a typical PV regime over a period of 2.5 years.

To apply the Kalman filter technique for data of a higher dynamic, e.g. for a hybrid electric vehicle (HEV), the second battery model (Fig. 6) has to be used. Since field data of HEVs are not available, the results presented are obtained using measurements performed on four 12 V, 52 Ah (Optima Yellow Top) batteries by means of synthetic hybrid cycles, generated with the simulation tool FAHR-SIM [19]. Fig. 7 shows the current and voltage evolution over time. The results of the SOC calculation with this data and the dynamic model is shown in Fig. 8. Because no other reference exists, the Kalman SOC is compared to the Ah balance with the above described loss calculation based on [2]. In total, only about 10 Ah were taken from the batteries. Both SOC curves are very similar, the maximum difference is 2% at the lowest SOC. Other cycles showed comparable results.

These are first results with dynamic data and SOC determination using the Kalman filter technique. At ZSW further work will be carried out to confirm the suitability of this method for high dynamic applications.

### 3. Conclusion

The paper has given a short overview of the existing techniques for the evaluation of battery SOC. Emphasis was given to the lead-acid system even though many techniques are also suitable for other systems. Fig. 9 summarises this overview.

The most used technique at this time for all systems is Ah counting because it is the most direct and transparent method and quite easily implemented. It also gives satisfyingly accurate results for short-time applications, especially if used in the range of low to medium SOC. The determination of SOC by the means of impedance spectroscopy, including ac and dc inductance measurements, is still a subject of debate because of its temperature sensitivity and the difficulty of its online implementation. New promising methods are:

- The linear model that is impressive for its simplicity and because it delivers satisfying results for photovoltaic applications.
- The Kalman filter that gives perspectives for high dynamic usage (HEV, EV).

- The artificial neural network that can be implemented for any battery and battery system provided enough training data can be supplied.

### References

- [1] D.U. Sauer, G. Bopp, A. Jossen, et al., State-of-charge — what do we really speak about? INTELEC, 1999.
- [2] A. Jossen, Betriebsführung photovoltaischer Anlagen mit Energiespeichern, Dissertation, Universität Stuttgart, 1994.
- [3] A. Jossen, H. Döring, J. Garche, Ladezustandsbestimmung von Bleibatterien an zwei ausgewählten Beispielen, 10, Symposium Photovoltaischer Solarenergie, Staffelstein, 1995.
- [4] ZSW (Hrsg.) & ISET & ISE, Referenzdaten zum Test von Verfahren zur Ladezustandsbestimmung von Bleibatterien, CD-ROM, 1999.
- [5] Ch. Ehret, S. Piller, W. Schroer, A. Jossen, State-of-charge determination for lead-acid batteries in PV-applications, in: Proceedings of the 16th European Photovoltaic Solar Energy Conference, Glasgow, 2000.
- [6] S. Piller, A. Jossen, Kalman-filter zur Ladezustandsbestimmung von Bleibatterien in PV-Anlagen, 14, Symposium Photovoltaischer Solarenergie, Staffelstein, 1999.
- [7] J. Alzieu, H. Smite, D. Glaize, Improvement of intelligent battery controller: state-of-charge indicator and associated functions, J. Power Sources 67 (1997) 157–161.
- [8] H.-P. Hönes, Elektrochemische Energiespeicher in photovoltaischen Anlagen, Dissertation, Universität Stuttgart, 1994.
- [9] M. Rothert, B. Willer, C. Schmitz, et al., Verschiedene Ansätze zur Ladezustandsbestimmung, Forschungsverbund Sonnenenergie Workshop Elektrochemische Speichersysteme für regenerative Energieversorgungsanlagen, May 1999.
- [10] Ph.E. Pascoe, A.H. Anbuky, Estimation of VRLA Battery Capacity Using the Analysis of Coup de Fouet Region, INTELEC, 1999.
- [11] D. Kray, D.U. Sauer, Neuro-Methoden zur Prognose und Fehlererkennung durch Analyse vor Daten aus Monitoring-Systemen, Internationales Sonnenforum, Köln, 1998.
- [12] M. Stoll, Ein Schätzverfahren über den inneren Zustand geschlossener Bleiakumulatoren, VDI Fortschritt-Berichte, Reihe 21, Nr. 167, 1994.
- [13] F. Huet, A review of impedance measurements for determination of the state-of-charge or state of health of secondary batteries, J. Power Sources 70 (1998) 5949.
- [14] A.J. Salkind, C. Fennie, P. Singh, et al., Determination of state-of-charge and state-of-health of batteries by fuzzy logic methodology, J. Power Sources 80 (1999) 293–300.
- [15] W. Burkner, Verfahren zur Ladezustandsbestimmung von Bleibatterien in Photovoltaikanlagen, IfE Schriftenreihe, Heft 27, Lehrstuhl für Energiewirtschaft und Kraftwerkstechnik, Technische Universität München, 1994.
- [16] R. Gretsche, Ein Beitrag zur Gestaltung der elektrischer Anlage in Kraftfahrzeugen Habilitationsschrift, Friedrich-Alexander-Universität Erlangen, Nürnberg, 1978.
- [17] S. Rodrigues, N. Munichandraiah, A.K. Shukla, A review of state of charge indication of batteries by means of ac impedance measurement, J. Power Sources 87 (2000) 12–20.
- [18] A. Jossen, H. Döring, J. Garche, Ladezustandsanzeiger für elektrochemische Akkumulatoren, UECT, 1995.
- [19] H. Kabza, C. Koerner, P. Seger, A. Wagener, FAHR-SIM: A Versatile Simulator for Drivetrain Modeling and Analysis, EVS 17, Montreal, 2000.

## Aging in chemically prepared divalent silver oxide electrodes for silver/zinc reserve batteries

David F. Smith<sup>a,\*</sup>, Curtis Brown<sup>b</sup>

<sup>a</sup>EMF Systems, Inc., 14670 Highway 9, Boulder Creek, CA 950065, USA

<sup>b</sup>Eagle Picher Technologies, LLC, P.O. Box 47, Joplin, MO 64802, USA

Received 4 December 2000; accepted 7 December 2000

### Abstract

The instability of silver(II) oxide electrodes used in silver/zinc reserve batteries is the well known cause of capacity loss and delayed activation in reserve batteries after they are stored in the dry, unactivated state for extended periods of time. Metal contaminants in sintered/electroformed electrodes destabilize the oxide and the solid state reaction between AgO and elemental silver results in the formation of the lower capacity monovalent oxide Ag<sub>2</sub>O. Chemically prepared (CP) AgO can be used to avoid the metal contaminants and to minimize the interfacial contact area between AgO and Ag, thus minimizing the affects of aging on the electrodes.

Electrodes were fabricated with CP AgO and polytetrafluoroethylene (PTFE) binder and expanded silver metal current collectors. Experimentally, both electrode active material compacts (AgO and binder only) and electrodes complete with AgO/binder and silver current collector were tested to evaluate the influence of the current collector on aging. The electrode samples were discharged at a constant rate of 50 mA cm<sup>-2</sup> before and after storage at 60°C for 21 days as well as after storage at room ambient temperature conditions for 91 months.

The results indicate that the affects of aging upon the AgO/binder compacts are insignificant for long term storage at room temperature. However, thermally accelerated aging at high temperature (60°C) affects both transient and stabilized load voltage as well as capacity. In terms of capacity, the AgO/binder mix itself loses about 5% capacity after 21 days dry storage at 60°C while electrodes complete with current collector lose about 8%. The 60% increase in capacity loss is attributed to the solid state reaction between AgO and elemental silver. © 2001 Elsevier Science B.V. All rights reserved.

**Keywords:** Silver oxides; Silver/zinc reserve batteries

### 1. Background

Silver/zinc reserve batteries are used in missiles and other military applications primarily because of their very high power density. The batteries can be stored in their dry, unactivated state for several years until they are called upon for operation. The batteries are activated by manually or automatically injecting the electrolyte (typically KOH solution) into the cells.

The battery voltage and capacity tend to decrease as the batteries age during the dry, unactivated storage period. A major cause for the decline in performance of silver/zinc reserve batteries is the instability of the silver electrode. To date, most silver/zinc batteries are produced with sintered silver electrodes which have been anodized in KOH solution to produce silver oxide. Typically, the electroformed electrodes contain a mixture of Ag, AgO, and Ag<sub>2</sub>O along with

Ag<sub>2</sub>CO<sub>3</sub> and residual H<sub>2</sub>O, KOH, K<sub>2</sub>CO<sub>3</sub> from the charging process. The higher oxide commonly referred to as AgO has been established to be Ag<sub>2</sub>O<sub>3</sub>·Ag<sub>2</sub>O [1].

Particular attention has been focused on the higher oxide AgO, which has nearly twice the capacity of the monovalent oxide (0.43 Ah g<sup>-1</sup> for AgO versus 0.23 Ah g<sup>-1</sup> for Ag<sub>2</sub>O). However, the AgO is thermodynamically unstable. Dallek et al. have reported a broad range for the activation energy of decomposition ( $E_a$ ) from 100 kJ mol<sup>-1</sup> to as high as 133 kJ mol<sup>-1</sup> [2]. The lowest  $E_a$  was from electroformed electrodes while chemically prepared AgO had the highest activation energy. Contaminant metals such as Cu can be introduced as part of the electroformation process and have been shown to significantly destabilize the AgO [3].

### 2. Chemically prepared silver oxide electrodes

In previous work, silver oxide (both AgO and Ag<sub>2</sub>O) electrodes were studied which were based upon the use of

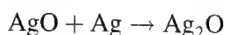
\* Corresponding author.

E-mail address: emfsys@pacbell.net (D.F. Smith).



chemically prepared oxides [4]. The AgO was prepared by persulfate oxidation of AgNO<sub>3</sub> and the Ag<sub>2</sub>O was prepared by precipitation of AgNO<sub>3</sub> solution with alkali. The stability of such electrodes is believed to be greater than electroformed electrodes for several reasons.

Electroformed electrodes include a dispersed phase of elemental silver particles because of incomplete conversion. The relatively high surface area of the interface between AgO and the Ag particles leads to the loss of AgO by the solid state reaction:



The destabilizing metal contaminants are completely absent in the chemical oxide electrodes, which contain only trace amounts of Ni, and Cu. Also absent are the residual water and carbonates which can also affect the stability of the AgO.

The most stable electrode is obviously made with the stable oxide Ag<sub>2</sub>O, which has a decomposition temperature of nearly 700 K. However, the higher capacity of AgO may be required in a limited number of applications.

The subject of this paper is the electrical characterization of electrodes produced with chemically prepared AgO as a function of age.

### 3. Experimental method

Chemically prepared AgO was obtained from Ames Goldsmith Company, Glens Falls, NY, USA. The oxide was produced by persulfate oxidation of AgNO<sub>3</sub> solution.

The AgO was blended with PTFE binder. No additives to increase the conductivity of the electrode active mass were used. Samples of the compacted AgO binder were stored for 91 months at room ambient temperature. Subsequent tests were performed to characterize the affects of the long term storage under benign conditions and after storage at elevated temperature.

### 4. Capacity after storage at 100°C

A baseline group of electrodes was prepared “fresh” before the AgO/binder compacts were stored for the 91 months period. The nominal thickness was 0.35 mm and the loading of AgO/binder mix was 120–140 mg cm<sup>-2</sup>. The test samples were then discharged in an excess of 6.3 M KOH solution at room ambient temperature against a nickel foam counterelectrode. The electrodes were discharged after various periods of dry oven storage at 100 ± 1°C. The voltage was measured against an amalgamated zinc reference electrode and the capacity was determined to a cutoff voltage of 1.00 V at the discharge current density of 80 mA cm<sup>-2</sup>. Corrected for the amount of binder and the assay amount as AgO and Ag<sub>2</sub>O, the utilization without storage at high temperature was 94.90% of the theoretical value.

Table 1

Utilization of oxides before and after storage at 100°C

Storage time at 100°C (h)	Utilization (to 1.00 V versus Zn(Hg) reference) (%)
Fresh, no storage	94.90
42.5	70.45
95.0	53.34
168.0	43.11
250.0	44.71

The remaining electrodes were removed from the storage oven after various periods of time, then discharged as described above.

The results are presented in Table 1 and in Fig. 1.

### 5. Real time aging of the AgO/binder mix before electrode fabrication

Compacted portions of the blend of AgO and PTFE were stored at uncontrolled room ambient temperature condition for 91 months. The compacts were then pressed onto silver expanded metal current collecting grids. The thickness and loading of the resulting electrodes was nominally 0.15 mm (50 mg cm<sup>-2</sup>) and 0.30 mm (125 mg cm<sup>-2</sup>).

The discharge tests characterize the affects of the long term (years) room temperature aging and the PTFE binder on the stability of the AgO. The electrodes were discharged in excess 6.3 M KOH at 20–21°C, at a current density of 50 mA cm<sup>-2</sup>. A machined acrylic test fixture was used which positioned a foam nickel counterelectrode, a separator (Celgard 3401), the working electrode, and an amalgamated zinc reference in a reproducible manner. Accordingly, the electrode was discharged from one face only, with the reaction zone being up to 0.30 mm in depth. The reference electrode was located 3 mm behind the centrepoint of the working electrode.

An EG&G Model 362 Scanning Potentiostat was used to discharge the test cells. The voltage of the working electrode (versus reference) was recorded with a 16 bits PC-based data acquisition system.

The capacity of the AgO electrode was calculated from the time to reach a cutoff voltage of 1.000 V versus reference. The utilization in terms of percentage of the theoretical value was corrected for the amount of inert binder, and the percent AgO and Ag<sub>2</sub>O in the original sample. The correction for the amount of binder assumed perfect dispersion of the PTFE. The data is presented in Table 2

The results are in rough agreement with the calculated decomposition rate predicted by Dallek [5] who calculated a minimal 0.4% conversion of CP AgO to Ag<sub>2</sub>O in a 101 months storage period at 25°C.

Given the experimental error in our tests, no measurable decrease in capacity was observed after the actual long term aging for the AgO-PTFE mix itself, indicating that the PTFE and the process itself had no significant destabilizing affect upon the AgO.



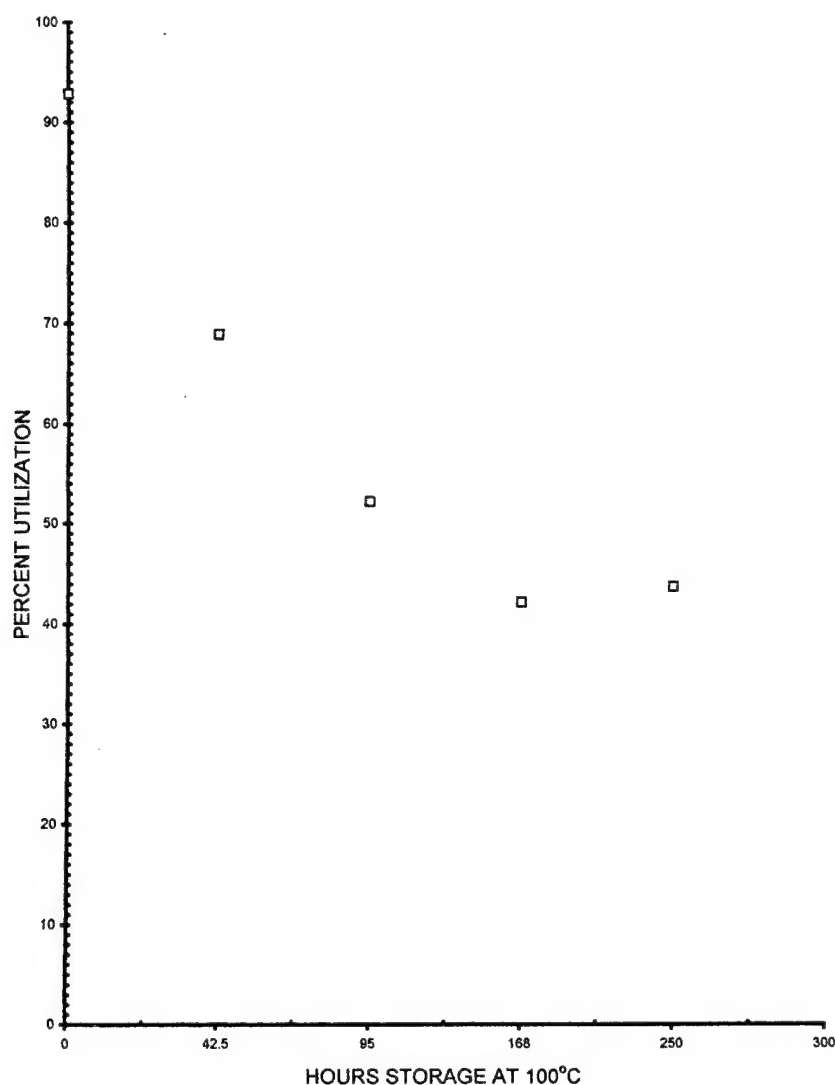


Fig. 1. Utilization of oxides before and after storage at 100°C.

## 6. Accelerated aging of the AgO/binder mix before electrode fabrication

One of the many thermally accelerated aging test methods is to subject batteries to oven storage at 60°C (333 K) for 21 days. Using the predictive model of Dallek [5], only 0.64%

Table 2  
Utilization of the AgO/binder mix to 1 V versus zinc reference electrode after storage for 91 months at room temperature

Test electrode number	Thickness (mm)	Utilization (%)	Average voltage (V) (versus Zn(Hg) reference)
1	0.15	97.77	1.54
2	0.30	100.99	1.55
3	0.30	101.84	1.56
4	0.30	100.28	1.55
5	0.30	100.19	1.57
6	0.30	100.11	1.56

of the CP AgO is predicted to decompose after the 21 days dry storage at 60°C (0.34% capacity loss).

The electrodes were prepared in an identical manner as described in clause 3. In this case, however, the AgO/binder compacts (no current collector) were heated at  $60 \pm 1^\circ\text{C}$  for 21 days in a mechanically convected oven. After heat treatment, the AgO/binder mix was then applied to silver expanded metal current collectors. The electrodes were then discharged in half cells under the same conditions as previously described, at a current density of  $50 \text{ mA cm}^{-2}$ .

The results are presented in Table 3

On average, the 60°C storage for 21 days resulted in a loss in capacity of about 5.6% rather than the predicted 0.34% loss. In addition to the loss in capacity, a degradation in voltage was noted. The initial open circuit potential (OCP), the initial load voltage at  $50 \text{ mA cm}^{-2}$ , and the stabilization voltage at 1 s is summarized in Table 4, comparing room temperature aging (91 months) and high temperature aging (60°C for 21 days).

Table 3

Utilization of the AgO/binder mix to 1 V versus zinc reference electrode after storage for 21 days at 60°C

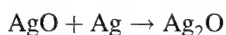
Test electrode number	Thickness (mm)	Utilization (%)	Average voltage (V) (versus Zn(Hg) reference)
7	0.30	95.78	1.50
8	0.30	92.97	1.55
9	0.30	94.34	1.52
10	0.30	94.83	1.50
11	0.29	94.02	1.47

As indicated in Table 4, the open circuit potential for room temperature aged AgO/binder electrodes was not reproducible and was somewhat less than expected. The deviation from the AgO/Ag<sub>2</sub>O potential is assumed to be the result of the 91 months room temperature storage of the AgO/binder. However, after storage at 60°C for 21 days, the OCP approached that of the Ag<sub>2</sub>O/Ag vs Zn.

It is assumed that the decomposition of AgO to Ag<sub>2</sub>O and/or the formation of Ag<sub>2</sub>CO<sub>3</sub> are surface phenomena, and when the mix compact was applied to the silver current collector (after thermal treatment) the Ag<sub>2</sub>O and/or Ag<sub>2</sub>CO<sub>3</sub> interface with the Ag is the cause of the depressed voltage.

## 7. Thermally accelerated aging with a silver grid in contact with the mix

Tests were performed to determine the affect of the solid state reaction between AgO active material and the silver metal current collector:



Electrodes were fabricated by applying the AgO/binder compact to silver current collectors, using the identical process described above. In this case, however, the complete electrodes with Ag current collector in place were heated at

Table 5

Utilization of electrodes to 1 V versus zinc reference electrode after storage for 21 days at 60°C

Test electrode	Thickness (mm)	Utilization (%)	Average voltage (V) (versus Zn(Hg) reference)
A	0.30	96.37	1.49
B	0.30	88.53	1.47
C	0.30	89.85	1.51
D	0.30	93.45	1.53
E	0.30	94.32	1.52
F	0.30	93.84	1.52
G	0.30	90.84	1.53

60°C for 21 days in a mechanically convected oven. The electrodes were then discharged in flooded half cells at the same current density (50 mA cm<sup>-2</sup>).

The capacity and average load voltage of the test electrodes is summarized in Table 5.

Fig. 2 shows the typical performance at 20°C, 50 mA cm<sup>-2</sup> current density, for a CPAgO electrode. Electrode A is shown.

The apparent affect of the current collector during storage at 60°C for 21 days is a greater reduction in capacity (on average about 7.5 versus 5.6% for the previous tests of AgO/binder without the current collector). The capacity loss is a significant deviation from the predicted 0.64% decomposition for CP AgO alone. The apparent difference is caused by the solid state reaction of the Ag grid with the AgO.

The data, however, indicates an increased stability over the typical for sintered and electroformed silver electrodes. Bagshaw and Brown [6] observed a 23.9% capacity loss after 1 month storage at 60°C, while Bowers and Gubner [7] found a reduced capacity loss of about 10% after 1 month at 54°C. The variability of the sintered electrodes is presumably caused by the influence of the grid, the unconverted silver phase, and the destabilizing contaminants which are associated with the electroformed electrodes.

Table 4

Comparison of electrode performances following room and 60°C storage of the constituent mix

Test electrode/aging temperature	Open circuit voltage (versus Zn(Hg) reference) (V)	Voltage at 100 ms (versus Zn(Hg) reference) (V)	Voltage at 1 s (versus Zn(Hg) reference) (V)
1 (Room)	1.7370	1.5317	1.5824
2 (Room)	1.8497	1.4900	1.5655
3 (Room)	1.7620	1.4952	1.5928
4 (Room)	1.6728	1.5055	1.5502
5 (Room)	1.7130	1.5502	1.5876
6 (Room)	1.6895	1.5340	1.5583
Average ± 1 S.D.	1.737 ± 0.064	1.517 ± 0.024	1.573 ± 0.017
7 (60°C)	1.6604	1.4422	1.4742
8 (60°C)	1.6950	1.5249	1.5515
9 (60°C)	1.6759	1.3824	1.4146
10 (60°C)	1.6725	1.5019	1.4782
11 (60°C)	1.6786	1.1632	1.3384
Average ± 1 S.D.	1.676 ± 0.012	1.403 ± 0.145	1.451 ± 0.079

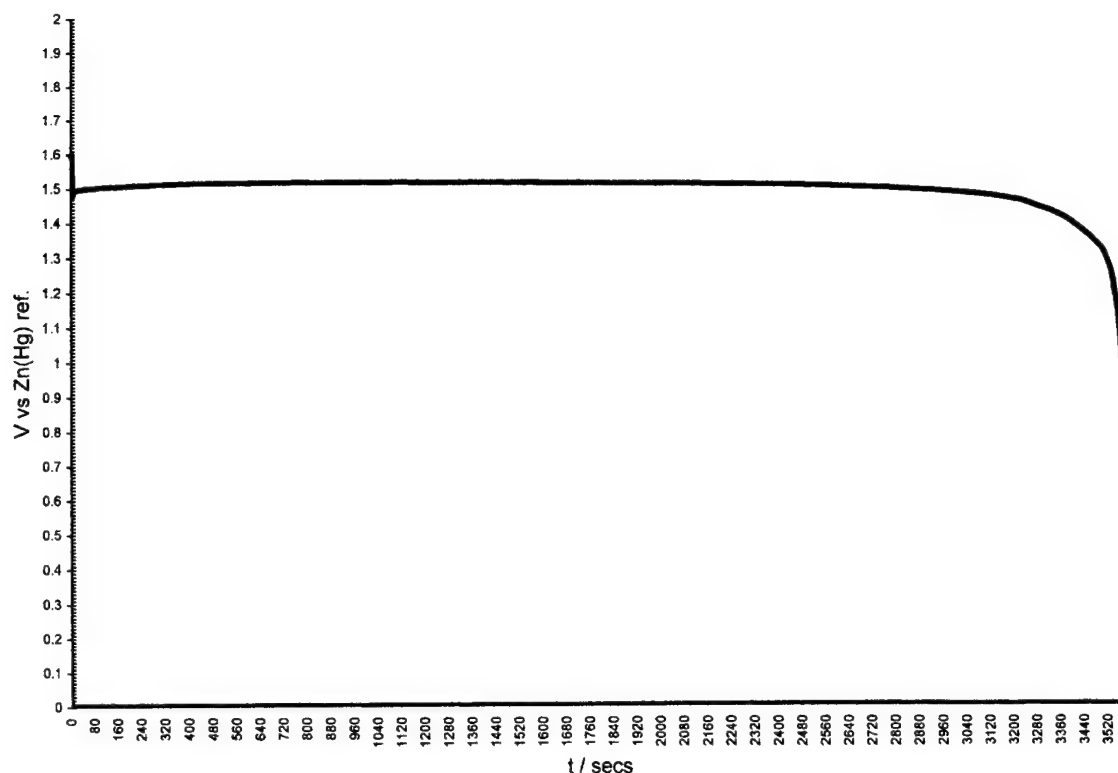


Fig. 2. Typical 20°C performance of chemically prepared AgO (electrode A) at 50 mA cm<sup>-2</sup>.

The initial OCP, the initial load voltage at 50 mA cm<sup>-2</sup> and the stabilization voltage for the thermally aged complete electrodes is summarized in Table 6.

As indicated in Tables 5 and 6, the open circuit potential has approached that of the Ag<sub>2</sub>O/Ag electrode. In this case, the Ag<sub>2</sub>O at the active material/grid interface is probably the Ag<sub>2</sub>O reaction product from the solid state reaction with the grid itself.

Of note is the data in Table 6, which shows much improved transient performance for the aged samples, which included the grid during the thermal treatment. It appears that the grid interface is much more uniform for this case.

Fig. 3 shows the onset of polarization of an electrode which has not been thermally aged and one which has been

subjected to dry storage at 60°C for 21 days. The tests chosen were those electrodes from the groups which exhibited the greatest voltage dip. There is scatter in the data, but the general trend of the limited number of tests is toward an increased magnitude of the voltage dip for the thermally treated samples. There is also an increased steady state polarization (by ~50 mV) resulting from the thermally accelerated aging.

## 8. Summary

The sintered and electroformed silver electrodes normally used are a mixed composition of Ag, Ag<sub>2</sub>O, AgO, and

Table 6  
Performance of thermally aged electrodes, following 21 days at 60°C

Test electrode	Open circuit voltage (versus Zn(Hg) reference) (V)	Voltage at 100 ms (versus Zn(Hg) reference) (V)	Voltage at 1 s (versus Zn(Hg) reference) (V)
A	1.5971	1.4773	1.4927
B	1.6244	1.4423	1.4586
C	1.6139	1.4773	1.4586
D	1.6182	1.5052	1.5162
E	1.6118	1.5575	1.5077
F	1.6233	1.5613	1.5120
G	1.6534	1.4882	1.5273
Average ± 1 S.D.	1.620 ± 0.017	1.501 ± 0.044	1.527 ± 0.022

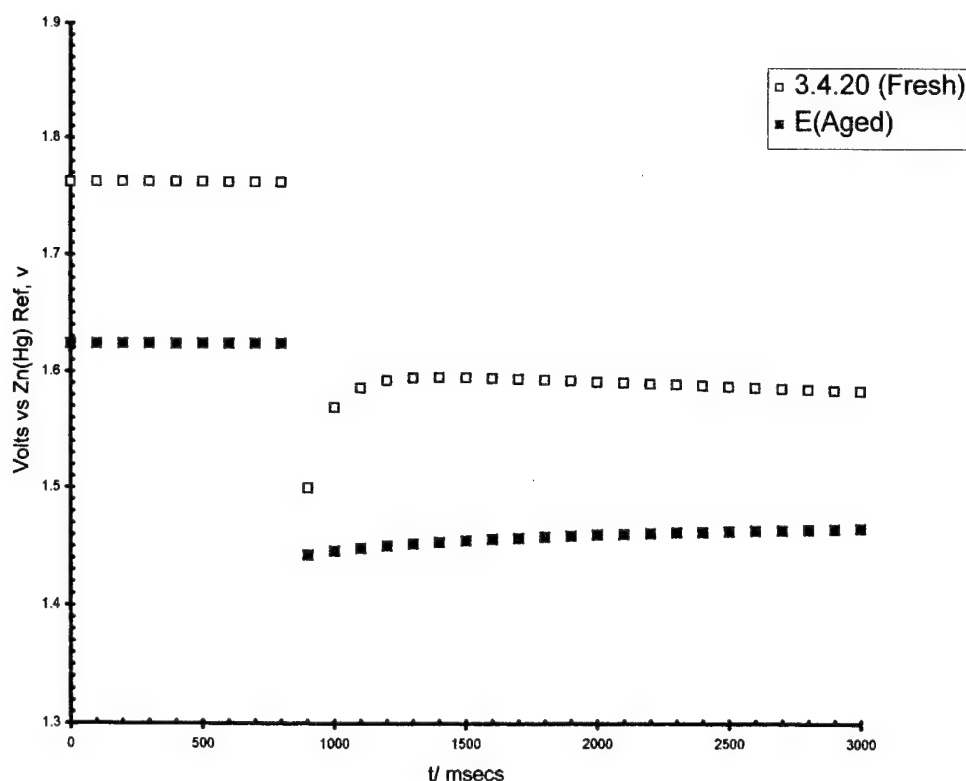


Fig. 3. Onset of polarization of an electrode which has not been thermally aged and one which has been subjected to dry storage at 60°C for 21 days.

$\text{Ag}_2\text{CO}_3$ . As a consequence of the random nature of the anodization process and the electrode morphology, the electrodes have a random chemical composition and morphology, which affects the performance of the electrodes, especially after aging.

Destabilizing contaminants such as Cu, residual water, and  $\text{K}_2\text{CO}_3$  are extremely difficult to exclude from the silver oxide plates which are processed by anodization in aqueous media. Particularly, troublesome are the metallic contaminants.

Many of the aforementioned problems can be avoided by the use of chemically prepared silver oxide and a non-reacting binder such as polytetrafluoroethylene. With such electrodes, a highly ordered structure free from a dispersed phase of elemental silver will be more stable than the sintered/electroformed variety, which can have a substantial amount of unreacted silver in random locations.

The decomposition of chemically prepared AgO itself follows an Arrhenius behavior which can be predicted with reasonable accuracy. The electrochemically converted electrode active material, however, is much more difficult to model, because of the random nature of the electrodes and the existence of destabilizing contaminants.

As shown in the tests which are the subject of this paper, the predicted conversion of AgO to  $\text{Ag}_2\text{O}$  as a consequence of aging is much less than the actual experience, presumably due at least partially to the reaction of between AgO and the grid.

Of prime importance is the fact that the efficiency of discharge for the chemically prepared AgO electrodes is extremely high, and there is only a small amount of inert binder. Accordingly, the electrodes have a much higher energy density at the plate level than normal sintered and electroformed electrodes. In previous work, the energy density of this type of AgO and sintered and electroformed electrodes was determined at high discharge rate. The tests were conducted in driven cells in flooded electrolyte in similar fashion to the tests described in this work [4]. The results are summarized in Table 7.

However, in some applications which require very precise voltage regulation and rapid activation, even chemically prepared AgO can cause problems. The data indicate a decline in the reproducibility of transient voltages with load changes after accelerated aging. The oxygen evolution as a consequence of AgO instability can also cause passive films to build on zinc electrodes which is known to impair the rapid activation of some batteries.

Table 7  
Comparison of the performances of chemically and sintered/electroformed AgO

Electrode type (AgO)	Average voltage (V)	Utilization (Ah g <sup>-1</sup> )	Wh g <sup>-1</sup>	Wh cm <sup>-3</sup>
Chemically prepared	1.526	0.428	0.446	2.585
Sintered/electroformed	1.594	0.233	0.259	1.825

## References

- [1] V. Scatturin, P.L. Bellon, A.J. Salkind, *J. Electrochem. Soc.* 108 (1961) 819.
- [2] S. Dallek, W.A. West, B.F. Larrick, Decomposition kinetics of AgO cathode material by thermogravimetry, *J. Electrochem. Soc.* 133 (1986) 2451.
- [3] A.J. Salkind, R.W. Freeman, J.J. Weckesser, W.A. West, S. Dallek, Self decomposition processes in silver electrodes, *J. Electrochem. Soc.* 135 (1988) 1882.
- [4] D. Smith, G. Graybill, R. Grubbs, J. Gucinski, New developments in very high rate silver oxide electrodes, *J. Power Sources* 65 (1997) 47.
- [5] W.A. West, R.W. Freeman, S. Dallek, A.J. Salkind, Instability in silver oxide electrode material (AgO), *Power Sources* 11 (1986) 349.
- [6] N.E. Bagshaw, A.C. Brown, Storage of dry-charged silver oxide–zinc reserve cells, *Power Sources* 5 (1974) 465.
- [7] F.M. Bowers, E. Gubner, The shelf life of unactivated dry-charged zinc–silver oxide cells, in: A. Fleischer, J.J. Lander (Eds.), *Zinc–Silver Oxide Batteries*, Wiley, New York, NY, 1971, p. 347.

## Advanced membranes for alkaline primary and rechargeable alkaline cells with zinc anodes

Harlan Lewis<sup>a,\*</sup>, Patricia Jackson<sup>a</sup>, Alvin Salkind<sup>b</sup>, Thomas Danko<sup>c</sup>, Roger Bell<sup>d</sup>

<sup>a</sup>NAVSEA Crane, 300 Highway 361, Code 609, B3287, Crane, IN 47522, USA

<sup>b</sup>College of Engineering, Rutgers University, Piscataway, NJ 08855, USA

<sup>c</sup>Viskase Corporation, 6855 W. 65th Street, Chicago, IL 60638, USA

<sup>d</sup>UCB Films plc, Wigton, Cumbria, Ca7 9BG, UK

Received 4 December 2000; accepted 14 December 2000

### Abstract

Several advanced cellulosic and radiation grafted polypropylene membrane materials are currently under evaluation in the laboratories at Navsea Crane and Rutgers University, for application to alkaline primary and rechargeable cell chemistries which employ zinc as the anode material. A portion of these tests involve model cell evaluations of cellulosic membranes for silver migration rates through the membranes as a function of separation layers and changes in the degree of polymerisation (DP), wet tensile strength (WTS) and voltage changes at both electrodes as a function of model rechargeable cell life cycle. Other testing on the actual membranes is generating data for both cellulosic and polypropylene materials on impedance, swelling properties, and silver and zinc penetration rates. The overall goal of these investigations is to obtain candidate separation membranes which will reduce zinc anode shape change and shedding and resist alkaline oxidative degradation to extend the active wet life in primary cells and both wet and life cycle in rechargeable cells. © 2001 Elsevier Science B.V. All rights reserved.

**Keywords:** Silver/zinc rechargeable cells; Separators/cellulosic; Separators/graft copolymer

### 1. Introduction

In previous papers [1–7] several of the authors developed concepts relating to the improvement of separations used in alkaline cells, particularly as they are applied to the rechargeable silver–zinc chemistry.

The standard separation for over 60 years has been cellulosic, because of its resistance to zinc dendrite growth, to alkaline and oxidative degradation, and because it is very inexpensive. However, its limitations which impact useful cell life are its gradual loss of tensile strength and degree of polymerisation (DP) under the alkaline oxidative effects of AgO and concentrated KOH, and the loss of volumetric energy density and large internal impedance which result from the required multiple layering.

This report presents the results of model cell studies with cellulosic membrane separations for changes in voltage at the plates, separation wet tensile strength (WTS) and DP, loss of discharge capacity, and rates of silver migration, all at

intervals in life cycle. In these studies, Viskase sausage casing and UCB cellophane films of an experimental nature were evaluated.

### 2. Experimental

The cell sets are identified as follows (five sets of seven rechargeable silver/zinc cells of nominal 26 Ah capacity were constructed at Eagle-Picher Industries on 21 September 1999):

Set 1 — Standard 1 mil (dry) Flexel film (Lot 139013 from 04/06/98, EPI no. 40330020): Cathode/1 × 3 mil Pellon/6 × 1 mil Flexel (U-wrap) Anode/1 × 3 mil Pellon.

Set 2 — New 1 mil (dry) UCB, Bridgwater, UK film (Lot 161602 from 02/24/99, EPI no. 40330020): Cathode/1 × 3 mil Pellon/6 × 1 mil UCB (U-wrap) Anode/1 × 3 mil Pellon.

Set 3 — PVA film with Viskase fibre-reinforced tubular sausage casing (FRSC), (1 month old, special preparation, Chicago plant): Cathode/1 × 3 mil Pellon/1 × 2 mil PVA/1 × 5.9 mil FRSC (tube wrap) Anode/1 × 3 mil Pellon and 10 × 10 mil Vinylite shims.

\* Corresponding author.

E-mail address: lewis\_h@crane.navy.mil (H. Lewis).

Set 4 — PVA film with Viskase unreinforced tubular sausage casing (USC), (2 weeks old, special preparation, Spain plant): Cathode/1 × 3 mil Pellon/1 × 2 mil PVA/1 × 2.3 mil USC (tube wrap) Anode/1 × 3 mil Pellon and 3 × 30 mil Plexiglass shims + 1 × 10 mil Vinylite shim.

Set 5 — New 1.75 mil (dry) UCB, Wigton, UK film (02/98, special preparation): Cathode/1 × 3 mil Pellon/3 × 1.75 mil UCB (U-wrap) Anode/1 × 3 mil Pellon and 1 × 30 mil Plexiglass shim + 2 × 10 mil Vinylite shims.

These five sets of seven cells each were all designated for life cycle study. All cells were filled to the red mark with 45% KOH in a standard filling procedure with vacuum application. All cells were charged at C/30 rate to 2.02 V + C/60 rate top-off to 2.04 V and discharged at C/6 rate to 1.20 V. The first three were “formation” cycles, which were counted towards life cycle. After 3 cycles one cell was withdrawn from each Set in a discharged state and dissected for baseline silver migration, DP and WTS for the separation. Additional cells were to be withdrawn at 25, 50, and 75 cycles for similar dissection evaluations. Failed cells were also dissected for failure mode and evaluation of properties.

The intent was to establish the degradation and failure processes and their rates. These data were to be compared to standard 1 mil (25 µm) cellophane degradation and failure rates (Set 1).

Cells were fitted with a third reference electrode consisting of a silver wire amalgamated with mercury to provide for anode potential versus the mercury electrode to obtain data on anode performance and cell impedance during testing.

Data evaluations included discharge Ah, silver migration, DP and WTS, all versus life cycle (in number of cycles) and state-of-health during testing from the plate voltage measurements.

### 3. Results and discussion

#### 3.1. Tensile strength measurements

Fig. 1 presents the comparison between 1 mil Flexel cellophane (Set 1) and 1 mil UCB cellophane (Set 2). A

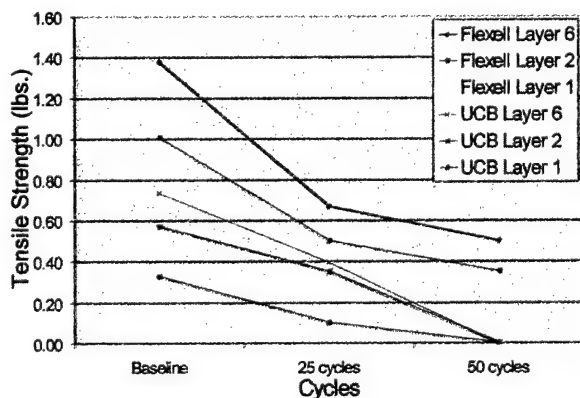


Fig. 1. Flexel vs. UCB tensile strength.

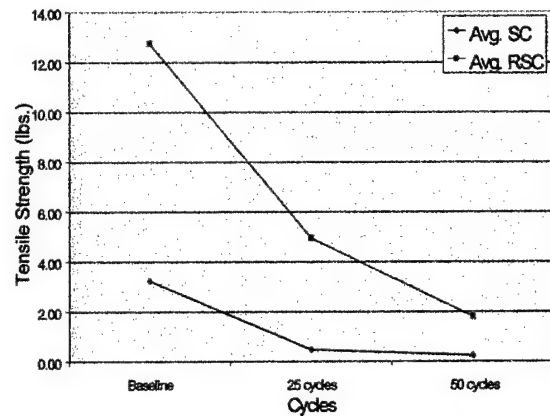


Fig. 2. RSC vs. USC tensile strength.

fourth datum point was available for Flexel for layer 6 because one cell failed at 12 cycles. This value, 1 × 10 lb, was right on line with the other layer 6 data. (layer 1 is the closest to the cathode.) Loss of tensile strength for the innermost layer in both cellophanes is greater with life cycle than for the outermost layer. Overall, the Flexel cellophane started with greater tensile strength and retained greater tensile strength with life cycle. All three layers of UCB cellophane were too weak for measurement at 50 cycles.

Fig. 2 shows the comparison between 1.75 mil USC (Set 3) and 5.9 mil FRSC (Set 4). The FRSC showed overall greater tensile strength, but its rate of degradation was much greater.

Fig. 3 presents data for the UCB single ply (1 mil, Set 2) versus double ply (1.75 mil, Set 5) cellophane.

Data for the double ply are problematical because in the baseline measurements the material showed two peaks, one for each layer, with the second break point at about twice the value for the first, and at 25 cycles, about 4×. The average values are plotted. At 50 cycles, both materials were too weak for measurement, as the cellophane fell apart during dissection. From the data, it appears that initially and through 25 cycles, the single layer film was stronger than the double.

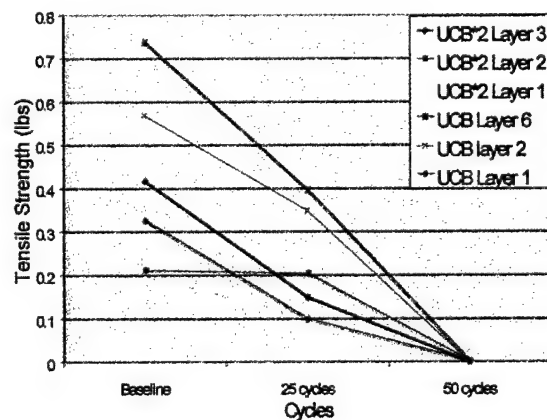


Fig. 3. UCB vs. UCB\*2 tensile strength.

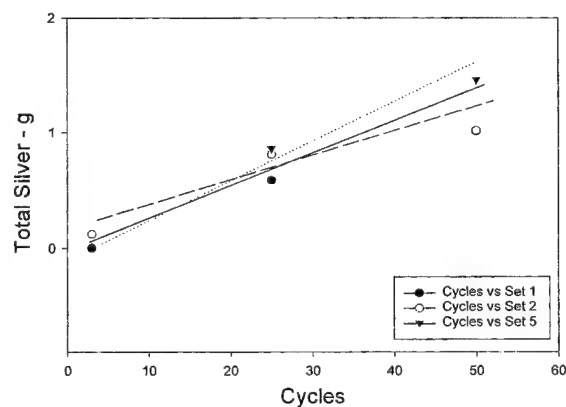


Fig. 4. Flexel vs. UCB silver migration.

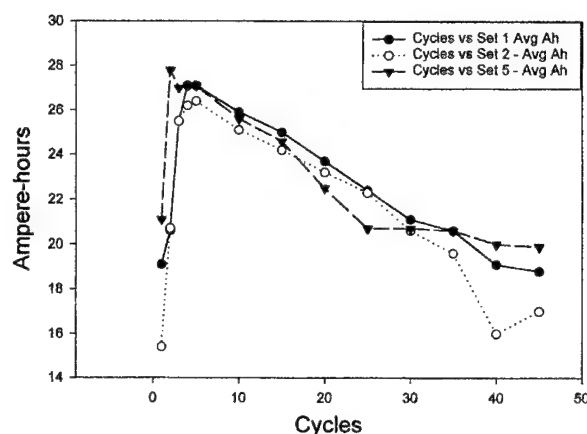


Fig. 6. Flexel vs. UCB discharge capacities.

### 3.2. Silver migration data

In Fig. 4, total silver migration data from Sets 1 (Viskase), 2 (UCB single ply), and 5 (UCB double ply) are plotted for life cycle. There appears to be no significant difference in the amounts of silver accumulating in the separations.

In Fig. 5, the same data for Sets 1, 3 (FRSC) and 4 (USC) are plotted, and here, there appears to be very little difference between the cellophane and the FRSC, however the USC separation exhibited a consistently higher rate of silver migration. But this did not influence performance because the silver was trapped in the PVA layer and did not appear in the SC layers.

#### 3.2.1. Discharge capacity data

In Fig. 6 are plotted the data for Flexel cellophane (Set 1) versus UCB (Sets 2 and 5), both single and double ply. The data plots for all three separations are about the same, with only a small advantage for the Flexel material. In Fig. 7 the data for Flexel (Set 1) versus the two SC separations (Sets 3 and 4) are plotted, and again there is very little difference, with a small advantage to Flexel out to 30 cycles, after which both SC materials exceed cellophane in discharge capacity.

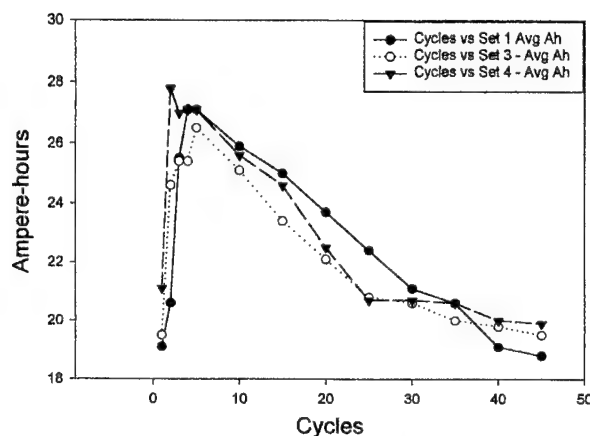


Fig. 7. Flexel vs. SC discharge capacities.

#### 3.2.2. Degree of polymerisation data

In Fig. 8 the data are plotted for DP changes with life cycle. The method of measurement is by an ASTM technique [8]. From the data plots, it is obvious that the DP decreases drastically in just the first few cycles and then

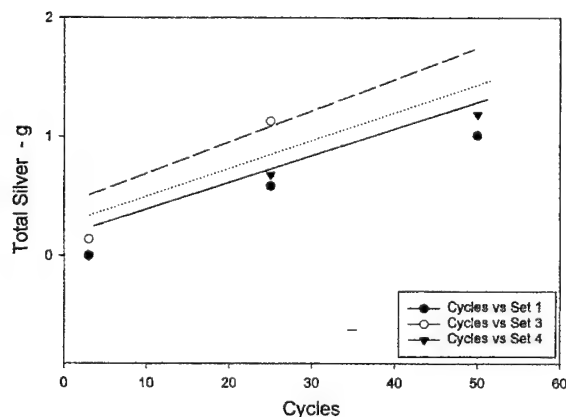


Fig. 5. Viskase vs. SC silver migration.

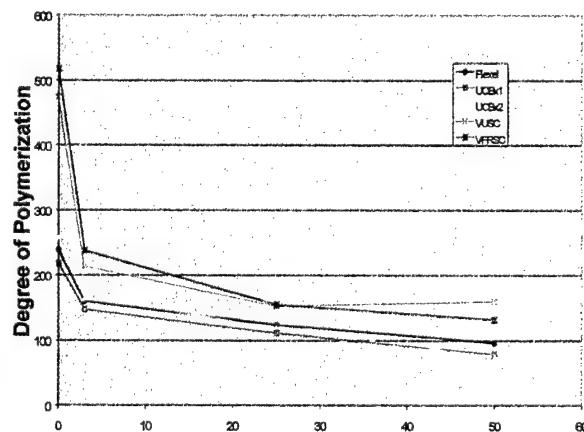


Fig. 8. Change in DP with cycling.



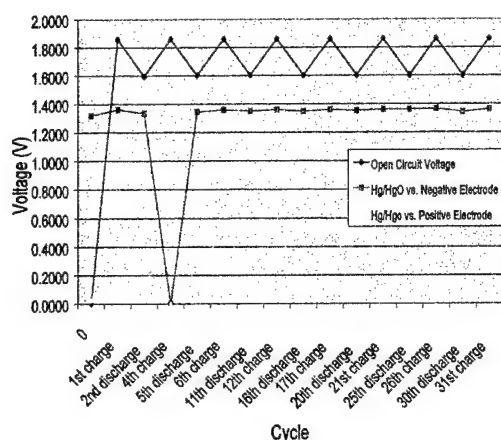


Fig. 9. Voltage measurement data for Set 1 cell 5.

decreases more slowly with cycling. All the plots appear to be trending toward a common minimum with cycling.

### 3.3. Voltage measurement data

The data for the voltage measurements with a third electrode are plotted for a single set in Fig. 9.

Voltages were only determined for Set 1 (Flexel cellophane) cells because the intent was to see if the anode voltage would change as it underwent shape change. No change in the voltage profiles was observed for any of the cells, and the data for cell 5 in Set 1 are representative of all the cells in this set. It was not possible to obtain voltage measurements beyond the 31st cycle because of zinc shedding in the cells.

## 4. Conclusions

### 4.1. Wet tensile strength and degree of polymerisation

From the WTS data (Figs. 1–3), it seems that both the UCB films and the USC tubing lose their tensile strength by the 50th cycle. The outermost layers of Flexel cellophane retained some strength, as did the FRSC tubing. The gradual alkaline hydrolysis and silver oxidation of cellulosic separations are the major contributors to loss of strength, and this loss is generally accompanied by shorting failure as the separations become more amorphous in character [9]. The loss of strength is also reflected in the DP data (Fig. 8), to a lesser extent, because all the separations, although the two SC maintained about 50% greater DP at 50 cycles than the cellophane films.

### 4.2. Silver migration rates

These data show that for the cellophane films (Fig. 4) the total silver accumulation in the respective films is constant with life cycle. Layer-by-layer data for the two 1 mil films

(Flexel and UCB) show that the migration beyond layer 3 was very small at 50 cycles, while for the 2 mil UCB film, the migration stopped at layer 2.

For the two SC materials versus Flexel (Fig. 5) the migration rates were about the same, while the layer-by-layer data show no silver beyond the PVA film layer at 50 cycles. So one layer of either SC in combination with the PVA film served as an effective silver barrier and also prevents zinc dendrite formation.

### 4.3. Discharge capacities

These data show identical behaviour (Fig. 6) for both UCB films versus Flexel, out to 40 cycles, after which the 1 mil UCB set cells began shorting. However, the double layer (2 mil, Set 5) cells were performing as well as the Flexel cells (Set 1) at 50 cycles.

The SC data in comparison to Flexel (Fig. 7) are especially interesting, because both SC separations tracked the Flexel performance out to 50 cycles, with no cells lost to shorting. The importance of these data is in the available volume generated by the reduction in separation wet swollen thickness (ca. 30 mil total for VUSC versus 48 mil total for Flexel) for energy density increases through the use of just one layer of tubular SC with PVA.

### 4.4. Reference voltage data

These measurements, in the way in which we performed them, did not provide useful data for evaluation of shape change in the anode in any of the Flexel cells used. There was no evident variation in anode voltage out to 31 cycles, where measurements were discontinued because the reference electrode shorted against the shed zinc.

## 5. Recommendations

The substitution of double-ply UCB cellophane film for UCB single-ply (which is the current film available for silver–zinc rechargeable cells) is a definite advantage, for at least two reasons:

1. it is much less subject to dendritic hard shorting by zinc and retains some DP after long cycling;
2. it may be possible to combine one or two layers of this separation with a layer of PVA film, yielding a volumetric savings which could be used to increase the energy density.

The substitution of a single tubular layer of either VUSC or VFRSC with a layer of PVA film for cellophane film is definitely an advantage in that:

1. the discharge capacity life is equally good;
2. the tubular sausage casings retain WTS and DP during cycling to as greater degree;

3. the additional volume available in the cell case will allow at least a 25% increase in volumetric energy density, which is very significant for mission capabilities in Navy undersea platform applications.

### Acknowledgements

NAVSEA and SPECWARCOM offices supported this work.

### References

- [1] H. Lewis, C. Grun, A. Salkind, *Proc. Electrochem. Soc.* 95/14 (1996) 68.
- [2] C. Grun, H. Lewis, A. Salkind, *Proc. Electrochem. Soc.* 95/14 (1996) 98.
- [3] H. Lewis, S. Wharton, in: *Proceedings of the 12th Annual Battery Conference on Applications and Advances*, 1997, p. 111.
- [4] H. Lewis, C. Grun, A. Salkind, in: *Proceedings of the 20th International Power Sources Symposium*, 1997, p. 29.
- [5] H. Lewis, A. Himy, in: *Proceedings of the 13th Annual Battery Conference on Applications and Advances*, 1998, p. 47.
- [6] H. Lewis, T. Danko, A. Himy, W. Johnson, in: *Proceedings of the 21st International Power Sources Symposium*, 1999, p. 61.
- [7] H. Lewis, S. Henderson, T. Danko, in: *Proceedings of the 16th Annual Battery Conference on Long Beach, CA*, 9–12 January 2001, in press.
- [8] ASTM D4243-86, in: *Proceedings of the American Society for Testing and Materials*, Philadelphia, PA, 1986.
- [9] R. Post, *Zinc-Silver Oxide Batteries*, in: A. Fleischer, J. Lander (Eds.), *Electrochemical Society, Inc.*, 1971, p. 263.



ELSEVIER

Journal of Power Sources 96 (2001) 133–139

JOURNAL OF  
POWER  
SOURCES

www.elsevier.com/locate/jpowsour

# High-rate capability of zinc anodes in alkaline primary cells

Jean-Yves Huot\*, Martin Malservisi

*Noranda Inc. — Technology Centre, 240 Hymus Blvd, Pointe-Claire, Que., Canada H9R 1G5*

## Abstract

This work is devoted to the electrochemical aspects of high-power testing of primary alkaline LR6 (“AA”) cells and to the factors influencing cell performance, namely the corresponding zinc anode behaviour under such high-rate conditions. The influence of the high-rate testing regime, such as the discharge mode and the end-potential, on zinc utilisation in alkaline cells has been monitored and its behaviour has been isolated by means of a pseudo-reference electrode.

As anticipated, anode formulation, including zinc alloy composition and size distribution, is found to affect the cell’s discharge curve and the corresponding zinc electrode potential and utilisation. The effects of these parameters on the discharge curve are discussed in terms of three stages of discharge.

Finally, the high-rate capability of commercial LR6 cells is analysed in terms of zinc anode formulation. It was concluded that zinc electrode polarisation is very small and is relatively independent of manufacturer, of zinc anode formulation and of zinc alloying. On the other hand, metallic zinc utilisation remains very low under high-rate conditions. © 2001 Elsevier Science B.V. All rights reserved.

**Keywords:** Zinc-alkaline primary cells; Zinc anodes

## 1. Introduction

Although aqueous and non-aqueous rechargeable battery markets have been growing very fast, the primary alkaline manganese (PAM) cell remains widely used in an impressive variety of applications and devices. Small sizes, such as LR6 (“AA”) and LR03 (“AAA”) alkaline cells, even demonstrated consistent growth over the past decade as a result of continuous improvement of their overall cell performance, namely their high-rate or high-power capability. This gain is closely related to major improvements in cell components and engineering, which resulted in lower cell impedance and improved active material utilisation.

High-performance and standard commercial PAM cells have been tested under various discharge conditions. Takei et al. [1] found a significant difference between commercial cells of different manufacturers for a continuous 1 A discharge. This difference was found to vanish at low discharge currents and higher temperatures [2]. Unfortunately, the potential–time discharge curves do not provide any insight into the electrochemical behaviour of zinc anodes. Modelling of cylindrical alkaline cells showed that cell performance under high discharge rates cannot be understood without modelling the zinc anode and by taking into account

anode porosity, KOH concentration, zincate ion distribution and (un)confinement to anode [3]. Previous out-of-cell anodic discharge capacities of gelled zinc alloy in electrochemical cell also showed the strong influence of zinc powder parameters on anode performance, namely the chemical composition and the presence of fine zinc particles [4].

The primary focus of this paper is to investigate the electrochemical aspects of high-power testing and factors influencing PAM cell performance, namely the corresponding zinc anode behaviour under high-rate conditions.

## 2. Experimental

Commercial and experimental LR6 alkaline cells were tested at room temperature and under controlled humidity with a Maccor Battery tester, System Series 4000. The cells were tested in triplicate.

Unless otherwise mentioned, commercial cells were purchased in 2000, with expiration dates after 2004. Experimental cells were half-cells supplied by a battery company, and filled with gelled zinc anode material containing a 2:1 ratio of zinc powder and alkaline solution mixed to 0.6 wt.% Carbopol 940. The alkaline solution was 40 wt.% KOH (Fisher SP236) containing 3 wt.% ZnO (Baker). Each experimental LR6 cell contained about 5.4 g of gelled zinc, or 3.6 g of zinc powder.

\* Corresponding author.

E-mail address: jean-yves.huot@ntc.noranda.com (J.-Y. Huot).

Unless otherwise mentioned, one pseudo-reference zinc electrode was inserted in the first layer of a multi-layer separator of a few LR6 cells, and both total potential and zinc potential with respect to this pseudo-reference zinc electrode were then recorded during cell discharge. In some cases, a second pseudo-reference electrode was inserted into the second layer of the separator. Cell component impedance was measured with a Solartron 1286 potentiostat and a 1260 frequency analyser.

Zinc alloy powders were made by gas atomisation of 99.995% molten zinc. Five alloys were tested, pure zinc, Bi–Zn, Bi–In–Zn, Bi–Al–Zn, and Al–Bi–In (ABI).

### 3. Results

#### 3.1. The high-rate discharge of alkaline LR6 cells

Cell discharge is associated with a cell impedance that consumes part of the cell energy and induces cell polarisation which decreases cell potential. Cell polarisation consists of activation/concentration polarisation of zinc anode, activation/concentration polarisation of  $\text{MnO}_2$  cathode, and IR loss in cell components such as electrodes, separator, and current collectors [5].

The contribution of cell components to the limited capacity and material utilisation of alkaline cells cannot be extracted from the overall discharge curve unless cell component potential and impedance are monitored as well. This was achieved by monitoring impedance and potential with respect to two reference zinc electrodes inserted in different layers of the separator. Cell impedance was measured from high to low frequencies, and ohmic contribution of cells and cell components was estimated at high frequencies, while electrochemical impedance associated with cell reaction or zinc oxidation was computed at the low end of the  $Z''$ – $Z'$  semi-circle (Bode plot). The contribution of mass transfer was not taken into account. These results are summarised in Table 1.

The ohmic loss in alkaline cells at 1 A ( $R_{\text{cell}}$ ) increases from 100 mV to 200 mV with increasing depth of discharge or decreasing cell potential, while the main contributors remain the increasing ohmic loss in active materials ( $R_{\text{Zn}}$  and  $R_{\text{MnO}_2}$ ). On the other hand, the electrochemical factor is

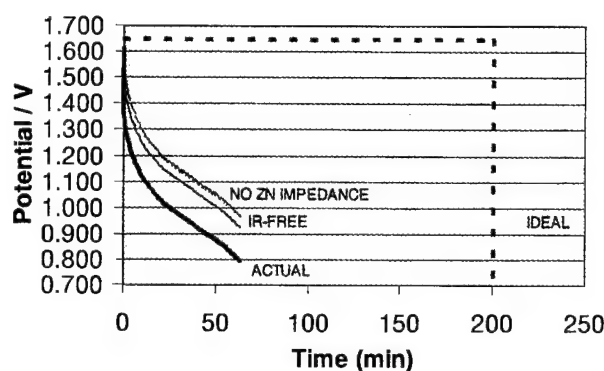


Fig. 1. Ideal and actual discharge curves of LR6 alkaline cells, and effects of cell impedance and electrochemical zinc impedance.

quite stable with increasing depth of discharge, and remains lower than the ohmic factor. The consistency of the electrochemical part means that the activation overpotential remains constant with increasing depth of discharge.

The impact of these factors is illustrated in the Fig. 1, wherein an actual discharge at 1 A is compared to the ideal cell discharge computed without any polarisation and ohmic loss. The ideal cell would provide about 5.5 Wh of energy per LR6 cell containing about 4 g of zinc, while the actual cell will deliver much less, with a material utilisation reaching 25% at 1 A continuous discharge. The absence of ohmic loss would actually double the energy output at the end-point potential of 1.0 V, while the absence of zinc overpotential (activation) would not significantly improve overall cell performance. The remaining gap between corrected and ideal cell potential curves can therefore be attributed to  $\text{MnO}_2$  discharge and mass transfer in zinc and  $\text{MnO}_2$  electrodes. Further reduction in cell polarisation will therefore not improve cell performance if the active materials utilisation remains low. It should be noted that increasing ohmic loss can be hardly distinguished from chemical passivation near the end-point potential of 0.9 V.

#### 3.2. High-rate testing of commercial cells

The cell and zinc potentials of commercial North-American (NA1 through 3) LR6 cells were monitored during continuous discharge at 1 A. Fig. 2 shows that the discharge curves of the three brands are quite similar and much better

Table 1  
Impedance of LR6 cell components at various end-point potentials<sup>a</sup>

Cell-potential (V)	Ohmic resistance				Electrochemical impedance	
	$R_{\text{cell}}$	$R_{\text{Zn}}$	$R_{\text{sep}}$	$R_{\text{MnO}_2}$	$R_{\text{cell}}$	$R_{\text{Zn}}$
Open circuit	0.106	0.032	0.018	0.054	0.048	0.036
1.2	0.117	0.021	0.018	0.060	0.053	0.019
1.0	0.100	0.028	0.024	0.083	0.042	0.035
0.9	0.131	0.048	0.018	0.068	0.061	0.043
0.6	0.180	0.048	Small	0.110	0.071	0.014

<sup>a</sup> Note: "Sep" stands for separator.

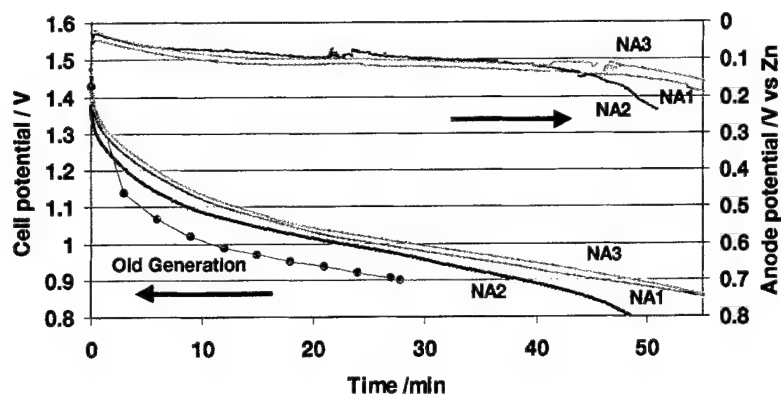


Fig. 2. Cell potentials and zinc potentials with respect to the pseudo-reference zinc electrode monitored during the continuous discharge at 1 A of commercial LR6 cells.

than the old PAM generation that was tested in 1998. Cell potential drops by about 500 mV over the entire discharge curve, while zinc anodic potential remains relatively flat at about 100 mV until cell potential reaches the end-point potential of 0.9 V. From the previous section, it can be stated that 50% of zinc polarisation is due to ohmic loss, while the other 50% is associated with the electrochemical oxidation of zinc in the early stage of the discharge.

The performance of these LR6 cells is cathode-limited as zinc potential does not drop simultaneously with the cell potential. NA2 cell performance was however found to be slightly lower than the others, while its zinc potential was quite similar to others up to 45 min, when it suddenly drops. This behaviour suggests that the NA2 zinc anode performs slightly less than NA1 and NA3, which are clearly cathode-limited. The lower performance of NA2 is much more apparent at 1  $\Omega$  and much less apparent at 1 W (Fig. 3). This is likely to be related to the initial discharge current that decreases in this order: 1  $\Omega$  > 1 A > 1 W, as the latter corresponds to a mid-rate discharge. On the other hand, it was well established that the constant load discharge is the least severe discharge mode, if performed at the same starting discharge current, when compared to constant current and constant power [6].

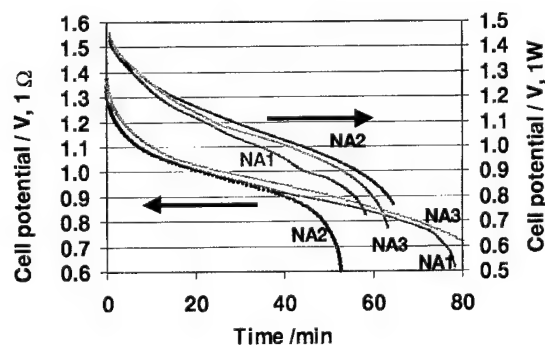


Fig. 3. Discharge profile of commercial LR6 cells under two continuous discharge modes, 1  $\Omega$  and 1 W.

As anticipated from previous work [7], the first part of both the cell and zinc discharge curves is found to follow a basic potential–time  $E-t^{1/2}$  function. This function for cell and zinc suggests some similar time dependence for the cathode that has actually been reported by Laig-Hörstebroek [8]. Table 2 shows that this slope depends upon both the discharge conditions and, to a lesser extent, the cell manufacturer. The zinc electrode contributes about  $3 \text{ mV s}^{-1/2}$  or 25% of cell potential drift, in perfect agreement with the extrapolated value of  $3 \text{ mV s}^{-1/2}$  at  $250 \text{ mA g}^{-1}$  for gelled zinc electrodes in electrochemical cells [9].

It appears that zinc electrode polarisation consumes about 100 mV. This begins in the first part of the zinc discharge curve, while zinc utilisation in commercial anodes is established in the third part of the zinc discharge curve and would hardly exceed 25% at 1 A, or about  $250 \text{ mA g}^{-1} \text{ Zn}$ . This result is in fairly good agreement with the alkaline cell discharge modelling that showed a similar zinc anode overpotential and a separator ohmic loss of about 100 mV each [6]. The actual cell potential curvature can therefore be largely attributed to the S-shaped discharge curve of  $\text{MnO}_2$  due to the homogeneous-phase discharge which generates an S-shaped open-circuit potential versus  $\text{Mn(III)/Mn(IV)}$  ratio [10].

### 3.3. The electrochemical aspects of high-rate discharges

A Ragone plot of commercial LR6 cells is illustrated for three end-point potentials in Fig. 4. The energy output drops

Table 2  
Initial  $E-t^{1/2}$  slope of discharge curve for three commercial LR6 cells

Cell	Slope $E$ vs. $t^{1/2}$ vs. discharge mode ( $\text{V s}^{-1/2}$ )			
	Zn anode at 1 A	1 A	1 $\Omega$	1 W
NA1	0.0031	−0.0134	−0.0158	−0.0114
NA2	0.0031	−0.0114	−0.0118	−0.0093
NA3	0.0034	−0.0114	−0.0110	−0.0095

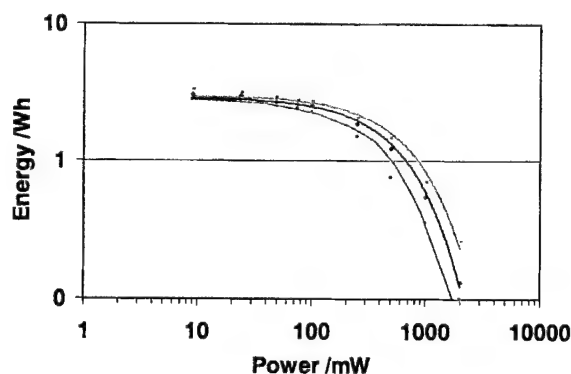


Fig. 4. Ragone plot of commercial LR6 cells for three end-point potentials.

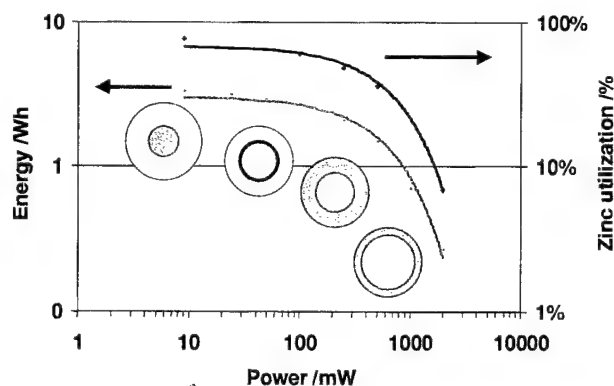


Fig. 5. Modified Ragone plot of commercial LR6 cells. A schematic cross-section of a discharged zinc anode is superimposed on the curves.

drastically when cell power reaches 0.5 W. As anticipated, this drop is more severe with increasing end-point potential.

In the Fig. 5, zinc utilisation and energy are plotted in a modified Ragone plot of commercial alkaline cells, where a schematic of the discharged anode at the end-point potential of 0.9 V is superimposed on energy and zinc utilisation curves. Schematics were drawn from color pictures of zinc cross-sections obtained from cut open cells which had been discharged down to 0.9 V. Basically, we can identify three types of zinc, gray-fresh zinc, blueish discharged zinc, and white-very discharged zinc. After high-rate discharge at 2 W, a very thin disk layer of blueish zinc precipitate is observed near the anode-separator interface, as reported for dissected discharged cells [3,11], while undischarged gray zinc is easily observed in the bulk of the anode. A Raman spectroscopy showed that blue coloration is due to ZnO [11]. The blue-discharged area expanded with decreasing power down to 100 mW, while a white-very discharged layer started forming within the blue-discharged zinc. This suggests that some deeper discharge of zinc and increased zinc utilisation are associated with the lower power. The center area remains undischarged until the extremely low power of

10 mW is reached, at which point zinc utilisation reached almost 100%.

Modelling of cylindrical alkaline LR6 cells demonstrated that the discharge layer moves toward the current collector with increasing discharge time [12], while a higher zincate concentration near the separator and corresponding zinc oxide precipitation near or in the separator could shorten cell life at increasing discharge rates.

### 3.4. Zinc alloy powders

Experimental LR6 cells containing various zinc alloy powders were discharged at 1 A after ageing for 7 days at room temperature. Discharge curves of five zinc alloys are shown in Fig. 6. The discharge curves basically superimpose down to 0.9 V, when the pure zinc alloy failed prematurely.

Zinc electrode potential drops in the first 10 min of continuous discharge at 1 A, where the electrode potential follows an  $E-t^{1/2}$  function. The potential of the five zinc alloys then reaches a plateau at 120–150 mV for 20 min (Fig. 7). The potential of the pure zinc electrode increases suddenly after 40 min at 1 A, and this change coincides with

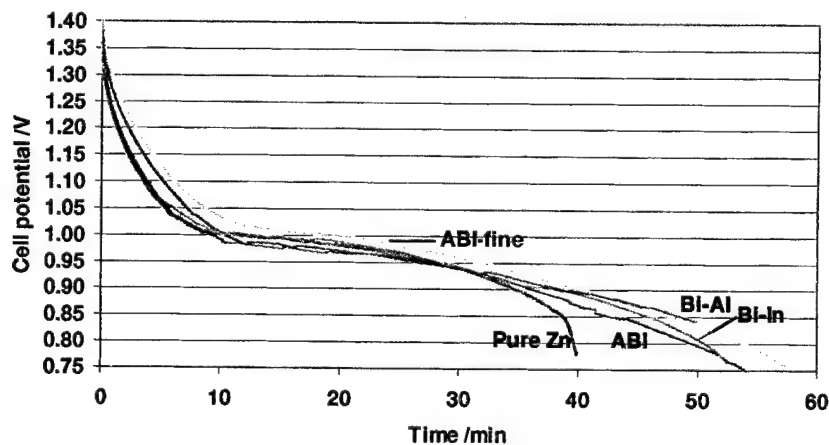


Fig. 6. Discharge curve at 1 A of LR6 cells containing various zinc alloy powders.

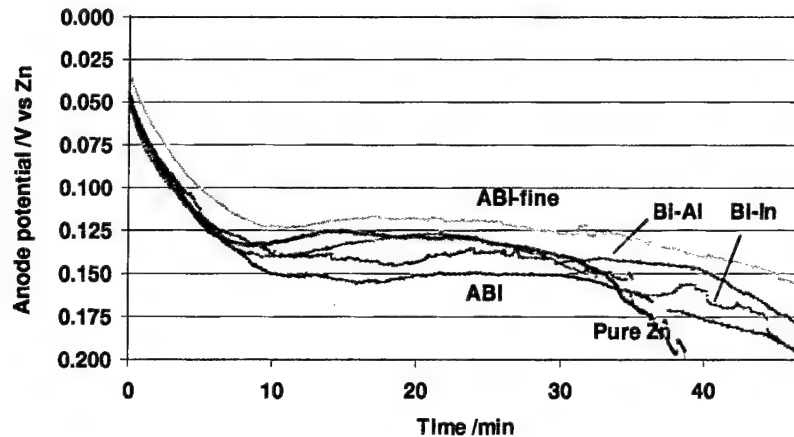


Fig. 7. Zinc electrode potentials of various alloy powders with respect to the zinc reference electrode.

the corresponding drop in cell potential. This result confirms the lower performance of pure zinc that was observed in an electrochemical cell [4]. The anodic behaviour of zinc alloy anodes suggest that pure zinc does limit cell performance, whereas cell performance is not anode-limited with the other zinc alloys, as the zinc electrode polarisation remains low when cell potential reaches the end-point potential of 0.9 V. The ultimate capacity of these zinc alloys was therefore not reached, as cell discharge was stopped as soon as the cell potential reached this end-point potential.

It can be observed that the presence of fines in the size distribution decreases zinc electrode potential by about

20 mV. This effect largely exceeds the chemical effect associated with the zinc alloys. These results are summarised in Tables 3 and 4. Again, the  $E-t^{1/2}$  slope of zinc alloys accounts for about 30% of cell  $E-t^{1/2}$  slope.

The anode polarisation at a given cell potential or at specific capacities remains constant for all the zinc alloys, except for pure zinc at 650 mAh. Again, these results do not tell us anything about the ultimate zinc utilisation in the cathode-limited LR6 cells.

The closed-circuit voltage (CCV) of zinc electrode contributes 30% or 50 mV to the cell CCV of 200 mV (versus open-circuit voltage (OCV)). Cell and anode resistances

Table 3  
Initial slope of discharge curve and zinc anode polarisation at different depth of discharge for various zinc alloys powder

Alloy	$E$ vs. $t^{1/2}$ slope		Anode polarisation (V vs. Zn)			
	Cell	Anode	at two cell potentials		at two capacities	
			1.2 V	0.9 V	150 mAh	650 mAh
Pure zinc	−0.0245	0.0071	0.075	0.167	0.133	0.212
Bi	−0.0203	0.0065	0.124	0.165	0.157	—
Bi-In	−0.0236	0.0066	0.087	0.159	0.139	0.157
Bi-Al	−0.0238	0.0069	0.074	0.146	0.134	0.146
ABI	−0.0163	0.0053	0.085	0.165	0.146	0.174
ABI fine	−0.0161	0.0046	0.078	0.140	0.122	0.139

Table 4  
Potentials and resistances of cell and zinc anode, and in-cell after-discharge gassing (PD) of various zinc alloy powders

Zinc alloy	Zinc gassing <sup>a</sup> ml/3 days	Zinc anode potential			Cell potential		
		OCV vs. Zn (V)	CCV vs. Zn (V)	$R_{Zn}$ ( $\Omega$ )	OCV (V)	CCV (V)	$R_{cell}$ ( $\Omega$ )
Pure zinc	10.3	−0.006	0.048	0.054	1.609	1.408	0.201
Bi	—	−0.013	0.068	0.081	1.614	1.396	0.218
Bi-In	2.8	−0.013	0.056	0.069	1.615	1.399	0.216
Bi-Al	0.4	−0.015	0.047	0.062	1.623	1.394	0.229
ABI	0.2	−0.015	0.050	0.065	1.618	1.418	0.200
ABI fine	0.3	−0.012	0.036	0.048	1.621	1.443	0.178

<sup>a</sup> Discharge at 3.9  $\Omega$ /450 mAh, then 3 days at 71°C. Gassing measurement by liquid displacement.

Table 5  
Zinc anode formulation and cell performance of commercial LR6 cells

Zn alloy <sup>a</sup>	Zn (g)	Zn (%)	D50 (μm)	OCV (V)	CCV (V)	Duration at 1 A min/s	PD <sup>b</sup> (μl g <sup>-1</sup> day <sup>-1</sup> )
PI	3.1	69	316	1.587	1.135	11,09	141
BI	3.1	69	321	1.592	1.369	34,08	150
PI	3.1	65	257	1.589	1.273	19,43	660
BIC	3.6	78	248	1.603	1.283	30,24	66
BIC	3.5	76	277	1.608	1.357	36,54	178
BI	3.9	74	290	1.606	1.201	14,13	445
BI	3.7	70	288	1.597	1.173	12,52	171
AbI	3.6	68	246	1.599	1.358	38,36	1671
AbI	3.7	73	218	1.610	1.380	10,43	133
AbI	3.3	71	301	1.597	1.350	33,26	150
ABI	3.4	71	264	1.612	1.393	40,59	87
ABI	3.6	75	250	1.559	1.207	21,00	505
BIP	3.1	68	248	1.510	1.166	6,54	1000
AbI	3.3	65	309	1.583	1.310	26,59	60
PI	3.4	71	220	1.590	1.381	16,23	N.A.
ABI	3.9	71	259	1.590	1.381	19,43	N.A.
BIP	3.1	69	266	1.566	1.360	10,40	288
Pb–Zn	3.7	78	212	1.589	1.276	18,3	390

<sup>a</sup> P, B, I, A and C stand for lead, bismuth, indium, aluminium and calcium. The lower case b means low concentration of the alloying element.

<sup>b</sup> Discharge at 1 A/0.75 V, then 24 h at 71°C. Gassing measurement by liquid displacement.

were calculated from (OCV–CCV)/I and these resistances were found to be independent of zinc alloys. Anode resistance accounts for about 30% of the whole cell resistance. These resistances agree quite well with the total ohmic and electrochemical resistances measured by impedance and presented in Table 1.

As anticipated from previous out-of cell gassing evaluations [7], after-discharge gassing of zinc alloys increases in this order: ABI < BA < BI < Bi < pure Zn (Table 4).

### 3.5. Behaviour of world-wide commercial cells

The variability in zinc anode formulations and high-rate cell performance of commercial LR6 cells acquired world-wide in 1998 were monitored. The results are summarised in Table 5. It should be noted that both anode formulation and cell performance may have changed since that time.

Zinc quantity, the percentage of zinc in anodes, zinc particle size and zinc alloys, as obtained from zinc anodes, were found to vary substantially from one cell to another. CCV, discharge time at 1 A down to the end-point potential of 0.9 V, and after-discharge (PD) gassing all vary substantially as well. Substantial OCV variations are surprisingly observed, but can be explained by differences in KOH–ZnO concentrations and the corresponding effect on the reversible (thermodynamic) electrode potential. More surprisingly, PD gassing of ABI alloys is not lower than PD gassing of non-aluminium/zinc alloys.

## 4. Discussion

Monitoring of zinc electrode potential during cell discharge revealed that the zinc discharge curve is flat and

slightly dependent on the alkaline cell manufacturer, anode formulation or zinc alloy powder. Zinc anode discharge at 1 A required an electrode polarisation ranging from 100 to 150 mV, which corresponds to an anodic zinc overpotential lower than 100 mV at about 200–250 mA g<sup>-1</sup>. The ohmic loss of about 50 mV can be associated with the anodic ohmic loss due to electrolytic resistance, tortuosity in the porous electrode, and ZnO precipitation.

The effect of zinc alloying on zinc anode polarisation remains small, but zinc alloying appears to extend zinc utilisation by delaying the passivation of pure zinc that occurs when cell potential reaches 1 V.

In other words, the absence of an alloying element was found to induce premature zinc passivation, which suddenly appeared when the zinc potential reached 200 mV. The difference, evidenced in an electrochemical cell [4] between zinc utilisation of the other zinc alloys, was however not assessed as the experimental LR6 cells were cathode-limited.

Cell and zinc discharges involve three stages, an initial stage with potential–time  $E-t^{1/2}$  function, a middle stage with a linear  $E-t$  function, and the final stage when the potential suddenly drops. This behaviour leads to three types of cell performance, (a) type I when the final stage is not observed with cells displaying a considerable ohmic drop, as the discharge is stopped when it reaches the end-point potential of 0.9 V, (b) type II, when the final stage is observed on the cell discharge curve whereas it is not observed with the zinc electrode if the cell is cathode-limited, (c) type III when the final stage is observed on both the cell and the zinc discharge curves, as the cell is anode-limited.

This work has shown that any reduction in ohmic drops in the separator and electrodes will improve the high-rate



performance of type I cells, while the benefits of reducing the overpotential of active materials will be very small. Separator impedance depends on layer thickness, porosity, the number of layers, and changes in the electrolyte composition associated with active material electrochemical reactions.

On the other hand, any reduction in cell impedance will result in a minor improvement of high-rate performance of type II and III cells if the active materials utilisation is not significantly improved. Parameters that affect zinc polarisation and zinc utilisation in alkaline cells still have to be identified and optimized in order to improve alkaline cell performance and to reduce the unit production cost of alkaline cells by reducing the zinc quantity in zinc anode material. Moreover, the electrochemical evaluation of high-rate discharge of the zinc anode in alkaline cells still needs to be addressed.

## 5. Conclusion

It has been shown that zinc electrode polarisation is very small, while it depends slightly on the cell manufacturer, zinc anode formulation and zinc alloying. The impact of size distribution of zinc alloy powders appears to be more

significant. Parameters that affect zinc utilisation in alkaline cells still have to be identified and optimised in order to improve cell performance, especially when the cell is clearly anode-limited, namely in the case of zinc-air cells.

## References

- [1] T. Takei, T. Kurosawa, Y. Wada, T. Ohtsuka, J. Kawasaki, A. Sato, *Prog. Batteries Batt. Mater.* 16 (1997) 367–376.
- [2] J. Matsumoto, B. Carter, A. Prater, D. Smith, J. Ross, in: *Proceedings of the 39th Power Sources Conference*, 12–15 June, 2000, p. 1.
- [3] E.J. Podlaha, H.Y. Cheh, *J. Electrochem. Soc.* 141 (1994) 15.
- [4] J.Y. Huot, E. Boubour, *J. Power Sources* 65 (1997) 81–85.
- [5] D. Linden (Ed.), *Handbook of Batteries*, 2nd Edition, McGraw-Hill, New York, 1995.
- [6] E.J. Podlaha, H.Y. Cheh, *J. Electrochem. Soc.* 141 (1994) 28.
- [7] J.Y. Huot, in: A.J. Salkind, F.R. McLarnon, V.S. Bagotzky (Eds.), *Proceedings of the Electrochemical Society on Rechargeable Zinc Batteries*, Vol. 22, 1996, pp. 14–95.
- [8] H. Laig-Hörstebroek, *J. Electroanal. Chem.* 180 (1984) 599.
- [9] J.Y. Huot, in: A. Attewell, T. Keily (Eds.), *Proceedings of the 18 International Power Source Symposium on Power Source*, 1993, p. 177.
- [10] A. Kozawa, R.A. Powers, *Electrochem. Technol.* 5 (11/12) 535.
- [11] W.B. Cai, Q. Shi, M.F. Mansuetto, D.A. Scherson, *Electrochem. Solid State Lett.* 3 (2000) 319.
- [12] E.J. Podlaha, H.Y. Cheh, *J. Electrochem. Soc.* 141 (1994) 15.

## Future talk

Mark Kniveton

*British Telecommunications Plc, Mondial House, PP 502.3, 90-94 Upper Thames Street,  
London EC4R 3UB, UK*

Received 8 January 2001; accepted 8 January 2001

---

### Abstract

The paper is divided into two distinct parts. The first part deals with a look at the progress made to date in the VRLA battery technology that has established itself as the primary source of emergency standby power within the BT network. This will include a review of maintenance procedures and the specifying of such products for central office and local switching centres, and will be discussed alongside an appreciation of how telecommunications networks are changing. The second part includes an assessment of future technology developments and how these changes will increase demand upon suppliers of battery power for network and hand-held devices of the future. The paper will conclude with a light-hearted look at potential technological developments of the future that will revolutionise the way we communicate with each other and our environment. © 2001 Published by Elsevier Science B.V.

**Keywords:** Lead-acid batteries/valve regulated; Applications/telecommunications; Applications/standby power

---

### 1. Introduction

Standby power, in the form of battery technology, is used throughout the telecommunications industry either as a means of portable power for hand-held devices or for providing emergency power in central office applications. This paper will describe the incredible and rapid change that is effecting the telecommunications industry, and review the progress made over the last 15 years in valve-regulated lead-acid (VRLA) battery technology. The author will also take a light-hearted look at future technological and social change that will continue to place great demands upon the battery industry to solve the insatiable appetite for power solutions that will make these products of the future a reality.

With so much of commerce reliant on their IT infrastructure, it is essential that any telecommunications network is resilient against the possibility of a mains power outage. At the same time, commercial pressure within the telecommunications industry is demanding a greater return on its network investment, and in particular questioning many aspects of the traditional way to power and maintain network equipment. This paper will review many of the standby power initiatives that have been introduced over the previous 20 years, and take a look at current and future network

technologies and the challenges that these represent for the standby power community.

### 2. Telecommunications technology review

#### 2.1. Changes in the telephone network

The current digital telephone network was introduced in the UK only 20 years ago, replacing the then decaying electro-mechanical analogue system, and it was thought at the time that this would be the network to meet all of the demands of the future. How wrong we were and how rapidly things have changed! The explosion of demand for broadband services fuelled by growth in the Internet and mobile communications has eaten into all of the available digital capacity and required a rapid reassessment of technology and infrastructure investment plans.

Powering these networks has seen a similar revolutionary change, as many operators found the world decided that their large-scale centralised dc power systems were too cumbersome for the digital age. Available technology had also changed, and the introduction of switch-mode rectifiers and valve-regulated lead-acid batteries enabled network operators to introduce smaller end-of-suite distributed power systems. The introduction of rapidly deployed Internet protocol (IP) equipment is also producing an intense debate within the telecommunications power community as

---

*E-mail address:* mark.kniveton@bt.com (M. Kniveton).

to whether the future of power equipment should be from a standby ac or dc platform.

## 2.2. *Changes in mobile communications*

Over the last 10 years, mobile hand-held devices have also changed out of all recognition. From the old style bulky handsets owned by the few, to today's wireless application protocol (WAP) miniature devices. The changes in technology have been surpassed only by the volume in use and this trend is set to continue for many years to come, as wireless bandwidth becomes cheaper and mobile Internet service providers exploit the potential of the new 3G networks.

Powering hand-held devices has also improved significantly with the introduction of new battery technologies (nickel/metal hydride, lithium-ion, lithium polymer) and sensible power control built into the handset. Improvements in radio technology, micro-electronics and smaller digital radio cells has also reduced the demand on the battery pack, correspondingly lower tariffs have increased talk time considerably and this has again burdened the power pack. Battery performance has and remains an inconvenience for the mass of users of mobile telephony despite the changes to more reliable battery technology and improved energy density. The future for mobile telephony is even more challenging, as greater reliability and higher power densities will be required for the next generation of always-on communicators that will transform all aspects of our lives.

## 3. Standby power: background and architecture

BT introduced VRLA battery designs to its network in 1984 as a means of simplifying its dc power system. Previously, the older centralised power plants consisted of large rectifier modules, some as large as 3000 A and associated large-scale, flooded electrolyte, Planté batteries. As the network evolved to the digital platform, it became clear that this type of dc infrastructure could not be built at the same speed as the telecommunications switching equipment, and therefore a new architecture was designed incorporating a rack-mounted power system installed alongside the switching equipment. This was made possible by recent improvements in smaller switch-mode rectifier designs.

Recombination VRLA battery technology was chosen because of its reduced gassing levels enabling the rack to be positioned in the switch room. Due to this close proximity of the power system to the switching equipment, distribution costs were reduced as the voltage drop from the battery was minimised and improved system reliability was anticipated due to the modular design of the new dc power system, both at component and system level. By comparison, failures of large central power plants, although rare, would be catastrophic over a large geographic area, as all switching and transmission units are connected to this one source.

As part of its modernisation plan for the digital network, BT also installed automatic-start diesel engine generator sets at all network sites. As these generators start within 27 s of the failure of the public electricity supply, battery autonomy times were reduced to a minimum of 1 h.

### 3.1. *Reliability of VRLA batteries*

Initially, all seemed well with the new battery technology. Then 4–5 years after their introduction, BT along with other network operators experienced increasing battery failures that primarily fell into two groups. The most serious were sudden and catastrophic failures caused by an open circuit battery and the second a premature reduction in battery capacity.

Investigations by BT and their battery suppliers identified one manufacturer whose products sometimes suffered severe corrosion of the interconnecting group-bar or top lead. At this time, most manufacturers employed a manual process to burn or form the group-bar onto the plate lugs. Subsequently, it became clear that the VRLA design was far more susceptible to manufacturing quality control than other lead designs and as a result BT introduced a monitoring programme and supported the introduction of the BSI standard (BS) 6290 pt 4 (1997).

Between 1989 and 1996, VRLA reliability became a major concern to BT and its battery suppliers, although it must be said that not all designs suffered from the same failure modes and there were also many examples of products that met their anticipated design life. Of notable merit were VRLA designs made from a pure lead prismatic plate that achieved an in-service life of 10 years. It became clear that there was nothing fundamentally wrong with the basic VRLA design other than the issue of quality control during manufacture, and BT's battery suppliers responded by introducing new automated manufacturing techniques that dispensed with the variability caused by older manual techniques. The group-bar problems were eradicated by the introduction of the automated cast-on-strap process, and incidences of premature capacity loss were reduced by improved active material mixing and pasting techniques.

As a result, BT has become increasingly satisfied by the performance of the VRLA product, and 98% of it is now meeting the 6-year-life criterion for lead–calcium–tin designs installed in an average equipment room temperature of 2°C. However, not all telecom operators feel the same, and there is move in some circles to go back to the older style centralised systems and flooded battery designs.

### 3.2. *Monitoring*

Due to our early experience with the VRLA product and with the number of monoblocs installed in the network now approaching 1 million units, it became essential to introduce a reliable monitoring programme. Even more essential was the need to register the make, age and location of each

battery on a network-wide inventory system. The basic fact that all batteries, especially lead-acid types, will ultimately require replacement means that a monitoring and replacement strategy is an essential service requirement of all network operators. Sadly (and this must be of some concern to the battery industry), many of the VRLA products installed within private networks have now decayed beyond their useful life and will ultimately present a safety hazard to the end user.

Automated power system controllers that can periodically perform a maintenance check by discharging batteries to the equipment load are a recent innovation, and until now manual methods had to be used. With so many batteries in a modern telecommunication network, it can prove to be an expensive time-consuming task if traditional discharge techniques are used. As a result, many batteries may remain untested and therefore their condition remains unknown. With so many batteries deployed within the BT network, it became necessary to introduce a faster manual method whilst continuing to deploy our ultimate strategy of automated battery testing for all modern power systems. To this end, BT introduced conductance/impedance testing as the primary annual maintenance check for all VRLA batteries. Initial scepticism over this method by industry was soon replaced by a better understanding of the limitations and advantages, coupled to the knowledge that BT's environmental control is within acceptable limits for a VRLA product (life is halved for every 10°C rise above 20°C).

Each field technician has a Midtronics conductance tester that uses a four wire ac signal method to measure and display the inverse of the impedance, conductance, of the monobloc under test. This is then compared to a reference figure for this type of battery. As BT is primarily interested in only potentially gross failures, due in part to the provision of an emergency engine generator, the chosen failure thresholds are purposely set outside of the scatter which is commonly seen around the 70–80% capacity value. In this way, only fully charged batteries are tested and a large variation in conductance can be identified as a problem battery. The technician can then choose either to subject this battery to a discharge test or replace it under warranty.

Careful monitoring of conductance trends and warranty replacements ensure that replacement strategies can be built with confidence.

BT is currently embarking on a further enhancement to its battery maintenance strategy by introducing automated battery capacity tests. This method exploits the potential of the power system controller to initiate an automated timed-battery discharge to the equipment load. This is a simplistic test to ensure that the battery can supply the equipment load for a predetermined time down to a minimum of 46 V. Once again, the test is only performed on a fully charged battery and the frequency of the test is designed to capture any significant degradation in battery capacity without any necessary cycling of the battery. In the event that a failure has been determined, a technician will

only then attend and perform a system load check and conductance test to further diagnose the problem and effect a repair.

Early indications of this method are suggesting that maintenance costs will be reduced by a further 15%, and those batteries that are exceeding their design life can remain in the network longer, thereby deferring capital replacement costs.

### *3.3. Specification, national and international battery standards*

An appreciation and understanding of the battery application and environment is essential to successfully specify the appropriate battery. A suitable National Standard for telecommunications batteries within the UK is BS 6290 pt4 (1997). This standard has been designed to assist in the formulation of a procurement specification and requires the user to specify the performance classification required to meet his requirements. The classification includes sections on safety, performance and durability. The user must specify a performance classification in each section.

Safety tests include container flammability and mechanical integrity tests as well as gas emission and high current endurance tests. These can be used by the designers of equipment cabinets to ensure that adequate ventilation and overcurrent protection can be built in from the start.

Performance tests confirm rated capacity tests between durations of 5 min and 10 h, as well as cyclic endurance, charge retention (for storage calculations) and internal resistance.

The durability classification is based upon elevated temperature tests in the laboratory that have been proven to relate to anticipated life at normal temperatures. The high temperature accelerates the corrosion of the lead plates and through a mathematical relationship (the Arrhenius equation); the high temperature life can be used to predict life at the actual temperature.

Work is also in progress on a new International Standard to reflect the global aspirations of telecommunications companies. This standard is an attempt to amalgamate National Standards from America, Japan and Europe, including BS 6290 pt4. If successful, IEC 60896-2 will be welcomed by many in the telecommunications industry, and simplify the global procurement of VRLA telecom batteries.

## **4. Future telecom platforms**

### *4.1. Network elements*

The real telecommunications revolution is only just beginning. The arrival of the Internet means that all networks are being forced to change beyond all recognition. A broadband network based on the new datacoms Internet

switching protocol (IP) enables voice, data or video streams to be sent at low cost over the high-speed part of the PSIN network. Advances in datacoms switching speeds enables vast amounts of data to be sent anywhere in the world, effectively by-passing the lower-order PSTN elements. The requirement to send and receive large amounts of data is enhanced further down-stream by cable TV networks, domestic modem or direct server access or by emerging XDSL platforms that can operate at increased speeds over a normal twisted-pair telephone line.

Commerce and Governments are demanding cheaper access to the Internet in order to benefit from the potential productivity gains of e-business within a society that embraces e-commerce. This will become a reality as Internet connections become affordable and are always on.

One of the most significant developments of this new IP network will be the emergence of voice over IP (VOIP) or video over IP. This is where voice or video data is transmitted over the IP network at a fraction of the cost of the PSTN network. These technology changes will force network operators to dispose-off assets that are not part of their new core businesses, and as a result the provision and maintenance of network power will move to external businesses. As a result, battery standby reserves may be reduced further and procurement pressure will see price as the dominating factor.

The reducing cost of bandwidth and the convergence of datacoms and telephony is making the traditional network operators move into media content as information service providers (ISPs) for their own products or as third party providers. The reliability of the necessary datacoms equipment will become increasingly important to these organisations and to their customers, as will the provision of standby power to backup the servers and routers.

In power and reliability terms, the convergence of the datacoms and telecoms networks will cause its own problems, as traditionally datacoms equipment has been fed from an ac source with limited backup power being provided from UPS systems having typical autonomy times of 5–30 min.

Safety and working practices are different too, with telecommunications equipments being the safer option using the traditional dc voltage of 48 and employing specific high impedance separation between ac protective and dc signalling earths.

#### 4.2. Wireless elements

Mobile networks will also be transformed with the introduction of 3G networks that will enable high bandwidth transmission via the newly licensed radio spectrum. This will require an increase in base stations, as the 3G network utilises smaller radio cells and each miniature radio base station will require its own backup battery. As these base stations will be subjected to varying environmental conditions, the chosen battery technology will have to be robust

enough to give reasonable life at summer temperatures in excess of 30°C. The downside to this rapid deployment of 3G infrastructure is cost, and therefore network providers will be reluctant to increase investment levels, and a fear exists that purchasing pressure could outweigh the use of a more suitable battery technology despite its superior engineering qualities.

The growth in personal communications is set to continue well into the next decade as mobile phone density rivals fixed network devices and the successful deployment of 3G networks enables a new range of personal communicators. Some operators believe that wireless networks will become the number one broadband access platform and that, despite the initial heavy costs of the 3G platform, will retain a significant cost-efficiency over rival fixed network. The evolution into higher speeds will also provide the opportunity to re-define basic telecommunications services. Always-on connectivity, bandwidth-on-demand and mobility will become the norm rather than the exception with speeds in excess of 64,000 bits/s becoming possible.

### 5. Futurology

In order to visualise the impact of these dramatic technology changes and the convergence of multimedia platforms, BT employs the services of a futurologist — a person who attempts to predict the endless possibilities of emerging technology, and how this will change and impact upon society. These predictions help technologists to develop new applications and devices that may well spin-off into commercial reality.

Futurologists have both optimistic and pessimistic views of the future. Optimistically, new technology will become all embracing and be a true commercial success that will change our human behaviour for the better, and will have an impact across all aspects of society. Pessimistically, the belief is that basic human needs of food, shelter, love, status and self-fulfilment cannot be altered by technology and are written deep into our DNA.

Clearly, the most rapid change is being experienced by the computer-based industries. This will continue with rapid advances being made in software developments that are not constrained to bandwidth. Personal computers, containing their own software packages, will be replaced by Internet software portals personalised to restrict unwanted junk mail and enhance speed of access to items of interest. Voice communication and recognition will rapidly prove to be a major success, and instantaneous multi-lingual translations will make the world seem even smaller.

Interactive software will develop personalities and synthetic talking life forms called *avatars* will add that personal touch when obtaining access to services or buying products on-line. By the year 2005, there will be more than 2 billion voice portals or voice-enabled web-sites. These devices will exploit Internet-based e-commerce and solutions to

customer/management relationships. The most popular avatars will have legal rights and some of our friends will be synthetic creations only existing in cyber space. All learning will become web-based and experience will be gained from time spent in a holographic simulator.

There will become one universal electronic currency accepted by any shop or web-site in the world with crediting and debiting performed instantaneously via your personal communicator. By 2003, there will be more than 350 million smart phones or personal communicators in use. The

integration of GPS technology into these devices will create myriad opportunities for location-based content and services. These personal communicators will also be able to monitor basic health functions and automatically alert your doctor, who may automatically e-mail a prescription or request a consultation.

These are just some of the views of our changing world, illustrations purely to remind the battery technologist that reliable portable and standby power will become essential part of our everyday life.

# VARTA micro batteries for wireless telecommunication devices

D. Ilic\*, J. Heydecke, M. Kilb, I. Knop, G. Schulz

VARTA Gerätebatterie GmbH, Daimlerstrasse 1, 73479 Ellwangen, Germany

Received 30 September 2000; accepted 4 December 2000

## Abstract

Newly developed nickel–metal hydride (Ni/MH) micro cells that are capable of high rates, meet the requirements of main power sources for modern wireless telecommunication devices, like GSM hand phones, PDAs and others. Besides having the capability to give high continuous and pulse discharge currents, they also ensure the realisation of a device with slim design and low cost.

For the back-up of the RTC function, a lithium-ion cell based on the carbon–manganese dioxide system provides high reliability by having a long cycle life and complete tolerance to deep discharge.

For MBU (which require higher rates), a Ni/MH cell only 2 mm thick is now being introduced. Other wireless devices, like headsets for comfortable use of mobiles whilst driving, wireless mice and keyboards and the upcoming “Bluetooth” technology will need suitable power sources. Besides the rather high currents, which exclude low-power lithium systems, miniaturisation is limiting the space available for the battery.

Some concepts using Ni/MH micro batteries will be discussed in this paper. © 2001 Elsevier Science B.V. All rights reserved.

**Keywords:** Nickel–metal hydride batteries; Lithium-ion batteries; Portable communications; Miniaturization

## 1. The 450 and 600 mAh Ni/MH cells

The design of new GSM phones, PDAs and other wireless devices is driven by the need to minimise dimensions as well as weight and, being a mass market consumer product, by continuous cost reduction.

To power these devices from a very fast growing market, Varta has developed two new Ni/MH cells, the V450HR and V600HR, with nominal capacities of 450 and 600 mAh

The main features of these cells are:

- slim design only about 5 mm thick;
- high short-duration discharge current capability, up to 10 C;
- fast charge capability, 1 C charge with  $-dV$  termination;
- low self-discharge characteristics,  $\sim 20\%$  per month at room temperature;
- long service life;
- attractive price/performance ratio;
- environmentally friendly: 0% lead, 0% mercury and 0% cadmium.

A successful GSM phone requires a total thickness of  $<20$  mm so a slim battery is needed. The alternatives,

prismatic Ni/MH or Li-ion cells (the latter with an advantage in weight) are rather costly.

The V450HR cell gives the design engineer the possibility of using a battery pack with a total thickness of 6–7 mm, but at a reasonable cost. A 3.6 V pack, using three V450HR cells to give dimensions of  $34\text{ mm} \times 24\text{ mm} \times 5\text{ mm}$ , in a plastic case or as a shrink-sleeved version can have either wire connectors or, to save costs, embedded directly onto the PCB of the phone.

Improvements in the chip technology have resulted in very long standby times, consequently the user usually needs only one battery and the option of a second battery is no longer needed. In addition the battery lifetime is improved, so this embedded option can be used. The battery is shown in Fig. 1.

Micro (button) cells are usually regarded as low power cells. The 450 HR cell was developed also to discharge at high currents. Its design, with a multi-electrode stack, enables it to be pulse discharged at up to 10 and 5 C continuously. Therefore, it can be used in GSM phones.

The performance of the V450HR under different loads is illustrated in Fig. 2. Cell impedance is about  $2\text{ m}\Omega$  and that of the complete pack is far below  $10\text{ m}\Omega$ . This ensures sufficient operational run time, even for digital devices with high pulse currents. In talk mode, GSM mobiles require up to 2 A pulses and standby currents in the range of 50–

\* Corresponding author.

E-mail address: dejan.ilic@vatra.com (D. Ilic).



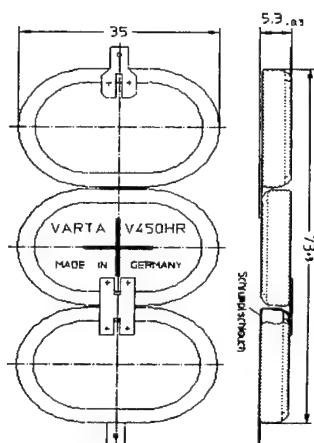


Fig. 1. Embedded version of three-cell V450HR Ni/MH cell.

200 mA, and under these conditions this battery provides more than 90% of the nominal capacity of 450 mAh (Fig. 3).

For convenience of use, a mobile phone requires a short recharging time. This battery can be recharged with currents up to 1 C, the decrease of the voltage ( $-dV$ ) when the battery is fully charged being used for termination, to avoid overcharging with such high currents. This performance is comparable to cylindrical and prismatic Ni/MH cells and the charging characteristic of the 450HR is shown in Fig. 4.

Compared to other Ni/MH micro batteries showing an extreme low self discharge rate of only 20% capacity loss

after 1 year, the multi-electrode design of this high rate cell resulted in a self discharge of 20% per month.

As in other button-type Ni/MH cells, a pressure relief vent is integrated at the bottom of the cell to avoid the built-up of high pressure inside the cell arising from abusive conditions. Under normal conditions the cell remains sealed, and even under abusive short-circuit conditions no activation of the safety vent is noticed. This cell offers the designers of wireless telecommunication devices an attractive option to realise a slim design without loosing the target of cost reduction.

## 2. Micro Li-ion cells for RTC back-up in GSM phones and pagers

When the main battery is changed or completely discharged, the RTC (or other) function of the device has to be backed-up by an additional battery. This requires a 3 V supply, but at very low currents in the range of micro amperes. The size of this battery should be as small as possible and a good cycle life even with deep discharges is required. For this purpose Li-ion cells, based on a carbon anode and a manganese dioxide cathode have been developed. Two sizes, both having a diameter of 6.8 mm and a height of 2.1 (the MC621) and 1.3 mm (MC614) enable the engineer to design in a 3 V back-up cell with minimum space requirement. The smaller cell, with tags, has a maximum height of 1.65 mm, which is a suitable size for mounting onto the PCB of many mobile phones.

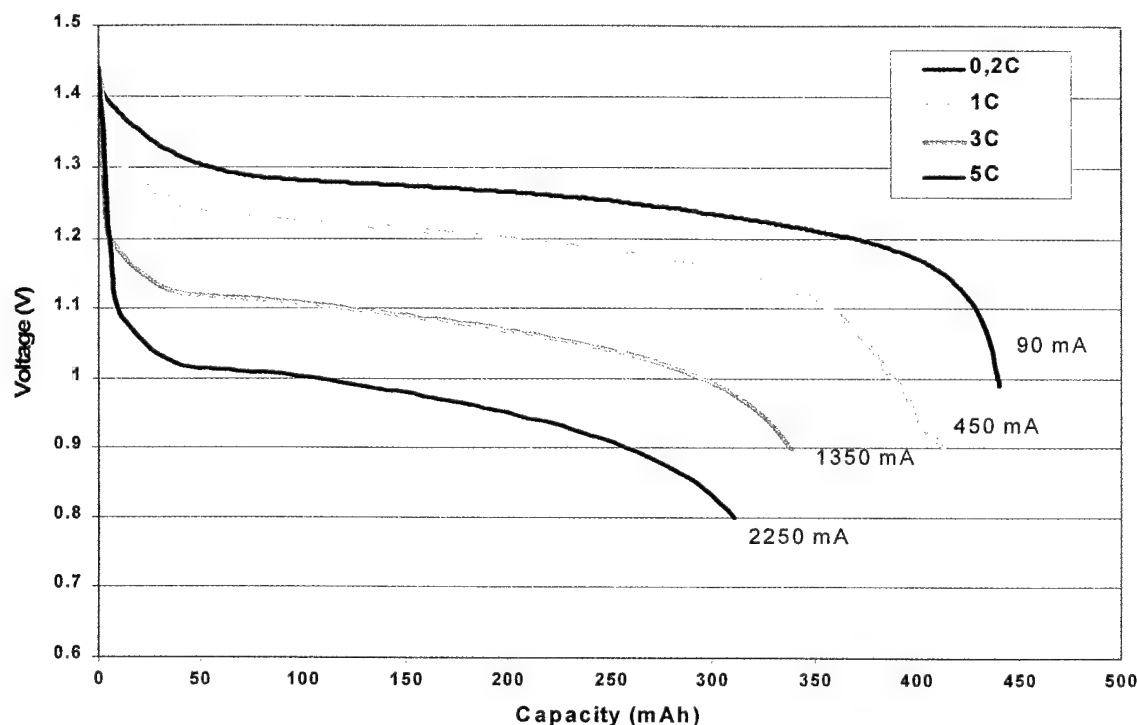


Fig. 2. High rate performance of V450HR Ni/MH cell.



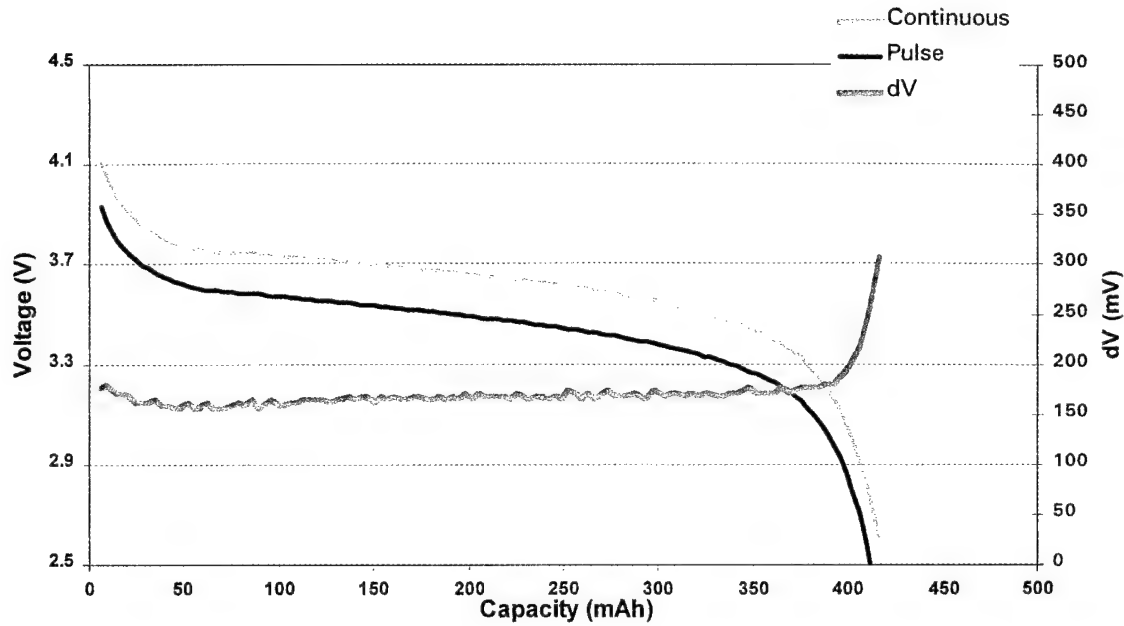


Fig. 3. GSM pulse discharge test on a three-cell V450HR battery. Repetitive regime: pulse, 1800 mA/0.6 ms. Continuous: 200 mA/4 ms.

The main advantages of these cells are:

- excellent cycle life (>200), even at 100%DOD to 1.8 V;
- insensitive to deep discharge, dischargeable down to 0.0 V (cycle life at 100% DOD to 0.0 V > 100);
- wide operational temperature range ( $-10$  to  $+60^{\circ}\text{C}$ );
- very low self discharge, <10% per year at room temperature;
- no safety risk, no metallic lithium is present;
- environmentally friendly.

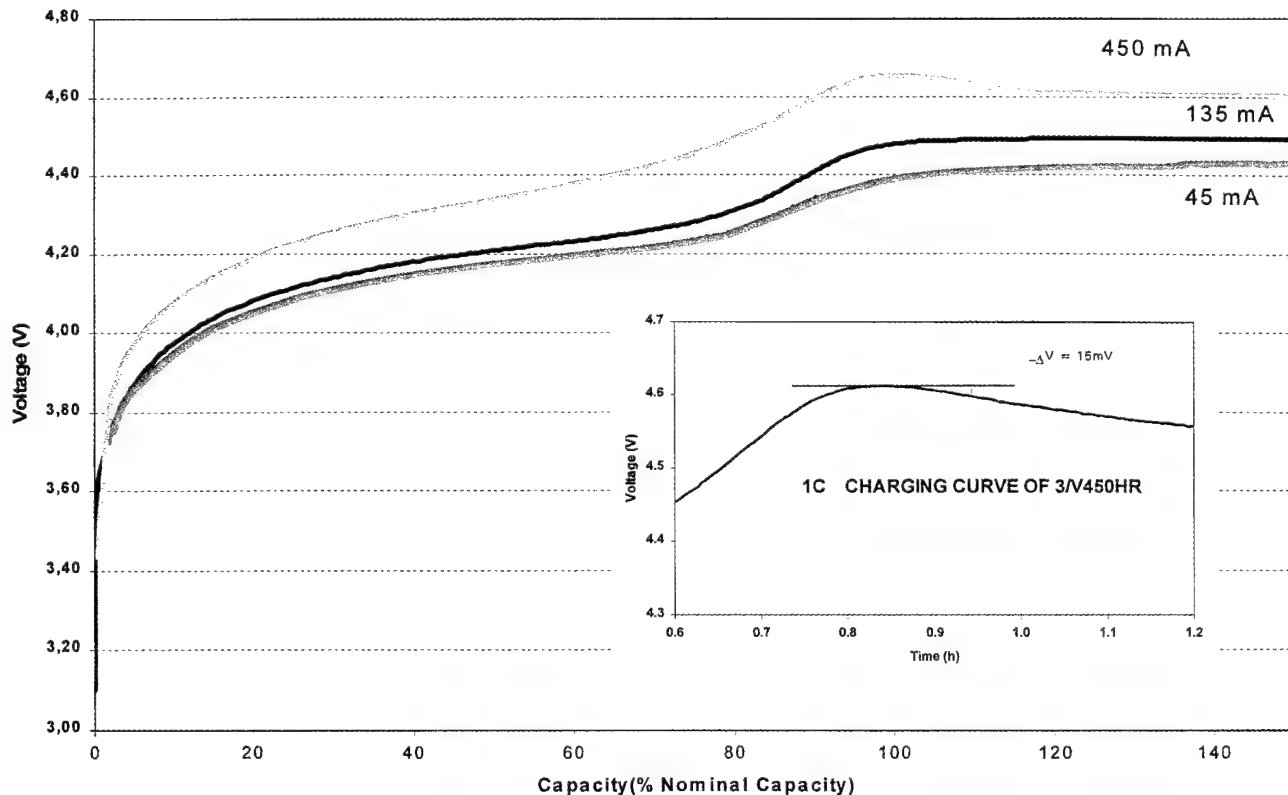


Fig. 4. Charging characteristics of a three-cell V450HR battery.

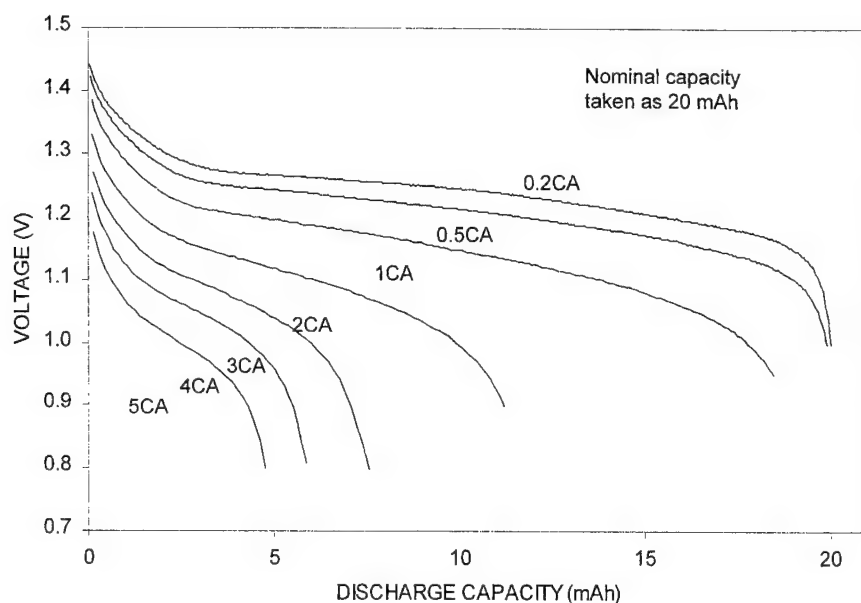


Fig. 5. Discharge curves for a V20HR cell.

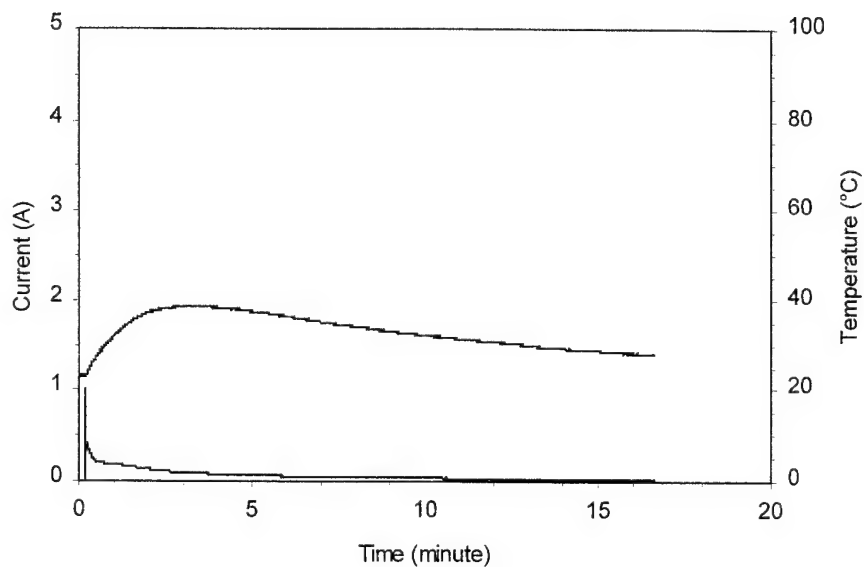
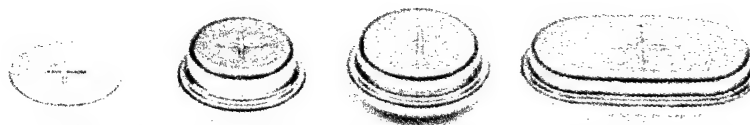


Fig. 6. Short circuit behaviour of a V20HR cell.



	V15H	V40H	V80H	V150H
Diameter/Length (mm)	11.5 <sub>-0.1</sub>	11.5 <sub>-0.2</sub>	15.5 <sub>-0.1</sub>	25.6 <sub>-0.2</sub>
Height (mm)	3.1 <sub>-0.2</sub>	5.35 <sub>-0.3</sub>	6.0 <sub>-0.2</sub>	5.9 <sub>-0.25</sub>
Width (mm)	-	-	-	14.1 <sub>-0.2</sub>
Weight, approx. (g)	1.3	1.7	4	6

Fig. 7. Range of small Ni/MH button cells.

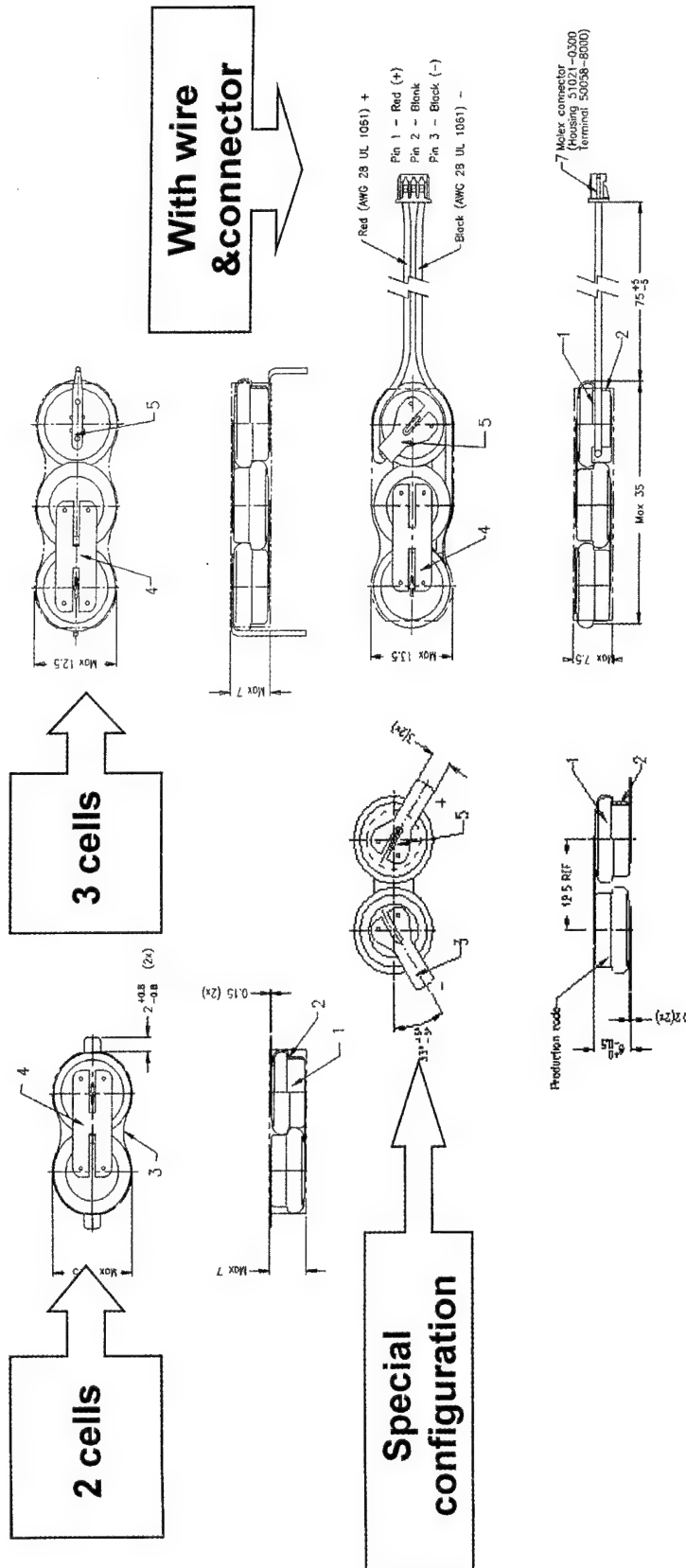


Fig. 8. Design concepts for button cells.

The cycling performance, even under deep discharge, is an especial criterion of enhanced reliability from this electrochemical couple compared to cells having lithium–aluminium alloy as their anodic material.

No protection against deep discharge is necessary, whilst charging can be done by using constant current up to 3.4 V (termination at this voltage) or directly from 3.4 V with a current limiting resistor.

### 3. V20HR-a back-up battery which meets the requirements for high rate capability and very slim design

For those applications which need more power for back-up, a Ni/MH micro battery, type V20HR, is now being introduced. This extremely slim cell, of thickness 2 mm, ensures a flat design for the device.

PDA's with additional cellular functions (GSM/CDMA) need to back-up memories when the main battery is changed or in case of failure. For this, a battery needs to provide currents in the range 10–20 mA. Advanced super-slim notebooks require, for RTC and/or bridging, a battery that is as flat as possible.

This new cell fulfils both demands. Having a nominal capacity of 20 mAh, it can be discharged up to the 5 C rate, and at 1 C (20 mA) it still delivers 18 mAh. The rate capability is shown in Fig. 5.

Besides these features, the V20HR cell shows the following characteristics

- charging can be done in a “normal” mode at 0.1 C (2 mA) within 14–16 h, or accelerated at the 0.5 C (10 mA) rate for 3 h after the cell has been fully discharged;
- continuous overcharge is possible at 2 mA (0.1 C);
- the expected life time under trickle charge of 0.6 mA is up to 6 years at 20°C and up to 3 years at +45°C;
- the cell can be discharged over the temperature range –20 to +65°C;
- the self-discharge rate is around 10% per month at room temperature;
- if short-circuited, the temperature increase is small. Fig. 6 shows an increase of about 12°C for a six-cell battery.

Depending on the requirements for MBU functions, very slim Li-ion or Ni/MH cells are available for back-up power and so help designers keep their devices small, yet reliable when the main battery is disconnected.

### 4. Main batteries for other wireless telecommunication devices

Other wireless devices like headsets for comfortable (and legally allowed) use of mobile phones whilst driving a car, wireless mice and keyboards, also the upcoming “Bluetooth” technology will need suitable power sources. These devices need rather high currents, so Li-ion rechargeable coin cells are not suitable.

Fig. 7 shows a range of Ni/MH button cells that combine light weight (for 3.6 V batteries between 5.5 and 19 g) with small form factors, have the ability to meet the current drain requirements, are “robust”, safe under abusive conditions and are environmentally friendly.

The main four types have capacities of 15, 40, 80 and 150 mAh. They can be designed into wireless devices or are under consideration. All can be continuously charged at the 0.1 C rate without capacity degradation. They lose only 20% of their capacity by self discharge during a 1-year storage. They will recover after deep discharge and when short circuited, their temperature will rise only by 10–15°C.

For voltage multiples of 1.2 V, single cells can be assembled in flat or stacked configurations, being connected to the device by tags or wire connectors and so conforming to the design criteria. For wireless headsets, the battery can be split, and mounted in different sections of the device to realise a comfortable weight balance. To provide a longer running time, a spare battery is often a consideration, which is charged in the base station when the other pack is in use. For reference, some battery design concepts are shown in Fig. 8.

### 5. Conclusions

Today's micro (or button) cells are not only for low rate applications, as they are suitable for use as main batteries in devices with rather high current drains. These new high-rate cells can power GSM phones. Depending on the current profile, Li-ion or Ni/MH cells are available to ensure MBU functions. For upcoming wireless telecommunication devices, including mobile phones, the designer will find a potential solution to his power requirements with the micro batteries described in this paper.

## Dynamic characterization of small lead-acid cells

Alvin Salkind<sup>a,d,\*</sup>, Terrill Atwater<sup>a,b</sup>, Pritpal Singh<sup>c</sup>, Sudarshan Nelatury<sup>c</sup>,  
Sangeetha Damodar<sup>c</sup>, Craig Fennie Jr.<sup>e</sup>, David Reisner<sup>e</sup>

<sup>a</sup>Center for Battery Materials & Engineering, Rutgers University, 98 Brett Road, Piscataway, NJ 08854-8058, USA

<sup>b</sup>US Army CECOM, RD&EC, Ft. Monmouth, NJ 07703, USA

<sup>c</sup>Villanova University, Villanova, PA 19085, USA

<sup>d</sup>UMDNJ-Robert Wood Johnson Medical School, Piscataway, NJ 08854, USA

<sup>e</sup>US Nanocorp Inc., 74 Batterson Park Road, Farmington, CT 06032, USA

Received 14 December 2000; accepted 23 December 2000

### Abstract

Three sizes of small valve regulated (VRLA) commercially available lead-acid cells were investigated and characterized for their dynamic properties by ac impedance spectroscopy and other electrochemical techniques. All cells were of the limited electrolyte type and no additional electrolyte was introduced during the studies.

The data indicates a very significant increase in cell impedance at lower states of charge, as expected. In charging studies close to the fully charged state, some unexpected impedance data were observed.

Complex impedance plots indicate a passive film formation, probably associated with the recombination surface film. The investigations included cells in various states of charge as well as cycling history including positional orientation studies. Equivalent circuits were derived from ac impedance spectroscopy and the parameters studied as a function of the cell's state-of-charge. Furthermore, the voltage response of the cells was theoretically generated from the ac impedance spectroscopy using Fourier transform analysis and found to be similar to the measured cell responses. © 2001 Published by Elsevier Science B.V.

**Keywords:** Lead-acid batteries; Electrochemical impedance spectroscopy; Time-domain spectroscopy; Fourier analysis; VRLA batteries

### 1. Introduction

Performance analysis of lead-acid cells continues to be of technical interest as they are recognized to be rapidly evolving among other successful commercial high power and electric vehicle power sources. The technique of assessing state-of-charge (SOC) based on electrochemical impedance spectroscopy (EIS) [1] is a very popular way to accomplish this. It is also known that for a valid and more thorough dynamic characterization of electrochemical devices, one might reinforce the experimental findings with model parameters derived from relevant mathematical analysis. Further, it is more assuring to have the same inference made from studies made on the basis of two different domains, i.e. both time and frequency.

Time-domain spectroscopy (TDS), which involves the application of a bipolar square wave current and measurement of the consequential terminal voltage, is an emerging

technique that attempts to predict the dynamics of cell chemistry by way of quantifying the time constants of the composite exponential response [2]. Be it the case of lead-acid battery, or for that matter any physical system in general, as long as linearity and time-invariance are prevalent, both EIS and TDS are bound to generate the same system-theoretic inference about the underlying processes. It is when these are violated that we find response ambiguities that call for more advanced, nonlinear, analytical methods.

In this paper, we shall show that it is possible to start with EIS data and by subjecting this to a Fourier technique, obtain a TDS response that compares quite well with the measured time domain response. Of particular attention is the distinction between charge and discharge half cycles. We found that during the charge process, the measured TDS almost matches with the Fourier-synthesized response, but during the discharge half-cycle, the predicted results differed from the measured results. To counter this, a small dc voltage bias is employed. This method worked well over the different states of charge considered.

\* Corresponding author. Tel.: +1-732-445-6858; fax: +1-732-445-5313.  
E-mail address: salkind@rci.rutgers.edu (A. Salkind).

In addition to ac impedance spectroscopy and time-domain spectroscopy, sweep voltammetry was used to investigate the electrochemical characteristics of the small VRLA lead-acid cells investigated for intermittent high power operations. The cell characteristics of impedance and polarization of these batteries throughout the life of the system were of the most interest and dictated the characterization methods used. To accomplish this, sweep voltammetry and ac impedance spectroscopy were used during both charge and discharge [3,4].

The cell designs of VRLA lead-acid cells investigated included

- a 2.5 Ah, cylindrical spiral wound design R20 ("D") size [8];
- a 2.0 Ah, flat plate prismatic single cell design [9];
- a 1.0 Ah cylindrical, spiral wound thin film design [10].

In the case of the 2.5 Ah R20 size cell, additional experimentation and modeling was undertaken. Besides impedance spectroscopy, these cells were interrogated with pulsed dc square waves. The 2.0 Ah prismatic and the 1.0 Ah thin film, spiral wound, cylindrical cell was investigated with ac impedance spectroscopy and sweep voltammetry during both charge and discharge.

## 2. The ac impedance spectroscopy

To study the electrochemical behavior of cells, dc techniques such as cyclic voltammetry, potentiostatic and galvanostatic polarization have been employed. When these techniques are correctly implemented, one might derive a vast amount of information about the kinetic and thermodynamic behavior of the electrodes. But as a variety of complex parallel processes occur at the electrodes, it is hard to elicit the required information. The dc techniques, by themselves, do not provide sufficient information to extract the various kinetic and thermodynamic processes occurring at the electrodes.

Recent literature [5,6] has dealt with deriving several physical models based on the differential equations governing the charge transfer rate and transport of species to the electrolyte/electrode interface. This approach is capable of explaining the occurrence of inductive behavior and negative resistance. Both analytical and numerical methods have been applied to solving these differential equations [5,6]. One useful technique to experimentally confirm the battery models is ac electrochemical impedance spectroscopy. In this method, a small amplitude ac signal (voltage/current) is used as the excitation and the resultant current/voltage response is measured from which the cell's impedance over a range of frequencies is derived. This impedance data is helpful for obtaining the equivalent circuit models for the cell. These models consist of discrete or distributed components. Also one might predict the rate-controlling step in the interfacial Faradaic process.

## 3. Time-domain spectroscopy

In this technique, a symmetrical, bipolar, square wave current is applied at the terminals of the battery and the consequential voltage is measured. We have developed two different schemes to get the same TDS response. In the first approach, we collect the EIS Data and fit an equivalent circuit model. Analytical expressions are available to get the voltage response due to a given current excitation. In the second approach, we use a Fourier technique to get the TDS response. Results indicate that there is a good match between the measured response and the predicted response.

## 4. Circuit-theoretical approach

The voltage response of an electrochemical system can be predicted using a purely circuit-theory approach. Equivalent circuits consisting of discrete or distributed components are used in combination to describe an electrochemical system. These circuits include the following subcircuits:

- a resistor in parallel with a capacitor (RC);
- a resistor in parallel with an inductor (RL);
- a constant phase element (CPE);
- a CPE in parallel with a resistor.

The voltage responses of these subcircuits (RC, RL, CPE and CPE in parallel with a resistor) to a step current excitation are shown in Eqs. (1)–(5), respectively. These equations define the temporal voltage response of the circuits for time ( $t$ ) greater than 0. The total voltage can be found from the sum of the individual contributions.

For the resistor in parallel with a capacitor, the response is given by

$$v(t) = R \left( 1 - \exp\left(-\frac{t}{RC}\right) \right) \quad (1)$$

where  $v(t)$  is the voltage across the circuit as a function of time,  $R$  the parallel resistance,  $C$  the parallel capacitance, and  $t$  time.

For the resistor in parallel with an inductor, the voltage response is given by

$$v(t) = R \exp\left(-\frac{tR}{L}\right) \quad (2)$$

where  $L$  is the parallel inductance. The voltage response of a single CPE element  $1/Ts^p$  is given by

$$v(t) = \frac{t^p}{T\Gamma(p+1)} \quad (3)$$

where  $\Gamma$  is the gamma function. The voltage response of a CPE element in parallel with a resistor  $R$  is given by

$$v(t) = R \left[ \sum_{i=1}^{\infty} (-1)^{i-1} \frac{1}{(RT)^i} \frac{t^{ip}}{\Gamma(ip+1)} \right] \quad (4)$$

A special case when  $P = 0.5$  results in a simplification to this equation:

$$v(t) = R \left( 1 - \exp\left(\frac{t}{R^2 T^2}\right) \operatorname{erfc}\left(\frac{\sqrt{t}}{RT}\right) \right) \quad (5)$$

where  $\operatorname{erfc}$  is the complementary error function.

The total voltage response derived from Eqs. (1)–(5) is due to a unit current step excitation. The voltage response due to a bipolar square wave current excitation,  $V_{\text{bpsw}}(t)$ , is then the corresponding sum of time shifted and weighted ( $\pm 2$ ) unit step responses as described by Eq. (6):

$$v_{\text{bpsw}}(t) = v_u(t) + 2 \sum_{i=1}^{\infty} (-1)^i v_u\left(t - i \frac{T}{2}\right) \quad (6)$$

where  $v_u(t)$  is the unit step response and  $T$  the period of the square wave excitation.

## 5. Fourier technique

In order to transform the frequency domain information to the time domain, we would like ideally to acquire the responses at the fundamental frequency and all of the odd harmonics (since the even harmonics are not present in a symmetric square wave). However, since the amplitude of the  $n$ th harmonic is  $1/n$  times the fundamental, we can window the response up to the 80th harmonic without loss of accuracy.

The Fourier synthesis procedure to derive the time domain voltage response from the measured EIS data is shown in Fig. 1. The measured EIS values at the  $n$ th harmonic ( $Z_n$ ) are multiplied by the windowed Fourier spectral coefficients of the bipolar square wave current ( $I_n$ ). The resultant is the Fourier coefficients of voltage response ( $v_n$ ). By adding all the individual contributions the total voltage response,  $v(t)$ , may be obtained, i.e.

$$v(t) = \sum_{n=-40}^{40} v_n \exp\left(\frac{j(2n-1)\pi t}{T}\right) \quad (7)$$

## 6. Polarization characterization

The electrochemical characteristics of thin film lead-acid cells were determined, as they are related to intermittent high power operations. Lead-acid cells are one of the primary candidates for a rechargeable component of an electrochemical hybrid system. These battery–battery hybrid systems are designed to provide pulse capability and with improved energy density as compared with standard batteries. The cell characteristics of impedance and polarization of these batteries throughout the discharge life of the system and at non steady-state conditions were of the most interest and dictated the characterization methods used. To accomplish this, sweep voltammetry and

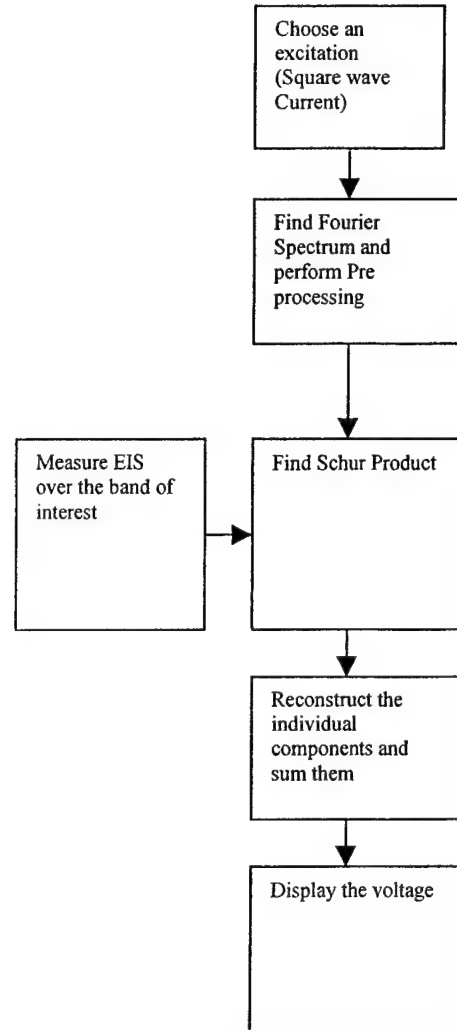


Fig. 1. Flow chart showing Fourier technique for determining a cell's voltage response to a unit step current.

impedance spectroscopy were used during both charge and discharge.

## 7. Experimental

Impedance data was obtained with a Solartron, SI-1287 Electrochemical Interface and SI-1260 Frequency Response Analyzer controlled by Scribner Associates Inc. CorrWare and Zplot software. The Impedance spectroscopy sweeps were conducted from 65000 to 0.65 Hz at a magnitude of 5 mV. Polarization data was obtained using an Arbin Instruments, Model BT-2043 Automated Battery Test System. The baseline and conditioning current for the cells was set at 200 mA throughout the experiments.

The impedance data on the cylindrical 2.5 Ah cells and some of the time domain data were taken using a Solartron 1280Z combined potentiostat/galvanostat and frequency response analyzer. Additional time domain data was taken with a Solartron 1470 battery analyzer/tester. These

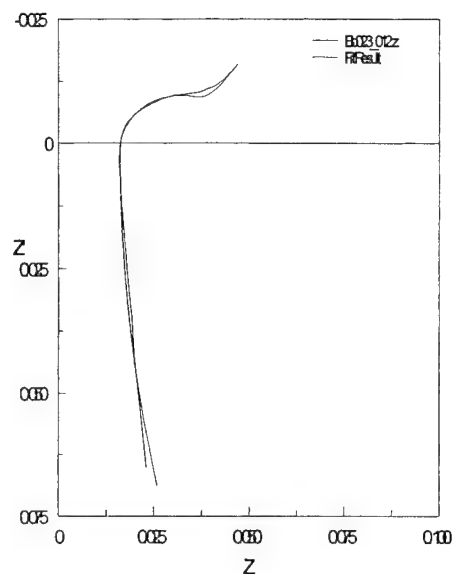


Fig. 2. Electrochemical impedance spectroscopy for a 2.5 Ah, R20 size lead-acid cell at 88% SOC. Real impedance ( $Z'$ ) vs. imaginary impedance ( $Z''$ ).

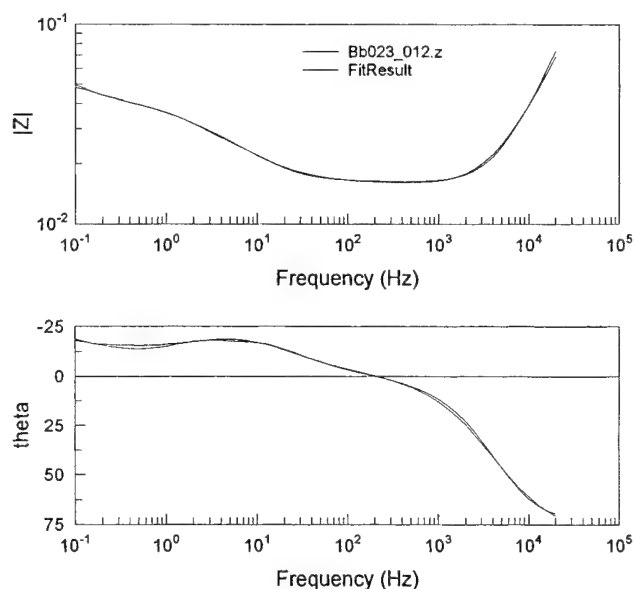


Fig. 3. Electrochemical impedance spectroscopy for a 2.5 Ah, R20 size lead-acid cell at 88% SOC. Magnitude and phase angle vs. frequency.

measurements were made over a frequency range of 0.01 Hz to 10 kHz with an ac amplitude of 10 mV. The time domain measurements were made using a square wave current of  $\pm 500$  mA and a period of 0.1 Hz.

## 8. Discussion

Fig. 2 shows a Nyquist plot for a 2.5 Ah, R20 size, cell at 88% SOC and Fig. 3 shows the Bode plots for both the

magnitude and phase of the impedance for the same cell and conditions of Fig. 2. The Fourier analysis of the impedance data shown in Figs. 2 and 3 resulted in the time domain response shown dashed in Fig. 4a. Also, Fig. 4a shows the measured time domain response of the cell as a solid line. As can be seen, the time domain response matches up quite well during the charging phase of the bipolar current pulse. However, during the discharging phase, the match is not as good. In order to get a better fit to the measured TDS data,

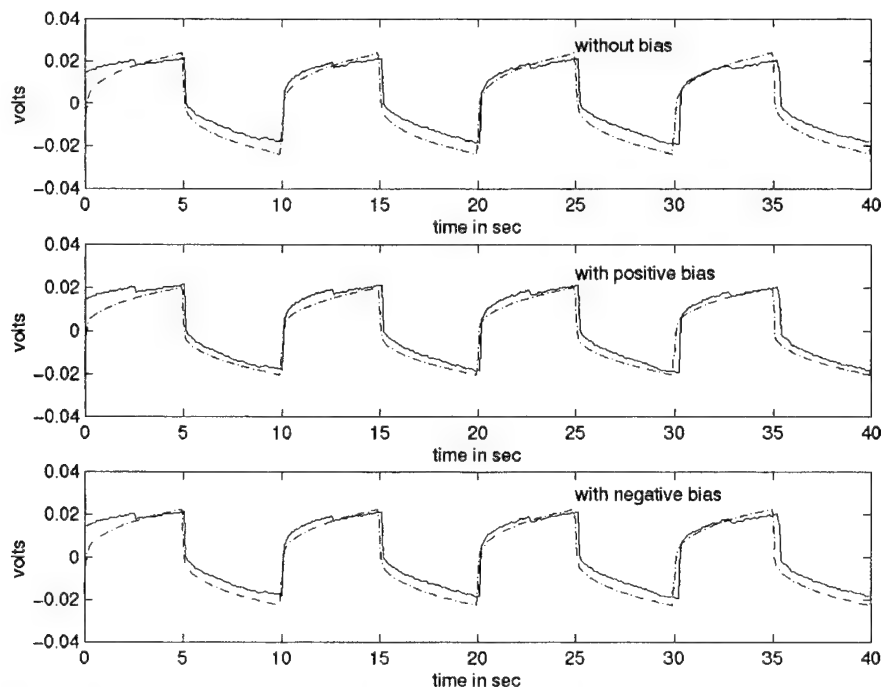


Fig. 4. Voltage response to a bipolar square-wave current obtained through Fourier synthesis technique for a 2.5 Ah, R20 size lead-acid cell. Dashed lines: computed; solid lines: measured results.





Element	Freedom	Value	Error	Error %
Rs	Free(+)	0.016048	8.6692E-5	0.5402
L1	Free(+)	5.6024E-7	3.6405E-9	0.64981
R3	Free(+)	0.49432	0.039841	8.0598
CPE1-T	Free(+)	60.67	2.9426	4.8502
CPE1-P	Free(+)	0.52469	0.026604	5.0704
C2	Free(+)	7.776	1.0188	13.102
R2	Free(+)	0.010493	0.0008137	7.7547
C1	Free(+)	2.349	0.19445	8.278
R1	Free(+)	0.0062609	0.00068376	10.921

Chi-Squared: 0.0014212  
 Weighted Sum of Squares: 0.14354

Data File: D:\aaTds\aeIS\_TDS\_data\Cell\_Bb023\Bb023\_012.z  
 Circuit Model File: D:\aaTds\aeIS\_TDS\_data\Zfit\Dd027.d.mdl  
 Mode: Run Fitting / Selected Points (0 - 54)  
 Maximum Iterations: 100  
 Optimization Iterations: 0  
 Type of Fitting: Complex  
 Type of Weighting: Calc-Modulus

Fig. 5. Electrochemical impedance spectroscopy, equivalent circuit model for a 2.5 Ah, R20 size lead-acid cell.

a voltage bias was added in the analysis. The results of the Fourier analysis with a +10 mV bias added is shown in Fig. 4b (dashed) and with a -10 mV bias added is shown in Fig. 4c (dashed). The figures show that the inclusion of a small, positive bias results in a better fit on the time domain discharge curve whereas a small negative bias results in a

worse fit than the zero bias case. This result suggests an inherent nonlinearity in the behavior of the cell as the applied bias is switched from a charging pulse to a discharging pulse.

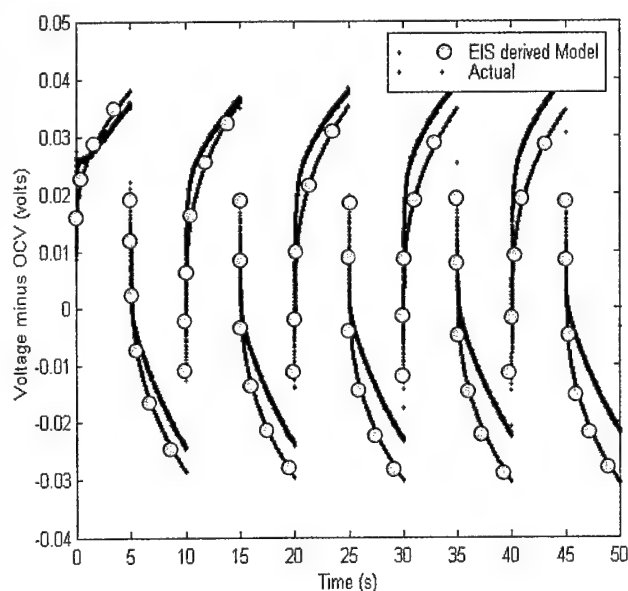


Fig. 6. Bipolar square-wave current for a 2.5 Ah, R20 size lead-acid cell. Voltage response minus open circuit potential.

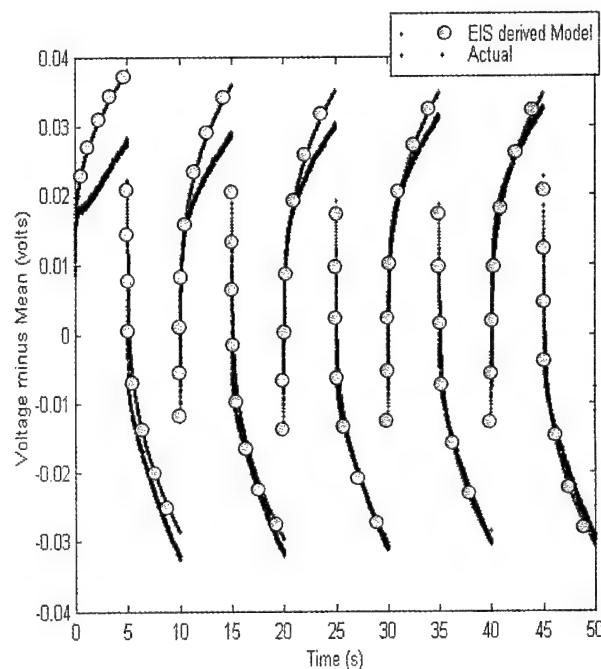


Fig. 7. Bipolar square-wave current for a 2.5 Ah, R20 size lead-acid cell. Voltage response minus mean potential.

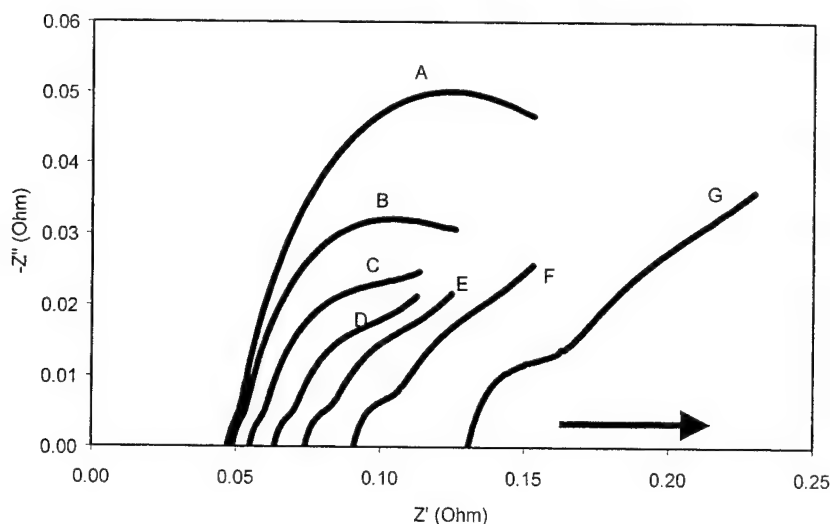


Fig. 8. Electrochemical impedance spectroscopy for a 2.0 Ah prismatic lead-acid cell during discharge cycles. Real impedance ( $Z'$ ) vs. imaginary impedance ( $Z''$ ). (A) 100% SOC; (B) 83% SOC; (C) 67% SOC; (D) 50% SOC; (E) 33% SOC; (F) 17% SOC; (G) 1% SOC.

The equivalent circuit of the 2.5 Ah cell was derived using Scribner Associates' Zview software. This equivalent circuit, which resulted in an excellent fit to the measured EIS data, comprises an ohmic series resistance, a series inductor in parallel with a resistor, a series CPE element, and two parallel  $R-C$  networks. It has been found that the equivalent circuit parameters vary in the anticipated manner with cell SOC. For example, the series resistance, which corresponds to the resistance of the cell's electrolyte increases as the cell SOC decreases. Details of the parametric variation with cell SOC will be reported elsewhere [7].

The time domain response of the cell calculated from the equivalent circuit of Fig. 5 (EIS derived) is shown in Figs. 6 and 7 together with the measured (actual) time domain response of the cell. The curves in Fig. 6 show the measured and the model-predicted cell voltage response curves with

the open-circuit voltage of the cells subtracted out, while Fig. 7 shows the corresponding curves with the mean potential subtracted out. Clearly the fit is much better when the voltage response is normalized against the mean potential of the cell. It is also noteworthy that the initial few cycles are of relatively poorer fit compared to later cycles. Furthermore, the discharge curve fit is much better than the charging portion of the cycles confirming the differing behavior of the cell to charging pulses compared to discharging pulses.

The ac impedance spectroscopy data presented in Figs. 8 and 9 show the shift from charge transfer controlled kinetics to diffusion controlled kinetics as the state of charge decreases for the prismatic lead acid cell. The data also shows the expected decrease in the electrolyte conductivity as the state of charge of the cell decreases. The data presented

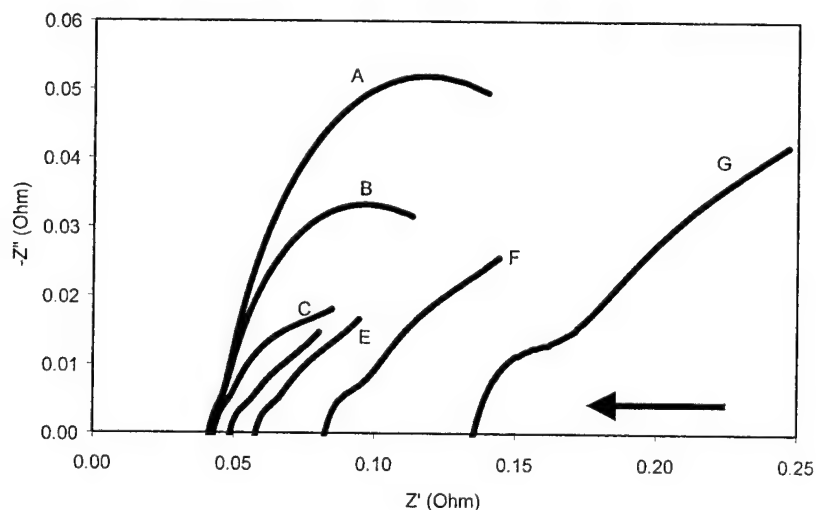


Fig. 9. Electrochemical impedance spectroscopy for a 2.0 Ah prismatic lead-acid cell during charge cycles. Real impedance ( $Z'$ ) vs. imaginary impedance ( $Z''$ ). (A) 100% SOC; (B) 83% SOC; (C) 67% SOC; (D) 50% SOC; (E) 33% SOC; (F) 17% SOC; (G) 1% SOC.

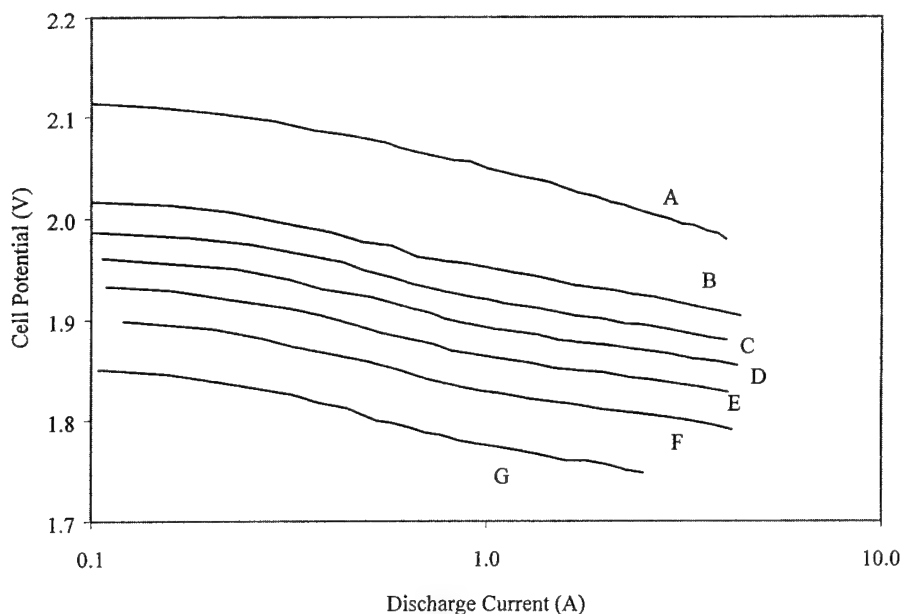


Fig. 10. Discharge polarization characteristics for a 1.0 Ah cylindrical lead-acid cell. (A) 100% SOC; (B) 83% SOC; (C) 67% SOC; (D) 50% SOC; (E) 33% SOC; (F) 17% SOC; (G) 1% SOC.

in Fig. 8 shows the complex impedance for the cell during discharge and Fig. 9 shows the complex impedance for the cell during charge. Comparison of the two sets of data show that at high (100 and 83%) and low (17 and 1%) states-of-charge (SOCs), the complex impedance is comparable. However, for SOC of 67, 50 and 33%, the data indicates reduced charge transfer for the charging cell compared to the discharging cell while conductivity remains comparable. The data also shows an increase in the complex impedance for the cell at high states of charge. This trend was found to be true for all lead-acid cells tested.

Figs. 10–13 show the discharge and charge polarization for lead-acid cells obtained through sweep voltammetry. A

comparison of the discharge characteristics (Figs. 10 and 12) of the cylindrical and prismatic lead-acid cell designs show the greater diffusional limits in the prismatic design during discharge. Figs. 11 and 13 shows that the polarization of both the cylindrical and prismatic cell designs are comparable during charge.

## 9. Conclusions and future plans

The two commonly utilized techniques of non-invasive interrogation of batteries and other electrochemical devices are impedance spectroscopy and time-domain spectroscopy.

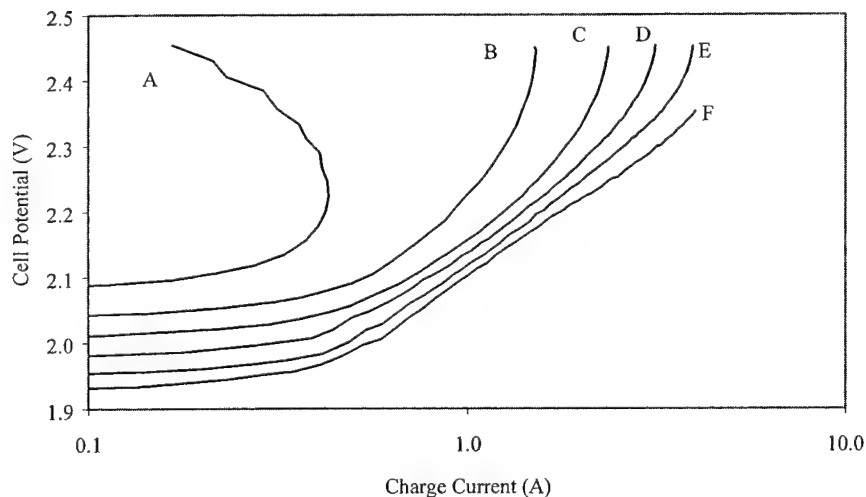


Fig. 11. Charge polarization characteristics for a 1.0 Ah cylindrical lead-acid cell. (A) 100% SOC; (B) 83% SOC; (C) 67% SOC; (D) 50% SOC; (E) 33% SOC; (F) 17% SOC; (G) 1% SOC.

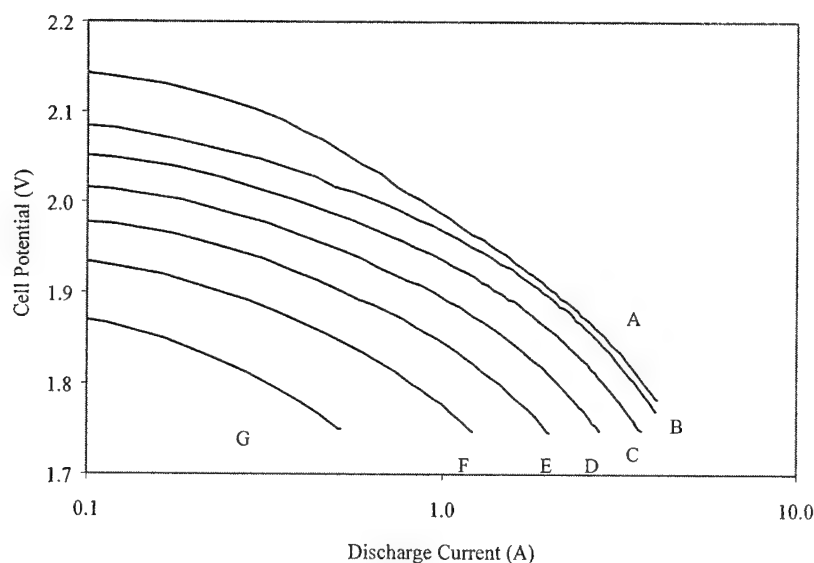


Fig. 12. Discharge polarization characteristics for a 2.0 Ah prismatic lead-acid cell. (A) 100% SOC; (B) 83% SOC; (C) 67% SOC; (D) 50% SOC; (E) 33% SOC; (F) 17% SOC; (G) 1% SOC.

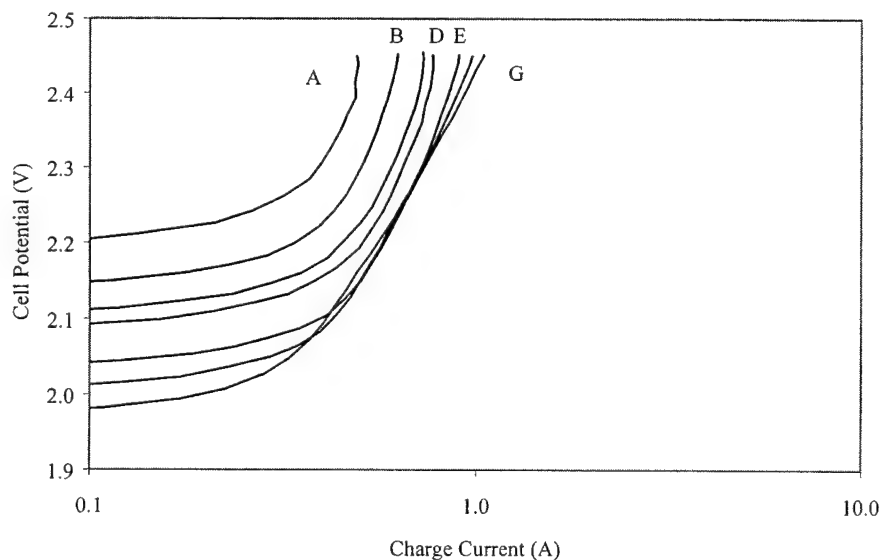


Fig. 13. Charge polarization characteristics for a 2.0 Ah prismatic lead-acid cell. (A) 100% SOC; (B) 83% SOC; (C) 67% SOC; (D) 50% SOC; (E) 33% SOC; (F) 17% SOC; (G) 1% SOC.

In this presentation, they have been shown to relate to the same fundamental properties of electrochemical systems and that the time-domain behavior can be derived from the impedance analysis. Each has some inherent advantages in certain applications, and combined they may provide some distinctive advantages. The data and techniques discussed will enable the fabrication of devices for determination of the SOC of small VRLA cells in the temperature and power range studied.

Other aspects of VRLA cells, for which we plan to seek support for additional studies, include temperature, aging, cycling, and charge techniques factors. In larger cells, there may also be orientation effects.

### Acknowledgements

Some of this work was funded through the Southern Coalition for Advanced Transportation under Model no. 35 to ARPA Contract no. MDA972-94-2-0003, dated 13 December 1993.

### References

- [1] J.R. McDonald, *Impedance Spectroscopy*, Wiley, New York, 1987.
- [2] W. Laletin, Private communication.
- [3] T.B. Atwater, L.P. Jarvis, P.J. Cygan, A.J. Salkind, Characteristics of thin film lead-acid cells, in: *Proceedings of the 7th ELBC Poster Session and Abstracts*, Dublin, Ireland, 19–22 September 2000.

- [4] S. Nelatury, S. Damodar, P. Singh, C. Fennie, D. Reisner, A.J. Salkind, A comparative study of time and frequency domain responses of spirally wound lead-acid cells, in: Proceedings of the 7th ELBC Poster Session and Abstracts, Dublin, Ireland, 19–22 September 2000.
- [5] J. Newman, W. Tiedemann, *AIChE J.* 21 (1975) 25.
- [6] W.B. Gu, C.Y. Wang, B.Y. Liaw, Numerical modeling of coupled electrochemical and transport processes in lead acid batteries, *J. Electrochem. Soc.* 144 (6) (1997) 2053–2061.
- [7] C. Fennie, S. Nelatury, Y.S. Damodar, P. Singh, D. Reisner, Time and frequency domain modeling of spirally wound lead acid cells, in preparation.
- [8] Commercial Product, Hawker North America, 617 N. Ridgeview Dr., Warrensburg, MO 64093-9301, USA.
- [9] Commercial Product, Portable Energy Products Inc., 940 Disc Drive, Scotts Valley, CA 95066, USA.
- [10] Commercial Product, Bolder Technologies, Corp., 4403 Table Mountain Dr., Golden, CO 80403, USA.

# Energy sources for the future dismounted soldier, the total integration of the energy consumption within the soldier system

Jillis W. Raadschelders<sup>a,\*</sup>, Tiny Jansen<sup>b</sup>

<sup>a</sup>*Department of Energy Technology, TNO-Environment Energy and Process Innovation, P.O. Box 3427300, AH Apeldoorn, The Netherlands*

<sup>b</sup>*Royal Netherlands Army, Army Staff, Directorate of Policy and Planning, Soldier Modernisation Programme, Bernhard kazerne Barchman Wuytierslaan, 198 3818 LN Amersfoort, The Netherlands*

Received 19 December 2000; accepted 19 December 2000

## Abstract

At present, the energy supply for the electronic equipment of the soldier is problematic. Each component has its own battery pack. These battery packs are not interchangeable and each requires its own charger. Furthermore, because they are all dimensioned to deliver the peak power for each item of equipment, this leads to a higher battery weight than necessary.

It is expected that the system of the future soldier will use a central power source to supply the energy for all the different components. An energy bus will be integrated within the soldier's system for this. The different components will generate their required voltages from the bus voltage by using high efficiency dc/dc converters. The use of an energy bus with local voltage conversion will facilitate interoperability between different forces. The energy sources can easily be exchanged.

For the near future, batteries are still considered to be the best option for the energy source. Rechargeable batteries are preferred above non-rechargeable ones due to logistic and environmental problems. For the long-term replacement of batteries, the direct methanol fuel cell (DMFC) is considered a viable option.

Several different battery packs were tested for their capability to supply both the required energy and power during a 24 h mission. The tests were carried out with a controlled power method, as maximum power should be deliverable during 10% of the operation time. © 2001 Elsevier Science B.V. All rights reserved.

**Keywords:** Applications/portable military equipment; Energy sources/choosing; Fuel cells/direct methanol; Portable batteries

## 1. Current operational system

Presently, soldiers of the Royal Netherlands Army (RNLA) as well as many other armies are equipped with an operational package of "separate best systems". The RNLA has always adopted a policy of purchasing the best available option for specific systems.

For the energy supply this has resulted in a situation with the following disadvantages.

- A variety of systems, each with its own energy source.
- The soldier has to carry several different batteries — which battery belongs to which system?
- Infrastructure — various types of batteries must be in storage and distributed in the field.
- Within each component, the current/power management systems are mostly low efficiency variable resistances.

These resistances convert the excess voltage of the energy sources into heat.

## 2. The challenge of an integrated system

This challenge may be defined as "To integrate all the different energy requirements into one, light weight, modular energy source for the future dismounted soldier".

So, one energy source powers all the different components (Fig. 1). The soldier is equipped with an energy bus. This could very well be integrated with the communication network also under development at TNO. The bus is supplied by different energy sources, operating at a set voltage. The different electronic components required by the future soldier are connected to this energy bus. Within each component the current/power management system, is replaced by a highly efficient dc/dc converter.

Representative energy/power requirements in the future for the Dutch dismounted soldier are

\* Corresponding author. Tel.: +31-55-549-37-38; fax: +31-55-549-37-40.

E-mail address: j.w.raadschelders@mep.tno.nl (J.W. Raadschelders).

Operation time	24 h
Energy consumption	400 Wh
Power	0–45 W

The expected duration of maximum power is 10% of total operation time in periods of 1, 2 or 3 min.

### 3. Advantages of an integrated system

#### 3.1. Inter-operability

Due to the ever increasing participation of the RNLA in international operations (NATO, UN) the RNLA has a need for inter-operability of its soldier system with those of other countries. The concept of the energy bus with local high efficiency dc/dc converters enables easy exchange of energy sources. The only demands laid down on each possible energy source are

- operating voltage within the possible input window of the dc/dc converters;
- connector compatible with the connectors used for the energy bus.

#### 3.2. Operating temperature window of the energy source

The required temperature window has until now been going as low as  $-40^{\circ}\text{C}$ . There are virtually no rechargeable



Fig. 1. Integration of power requirements on the future soldier.

batteries which can meet this without losing a significant part of their rated capacity at  $20^{\circ}\text{C}$ .

The energy grid concept allows the positioning of the energy sources at any place in the soldier's system. If this place is chosen close enough to the body heat might be sufficient to keep the operating temperature of the energy source above  $0^{\circ}\text{C}$  or even above  $+10^{\circ}\text{C}$ .

#### 3.3. Energy source changes during missions

With the present system, each component has its own energy source, with its own operating time. This means that at different time intervals the soldier has to change the energy source of a component. During this operation, the soldier is inactive/not using equipment and also the component is inactive. The future soldier system circumvents this problem by utilising a central energy source.

#### 3.4. Gradual implementation of the system

The implementation of an energy network can be done gradually. There is no need to replace all systems which are currently in use. Only the replacement of the power management system is required. This also does not have to be done all at once. The energy network can be used together with all the operational systems.

#### 3.5. Grid/bus voltage

The voltage on the energy grid will vary with energy consumption. The possible operating window depends on the input voltage window of the converters being used, or vice versa!

The efficiency of the converter depends on its input voltage and input voltage window.

General dc/dc converters in high volume production have input windows of between 9 and 18 V or even between 9 and 36 V. This allows the use of four, series connected, Li-ion cells, to give a 16.8–11.0 voltage window (4.2–2.75 V per cell).

### 4. System electronics

Prior to leaving for a mission, the soldier connects all the energy sources he requires for his mission. The system connects only one energy source directly to the bus, only one being used at a time. After the first one is empty, or fails, the system switches to the next energy source. This will prevent the future soldier from returning with half empty battery packs. Instead, the soldier will have both empty and full battery packs if he returns early from his mission. LED indicators will show which battery packs should be changed and which ones have not been used.

The regulating electronics of the energy network have to fulfil several requirements.

- Uninterruptable power supply to the energy bus.

- Single operating energy source.
- Automatic switching between energy sources.
- Protection of energy sources.
- Minimal energy consumption.

When the energy source that is connected to the bus fails, instantaneously the system electronics have to be able to maintain a minimum voltage on the bus. Switching times of state-of-the-art relays are too long to prevent a reboot of computer systems. For a normal decrease in the output voltage of an energy source, the system can switch to another source before the first reaches its lower operating point.

To avoid having all battery packs half empty, only one may be used at a time. The monitoring of the batteries is made easy since they have comparable duty cycles.

The switching between energy sources must be done automatically. This avoids distracting the soldier at inconvenient moments.

The life cycle of rechargeable batteries decreases when they are discharged too far. The electronics have to disconnect the packs before this happens. A manual override may be introduced for emergencies. The electronics are to be designed to minimise energy consumption of the total system.

#### 4.1. Power management of components

To be able to introduce this soldier systems energy network, several alterations to the existing equipment are required. The power management sections of the different items presently in use have to be replaced. The new power management sections will have to consist of at least a dc/dc converter and an emc filter. The dc/dc converter might have to have multiple output voltages if more than one operating voltage is required within an equipment.

### 5. Possible energy sources

The “energy sources” project began with the selection of possible energy sources for the dismounted soldier.

The following points of consideration were used to select the possible energy sources:

- weight;
- volume;
- stage of development;
- different signatures on the battlefield (sound, radiation, thermal).

By not meeting these requirements, a thermophotovoltaic system operating at 2000°C, the quasiturbine or a small nuclear power plant are considered not to be realistic options. Also noisy transportable generators, mostly of >100 W output, were not put on the list of realistic options,

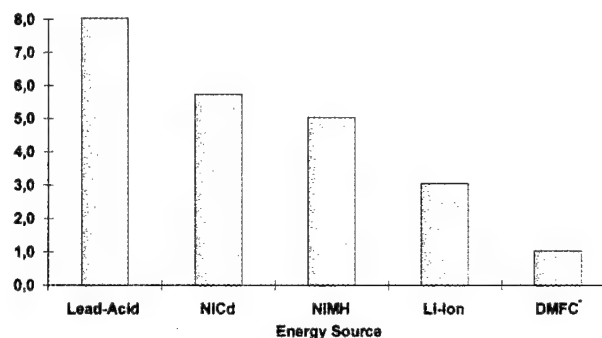


Fig. 2. Weights of rechargeable energy sources for a 24 h mission.

as well as human power and some other less realistic options.

This led to the following short list of possible energy sources (Fig. 2):

- for the near future batteries are still the desired energy sources;
- for the long term future fuel cells are considered to be able to replace most batteries.

Our conclusion from this survey is that the direct methanol fuel cell (DMFC) is the expected long-term solution.

#### 5.1. Batteries

For the near future, batteries are still the energy source of choice. Rechargeable batteries are preferred above non-rechargeable ones due to the logistic problems with non-rechargeable batteries. The recharging is more easily dealt with, and in most cases logistic fuels are used to power the battery chargers. However the specific energy ( $\text{Wh kg}^{-1}$ ) of non-rechargeable batteries is generally higher than that of rechargeable batteries.

#### 5.2. Fuel cells

In the long term, in a number of applications, batteries are expected to be replaced by fuel cells or combinations of both.

The fuel cell for the soldier application can be either a solid polymer fuel cell (SPFC) or a direct methanol fuel cell Fig. 3, using, respectively, hydrogen and methanol as fuel. Other fuel cell types are not suitable due to their high operating temperature.

The fuel cell principle enables a separation between power and energy. The maximum required power determines the size of the fuel cell, the required energy for a mission determines the amount of fuel to be carried. The specific power ( $\text{W kg}^{-1}$ ) of the SPFC is roughly twice that of the DMFC. This means the DMFC will be twice the size and weight than that of the SPFC, for the same power output.



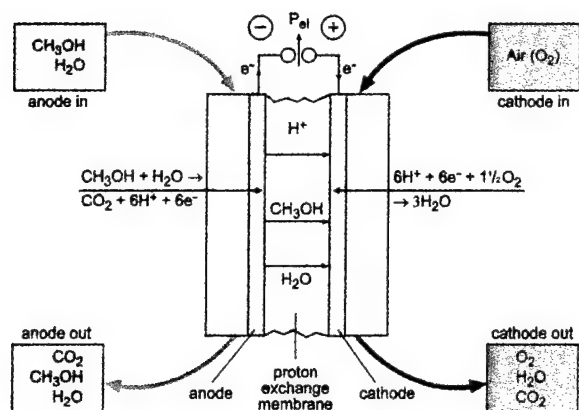


Fig. 3. Schematic representation of the reactions in the direct methanol fuel cell.

Table 1  
Properties of fuel

Fuel	Specific energy (Wh kg <sup>-1</sup> )	Density (kg dm <sup>-3</sup> )	Energy density (Wh dm <sup>-3</sup> )
Methanol	5500 <sup>a</sup>	0.8	4400
Hydrogen (pure)	32800 <sup>a</sup>	8.9 × 10 <sup>-5</sup>	2.94
Hydrogen (pressurised)	<350		
Metal hydride	<600		

<sup>a</sup> These values do not include auxiliary equipment.

Hydrogen can be packed either as liquid, pressurised or as a metal hydride. Methanol is a liquid and has a very high specific energy (Wh kg<sup>-1</sup>), see Table 1.

## 6. Problems with fuel cells

For the long term, a partial replacement of the batteries by fuel cells is expected, but they have some specific challenges, besides the technical ones.

### 6.1. Air supply to the fuel cell.

When a soldier operates within wet areas, the air supply to the fuel cell may be temporarily blocked. This would stop the energy supply to all of the components of the soldier system. One possible solution would be to utilise small rechargeable battery packs to overcome these periods of air supply blockage.

This introduces the requirement for a sophisticated electronic circuit. The fuel cell voltage window is rather large — compare 4.1–2.75 V for a single Li-ion cell.

### 6.2. Methanol fuel

Hydrogen, in any of the storage methods, is not considered a viable option for fuel supply. Methanol is a liquid and therefore can be easily stored and transported. In some countries it is used as car fuel (sometimes mixed with gasoline). However, methanol is toxic and must not be consumed.

## 7. Experimental testing

On the basis of the short list of options, a test programme was developed to obtain insight into the performance and problems to be expected from the use of batteries and, in a later stage, fuel cells. The experiments were carried out with Digatron BTS600 battery test equipment, so enabling us to use fully reproducible test sequences. The computer can control current, potential and power, both for charge and discharge. The test profiles are scaled to the nominal energy content of the tested battery packs.

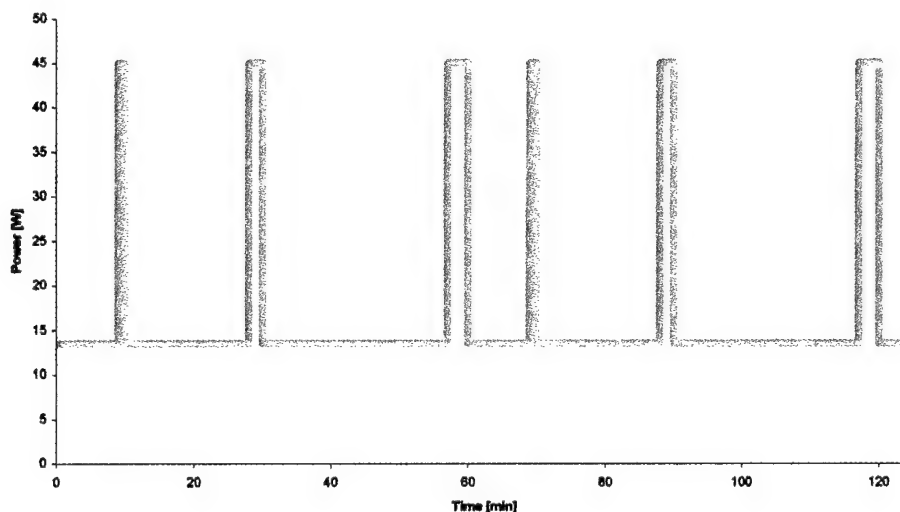


Fig. 4. Load profile for SMP application. 13.5 W continuous, plus three distributed single 21.5 W pulses of 1, 2 and 3 min duration every hour.

Table 2  
Battery packs tested<sup>a</sup>

Battery chemistry	Non-rechargeable (NR/R)	Cell capacity (Ah)	Cell voltage (max–min) (V)	Battery capacity (Ah)	Battery voltage (V)	Battery energy (Wh)	Battery weight (kg)	Specific energy (Wh kg <sup>-1</sup> )
Alkaline	NR	10	1.3–0.7	10	8.0–3.5	80	0.70	114
Li-SOCl <sub>2</sub>	NR	13	3.7–2.0	39	7.4–4.0	280	0.60	465
Li-SO <sub>2</sub>	NR	7.5	3.0–2.0	37.5	15.0–10.0	560	2.30	245
Li-ion <sup>b</sup> (1)	R	5.5	4.1–2.7	5.5	16.4–11.0	80	0.60	135
Li-ion(2)	R	5.0	4.2–2.7	5.0	16.8–11.0	70	0.50	144

<sup>a</sup> The values in this table are the nominal values, supplied by the manufacturers.

<sup>b</sup> These Li-ion cells showed peculiar behaviour after cycling at –10°C and tests were stopped with these battery packs.

Table 3  
Weights of the battery packs<sup>a</sup>

Battery	Weight (kg)
Alkaline	3.50
Li-SOCl <sub>2</sub>	0.86
Li-SO <sub>2</sub>	1.51
Li-ion <sup>b</sup> (1)	2.96
Li-ion(2)	2.78

<sup>a</sup> These numbers do not include any packaging, protection or external wiring of the battery packs.

<sup>b</sup> These Li-ion cells showed peculiar behaviour after cycling at –10°C and tests were stopped with these battery packs.

The operational requirements for the future soldier system (SMP), led to the repetitive power versus time test profile shown in Fig. 4 (see Table 2).

The nominal values for the specific energy of the different batteries are used to calculate the required battery weight for an energy content of 400 Wh (see Table 3).

The rechargeable battery packs are full-scale test packs. They have an operating voltage of 16.8–11.0 V, and should be capable of delivering the maximum power requirement of 45 W, required by the SMP system. The energy content of the battery pack determines how many repetitive 1 h discharge cycles (Fig. 3) it can, or should be able to, deliver. Other batteries are being, or will be tested in the near future. Results will be presented when they will be available.

## 8. Results

### 8.1. Charging and discharge capacities of the rechargeable battery packs

Capacity tests have only been done with the rechargeable battery packs. The non-rechargeable batteries were only tested with the actual load profile. The following capacities were obtained (see Table 4).

Both charging and discharging was done at the stated temperatures. Future tests of the discharge capacities at different temperatures will include charging at room temperature. Several battery manufacturers do not recommend the charging Li-ion batteries below 0°C. Fig. 5 shows the room-temperature performance of a single Li-ion cell from manufacturer 1, at constant current loads between 1 and 5 A.

### 8.2. Voltage–time profiles obtained during the SMP test

#### 8.2.1. Room temperature (20–25°C)

The Li-ion battery pack from manufacturer 1 was able to deliver the required power, 13.5 W continuous and 45 W pulsed, for 4 h. A total of 4.5 Ah and 67 Wh were supplied by the pack in that period, 84% of its nominal capacity.

The Li-ion battery pack from manufacturer 2 was able to deliver the required power for a little over 4 h. A total of 4.8 Ah and 69 Wh were supplied by the pack in that period, 96% of its nominal capacity.

Table 4  
Performance of Li-ion batteries at different currents and temperatures

Discharge current (A)	–10°C Li-ion(1)		0°C Li-ion(1)		20–25°C Li-ion(1)		20–25°C Li-ion(2)	
	In Ah	In Wh	In Ah	In Wh	In Ah	In Wh	In Ah	In Wh
1	4.16	13.8	5.17	19.0	5.58	21.1	4.79	17.5
2	3.97	13.0	5.03	17.9	5.60	21.0	4.87	17.6
3	3.60	11.7	5.18	18.1	5.60	20.7	4.86	17.2
4	3.36	10.7	5.17	17.8	5.59	20.5	4.85	16.8
5	3.25	10.2	5.15	17.5	5.57	20.2	4.83	16.4

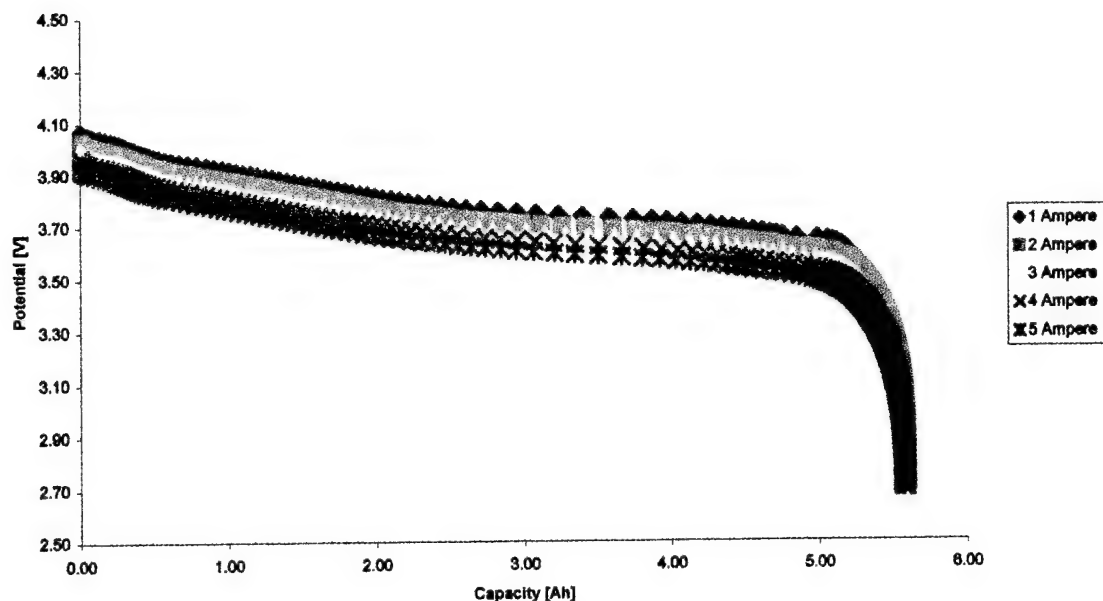


Fig. 5. Voltage vs. withdrawn capacity for different discharge currents from a Li-ion(1) cell.

The alkaline batteries were capable of supplying energy for 10 h under load. The maximum power obtained was 7 W (three-seventh of the continuous load profile). Total delivered energy and capacity was 32 Wh and 5.5 Ah. The nominal values were 75 Wh and 10 Ah. So, only 42% of the theoretical energy was released.

The Li-SOCl<sub>2</sub> battery showed very poor rate capability. The power rating of the test profile had to be scaled down to a 7 W continuous/20.5 W pulse profile. The pack was able to supply energy at this rate for 15 h. Total delivered energy and capacity was 125 Wh and 19.7 Ah. The nominal values were 280 Wh and 39 Ah. So only 45% of the theoretical energy was released.

The Li-SO<sub>2</sub> battery pack had an extremely flat voltage profile. During the required 24 h of the SMP cycle it showed no significant voltage decrease (Fig. 6). However, the battery pack was over-rated at 560 Wh instead of the required 400 Wh. In consecutive 30 h, it delivered 500 Wh, so 90% of the theoretical energy was released. The Li-SO<sub>2</sub> battery also showed good performance at the maximum power level.

#### 8.2.2. Low temperature

The Li-ion battery pack(1) was able to deliver the full-required power, 13.5 and 45 W for 2 h at  $-10^{\circ}\text{C}$ . A total of 2.5 Ah and 33 Wh were supplied by the pack in that period,

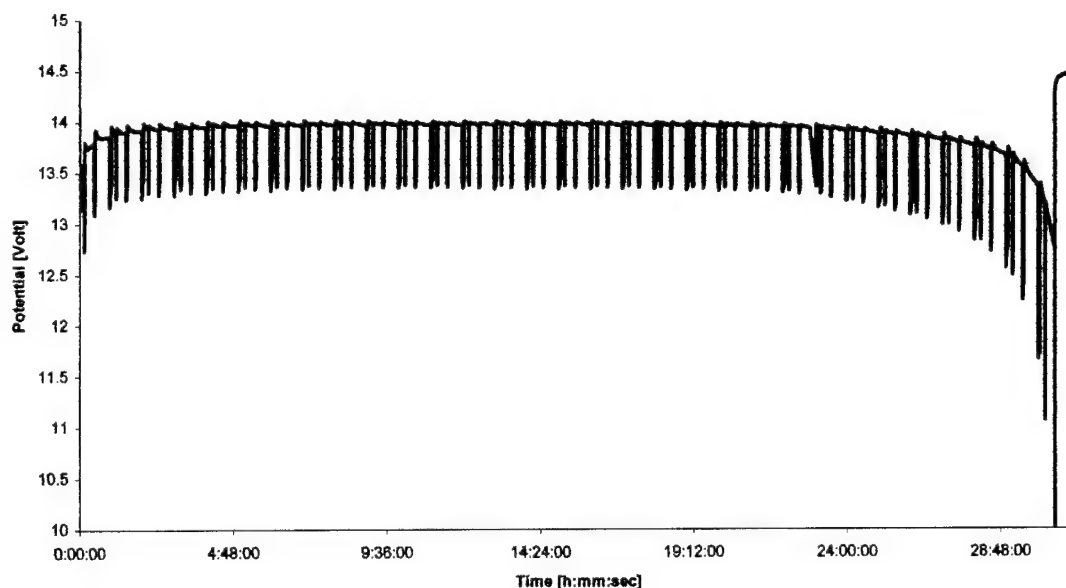


Fig. 6. 12 V, 37.5 Ah Li-SO<sub>2</sub> battery pack discharged at room temperature to the SMP profile of Fig. 4.

42% of its nominal capacity. That is only 50% of the energy released at room temperature. The pack showed dimensional changes after charging at  $-10^{\circ}\text{C}$  and the tests were stopped.

## 9. Future research

The Li-ion packs will be tested for their performance at low and high temperatures. Charging at low or high temperatures will be investigated and also the effects of charging at room temperature followed by discharge at low or high temperature.

We will be testing the battery packs at different temperatures to determine their cycle lives. Discharge will be carried out to the SMP profile and charging according to the charge regime given by the manufacturer.

Decrease in capacity and rate capability will be monitored by capacity tests at various constant currents. A first version of the electronic power control unit will be tested in 2001. Integration of actual soldier equipment with the energy grid is also scheduled for 2001.

The possible operating conditions of the energy source will be determined in close co-operation with the TNO institutes involved in the development of different soldier system components. Special attention will be given to the operating temperature and the possibilities for influencing its lower limit.

## 10. Conclusions

The integration of the energy consumption of the soldier system has several advantages.

- Each separate component can become lighter and smaller, the energy source can be placed more comfortably, the soldier has less concern about the changing of batteries for all his systems. The total energy consumption of the system can be reduced by implementing high efficiency power management (dc/dc converters) within the separate

components, hence reducing the amount of energy the soldier has to carry.

- National Forces are more and more faced with international operations. The principle of the energy network for the future dismounted soldier would enable more interoperability between European and International forces. The system requires only small stepwise changes towards operational systems, not complete replacement at one time.
- It enables easy modernisation of equipment in the future.
- The specifications for the energy source allows the use of a wide variety of possible energy sources. On the other hand it also enables more and more uniformity in the operational energy sources.
- Batteries are still considered the best option for the near future. Rechargeable ones are preferred. For the long-term future it is believed that the direct methanol fuel cell holds enough promises to become a viable option. The use of liquid methanol on the future battlefield is considered more realistic than using hydrogen, in any form.
- Batteries, or any energy source, for the energy network have to comply with only a few specifications: (a) Their operational voltages must lie within the input voltage window of the dc/dc converters used. (b) They must be able to deliver both the power and energy required by the specifications.

The experiments showed good performance of the two Li-ion battery packs at room temperature. However their capacity dropped significantly at lower temperatures, where charging becomes problematic. Charge time increases highly and one of the Li-ion battery packs showed dimensional changes after being charged at  $-10^{\circ}\text{C}$ .

## Acknowledgements

We would like to thank the RNLA and the TNO-Defence Research Organisation for their financial support of this project.



ELSEVIER

Journal of Power Sources 96 (2001) 167

JOURNAL OF  
**POWER  
SOURCES**

[www.elsevier.com/locate/jpowsour](http://www.elsevier.com/locate/jpowsour)

### Abstract

## Development of an intelligent rechargeable lithium-ion battery and charger system for military applications

Quintin Moore

*Lincad Ltd., Cornwall House, 8 Albany Park, Camberley, Surrey GU16 7AF, UK*

---

### Abstract

Development of a power system based upon lithium-ion technology for military applications requires expertise in cell, battery and charging systems to provide the optimum integrated power solution. To achieve this objective, Lincad Ltd. has teamed with SAFT (UK) to develop the Extended Capability Lithium-Ion Power System (ECLIPS). The first application for the ECLIPS solution is under a contract from the UK MoD for the development of a rechargeable lithium-ion battery and charger system for a new generation of portable electrical equipment for the British Armed Forces.

To satisfy this new requirement, which could replace current in-service primary and secondary power systems, the ECLIPS team proposed the 24 V; 12 Ah lithium-ion battery from the ECLIPS battery range. This is supported by the ECLIPS charger which provides for the fast charging of the ECLIPS battery and existing in-service nickel/cadmium batteries.

In addition to the key benefits provided by a lithium-ion solution, namely increased capacity, reduced weight and a more compact solution, other major factors are involved in the development of ECLIPS to fully satisfy the requirements of a military power solution. These factors include optimisation of cycle life, cell balancing and protection, high accuracy capacity gauging, communications to hosts and charger, also charging rates, all to meet the mission requirements of a military power solution.

The key development aspects associated with the development of the ECLIPS power solution through to the generation of the initial production of batteries and chargers will be discussed in the paper. © 2001 Published by Elsevier Science B.V.

**Keywords:** Lithium-ion batteries; Applications/military communications

---

---

*E-mail address:* [sales@lincad.co.uk](mailto:sales@lincad.co.uk) (Q. Moore).

# Renewable energy systems based on hydrogen for remote applications

K. Agbossou<sup>\*</sup>, R. Chahine, J. Hamelin, F. Laurencelle, A. Anouar,  
J.-M. St-Arnaud, T.K. Bose

*Institut de recherche sur l'hydrogène, Université du Québec à Trois-Rivières, P.O. Box 500, Trois Rivières, Que., Canada G9A 5H7*

Received 5 December 2000; accepted 15 December 2000

## Abstract

An integrated renewable energy (RE) system for powering remote communication stations and based on hydrogen is described. The system is based on the production of hydrogen by electrolysis whereby the electricity is generated by a 10 kW wind turbine (WT) and 1 kW photovoltaic (PV) array. When available, the excess power from the RE sources is used to produce and store hydrogen. When not enough energy is produced from the RE sources, the electricity is then regenerated from the stored hydrogen via a 5 kW proton exchange membrane fuel cell system. Overview results on the performances of the WT, PV, and fuel cells system are presented. © 2001 Elsevier Science B.V. All rights reserved.

**Keywords:** Hydrogen; Renewable energy; Wind turbine; Photovoltaic array; Electrolyzer; Fuel cells

## 1. Introduction

The last few years have seen the development of renewable energy (RE) systems based mainly on wind and solar power. Such systems are especially relevant to off-network communities, and remote areas like the Canadian north, which is particularly sensitive to pollution. These RE systems rely on highly transient energy sources and exhibit strong short-term and seasonal variations in their energy outputs. They thus need to store the energy produced in period of low demand in order to stabilize the output when the demand is high. While batteries are most commonly used for this purpose, they typically lose 1–5% of their energy content per hour and thus can only store energy for short periods of time [1,2]. There are presently no practical means available for long-term storage of excess electrical energy produced by the RE sources.

Few studies are related to the use of hydrogen for the electrical energy produced by RE sources such as wind and solar power [3–7]. This is being investigated at the hydrogen research institute (HRI). Hydrogen is produced by an electrolyzer powered by the excess electrical energy from the RE source. The hydrogen can then be used to feed an energy conversion device (such as a fuel cell or an internal combustion engine), which will act as a secondary power source in

periods of high demand. Such a system is set up at HRI for remote areas applications such as communication stations. The RE sources at HRI are a wind turbine (WT) capable of generating a maximum electrical power of 10 kW and photovoltaic (PV) cells of 1 kW maximum power. The excess energy available from the RE sources is directed to an electrolyzer. The hydrogen produced is then stored in a pressurized tank. This hydrogen is then fed to a proton exchange membrane fuel cell (PEMFC) system [7] that would be used as a load-leveling electrical system when unfavorable weather conditions arise.

The objectives of these studies include the development and experimental testing of the best methods for design optimization and control strategies. Here, we present an overview of the PEMFC system, the hydrogen production and storage subsystem. The integration of the fuel cell into a power source for the remote communication station is also discussed.

## 2. Description

A schematic of the complete RE system is presented in Fig. 1. It includes the following components:

1. An hybrid energy system from Bergey Windpower Co, model Excel. This is composed of a permanent magnet WT that can deliver a maximum output power of 10 kW. The wind system is coupled to a PV array that can

<sup>\*</sup> Corresponding author. Tel.: +1-819-376-5011/ext. 3911;  
fax: +1-819-376-5164.  
E-mail address: kodjo\_agbossou@uqtr.quebec.ca (K. Agbossou).

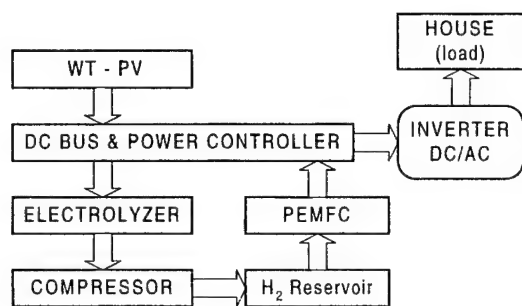


Fig. 1. RE system diagram.

deliver a maximum output power of 1 kW. The voltage produced by these sources is regulated and converted to a 48 V on a controlled dc bus. A set of deep-discharge batteries, connected in a series/parallel configuration, act as a buffer between the load and the power sources.

2. A 5 kW electrolyzer made by Stuart Energy Systems that can deliver up to  $1 \text{ m}^3 \text{ h}^{-1}$  of purified hydrogen compressed at 7 bars.
3. The hydrogen is further compressed to 10 bars, and directed to a storage tank of  $3.8 \text{ m}^3$  (water capacity). This represents 125 kWh of stored energy based on high heating values (HHV) (the maximum energy density of  $\text{H}_2$  is  $285 \text{ kJ mole}^{-1}$ ).
4. A 5 kW-24 V dc Ballard fuel cell stack model MK5-E.
5. Some 48 V deep-discharge batteries for voltage stabilization.
6. A dc bus controller that includes the batteries for energy transfer.
7. An intelligent dc-ac inverter that can deliver a constant 60 Hz 115 V output to the load.

In addition to the above basic system, we use a 10 kW Elgar programmable source to simulate the output of the WT-PV power sources for a given set of wind speed and sunlight data. In order to make preliminary tests on the fuel cell system, we use a 12 kW water-cooled TDI-Dynaload programmable load.

Each component of the RE system was tested under real operational conditions. We also investigated different operational strategies. The control system is composed of a dc bus and a power controller. The dc bus receives the electricity from the WT, PV array and fuel cells. The load, the electrolyzer and the compressor are connected to the same bus. A battery array maintains the stability of the voltage on the bus. The test bench controller manages the available power and the load demand.

### 3. Hydrogen production and storage subsystem

The electrolysis process is inherently clean and efficient. The hydrogen production rate of the electrolyzer is  $1 \text{ N m}^3 \text{ h}^{-1}$  at 5 kW input. Figs. 2 and 3 show, respectively, the polarization curve for two different temperatures and the operating curves (voltage, temperature and hydrogen flow) of the electrolyzer. The electrolyzer efficiencies without compressor are 65% at ambient temperature around  $23^\circ\text{C}$  and 71% for  $55^\circ\text{C}$ . These efficiencies decrease by 5% when the hydrogen is compressed. Compressor drive currents are the ripples on the current curve of Fig. 3. Thus, for an average wind speed at the test location of  $6 \text{ m s}^{-1}$  which translates in an average WT power of 2 kW, the hydrogen production rate is about  $0.4 \text{ N m}^3 \text{ h}^{-1}$ . This is fed from the buffer tank via a compressor to the hydrogen storage system

Hydrogen Research Institute

#### Electrolyser polarization curves Test with programmable power source

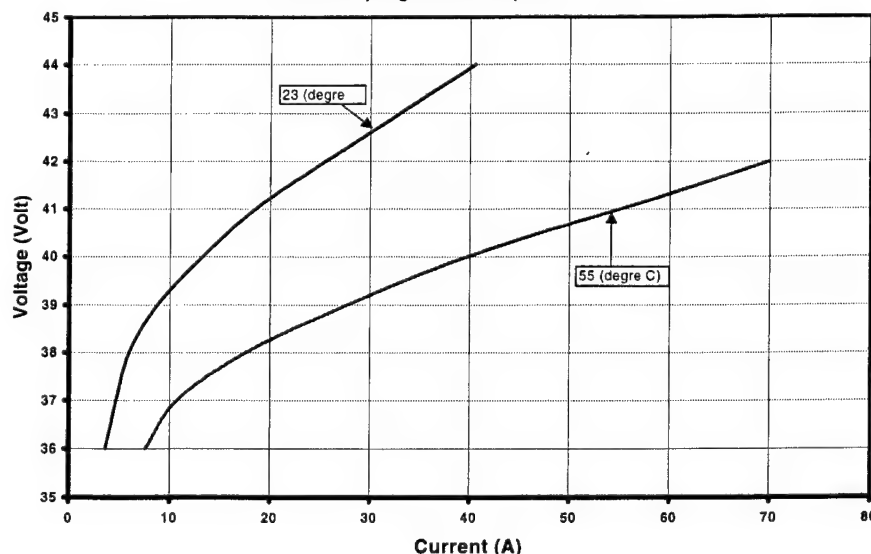


Fig. 2. Electrolyzer polarization curves.

Hydrogen Research Institute

### Operating curves of the electrolyzer Test with programmable power

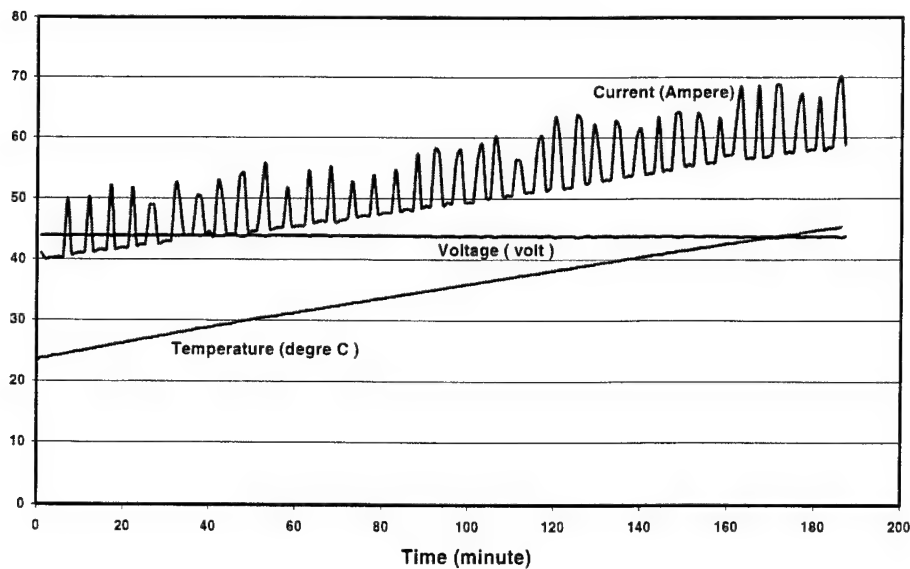


Fig. 3. Operating curves of the electrolyzer.

at 10 bar. In addition to the low-pressure storage, we are also testing a high-pressure storage option at 207 bar using a small high-pressure compressor made by FuelMaker Corporation. It has a  $4.5 \text{ N m}^3 \text{ h}^{-1}$  flow and uses 1.6 kW input power. The compressed hydrogen will be stored in seven high-pressure tanks of 110 L each. This represents  $154 \text{ m}^3$  of hydrogen at normal temperature and pressure and a capacity of 507 kWh.

Hydrogen is considered the fuel of the future and many resources have been invested in the development of advanced production and storage. Other storage techniques are under development at our institute. Nanocrystalline metal hydrides can be used advantageously as safe, reversible, hydrogen storage materials and can contribute significantly to an environmentally clean storage energy technology [8]. It is characterized by the presence of a large number of grain boundaries and interfaces which confer to this alloy enhanced kinetics and volumetric hydrogen packing densities. Physisorption on carbon offers a promising avenue for lowering the storage pressure of compressed gas fuels such as hydrogen [9]. The recent advent of carbon nanotubes capable of storing large amounts of hydrogen similar to the amount absorbed by metal hydrides at ambient pressure and temperature makes the adsorption storage technology quite promising.

#### 4. WT system and hydrogen production

The WT is installed on a 30 m tower. The production of electricity starts from a minimum wind speed of about  $3.4 \text{ m s}^{-1}$  and reaches the maximum rated output power of 10 kW for winds attaining  $13.0 \text{ m s}^{-1}$ . Fig. 4 represents

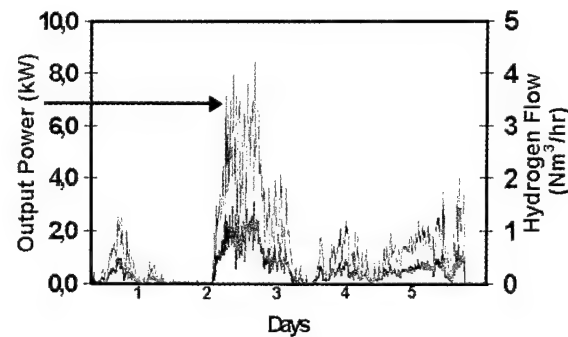


Fig. 4. Hydrogen flow and output power versus time.

the power output during a 5-day period. The figure also shows the corresponding hydrogen production during the same period when all produced electricity is fed to electrolyzer.

The efficient operation of the WT station requires a minimum amount of information about the wind characteristics. The anemometer on the WT tower at a height of 15 m provides these data. The information on the wind characteristics at our observation site is obtained by measuring wind speed (with a NRG Systems anemometer) every 2 s and obtaining an average every 10 min.

#### 5. Load-leveling electrical system

This part of the system is composed of a 5 kW fuel cells system connected to the dc bus, via a regulated dc/dc converter (24/48 V) designed at our institute and acts as a load-leveling device.



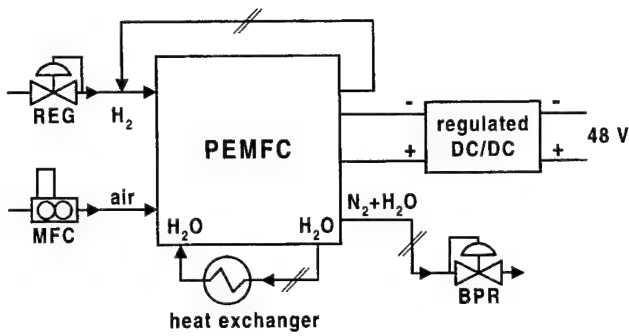


Fig. 5. PEMFC system diagram.

Fig. 5 depicts a simplified diagram of the fuel cell system and the dc/dc converter. Fuel cells have the advantage of being environmentally clean, highly efficient, and reliable since they do not have moving parts [7]. The fuel cell system is the model PGS-105 from Ballard Power Systems. The heart of this system is a Ballard fuel cell stack model MK5-E, which has a total of 35 cells connected in series. Each cell has a surface area of 225 cm<sup>2</sup>/sup/2. The membrane electrode assembly (MEA) consists basically of graphite electrodes and a Dow<sup>TM</sup> membrane. The reactant gases (hydrogen and air) are humidified within the stack. The hydrogen is recirculated at the anode, while the oxidant (air) is flowing through the cathode. The hydrogen pressure at the stack anode inlet is kept at 3 bars by a regulator (REG) and the air pressure at the cathode inlet and outlet is maintained at 3 bars by a backpressure regulator (BPR). The oxygen flow is automatically adjusted by computer as a function of the load via a mass flow controller (MFC).

The dc/dc converter has efficiency better than 95% and the use of eight conversion circuit (power switch MOSFET) levels minimizes the ripples normally associated with this kind of device.

An automatically controlled switching device in the converter drives the required power from the fuel cells. We have shown in a previous publication [10] that the efficiency of the fuel cell system in converting hydrogen into electricity is better than 45% when delivering a power of 4 kW. Therefore, the total efficiency of the load leveling system is better than 42%. Fig. 6 plots the electrical efficiency, defined as the fuel cell output power measured ( $P_{\text{expt}}$ ) over the theoretical power ( $P_{\text{theoretical}}$ ) of the fuel cell system as a function of the load current, for the case when air and pure oxygen are used as an oxidant. The theoretical power is defined as

$$P_{\text{theoretical}} = \frac{\text{HHV} \times N_{\text{cells}} \times I}{2e^- \times F} \quad (1)$$

where HHV = 285.8 kJ mol<sup>-1</sup>, is the high heating value of hydrogen,  $N_{\text{cells}}$  = 35, the number of cells,  $I$  the load current, and  $F = 9.6487 \times 10^{-7}$  C, the Faraday constant.

Fuel cell power as a function of temperature is plotted in Fig. 7. The stack can produce a maximum continuous power

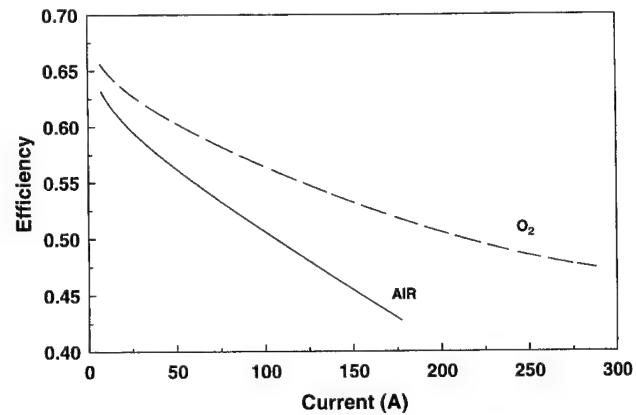


Fig. 6. Fuel cell stack efficiency curves for air and oxygen.

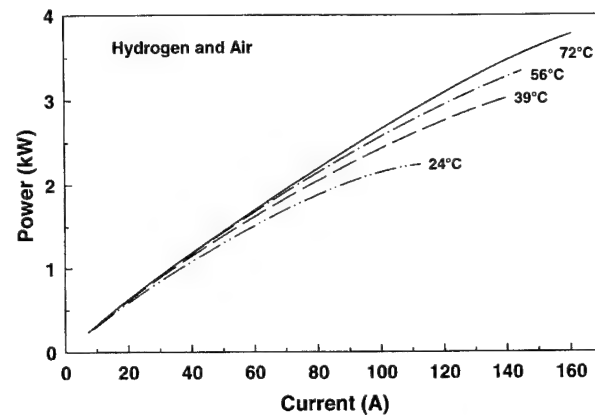


Fig. 7. Fuel cell stack power curves at different temperatures.

of 4 kW when its temperature is in the range of 72–77°C. The stack can generate a peak power of up to 5 kW, but only for a short period of time because of the poor water management of this specific model. The response of the stack to fast switching loads has also been measured and is plotted in Fig. 8. The observed transients actually show how the load reacts to a specific change.

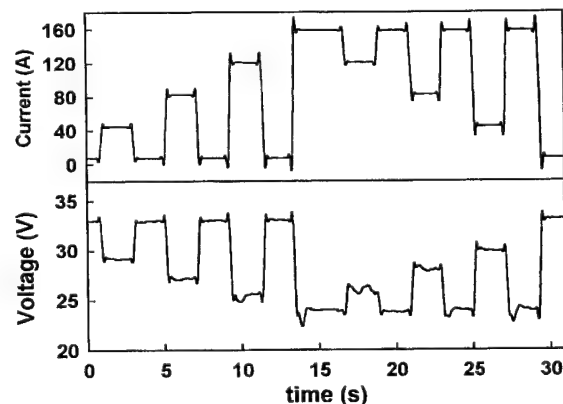


Fig. 8. Current and voltage responses to fast load switching.

## 6. Conclusion

The WT power available shows that excess electrical energy produced during the best wind periods can be used to produce hydrogen. When unfavorable weather conditions arise, it will then be necessary for the stand-alone site to produce electrical energy via a PEMFC. We have shown that a PEMFC stack can respond to fast load switching, through a dc/dc converter, with efficiency better than 42%. This system will also give stabilized electrical power for communication stations. Different storage techniques have also been presented and the simple technique of storing hydrogen at 10 bar in a fuel tank is retained.

## Acknowledgements

This work has been supported by the Ministère de la Recherche, de la Science et de la Technologie Québec, Canada Foundation of Innovation, LTEE-Hydro Québec and Stuart Energy Systems Inc. (SESI). We thank Ballard Power Systems for their fuel cell system.

## References

- [1] C.V. Nayar, Stand alone wind/diesel/battery hybrid energy systems, *Wind Eng.* 21 (1) (1997) 13–19.
- [2] B. Wichert, C.V. Nayar, W.B. Lawrance, photovoltaic-diesel hybrid energy systems for off-grid rural electrification, *Int. J. Renewable Energy Eng.* 1 (1) (1999) 7–17.
- [3] S.R. Vosen, J.O. Keller, Hybrid energy storage systems for stand-alone electric power systems: optimization of system performance and cost through control strategies, *Int. J. Hydrogen Energy* 24 (1999) 1139–1156.
- [4] F. Menzl, M. Wenske, J. Lehmann, Hydrogen production by windmill powered electrolyser, *Hydrogen Energy Prog.* XII 1 (1998) 757–765.
- [5] T.K. Bose, K. Agbossou, P. Bénard, J.M. St-Arnaud, Nouvelles perspectives des systèmes à énergies renouvelables basés sur l'hydrogène, in: *Proceedings of the 15th Conférence et exposition de l'Association canadienne d'énergie éolienne*, Rimouski, September 1999.
- [6] H. Bargthels, W.A. Brocke, K. Bonhoff, PHOEBUS Jülich: an autonomous energy supply system comprising photovoltaic, electrolytic hydrogen, fuel cell, *Hydrogen Energy Prog.* XI 2 (1996) 1005–1015.
- [7] G.E.H. Ballard, Engines of changes, *Hydrogen Energy Prog.* XI 2 (1996) 1357–1371.
- [8] Z. Dehouche, R. Djaozandry, J. Goyette, T.K. Bose, Evaluation techniques of cycling effect on thermodynamic and crystal structure properties of  $Mg_2Ni$  alloy, *J. Alloys Compounds* 288 (1999) 269–276.
- [9] R. Chahine, T.K. Bose, Low-pressure adsorption storage of hydrogen, *Int. J. Hydrogen Energy* 19 (2) (1994) 161–164.
- [10] J. Hamelin, K. Agbossou, A. Laperrière, F. Laurencelle, T.K. Bose, Dynamic behavior of a PEM fuel cell stack for stationary applications, *Int. J. Hydrogen Energy*, in press.

## Solar photovoltaics: an industry of today or tomorrow?

Mark Hammond

*BP Solar Ltd., P.O. Box 191, Chertsey Road, Sunbury on Thames, Middlesex TW16 7XA, UK*

---

A copy of this paper may be obtained from the author.

# Polymer electrolyte membrane fuel cells for communication applications

Deryn Chu<sup>a,\*</sup>, R. Jiang<sup>a</sup>, K. Gardner<sup>b</sup>, R. Jacobs<sup>b</sup>, J. Schmidt<sup>c</sup>,  
T. Quakenbush<sup>c</sup>, J. Stephens<sup>b</sup>

<sup>a</sup>US Army Research Laboratory, 2800 Powder Mill Rd., Adelphi, MD 20783-1197, USA

<sup>b</sup>US Army CECOM, 10108 Gridley Rd., Suite 1, Fort Belvoir, VA 22060, USA

<sup>c</sup>Ball Aerospace Technologies Corp., Boulder, CO 80306, USA

Received 21 December 2000; accepted 4 January 2001

## Abstract

An advanced portable power source using a 50 Watt (PPS-50) polymer electrolyte membrane cell EMFC system was developed by Ball Aerospace under the US Army, Defense Advanced Research Project Agency (DARPA) and the Office Special Technology (OST) joint program. The PEMFC system was designed as required for commercial and military applications. The system was evaluated extensively under different environmental temperatures and humidity conditions. The thermal behavior and discharge performances of the PEMFC system at different discharge currents, temperatures and relative humidities were also investigated. The temperature range was from –10 to 50°C and the relative humidity (r.h.) from 10 to 90%. The PPS-50 system can provide a normal power output about 50 W at 12 V, while the peak power output can reach approximately 65 W (11 V, 6 A). The water production efficiency from the cathode was approximately 70%, and the residual 30% diffused to the anode side. The system was also used to power PRC-119 radios for communication applications, and it performed extremely well during the retransmission site test, operating continuously for over 25 h. © 2001 Elsevier Science B.V. All rights reserved.

**Keywords:** Fuel cells; Polymer electrolyte membrane; Applications; Portable communications

## 1. Introduction

The US Army requires extremely lightweight, quiet, efficient and reliable power-sources for a variety of portable electronics and other applications in the modern battlefield. Polymer electrolyte membrane fuel cells (PEMFCs) are most favored as portable power supply devices, primarily because of their lightweight and high power density. At the present time, the best candidate for a high-energy power source for long-duration Army missions is the hydrogen/polymer electrolyte membrane fuel cell, in which hydrogen (tanked, metal hydride or chemical hydride) and oxygen from the air are combined to produce electricity, heat and water. A PEMFC will provide power indefinitely as long as it is supplied with fuel. The PEMFC power sources are also being developed for a wide variety of applications that now use batteries. These range from laptop computers to electric vehicles. Future man-portable power source systems will need to have a high power density and a long operating life and they must be small and lightweight. Using a lightweight

PEMFC system as the portable source can reduce the physical burden on the carrier.

The following key areas need to be addressed to produce successfully the desired high-performance, lightweight, ambient temperature and pressure, fuel cell system:

1. thermal and heat transfer management;
2. water management;
3. environmental factors;
4. hydrogen storage conditions;
5. determination of the optimum stoichiometry of fuel and oxidant;
6. system integration for high-performance PEMFCs [1–7].

This paper addresses the performance of the PPS-50 system, as developed by Ball Aerospace, at discharge currents between 3.5 and 6 A (maximum power output approximately 72 W at 12 V) under the different environmental temperatures, and relative humidities.

The PPS-50 contains two fuel cell stacks connected by parallel, each of them with 18 single cells connected by series. The dimensions of the system are: 107 mm × 178 mm × 198 mm (4.2 in. × 7 in. × 7.8 in.) and the total

\* Corresponding author. Tel.: +1-301-394-0308; fax: +1-301-394-0273.  
E-mail address: dchu@arl.army.mil (D. Chu).

weight is 2.95 kg (6.5 pounds). The system provides a user-friendly LCD interface for system start-up and shutdown. An RS-232 data port is available to status the system parameters and to provide atmospheric data to the user. Behavior of the system when used for communication applications is also reported.

## 2. Experimental

High purity hydrogen was used as fuel. The oxygen was taken directly from the environmental air by the internal air pump in the PPS-50 system. The environmental temperature and humidity were control within a Tenney Environmental Chamber, which was programmed through a computer with Linktenn II software. An Arbin Tester was used to control discharge tests. In order to get reproducible results, the time interval between tests were at least several hours or overnight to allow temperature and humidity to reach an equilibrium between the internal power system and the environment.

## 3. Results and discussion

The PPS-50 systems are designed to protect themselves from permanent failure by shutting off the load during some out-of-specification conditions or aborting the program in others. Constant current discharges at 3.5, 4 and 6 A were carried out to evaluate the PPS-50 system. The system was evaluated at all possible relative humidities and over a wide range of temperatures.

Fig. 1 shows the performance of the PPS-50 fuel cell system under different discharge currents at 20°C and 32% r.h. The PPS-50 is a 12 V fuel cell supply that is able to provide 60 W continuously and 70 W in bursts for a few minutes. As operating time and current increased, the membrane became more hydrated and stack performance improved significantly. The performance results obtained at relative humidities of 10, 40, 60 and 90% at 40°C and at the 4 A discharge current are almost identical (Fig. 2). The system was designed to be self-humidifying, and the

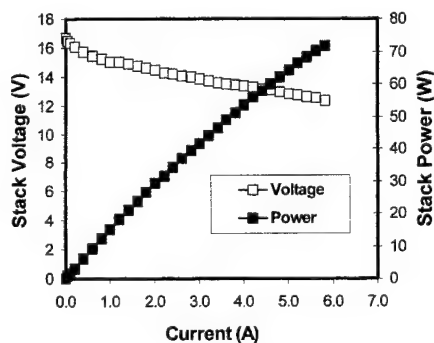


Fig. 1. Performance of the PPS-50 system at 20°C and 32% r.h.

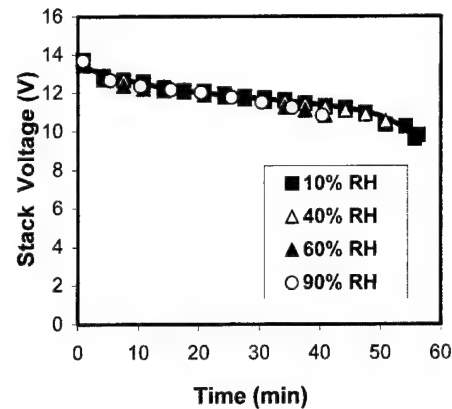


Fig. 2. Effect of relative humidity on the performance of the PPS-50 system at a constant discharge current of 4 A in an ambient temperature of 40°C.

environmental relative humidity seems to have no effect on the discharge performance of the system.

The effect of environmental temperatures over the wide range of +2 to 50°C was also tested to evaluate the discharge performance of the system at 60% r.h. This is shown in Fig. 3. At the beginning, the stack has a voltage of approximately 13.5 V for all the different environmental temperatures. As discharge time increases, the performance of the stack becomes significantly different at various temperatures. The performance at the lowest tested temperature (2°C) has the highest stack voltage and the voltage remain constant during the whole operating time. At 20°C or less, the long-term operating voltage can remain above 12 V. However, at 40°C or higher, the stack voltage drops so quickly that the PPS-50 System can only run for a short time because of the stack system overheating (i.e. when the internal fuel cell stack temperature gets higher than 65°C).

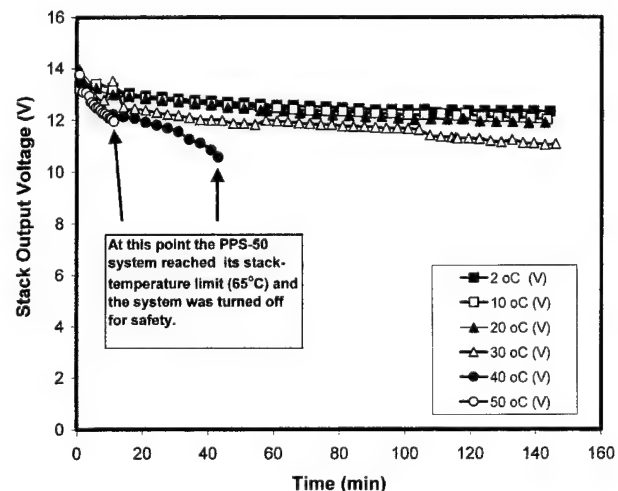


Fig. 3. Effect of ambient temperature on the performance of the PPS-50 system at a constant discharge current of 4 A in an ambient temperature of 60% r.h.

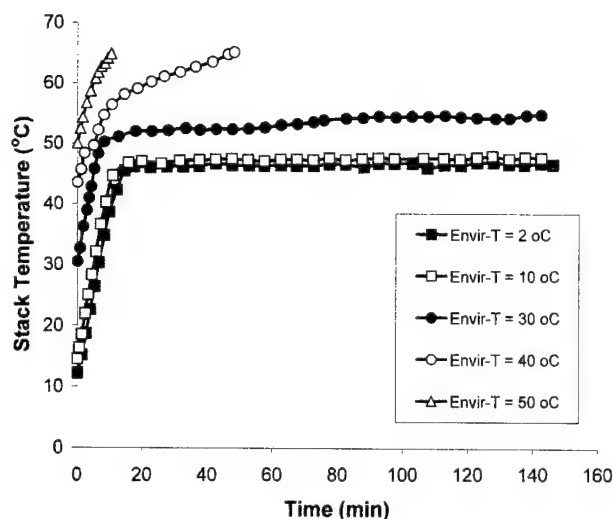


Fig. 4. Effect of ambient temperature on the internal stack temperature of the PPS-50 system at a constant discharge current of 4 A in an ambient temperature of 40°C.

Fig. 4 shows the fuel cell stack temperatures as a function of time at the different environmental temperatures and at 60% relative humidity. In general, the system performance is better at the low operating environmental temperatures, where heat, which is one of the products of the fuel cell reaction, is more readily dissipated. High discharge currents will generate more heat and Fig. 5 shows the stack temperatures at different discharge currents at 40°C and 40% r.h. ambient conditions for discharge currents of 3.5 and 4 A. The stack temperature increases very quickly and then remains at a constant level after about 10 min at 3.5 A. The system demonstrates a good performance for 1 h at the 4 A discharge current before the cut-off temperature of 65°C was reached. So the system performed very well at the 3.5 A discharge current, but heat generation is high at 4 A.

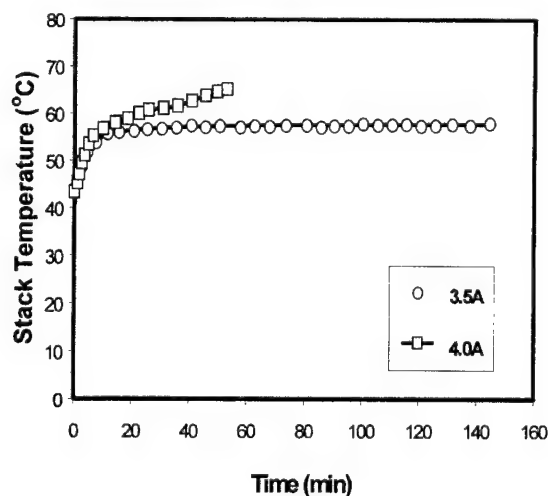


Fig. 5. Effect discharge current on the internal stack temperature of the PPS-50 system in an ambient of 40°C, 40% r.h.

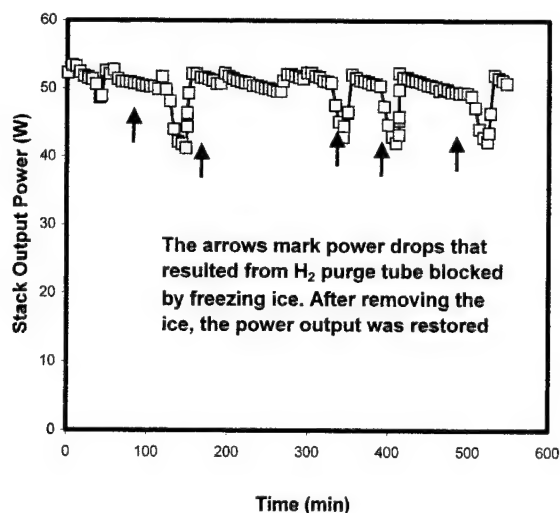


Fig. 6. Performance at constant discharge current of 4 A from a PPS-50 system in an ambient of -10°C.

Operating the system at sub-zero temperature was also evaluated. Fig. 6 shows the plot of stack voltage output versus time at 4 A constant current discharge during the -10°C experiment. Because the hydrogen purge tube was blocked by freezing ice, several voltage drops can be seen on the voltage-time curve in the figure. However, after removing the ice from the hydrogen purge tube the stack voltage recovered. The system operated at -10°C for more than 9 h.

Our experimental results showed that the PPS-50 system performance was excellent at different environmental temperatures and humidity. The temperature range was from -10 to 50°C. The system performance is independent of environmental humidity. At lower temperatures, the bipolar PEMFC stack shows better discharge performance.

Fig. 7 shows the long-term 6 A discharge current performance of the PPS-50 system at 20°C and 32% r.h. The

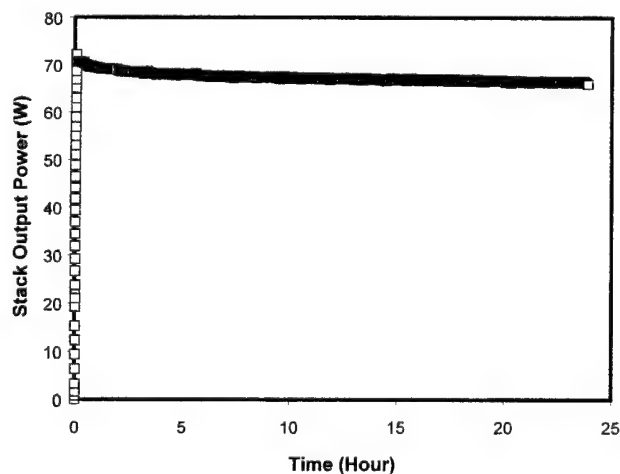


Fig. 7. Performance at constant discharge current of 6 A from a PPS-50 system in an ambient of 21°C, 22% r.h.

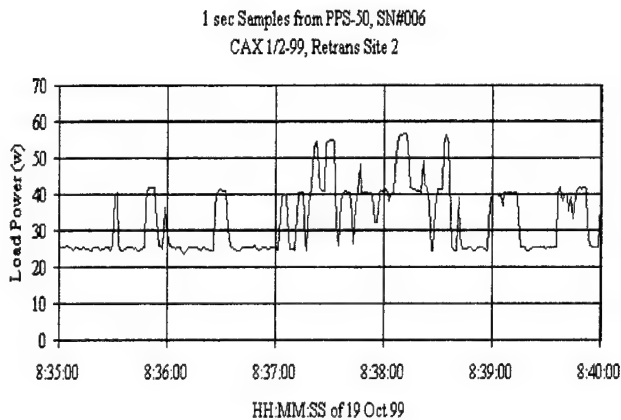


Fig. 8. Load profile over a 5 min period with the PPS-50 system powering two radio nets.

system can provide a constant power output of approximately 65 W, which is higher than the designed normal power output of 50 W. As the operating time and current increase, the membrane became more hydrated and stack performance improved significantly.

The PPS-50 W system was also tested in field exercises by the Marine Corps at 29 Palms Marine Base in October 1999. The PPS fuel cell system was used for communication applications and to power nine PRC-119 radios (system capacity is 12 radios simultaneously) and a laptop computer for 20 h with no glitches in power. The fuel cell system tracked changes in power demand fast enough to avoid any brownout conditions for the radio. Fig. 8 shows load power logged over a 5 min period from a PPS-50 powering two nets of PRC-119 radios. Two idling nets drew 25 W, one idle net and one transmitting net drew 40 W, and both nets transmitting drew an average 55 W.

The fuel cell power systems are also able to respond in real-time to the load. Fig. 9 shows the load power for the 24 h of operation on the PRC-119 radios. It shows that there was light radio traffic through the night with a large increase at the morning of 19 October 1999. The gap between 11.00 and 13.00 h is because the computer was

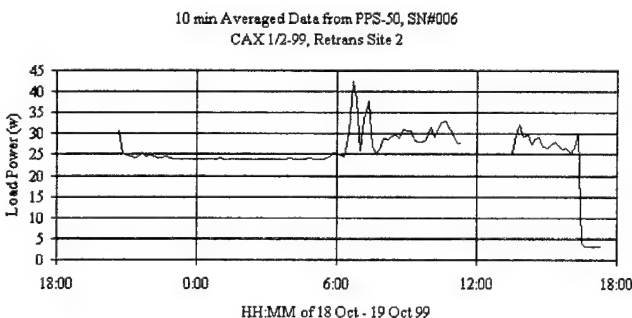


Fig. 9. Load profile over a 24 h period with the PPS-50 system powering two radio nets.

logging data from a PPS-100 instead of the PPS-50. The end of the curve drops to about 3.5 W when the eight net radios were shut down. All of the exercises were accomplished in good time and the PRC-119 radios were operated properly.

This field test, conducted by the US Marine Corps, demonstrated that small fuel cells are a reliable, lightweight and cost-effective means of providing power for military applications. The fuel cells performed extremely well during the retransmission site test, operating continuously for over 25 h. The use of fuel cells in place of traditional batteries can reduce the cost of energy by up to 80%.

#### 4. Conclusions

The thermal behavior and discharge performances of the PPS-50 system at different discharge currents, temperatures and relative humidities were investigated. In general, the system performance is better at low operating environmental temperatures, because the heat generated from the fuel cell reaction is more easily dissipated to the environment at lower temperatures. Our tests showed that the PPS-50 system performance was excellent at different environmental temperatures and humidity, the temperature range tested being  $-10$  to  $50^{\circ}\text{C}$ . The system performance is independent of environmental humidity.

The PPS-50 fuel cell system was also used successfully in field exercises by the Marine Corps, a test which demonstrated that small fuel cells are a reliable, lightweight and cost-effective means of providing power for military applications. The fuel cells performed extremely well during the retransmission site operating continuously for over 25 h. To use fuel cells in place of traditional batteries can reduce the cost of energy up to 80%.

Understanding the performance characteristics of stack systems is clearly important for the realization of the optimum cost/weight/volume/performance ratios. The results of this study advance the development of the PEMFC stack system for practical power for the soldier and future combat system applications.

#### Acknowledgements

The authors wish to thank the Army Research Laboratory/Army Research Office Directorate (ARL/ARO), Army Research Laboratory/Sensors and Electron Devices Directorate (ARL/SEDD), Communication Electronic Command (CECOM), Defense Advanced Research Project Agency (DARPA), Office Special Technology (OST) and Ball Aerospace for teamwork on the fuel cell program. The authors also wish to thank the Department of the Army and the Army Materiel Command (AMC) for their financial support.

## References

- [1] D. Chu, The high performance of polymer electrolyte membrane fuel cells for army applications, in: *Proceedings of The 21st Army Science Conference*, June 1998, Norfolk, VA.
- [2] D. Chu, R. Jiang, in: *Proceedings of the Electrochemical Society*, 1998, pp. 470–478.
- [3] D. Chu, R. Jiang, *J. Power Sources* 80 (1999) 226–234.
- [4] D. Chu, R. Jiang, *J. Power Sources* 83 (1999) 128–133.
- [5] D. Chu, R. Jiang, C. Walker, *J. Appl. Electrochem.* 30 (2000) 365.
- [6] R. Jiang, D. Chu, *Electrochim. Acta* 45 (2000) 4025.
- [7] D. Chu, R. Jiang, C. Walker, K. Gardner, R. Jacobs, J. Stephens, in: *Proceedings of the 39th Power Sources Conferences*, Cherry Hill, NJ, pp. 136–139.





Abstract

## Powering the 21st century with Ballard fuel cells

Henry Voss

*Ballard Power Systems, 9000 Glenlyon Parkway, Burnaby, BC, Canada V5J 5J9*

---

**Abstract**

It is widely accepted that fuel cell technology will create a critical and lasting shift in energy generation and use during the 21st century. This paper will discuss Ballard's product development, demonstration and market development activities focused on the introduction of products into portable and compact power applications. © 2001 Published by Elsevier Science B.V.

*Keywords:* Fuel cells/polymer electrolyte; Applications/portable power

---



ELSEVIER

Journal of Power Sources 96 (2001) 180–183

JOURNAL OF  
POWER  
SOURCES

www.elsevier.com/locate/jpowsour

# Further development of lithium/polycarbon monofluoride envelope cells

A.G. Ritchie<sup>a,\*</sup>, C.O. Giwa<sup>a</sup>, P.G. Bowles<sup>a</sup>, J. Burgess<sup>a</sup>, E. Eweka<sup>a</sup>, A. Gilmour<sup>b</sup><sup>a</sup>DERA, Haslar, Gosport, Hants PO12 2AG, UK<sup>b</sup>Lexcel Technology Ltd., Henley-on-Thames, Oxonia RG9 1LU, UK

## Abstract

Lithium primary cells in a light weight plastic envelope format have been made using carbon monofluoride ( $\text{CF}_x$ ) as cathode material, because previous work showed that this cathode material has the highest energy density in lithium primary batteries. Energy densities of around  $650 \text{ Wh kg}^{-1}$  were obtained in an envelope cell. Different electrolytes have been examined for high rate and low temperature performance. © 2001 Published by Elsevier Science B.V.

**Keywords:** Lithium primary cells; Polycarbon monofluoride

## 1. Introduction

Lithium/carbon monofluoride ( $\text{CF}_x$ ) primary cells are known to give the highest energy density of all lithium primary cells, with a theoretical energy density of  $2180 \text{ Wh kg}^{-1}$ , cf.  $1470 \text{ Wh kg}^{-1}$  for lithium/thionyl chloride or  $1005 \text{ Wh kg}^{-1}$  for lithium/manganese dioxide [1–3]. Other cathode materials (iron disulphide,  $\lambda$ -manganese dioxide) for lithium primary cells and a metal-free rechargeable lithium cobalt oxide cell have been shown to have lower energy densities [4]. Polycarbon monofluoride has the further advantage that  $\text{CF}_x$  is a solid so that light weight envelope cell packaging can be used, similar to that already described [4,5] and illustrated in Fig. 1.

Lithium/carbon monofluoride primary cells are commercially available, e.g. as button cells [2,3,6], but are largely used for low rate applications, such as pagers, cameras, computer clock and memory back-up [3], gas meters [7], electronic and communications equipment. The envelope or ‘pouch’ construction has previously been used for lithium/manganese dioxide primary cells [8,9], so it is an established technology for primary lithium/solid cathode cells though the theoretical energy density for  $\text{Li/MnO}_2$  is much lower. Hence, lithium/carbon monofluoride envelope cells have the potential for the highest possible energy density both on grounds of chemistry and of construction.

Previous work [10] has shown that envelope cells could be made in thickness from 0.8 mm upwards, with five-fold cells

reaching 10.5 mm. Capacities were from 1.125 to 18 Ah. These cells used the EC/DEC/ $\text{LiPF}_6$  electrolyte as used in lithium-ion secondary batteries. However, laboratory cells showed higher voltages on discharge with other electrolytes (e.g. EC/PC/DME/ $\text{LiBF}_4$ ). Further studies on the effect of different electrolytes have been carried out over a range of temperatures. Energy densities up to  $516 \text{ Wh kg}^{-1}$  were achieved but  $750 \text{ Wh kg}^{-1}$  was predicted for optimised designs. This work describes the use of these better electrolytes and the optimisation of design to achieve balanced cells, with resulting higher energy density.

## 2. Experimental

Experimental techniques were similar to those described previously [10]. By varying the concentration and hence viscosity of the cathode mixture, the thickness of the cathode coatings could be adjusted. Cathode capacities between 10 and  $17 \text{ mAh cm}^{-2}$  were achieved.

Two electrolytes were studied in laboratory cells:

- 1 M lithium tetrafluoroborate,  $\text{LiBF}_4$ , in PC:DME (1:1 w/w).
- 1 M lithium hexafluorophosphate,  $\text{LiPF}_6$ , in EC:EMC (1:1) (Merck LP50).

where EC = ethylene carbonate, PC = propylene carbonate, EMC = ethyl methyl carbonate, DME = dimethoxy ethane.

In envelope cells, cathode sheets were folded around a central lithium anode so, for a balanced cell, the cathode capacity should be half the anode capacity ( $27.2 \text{ mAh cm}^{-2}$

\* Corresponding author. Tel.: +44-2392-335429;  
fax: +44-2392-335102.  
E-mail address: agritchie@dera.gov.uk (A.G. Ritchie).

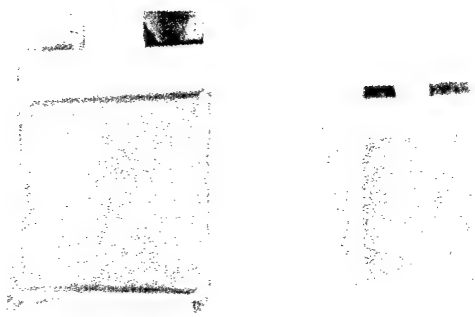


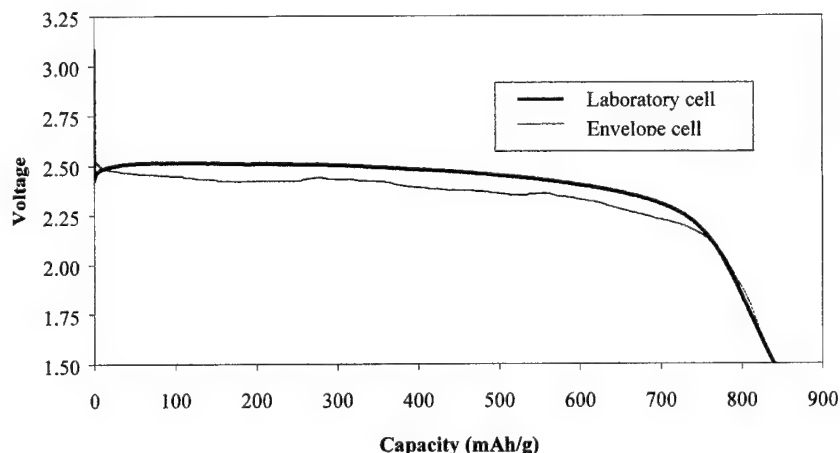
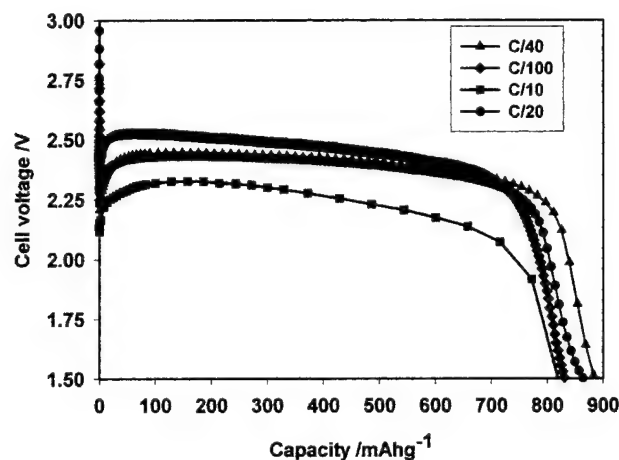
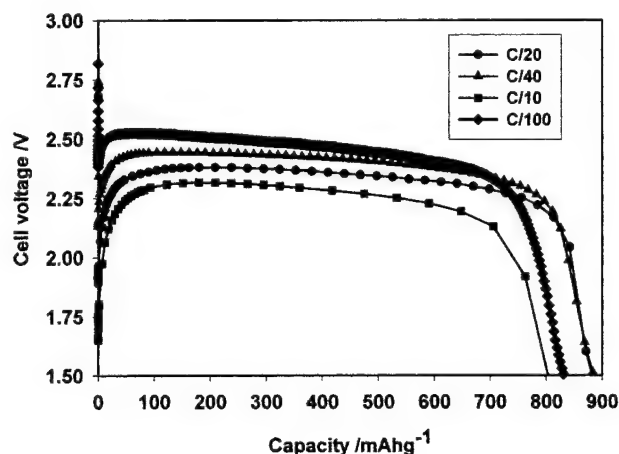
Fig. 1. Packet and envelope cells.

for  $132\ \mu\text{m}$  lithium foil), i.e.  $13.6\ \text{mAh cm}^{-2}$  for the cathode. The cells used a folded construction with each fold being  $75\ \text{mm} \times 75\ \text{mm}$ . The cells were folded successively, giving  $225\ \text{cm}^2$  for a two-fold cell. Folded cells were put into a Surllyn bag, the electrolyte was added then the cells were evacuated and vacuum sealed. Flat packs without bulging were readily obtained. During testing, no external pressure needed to be applied. In laboratory cells, a single sheet of cathode material was used, so the lithium was in excess.

### 3. Discharge tests in laboratory cells

These tests studied the effects of cathode thicknesses, temperatures ( $-30$  to  $+40^\circ\text{C}$ ), discharge rate ( $10$ – $100\ \text{h}$ ) and different electrolytes in laboratory cells whose design has been described previously [5]. Previous results [4] and Fig. 2 have shown similar results in envelope and laboratory cells so laboratory cell results should be readily transferable to envelope cells, which would be used for actual battery construction.

Different cathode loadings are compared in Figs. 3 and 4. They show similar discharges for coatings of  $13.6$  and  $17\ \text{mAh cm}^{-2}$ .

Fig. 2. Comparison of  $\text{Li}/\text{CF}_x$  primary laboratory and envelope cells discharged at  $0.05\ \text{mA cm}^{-2}$  ( $200\ \text{h}$  rate).Fig. 3. Electrochemical discharges of lithium/ $\text{CF}_x$  primary laboratory cells at room temperature with  $\text{PC}/\text{DME}/\text{LiBF}_4$  electrolyte for a cathode loading of  $13.6\ \text{mAh cm}^{-2}$ .Fig. 4. Electrochemical discharges of lithium/ $\text{CF}_x$  primary laboratory cells at room temperature with  $\text{PC}/\text{DME}/\text{LiBF}_4$  electrolyte for a cathode loading of  $17\ \text{mAh cm}^{-2}$ .

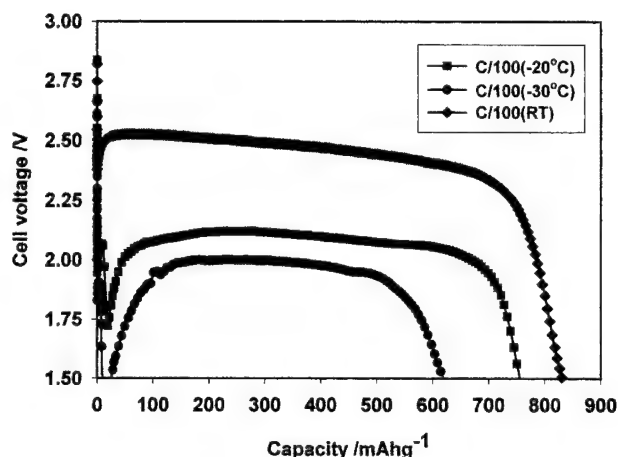


Fig. 5. Electrochemical discharges of lithium/CF<sub>x</sub> primary laboratory cells at the 100 h rate at different temperatures.

The capacities were close to the theoretical value of 864 mAh g<sup>-1</sup> showing that the cathode material was being discharged efficiently for both coating thicknesses. Good discharges were obtained at the 20, 40 and 100 h rates but slightly lower capacity and discharge voltage were found at the 10 h rate.

Figs. 5 and 6 show the effect of different temperatures at the 100 and 20 h rates, respectively. Cells could be discharged at temperatures as low as -30°C but performance was better at room temperature or +40°C.

Previous work [10] used EC/EMC/LiPF<sub>6</sub> electrolyte. Discharges using this electrolyte are illustrated in Fig. 7.

Comparison of Figs. 4, 7 and 8 shows the higher on-load voltage found when using the PC/DME/LiBF<sub>4</sub> electrolyte instead of the EC/DMC/LiPF<sub>6</sub> electrolyte used previously in [10].

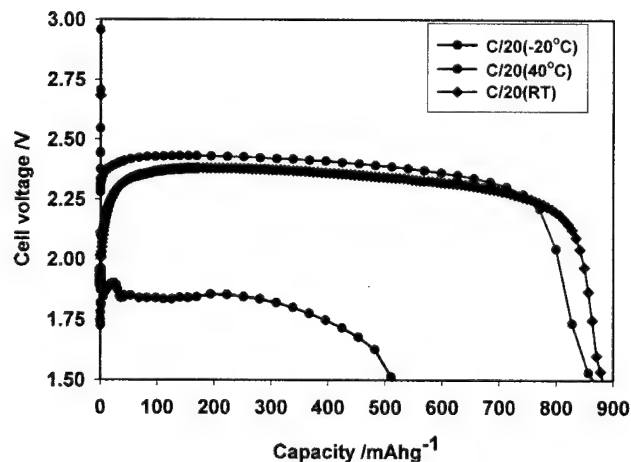


Fig. 6. Electrochemical discharges of lithium/CF<sub>x</sub> primary laboratory cells at the 20 h rate at different temperatures.

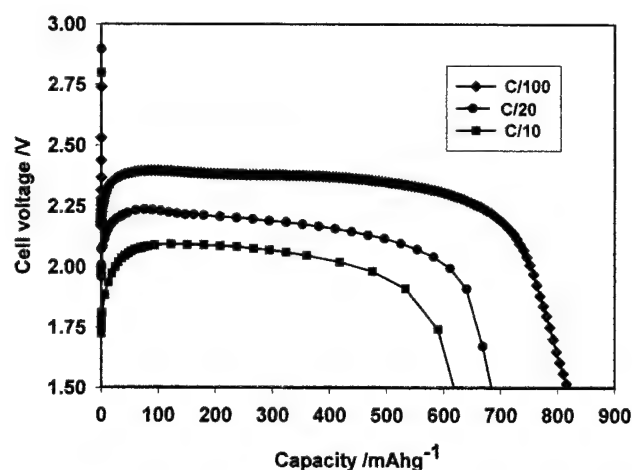


Fig. 7. Electrochemical discharges of lithium/CF<sub>x</sub> primary laboratory cells at room temperature with EC/DMC/LiPF<sub>6</sub> electrolyte at a cathode loading of 17 mAh cm<sup>-2</sup>.

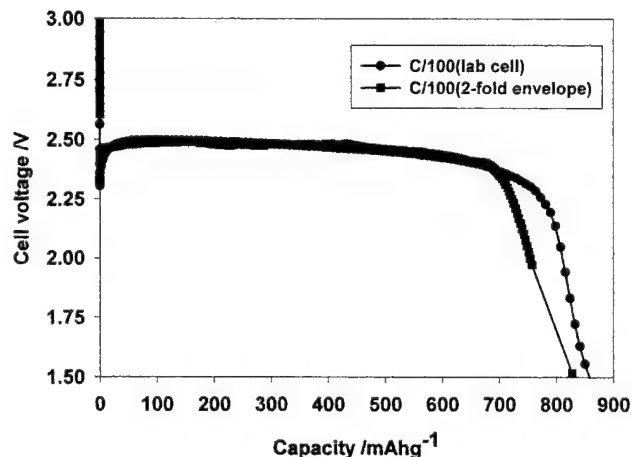


Fig. 8. Electrochemical discharge of a two-fold lithium/CF<sub>x</sub> primary envelope cell at the 100 h rate at room temperature with 13.6 mAh cm<sup>-2</sup> cathode loading and PC/DME/LiBF<sub>4</sub> electrolyte.

#### 4. Discharge of envelope cell

A two-fold envelope cell was made as described previously [10] but with an increased cathode loading of 13.6 mAh cm<sup>-2</sup> to provide a balanced design. A PC/DME/LiBF<sub>4</sub> electrolyte was used to provide higher conductivity, and hence a higher on-load voltage than the EC/DMC/LiPF<sub>6</sub> electrolyte used in the earlier work. In accordance with earlier predictions [10], this produces a higher energy density, 642 Wh kg<sup>-1</sup> for a two-fold cell. Compare this value with 385 Wh kg<sup>-1</sup> for the three-fold cell reported earlier. The cathode capacity was close to theoretical and the discharge was similar to a laboratory cell discharged under similar conditions.

## 5. Conclusions

An energy density of around  $650 \text{ Wh kg}^{-1}$  has been achieved from a lithium/polycarbon monofluoride envelope cell. This demonstrates the benefits in terms of energy of this chemical system and of the envelope cell construction. Different electrolytes have been investigated for good low temperature performance.

## References

- [1] D. Linden, *Handbook of Batteries*, 2nd Edition, McGraw-Hill, 1994 (Table 14.4).
- [2] D. Rohde, M.J. Root, in: *Proceedings of the 37th Power Sources Conference, Li/CF<sub>x</sub> Cell and Material Development for High Rate Applications*, Cherry Hill, USA, June 1996, pp. 350–352.
- [3] M.J. Root, K. Dittberner, in: *Proceedings of the 6th Workshop for Battery Exploratory Development, Investigation and Development of Lithium Carbon Monofluoride Cells*, Williamsburg, USA, June 1999.
- [4] C.O. Giwa, A.G. Ritchie, J.C. Lee, P. Bowles, R. Luxton, A. Gilmour, J. Allan, Lithium primary envelope cells, in: *Proceedings of the 16th International Seminar and Exhibit on Primary and Secondary Batteries*, Fort Lauderdale, FL, March 1999.
- [5] A. Gilmour, C.O. Giwa, J.C. Lee, A.G. Ritchie, in: *Proceedings of the 20th International Power Sources Symposium on Power Sources*, Vol. 16, Brighton, April 1997, Lithium rechargeable envelope cells, *J. Power Sources* 65 (1997) 219–224.
- [6] D.D. Pagoria, S.A. Megahed, J.L. Lautzenhiser, R.J. Ekern, in: *Proceedings of the 35th International Power Sources Symposium on Lithium Carbon-Monofluoride Batteries for Extended Ultra-High Temperature Storage and Surface Mount Applications*, Cherry Hill, USA, June 1992, pp. 7–9.
- [7] M.-L. Chan, in: *Proceedings of the 21st International Power Sources Symposium on Power Sources*, Vol. 17, Brighton, May 1999, Reliability and performance of primary lithium batteries for ultrasonic gas meters, *J. Power Sources* 80 (1999) 273–277.
- [8] K. Almond, S. Wessel, L. Marcoux, in: *Proceedings of the 38th Power Sources Conference on State of the Art High Performance Ultrasafe Pouch Cell Li/MnO<sub>2</sub> Batteries*, Cherry Hill, USA, June 1998, pp. 131–134.
- [9] L. Malinovsky, B. Hoge, B. Coffey, in: *Proceedings of the 38th Power Sources Conference, Prismatic Lithium/Manganese Dioxide Batteries for High Rate, Low Temperature Applications*, Cherry Hill, USA, June 1998, pp. 135–138.
- [10] C.O. Giwa, A.G. Ritchie, P.G. Bowles, E.L. Price, J. Burgess, A. Gilmour, J. Allan, in: *Proceedings of the 39th Power Sources Conference, Scale-up of Lithium Carbon Monofluoride Envelope Cells*, Cherry Hill, USA, June 2000, pp. 32–35.

## Ultralife's polymer electrolyte rechargeable lithium-ion batteries for use in the mobile electronics industry

Edward A. Cuellar\*, Michael E. Manna, Ralph D. Wise, Alexei B. Gavrilov,  
Matthew J. Bastian, Rufus M. Brey, Jeffrey DeMatteis

*Ultralife Batteries Inc., 2000 Technology Parkway, Newark, NY 14513, USA*

Received 30 November 2000; accepted 5 December 2000

---

### Abstract

Ultralife Polymer™ brand batteries for cellular phones as made by Nokia Mobile Phones Incorporated were introduced in July 2000. Characteristics of the UBC443483 cell and UB750N battery are described and related to the power and battery requirements of these cellular phones and chargers. Current, power, and pulse capability are presented as functions of temperature, depth of discharge, and storage at the cell level. Safety protection devices and chargers are discussed at the battery pack level, as well as performance in cellular phones under various wireless communication protocols. Performance is competitive with liquid lithium-ion systems while offering opportunity for non-traditional form factors. © 2001 Elsevier Science B.V. All rights reserved.

**Keywords:** Lithium-ion batteries; Polymer electrolytes; Mobile telephones

---

### 1. Introduction

The ever increasing and aggressive power demands of portable electronic devices continue to challenge battery design and performance. Lithium-ion polymer batteries are an emerging force in this marketplace [1],<sup>1</sup> addressing needs for high energy and for thin and lightweight batteries with customizable shapes and sizes. Ultralife batteries is a leader in the development and manufacture of a wide range of lithium-ion polymer cells and battery packs to meet these needs in consumer, commercial, and military markets.

Ultralife Polymer™ brand after-market batteries for 51xx, 61xx, and 71xx series cellular phones from Nokia were introduced in July 2000. Characteristics of one production polymer cell used in these batteries, the UBC443483, and one battery, the UB750N, are described below. Power and battery requirements of several models of cellular phones and chargers from Nokia are also presented and related to UBC443483 and UB750N design, performance and safety characteristics. Performance for cells under development, both in form factor and chemistry, are also described.

### 2. Cell design and manufacture

Ultralife Polymer™ brand cells described in this paper use a stacked electrode architecture [2], polymer electrolyte, and fabrication procedures based on Bellcore's plastic lithium-ion (PLion™) technology [3]. Ultralife commercial cells use LiCoO<sub>2</sub> as the cathode active material, graphite as the active material for the anode, and Al-laminated film packaging. Higher energy cathode and anode materials are being developed under a NIST ATP award [4]. Ultralife can also manufacture polymer cells using Li<sub>1+x</sub>Mn<sub>2-x</sub>O<sub>4</sub> as the active cathode [2]. Cells are made in a variety of form factors up to 15 Ah in capacity. High volume manufacturing facilities are in place for the UBC443483 (725 mAh) and UBC543483 (930 mAh). These cells are 34 mm wide, 83 mm long, and 4.4 and 5.4 mm thick, respectively. Cells as thin as 0.9 mm thick can be made in this form factor using central anode electrodes. An example of the C rate capacity distribution for a typical production lot of UBC443483 at ambient temperature is shown in Fig. 1. The average C rate capacity is 717 mAh. One standard deviation is 16 mAh. The cells are conservatively rated at 725 mAh at 0.2C as sold, typical average capacity is 735 mAh. Unless noted otherwise, UBC443483 cells are rated at 725 mAh at C rate in this paper. Cells are tested with or without a Raychem® LR4-380 PPTC (polymer positive temperature coefficient) device as noted. Ambient temperature is taken as 23 ± 2°C.

---

\* Corresponding author. Tel.: +1-315-332-7100; fax: +1-315-331-8010.  
E-mail address: ecuellar@ulbi.com (E.A. Cuellar).

<sup>1</sup> Approximately 50% of the battery papers were lithium-ion polymer.

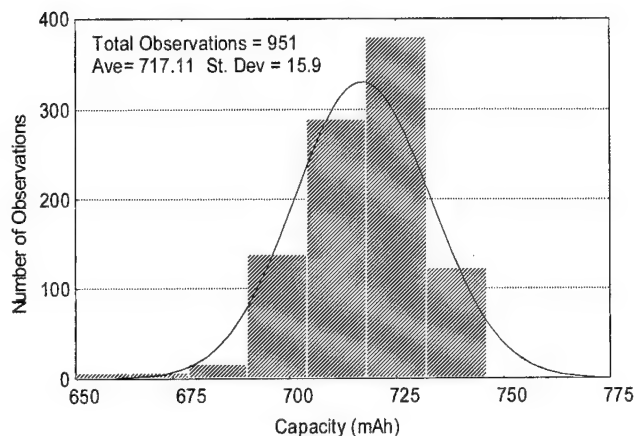


Fig. 1. Distribution of capacity for a typical production run of UBC443483 cells at  $C$  rate, cells discharged at 725 mA at ambient temperature.

### 3. Cell performance

#### 3.1. Charge and discharge characteristics at ambient temperature

Typical charge characteristics for the UBC443483 with a PPTC are shown in Fig. 2. Constant current charge to a specified voltage limit, followed by constant voltage charge at the voltage limit to a specified current limit cut-off is recommended. The constant current charge rate is a function of the electrode coat weights, 350 mA for the UBC443483, having seven electrodes in parallel as described in this paper. A charge limit of 4.2 V is recommended for  $\text{LiCoO}_2$  cathodes. Typical current limit cut-offs in the constant voltage charge are  $C/10$  to  $C/20$ . A lower voltage cut-off of 3.0 is recommended during active discharge, drift to lower voltages on stand do not appear to be detrimental to cell performance.

The rate capability from 1 to 10C at ambient temperature of the UBC443483 with a PPTC is shown in Fig. 3. The cells deliver 91% of 1C capacity at 3C rate. Constant power discharges provide flat discharge profiles even at high power rates, such as 2.8 W, where the current reaches 1.3C at end of discharge. Typical constant power discharges for cells with a PPTC are shown in Fig. 4.

#### 3.2. Charge and discharge characteristics below ambient temperature

Low temperature performance of the UBC443483 with a PPTC device was measured from  $-20$  to  $+20^\circ\text{C}$  under group special mobile (GSM) simulated pulse discharges. Charges were at ambient temperature with a 4 h soak at the discharge temperature. The discharge consisted of a 1.64 A current pulse of 550  $\mu\text{s}$  duration every 4.6 ms on a background current of 0.2 A. The voltage during the high current pulse is shown in Fig. 5. Resistance measured during the pulse, measured as the difference in the pulse and background voltages divided by 1.44 A, is stable over a wide temperature range. There is little to no performance dependence on state-of-charge.

Rate performance of the UBC443483 cell at  $-20^\circ\text{C}$  is shown in Fig. 6. Capacity at 1C approaches 65% of the 1C capacity of 725 mAh at ambient temperature, while 0.2C rate delivers 98% of ambient 1C capacity.

Low temperature charge of the UBC443483 is excellent, with fully discharged cells charging at  $0^\circ\text{C}$  after 4 h soak at temperature to over 96% of the ambient 1C capacity. The charge was 350 mA constant current to 4.15 V, followed by a constant voltage charge at 4.15 V until the current fell to 72.5 mA (see Table 1).

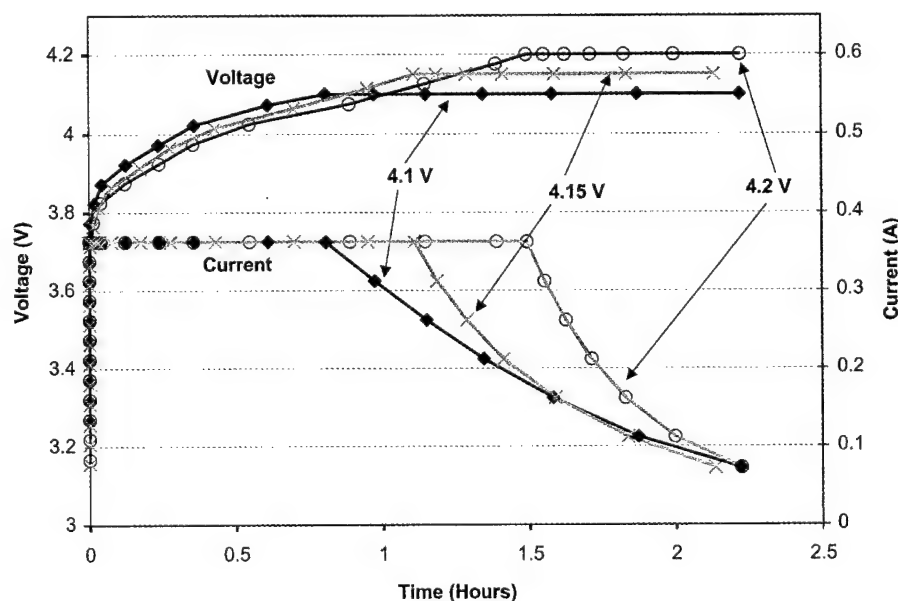


Fig. 2. Typical charge profiles for UBC443483 cells with a PPTC charged at 362.5 mA to specified voltage at ambient temperature.

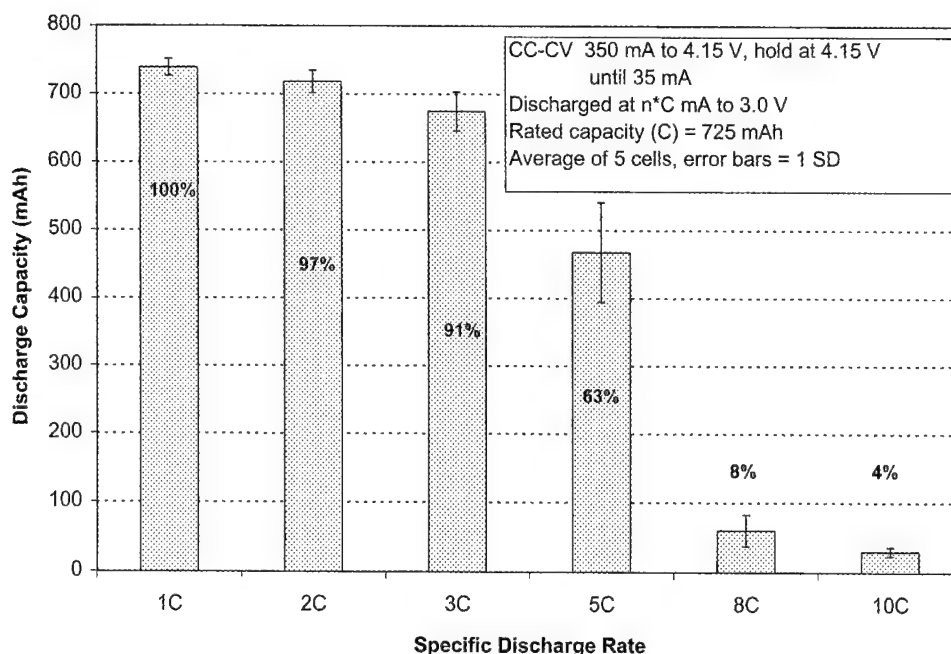


Fig. 3. Constant current discharge capacity vs. rate at ambient temperature for UBC443483 with PPTC.

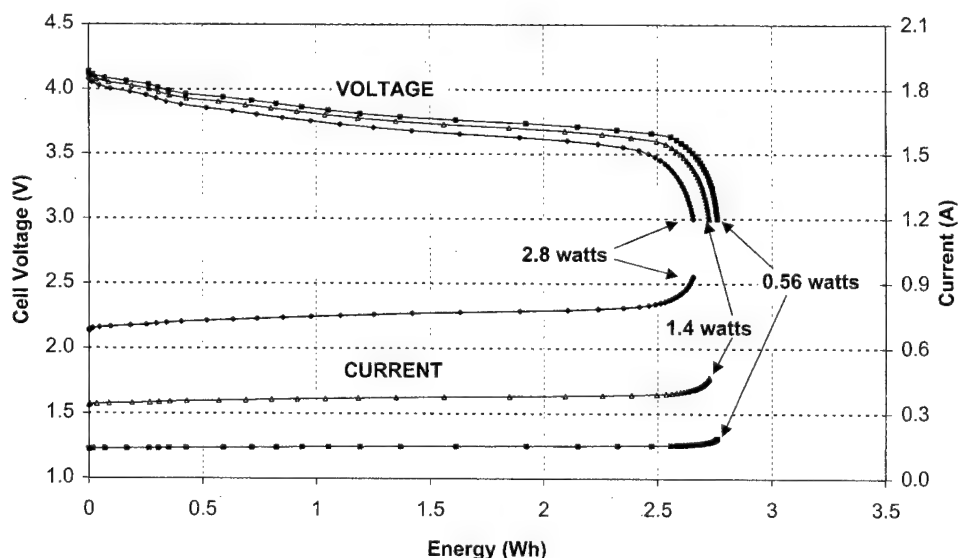


Fig. 4. Constant power discharge profiles for UBC443483 with a PPTC at ambient temperature.

### 3.3. Long-term cycling: discharge at constant current and constant power

Ambient and 45°C life cycle characteristics are comparable with liquid lithium-ion systems.<sup>2</sup> Both constant current, Fig. 7, and constant power, Fig. 8, interrupted long-term cycle performances (with 30 min rests between half cycles)

typically exceed 300 cycles to 80% of ambient 1C capacity. Fig. 9 shows comparative information for UBC443483 cells with a PPTC undergoing continuous cycling at ambient and 45°C. Figs. 10 and 11 show the voltage versus time discharge curves for various cycles of a single cell at the temperatures in Fig. 9.

### 3.4. Long-term cycling: GSM discharge

Long-term cycling, with 30 min rests between half cycles, was performed at ambient conditions using the same GSM simulated pulse discharges described above. Retained capa-

<sup>2</sup>For example, see specification sheets for Sony US063048G3 (700 mAh), UP383562 (540 mAh) and US18650G3 (1800 mAh) at [www.world.sony.com](http://www.world.sony.com) and Panasonic CGP30486 (630 mAh) and CGR18650H (1500 mAh) at [www.panasonic.com](http://www.panasonic.com).



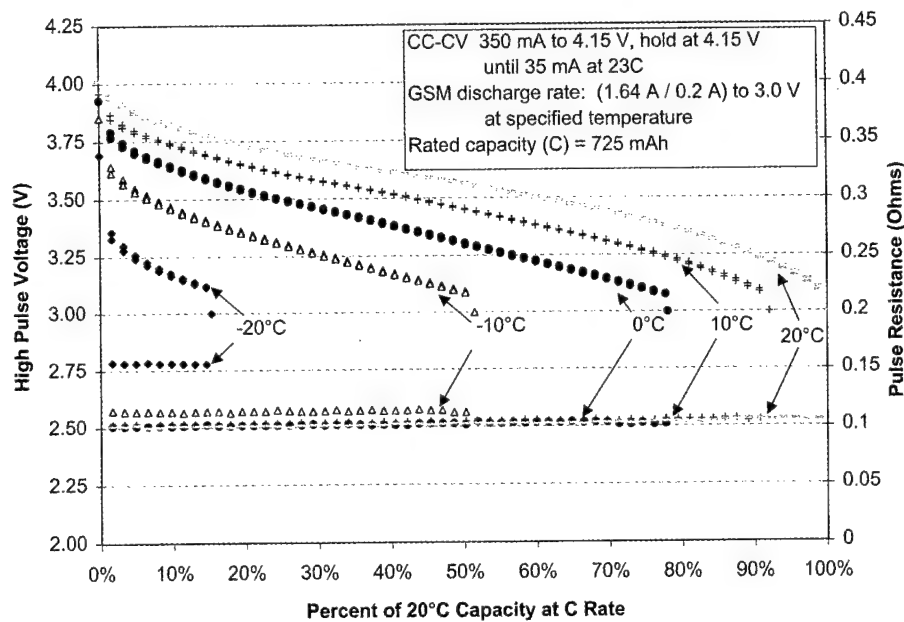


Fig. 5. GSM pulse discharge characteristics of UBC443483 with a PPTC. Ambient temperature charge, GSM discharge (1.64 A/0.2 A) at specified temperature.

city is greater than 80% of ambient 1C capacity for over 250 cycles with concurrent resistance growth measured during the pulse changing from 80 to 94 mΩ, a 17% change (see Fig. 12).

### 3.5. Cycle life as a function of depth of discharge and rate

Cell and battery performance varies widely depending upon usage habits. Since in-field use is so difficult to model and so random, worst case scenarios are often chosen for life

testing of portable power products. This can be extremely misleading regarding the real world application and often misrepresents the actual battery life in the application. This is brought to the forefront when one starts to model the cycle life of batteries in cellular phone applications, taking into consideration depth of discharge (DOD) effects at various discharge rates.

UBC443483 cells were cycled at DOD varying from 10 to 100% under several different discharge rates. To make testing equal, all cells were charged to the specified voltage,

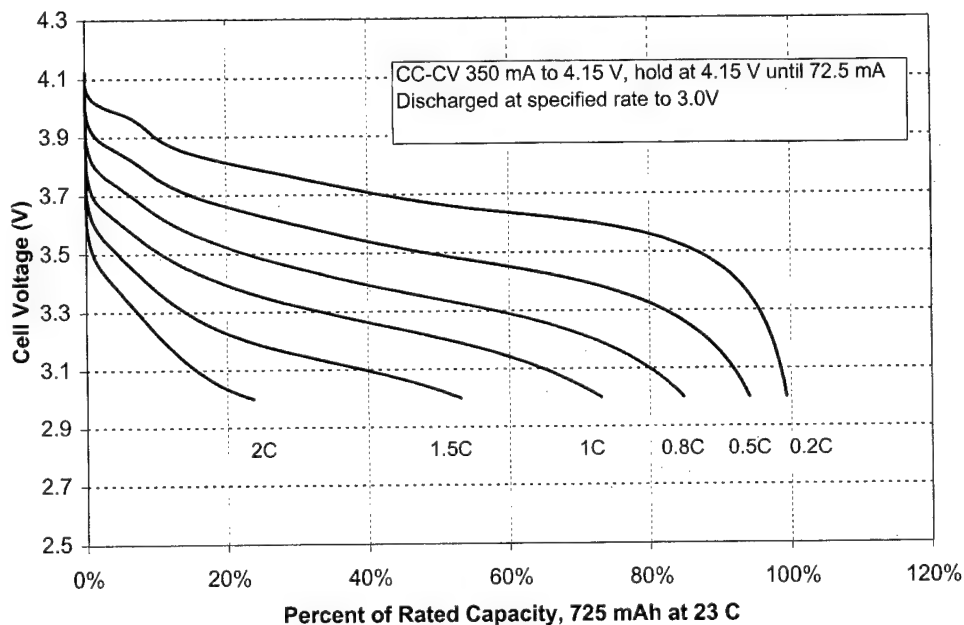


Fig. 6. Constant current discharge capacity vs. rate at -20°C for UBC443483.

Table 1  
Capacity obtained during 0°C charge

Samples	Capacity (mAh)	Energy (Wh)
1	717	2.84
2	691	2.74
3	692	2.74
4	697	2.77
5	702	2.78
Average	699.7	2.78
S.D.	10.7	0.04

and then discharged until a percent of rated capacity was removed. If in removing the capacity, the voltage on any cell reached the lower cut-off voltage before the capacity was removed, the test was ended. The exception to this rule was 100% DOD cycling, where cells were discharged to 3.0 V on every cycle. There were three separate tests initiated, each using different discharge rates.

The first test was to charge UBC443483 cells to 4.10 V (column A in Table 2) at 350 mA, or approximately 0.5C (column C in Table 2). The cells were then charged at a constant voltage of 4.10 V until the current fell below 72.5 mA. The cells were then discharged at 350 mA

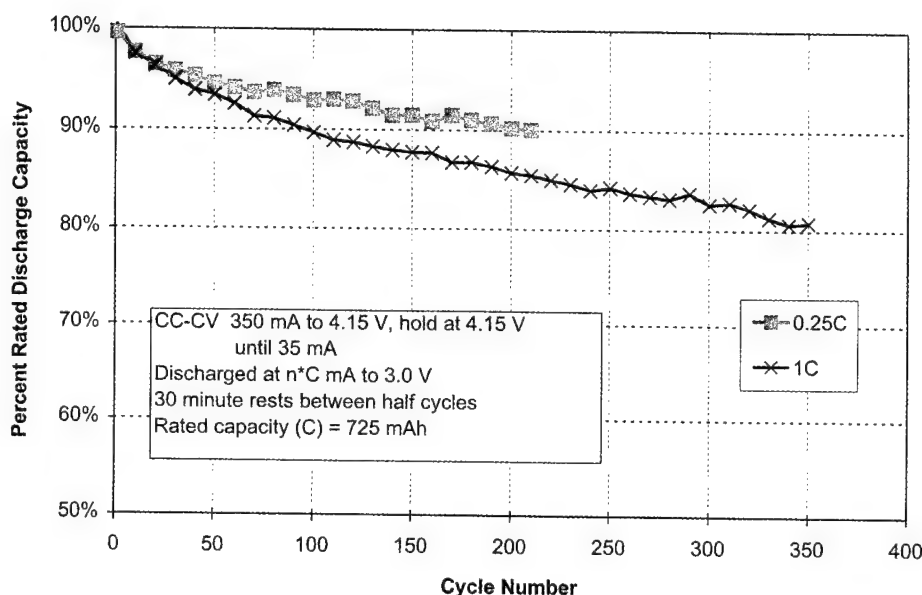


Fig. 7. UBC443483 interrupted constant current long-term cycling at ambient temperature.

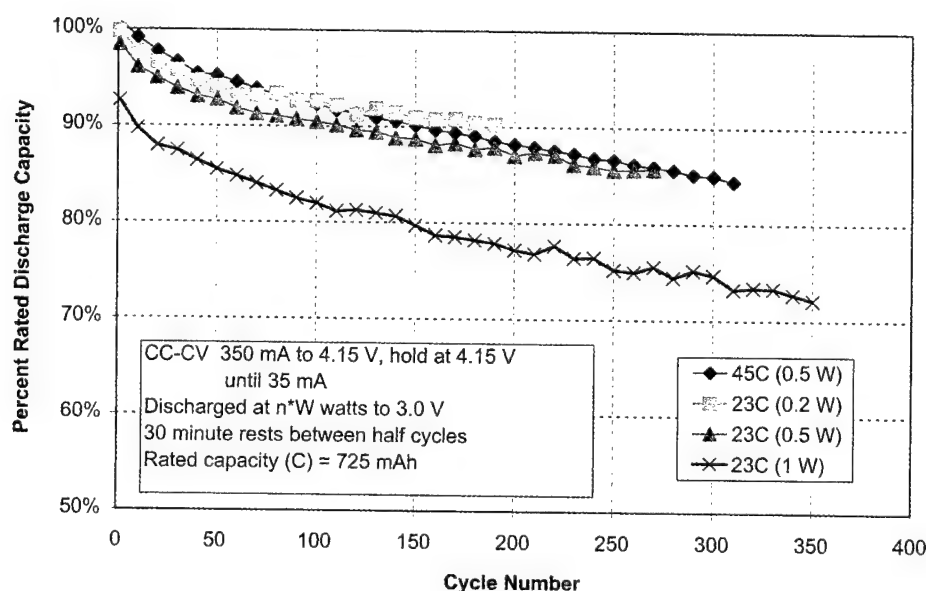


Fig. 8. UBC443483 interrupted constant power long-term cycling at 23 and 45°C. In the figure legend 1W = 2.8 watts.

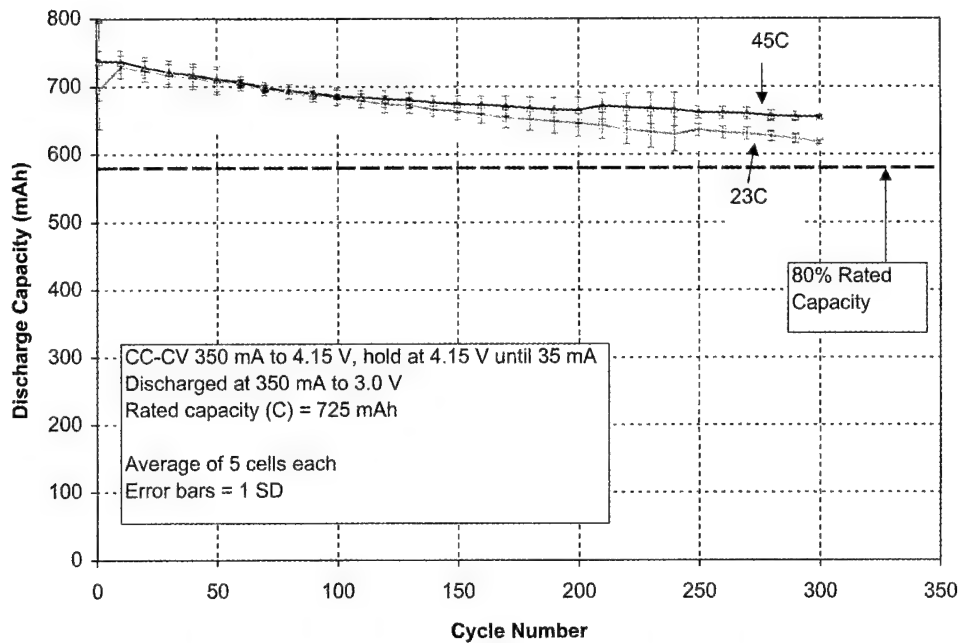


Fig. 9. UBC443483 with a PPTC undergoing continuous constant current long-term cycling at 23 and 45°C.

constant current (column D in Table 2) until the chosen percent DOD was obtained or 3.10 V (column B in Table 2) was reached. Cells were cycled at 10, 20, 40, 60, 80, and 100% DOD. Every 100–500 cycles, cells were charged as above, but only to 4.15 V (column E in Table 2), then discharged at a constant current of 350 mA (column D in Table 2) to 3.0 V (column F in Table 2) to obtain retained capacity information. These conditions were used to parallel the Nokia phone, closely approximating the charge and discharge rates, along with the reduced voltage window (vide infra). Several variants of this test were performed, see Table 2's figure numbers and related test differences.

When results are examined from the test conditions above, it becomes clear that the number of cycles expected to a given level of retained capacity for a cell is extremely dependent upon DOD. As shown in Fig. 13, a cell cycling at 100% DOD at 1C charge, 1C discharge, would be expected to average 330 cycles to 80% retained capacity. A decrease to 80% DOD increases the number of cycles to 450 — an over 25% improvement. The effect continues as one decreases the DOD cycle percentage, with 1000 cycles at 1C charge, 1C discharge possible to 80% retained capacity at 20% DOD. When a logarithmic trend line is plotted against the 90 and 80% retained capacity lines, a strong

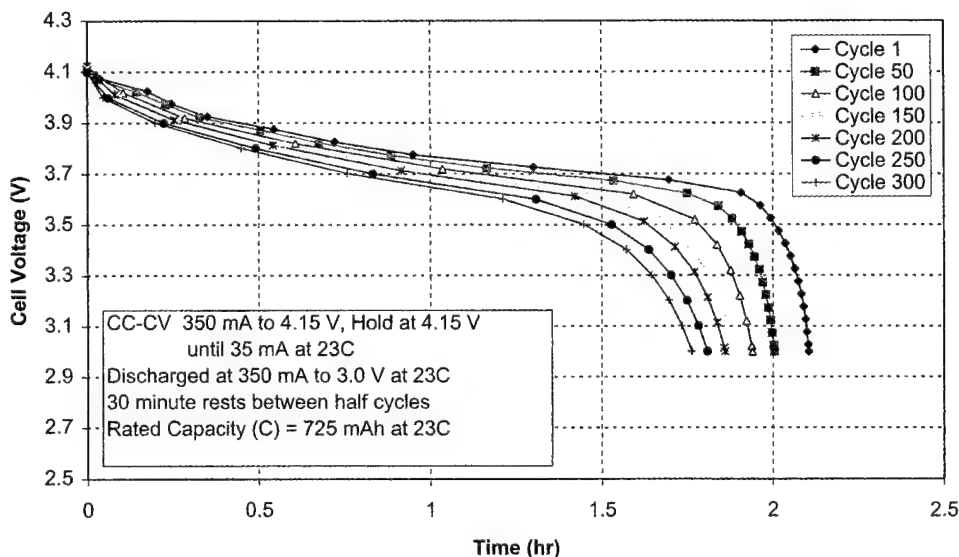


Fig. 10. UBC443483 with a PPTC discharge curves as a function of cycle number at 23°C.

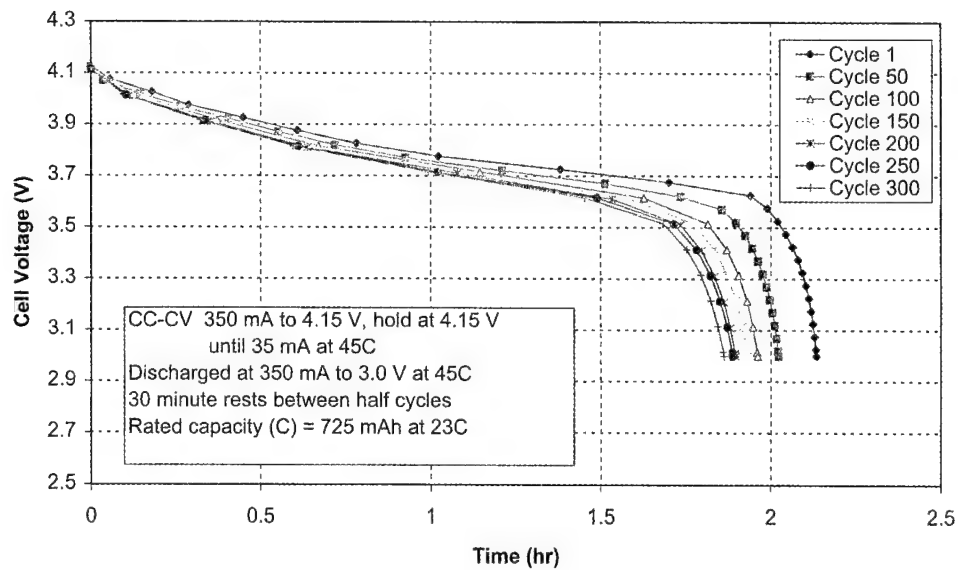


Fig. 11. UBC443483 with a PPTC discharge curves as a function of cycle number at 45°C.

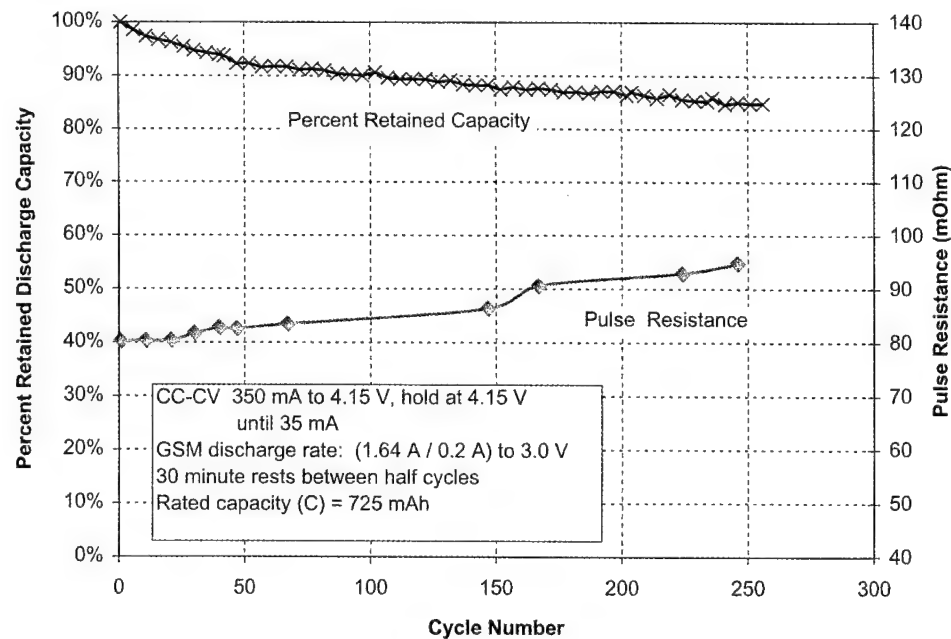


Fig. 12. UBC443483 with a PPTC interrupted long-term GSM discharge characteristics. Ambient temperature charge, GSM discharge (1.64 A/0.2 A) at ambient temperature.

Table 2  
Depth of discharge experimental matrix

Figures	A DOD cycle charge voltage	B DOD cycle end test voltage	C DOD charge rate (mA)	D DOD discharge rate	E Retained capacity charge voltage	F Retained capacity discharge voltage
13	4.10	3.1	350	350 (mA)	4.15	3.0
14	4.15	3.0	725	725 (mA)	4.15	3.0
15	4.15	3.0	725	2.8 (W)	4.15	3.0

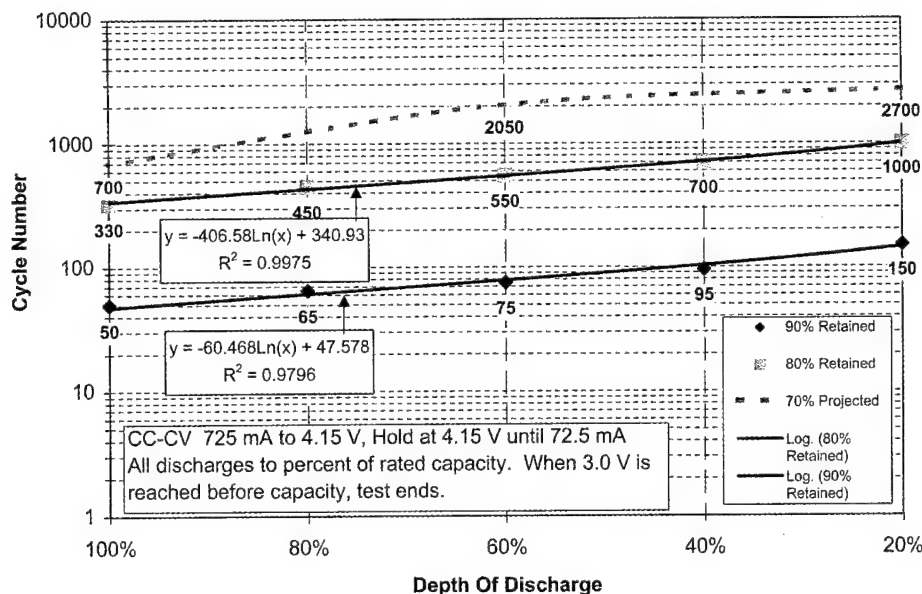


Fig. 13. UBC443483 with a PPTC cycle life vs. depth of discharge at ambient temperature. Constant current discharge at 1C. 100% DOD at 1C discharge every 100–500 cycles.

correlation with  $R^2$  values of 0.97 and 0.99, respectively, is present between DOD and cycle number. A linear projection based on fade between the most recent two full DOD cycles has been added to estimate the number of cycles to 70% of retained capacity.

With examination of the lower rate and constant power test conditions in Table 2, the effect of rate on cycle life is evident. As shown in Fig. 14, the decrease in the charge and discharge rate to 350 mA from 1C charge 1C discharge dramatically increases the number of cycles to 80% retained capacity. At 80% DOD, the number of cycles increases from

450 at 1C charge, 1C discharge, to 600 cycles at 350 mA charge, 350 mA discharge. At 60% DOD, the number of cycles increases dramatically from 550 to 1150. The 20% DOD cycling is enhanced as well, with the number of cycles to 80% retained capacity increasing from 1000 to over 4800. The data obtained in Fig. 14 were obtained from an experimental cell using a doped nickel oxide cathode, but similar results are expected for  $\text{LiCoO}_2$  cathodes.

Cycling the cells at constant power also supports the rate relationship, as shown in Fig. 15. Using the 0.2C rated power of 2.8 W, the cells being cycled are exposed to a varying

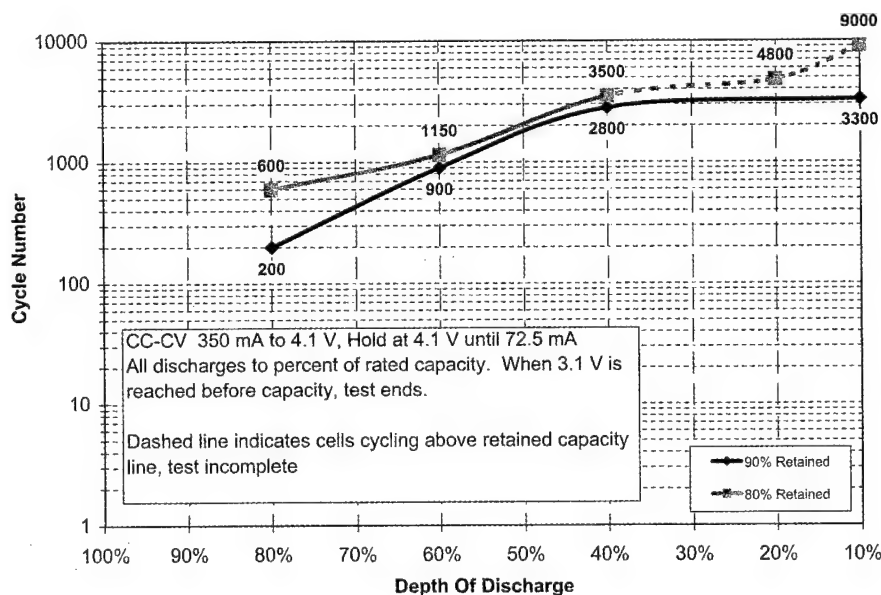


Fig. 14. Cycle life vs. depth of discharge at ambient temperature. Constant current discharge at 350 mA ( $C = 685$  mA). 100% DOD at 350 mA discharge every 100–500 cycles.

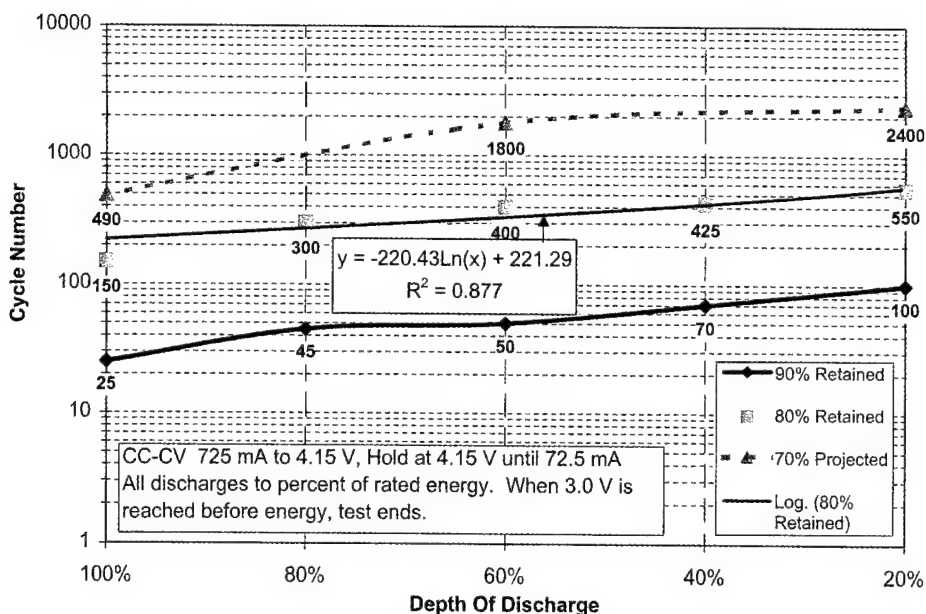


Fig. 15. UBC443483 with a PPTC cycle life vs. depth of discharge at ambient temperature. Constant power discharge at 2.8 W. 100% DOD at 2.8 W every 100–500 cycles.

current throughout discharge. To make results comparable to the other test conditions, the DOD percentages are based on the rated cell capacity in mAh, and retained capacity is measured by constant power discharges every 100–500 cycles. At low DOD the cells cycle near the 1C rate, while at higher depths of discharge the current can approach 1.3C at end of discharge as illustrated in Fig. 16. Cells cycling at constant power discharges to various DODs have decreased performance when compared to the cells cycling at 1C charge, 1C discharge. A linear projection based on fade between the most recent two full DOD cycles has been added to estimate the number of cycles to 70% of retained capacity.

### 3.6. Temperature storage studies

Testing was conducted in what is expected to be extreme storage conditions for cells in cellular phone packs under normal usage. This testing used a temperature cycling regime that varied the cell temperature from 0 to 60°C. Cells with a PPTC were held at each temperature for 6 h, then transitioned to the alternate temperature over 6 h. Total temperature cycle was 24 h. Cells were stored at 0 and 100% state of charge (SOC). The cells were removed periodically and tested for impedance growth at 1 kHz frequency and cycled to determine reversible capacity. The cells were charged to 4.1 V and discharged to 3.1 V to closely simulate

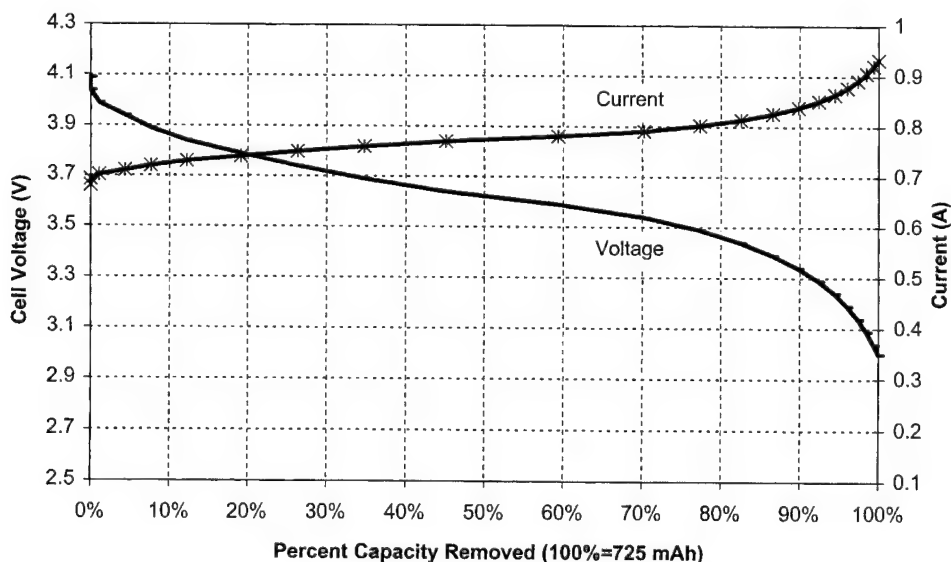


Fig. 16. UBC443483 with a PPTC at 2.8 W constant power discharge to 3.0 V at ambient temperature.

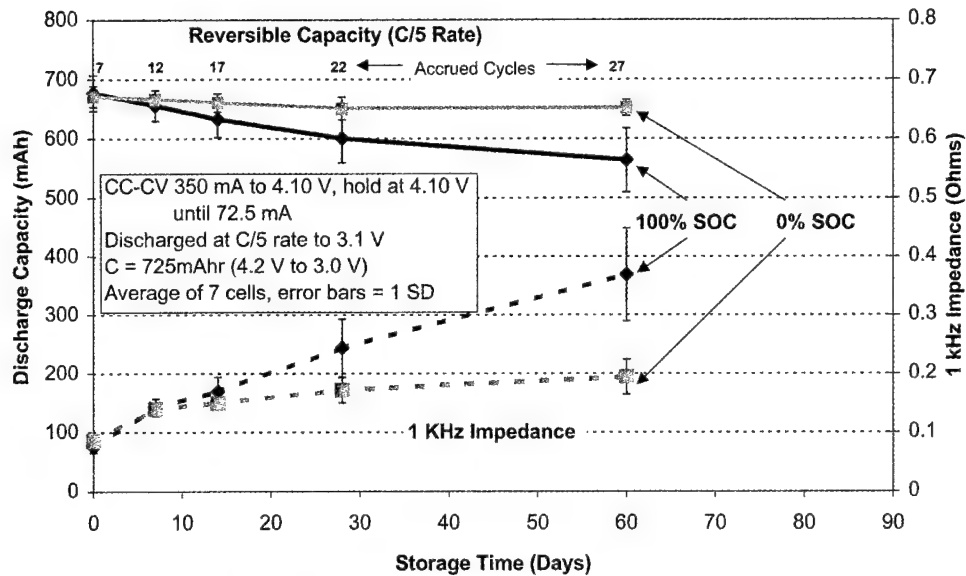


Fig. 17. The 0–60°C temperature cycle storage data for UBC443483 with a PPTC. Temperature cycle: 0°C for 6 h, 6 h ramp to 60°C; 60°C for 6 h, 6 h ramp to 0°C, repeat.

a cellular phone operational voltage window. Results are shown in Fig. 17. There is a charge state dependence on retained capacity and impedance growth at 1 kHz. All impedance measurements were performed prior to storage in the storage charge state, so all are charged to a similar voltage level.

Comparative data has been gathered at a continuous 60°C temperature storage on the UBC443483 cell in 100% SOC as shown in Fig. 18. These cells do not contain PPTC devices, so impedance is decreased by 35 mΩ at the start and throughout the test compared to cells in Fig. 17. Similarity in the results of Fig. 17 (temperature cycling, so

reduced time at 60°C) and 18 (continuous 60°C), suggests that thermal shock is a harsher test.

### 3.7. Float charge

Cells with PPTC devices were put on ambient temperature float charge at 1.075C rate for 1 week intervals. The voltage was set at 3 levels: 4.1, 4.2, and 4.3 V, while the maximum current was set at 780 mA. The cells were discharged at 780 mA to 3.0 V after each week of storage and the float test repeated. A total of 7 weeks of float charge

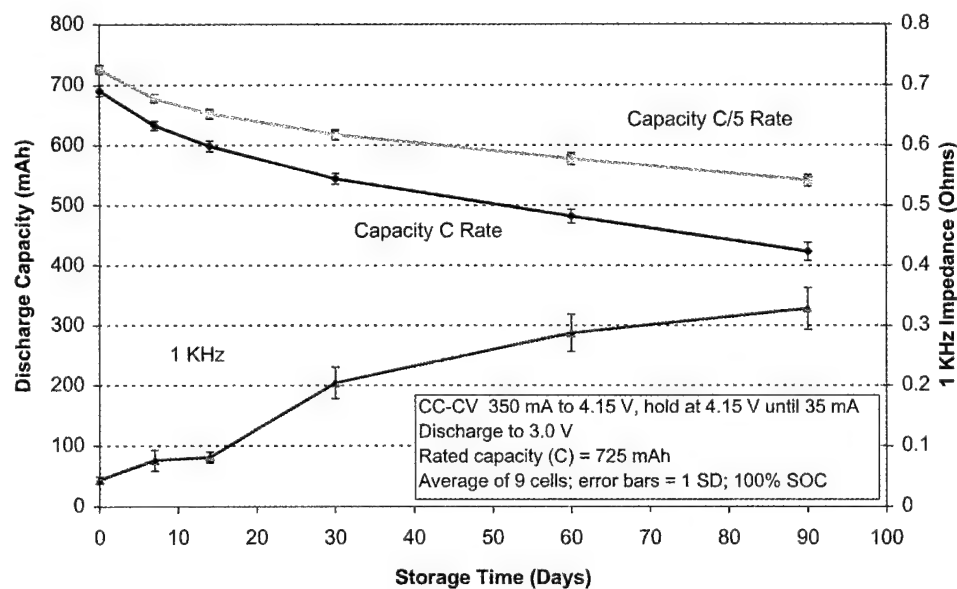


Fig. 18. The 60°C temperature storage data for UBC443483.

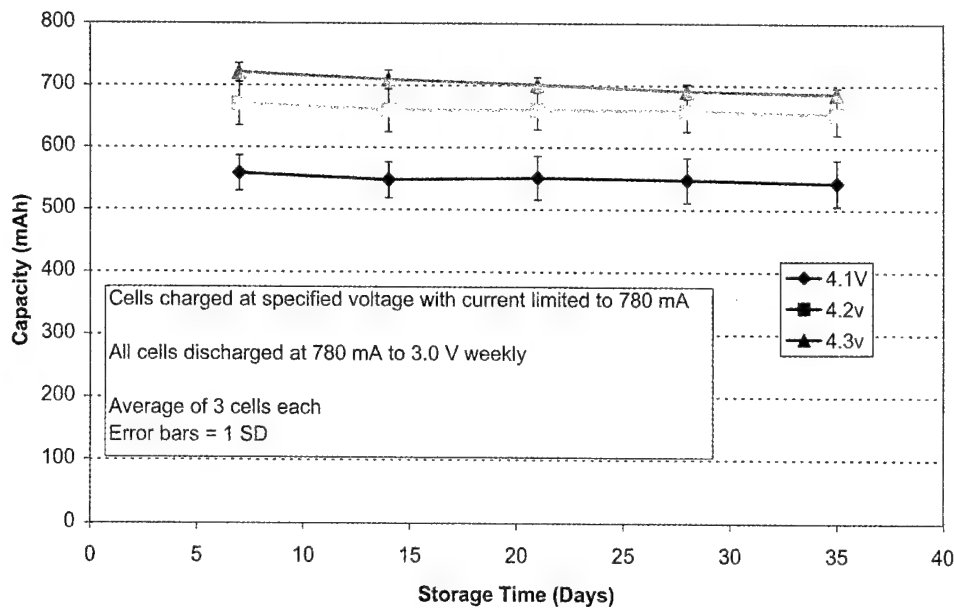


Fig. 19. UBC443483 with a PPTC on float charge at various voltages.

show little degradation of initial capacity and no safety problems, as shown in Fig. 19.

### 3.8. Advanced product development

Several energy density improvements are expected over the next few years and several prototype and commercial-scale builds are in testing [4]. One such development, yielding a 10% volumetric energy density improvement over current production product has been cycled to over 300 cycles. The cycle profile was a 0.5C charge to 4.15 V,

hold at 4.15 V until current drops below 0.1C, and discharge at 1C to 3.0 V. A non-packaged energy density comparison to the current product can be found in Fig. 20.

### 3.9. Advanced form factors

One of the key advantages of the Ultralife Polymer™ brand cell is that the form factor can be manipulated. The designer is no longer limited to a round or prismatic shape for powering a consumer device. Many shapes and sizes are possible with the advent of lithium polymer technology.

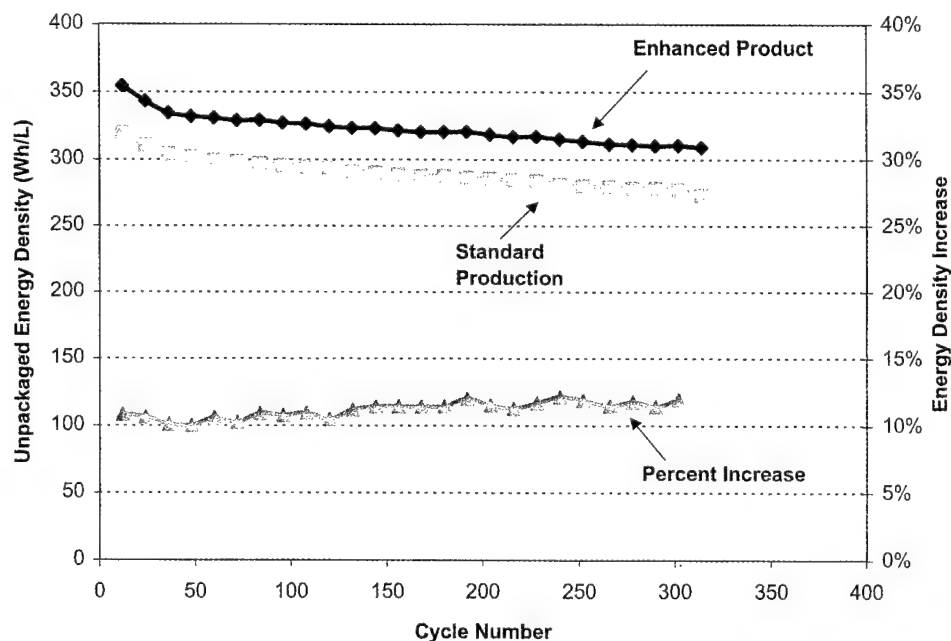


Fig. 20. Enhanced product comparison to current production product in a UBC093562 form factor.



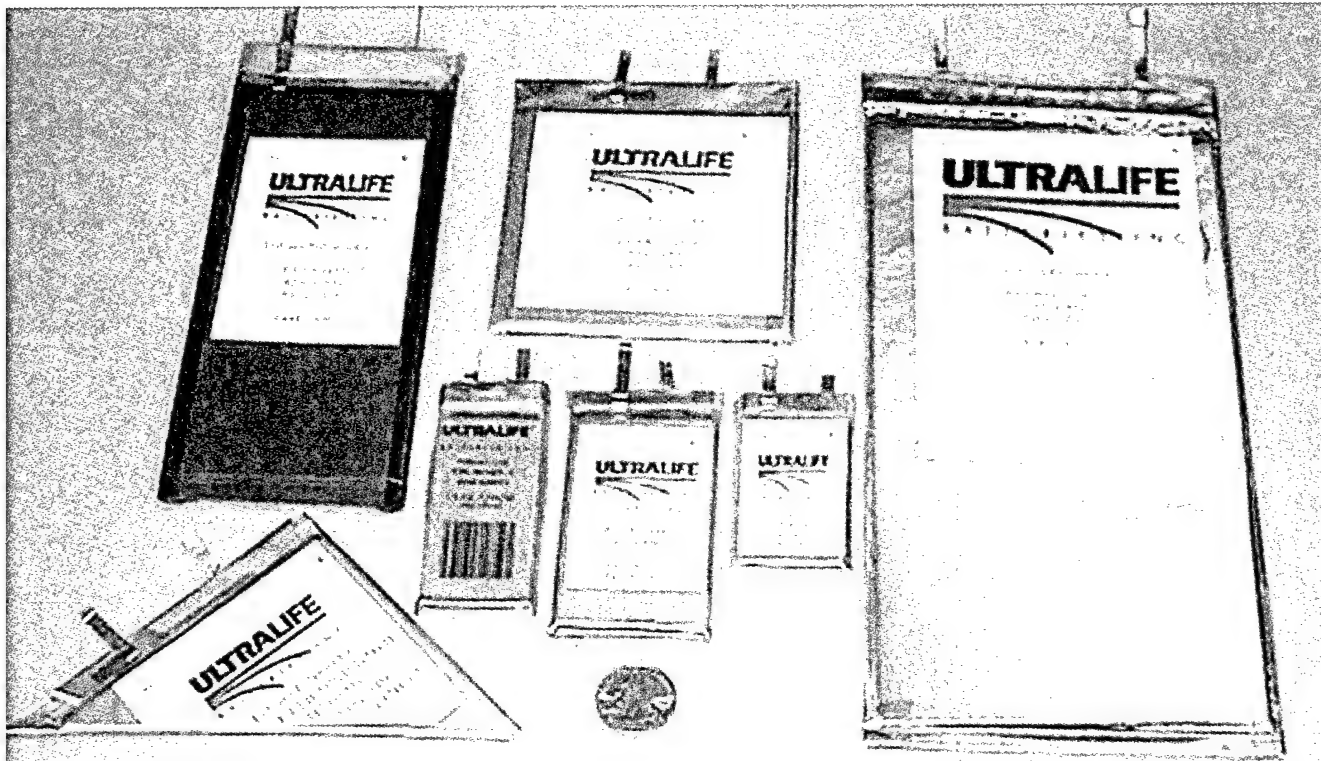


Fig. 21. Array of prototype and commercial Ultralife Polymer™ brand cells. The UBC443483 is the cell without the white label and with the bar code.

Two-dimensional shapes such as triangles, parallelograms, trapezoids, and tori could be easily accommodated with present processing methods, three-dimensional shapes can be envisioned or constructed from two-dimensional building blocks. This will allow designers in the future to more freely take advantage of design options available with shaped power sources. An example of this technology is the triangle cell viewed in Fig. 21. This cell has dimensions of  $102\text{ mm} \times 102\text{ mm} \times 154\text{ mm}$ , a thickness of  $3.1\text{ mm}$ , a capacity of  $1130\text{ mAh}$ , and an energy density of  $268\text{ Wh dm}^{-3}$ .

#### 4. Battery pack design

There are several design considerations that are instrumental in the development of a battery pack system. These include the type of housing, interconnects, and series and parallel combinations of cells used to achieve, respectively, the required voltage and capacity. Thermal management, safety devices, and specialized chargers may also be required. For safety, lithium-ion cell manufacturers usually recommend use of protection circuitry to prevent cell overcharge and overdischarge, as well as PTC devices or fuses to limit current. Impedance, assembly cost, and availability all factor in the final pack design. Ultralife Polymer™ brand batteries incorporate a charge control circuit and a PPTC device (vide supra) for pack protection and safety for the consumer. The incorporation of a protective circuit and a

PPTC device is important to protect against non-specified aftermarket chargers that can charge cell packs in an extremely harsh manner. Some aftermarket chargers tested at Ultralife have extremely high pulse and average charge currents, approaching  $3C$  with the UBC443483. This is much higher than the specified cell charge rate of  $C/2$  for the UBC443483, thus necessitating the need for charge control circuitry.

The charge control circuitry in use by Ultralife in cellular phone packs limits charge voltage to no more than  $4.25\text{ V}$  at the cell. If the cell voltage reaches  $4.25\text{ V}$ , the charge control will open the charge circuit, disallowing further charge. On discharge a similar protection is in place, where the charge control circuit will open and stop any overdischarge when the cell voltage is below  $2.3\text{ V}$ .

The use of charge control circuitry and a PPTC does add impedance to the battery system, thus reducing the average voltage of the battery pack, as shown in Fig. 22. This directly results in lower capacity and, therefore, talk and standby times when going from a cell to a completed battery pack. This results in a need to produce cells with as low impedance as possible to offset some of the impedance associated with protective devices, thereby increasing available capacity and talk time.

#### 5. Battery pack performance

There are varying power requirements for cellular phones across the world, based upon infrastructure setup, network

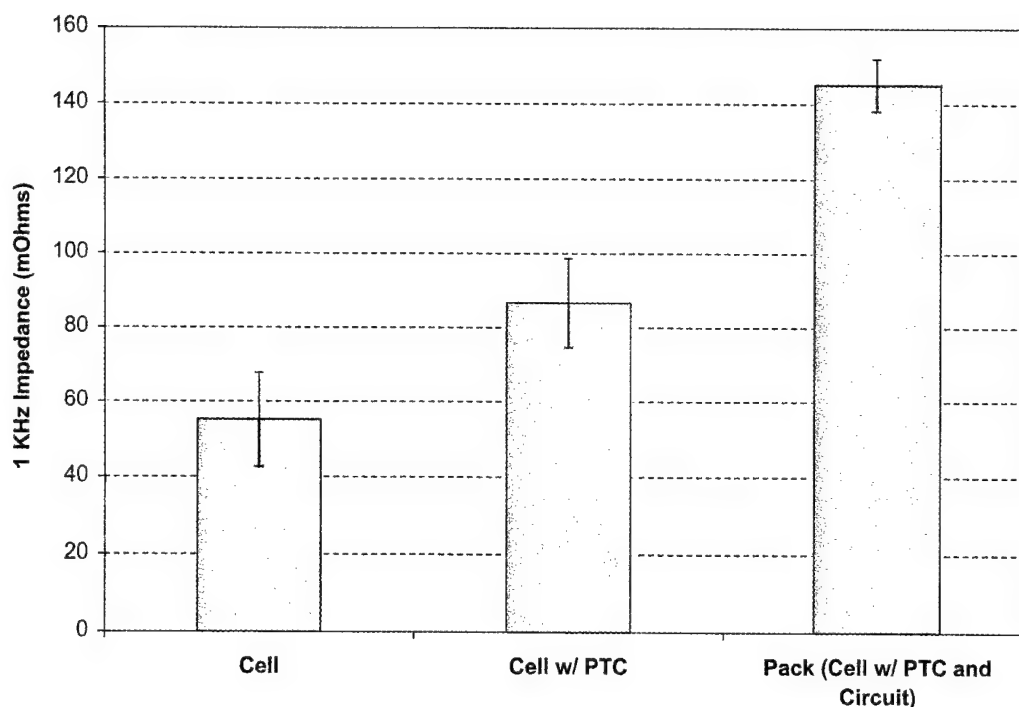


Fig. 22. Impedance comparison of UBC443483 cells with and without a PPTC device and with and without PPTC/circuit elements.

system, phone type, manufacturer, and usage habits. When evaluating several cellular phone types from Nokia in upstate New York using the UB750N battery pack, it is apparent that some of the inherent differences in power requirements are dependent on service provider's type of system. Service providers and system types tested included Sprint personal communication system (PCS), Verizon code division multiple access (CDMA), Frontier time division multiple access (TDMA), Cellular One Analog, and Cellular One Digital.

The analog system places the most aggressive power requirement on the battery. During standby the power consumption is pulse based, with a 100 mA high current for 50 ms every 1.25 s. While talking the system consumes 800 mA constant current, with 1 A  $\mu$ s pulses. The discharge current is constant whether a user is quiet or talking.

Digital systems are more power friendly. For example, a Verizon 5180 Nokia CDMA phone uses a standby profile that consists of a 200 mA pulse for 150 ms of duration every 2.5 s which does not differ much from the example above. Compared to analog, digital systems conserve power by reducing power levels during periods of inactivity (quiet), and raising power levels during active periods (talking). The talking current profile of the CDMA digital phone determined by test was 500 mA background current with 600 mA  $\mu$ s pulses, every 300  $\mu$ s, while the profile during quiet time periods reduced to 250 mA, with 300 mA high pulses every 5 ms.

Although European phone systems were not actually characterized for average current usage, most European

phones are GSM phones with well-known power requirements [5]. Actual usage tests were performed in Europe. The tests used a Nokia phone and confirms the decreased power consumption and increased talk time over United States systems. Results are summarized in Table 3 for the UB750N battery pack.

The cellular phones were also tested for low battery and cut-off voltage ranges. The phone ceases to operate and the display will not light if the pack voltage is below 3.2 V. The phones start going into low battery alarm below 3.6 V. Due to the high current drain and corresponding voltage drop in the pack, analog phone operation is limited once the low battery alarm sounds. The digital phones are slightly better, with roughly 10–15% of talk time available after low battery alarm sounds.

One of Ultralife's main goals is to produce the lightest, highest capacity, polymer cell phone battery. To this end, several original equipment manufacturer (OEM) and competitor products were tested for specific energy. The results are favorable for the Ultralife cellular phone product, as shown in Fig. 23.

Table 3  
Average actual talk times associated with three different cellular phone service provider systems

System	Phone	Location	Talk time (min)
Cellular One Analog	5120	US	44–48
Sprint PCS Digital	6185	US	110–125
European GSM	6110 GSM	UK	200–210

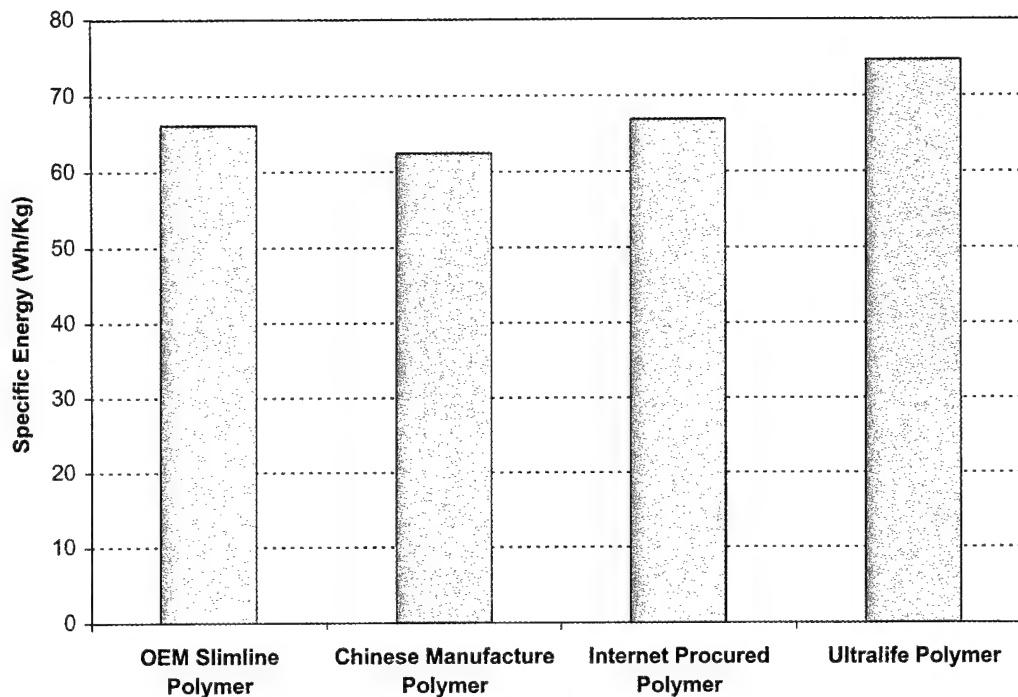


Fig. 23. Comparison by energy density of various polymer battery packs available on the market. Nokia 51xx, 61xx, and 71xx platforms.

Table 4  
Comparison of various currently available charge devices

Power supply	Connected to	Method	$I_{P-P}$	$I_{AVE}$	$I_{RMS}$
ACP-7U	Phone model: 6185	Pulse	718.7	216.8	333.3
ACP-7U	DCH-9 base	Pulse	662.5	180	240
ACP-9U	Phone model: 6185	Constant current	NA	729	NA
ACP-9U	DCH-9 base	Constant current	NA	270	NA
LCH-9U (car)	Phone model: 6185	Constant current	NA	776	NA

## 6. Battery pack charger

Standard Nokia chargers were evaluated for charge currents and voltages. The standard power supply that comes with most Nokia phones is the ACP-7U. This power supply is relatively low rate, and when attached to the phone for charging, uses a peak current nearing 720 mA, with an average current of 220 mA. The charge method is a pulse

width modulation method, whereby as the pack reaches full charge, the period between pulses increases. Several power supplies were evaluated in the same manner.

The fast charge models, ACP-9U and LCH-9U, differ from the ACP-7U in that a constant current charge method is used. These chargers charge at relatively high rates of 720–770 mA until the voltage reaches 3.9 V. The charger then enters a trickle charge mode for the remaining charge. When

Table 5  
Various 350 mA ambient discharge capacities at cycle 50 for UBC443483 cells

Description	High voltage cut-off	Low voltage cut-off	Discharge capacity (Ah) at cycle 50	Notes
No PTC	4.20	3.00	0.700	Cell in normal cycle voltage range
With PTC	4.20	3.00	0.683	PTC influence on cell in normal range
No PTC	4.10	3.10	0.580	Cell in "phone" cycle range
With PTC	4.15	3.00	0.572	Cell between normal and "phone" cycle range + PTC is similar to cell without PTC cycling at 4.10–3.0 V
With PTC	4.10	3.10	0.540	Cell in "phone" cycle range with PTC
With PTC and circuit	4.10	3.10	0.526	Cell in "phone" cycle range with PTC and protection circuit board

the ACP-9U is attached to the DCH-9 base, the charge current is reduced to 270 mA at the rear slot. The maximum charge voltage was 4.101 V at the pack for all charge combinations (see Table 4 for the testing matrix).

The maximum charge voltage is important, as a voltage of 4.2 V must be obtained at the cell to fully charge a  $\text{LiCoO}_2$  lithium-ion cell. When the pack is charged to 4.1 V, greater than 10% reduction in capacity from the rated cell capacity is possible. Impedance losses due to circuit protection, fuses, and connections further reduce available cell capacity at the pack level. This can be seen in Table 5, which compares the capacity of a cell and a battery pack cycling at the same rates over various voltage windows. The battery pack has reduced capacity due to the reduction in voltage at the cell by the additional circuit and protection devices.

## 7. Summary

One of the most aggressive and varied power requirements is in the application of today's cellular phones.

Ultralife is a leader in providing next generation portable power for cellular phones and other wireless devices. Current generation Ultralife technology is a significant step forward in the portable power area, and future developments will allow Ultralife to continue to be competitive in this market segment.

## References

- [1] The Eighth Annual International Conference on Power Requirements for Mobile Computing and Wireless Communications, 24–27 September, 2000, San Diego, CA.
- [2] J.S. Xue, R.D. Wise, X. Zhang, M.E. Manna, Y. Lu, G. Ducharme, E.A. Cuellar, *J. Power Sources* 80 (1999) 119–127.
- [3] A.S. Gozdz, J.-M. Tarascon, P.C. Warren, US Patent 5,460,904.
- [4] National Institute of Standards Technology, Advanced Technology Program, Advanced Lithium Solid Polymer Battery Development Awarded on October 1998 to Ultralife Batteries Inc., Eagle-Picher Technologies, LLC, Lockheed Martin Missiles and Space Company, Award Number 70NANB8H4073.
- [5] R. Kurupillai, M. Dontamsetti, F.J. Cosentino, *Wireless PCS*, McGraw-Hill, New York, 1997, pp. 201–202.

Abstract

## The development of higher energy density lithium-ion cell designs

F. Coowar, J.S. Weaving, M. Lee, C.R. Jarvis, W.J. Macklin\*

*AEA Technology Batteries, Culham Science Centre, El Culham, Abingdon, Oxfordshire OX14 3ED, UK*

---

**Abstract**

Progress in the development of higher energy density lithium-ion cell designs for a range of consumer and military applications will be described. Strategies for improvements in energy density based on the introduction of higher capacity electrode materials such as the  $\text{LiNi}_{1-x-y}\text{Co}_x\text{Al}_y\text{O}_2$  cathode material with a high reversible capacity of  $184 \text{ mAh g}^{-1}$  will be presented. Electrochemical data will be used to illustrate the benefits of optimisation of electrolyte system to maximise lithium-ion cell capacity.

The performance characteristics of 'flat' cell designs utilising flexible laminate packaging materials will be presented in order to demonstrate that projected lithium-ion energy densities of  $180 \text{ Wh kg}^{-1}$  are achievable. Finally, comparisons between alternative lithium-ion and lithium-ion polymer cell designs will be discussed. © 2001 Published by Elsevier Science B.V.

**Keywords:** Lithium batteries/polymer electrolyte

---

---

\* Corresponding author.

## Direct methanol–air fuel cells with membranes plus circulating electrolyte

Karl Kordesch<sup>a,\*</sup>, Viktor Hacker<sup>b</sup>, Udo Bachhiesl<sup>b</sup>

<sup>a</sup>*Institute for Chemical Technology of Inorganic Materials, Graz University of Technology, Stremayrgasse 16/III, A-8010 Graz, Austria*

<sup>b</sup>*Department of Electricity Management and Energy Innovation, Graz University of Technology, Inffeldgasse 18, A-8010 Graz, Austria*

Received 19 December 2000; accepted 19 December 2000

### Abstract

A new approach for direct methanol–air fuel cells (DMFC), with the advantage of reduced methanol crossover is discussed in this paper. Methanol traces in the circulated electrolyte are recovered and CO<sub>2</sub> bubbles in the cells are removed due to the forced methanol–electrolyte stream through the cell.

Degradation of the catalyst is reduced since fuel cell electrodes degrade on activated stand without load to a higher extent than under load because high voltage on open circuit promotes carbon oxidation, catalyst changes, etc. Therefore, life expectancy increases with circulating electrolyte by removing the electrolyte from the cells between operating periods. © 2001 Elsevier Science B.V. All rights reserved.

**Keywords:** Fuel cells/direct methanol; Fuel cells/acidic electrolytes

### 1. Fuel cells with circulating electrolyte

The classical example of a fuel cell with liquid electrolyte is the alkaline fuel cell (AFC). The introduction of AFC for space applications led to the elimination of circulating electrolyte due to removal of any mechanical pumps, which were not reliable enough. The use of matrices (for instance, micro-porous asbestos) soaked with KOH became standard for NASA space fuel cells. The fact that liquid circulating electrolytes offered great advantages for heat management and water removal requirements was believed to be overcome by the disadvantage of creating parasitic shunt currents in cell assemblies connected in series. Delayed start-up procedures often led to the reversal of cells and irreversible cell failures. The advantages of combining fuel cells with rechargeable batteries in a hybrid system were not recognised. As a matter of convenience and for time saving, all the testing of fuel cells was (and is) done in a continuous operation mode. The need to operate fuel cells in an interrupted fashion, sometimes with long idle periods did not seem to be important — but surely it is. The fuel cell must be able to shut down completely for longer time periods, hours, days, weeks, etc. it must be safe in the garage, with

turned-off fuel supply, at ambient and even low temperatures. It should also be mentioned that on activated stand, without load, fuel cell electrodes and catalysts degrade more than under load. The high voltage on open circuit is the reason for carbon oxidation processes, catalyst changes, etc. [1–3].

Direct methanol fuel cells with KOH or NaOH as electrolytes have been built by Vielstich [4] and high current densities had been achieved with flow-through Raney type electrodes [5]. The air electrodes produced high voltages and good current densities due to the alkaline pH of the electrolytes. However, the anodic reaction products of the methanol are CO<sub>2</sub> and H<sub>2</sub>, and therefore, the KOH is used up, requiring an exchange of the electrolyte after use.

The historic alkaline direct methanol systems can be improved by using circulating electrolytes and separator systems designed to cut down the cross leakage and preventing the destruction of the hydrophobic property of the air cathodes by methanol. It will then be possible to use alkaline methanol–air fuel cells in the same way as zinc–air batteries with replaceable zinc anodes. Actually the procedure of emptying the spent electrolyte and filling up the tank again with a near stoichiometric methanol–electrolyte mixture instead of an equivalent methanol–water mixture would be quite simple.

Acidic fuel cell electrodes have been extensively developed for phosphoric acid fuel cells. Formulations for carbon activation and catalysts used in phosphoric acid cells [6]

\* Corresponding author. Fax: +43-316-83-76-19.  
E-mail address: kkmno2@aol.com (K. Kordesch).

have been useful for acidic methanol cells. Acidic DMFCs have been investigated by Shell and Exxon using sulphuric acid, later also fluoroboric acid and bicarbonates have been tested. Though  $\text{CO}_2$  sensitivity was avoided, no solution was found to the problem of corrosion and performance reduction due to methanol crossover. The projects were suspended. No research is reported with circulating electrolyte [7–10].

## 2. Direct methanol fuel cell with circulating electrolyte

A new system of a direct methanol fuel cell with circulating electrolyte is suggested [11–13]. The DMFC with circulating electrolyte has the potential to solve the problem of methanol crossover and at the same time has the advantages of a circulating electrolyte. The liquid electrolyte is arranged between two matrices. The matrix could be a proton exchange membrane, but the goal is to find a more inexpensive material for the matrix to reduce methanol diffusion into the electrolyte. The circulating liquid electrolyte containing methanol leaves the cell and thereby prevents crossover (chemical short circuiting). Since the liquid electrolyte is pumped through the system, the fuel cell can easily be interrupted and deactivated. A loss of methanol between operating periods is avoided as well. The small amount of methanol in the electrolyte will be recovered and the electrolyte recycled into the cells.

Fig. 1 shows in principle how membrane DMFC systems can be modified by adding a liquid electrolyte, demonstrating the principle of an acidic DMFC with a circulating electrolyte. The out-flowing liquid carries any small amounts of permeated methanol out of the cell into a

recovery (distillation) unit. The fuel mix can now be fed even at a higher concentration as before and no damage to the air electrode will occur. Fig. 2 shows mass flows in a direct methanol fuel cell with liquid electrolyte and (optionally) with matrix or membrane on the anode or cathode (or on both) sides. Several possible combinations of electrodes, membranes or separators and liquid flow fields are shown in Fig. 3. The optimal arrangements will have to be explored with performance and cost considered. Very promising to improve the cost situation, is a system arrangement without a polymer electrolyte membrane (Fig. 3a).

Presently the acidic DMFCs are built with PEM membranes. The introduction of an acidic liquid electrolyte in addition to PEMs will also change the membrane characteristics. This is expected also in hydrogen–air PEM systems. Especially the water transport (water is attached to the protons) can be influenced and changes in ionic mobility are expected. The  $\text{H}_2\text{SO}_4$  electrolyte for example has conductivities in the fractional Siemens ranges. The system can be completely shut down if needed, whereby the catalysts re-activate. Membranes are re-wetted immediately when the cells start again, no complicated wetting procedures are required. However, the biggest advantages are probably obtained in the higher temperature ranges where water vapour (relative humidity) control and cooling becomes a major effort. Performance criteria for PEMs, mechanical, influences of cations on water content, gas permeability, cross leakages as function of thickness and current densities, ion exchange capacity versus resistances, differences between ac and dc resistance values, etc. [14–16].

The system built first (Fig. 4) was operated with hydrogen and oxygen using a 0.5 M  $\text{H}_2\text{SO}_4$  electrolyte between the anode and cathode up to  $550 \text{ mA cm}^{-2}$  at 0.35 V.

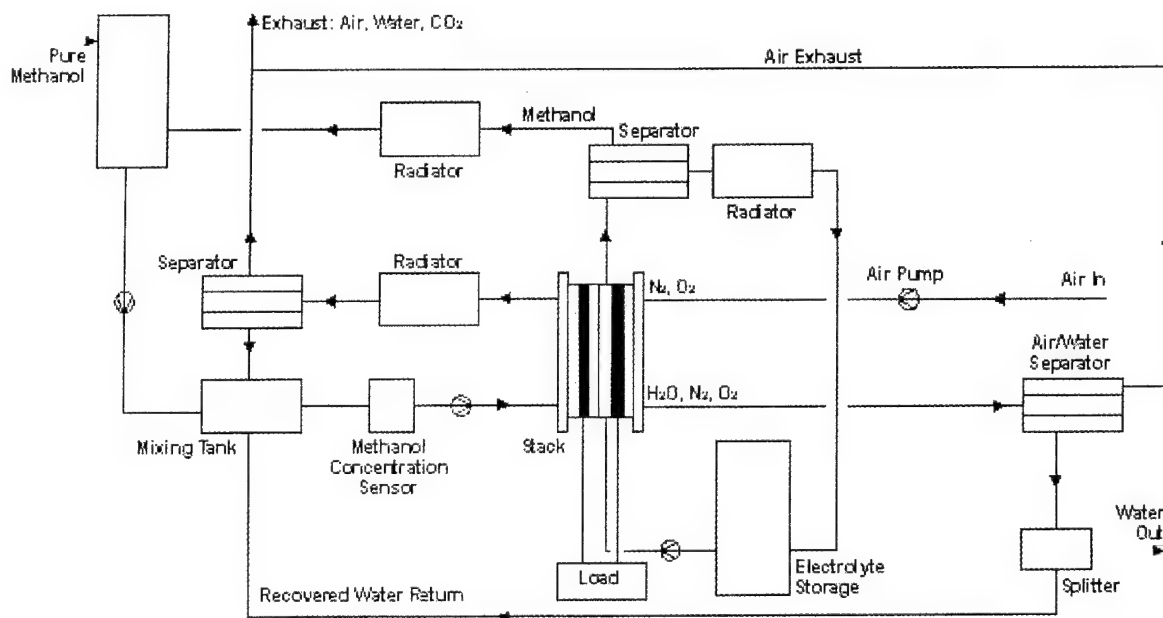


Fig. 1. Concept of a DMFC system with liquid acidic electrolyte, operating at  $70^\circ\text{C}$ .

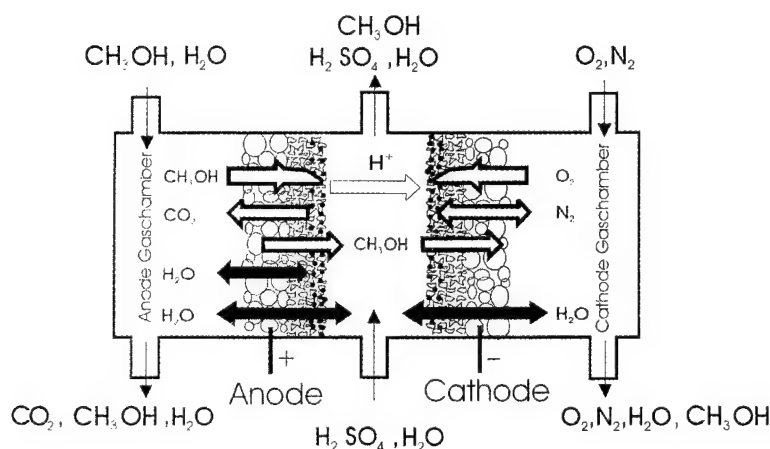


Fig. 2. Mass flows within a direct methanol fuel cell.

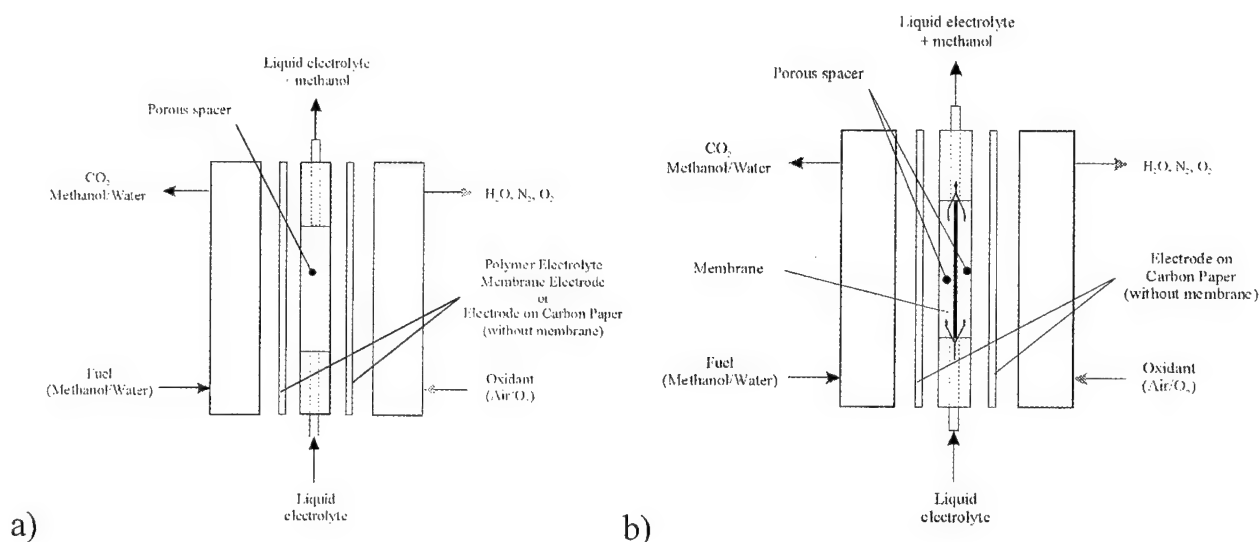
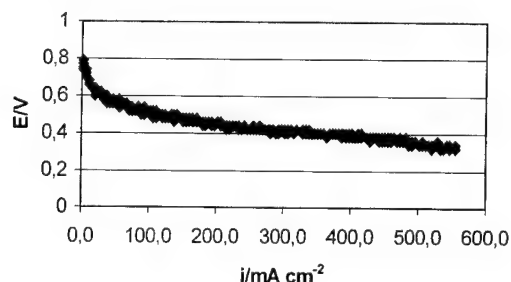


Fig. 3. Possible variations of direct methanol fuel cells with circulating electrolyte.

The result of a preliminary experiment with a single DMFC is shown in Fig. 5. It was done with E-TEK EFCG electrodes on TGP-120 Toray Carbon (two PAFC electrodes with a catalyst loading of  $4 \text{ mg cm}^{-2} \text{ Pt/Ru}$ ). No membrane was used.

Fig. 4. Voltage/current density curve obtained with hydrogen and oxygen at  $20^\circ\text{C}$ , not under pressure and  $0.5 \text{ M H}_2\text{SO}_4$  as electrolyte.

The electrolyte ( $0.5 \text{ M}$  sulphuric acid) is pumped through the system by using a tubing pump. The electrolyte in the cell is being circulated at an exchange rate of approximately four times a minute. The experiment was done at ambient temperature. At the cathode pure oxygen, at the anode a  $10 \text{ M}$  methanol–water mixture, was used. As shown in Fig. 5, the open circuit voltage (OCV) reaches approximately  $0.8 \text{ V}$  in the starting phase. Thereafter, phase 1 shows that the OCV remains stable although methanol can easily go through the membrane because no PEM is used. At the beginning of phase 2 the circulation was stopped and the OCV falls rapidly. Summarising, it can be said that while pumping electrolyte through the system (phase 1) the OCV remains constant, while after interruption of the circulation of the electrolyte (phase 2) the OCV decreases by the effect of methanol crossover.



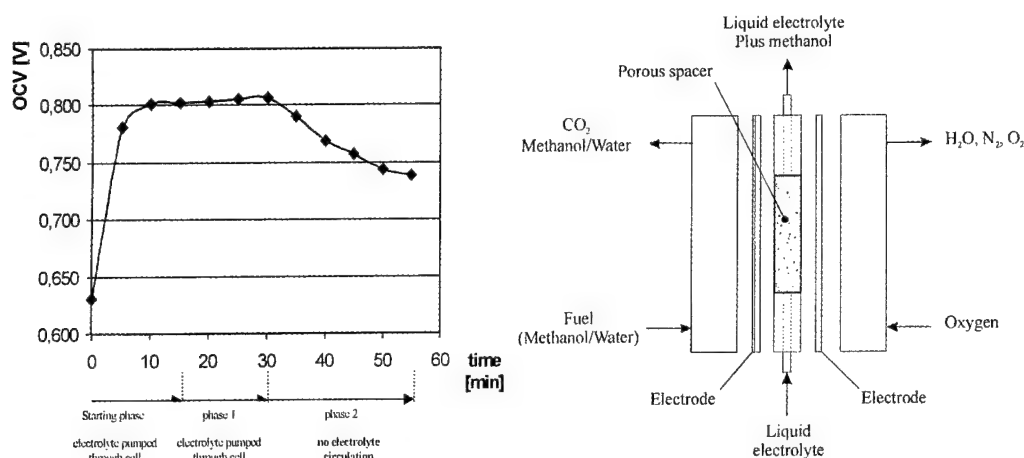


Fig. 5. Influence of electrolyte circulation on open circuit voltage of a DMFC cell (left), schematic of the system, which had an active electrode area of  $4.5 \text{ cm}^2$  (right).

### 3. Conclusion and future work

Preliminary test results confirm the assumptions that a circulating electrolyte helps to avoid methanol crossover in DMFCs. Experiments with different systems of DMFC with circulating electrolytes and at different temperature levels are planned whereby it is expected that the combination of a liquid electrolyte with a polymer electrolyte membrane controls drying and humidification and also makes it possible to influence the water transport via the protons of the membrane and that heat management of the stack will be eased.

Operation at higher temperature becomes possible by using different electrolytes. For cost reduction, a replacement of the polymer electrolyte membrane will be sought.

From the experiences with acidic electrolyte fuel cells it can be concluded that life expectancy for DMFC with circulating electrolyte can be increased by emptying the electrolyte between operating periods since this shuts down the system and eliminates all parasitic currents.

### Acknowledgements

The acidic DMFC program at Graz University of Technology is supported by Energy Ventures Inc., Canada (President: Wayne D. Hartford) in co-operation with the National Research Council (NRC) of Canada in Ottawa.

### References

- [1] K.V. Kordesch, J. Gsellmann, M. Cifrain, S. Voss, V. Hacker, R.R. Aronson, C. Fabjan, T. Hejze, J. Daniel-Ivad, *J. Power Sources* 80 (1999) 190.
- [2] K.V. Kordesch, R.F. Scarr, *Thin Carbon Electrodes for Acidic Fuel Cells*, IECEC, 1972, No. 729003.
- [3] V. Hacker, G. Faleschini, P. Enzinger, M. Muhr, K. Friedrich, in: *Proceedings of the 3rd International Fuel Cell Conference on Alkaline Fuel Cells For Electric Vehicles*, Nagoya, 30 November–3 December 1999, p. 165.
- [4] W. Vielstich, *Alcohol–air fuel cells*, in: B. Baker (Ed.), *Hydrocarbon Fuel Cell Technology*, Academic Press, New York, 1965.
- [5] H. Binder, A. Köhling, G. Sandstede, *Raney Catalysts, From Electrocatalysts to Fuel Cells*, Battelle Seattle Research Center, University of Washington, PR, USA, 1972.
- [6] K.V. Kordesch, *Survey of Carbon and its Role in Phosphoric Acid Fuel Cells*, DOE-Contract 464459-s, Brookhaven Natl. L. 51418-Uc-94d, 31 December 1979.
- [7] A. Heinzel, V.M. Barragan, *A review of the state-of-the-art of the methanol crossover in direct methanol fuel cells*, *J. Power Sources* 84 (1999) 70.
- [8] J. Cruickshank, K. Scott, *The degree and effect of methanol crossover in the direct methanol fuel cell*, *J. Power Sources* 70 (1998) 40.
- [9] X. Ren, P. Zelenay, S. Thomas, J. Davey, S. Gottesfeld, *Recent advances in direct methanol fuel cells at Los Alamos National Laboratory*, *J. Power Sources* 86 (2000) 111.
- [10] B.D. McNicol, D.A. Rand, K.R. Williams, *J. Power Sources* 83 (1999).
- [11] K. Kordesch, M. Cifrain, T. Hejze, V. Hacker, U. Bachhiesl, in: *Proceedings of the Fuel Cell Seminar 2000 on Fuel Cells with Circulating Electrolytes*, Portland, OR, 30 October–2 November 2000, p. 432–435.
- [12] K. Kordesch, V. Hacker, in: *Proceedings of the 17th International Electric Vehicle Symposium & Exhibition on Fuel Cells with Circulating Electrolyte and their Advantages for DMFCs*, EVS 17, Montreal, Session 2C-3, 15–18 October 2000.
- [13] K. Kordesch, et al., in: *Proceedings of the 39th Power Sources Conference*, Cherry Hill, NJ, 12–15 June 2000, p. 190.
- [14] K. Kordesch, G. Simader, *Fuel Cells and Their Applications*, VCH-Verlag, Weinheim, 1996.
- [15] *Proceedings*, Vol. 575, pp. 201–275, Publisher: National Research Society Warrendale, PA (1999), Editor: Daniel H. Doughty et al. *Proceedings of the Symposium on New Materials for Batteries and Fuel Cells*, San Francisco, 5–8 April 1999.
- [16] J. Larminie, A. Dicks, *Fuel Cell Systems Explained*, Wiley, New York, 2000.

# The effect of anode flow characteristics and temperature on the performance of a direct methanol fuel cell

John C. Amphlett, Brant A. Peppley\*, Ela Halliop, Aamir Sadiq

*Department of Chemistry and Chemical Engineering, Royal Military College of Canada, Kingston, Ont., Canada K7K 7B4*

Received 6 December 2000; accepted 16 December 2000

---

## Abstract

An experimental direct methanol fuel cell (DMFC), designed and manufactured in-house, was used in this study. The cell is of standard filter-press configuration with parallel rectangular single-pass anode channels. The membrane electrode assembly (MEA), with a suitable Pt–Ru anode electrocatalyst, was purchased from E-TEK Inc. A 1.0 M methanol in water solution was used as the fuel and pure oxygen was used as the oxidant in all experiments. Three graphite anode plates were machined with the same flow channel configuration but each with different depth of channels. The cathode was kept the same for all experiments. Polarisation curves and ac impedance spectra were obtained for varying temperatures and channel depths. To separate the contribution of the oxygen reduction reaction to the overvoltage from the anode and membrane contributions, reference hydrogen electrode (RHE) measurements were taken. By comparing the RHE polarisation with the methanol–oxygen polarisation experiments, it was found that polarisation losses at the oxygen cathode accounted for a 40–50% of the overpotential.

The variation in the performance of the cell with flow of methanol/water mix, with temperature and with current density was studied. Polarisation measurements indicate that the medium channel depth flow channels performed better than either the shallow depth or deep depth flow channels indicating that there is a complex relationship between the effect of flow velocity and the influence of the rate of production of product  $\text{CO}_2$ . AC impedance spectroscopy measurements confirmed the observed polarisation results. This method proved to be able to provide a reliable indication of the performance of the cell even when the cell had not yet achieved steady-state. In the case of the shallow channel depth anode, ac impedance revealed that it required considerably longer to achieve steady-state than the time required for the medium and deep channel depths. © 2001 Elsevier Science B.V. All rights reserved.

**Keywords:** Fuel cells/direct methanol; Impedance spectroscopy (ac)

---

## 1. Introduction

Direct methanol fuel cells (DMFCs) have considerable advantages when compared to polymer electrolyte membrane (PEM) hydrogen/air fuel cells: simplicity and convenience. However, DMFCs are also marred by a number of technical challenges: very wet environment, slow anode kinetics and mixed potential [1–3].

The wet environment has important implications for the cell operation. An excess of water in DMFCs can lead to cathode flooding and, in consequence, results in less than optimal performance. The cell has to be designed in such a way as to keep water away from electrical connections. This is further complicated by the fact that corrosion restricts the choice of the material for channel plates.

A number of different approaches are being investigated to improve anode kinetics. The greatest effort is being directed toward the development of more active electrocatalysts: binary to quaternary platinum alloys [4], supported and unsupported Pt/Ru [5–8]. Other approaches for dealing with slow anode kinetics involve increased cell temperature and pressure [9].

A critical issue to the advancement of DMFC is methanol permeation through the membrane. Methanol is being ionised in the cathode catalyst layer, but the ions and electrons do not contribute to the overall current. Instead this consumes oxygen and, in consequence, lowers the overall voltage.

Until a methanol impermeable membrane is discovered [10–14] or the cathode catalyst possesses the specific function to selectively catalyse oxygen reduction without allowing methanol oxidation [15,16], the only known tools to reduce methanol crossover are lower methanol feed concentration and optimised cell design [17].

---

\* Corresponding author. Tel.: +1-613-541-6000/ext. 6702;  
fax: +1-613-542-9849.  
E-mail address: peppley-b@rmc.ca (B.A. Peppley).

There has recently been a significant amount of work done in modelling the flow behaviour in DMFCs [18–23]. The performance of a variety of flow channel designs were also recently compared [24,25]. It is clear that the geometry of the flow channels (especially the anode channel) can have a significant effect on fuel cell performance.

Various approaches have been used in our laboratory to study the effect of anode flow characteristics on DMFC performance. The first experimental set-up used a transparent cell (Plexiglas<sup>TM</sup> and Cyrolon) with grid pattern flow channels. Current collectors, both mesh and foil, of various materials (graphite, stainless steel, titanium and molybdenum) were used in an attempt to achieve low contact resistance.

The transparent cell proved to be an excellent tool for gaining knowledge of the flow dynamics inside the DMFC. For example, it could be visually confirmed that the performance of the cell was significantly effected both by cathode flooding, and when the surface of the anode became covered with bubbles of carbon dioxide. This cell, however, had a somewhat limited operating temperature and pressure.

In the present work, a cell of standard filter-press configuration with parallel rectangular single-pass flow channel plates was used. Both the anode and cathode were made of electrochemical grade graphite. The variation of the performance of the cell was investigated with respect to flow velocity, temperature and concentration gradients in the boundary layer between the electrode and the flowing liquid, also for different depths of anode flow channels.

Anode and cathode characterisation by ac impedance was performed using a procedure similar to the one discussed in [26,27].

## 2. Experimental

The cell consisted of a membrane/electrode assembly sandwiched between two rectangular graphite plates which had been treated with zinc-phosphate resin to reduce gas permeation and fluid penetration (supplied by Poco Graphite Inc.). The active area of the cell was approximately 50 mm × 50 mm. Flow channels were machined into the graphite blocks. Three anode plates were fabricated with channel depths of 1.1905, 2.381 and 4.763 mm (shallow, medium and deep). The schematic representation of the flow channel configuration used in this study is shown in Fig. 1.

A single cathode plate was fabricated from graphite with a 1.1905 mm channel depth. The cathode was the mirror image of the shallow channel depth anode plate. The current collectors were made from molybdenum foil and placed to the back face of graphite plates. The cell was clamped between two GPO-3 fibreglass (glass polyester laminates) boards, two 6061-T6 aluminium plates and eight steel bolts to provide rigidity for the system and to distribute pressure equally across the plate surface/electrode interface. The methanol entered at the bottom and oxygen from the top. This orientation was chosen based on observation of

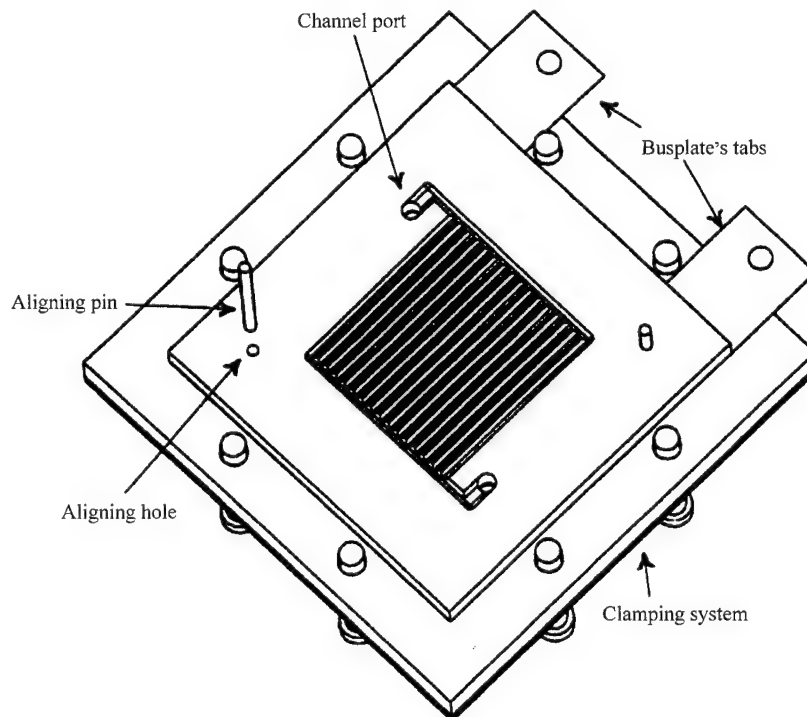


Fig. 1. Perspective view of the cell in its operational orientation. The top right aligning pin is shown inserted in the plate, as is the case during cell assembly.

the product  $\text{CO}_2$  removal at the anode and liquid crossover at the cathode, within the transparent cell studied previously.

The membrane electrode assembly (MEA) used in the cell was purchased from E-TEK. It consisted of two electrodes containing the catalysts: anode ( $4 \text{ mg cm}^{-2} (\text{Pt-Ru})\text{O}_x$  (1:1 a/c)) and cathode ( $4 \text{ mg cm}^{-2}$  Pt black) laminated to either side of a proton conducting solid polymer membrane (Nafion 117). The active surface area was  $3025 \text{ mm}^2$ . The space under the ridges between the channels was included in this value.

The cell was placed in the test rig, that consisted of a HPLC reciprocating piston pump (ISCO Model 2350) used to supply methanol solution from the reservoir, a programmable mass flow controller with digital signal processing from AALBORG to indicate and control oxygen flow rates (see Fig. 2). Methanol pressure was controlled by maintaining a back pressure of nitrogen in the collection vessel. This system, which was developed in-house, was able to compensate for fluctuations in the anode stream density caused by intermittent discharges of product  $\text{CO}_2$ . Ultra high purity oxygen was provided, at the required pressure, from a cylinder equipped with a two-stage stainless steel, low

pressure, regulator. All the inlet connections between the cell and equipment were made of annealed 304 stainless steel ASTM A269 tubing. About 2.5 m of the tubing, in the form of a coil, was placed inside the oven in order to preheat the gas before being fed to the cell. Cole-Palmer pressure transmitters, range 0–6.9 bar (0–100 psi)  $\pm 0.25\%$  of full scale, were mounted on the outlets of the streams. FEP fluoropolymer translucent tubing was used on all outlet connections to enable visual observations of the flow streams. The oven was equipped with a transparent door in order to monitor for methanol leaks.

The internal resistance of the cell was taken between the tabs of the anode current collectors and the tabs of the cathode current collector using a four terminal ac Hewlett-Packard milliohmeter (model 4328A).

A Labview data acquisition system was used to collect and store flow rates, pressures, temperature, voltage, current and internal resistance. Power and current densities were calculated and graphed continuously as voltage and applied load values were acquired. A bipolar operational power supply (BOP, 20–20 M) from Kepco was used to apply an appropriate load to the DMFC.

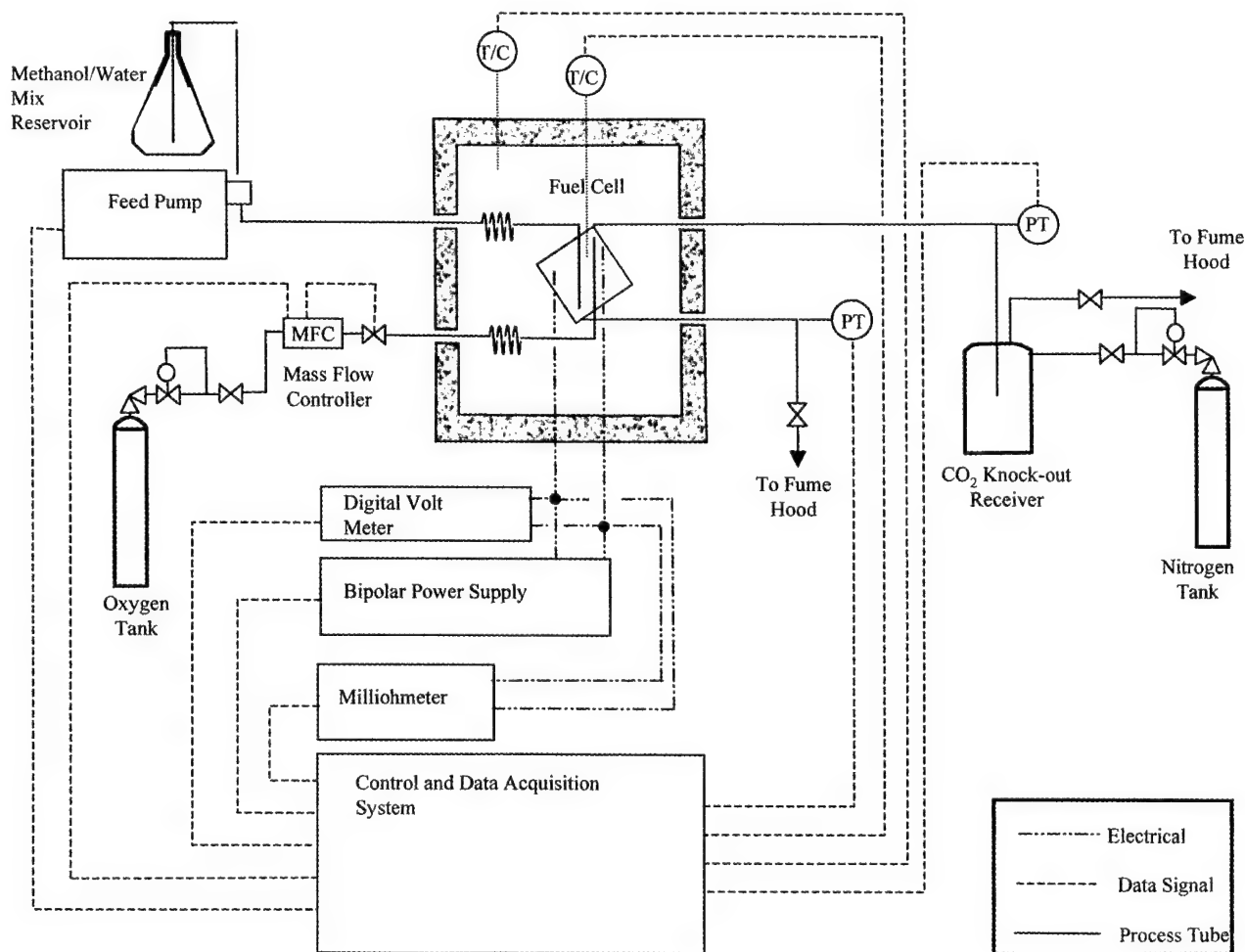


Fig. 2. Schematic of the test rig.

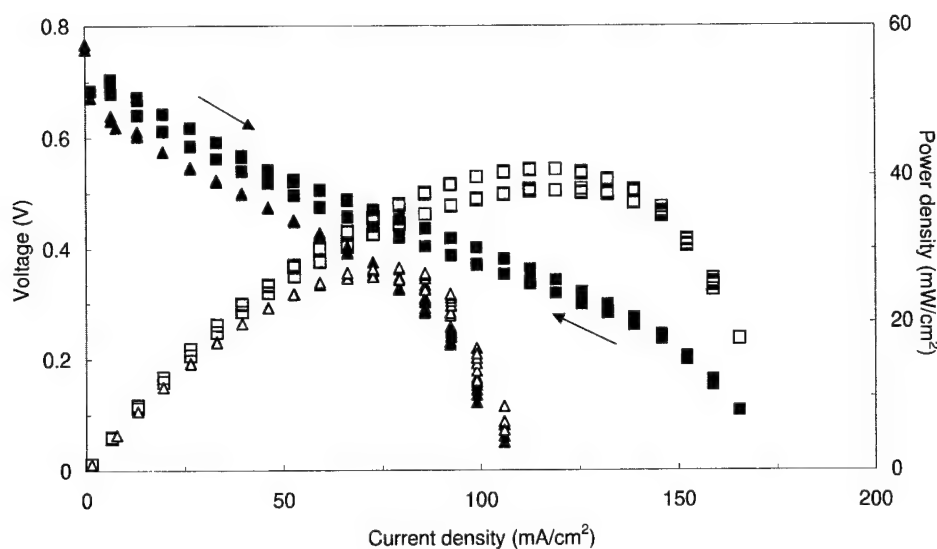


Fig. 3. Variation in fuel cell performance with temperature shown for medium channel depth. Methanol flow stoichiometric ratio = 4,  $O_2$  flow = 0.25 SLM (kept constant throughout). (■) Voltage at 95°C; (□) power density at 95°C; (▲) voltage at 70°C; (△) power density at 70°C.

A Solartron (1255) hf frequency response analyser was used to perform ac impedance spectroscopy measurements. The BOP was adapted to work as a potentiostat in connection with the Solartron. A voltage divider (20:1) was placed between BOP and generator output from the Solartron.

Initial conditioning of the MEA was done in the cell. The anode was supplied with 1 M aqueous solution of methanol at  $0.2 \text{ ml min}^{-1}$ . The cathode was supplied with oxygen at  $0.25 \text{ l min}^{-1}$ . The cell was kept at 70°C for 48 h. No pressure was applied during conditioning.

To insure the same conditions for each experiment, the cell was conditioned for 2 h daily with an applied load

corresponding to  $40 \text{ mA cm}^{-2}$  at pressure (50/50 psi, anode/cathode) and temperature (70 or 95°C).

If it is not stated otherwise, the methanol flows were adjusted relative to the current to maintain a four times stoichiometric ratio. Oxygen flow was kept constant at 0.25 SLM.

At each set of anode operating conditions, the cathode was supplied at first with oxygen and the polarisation and ac impedance were measured. The polarisation measurements were repeated after the ac impedance, to ensure that the fuel cell conditions were steady. Next nitrogen was fed to the cathode instead of oxygen. This is equivalent to having a

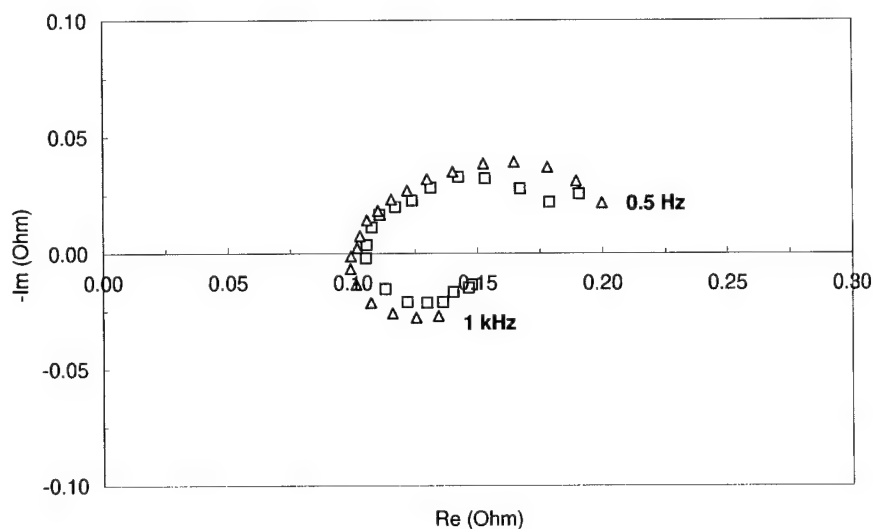


Fig. 4. Variation in ac impedance spectra with cell temperature. Channel depth = 2.4 mm, current density =  $40 \text{ mA cm}^{-2}$ ,  $O_2$  flow = 0.25 SLM. Methanol flow stoichiometric ratio = 4, ac amplitude = 5 mV. (□) 95°C; (△) 70°C.

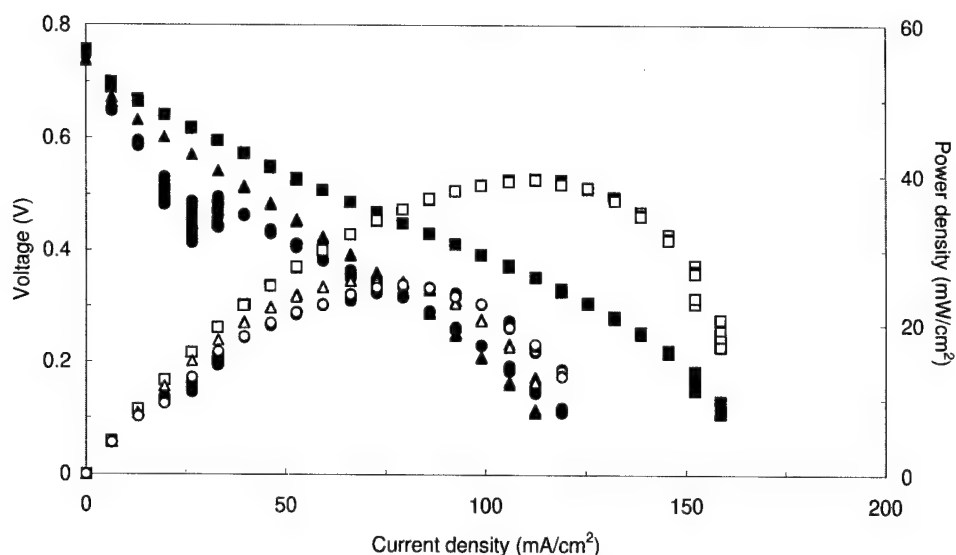


Fig. 5. Variation in fuel cell performance with channel depths. Other conditions as in Fig. 3. (●, ○) 1.2 mm; (□, ■) 2.4 mm; (▲, △) 4.8 mm. Solid symbols: voltage; outline symbols: power.

reference hydrogen electrode (RHE) since hydrogen is being generated at the cathode. The polarisation and ac impedance were measured after 1 h and repeated 18 h later.

For the polarisation curves, the applied current was increased by uniform intervals until the cell voltage reached 0.1 V. The current was then decreased in uniform intervals so that polarisation curves for increasing and decreasing loads were obtained.

AC impedance measurements were done at a base current density of  $40 \text{ mA cm}^{-2}$  ( $20 \text{ mA cm}^{-2}$  for some measurements at  $70^\circ\text{C}$ ) with the amplitude of the sinusoidal current signal adjusted so that potential amplitude was 5 mV. Impedance spectra were obtained at frequencies between 1 kHz and 0.5 Hz. The integration time was set at 10 s.

The data reported here were obtained with one MEA. All three anode channels were investigated with the medium channel depth (2.381 mm) repeated.

### 3. Results and discussion

#### 3.1. Results from methanol/oxygen operation

Steady-state current–voltage characteristics of the cell were obtained at 70 and  $95^\circ\text{C}$  for all three channel depths. The polarisation and ac impedance results for medium channel depth at both temperatures are shown in Figs. 3 and 4, respectively. The flow rate of methanol was increased

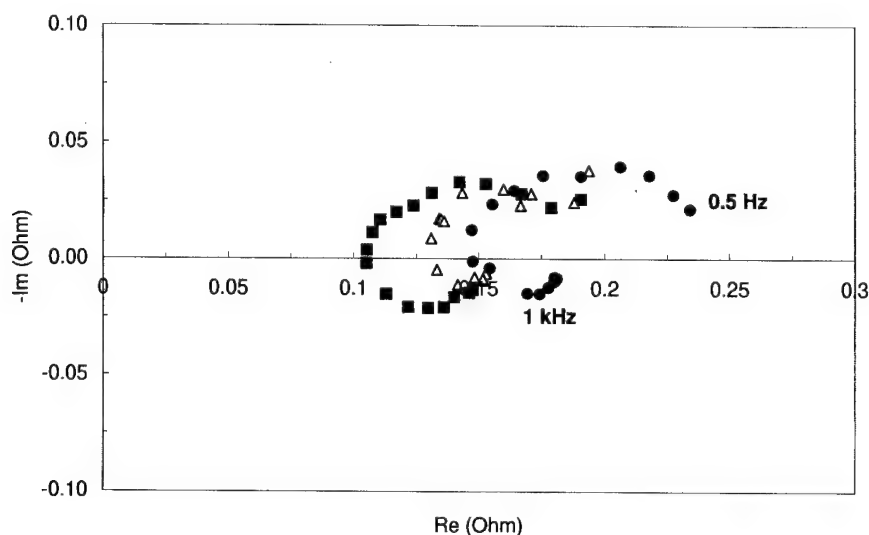


Fig. 6. An ac impedance spectra for (●) shallow; (■) medium; (△) deep channels at  $95^\circ\text{C}$ . Other conditions as in Fig. 4.

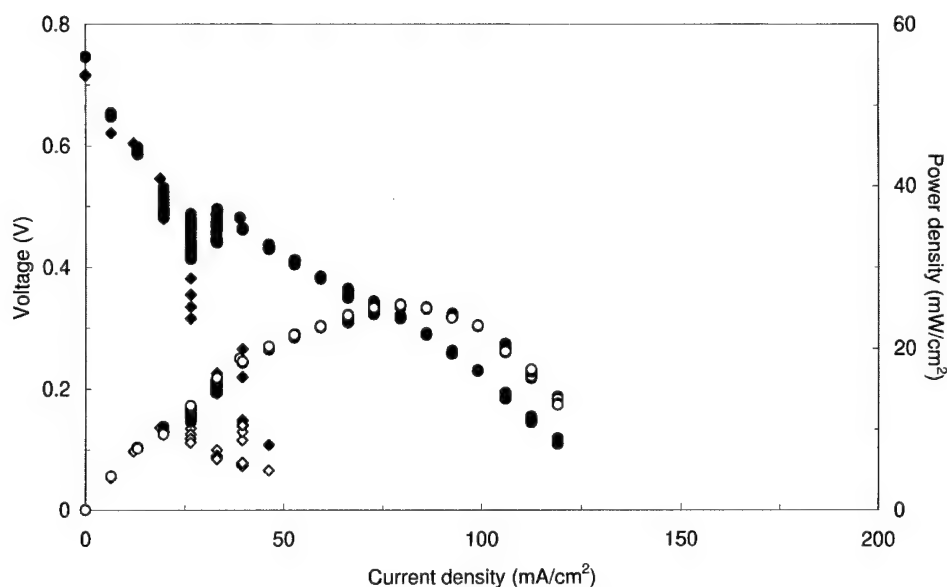


Fig. 7. Polarisation curves for shallow channel depth showing effect of slow response to load changes. Other conditions as in Fig. 3. (◆, ◇) Measurement 1; (●, ○) measurement 2. Solid symbols: voltage; outline symbols: power.

during polarisation measurements to maintain the stoichiometric ratio equal to four. A significantly lower power density and a lower maximum current density was obtained at 70 than at 95°C.

The ac impedance data for medium channel were obtained when the system was under a load corresponding to 40 mA cm<sup>-2</sup> at 95 and at 70°C. Consistent with the polarisation data, Fig. 4 shows increased impedance at lower temperature in the high and low frequency regions.

Fig. 5 shows the variation in fuel cell performance with channel depth. From the three channel depths tested, the medium channel gave the best performance. The other channels (shallow and deep) gave similar values for power

density, although the shallow one was more problematic to operate.

AC impedance spectra for the three channels depth at 95°C, current density of 40 mA cm<sup>-2</sup> and methanol flow rate equivalent to a stoichiometric ratio of four, are shown in Fig. 6. As expected, the impedance in the real domain was greatest for the shallow channel depth flow plate.

Fig. 7 shows two polarisation curves obtained at 95°C for the shallow channel depth. Both measurements were done at a pressure of 350/350 kPa, anode/cathode and with anode feed rate increased with increasing load, to maintain a stoichiometric ratio of four. Fig. 8 shows the ac impedance spectra that were collected immediately following the

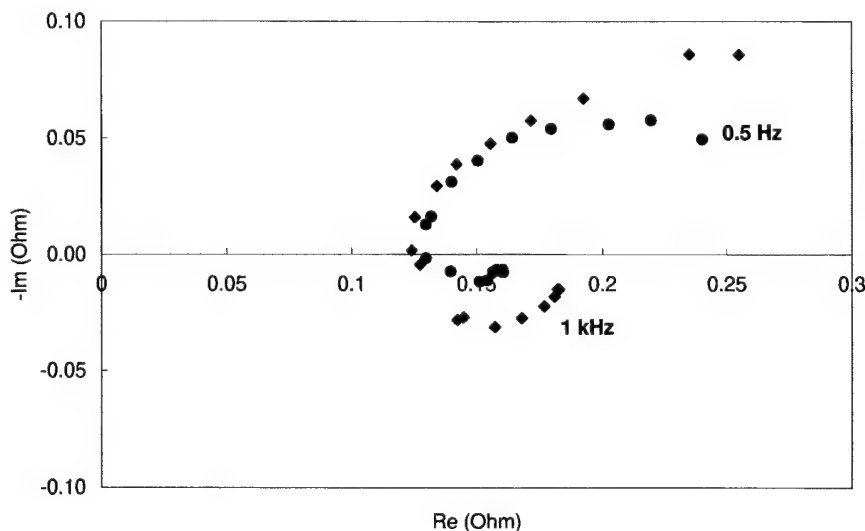


Fig. 8. An ac impedance spectra for shallow channel at 95°C. Current density = 20 mA cm<sup>-2</sup>, O<sub>2</sub> flow = 0.25 SLM. Methanol flow stoichiometric ratio = 4. (◆) Measurement 1; (●) measurement 2. Performed after polarisation curves of Fig. 7.

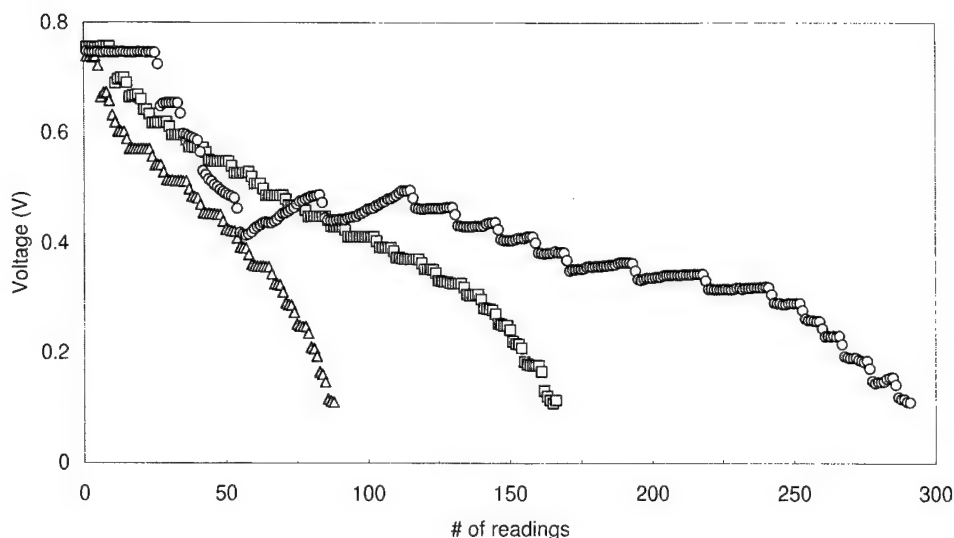


Fig. 9. Channel depth effect on achieving steady-state. Time between readings is 5 s. ( $\Delta$ ) 1.2 mm; ( $\square$ ) 2.4 mm; ( $\circ$ ) 4.8 mm.

polarisation measurements in Fig. 7. As can be seen, the difference in the impedance spectra is not as significant as would be expected given the difference in polarisation curves. It was later determined, after reviewing the data collection files, that the first polarisation curve for the shallow channels had been collected from approximately 90 readings whereas the second polarisation curve had required nearly 300 readings. Clearly, the first polarisation curve did not represent steady-state performance. Fig. 9 shows this graphically. As can be seen, stable steady performance was achieved relatively quickly for the deep and medium depth flow channels; whereas, for the shallow flow channels there is a relatively slow recovery when the load is changed.

Additional investigations were completed to determine whether fuel cell performance with the shallow anode

channels could be improved by increasing the flow velocity of the methanol solution. Figs. 10 and 11 shows that a stoichiometric ratio of four seems to be sufficient. Increasing the ratio to six did not significantly improve power density, but decreasing it to two lowered it drastically. In the lower current density range, between 10 and 50  $\text{mA cm}^{-2}$ , the stoichiometric ratio of six appears to give slightly more stable performance than was observed for a stoichiometric ratio of four.

### 3.2. Results from reference hydrogen electrode

To separate the contribution of the oxygen reduction reaction to the overvoltage from the anode and membrane contributions, reference hydrogen electrode (RHE)

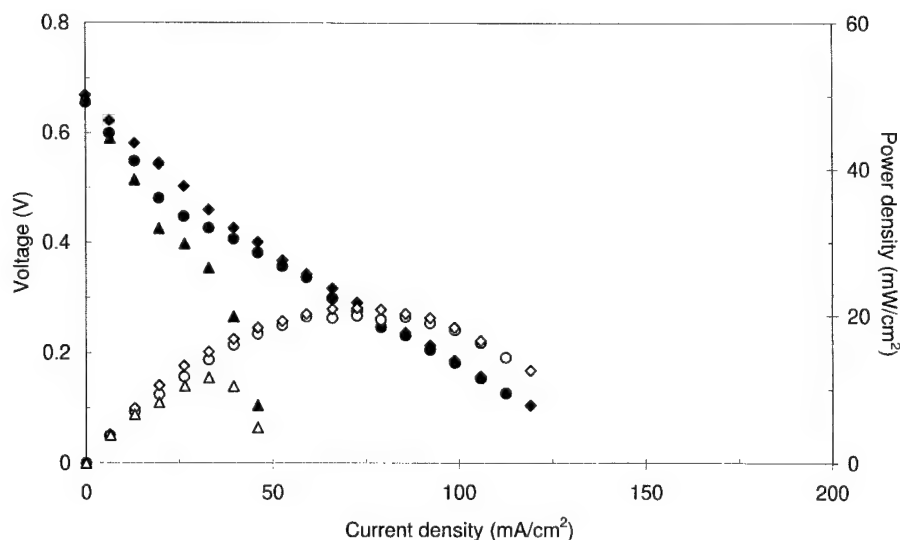


Fig. 10. Polarisation data for shallow channel at 95°C for methanol flow stoichiometric ratio of: ( $\bullet$ ) four; ( $\blacklozenge$ ) six; ( $\blacktriangle$ ) two.  $\text{O}_2$  flow = 0.25 SLM. Solid symbols: voltage; outline symbols: power.



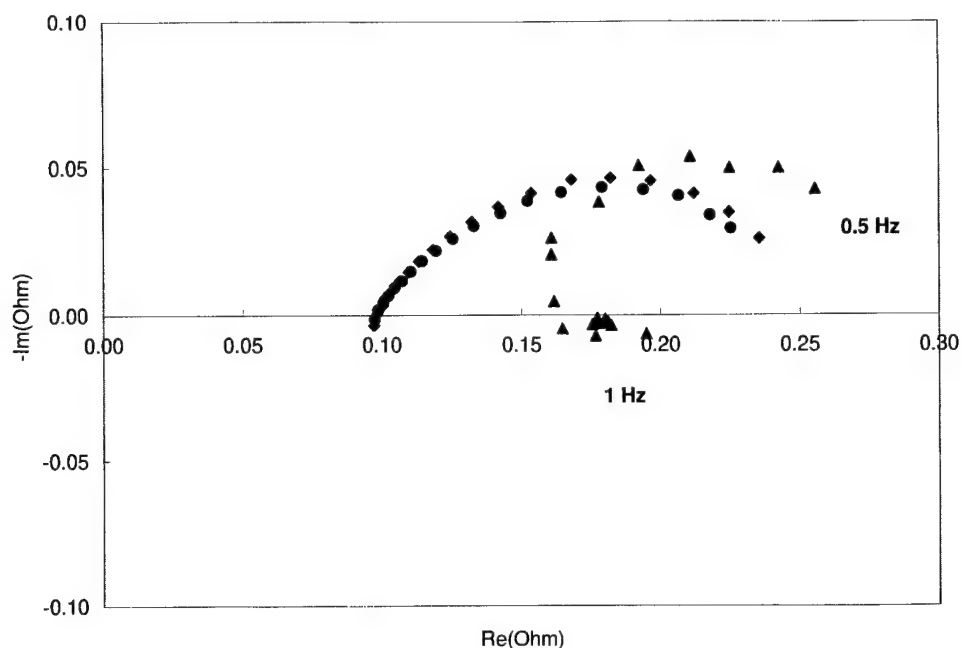


Fig. 11. AC impedance spectra for shallow channel at 95°C for methanol flow stoichiometric ratios of: (●) four; (◆) six; (▲) two.

measurements were taken. This was accomplished by feeding nitrogen to the cathode at a flow rate equal to that of the previous oxygen flow. Polarisation curves and impedance spectra were collected for this RHE configuration. By comparing these results with the methanol–oxygen performance measurements, an indication of the impact of the oxygen cathode performance on the cell can be separated from the anode–membrane effects.

Figs. 12 and 13 show the polarisation curve and the ac impedance spectrum taken when the cathode was supplied with nitrogen to give an equivalent to RHE configuration at

95°C for the medium depth channels. The oxygen–methanol polarisation curve and impedance spectrum are also shown for comparison. The methanol flow was four times stoichiometric for these measurements. As can be seen from Fig. 12, the cell voltage is negative for the RHE configuration. The open circuit voltage should be approximately  $-0.016$  V according to the Nernst potential so that the overvoltage contribution of the oxygen electrode varies from  $0.48$  V at open circuit voltage to the  $0.42$  V at  $160 \text{ mA cm}^{-2}$ . By subtracting the cathode overvoltage from the total overvoltage, the overvoltage contribution of the anode–MEA

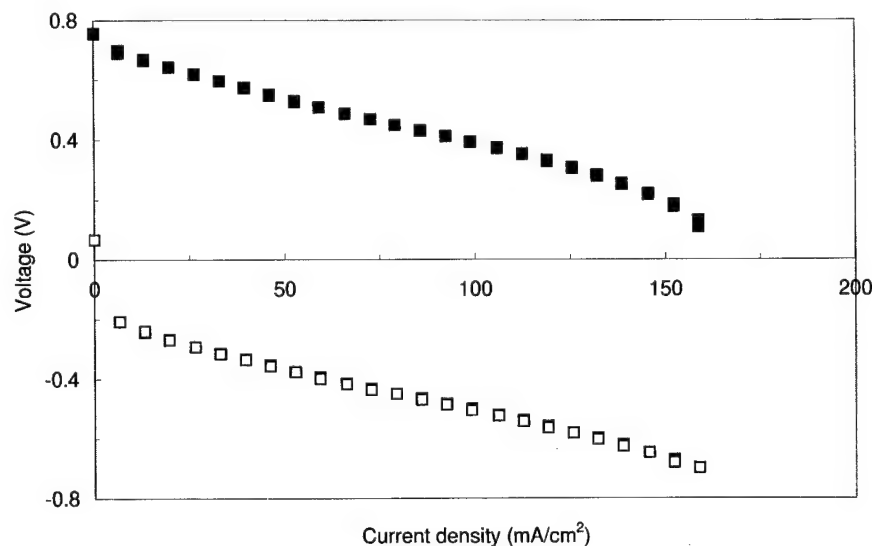


Fig. 12. The RHE–methanol and oxygen–methanol polarisation measurements for medium channel depth at 95°C. Other conditions as in Fig. 3. (■) Oxygen–methanol; (□) RHE–methanol.

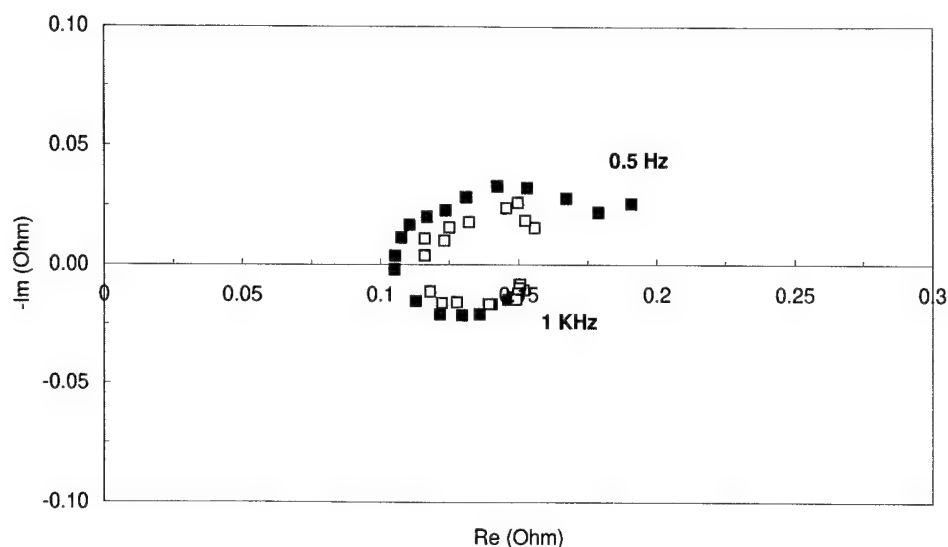


Fig. 13. The RHE-methanol and the oxygen-methanol ac impedance spectra for medium channel depth at 95°C. Other conditions as in Fig. 4. (■) Oxygen-methanol; (□) RHE-methanol.

was calculated to be zero at open circuit and 0.68 V at 160 mA cm<sup>-2</sup> was calculated. By comparing this value with the total polarisation losses, we see that the anode-MEA accounts for approximately 60% of the voltage losses observed in the methanol-oxygen polarisation but there is clearly a contribution due to the oxygen electrode overpotential of 40% at 160 mA cm<sup>-2</sup>. If we examine the ac impedance spectra, we see that the spectrum for the RHE measurements form an arc that is inside the methanol-oxygen spectrum. This confirms that the oxygen electrode makes a significant contribution to losses in the overall cell performance. The RHE polarisation measurements and ac impedance spectrum indicate that the overvoltage of the oxygen electrode accounts for more of the polarisation losses in the shallow (50% at 120 mA cm<sup>-2</sup>) and deep (45% at 110 mA cm<sup>-2</sup>) channel depths than in the medium channel depth configurations. It appears that the flow channel geometry has an effect on the rate of methanol crossover and consequently on the polarisation losses at the cathode, attributable to the parasitic oxidation of methanol. This effect on crossover may be associated with the masking of the anode by product CO<sub>2</sub> but more testing is required to confirm this hypothesis.

#### 4. Conclusions

This is the first time that results from this test system have been published. The experimental apparatus performed well and has been able to generate accurate and reproducible results. The most significant control problem has been maintaining a uniform flow and pressure on the anode as the discharge of product CO<sub>2</sub> causes large changes in the density of the flowing fluid. The use of a pressurised

receiving vessel to create a stable back pressure on the anode appears to have resolved this problem.

The effect of temperature on DMFC performance was as expected. The maximum power density at 95°C was approximately 50% greater than at 70°C. The performance at the higher temperature in general was more stable.

The initial study of the effect of flow channel depth has revealed that there is a complex relationship between flow geometry and DMFC performance. The medium channel depth anode flow field consistently showed the best performance. The polarisation losses for the shallow channel depth and the deep channel depth anodes were similar and were significantly and consistently less than the medium channel depth anode. A key characteristic of the shallow channel depth performance was that it took a much greater amount of time to reach steady-state than for the other two channel configurations. This may be due to the larger pressure drop through the anode and time required to achieve a stable pressure gradient following a change in methanol flow. An ac impedance spectroscopy gave an indication that there was an initial polarisation data for the shallow depth channels.

Comparing the RHE measurements with the oxygen-methanol data provides an indication of the relative importance of the cathode polarisation to the performance of the DMFC. From this analysis it has been determined that the contribution of the cathode to the fuel cell overvoltage is less than the anode-membrane contribution but is still quite significant.

#### Acknowledgements

Support for this work was provided by the Canadian Department of National Defence through the Defence Research and Development Branch.

## References

- [1] M. Baldauf, W. Preidel, J. Power Sources 84 (1999) 161.
- [2] A. Heinzl, V.M. Barragan, J. Power Sources 84 (1999) 70.
- [3] S. Wasmus, A. Küver, J. Electroanal. Chem. 461 (1999) 14.
- [4] B. Gurau, R. Viswanathan, R. Liu, T.J. Lafrenz, K.L. Ley, E.S. Smotkin, E. Reddington, A. Sapienza, B.C. Chan, T.E. Mallouk, S. Sarangapani, J. Phys. Chem. B 102 (1998) 9997.
- [5] D.R. Rolison, P.L. Hagans, K.E. Swider, J.W. Long, Langmuir 15 (1999) 774.
- [6] K.A. Friedrich, M. Huber, M. Stefener, U. Stimming, Fuel Cell Seminar Abstracts, Portland, USA, 2000, p. 190.
- [7] A.S. Arico, V. Baglio, P. Creti, V. Antonucci, Fuel Cell Seminar Abstracts, Portland, USA, 2000, p. 75.
- [8] L. Liu, C. Pu, R. Viswanathan, Q. Fan, R. Liu, E.S. Smotkin, Electrochem. Acta 43 (1998) 3657.
- [9] A.S. Arico, P. Creti, P.L. Antonucci, J. Cho, H. Kim, V. Antonucci, Electrochem. Acta 43 (1998) 3719.
- [10] P. Staiti, M. Minutoli, S. Hocevar, J. Power Sources 90 (2000) 231.
- [11] C. Pu, W. Huang, K.L. Ley, E.S. Smotkin, J. Electrochem. Soc. 142 (1995) L119–120.
- [12] B.S. Pivovar, Y. Wang, E.L. Cussler, J. Membr. Sci. 154 (1999) 155.
- [13] E. Peled, T. Duuvdevani, A. Melman, Electrochem. Solid State Lett. 1 (1998) 210.
- [14] N. Yoshida, T. Ishisaki, A. Watakabe, M. Yoshitake, Electrochem. Acta 43 (1998) 3749.
- [15] D. Chu, R. Jiang, Ch. Walker, Fuel Cell Seminar Abstracts, Portland, USA, p. 160.
- [16] R.W. Reeve, P.A. Christensen, A. Hamnett, S.A. Haydock, S.C. Roy, J. Electrochem. Soc. 145 (1998) 3463.
- [17] X. Ren, P. Zelenay, S. Thomas, J. Davey, S. Gottesfeld, J. Power Sources 86 (2000) 111.
- [18] K. Scott, W. Taama, J. Cruickshank, J. Appl. Electrochem. 28 (1998) 289.
- [19] D. Xue, Z. Dong, J. Power Sources 76 (1998) 69.
- [20] S.F. Baxter, V.S. Battaglia, R.E. White, J. Electrochem. Soc. 146 (1999) 437.
- [21] P. Argyropoulos, K. Scott, W.M. Taama, J. Appl. Electrochem. 30 (2000) 899.
- [22] A.A. Kulikovskiy, J. Appl. Electrochem. 30 (2000) 1005.
- [23] H. Dohle, J. Divisek, R. Jung, J. Power Sources 86 (2000) 469.
- [24] K. Scott, P. Argyropoulos, C. Jackson, W.M. Taama, J. Horsfall, K. Lovell, K. Soundmacher, Fuel Cell Seminar Abstracts, Portland, USA, 2000, p. 110.
- [25] H. Dohle, T. Bewer, J. Merger, R. Neitzel, D. Stolten, Fuel Cell Seminar Abstracts, Portland, USA, 2000, p. 130.
- [26] J.T. Mueller, P.M. Urban, J. Power Sources 75 (1998) 139.
- [27] J.T. Müller, P.M. Urban, W.F. Hölderich, J. Power Sources 84 (1999) 157.

# An innovative technique for pore structure analysis of fuel cell and battery components using flow porometry

Akshaya Jena, Krishna Gupta<sup>\*</sup>

*Porous Materials, Inc., 83 Brown Road, Ithaca, NY 14850, USA*

Received 30 November 2000; accepted 10 December 2000

---

## Abstract

Some of the porous sheet materials used in fuel cells and batteries hardly permit gas flow through the thickness of the sheet, although flow parallel to the sheet is appreciable. Determination of the porosity of such materials is not possible by the available techniques. A novel technique based on flow porometry is reported. This technique can measure the pore structure of such porous sheets. A composite porous sheet material containing one of the electrodes and the separator in two layers was investigated. The largest pore diameter, the mean flow pore diameter and the pore size distributions were measured. The pore structures of both layers were identified. © 2001 Elsevier Science B.V. All rights reserved.

**Keywords:** Capillary flow porometry; Pore structure; Fuel cell separators; Battery separators

---

## 1. Introduction

Recent research efforts to design more efficient batteries and fuel cells have resulted in the development of thin composite sheets of porous materials. Composites of electrode and separator materials and composite separators are examples of such porous sheets. These sheet materials often hardly permit gas flow through the thickness of the sheet, although flow parallel to the sheet is appreciable. Porosity of such composite materials is vital for design applications. However, determination of the pore structure of such materials is not possible by the available techniques. The widely used mercury intrusion technique and the vapor condensation technique cannot be employed because the pore volume in the thin sheet is too small to be detectable. Flow porometry measures flow rate parallel to the thickness of the sheet. This technique cannot measure the pore structures of composites consisting of several layers.

In order to measure the pore structure of composite porous sheets, a novel technique based on flow porometry has been designed. In this paper the new technique is described and results obtained with a two layered composite battery material are discussed.

## 2. Material and techniques

### 2.1. Material

A composite sheet material consisting of an electrode and the separator was investigated. The two layers had different pore sizes. Fig. 1 is an illustration of the structure of the material. The pore size in layer no. 1 is much smaller than the pore size in layer no. 2.

### 2.2. Principle of the technique

The sample of the material to be tested is soaked in a liquid that fills spontaneously the pores in the material. The liquid is known as the wetting liquid. Filling of the pores by the liquid results in replacement of the solid/gas interface by a solid/liquid interface. Spontaneous filling occurs because the interfacial free energy of the solid/liquid interface is lower than that of the solid/gas interface and the net free energy change associated with the filling process is negative. Removal of the wetting liquid from pores is not spontaneous. Therefore, pressure of a non-reacting gas is slowly increased on one side of the sample to remove the liquid from pores and permit gas flow to occur.

Gas displaces the liquid in the pore, when work done by the gas is equal to the increase in surface free energy (Fig. 2).

---

<sup>\*</sup> Corresponding author. Tel.: +1-607-257-5544; fax: +1-607-257-5639.  
E-mail address: info@pmiapp.com (K. Gupta).

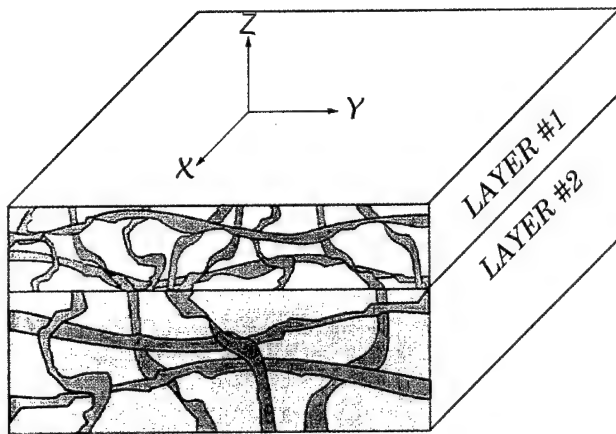


Fig. 1. The two layered battery material.

Considering displacement of a small volume of liquid

$$p dV = \gamma_{s/g} dS_{s/g} + \gamma_{s/l} dS_{s/l} + \gamma_{l/g} dS_{l/g} \quad (1)$$

Where,  $p$  is the differential pressure;  $V$  the volume of gas in the pore;  $\gamma_{s/g}$  the solid/gas interfacial free energy;  $S_{s/g}$  the solid/gas surface area;  $\gamma_{s/l}$  the solid/liquid interfacial free energy;  $S_{s/l}$  the solid/liquid interfacial area;  $\gamma_{l/g}$  the liquid/gas interfacial free energy;  $S_{l/g}$  the liquid/gas interfacial area.

Increase in solid/gas surface area is equal to the decrease in the solid/liquid surface area.

$$dS_{s/g} = -dS_{s/l} \quad (2)$$

Substituting in Eq. (1)

$$p = \gamma_{l/g} \left( \frac{dS_{s/g}}{dV} \right) \left\{ \left[ \frac{\gamma_{s/g} - \gamma_{s/l}}{\gamma_{l/g}} \right] + \left[ \frac{dS_{l/g}}{dS_{s/g}} \right] \right\} \quad (3)$$

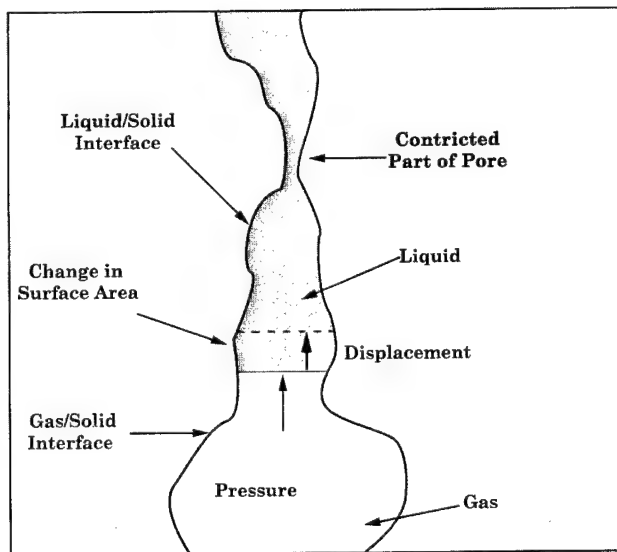


Fig. 2. Displacement of liquid in the pore by gas.

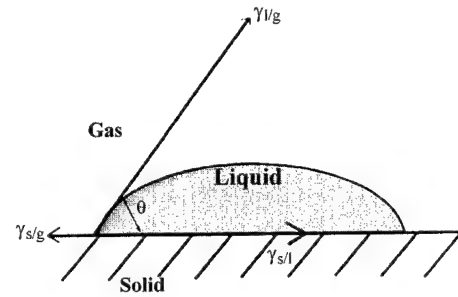


Fig. 3. Equilibrium between the three surface tensions.

In the case of consolidated materials and high fiber density materials the term,  $[dS_{l/g}/dS_{s/g}]$  is very small.

$$\left[ \frac{dS_{l/g}}{dS_{s/g}} \right] \approx 0 \quad (4)$$

The surface tensions can be expressed in terms of contact angle,  $\theta$ , of the wetting liquid with the solid. Equilibrium between the surface tensions depicted in Fig. 3 shows that

$$\cos \theta = \left[ \frac{\gamma_{s/g} - \gamma_{s/l}}{\gamma_{l/g}} \right] \quad (5)$$

It has been demonstrated that for wetting liquids with very low surface tensions [1]:

$$\cos \theta \approx 1 \quad (6)$$

Substituting from relations 4, 5 and 6 in Eq. (3)

$$p = \gamma_{l/g} \left( \frac{dS_{s/g}}{dV} \right) \quad (7)$$

It follows from this relation that the lowest pressure is required to empty the largest pore (lowest  $[dS/dV]$ ). Therefore, there will be no flow through the sample containing liquid filled pores and flow of gas begins when the pressure is increased to a value sufficient to empty the largest pore. Further increase of pressure will empty smaller pores and increase gas flow. Measurement of flow rate as a function of differential pressure permits many pore characteristics to be measured.

### 2.3. The instrument

In order to obtain reliable and reproducible results, the instrument was fully automated and contained many novel design features and state-of-the-art components. Windows-based operation of the instrument made testing objective easy. The instrument is shown in Fig. 4.

The unique design of the sample chamber shown in Fig. 5 allows gas flow to occur only along the  $x$  and  $y$  directions (Fig. 1). We call this flow parallel to the plane of the sheet in-plane flow. The wet sample is placed between two non-porous plates. The bottom plate has a small central opening.

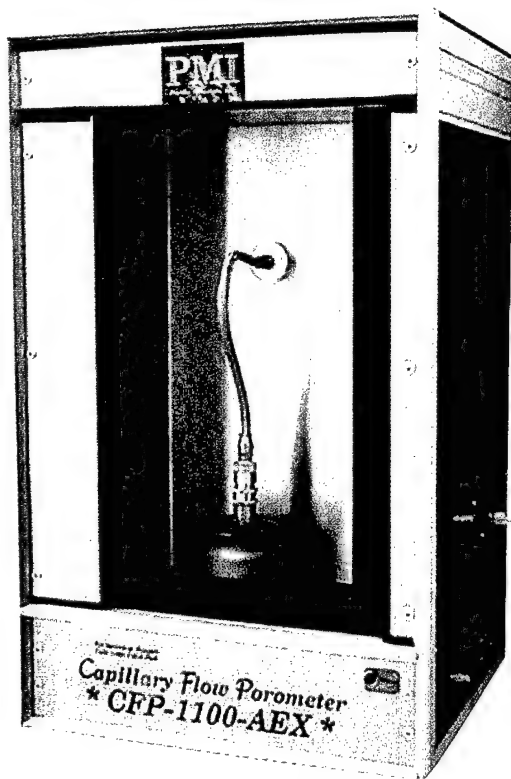


Fig. 4. Capillary flow porometer.

Compressed gas reaches the wet sample through the central hole. Gas is permitted to pass through the  $x$  and  $y$  directions in the plane of the sheet material. Differential pressure and flow rate in the in-plane directions are measured.

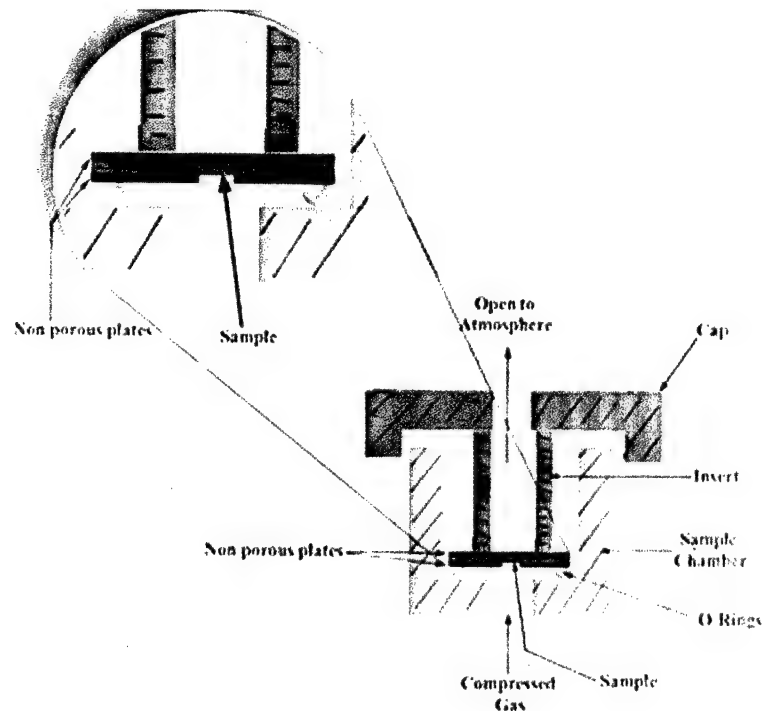


Fig. 5. Sample chamber for determination of in-plane pore structure.

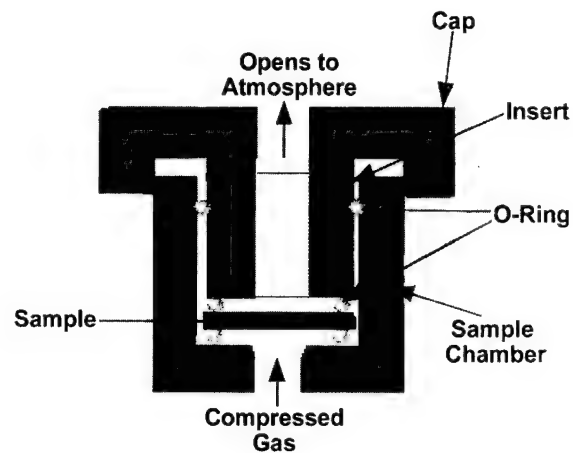


Fig. 6. Sample chamber for determination of through-plane pore structure.

The sample chamber shown in Fig. 6 allows gas to flow only along the  $z$  direction (Fig. 1). We call this through plane flow. The in-plane flow is prevented by O-rings. The differential pressure and through-plane flow rates are measured.

### 3. Results and discussion

#### 3.1. Variation of flow rate with differential pressure

Fig. 7 shows the variation of flow rate with differential pressure when the sample chamber for flow along the  $z$  direction (through-plane) was used (Fig. 6). The data are

presented as three curves. The dry and wet curves are obtained with dry (liquid free) and wet (liquid filled) samples, respectively. The half-dry curve is calculated from the dry curve and yields half of the flow rate through the dry sample at any given pressure.

All the pores in the dry sample are open. Therefore, the flow continuously increases with increase of pressure. The pores in the wet sample are filled with liquid. Therefore, there is no flow at the start. When the pressure is sufficient to empty the largest pore, flow starts and on further increase of pressure flow rate increases.

Gas pressure required to displace the liquid in the pore and start flow through the pore is determined by pore size. The size of a pore varies along its length (Fig. 2) and the gas pressure required to displace the liquid also varies along the length of the pore. The pressure is maximum at the most constricted part of the pore because  $(dS/dV)$  of the pore has its maximum value at this part. Only when the pressure reaches this maximum, is the liquid in the pore completely removed and gas flows through the pore. Thus, measured pressure for flow to occur through a pore corresponds to the size of the narrowest part of the pore. For through-plane flow, the layers in the sample are in series and the pores extend from layer no. 2 to layer no. 1. Therefore, the measured differential pressure is due to the size of the smaller pores in layer no. 1.

Fig. 7 also contains data from the specimen loaded in the sample chamber (Fig. 5) which permitted flow in the  $x$  and  $y$  directions (in-plane). The layers in the sample are parallel and gas could flow in the  $x$  and  $y$  directions in both layers simultaneously. However, the pores in layer no. 2 are larger than the pores in layer no. 1. Therefore, the pores in layer no.

2 require less pressure to be emptied. In-plane flow at low pressures occurs through the large pores in layer no. 2 and when the pressure is sufficiently high flow also occurs through the small pores in layer no. 1. Therefore, the in-plane flow rate is expected to be much larger than the through-plane flow rate. This is observed in Fig. 7.

### 3.2. Pore diameter

Pore cross-sections are normally irregular. Therefore, pore size is not defined. We define pore diameter as the diameter,  $D$  of an opening such that:

$$\left(\frac{dS}{dV}\right)_{\text{pore}} = \left(\frac{dS}{dV}\right)_{\text{opening}} = \frac{4}{D} \quad (8)$$

Substituting in Eq. (7)

$$D = \frac{4\gamma_{l/g}}{P} \quad (9)$$

Eq. (9) is used to calculate pore diameter.

The largest pore diameter is obtained from the pressure at which the flow of gas begins. This pressure is known as the bubble point pressure. The instrument uses a sophisticated technique to detect this pressure accurately. The largest pore diameters were calculated after Eq. (9) using the measured bubble point pressures and surface tension of the wetting liquid. The results are listed in Table 1. The largest pore diameter obtained by in-plane flow is for layer no. 2 and the one obtained by through-plane flow is for layer no. 1. As expected, the largest pore diameter in layer no. 1 is much smaller (about one fifth) than that in layer no. 2. The ability of the separator to act as a barrier to certain ions and particles

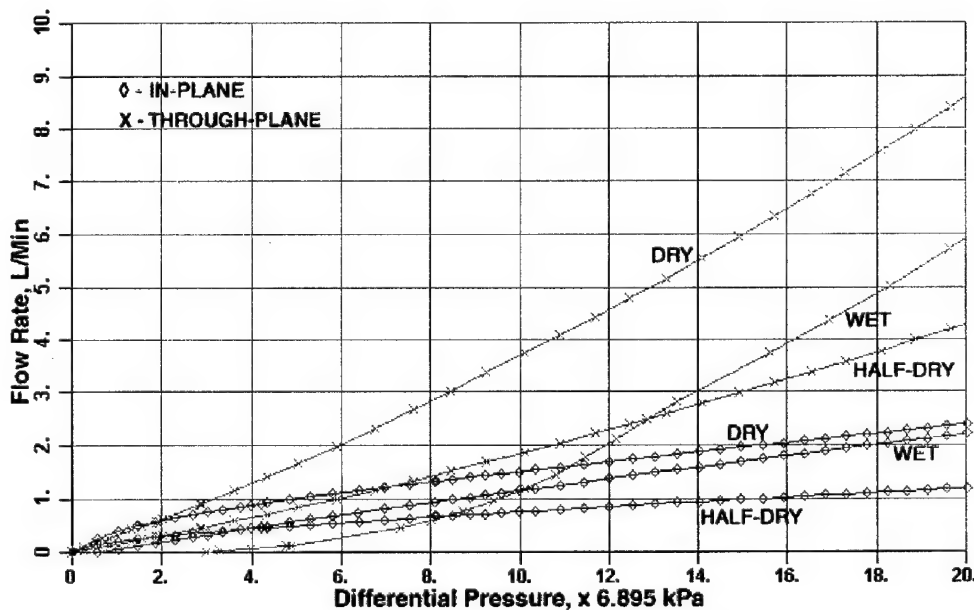


Fig. 7. Variation of flow rate with differential pressure for through-plane and in-plane flow.

Table 1  
Pore diameters in the two layers of the composite battery material

Layer no.	The largest pore diameter ( $\mu\text{m}$ )	The mean flow pore diameter ( $\mu\text{m}$ )	Technique
1	2.214	0.514	Through-plane
2	11.57	1.72	In-plane

is determined by its largest pore diameter. Any flaw present in the separator may also show up as the largest pore diameter.

The intersection of the wet curve and the half-dry curve gives the mean flow pressure which is converted to mean flow pore diameter. Half of the flow through the sample is through pores larger than the mean flow pore diameter. The mean flow pore diameters are listed in Table 1. Mean flow pore diameter is a measure of the permeability of fluids through the material [2].

### 3.3. Pore size distribution

The flow rate through a material is a function of pressure, properties of the gas and properties of the sample. For viscous flow the variable, pressure, can be separated from other variables [3]. We assume that flow rate can be expressed as the product of two functions such that one of these functions depends on pressure only and the other function is independent of pressure. The ratio of flow rates through the wet and the dry samples at the same pressure does not depend upon pressure. If  $F_w$  and  $F_d$  are flow rates through wet and dry samples respectively at the same pressure  $p_i$ ,  $\left(\frac{F_w}{F_d}\right)_{p_i}$  is independent of pressure. The cumu-

lative filter flow percent,  $(100 \times (F_w/F_d))$  obtained from Fig. 7 is shown in Fig. 8. The pores in layer no. 2 that are larger than those in layer no. 1 and are in the range of about 2–11.5  $\mu\text{m}$  are responsible for almost 50% of flow (Fig. 8). Other differences between the layers are brought out by the pore size distribution.

The pore size distribution function,  $f$  is defined as:

$$f = - \frac{d[100 \times (F_w/F_d)]}{dD} \quad (10)$$

The leading negative sign on the right hand side of this Eq. is due to the fact that increase in pore diameter decreases the flow rate. The distribution functions were calculated from data in Fig. 7 and are shown in Fig. 9. The area under the distribution curve in a given pore diameter range yields percentage of flow through pores in that size range.

The through-plane test shows a group of small pores in the range of about 0.2–1.5  $\mu\text{m}$ , while the in-plane test shows a group of small pores in the same range and a group of large pores over a wide range of about 2–11.5  $\mu\text{m}$ . The small group of pores obtained from the through-plane test is in layer no. 1. The group of large pores found in the in-plane test is in layer no. 2. The group of small pores found in the in-plane test could be in both layers or in one of the layers. This small group of pores appears in a size range which is almost identical with that in layer no. 1. Therefore, the small group of pores found in the in-plane test is expected to be of layer no. 1. The pores in both layers are identified.

In the material investigated, the flow rates through the two groups of large and small pores are comparable. In many other composites the flow through the large pores dominates the in-plane flow. In such cases, determination of pore structures of the two layers by this technique becomes even easier.

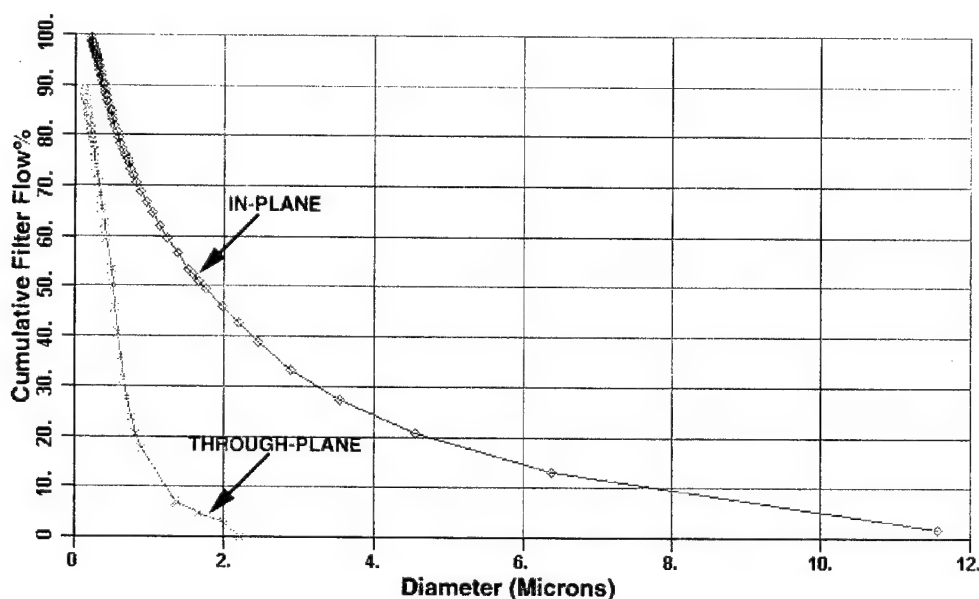


Fig. 8. Cumulative filter flow.



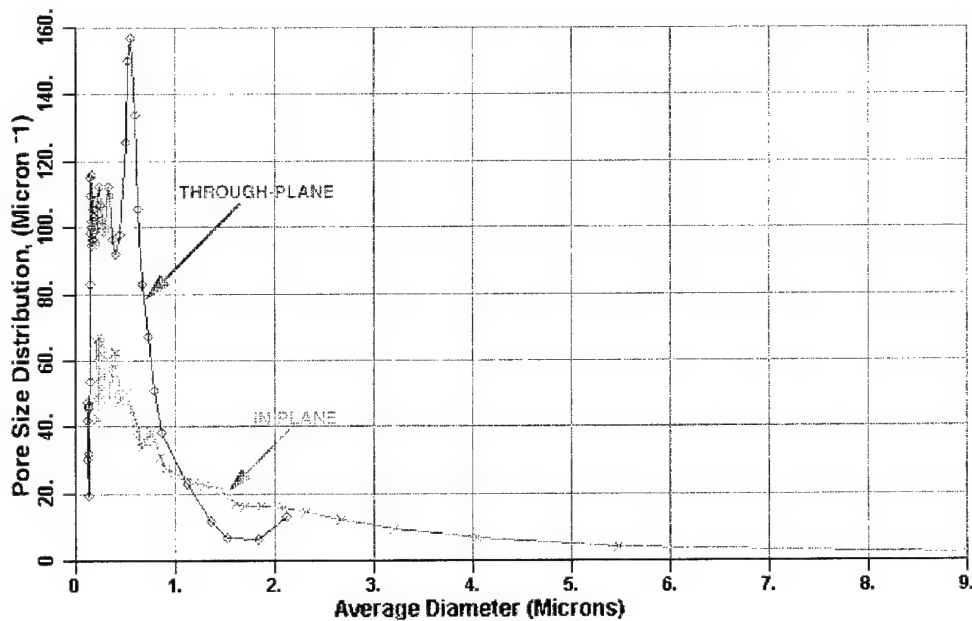


Fig. 9. Pore size distribution.

#### 4. Conclusions

1. The technique for measurement of change of flow rate with increase in differential pressure in the  $x$  and  $y$  directions and the  $z$  direction of a sheet material was described.
2. Flow through a composite sheet material for battery consisting of one of the electrodes and the separator in two layers was measured in the in-plane ( $x$  and  $y$  directions) and the through-plane ( $z$  direction).
3. The measurements yielded the largest pore diameter, the mean flow pore diameter, cumulative flow percent and pore size distribution.
4. For layer no. 1, the largest pore diameter was  $2.214\text{ }\mu\text{m}$ ,

the mean flow pore diameter was  $0.514\text{ }\mu\text{m}$  and the pores were in the range of about  $0.2\text{--}1.5\text{ }\mu\text{m}$ . For layer no. 2, the largest pore diameter was  $11.57\text{ }\mu\text{m}$ , the mean flow pore diameter was  $1.72\text{ }\mu\text{m}$  and the pores were in the range of about  $2\text{--}11.5\text{ }\mu\text{m}$ .

5. The pore structure of the two layers of the composite could be easily determined.

#### References

- [1] V. Gupta, A.K. Jena, *Adv. filtr. Sep. Technol.* 13b (1999) 833.
- [2] E. Mayer, *Fluid/Particle Sep. J.* 10 (2) (1997) 81.
- [3] C.R. Scheidegger, *The Physics of Flow Through Porous Media*, Macmillan, New York, 1957.

# Possibilities of prevention of formation of poisoning species on direct methanol fuel cell anodes

Ramasamy Manoharan\*, Joghee Prabhuram

HEB R&D Laboratories, High Energy Batteries (India) Ltd., Mathur 622 515 Pudukkottai (Dt), Tamil Nadu, India

Received 25 October 2000; accepted 30 November 2000

## Abstract

Porous unsupported Pd, Pt and Pt–Ru single phase alloy electrodes with different compositions viz. 9:1, 7:3 and 5:5 were prepared by  $\text{NaBH}_4$  reduction method at room temperature.

Extensive cyclic voltammetric investigations in different solutions have been performed on these electrodes, as well as on smooth electrodes, with the aim of identifying suitable combinations of electrode structure and electrolyte/methanol mixtures which can prevent the formation of organic poisoning species.

Various electrochemical processes occurring in different potential regions are discussed. Meanings of the appearance/disappearance of oxidation peaks during both forward and backward sweeps on the present electrodes are pointed out. © 2001 Elsevier Science B.V. All rights reserved.

**Keywords:** Fuel cells/alkaline electrolyte; Fuel cells/acid electrolyte; Noble metal catalysts; Methanol oxidation: formation of poisoning species

## 1. Introduction

The formation of intermediate organic poisoning species during the course of the methanol oxidation reaction (MOR) on noble metals and their alloy electrodes in aqueous solutions of alkali and acid is considered to be a common phenomenon and has been posing a problem for developing direct methanol fuel cell anodes [1–9]. These intermediate organic poisoning species has been identified by in situ IR spectroscopic studies and found to exist in the form of  $(\text{CHO})_{\text{ads}}$  in alkaline solution and in the form of linearly bonded  $=\text{C}=\text{O}$  in acid solution on smooth Pt and Pt-based alloy electrodes [4,10–14]. On smooth Pd, it has been identified that the bridge bonded  $>\text{CO}$  is the poisoning species [15]. With the aim of avoiding the formation of these poisoning species on the electrodes surfaces, binary Pd-based alloy catalysts and binary, ternary and quaternary Pt alloy catalysts have been employed for the MOR. However, the complete removal of these species has not been completely realised [14–25] in these studies. In the present investigation, extensive cyclic voltammetric (CV) measurements for the MOR on several smooth and carbon unsupported porous Pd, Pt and Pt–Ru alloy electrodes of

compositions 9:1, 7:3 and 5:5 in different aqueous electrolytes of high and low pH that contain different quantities of methanol have been carried out.

The CVs of the porous unsupported Pt and Pt–Ru alloy electrodes in different alkaline and acidic solutions and those of the Pd electrodes in different alkaline solutions have exhibited both featured curves (i.e. the curves with the formation of anodic oxidation peaks namely  $\text{O}^{\text{f}}$  and  $\text{O}^{\text{b}}$ ) and featureless polarisation curves (i.e. the curves without forming the  $\text{O}^{\text{f}}$  and  $\text{O}^{\text{b}}$  peaks). In the case of the smooth Pt and Pd electrodes, only featured CV curves have been obtained in all the electrolyte/methanol combinations tested in the present study. The various processes that occur on the unsupported porous electrodes and the smooth electrodes are discussed [1,3,4,21,26].

It is inferred from this study that by choosing the proper porous electrode structure and the proper ratio of  $\text{OH}^-$  and  $\text{CH}_3\text{H}$  in solution, it may be possible to avoid completely the intermediate organic species and/or poisoning species that retard the MOR rate on the electrode surface.

## 2. Experimental preparation of the porous unsupported Pd, Pt and Pt–Ru alloy electrodes

The porous unsupported Pd, Pt and Pt–Ru (9:1), (7:3) and (5:5) single phase alloy electrodes were prepared from the

\* Corresponding author. Tel.: +91-431-660-311; fax: +91-4339-50-516.  
E-mail address: hinergy@tr.dot.net.in (R. Manoharan).

metal powders by the compaction method. These metal powders were prepared by aqueous phase reduction method as reported elsewhere [27]. The Pd, Pt and Pt–Ru alloy electrodes, thus, prepared offered a porosity of 60–65% void volume. The real area of the electrode has not been determined in the present study and only the geometrical area has been utilised to calculate current densities.

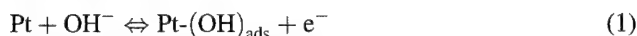
Foils of Pt and Pd were used as smooth working electrodes. The smooth Pt electrode was pre-treated with acetone and 5% solution of aqua regia followed by washing with demineralised water. The smooth Pd electrode was pre-treated by mildly abrading with fine grade emery paper followed by washing with demineralised water. The Pt smooth electrodes were scanned in the region between –0.25 and 1.8 V and the Pd smooth electrodes in the region between 0.3 and 1.8 V at 25 mV s<sup>–1</sup> initially to ensure that the expected CV behaviour of the system is observed.

A conventional, three-electrode system was employed for electrochemical measurements. All the CVs were obtained at a scan rate of 25 mV s<sup>–1</sup>, unless stated otherwise, as reported in [27]. The electrode potentials are reported with respect to reversible hydrogen electrode (RHE).

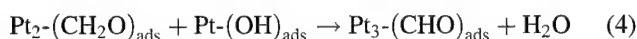
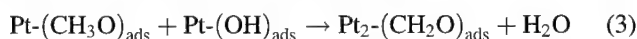
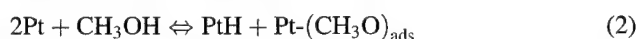
### 3. Results and discussion

#### 3.1. Cyclic voltammograms for the oxidation of methanol on Pt and Pt–Ru electrodes in alkaline solutions<sup>1</sup>

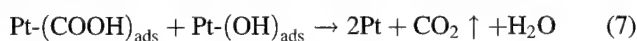
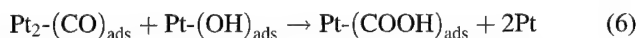
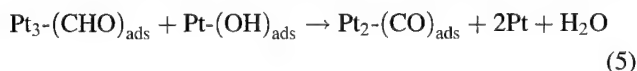
The MOR mechanistic pathways in alkaline solutions are as follows [3]:



The OH<sup>–</sup> ions required for this equilibrium are mainly supplied by the solution OH<sup>–</sup> ions at  $E > 0.3$  V [28].

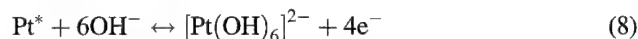


The strength of the bonding of (CHO)<sub>ads</sub> on the surface determines the entire rate of the reaction. The chemisorptive bonding of CHO on platinum in alkali is weak, such that further oxidation takes place without much difficulty, i.e. without irreversibly blocking the electrode's active sites.



A low level of hydrous oxide, which may be formed at metal sites and surface defects [29] via the reaction of

Eq. (8), may also contribute the active oxygen atoms responsible for “burning off” the organic species in the reactions of Eqs. (2)–(7).



CVs have been recorded on the unsupported porous Pt, Pt–Ru and the smooth Pt electrodes in electrolytes that contain varying concentrations of alkali and methanol.

In Fig. 1, the CVs recorded for the porous unsupported Pt electrode in 6 M KOH solutions that contain varying concentrations of methanol (1, 3, 6, 9 and 11 M CH<sub>3</sub>OH) are shown. During the forward sweep, the MOR begins at 0.18 V for all the electrolyte/methanol mixtures. For the 6 M KOH/1 M CH<sub>3</sub>OH mixture, the anodic peak O<sup>f</sup> occurs in the region 0.18–0.92 V with  $E_p = 0.7$  V. The reactions (1–4) occur in the early potential region of the O<sup>f</sup> peak and the reactions of Eqs. (5)–(7) occur in the region 0.18–0.92 V. A less active PtO monolayer film is formed at  $E > 0.8$  V during the forward sweep. It blocks the supply of the active oxygen atoms and hence further occurrence of the MOR is suppressed.

During the backward sweep, the oxidation peak O<sup>b</sup>, appears in the region 0.8–0.17 V with  $E_p = 0.5$  V. In this region, the oxide layer becomes reduced and gives room for the electrode surface to acquire a large quantity of active oxygen atoms from the solution. These atoms then oxidise the weakly bonded residual CHO species that remain at the end of the forward sweep as well as freshly chemisorbed methanol molecules and give rise to the O<sup>b</sup> peak.

On increasing the methanol concentration to 3 M, the electrode tries to oxidise the organic species completely but it does not quite succeed in doing so. The formation of the less active PtO is not completely suppressed in this case. At  $E > 1.05$  V, some PtO is formed during the forward sweep and it reduces the rate of oxidation of the organic species. This accounts for the current-declining portion of the CV

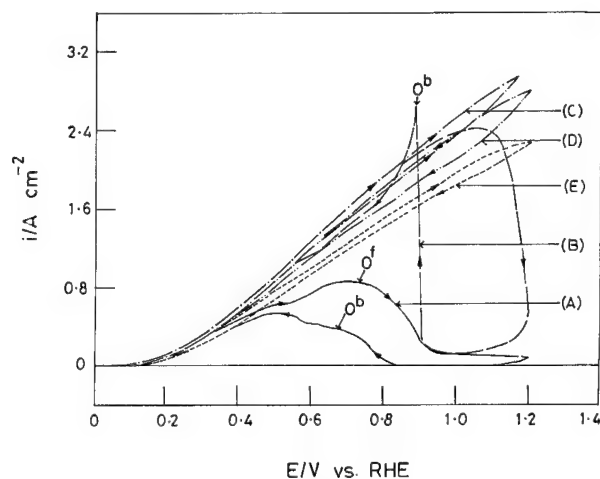


Fig. 1. CVs for the MOR on porous unsupported Pt electrodes in 6 M KOH solutions that contain varying concentrations of CH<sub>3</sub>OH: (A) 1 M; (B) 3 M; (C) 6 M; (D) 9 M; (E) 11 M.

<sup>1</sup> In the case of the Pt–Ru alloy electrodes, the active oxygen atoms are supplied via some of the Pt and some Ru sites.

curve. During the backward sweep, the PtO is reduced in the potential region 1.2–0.9 V and the remaining CHO species are immediately oxidised. Following this, freshly chemisorbed methanol molecules are oxidised at  $E < 0.8$  V.

On increasing further the methanol concentration to 6 M, it appears that complete oxidation of chemisorbed organic species takes place without permitting any CHO species to remain on the electrode surface and the peaks  $O^f$  and  $O^b$  are not observed [30]. Instead, a featureless polarisation curve is obtained ( $3 \text{ A cm}^{-2}$  at 1.17 V). The active oxygen atoms, provided by the porous network of the unsupported carbon catalytic electrodes, seem to be greatly efficient oxidisers. It is noteworthy that no previous work has discussed such featureless CV curves for the MOR.

For higher methanol concentrations viz. 9 and 11 M, the featureless polarisation curves are again noted. However, in these higher concentrations, relatively lower current densities are obtained.

On recording the CVs in 1 M KOH solutions containing varying concentrations of methanol (1, 3 and 6 M), small  $O^f$  and  $O^b$  peaks are observed for the 1 M KOH/1 M  $\text{CH}_3\text{OH}$  and 1 M KOH/3 M  $\text{CH}_3\text{OH}$  mixtures in the higher potential region. On increasing the methanol concentration to 6 M, the formation of these peaks is suppressed and the featureless polarisation curve is formed.

In the case of 11 M KOH with 1, 3, 6, 9, 11 and 13 M  $\text{CH}_3\text{OH}$ , the  $O^f$  and  $O^b$  peaks are formed in concentrations up to 9 M. Upon further increasing the methanol concentration (11 and 13 M), the featureless polarisation curves are obtained.

In the case of the porous unsupported Pt–Ru alloy electrodes, the active oxygen atoms are supplied by both Pt and Ru atoms, the ratio of supply being governed by the alloys' compositions. The anodic peaks  $O^f$  and  $O^b$  appear in the CVs in the 6 M KOH/1 M  $\text{CH}_3\text{OH}$  and 3 M  $\text{CH}_3\text{OH}$  mixtures. On raising the methanol concentration to 6 M, the featureless polarisation curves are obtained for all of the Pt–Ru compositions [31].

Fig. 2 presents the CVs recorded for the smooth Pt electrodes in 6 M KOH solutions that contain 1, 3, 6, 9, 11, 13, 15 and 18 M  $\text{CH}_3\text{OH}$ . For all of these mixture combinations, onset of the MOR takes place at 0.37 V, which is 190 mV more positive than for the porous unsupported Pt electrodes. The  $O^f$  and  $O^b$  peaks appear in all the CVs.

For the 6 M KOH/1 M  $\text{CH}_3\text{OH}$  mixture, the  $E_p$  values of the  $O^f$  and  $O^b$  peaks are 0.73 and 0.55 V, respectively. On gradually increasing the methanol concentration (1–18 M) in the solution, the positions of both the  $O^f$  and  $O^b$  peaks shift slightly in the positive direction. The current densities of the  $O^f$  peaks increase up to 13 M  $\text{CH}_3\text{OH}$  and on further increasing the methanol concentration (15 and 18 M), the current densities of the peaks decline.

On recording the CVs in 1 M KOH solutions containing varying concentrations of methanol (1, 3, 5, 7, 9 and 11 M), only featured curves are recorded. The 1 M KOH/9 M

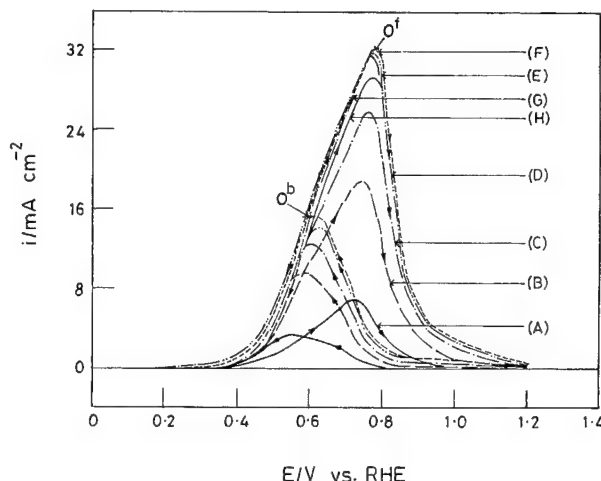


Fig. 2. CVs for the MOR on smooth Pt electrodes in 6 M KOH solutions that contain varying concentrations of  $\text{CH}_3\text{OH}$ : (A) 1 M; (B) 3 M; (C) 6 M; (D) 9 M; (E) 11 M; (F) 13 M; (G) 15 M; (H) 18 M.

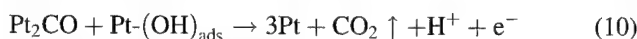
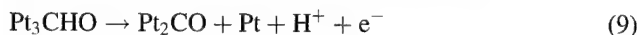
$\text{CH}_3\text{OH}$  mixture has yielded the highest current density peak.

Similarly the  $O^f$  and  $O^b$  peaks have only been observed in the CVs recorded in highly concentrated (11 M) KOH solutions containing varying concentrations of methanol (1, 3, 6, 9 and 11 M).

From the observations of the appearance of the  $O^f$  and  $O^b$  peaks and higher MOR polarisations in all KOH/methanol mixtures, it can be inferred that the oxidation of the intermediate organic species  $(\text{CHO})_{\text{ads}}$  does not take place easily and completely on the smooth Pt electrodes. Population of the active sites that are present on the smooth electrodes are lower compared to those in the porous electrodes. Hence inadequate amounts of the active oxygen atoms may be extracted from the electrolyte on the smooth Pt electrodes to completely oxidise the  $(\text{CHO})_{\text{ads}}$  species in the lower potential region and these organic species remain as the “poisoning species” on the surface of the electrodes.

### 3.2. Cyclic voltammograms for oxidation of methanol on Pt and Pt–Ru alloy electrodes in acid solutions

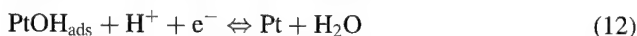
The dehydrogenation of methanol molecules occurs in acid solutions via the reactions (1–4) and the  $(\text{CHO})_{\text{ads}}$  species are further oxidised as follows [32]:



The unreacted  $\text{Pt}_2\text{CO}$  may also rearrange to give a linearly bonded CO species which acts as poison



On reversing the sweep, the linear species  $\text{Pt}=\text{C}=\text{O}$  are oxidised according to the following reactions:



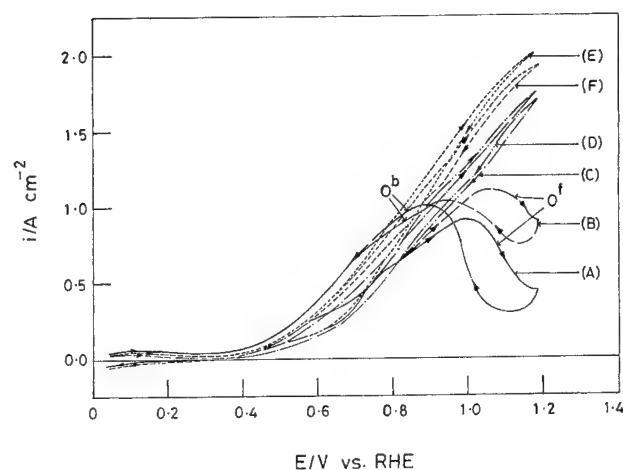
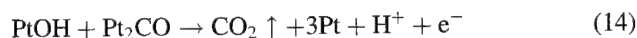


Fig. 3. CVs for the MOR on porous unsupported Pt electrodes in 2.5 M  $\text{H}_2\text{SO}_4$  solutions that contain varying concentrations of  $\text{CH}_3\text{OH}$ : (A) 1 M; (B) 2.5 M; (C) 4 M; (D) 6 M; (E) 8 M; (F) 10 M.



The active oxygen atoms may also be provided by the Ru atoms during the occurrence of the reactions of Eqs. (10) and (11) while employing the Pt–Ru electrodes.

The CVs recorded for the unsupported porous Pt electrode in 2.5 M  $\text{H}_2\text{SO}_4$  solutions that contain 1, 2.5, 4, 6, 8 and 10 M methanol are shown in Fig. 3. For the 2.5 M  $\text{H}_2\text{SO}_4$ /1 M  $\text{CH}_3\text{OH}$  mixture, the MOR begins at 0.06 V, and after the initial anodic reactions of Eqs. (1)–(4) have taken place at potentials below 0.44 V, the peak  $\text{O}^f$  appears at potential 150 mV more positive than that observed in alkaline solutions. The  $E_p$  of  $\text{O}^f$  is 1 V.

The reactions of Eqs. (9) and (10) occur in the potential region of the  $\text{O}^f$  peak. The appearance of the  $\text{O}^b$  peak ( $E_p = 0.85$  V) during the backward sweep suggests that all the  $\text{Pt}_2\text{CO}$  species are not reacting completely during the forward sweep; some  $\text{Pt}_2\text{CO}$  species remain unreacted and they rearrange themselves into a linear  $\text{Pt}=\text{C}=\text{O}$  structure. The peak  $\text{O}^b$  is associated with the removal of the linear species  $\text{Pt}=\text{C}=\text{O}$  according to the reactions of the Eqs. (12)–(14) [26].

When the methanol concentration is raised to 2.5 M, small  $\text{O}^f$  and  $\text{O}^b$  peaks are observed at  $E > 0.8$  V. On further raising the methanol concentration (up to 10 M), the featureless CV curves are observed [27]. It is apparent that on raising the methanol concentration above 2.5 M, all the linearly bonded poisoning  $\text{PtCO}$  species are completely oxidised by the active oxygen atoms supplied by the porous network of the unsupported catalytic electrodes. The current densities of these CV curves increase on adding further quantity of methanol (4–8 M). On increasing the methanol concentration above 8 M, the current densities of the peaks decline.

In the case of 1 M  $\text{H}_2\text{SO}_4$  solutions with varying concentrations of methanol (1, 2, 4, 6, 8 and 10 M), the  $\text{O}^f$  and

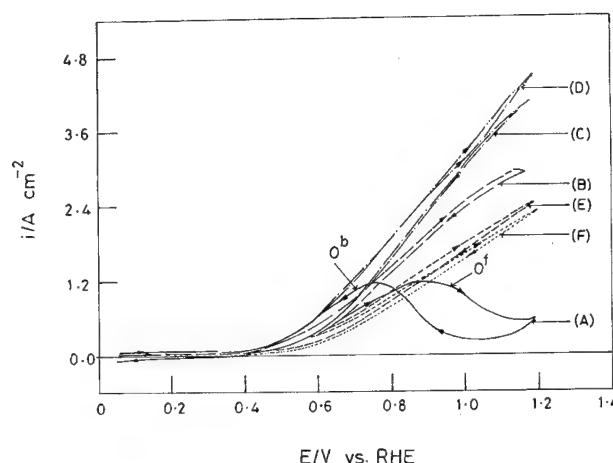


Fig. 4. CVs for the MOR on porous unsupported Pt–Ru (7:3) electrodes in 2.5 M  $\text{H}_2\text{SO}_4$  solutions that contain varying concentrations of  $\text{CH}_3\text{OH}$ : (A) 1 M; (B) 2.5 M; (C) 4 M; (D) 6 M; (E) 8 M; (F) 10 M.

$\text{O}^b$  peaks appear only in the 1 M  $\text{H}_2\text{SO}_4$ /1 M  $\text{CH}_3\text{OH}$  mixture. On increasing the methanol concentration, the featureless CV curves are obtained. The current densities of the peaks increase only up to 3 M, and above this concentration, the current density falls down.

In higher concentrations of acidic solutions (up to 5 M  $\text{H}_2\text{SO}_4$ ), only the featureless CV curves are obtained.

The porous unsupported Pt–Ru alloy electrodes of all the compositions show featureless polarisation curves in all acidic solutions except in 2.5 M  $\text{H}_2\text{SO}_4$ /1 M  $\text{CH}_3\text{OH}$  and 1 M  $\text{H}_2\text{SO}_4$ /1 M  $\text{CH}_3\text{OH}$  [31]. The CVs recorded for the best performing 7:3 electrode in 2.5 M  $\text{H}_2\text{SO}_4$  solutions with varying concentrations of methanol (1, 2.5, 4, 6, 8 and 10 M) are shown in Fig. 4.

Fig. 5 shows the CVs for the smooth Pt electrodes in 2.5 M  $\text{H}_2\text{SO}_4$  solutions containing varying concentrations of methanol 1, 3, 6, 8 and 10 M  $\text{CH}_3\text{OH}$ . During the forward sweep, the MOR begins at 0.6 V in all these mixtures, which

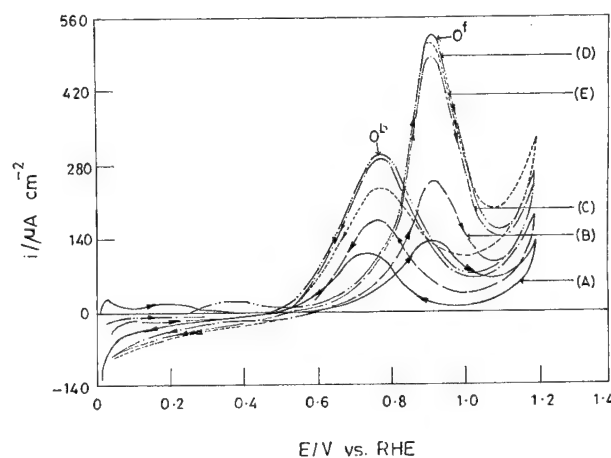


Fig. 5. CVs for the MOR on smooth Pt electrodes in 2.5 M  $\text{H}_2\text{SO}_4$  solutions that contain varying concentrations of  $\text{CH}_3\text{OH}$ : (A) 1 M; (B) 3 M; (C) 6 M; (D) 8 M; (E) 10 M.

is 250 mV more positive than with the porous Pt electrodes. The maximum current density for the  $O^f$  peak is observed for the 2.5 M  $H_2SO_4$ /8 M  $CH_3OH$  mixture and on further increasing the methanol concentration to 10 M, the current density decreases.

In the case of 1 M  $H_2SO_4$  with varying concentrations of methanol (1, 3 and 6 M), all the CVs show  $O^f$  and  $O^b$  peaks. The 1 M  $H_2SO_4$ /1 M  $CH_3OH$  mixture has yielded the highest current density among these combinations. On raising the methanol concentration beyond 1 M, the current density of the  $O^f$  peak declines.

It can be surmised from the investigation on the smooth Pt electrodes in acid solutions that the oxidation of the poisoning  $=C=O$  does not take place completely on these electrodes.

### 3.3. Cyclic voltammograms for the oxidation of methanol on Pd electrodes in alkaline solutions

The MOR on the Pd electrodes in alkaline solutions proceeds via chemisorptive dissociation pathways and the strongly held intermediate organic species is bridge bonded  $Pd_2CO$  [15].

Fig. 6 shows the CVs for the porous unsupported Pd electrodes in 6 M KOH solutions that contain 1, 3, 5, 6, 8 and 9 M  $CH_3OH$ . The  $O^f$  and  $O^b$  peaks are observed up to 5 M  $CH_3OH$ ; probably the process of formation of less active PdO dominate in these mixtures [33].

On increasing further the methanol concentration to 6 M, the  $O^f$  and  $O^b$  peaks are not observed, and the featureless CV curve is observed. In this mixture, dissociatively chemisorbed methanol and  $OH_{ads}$  cover the Pd sites in such a way that the complete oxidation of chemisorbed organic species take place without permitting any CO species to remain on the electrode surface [34]. On raising the methanol concen-

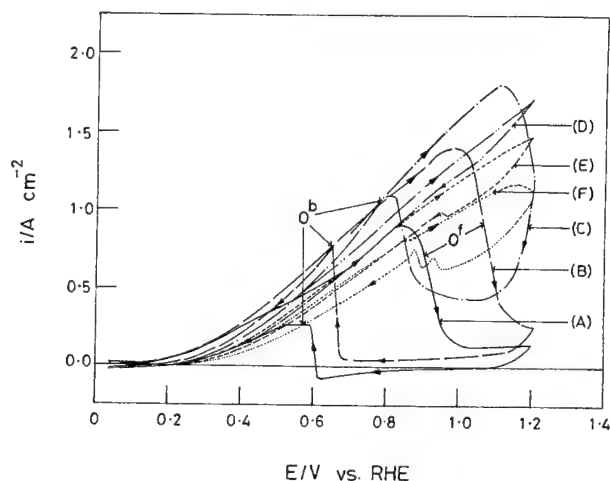


Fig. 6. CVs for the MOR on porous unsupported Pd electrodes in 6 M KOH solutions that contain varying concentrations of  $CH_3OH$ : (A) 1 M; (B) 3 M; (C) 5 M; (D) 6 M; (E) 8 M; (F) 9 M.

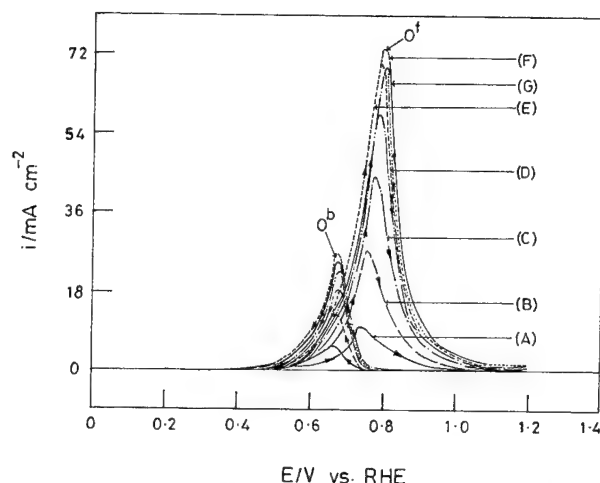


Fig. 7. CVs for the MOR on smooth Pd electrodes in 6 M KOH solutions that contain varying concentrations of  $CH_3OH$ : (A) 1 M; (B) 3 M; (C) 6 M; (D) 9 M; (E) 11 M; (F) 13 M; (G) 15 M.

tration above 6 M (i.e. 8 and 9 M), again small  $O^f$  and  $O^b$  peaks appear in the CVs and, also, the current densities of these peaks decrease. This suggests that the active oxygen atoms extracted by the Pd electrodes from 6 M KOH solution are not able to oxidise completely the bridge bonded CO species that arises from the excess methanol.

The CVs recorded for 1 and 11 M KOH solutions containing varying concentrations of methanol show only  $O^f$  and  $O^b$  peaks.

Fig. 7 shows the CVs recorded for the smooth Pd electrodes in 6 M KOH solutions that contain 1, 3, 6, 9, 11, 13 and 15 M  $CH_3OH$ . All these mixtures show  $O^f$  and  $O^b$  peaks. The current densities of the peaks increase up to the concentration of 13 M. In 15 M, the current density is lower.

On lowering the KOH concentration to 1 M and on adding various amounts of methanol (1, 3, 6 and 9 M) the positions of the  $O^f$  and  $O^b$  peaks are shifted in the positive direction.

In the case of 11 M KOH solutions with 1, 3, 6, 9 and 11 M  $CH_3OH$ , the positions of the  $O^f$  and  $O^b$  peaks are slightly shifted in the negative side suggesting that the MOR may take place somewhat more easily on increasing the KOH concentration in the electrolyte/methanol mixtures.

It is learnt from these investigations that on the smooth Pd electrodes, the intermediate bridge bonded  $>CO$  species does not become completely oxidised in the KOH/methanol mixtures of all concentrations and they remain as poisoning species on the surface of the electrodes.

The Pd electrodes corrode in acid solutions and hence they do not catalyse the MOR [27,34].

## 4. Conclusions

From the extensive cyclic voltammetric investigations of the MOR on the porous unsupported Pd, Pt and Pt–Ru alloy

electrodes of compositions 9:1, 7:3 and 5:5 and the smooth Pt and Pd electrodes in different aqueous electrolytes of high and low pH, the following conclusions have been drawn:

The CVs recorded for the porous unsupported Pd, Pt and Pt–Ru alloy electrodes in some electrolyte/methanol mixtures exhibit featureless polarisation curves. If  $O^f$  and  $O^b$  peaks do not appear in the CVs, then it can be inferred that the poisoning species do not arise under such circumstances and that the intermediate organic species are rapidly oxidised by the active oxygen atoms provided by the porous network of the catalytic electrodes.

The anodic peaks  $O^f$  and  $O^b$  appear in the CVs in some electrolyte/methanol mixtures. Appearance of these peaks in the CVs mean that both the methanol and the active oxygen atoms do not meet at the electrodes surface in a suitable ratio and the complete oxidation of chemisorbed organic species does not take place. The strongly bonded organic species persist as the “poisoning species” on the surface of the electrodes during the forward sweep.

On the smooth Pt and Pd electrodes where a porous structure does not exist, the poisoning species seem to persist in any electrolyte/methanol combination. The  $O^f$  and  $O^b$  peaks appear in all the CVs. On the smooth electrodes, the number of active sites are lower. Adsorption of the active oxygen atoms and methanol takes place in ratios such that the complete oxidation of the intermediate organic species do not take place.

It is concluded that it is possible to prevent the formation of the poisoning species provided unsupported porous structured methanol anodes are chosen and a suitable combination of electrolyte/methanol is employed. In situ IR spectroscopic investigations would be desirable to further corroborate these findings.

## References

- [1] V.S. Bagotsky, Y.B. Vassiliev, O.A. Khazova, J. Electroanal. Chem. 81 (1977) 229.
- [2] D. Pletcher, V. Solis, Electrochim. Acta 27 (1982) 775.
- [3] B. Beden, F. Kadirgan, C. Lamy, J.M. Leger, J. Electroanal. Chem. 142 (1982) 171.
- [4] C. Lamy, Electrochim. Acta 29 (1984) 1581.
- [5] K. Ota, Y. Nakagawa, T. Takahashi, J. Electroanal. Chem. 179 (1984) 179.
- [6] F. Hahn, B. Beden, F. Kadirgan, C. Lamy, J. Electroanal. Chem. 216 (1987) 169.
- [7] R. Parsons, T. Vandernoot, J. Electroanal. Chem. 257 (1988) 9.
- [8] K. Kunimatsu, Ber. Bunsenges. Phys. Chem. 94 (1990) 1025.
- [9] P.A. Christensen, A. Hamnett, J. Munk, G.L. Troughton, J. Electroanal. Chem. 370 (1994) 251.
- [10] F. Hahn, B. Beden, C. Lamy, J. Electroanal. Chem. 216 (1987) 169.
- [11] F. Hahn, B. Beden, F. Kadirgan, C. Lamy, J. Electroanal. Chem. 216 (1983) 505.
- [12] K. Kunimatsu, J. Electroanal. Chem. 213 (1986) 149.
- [13] B. Beden, A. Bewick, K. Kunimatsu, C. Lamy, J. Electroanal. Chem. 142 (1982) 345.
- [14] M.M.P. Janssen, J. Moolhuysen, Electrochim. Acta 21 (1976) 869.
- [15] K. Nishimura, K. Kunimatsu, M. Enyo, J. Electroanal. Chem. 260 (1989) 167.
- [16] H.A. Gasteiger, N. Markovic, P.N. Ross Jr., E.J. Cairns, J. Phys. Chem. 97 (1993) 12020.
- [17] D. Chu, S. Gilman, J. Electroanal. Chem. 143 (1996) 1685.
- [18] A.S. Arico, P. Creti, N. Giordano, V. Antonucci, P.L. Antonucci, A. Chuvilini, J. Appl. Electrochem. 26 (1996) 959.
- [19] K.J. Cathro, J. Electrochem. Soc. 116 (1969) 1608.
- [20] W. Vielstich, P.A. Christensen, S.A. Weeks, A. Hamnett, J. Electroanal. Chem. 242 (1988) 327.
- [21] M. Shibata, S. Motoo, J. Electroanal. Chem. 209 (1986) 151.
- [22] A.S. Arico, Z. Poltarzewski, A. Morana, N. Giordano, V. Antonucci, J. Power Sources 55 (1995) 159.
- [23] J.B. Goodenough, A. Hamnett, B.J. Kennedy, R. Manoharan, S.A. Weeks, J. Electroanal. Chem. 240 (1988) 133.
- [24] P.K. Guha, A. Bhattacharya, K.K. Kundu, Ind. J. Chem. 28A (1989) 825.
- [25] B. Gurau, R. Viswanathan, R. Liu, T.J. Lafrenz, K.L. Ley, E.S. Smotkin, E. Reddington, A. Sapienza, B.C. Chan, T.E. Mallouk, S. Sarangapani, J. Phys. Chem. 102 (1998) 9997.
- [26] R. Manoharan, J.B. Goodenough, J. Mater. Chem. 2 (8) (1992) 875.
- [27] J. Prabhuram, Ph.D. Thesis, Bharathidasan University, Tiruchirapalli, 1999.
- [28] A.N. Frumkin, O.A. Petry, A.M. Kossaya, Elektrokhimiya 4 (1968) 475.
- [29] L.D. Burke, K.J. O'Dwyer, Electrochim. Acta 35 (1990) 1821.
- [30] J. Prabhuram, R. Manoharan, J. Power Sources 74 (1998) 54.
- [31] J. Prabhuram, R. Manoharan, Portugaliae Electrochim. Acta 16 (1998) 181.
- [32] I. Iwasita, W. Vielstich, J. Electroanal. Chem. 250 (1988) 452.
- [33] J. Prabhuram, R. Manoharan, H.N. Vasan, J. Appl. Electrochem. 28 (9) (1998) 935.
- [34] J. Prabhuram, R. Manoharan, Bull. Electrochem. 14 (1998) 255.



## In situ X-ray absorption spectroscopy and X-ray diffraction of fuel cell electrocatalysts

Andrea E. Russell<sup>a,\*</sup>, Stephanie Maniguet<sup>a</sup>, Rebecca J. Mathew<sup>a</sup>, Jun Yao<sup>a</sup>,  
Mark A. Roberts<sup>b</sup>, David Thompson<sup>c</sup>

<sup>a</sup>Department of Chemistry, University of Southampton, Highfield, Southampton SO17 1BJ, UK

<sup>b</sup>CLRC, Daresbury Laboratory, Warrington, Cheshire WA4 4AD, UK

<sup>c</sup>Johnson Matthey Technology Centre, Blounts Court, Sonning Common, Reading RG4 9NH, UK

Received 12 January 2001; accepted 14 January 2001

### Abstract

The utility of in situ X-ray absorption spectroscopy (XAS) in determining structural parameters, through analysis of the extended X-ray absorption fine structure (EXAFS), and electronic perturbations, through a white line analysis of the X-ray absorption near edge structure (XANES), is demonstrated for Pt/C, PtRu/C and PtMo/C fuel cell electrodes. The results provide verification that the enhancement of CO tolerance of the alloy catalysts occurs via an intrinsic mechanism for the PtRu alloy, whilst a promotion mechanism is in operation for the PtMo alloy. Preliminary results of an in situ powder X-ray diffraction (XRD) method which utilises synchrotron radiation (SR) and a curved image plate detector are also presented, using Pd/C as an example. The lattice expansion upon formation of the  $\beta$ -hydride is clearly observed. © 2001 Elsevier Science B.V. All rights reserved.

**Keywords:** Fuel cell catalysts; X-ray absorption spectroscopy; X-ray diffraction

### 1. Introduction

In recent years there has been an increased interest in electricity generation using fuel cells for both stationary and mobile applications. In particular, following announcements by several automotive manufacturers [1,2], the research and development effort in the area of PEM (proton exchange membrane) fuel cells has intensified. Such cells either use H<sub>2</sub> or CH<sub>3</sub>OH as the fuel and O<sub>2</sub> or air as the oxidant. The electrocatalysts are usually based on small Pt metal particles dispersed on a conductive supporting medium, often carbon.

In the case of the H<sub>2</sub> or PEM fuel cell, the source of the fuel is usually reformat, which is a mixture of H<sub>2</sub> and CO<sub>2</sub> obtained by processing (reforming) a hydrocarbon feed stock. Reformate produced by steam or partial oxidation, contains 0.5 to 2% CO. The CO contamination is then reduced to ppm levels prior to entering the fuel cell by clean up stages (selective oxidation). However, even at 10 ppm CO, a further reduction is required as, even at such levels, CO can cause deactivation of the anode catalyst by strongly adsorbing to the more active sites; a site blocking

mechanism. Adding an air bleed to the anode fuel stream and performing the final CO clean up within the membrane electrode assembly (MEA) are the most generally applied approaches to improving CO tolerance. However, the more elegant alternative is to develop electrocatalysts that are 'tolerant' to the presence of CO in the fuel. The most promising electrocatalysts are now based on binary and ternary alloys of Pt. The ultimate performance of the H<sub>2</sub> fuel cell is also limited by the rate of the O<sub>2</sub> reduction reaction at the cathode.

As in the case of the electrocatalysts for the anode, alloys of Pt have been investigated in an effort to improve the performance of the cathode. In the case of the direct methanol fuel cell (DMFC), the anode catalyst may be slowly deactivated by the accumulation of partial oxidation products such as CO, while the cathode is depolarised by crossover of methanol from the anode side of the cell. Alloy electrocatalysts may also provide solutions to these difficulties.

Characterisation of the electrocatalyst materials is usually conducted ex situ using BET, TEM, or XRD measurements. Recently, with the increased availability of synchrotron radiation (SR), the use of in situ X-ray absorption spectroscopy (XAS) has been shown to be uniquely suited to

\* Corresponding author. Fax: +44-1703-593781.

E-mail address: a.e.russell@soton.ac.uk (A.E. Russell).



determining the structure of such electrocatalysts. In situ XAS enables the probing of both the d-electronic structure of the metal particles (oxidation state and size/delocalization) and the interaction of these particles with their support and adsorbates (near neighbour interactions). The in situ study of carbon supported Pt (Pt/C) fuel cell electrodes was first successfully demonstrated by O'Grady and Koningsberger [3]. Mathew and Russell have recently presented a comprehensive review of the use of XAS for the characterisation of Pt/C, highlighting the development of the technique [4]. The most significant advances have been in the development of energy dispersive EXAFS (EDE) methods, which enable dynamic or time resolved studies of the catalyst structure.

In this paper the utility of in situ XAS methods in determining the structure of Pt/C, PtRu/C and PtMo/C catalysts is demonstrated. The results are related to the improvement in CO electro-oxidation for the binary catalysts over that of Pt/C. In addition, in situ X-ray diffraction (XRD) measurements using SR and a curved image plate camera is presented for the Pd/C system.

## 2. Experimental

### 2.1. Electrodes

An appropriate quantity of 40 wt.% Pt/XC-72R, or 40 wt.% Pt plus 20 wt.% Ru/XC-72R, or 35 wt.% Pt plus 5 wt.% Mo/XC72-R catalyst (supplied by Johnson Matthey, the preparation of which has been previously reported [5]) or 40 wt.% Pd/XC72-R (E-TEK) was suspended in Nafion<sup>®</sup> and water to form an ink-like paste. The paste was stirred for 15 min and then spread onto carbon paper (E-TEK TGHP-120). The sheet was pressed at 14 kg cm<sup>-2</sup> for 20 s at room temperature. Electrodes of area 2.5 cm<sup>2</sup> were cut from the compressed sheet for the in situ EXAFS and XRD measurements and 1 cm<sup>2</sup> for cyclic voltammetric (CV) testing. Electrodes were boiled in triply distilled water prior to EXAFS and CV studies to ensure a fully flooded state.

### 2.2. Cyclic voltammetry

The wetted electrodes were placed in a standard three-electrode cell for the CV experiments. Potentials were measured either with respect to a Hg/Hg<sub>2</sub>SO<sub>4</sub> (MMS) reference electrode or a H<sub>2</sub> purged Pd on carbon electrode strip acting as a reversible hydrogen electrode (RHE). When the MMS reference electrode was used the potentials have been corrected to the RHE scale.

For CO electro-oxidation experiments, the catalyst electrodes were held at 0.15 V versus RHE while CO and N<sub>2</sub> was purged through the electrolyte for 15 and then 30 min, respectively. The electrode potential was then cycled to the positive limit and back to 0.05 V at a sweep rate of 10 mV s<sup>-1</sup>.

### 2.3. X-ray absorption spectroscopy measurements

The in situ transmission data was collected using a cell described previously [6]. The carbon paper backed catalyst working electrode was placed against a gold wire current collector and several layers of filter paper soaked in electrolyte, 1.0 mol dm<sup>-3</sup> H<sub>2</sub>SO<sub>4</sub> prepared with 18 MΩ cm water, were placed over the electrode. This assembly was compressed between Kapton<sup>®</sup> or polycarbonate windows, through which the X-rays passed.

All X-ray data were collected on Wiggler station 9.2 of the synchrotron radiation source (SRS) at Daresbury Laboratory, Warrington, England. The ring operated with 2.0 GeV energy and 100–250 mA current. The station was operated with a Si(2 2 0) double crystal monochromator, which was detuned to 50% intensity to minimise the presence of higher harmonics. Three ion chambers, optimised for the platinum L<sub>III</sub> edge, were used in series to measure the intensities of the incident beam,  $I_0$ , the beam transmitted by the sample,  $I_t$ , and the beam subsequently transmitted by a platinum foil,  $I_m$ . The Pt foil was used as an internal reference, enabling calibration of the X-ray beam energy.

The absorption spectra were processed using EXBROOK. The zero point of the energy scale was taken to be the point of inflection in the L<sub>III</sub> edge. The pre-edge region was fitted by a straight line and extrapolated to zero energy. A polynomial spline was fitted to the non-oscillatory component of the post-edge region and was extrapolated back to zero energy. The difference between the extrapolated values was taken to be the step height and the spectrum was normalised to this value. The EXAFS components,  $\chi(k)$ , were then isolated from the absorption spectra and subsequently analysed using EXCURV98 [7], a least squares fitting programme based on curved-wave theory, using a  $Z + 1$  2p core hole approximation.

### 2.4. X-ray diffraction measurements

The in situ XRD data was collected using a similar electrochemical cell to that used for the XAS measurements. On the exit side of the cell an enlarged slit was cut into the cell body and support to enable collection of the diffracted signal over a greater angular spread. The data was collected using Station 9.1 of the SRS. This station accepts a high energy X-ray spectrum of radiation from a 5 Tesla superconducting Wiggler. The monochromator was a Si(1 1 1) channel-cut crystal mounted at 15 m from the source and was used to select a wavelength, typically between 0.46 and 0.70 Å when using the Curved Image-Plate (CIP) camera [8]. This wavelength range is restricted because the high-energy flux is diminishing rapidly and the longer wavelength is a maximum at 0.70 Å since  $\lambda/3$  harmonics become prominent and contaminate the data. A wavelength of 0.6920 Å was selected and calibrated using a Zr metal absorption foil. The monochromatised beam was reduced in size to 0.5 mm × 0.5 mm and this was passed down the

anti-scatter tube arrangement to impinge on the sample in the cell approximately 1 m from the monochromator. The sample was located at the centre of curvature of the 350 mm radius camera arc. Any positional discrepancy is corrected by collecting data from an NBS 640b silicon standard and spatial distortions introduced during the image-plate reading are corrected using a grid calibration. Utilising a significant proportion of the area of the image-plate it is possible to collect high quality data on materials over a few minutes.

The processed data were subsequently analysed by the Le Bail method using the program WinMPProf. The Le Bail method is used to extract the intensities of the overlapping peaks from powder data without a structural model, given a starting set of unit cell parameters, and a list of possible reflections. Essentially, the method is similar to Rietveld in that a calculated profile is refined by least-squares against the observed diffraction pattern. Hence lattice parameters, peak widths, peak-shape parameters are allowed to vary. The same procedure was used for each data set.

### 3. Results and discussion

#### 3.1. Cyclic voltammetry

Fig. 1 shows the cyclic voltammograms obtained for electro-oxidation of adsorbed carbon monoxide for each of the Pt and Pt-alloy catalyst electrodes. For each of the electrodes, during the first forward sweep (from 0.05 to 1.0 V) the peaks characteristic of hydrogen desorption were

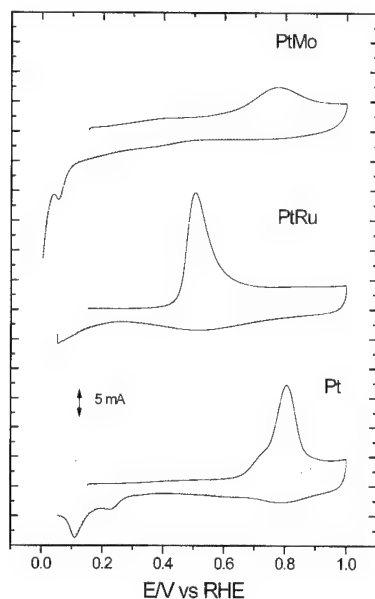


Fig. 1. Cyclic voltammograms of Pt/C, PtRu/C, and PtMo/C catalysts in  $1 \text{ mol dm}^{-3} \text{ H}_2\text{SO}_4$  at  $10 \text{ mV s}^{-1}$  (electrode area  $1 \text{ cm}^2$ ). The electrode surface was exposed to CO saturated solution while the potential was held at 0.15 V vs. RHE. After adsorption, CO was displaced from the solution by purging with  $\text{N}_2$  for 15 min. The solid lines represent the first cycle and the dashed lines the second.

suppressed by the presence of adsorbed CO, indicating nearly full CO coverage. The peak at 0.8 V in the Pt/carbon CV corresponds to the oxidative stripping of the adsorbed CO layer. On the second sweep the voltammogram returns to that observed in the absence of CO purging and corresponds to that of Pt in the base electrolyte. Similar features are apparent in the PtRu/C and PtMo/carbon CVs with the peak potential of the CO oxidation shifting to 0.48 and 0.78 V, respectively. The lack of distinct hydrogen adsorption/desorption peaks in the PtRu/carbon CV is characteristic of the response of a PtRu alloy. On close inspection of the PtMo/carbon CV, an oxidation current is observed throughout the first forward sweep, from 0.15 to 1.00 V, suggesting that some of the adsorbed CO is being oxidised at lower potentials. An additional oxidation peak is observed in the second forward sweep at 0.45 V, which has previously been attributed redox reactions of the Mo on the surface of the metal particles [9]. These results have been discussed recently in terms of the heterogeneity of the PtMo/C electrocatalyst in comparison to PtRu/C [10].

#### 3.2. X-ray absorption

The XANES (X-ray absorption near edge structure) or white line region of the Pt  $L_{\text{III}}$  and  $L_{\text{II}}$  absorption edges provides information regarding the d-electron occupancy of the metal particles. Comparisons of the area under the white lines of the sample and a Pt foil have been used previously [11–14] to quantify the changes in the relative occupancy,  $f_d$ , of the Pt as a function of the applied electrode potential.  $f_d$  is defined as follows [15]:

$$f_d = \left( \frac{\Delta A_3 + 1.11 \Delta A_2}{A_{3r} + 1.11 A_{2r}} \right) \quad (1)$$

where  $\Delta A_3$  is the difference in the area under the white line at the  $L_{\text{III}}$  absorption edge between the sample and the Pt reference foil ( $\Delta A_3 = A_{3s} - A_{3r}$ ). Similarly  $\Delta A_2 = A_{2s} - A_{2r}$ , is the difference at the  $L_{\text{II}}$  absorption edge. Thus, a smaller value of  $f_d$  indicates a greater occupancy of d electrons per Pt atom.

Fig. 2 shows the effect of variation of the applied electrode potential on the white line features at the Pt  $L_{\text{III}}$  and  $L_{\text{II}}$  absorption edges for the Pt/C sample. The effect of increasing the applied potential is to increase the area in the white line region, this corresponds to an increase in the  $f_d$  value. The  $f_d$  values as a function of the applied potential for the Pt and Pt-alloy catalysts are shown in Table 1. The effect of incorporation of the secondary metal is to decrease the d-electron occupancy per Pt atom (increased  $f_d$ ) at the lower potentials. Thus, the electronic state of the Pt in the alloy catalysts at these potentials corresponds to a pre-oxidised state. As the potential is increased the  $f_d$  values of all the catalysts increases, but that of the alloy catalysts do not change as much as that of the Pt/C.

The  $k^1$  weighted raw EXAFS data for the Pt/C electrode at 0.05 V is shown in Fig. 3. The corresponding  $k^3$  weighted

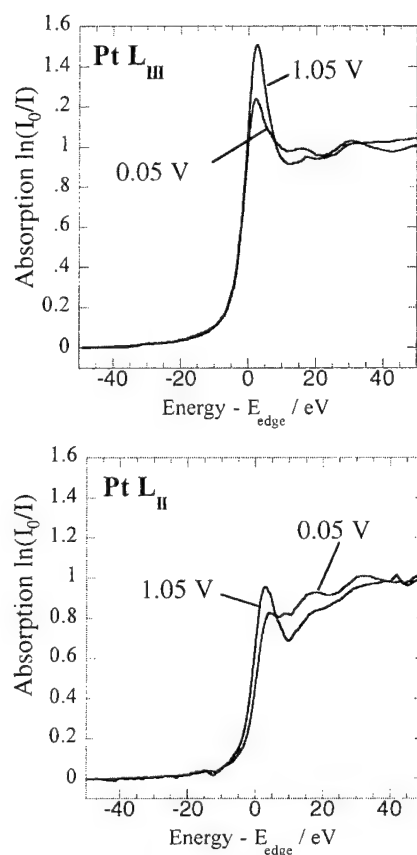


Fig. 2. XAS in 1 mol dm<sup>-3</sup> H<sub>2</sub>SO<sub>4</sub> showing the XANES region at the Pt L<sub>III</sub> and L<sub>II</sub> absorption edges for Pt/C at 0.05 and 1.05 V vs. RHE.

Table 1  
Fractional d-electron occupancy,  $f_d$ , as a function of applied potential

E/V vs. RHE	Pt/C	PtRu/C	PtMo/C
0.05	-0.095	-0.029	-0.055
0.25	-0.002	-0.019	-0.024
0.55	0.024	0.000	0.012

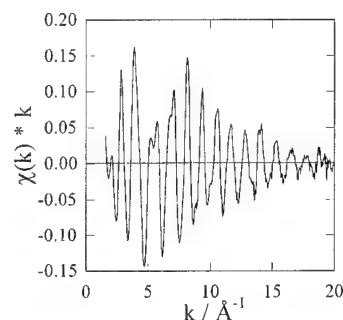


Fig. 3.  $k^1$  weighted EXAFS at 0.05 V vs. RHE for Pt/C fuel cell electrode in 1 mol dm<sup>-3</sup> H<sub>2</sub>SO<sub>4</sub>.

Pt–Pt phase corrected Fourier transform is shown in Fig. 4, with those for the PtRu/C and PtMo/C catalysts. The dashed lines indicate the best fit of the data. The splitting of the peak corresponding to the first coordination shell for the PtRu/C catalyst is caused by interference between the backscattering from Pt and Ru neighbours. The parameters for the fits of the EXAFS data are given in Table 2. The smaller coordination numbers and distances for the supported particles compared to those for a Pt foil,  $N = 12$  and  $R = 2.779$  Å, are consistent with the small size of the particles and other EXAFS studies ([4] and references contained therein). The smaller total number of neighbours in the first coordination shell ( $N(\text{Pt–Pt}) + N(\text{Pt–X})$ , where  $X = \text{Mo or Ru}$ ) indicates that the particles are smaller than for the Pt/C sample, in agreement with TEM measurements of the particle sizes [10]. The fits indicate that the PtRu/C is a well mixed alloy with almost equal numbers of Pt and Ru in the first coordination shell, whilst the PtMo/C catalyst has very little Mo in the first coordination shell. For icosahedral or cuboctahedral particles less than 5 nm in diameter, the fraction of the Pt atoms which are on the surface is approximately 0.5. Thus, the PtMo/C sample may consist of a Pt core with less than a full monolayer of Mo on the surface, or it may represent a mixed system with less than the stoichiometric quantity of

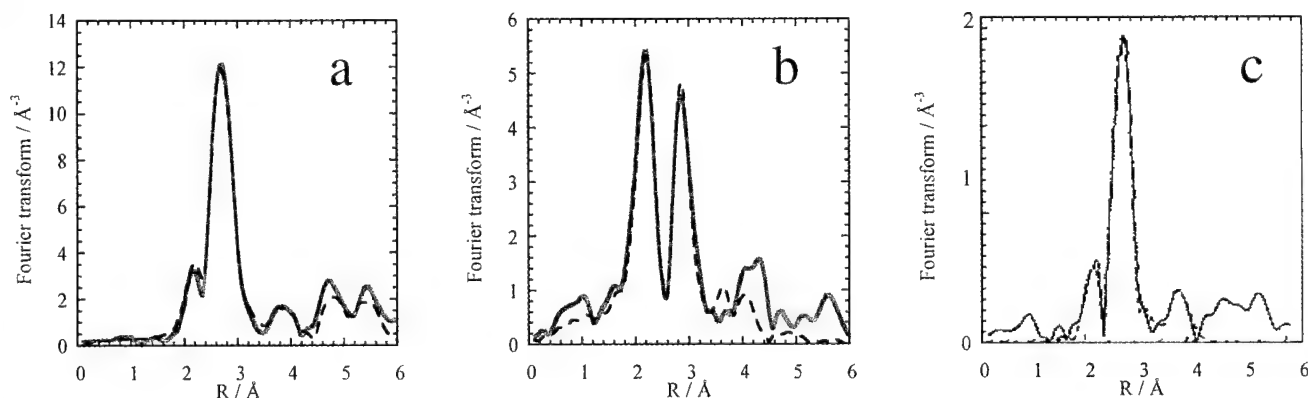


Fig. 4.  $k^3$  weighted Pt–Pt phase corrected Fourier transforms of the data (solid lines) and model spectra (dashed lines) for the (a) Pt/C, (b) PtRu/C and (c) PtMo/C fuel cell electrodes at 0.05 V versus RHE in 1 mol dm<sup>-3</sup> H<sub>2</sub>SO<sub>4</sub>.

Table 2  
Fit parameters and variances for model spectra at 0.05 V vs. RHE<sup>a</sup>

Catalyst	Neighbour	N	R (Å)	2σ <sup>2</sup> (Å <sup>2</sup> )
Pt/C R = 23%	Pt–Pt	9.1	2.755	0.011
	Pt–Pt	4.4	3.912	0.016
	Pt–Pt	7.1	4.798	0.012
PtRu/C R = 25%	Pt–Pt	4.4	2.732	0.011
	Pt–Ru	3.2	2.710	0.013
	Pt–Pt	1.9	3.850	0.017
PtMo/C R = 37%	Pt–Pt	6.0	2.756	0.011
	Pt–Mo	0.3	2.431	0.014
	Pt–Pt	3.5	3.893	0.013

<sup>a</sup> Errors are ±10% in coordination number for the first Pt–Pt and Pt–X distances and ±50% for the higher shells, ±0.004 Å in coordination distance for the first and second Pt–Pt and Pt–X distances, and 0.003 for the Debye Waller term (2σ<sup>2</sup>). The goodness of fit parameter, R, is  $R_{\text{EXAFS}} = \left\{ \sum_i^N (1/\sigma_i^{\text{exp}}) (|\chi_i^{\text{exp}} - \chi_i^{\text{th}}|) \right\} \times 100\%$  where N is the total number of data points, σ the standard deviation for each data point, and χ the experimental and theoretical EXAFS.

Mo in the particle. EXAFS measurements obtained at the Mo edge are required to discriminate between these two possibilities.

Improvements in the tolerance of electrocatalysts to carbon monoxide exposure or methanol crossover upon alloy formation are thought to be related to either variations in the chemisorptive properties of the particles (intrinsic mechanism) or electronic effects which lead to a reduction in the activation overpotential (promotion mechanism). For PtRu/C the intrinsic mechanism is thought to dominate, whilst for PtMo/C the promotion mechanism is thought to be more important [16]. The in situ XAS results described above provide evidence supporting these conclusions.

The PtRu/C catalyst used in this study was shown to be a well mixed alloy, in contrast to those investigated by Rolison et al. [17]. In their work, using ex situ XPS analysis of as prepared PtRu/C materials (obtained from E-TEK), they showed that much of the Ru in such catalysts exists as a separate amorphous RuO<sub>x</sub> phase. In conclusion, they proposed that these ruthenium oxides are beneficial in that they enhance the proton conductivity of the catalyst material. In a separate study we have obtained XAS data at both the Pt L<sub>III</sub> and Ru K absorption edges for well mixed and poorly mixed PtRu/C catalysts [18]. Examination of the Ru EXAFS data verified that at the potentials at which H<sub>2</sub> oxidation occurs (for well mixed PtRu/C catalysts) the Ru is metallic in nature. In fact, Cooper et al. [19], have shown that the oxidation of 100% CO on well alloyed PtRu/C does not occur at a significant rate below 0.2 V versus RHE. The EXAFS results also show a significant contraction in the Pt–Pt distance for the PtRu/C as compared to the Pt/C sample. This contraction, along with the electronic effect of alloying with Ru on the Pt atoms in the particles, is likely to result in a modification of the chemisorptive behaviour of CO on the Pt sites. We have recently shown that EXAFS is a useful probe for the investigation of the bonding of CO to Pt in Pt/C catalysts [6]. Further EXAFS investigations of the

effect of Ru on the bonding of CO to the Pt sites are underway.

The PtMo/C catalyst used in this investigation was not shown to be a well mixed alloy system. In fact, the small number of Mo atoms in the first coordination shell and the lack of a significant variation in the Pt–Pt coordination distance, indicate that it is likely that the Mo is situated on the surface of the Pt particles. Preliminary analysis of the Mo K edge XAS data of an E-TEK PtMo/C catalyst has recently been reported by Mukerjee et al. [20]. They showed that the Mo exists as Mo(OH)<sub>2</sub><sup>2+</sup> at 0.0 V and that the oxidation state of the Mo is potential dependent. The electronic effect of the addition of Mo on the Pt atoms in the particles is much weaker than that observed for the PtRu/C (see Table 1). The promotion of the oxidation of chemisorbed CO at low potentials, <0.1 V versus RHE, upon the addition of Mo is thus attributed to the formation of oxy-hydroxide species at the Mo sites rather than a change in the Pt–CO bond.

Ex situ XRD is commonly used to determine the extent of intermixing in alloy catalysts. The lattice constants obtained for fcc crystallites, such as Pt/C, may be compared with the second Pt–Pt distance in the model of the EXAFS data. However, XRD only probes the crystalline portion of the sample, whilst EXAFS probes the entire sample. In fact, we have obtained very different EXAFS results for several PtRu/C catalysts which all had similar lattice constants as determined by XRD [18]. In addition, the EXAFS data may be collected in situ, under electrochemical control. To enable more realistic comparison between XRD and EXAFS studies, we have sought to develop an in situ XRD method.

### 3.3. In situ X-ray diffraction

The Pd/C system was chosen as a first illustrative example, as the lattice is known to expand at potentials where hydrogen is incorporated. Cyclic voltammograms of the Pd/C electrode in 1 mol dm<sup>−3</sup> H<sub>2</sub>SO<sub>4</sub> are shown in Fig. 5. The large peaks observed in the first cycle from 0.05 to 0.45 V are attributed to desorption of adsorbed hydrogen incorporated into the Pd lattice when the potential is held below 0.05 V. The XRD patterns obtained using the CIP detector as a function of the applied potential for the Pd/C electrode are shown in Fig. 6.

The lattice constants obtained are summarised in Table 3. The lattice constants obtained may be compared with those of bulk Pd metal, 3.8900 Å [21], and the β-hydride (PdH<sub>0.56</sub>), 4.018 Å [22]. The lattice constants obtained at 0.55 and 0.15 V are both slightly larger than that obtained for Pd metal, but show little effect of adsorbing H (at 0.15 V). That at −0.05 V, where H is absorbed, is also larger than that of the bulk β-hydride. The differences may represent a systematic error, caused by imprecise positioning of the electrochemical cell at the focus of the CIP. However, these preliminary results do demonstrate the utility of the in situ XRD method using the CIP.

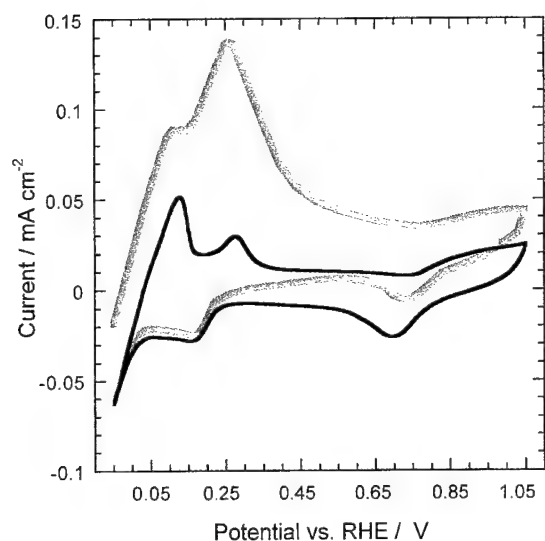


Fig. 5. Cyclic voltammogram of Pd/C fuel cell electrode (electrode area  $1 \text{ cm}^2$ ) in  $1 \text{ mol dm}^{-3} \text{ H}_2\text{SO}_4$  at  $20 \text{ mV s}^{-1}$ . Grey line shows the first cycle after the potential was held at  $-0.05 \text{ V}$  vs. RHE for 10 min, black line shows the fourth cycle.

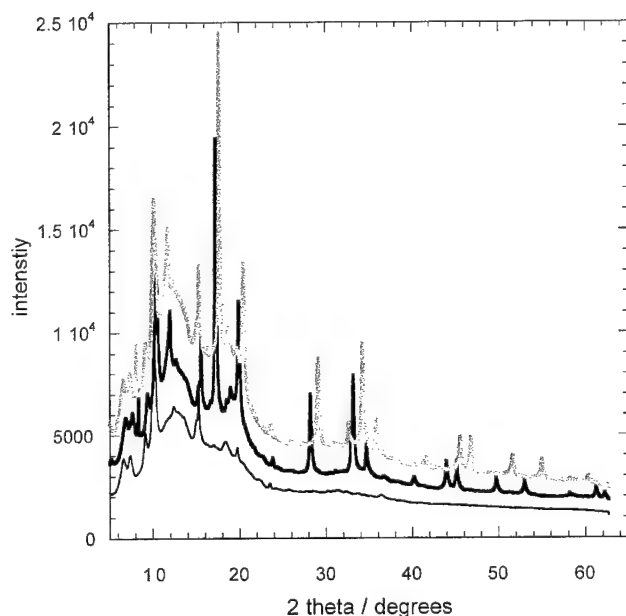


Fig. 6. XRD patterns for empty electrochemical cell (thin black line), Pd/C electrode at  $0.15 \text{ V}$  vs. RHE in  $1 \text{ mol dm}^{-3} \text{ H}_2\text{SO}_4$  (thick grey line) and at  $-0.05 \text{ V}$  vs. RHE (thick black line). Data were collected using a curved image plate detector with 20 min exposures.

Table 3

Lattice parameters and standard deviations for Pd/C as a function of applied electrode potential

$E$ vs. RHE (V)	Lattice parameter ( $\text{\AA}$ )	ESD ( $\text{\AA}$ )
0.55	3.8957	0.0008
0.15	3.8955	0.0010
$-0.05$	4.0504	0.0010

#### 4. Summary

The increased availability of SR has enabled the use of in situ XAS to become more routine in the investigation of carbon supported catalysts used in PEM fuel cells. For the examples described in this paper, Pt/C, PtRu/C, and PtMo/C, the information obtained from analysis of the white line or near edge and EXAFS regions of the XAS has added weight to the assertion that the mechanisms by which Ru and Mo increase the CO tolerance of Pt/C catalysts are different. Ru promotion occurring by the intrinsic mechanism is thought to dominate, whilst Mo acts via the promotion mechanism. Finally, preliminary results describing an in situ XRD method based on SR and the curved image plate detector were presented.

#### Acknowledgements

The authors would like to thank Johnson Matthey for the loan of the electrocatalyst materials and Fred Mosselmanns and Chris Corrigan (Daresbury Laboratory) for their assistance while at the SRS. RJM and JY acknowledge the support of the EPSRC through Quota studentships. The project is jointly supported by the EPSRC (GR/L69817), DERA through the Joint Grants Scheme, and Johnson Matthey.

#### References

- [1] [http://www.daimlerchrysler.de/index\\_e.htm?news/top/t90317\\_e.htm](http://www.daimlerchrysler.de/index_e.htm?news/top/t90317_e.htm); Daimler Chrysler Necar announcement.
- [2] <http://www.hfcletter.com/letter/march98/feature.html>; GM PEM Fuel cell car to be launched with its European subsidiary, Opel.
- [3] W.E. O'Grady, D.C. Koningsberger, *Electrochem. Soc. Extended Abstr.* 88 (1) (1988) 513.
- [4] R.J. Mathew, A.E. Russell, *Topics Catal.* 10 (2000) 231.
- [5] L. Keck, H. Buchanan, G. Hards, US Patent, 5,068,161 (1991).
- [6] S. Maniguet, R.J. Mathew, A.E. Russell, *J. Phys. Chem. B* 104 (2000) 1998.
- [7] M.A. Roberts, J.L. Finney, G. Bushnell-Wye, *Mater. Sci. Forum* 278 (1998) 318.
- [8] N. Binstead, EXCURV98: CCLRC Daresbury Laboratory computer program (1998).
- [9] B.N. Grgur, N.M. Markovic, P.N. Ross, *Electrochem. Soc. Proc.* 98 (27) (1998) 176.
- [10] S.C. Ball, A. Hodgkinson, G. Hoogers, S. Maniguet, D. Thompson, B. Wong, *Electrochem. Solid State Lett.*, submitted for publication.
- [11] H. Yoshitake, T. Mochizuki, O. Yamazaki, K.-I. Ota, *J. Electroanal. Chem.* 361 (1993) 229.
- [12] H. Yoshitake, O. Yamazaki, K.-I. Ota, *J. Electroanal. Chem.* 371 (1994) 287.
- [13] H. Yoshitake, O. Yamazaki, K.-I. Ota, *J. Electrochem. Soc.* 141 (1994) 2516.
- [14] S. Mukerjee, J. McBreen, *J. Electroanal. Chem.* 448 (1998) 163.
- [15] A.N. Mansour, J.W. Cook Jr., D.E. Sayers, *J. Phys. Chem.* 88 (1984) 2230.
- [16] G. Hoogers, D. Thompson, *Cattech.* 3 (2000) 106.

- [17] D.R. Rolison, P.L. Hagans, K.E. Swider, J.W. Long, *Langmuir* 15 (1999) 774.
- [18] S. Maniguet, R. Mathew, J. Yao, D. Thompsett, A.E. Russell, unpublished results.
- [19] S.J. Cooper, A.G. Gunner, G. Hoogers, D. Thompsett, in: *Proceedings of the 2nd International Symposium on New Materials for Fuel Cells and Modern Battery Systems*, Montreal, Quebec, Canada, 1997.
- [20] S. Mukerjee, S.J. Lee, E.A. Ticianelli, J. McBreen, B.N. Grgur, N.M. Markovic, P.N. Ross, J.R. Giallombardo, E.S. De Castro, *Electrochem. Solid State Lett.* 2 (1999) 12.
- [21] D.W. Murphy, S.M. Zahurak, B. Vyas, M. Thomas, M.E. Badding, W.-C. Fang, *Chem. Mater.* 5 (1993) 767.
- [22] A.F. Wells, *Structural Inorganic Chemistry*, 5th Edition, Clarendon Press, Oxford, 1984.

## New lightweight bipolar plate system for polymer electrolyte membrane fuel cells

D.R. Hodgson<sup>a,\*</sup>, B. May<sup>a</sup>, P.L. Adcock<sup>b</sup>, D.P. Davies<sup>b</sup>

<sup>a</sup>ICI Chemical and Polymers Ltd, ETB Technical Centre, PO Box 9, Runcorn Site, Runcorn, Cheshire, WA7 4JE, UK

<sup>b</sup>Fuel Cell Research Group, Department of AAE, Loughborough University, Loughborough, Leicestershire, LE11 3TU, UK

Received 21 December 2000; accepted 3 January 2001

---

### Abstract

The use of metal based bipolar plates in polymer electrolyte membrane (PEM) fuel cells, with an active coating on titanium to reduce voltage losses due to the formation of passive layers has been demonstrated. Lifetime data in excess of 8000 h has been achieved and power densities in excess of  $1.8 \text{ kW dm}^{-2}$  and  $1 \text{ kW kg}^{-1}$  are predicted. © 2001 Elsevier Science B.V. All rights reserved.

**Keywords:** Fuel cells/polymer electrolyte membrane; Catalysis

---

### 1. Introduction

A key prerequisite for many power applications is the production of compact and lightweight polymer electrolyte membrane fuel cell (PEM FC) stacks. With bipolar plates accounting for the bulk of the stack, it is desirable to produce plates with the smallest possible dimensions permissible. Traditionally, carbon based materials have been chosen, as these are chemically stable in a fuel cell environment and produce the highest electrochemical power output. However, the lack of mechanical strength inherent with carbon limits the size and hence the volumetric power density. Other materials are being evaluated by a number of academic and industrial research groups, with the aim of producing low voltage drop, long lifetime materials. The alternatives to graphite fall into three categories: carbon–carbon composites [1], carbon–polymer composites [2] and metals [3]. It is likely that only carbon–polymer composites and metal systems will meet the long term cost requirements for fuel cell technology. For portable PEM systems, both the mass and volume of the stack are key considerations and the present thickness of polymer composite bipolar plates [4] results in stacks with low volumetric power densities (as measured on  $\text{kW dm}^{-2}$  basis).

Consequently, work at Loughborough University has focused primarily on stainless steel and titanium plate technology, which enables thin bipolar plates to be used

and, in the case of titanium, plates with low mass. Unfortunately, although the passive films on the surface of these metals protect them from corrosion, it also acts in part as an electrical insulator and thus reduces cell performance due to ohmic losses. To reduce this parasitic loss, the plate surface has to be modified.

Coating systems for metal plates have been investigated by many workers in the field (e.g. [3]), but little data has been presented on the long term performance of suitably coated metal bipolar plates. This paper describes the short and long term performance of coated metal plates, with particular emphasis on the coating designated FC5 and developed by ICI's Electrochemical Technology Business.

### 2. Experimental

Screening tests for the performance of the coating comprise: contact resistance, corrosion testing, short term polarisation performance and long term durability data. The experimental conditions for the measurement of contact resistance, short term polarisation performance and the long term performance evaluation have been described earlier [5].

Corrosion testing was performed using a series of potentiodynamic sweeps in a mixture of sulphuric and hydrofluoric acids at elevated temperature. Observations of the magnitude of the corrosion currents and changes in contact resistance before and after exposure to the acidic environment of the corrosion test were made.

---

\* Corresponding author.

E-mail address: david\_hodgson@ici.com (D.R. Hodgson).

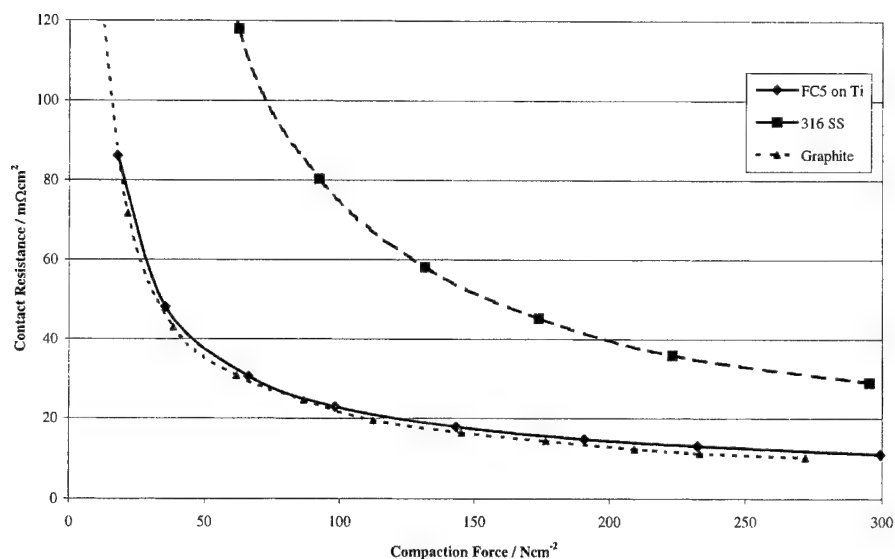


Fig. 1. Contact resistance of different materials as a function of compaction force.

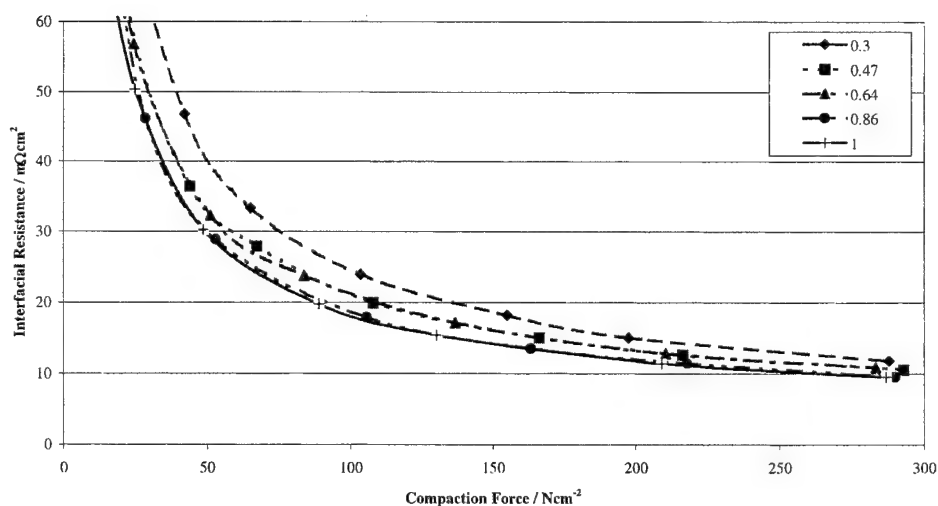


Fig. 2. Effect of coating thickness on contact resistance. The legend indicates the fraction of coating applied compared to that deposited on plates to generate the data in Fig. 1.

The coating of FC5 onto titanium was performed using proprietary methods. The coating method can be used for any structure of bipolar plate and does not significantly affect the dimensions of the flow channels.

### 3. Results and discussion

The contact resistance of the FC5 system compared to Poco™ graphite and stainless steel is shown in Fig. 1. It can be clearly seen that the contact resistance of the FC5 coated titanium approaches that of the graphite and is far superior to that of uncoated 316 stainless steel. Interestingly, the contact

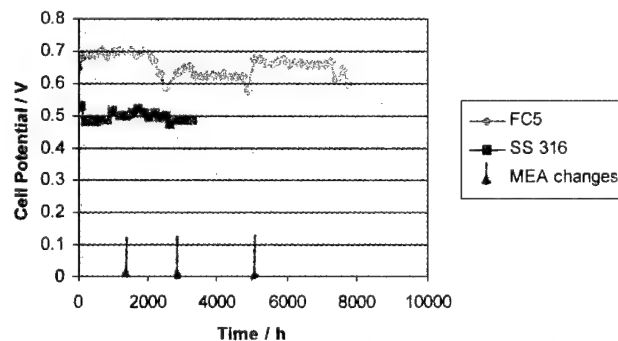


Fig. 3. Durability with time of operation data for FC5 coated titanium plates and 316 SS, in operation of a single laboratory cell.



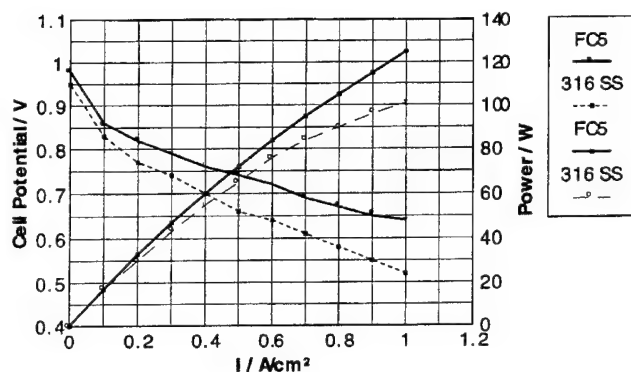


Fig. 4. Polarisation data from a 200 cm<sup>2</sup> APS cell design for FC5 coated titanium plates and 316 SS.

resistance varies with thickness of the coating layer (Fig. 2), suggesting a minimum amount of coating is required to avoid formation of passive layers.

No affect on the contact resistance from potentiodynamic sweeps in mixtures of sulphuric and hydrofluoric acids, was observed. No measurable metal corrosion took place under the same potentiodynamic conditions.

The most significant data is that of the longer term performance of the FC5/Ti system, as shown in Fig. 3. Also shown in Fig. 3 is comparative data for 316 SS taken from [5]. Fig. 3 not only shows the long term performance data of the two materials, but also the much higher voltage output of the cell with the FC5 coated plates, compared to the 316 SS plates. Membrane/electrode assembly (MEA) changes are indicated in Fig. 4, and it can be seen that in the FC5 case, cell performance declines to a point where the MEA has to be changed, but that the cell performance comes back to that expected after changing the MEA. Analysis of the MEA for metal ion impurities revealed no contamination and it is thought that problems with the cell design led to the decrease

in MEA performance (the same voltage profile has been observed with other plate materials, including non-metallics). Periodic ex situ assessment of the plate contact resistance revealed no change with time from the FC5 coated plate.

Larger scale experiments to assess the performance of FC5 and 316 SS in a 200 cm<sup>2</sup> plate were performed and the data generated is shown in Fig. 4. The increase in voltage and power output at any given current density for FC5 over 316 SS can be clearly seen. Previously reported data indicate that the volumetric and gravimetric power densities using a proprietary APS plate design are 1.8 kW dm<sup>-3</sup> and 0.6 kW kg<sup>-1</sup>, respectively. Using the FC5 coated titanium plate design, power densities of 1.8 kW dm<sup>-3</sup> and >1 kW kg<sup>-1</sup> can be estimated from the single cell data.

#### 4. Conclusions

Titanium can be employed to produce fuel cells with very high volumetric and gravimetric power densities, ideal for portable applications. Lifetime of the FC5 plate system has also been shown to be very high. Stack performance is now to be evaluated.

#### References

- [1] T.M. Besmann, J.W. Klett, J.J. Henry Jr., E. Lara-Curzio, J. Electrochem. Soc. 147 (2000) 4083.
- [2] D.N. Busick, M.S. Wilson, Fuel Cell Seminar, Palm Springs, 1998, Abstract 1186.
- [3] R.C. Makkus, A.H.H. Janssen, F.A. de Bruijn, R.K.A.M. Mallant, J. Power Sources 86 (2000) 274.
- [4] D. Weng, G. Woodcock, T. Rehg, Z. Iqbal, J. Guiheen, J. Matrunich, Fuel Cell Seminar, Portland, 2000, Abstract 52.
- [5] D.P. Davies, P.L. Adcock, M. Turpin, S.J. Rowen, J. Power Sources 86 (2000) 237.

# Optimization of the magnesium-solution phase catholyte semi-fuel cell for long duration testing

Maria G. Medeiros<sup>a,\*</sup>, Russell R. Bessette<sup>b</sup>, Craig M. Deschenes<sup>c</sup>, Delmas W. Atwater<sup>a</sup>

<sup>a</sup>Naval Undersea Warfare Center, Newport Division, Newport, RI 02841, USA

<sup>b</sup>University of Massachusetts Dartmouth, N. Dartmouth, MA 02747, USA

<sup>c</sup>Systems Integration and Research Inc., Middletown, RI 02840, USA

Received 29 November 2000; accepted 16 December 2000

## Abstract

A magnesium semi-fuel cell (Mg-SFC) was investigated as an energetic electrochemical system for low rate, long endurance undersea vehicle applications. This electrochemical system uses a Mg anode, a sea water electrolyte, a Nafion membrane, a carbon paper cathode catalyzed with Pd and Ir, and a catholyte of hydrogen peroxide in a sea water/acid electrolyte. Unique to the approach described here is the use of a magnesium anode together with the introduction of the catholyte in solution with the sea water, thus operating as a semi-fuel cell as opposed to a battery. Five critical operating parameters were optimized using a Taguchi matrix experimental design. Using these optimized conditions, high voltage and high efficiencies were obtained during long duration tests. © 2001 Elsevier Science B.V. All rights reserved.

**Keywords:** Magnesium anodes; Semi-fuel cells; Hydrogen peroxide; Taguchi matrix

## 1. Introduction

Primary batteries employing aqueous electrolytes [1,2] have been under development by the USA and other countries [3], both government and commercial, since the 1940s. Emphasis has been placed on aluminum [4–6] and magnesium anodes [7] due to their high faradaic capacity, low atomic weight and high standard potentials. Of particular interest is their application for undersea vehicles due to the

silver oxide (Al–AgO) [10] or aluminum–hydrogen peroxide (Al–H<sub>2</sub>O<sub>2</sub>) [11–13]. In addition, the Mg–H<sub>2</sub>O<sub>2</sub> system is lighter in weight, environmental-friendly and less expensive. This new solution phase system should be capable of performing as a high energy density source for low power, long endurance UUV applications.

The theoretical half-cell and overall cell voltages for the magnesium–hydrogen peroxide semi-fuel cell system [14,15] are the following.

Anode	$\text{Mg} \rightarrow \text{Mg}^{2+} + 2\text{e}^-$	$E^0 = 2.37 \text{ V vs. SHE}$
Cathode	$\text{H}_2\text{O}_2 + 2\text{H}^+ + 2\text{e}^- \rightarrow 3\text{H}_2\text{O}$	$E^0 = 1.77 \text{ V vs. SHE}$
Cell reaction	$\text{Mg} + \text{H}_2\text{O}_2 + 2\text{H}^+ \rightarrow \text{Mg}^{2+} + 2\text{H}_2\text{O}$	$E_{\text{cell}} = 3.58 \text{ V}$

availability of sea water to act as an electrolyte or electrolyte solution; further enhancing their effectiveness as an energy source on a systems basis.

Development of affordable, long endurance semi-fuel cell technology to meet the demands of current and future unmanned underwater vehicles (UUVs) is a major technical challenge. The magnesium–hydrogen peroxide electrochemical couple [8,9] has a theoretical cell potential of 4.14 V, which is higher than the present energy sources, aluminum–

The performance of the magnesium–hydrogen peroxide semi-fuel cell is principally dependent on five parameters: (1) the H<sub>2</sub>O<sub>2</sub> catholyte concentration; (2) the electrolyte temperature; (3) the catholyte flow rate; (4) the electrolyte flow rate and (5) the current density. With all these variables in mind, determination of the maximum performance and efficiency would require an unacceptably large number of tests by the conventional method of changing one variable at a time while keeping all others constant. However, a Taguchi method [16] multi-variable array was utilized to maximize the data collection and minimize the number of tests.

\* Corresponding author. Tel.: +1-401-832-2454.

E-mail address: medeirosmg@npt.nuwc.navy.mil (M.G. Medeiros).

Measuring the effects of changing these variables one at a time while holding the rest constant (conventional experimental approach) would require 243 tests ( $3^5$  or five parameters at three levels for each parameter). Through the use of orthogonal arrays via the Taguchi method, the number of tests was reduced to only 18 for the magnesium–hydrogen peroxide system.

## 2. Experimental

Chemicals used included: sea salt (ASTM-D 1141-52, Lake Products), hydrogen peroxide (50% CG-grade, Elf Atochem), and sulfuric acid (ACS grade, 96%, Aldrich Chemicals).

Each test was performed over a 4 h time period using the apparatus pictured in Fig. 1. This ensured a fair length of time to judge the validity of the test. The flowing electrolyte apparatus contained two electrolyte tanks and two flow loops. One tank contained the sea water electrolyte that was pumped to the magnesium anode. The second electrolyte tank contained sea water, hydrogen peroxide and acid; this electrolyte was pumped to the cathode side of the cell. The cell fixture used could accommodate a separator/membrane in the cell, thus separating the anode reaction from the cathode side.

The five parameters and the three levels for each parameter are summarized in Table 1. Application of the Taguchi method is accomplished by adjusting each parameter concurrently throughout the formulated matrix in an equal number of times. For any pair of columns, all combinations of parameter levels occur an equal number of times. Once data had been collected an error analysis was performed on each individual test. Table 2 summarizes the 18 experiments devised by the Taguchi matrix.

## 3. Results

Once the test matrices were completed, a function  $\eta$  based on the signal to noise ratio was determined. This value of  $\eta$  was determined by the following equation.

$$\eta = -10 \log_{10} (\text{mean square reciprocal quality characteristic})$$

$$\eta = -10 \log_{10} \left[ \frac{1}{\mu^2} + 3 \left( \frac{\sigma^2}{\mu^2} \right) \right]$$

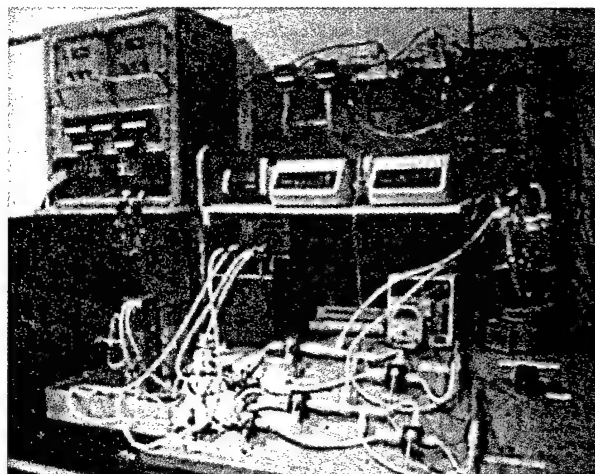


Fig. 1. The dual-flow electrolyte apparatus.

where  $\mu$  is specific energy density ( $\text{Wh kg}^{-1}$ ), total energy produced divided by the total mass of energetic materials consumed (anode material and catholyte).  $\sigma$  is standard error of  $\mu$ . A unique  $\eta$  value is calculated for each specific test ( $\eta_i$ ). A new overall average  $\eta$  ( $\eta_0$ ) value for a specific parameter is then calculated by averaging the  $\eta_i$  values of all tests that contain the parameter.

Fig. 2 is a plot of all the  $\eta$  (signal to noise ratio dependent) values for the magnesium–hydrogen peroxide semi-fuel cell matrix tests. Each  $\eta$  value is based on the average of six individual tests, which contain that parameter. The optimum value of each of the variables is determined by the largest  $\eta$  value as compared to the other members of the group. The values used for the optimum conditions test were chosen by interpreting the data from this figure.

As a result, it was concluded that for maximum specific energy, the optimum conditions are as follows:

- flow rate, anode:  $200 \text{ cm}^3 \text{ min}^{-1}$ ;
- flow rate, cathode:  $100 \text{ cm}^3 \text{ min}^{-1}$ ;
- $\text{H}_2\text{O}_2$  concentration: 0.20 M;
- current density:  $25 \text{ mA cm}^{-2}$ ;
- temperature:  $25^\circ\text{C}$ .

Under these optimum conditions, a single-cell Mg-SFC ( $77 \text{ cm}^2$ ) test was conducted and the voltage, current, power versus time results are pictured in Fig. 3. Utilizing the optimum conditions resulted in  $\eta = 59.8$ . Anodic and cathodic efficiencies of 80 and 60% were achieved, respectively.

Table 1  
Mg– $\text{H}_2\text{O}_2$  test parameters

$[\text{H}_2\text{O}_2]$ (M)	Temperature ( $^\circ\text{C}$ )	Catholyte flow rate ( $\text{cm}^3 \text{ min}^{-1}$ )	Electrolyte flow rate ( $\text{cm}^3 \text{ min}^{-1}$ )	Current density ( $\text{mA cm}^{-2}$ )
0.20	0.0	25.0	25.0	10.0
0.30	25.0	100.0	100.0	25.0
0.40	50.0	200.0	200.0	50.0

Table 2  
Eighteen experiments of the Taguchi matrix

Test No.	Flow rate, anode (cm <sup>3</sup> min <sup>-1</sup> )	Flow rate, cathode (cm <sup>3</sup> min <sup>-1</sup> )	[H <sub>2</sub> O <sub>2</sub> ] (M)	[H <sub>2</sub> SO <sub>4</sub> ] (M)	Current density (mA cm <sup>-2</sup> )	Temperature (°C)
1	25	25	0.4	0.01	10	0
2	25	100	0.2	0.05	25	25
3	25	200	0.3	0.1	50	50
4	100	25	0.4	0.05	25	50
5	100	100	0.2	0.1	50	0
6	100	200	0.3	0.01	10	25
7	200	25	0.2	0.01	50	25
8	200	100	0.3	0.05	10	50
9	200	200	0.4	0.1	25	0
10	25	25	0.3	0.1	25	25
11	25	100	0.4	0.01	50	50
12	25	200	0.2	0.05	10	0
13	100	25	0.2	0.1	10	50
14	100	100	0.3	0.01	25	0
15	100	200	0.4	0.05	50	25
16	200	25	0.3	0.05	50	0
17	200	100	0.4	0.1	10	25
18	200	200	0.2	0.01	25	50

Following the optimization of the parameters for the Mg–H<sub>2</sub>O<sub>2</sub> system, several experiments were conducted to determine catalyst stability with time along with the start/restart capabilities. Experiments were conducted for 8 h, utilizing the optimum conditions. At the end of the 8 h; the magnesium anode was replaced (due to thickness limitations) and the experiment was restarted and continued for another 8 h. This was conducted for five experiments, the last experiment utilized ‘real’ versus synthetic sea water purchased from Lake Products. No differences in voltage or performance efficiency were evident between the ‘real’ and the synthetic sea water. Fig. 4 illustrates the five experiments, the start/restart performance and the anodic and cathodic efficiencies associated with each experiment. It is evident from Fig. 4 that the system recovers well and maintains its voltage with time. The second experiment shows a voltage

decrease from the normal 1.7–1.8 V to a voltage decay below 1.5 V. This was attributed to a contact problem between the magnesium anode and the current collector, as was evident once the cell was taken apart after 5 h under load.

#### 4. Summary

Demonstrated was the effective use of the Taguchi method to determine the optimum conditions for the magnesium–hydrogen peroxide semi-fuel cell system in a reasonable time frame with a minimum number of tests.

The magnesium–hydrogen peroxide system had an  $\eta$  value ranging from (based on signal to noise ratio) 52.5 to 57.9 over all of the Taguchi orthogonal array tests

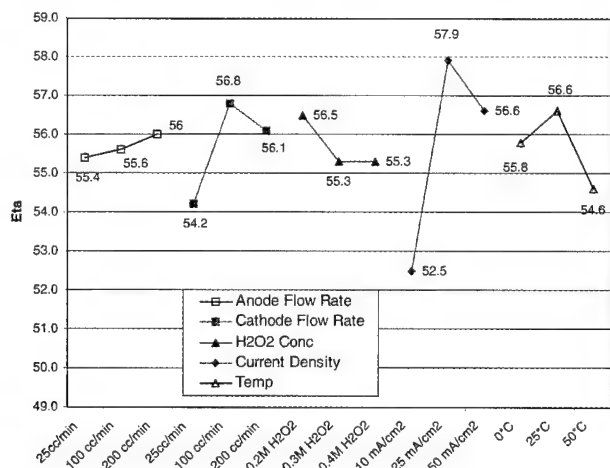


Fig. 2. Summary of the Taguchi matrix.

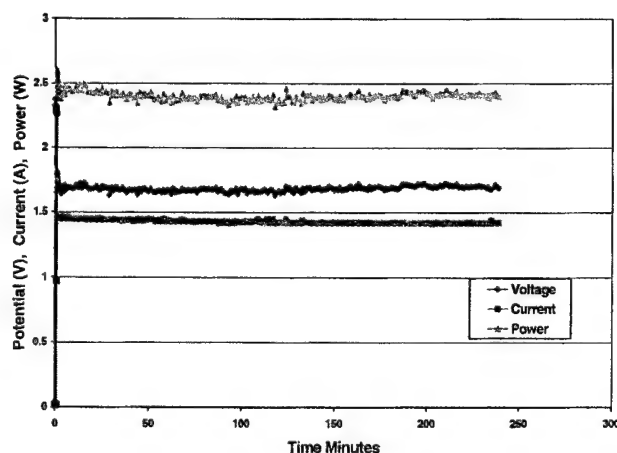


Fig. 3. Optimum Taguchi test.

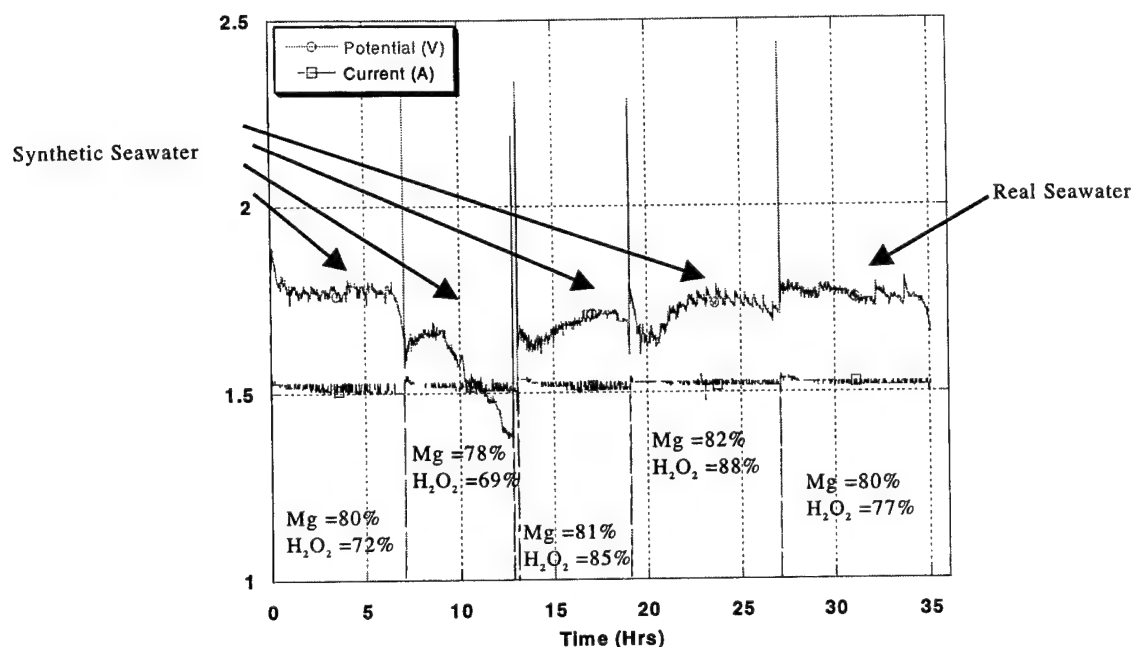


Fig. 4. Start/restart experiments.

performed. The test performed with all the optimum conditions resulted in an  $\eta$  value of 59.8; clearly the Taguchi Method predicted optimum conditions which yielded the best performance.

The optimum test conditions for the magnesium–hydrogen peroxide system are:

- flow rate, anode:  $200 \text{ cm}^3 \text{ min}^{-1}$ ;
- flow rate, cathode:  $100 \text{ cm}^3 \text{ min}^{-1}$ ;
- $\text{H}_2\text{O}_2$  concentration: 0.20 M;
- current density:  $25 \text{ mA cm}^{-2}$ ;
- temperature:  $25^\circ\text{C}$ .

### Acknowledgements

This study was supported by the Naval Undersea Warfare Center (NUWC) In-House Laboratory Independent Research (ILIR) Program, Mr. Richard Philips and the Office of Naval Research (ONR-333), Dr. Richard Carlin.

### References

- [1] O. Hasvold, H. Henriksen, E. Melvaer, G. Citu, B. Johansen, T. Kjonigsen, R. Galetti, Sea water battery for subsea control systems, *J. Power Sources* 16 (1997) 39.
- [2] O. Hasvold, C. Battaia, B. Johansen, Operational experiences with sea water batteries, *J. Power Sources* 38 (1998) 358.
- [3] D. Linden, *Handbook of Batteries*, 2nd Edition, McGraw-Hill, New York, 1995.
- [4] J. Hunter, G. Scamans, W. O'Callaghan, P. Wycliffe, Aluminum batteries, European Patent Application #0354752, Alcan International Ltd., 1989.
- [5] G. Scamans, J. Hunter, C. Tuck, R. Hamlen, N. Fitzpatrick, Further development of aluminum batteries, in: *Power Sources*, Vol. XII, Kelly and Baxter, 1988, p. 363.
- [6] G. Tarcy, R. Mazgaj, Aluminum alloys and associated anodes, US Patent #4,808,498 (1989).
- [7] S. Ono, K. Asami, T. Osaka, N. Masuko, Structure of anodic films on magnesium, *J. Electrochem. Soc.* 143 (1996) 106–109.
- [8] M.G. Medeiros, R. Bessette, D. Dischert, J. Cichon, Magnesium-solution phase catholyte seawater electrochemical system, Navy Patent Case #78609 (1998).
- [9] M.G. Medeiros, C. Marsh, J.R. Moden, H. Meunier, An aluminum hypochlorite electrochemical system, Navy Patent Case #78608 (1998).
- [10] G. Anderson, Aluminum–silver oxide primary battery, US Patent #3,953,239 (1976).
- [11] E.G. Dow, R. Bessette, M.G. Medeiros, H. Meunier, G.L. Seebach, J. Van Zee, C. Marsh-Orndorff, Enhanced electrochemical performance in the development of the aluminum–hydrogen peroxide semi-fuel cell, *J. Power Sources* 65 (1997) 207–212.
- [12] C. Marsh, R. Bessette, M.G. Medeiros, J. Van Zee, G. Seebach, An effective method for the reduction of  $\text{H}_2\text{O}_2$ , Navy Patent Case #73161 (1990).
- [13] C. Marsh, H. Munier, R. Bessette, J. Van Zee, G. Seebach, M.G. Medeiros, Aluminum–hydrogen peroxide battery development, anode polarization studies. Part V. The effect of NaOH,  $\text{H}_2\text{O}_2$ , temperature and sea salt, Naval Undersea Warfare Center (NUWC) TM #922070 (1992).
- [14] A.J. Bard, R. Parsons, J. Jordan, *Standard Potentials in Aqueous Solution*, IUPAC, Marcel Dekker, New York, 1985.
- [15] W. Latimer, *Oxidation Potentials*, 2nd Edition, Prentice-Hall, New York, 1953.
- [16] M. Phadke, *Quality Engineering Using Robust Design*, Prentice-Hall, New Jersey, 1989.

# Development and characterization of a novel carbon fiber based cathode for semi-fuel cell applications

Russell R. Bessette<sup>a,b,\*</sup>, Maria G. Medeiros<sup>b</sup>, Charles J. Patrissi<sup>b</sup>,  
Craig M. Deschenes<sup>b,c</sup>, Christopher N. LaFratta<sup>a,b</sup>

<sup>a</sup>University of Massachusetts Dartmouth, N. Dartmouth, MA 02747, USA

<sup>b</sup>Naval Undersea Warfare Center, Newport, RI 02841, USA

<sup>c</sup>BAE Systems, Middletown, RI 02842, USA

## Abstract

Fabrication of a microfibre carbon electrode (MCE) using a textile science flocking technique is described. Carbon fibers, 0.5 mm long and 10  $\mu\text{m}$  in diameter are aligned perpendicular to the surface of a conductive carbon epoxy coated carbon paper substrate in a high voltage (typically 70 kV) field. SEM images are used to confirm high carbon fiber density and associated high volumetric surface area. Coverage of the carbon fiber surface with stable Pd–Ir clusters is shown. Performance of the MCE in a magnesium–hydrogen peroxide semi-fuel cell (SFC) under optimum conditions and at reduced concentration of  $\text{H}_2\text{O}_2$  is reported upon. © 2001 Elsevier Science B.V. All rights reserved.

**Keywords:** Semi-fuel cells; Carbon fibers; Carbon electrodes

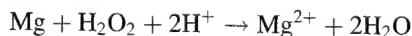
## 1. Introduction

Development of affordable, safe and environmentally compatible energy sources for unmanned undersea vehicle (UUV) propulsion continues to attract a great deal of interest. Aluminum and magnesium anodes [1] have received considerable attention due to their high standard potentials and Faradaic capacity [2]. Their application to UUVs is of particular interest due to the availability of seawater to act as an electrolyte or catholyte solvent. This to further enhance their effectiveness as an energy source on a systems basis.

Semi-fuel cell (SFC) technology refers to the use of a solid reductant anode (e.g. aluminum or magnesium) and a soluble oxidant (e.g.  $\text{H}_2\text{O}_2$ ) dissolved in the electrolyte to form a catholyte, which is metered into the cell as required. These new solution phase systems should be capable of performing as high energy density sources, providing a broad power turn-down ratio; making them useful for torpedo propulsion. They may, however, be better suited for the low power/long endurance applications of UUVs. This paper focuses on the development of microfibre carbon electrodes (MCEs) for the solution phase of SFC systems possessing low rate, very long endurance capabilities.

The combination of aluminum metal and hydrogen peroxide as an energy source has been studied extensively. Scamans and coworkers focused on the development of specialized aluminum alloys [3,4]. Collaborators from the University of Massachusetts, Dartmouth and the Naval Undersea Warfare Center have reported on performance studies of Al– $\text{H}_2\text{O}_2$  semi-fuel cells [5,6].

The use of a magnesium anode in place of the aluminum anode to achieve higher cell potentials and to exclude the use of the sodium hydroxide in the seawater electrolyte, as well as focus on current densities below 50  $\text{mA cm}^{-2}$ , has been investigated by Medeiros et al. [7,8]. The microfibre carbon cathode substrates described herein are for use in the acidic Mg– $\text{H}_2\text{O}_2$  system. The overall cell reaction for the Mg–SFC in an acidic medium is



Several catalysts have been investigated for use in fuel cells [9]. Many of these catalysts (including palladium and iridium independently) have been incorporated in carbon based pastes [10]. Collman and Kim have reported that iridium porphyrin complexes are very active catalysts [11]. Cox and Jaworski have used a palladium–iridium combination on a glassy carbon microelectrode for the quantitative determination of  $\text{H}_2\text{O}_2$  [12]. A combination of palladium and iridium has been shown in the NUWC

\* Corresponding author. Tel.: +1-508-999-8587; fax: +1-508-999-9167.  
E-mail address: rbessette@umassd.edu (R.R. Bessette).

electric propulsion laboratories to improve the electrochemical efficiency for the reduction of  $\text{H}_2\text{O}_2$  and to improve cell voltage relative to the use of a metallic silver cathode [13].

Hasvold et al. have studied the use of large “bottle brush” catalyzed carbon fiber electrodes in a non-separated Al– $\text{H}_2\text{O}_2$  system at the 5 mM level of  $\text{H}_2\text{O}_2$  [14]. Their success was attributed to an increase in the ratio of cathode to anode area. Because of more stringent system power and volume requirements, our investigations have centered on the use of magnesium anodes and on achieving very large cathode surface area to volume ratios. Achievement of small volume, large surface area cells will permit operation at low  $\text{H}_2\text{O}_2$  levels and result in

1. reduction in the size of the  $\text{H}_2\text{O}_2$  storage tank,
2. higher electrochemical reaction efficiencies (less  $\text{H}_2\text{O}_2$  decomposition), and
3. elimination of the need for a cell separator membrane (negligible direct reaction of catholyte with the anode).

This latter result will bring about greater system simplicity, a modest gain in cell voltage at low rate and a significant increase in cell voltage at high rate.

## 2. Experimental

All chemicals used in this investigation were of reagent grade quality and were used as obtained from the supplier (Alfa Aesar, Aldrich, and Fisher Scientific) without further purification. All solutions were prepared using glass distilled, deionized water. The sea salt used was ASTM-D 1141-52 (Lake Products), the hydrogen peroxide was 50% grade (Elf Atochem) and the carbon microfibres were pitch based and 10  $\mu\text{m}$  diameter (Mitsubishi Chemical). The fibers were accurately cut to 0.50 mm in length by Engineered Fibers Technology, LLC. The carbon microfibres were applied to the substrate using a Maag Flockmaschinen Model SPG 1000. The conductive carbon epoxy was obtained from Creative Materials Inc. The carbon paper was 0.25 mm thick, Spectracarb type 2050A-1040, available from E-Tek Incorporated.

The simultaneous deposition of Pd and Ir on the carbon substrate was carried out by cyclic voltammetry from  $-150$  to  $-300$  mV versus Ag–AgCl at a rate of  $1.0 \text{ mV s}^{-1}$  using a EG&G Instruments, Inc. Model 273A potentiostat/galvanostat and associated data acquisition system. The degree of loading was controlled by carrying out the deposition for exactly 25 cycles.

The solutions used for the deposition were heated to  $70^\circ\text{C}$  and contained 2.0 mM palladium(II) chloride ( $\text{PdCl}_2$ ), 2.0 mM sodium hexachloroiridate ( $\text{Na}_2\text{IrCl}_6$ ), 0.2 M KCl, and 0.1 M HCl. The carbon fiber electrode was soaked in 6 M HCl for 15 min and rinsed with distilled water prior to use. A three-electrode cell consisting of the substrate carbon fiber working electrode, a Ag–AgCl reference electrode, and a Pt auxiliary electrode was used for the depositions.

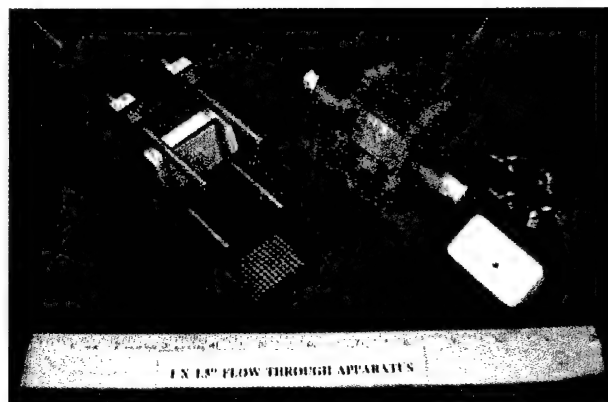


Fig. 1. Flow-through test cell.

Full cell performance was carried out using a 25 mm  $\times$  38 mm (1"  $\times$  1.5") cell made of polycarbonate (Fig. 1).

A Vexar spacer maintained the cell gap at 0.7 mm. The anode and cathode were mounted on individual current collector bus bars. The two electrodes were mounted vertically and were separated by the Vexar screen spacer. When a Nafion 115 membrane was used, Vexar spacers were used on each side of the membrane. The flowing electrolyte apparatus consisted of two electrolyte tanks and two flow loops. One tank contained the seawater electrolyte that was pumped to the magnesium anode side. The second electrolyte tank contained seawater, hydrogen peroxide and acid. This electrolyte was pumped to the cathode side of the cell. The catholyte and the electrolyte were pumped into the bottom of the cell, flowed between the anode and the cathode surfaces and the membrane and exited at the top of the cell. The closed loop flowing electrolyte apparatus consisted, in series, of the electrolyte reservoirs, peristaltic pumps, a heat exchanging coil in a constant temperature bath to maintain temperature, the flow through cell and a return to the reservoir. Cell current was regulated by means of a multistep load resistance substitution box. Cell current, voltage, inlet and outlet temperatures, and evolved gas flow rate were simultaneously monitored and recorded by the computer data logging system. The software used for the data acquisition was Lab Tech Notebook.

Scanning electron microscopy (SEM) was carried out using a JEOL USA Model 6300 instrument. The SEM working distance was 15 mm giving a resolution of 5 nm.

## 3. Results and discussion

Fabrication of microfibre carbon electrodes (MCEs) using a textile science flocking technique has been studied. To our knowledge use of the flocking technique, which involves application of very high electric fields (40–70 kV), with highly conductive and high surface charge carbon fibres, has



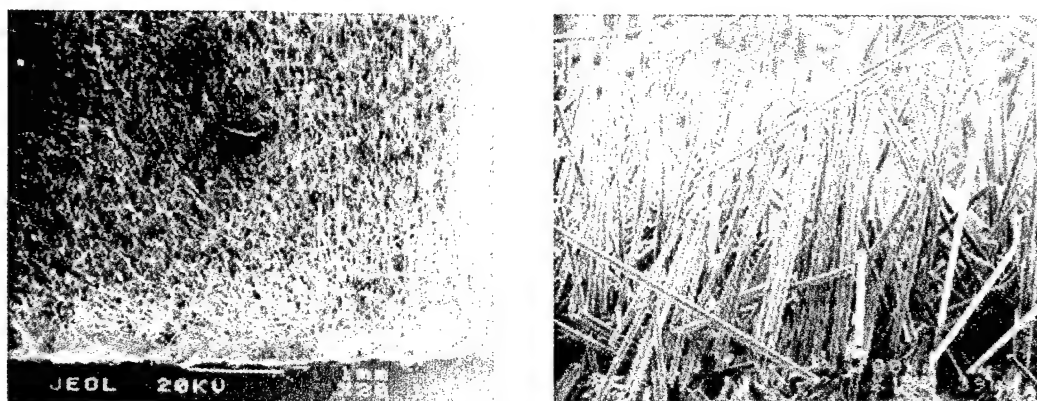


Fig. 2. S.E.M. micrographs of a microfiber carbon electrode. Left: top view at 20 $\times$ . Right: cross-sectional view at 150 $\times$ . Fibres are 0.5 mm long  $\times$  10  $\mu$ m diameter.

not been reported upon in the scientific literature. Flocking of the carbon fibers onto a substrate is accomplished by placing the substrate at ground potential and locating the flocking apparatus anode vertically above the substrate at a distance between 170 and 300 mm. A hopper, which contains the fibers to be flocked, is concentric to the anode.

Upon application of the voltage field (typically 70 kV), the fibers are expelled from the hopper toward the substrate. Since the substrate is coated with a conductive epoxy binder, the fibers will be held perpendicular to the surface.

Fig. 2 depicts SEM images showing top and cross sections of a microfibre carbon electrode. This electrode was fabricated using a 250  $\mu$ m thick film of conductive epoxy to bind the fibers to the carbon paper substrate.

The conductive epoxy used in the fabrication of the MCE is a key component. It must bind the fibers and bind itself effectively to the substrate while not introducing significant potential (IR) loss in the cell. Initial fabrication experiments have shown a carbon conductive epoxy (Creative Materials, Inc.) to have excellent physical properties for our use. Excellent adhesion of the fibers has been obtained. A Bird type applicator allowed application of a uniform film of the

epoxy on the substrate. A porous carbon paper (0.25 mm thick, Spectracarb) has proven to be an excellent substrate for bonding of the conductive epoxy. In addition, it remains rigid during electrochemical deposition of the Pd–Ir catalyst at 70°C.

Using SEM images, the fiber density of the electrode shown in Fig. 2 was determined to be 55,700 fibers per cm<sup>2</sup> of electrode geometric area, i.e. the two dimensional area defined by the carbon paper. MCEs having 112,000 fibers per cm<sup>2</sup> of geometric area have been prepared. The electrode having the latter fiber density has 182 cm<sup>2</sup> of surface area per cm<sup>3</sup> of electrode volume. This electrode volume includes the thickness of the conductive epoxy binder and the carbon paper substrate.

Application of a palladium–iridium catalyst to carbon microfibres with a 100:1 aspect ratio (1.0 mm long, 0.010 mm diameter) was non-uniform. The catalyst was deposited in the top one third of each fiber. Fairly complete coverage of each fiber by the catalyst was achieved with fibers having 50:1 and 25:1 aspect ratios. Fig. 3A and B show top views at 100 and 950 $\times$ , respectively, of the 50:1 aspect ratio fibers (0.5 mm long; 0.010 mm diameter) of the

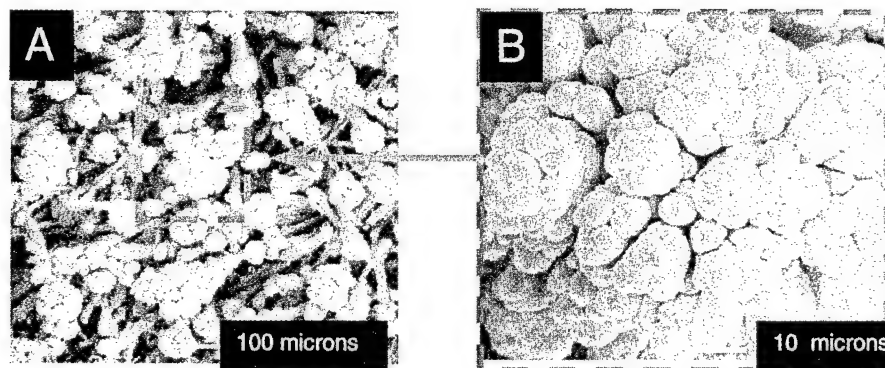


Fig. 3. S.E.M. micrographs of the Pd–Ir catalysed microfiber electrode at 100 $\times$  (3A) and 950 $\times$  (3B). 3B shows the morphology of the Pd–Ir at the center of 3A.



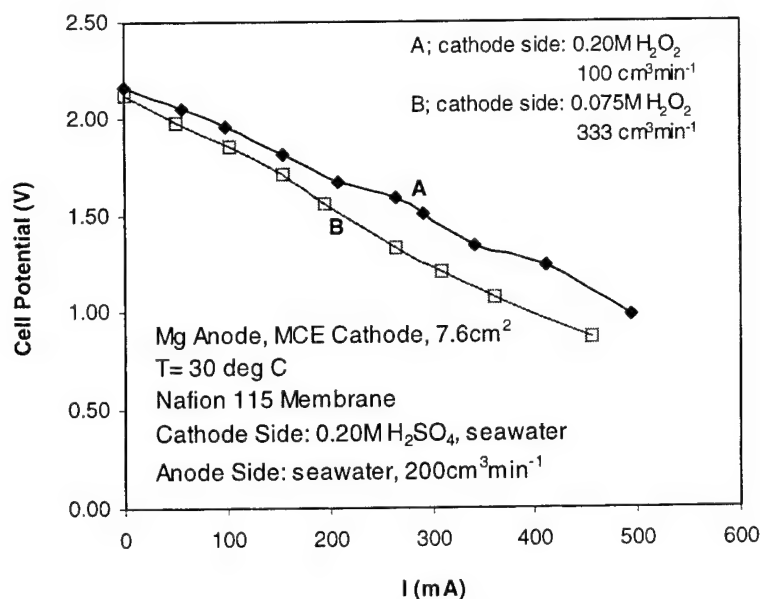


Fig. 4. Performance of the microfiber carbon electrode.

MCE covered with catalyst for the entire length of the fibers. Well formed palladium and iridium clusters are clearly shown. One can conclude that an increase in surface area of several times occurs with the application of the catalyst. For the electrode with 11,200 fibers per  $\text{cm}^2$  of geometric area, the total volumetric surface area will be several times —  $182 \text{ cm}^2 \text{ per cm}^3$  — of electrode volume. BET determination of the total surface area will be performed to ascertain the increase in surface area with formation of the catalyst clusters.

Magnesium– $\text{H}_2\text{O}_2$  cell data show unhindered flow of catholyte through the carbon fiber microelectrode. The full surface area of the catalyzed MCE appears to be accessible. Stability of this catalyst on a carbon surface is excellent. Catalyzed carbon paper substrates have been used repeatedly without any loss of catalyst performance. Curve A of Fig. 4 shows the superior cell voltage to current performance of the MCE in a membrane separated  $\text{Mg-H}_2\text{O}_2$  cell. The operating conditions for curve A are those established as optimum for a  $\text{Mg-H}_2\text{O}_2$  cell incorporating a Pd–Ir catalyzed carbon paper cathode. The optimization of the conditions is reported upon by Medeiros et al. [15]. The cell potential of 1.7 V at 190 mA ( $25 \text{ mA cm}^{-2}$ ) agrees very favorably with the voltages obtained upon optimizing the operating conditions.

Curve B of Fig. 4 shows the cell voltage to current relationship with a decrease in  $\text{H}_2\text{O}_2$  concentration to 0.075 M and an associated increase in the catholyte flow rate to  $333 \text{ cm}^3 \text{ min}^{-1}$ . The slight decrease in voltage of approximately 0.100 V at  $25 \text{ mA cm}^{-2}$  (190 mA total current) is encouraging in our attempts to significantly lower the concentration of  $\text{H}_2\text{O}_2$  at which the cell can be operated efficiently.

#### 4. Summary

Microfiber carbon electrodes (MCEs) of significant density have been fabricated using a textile science flocking technique. Volumetric surface area of  $182 \text{ cm}^2 \text{ per cm}^3$  has been achieved.

Stable Pd–Ir catalyst cluster formation over most of the carbon fibre surface area is demonstrated. The Pd–Ir catalyst cluster formation is expected to increase the volumetric surface area several fold.

Superior cell voltage to current performance in a  $\text{Mg-H}_2\text{O}_2$  membrane separated cell has been obtained. Cell voltage at  $25 \text{ mA cm}^{-2}$  for the cell containing a MCE cathode is similar to the voltage obtained for a cell operating under optimum conditions and employing a Pd–Ir catalyzed carbon paper cathode.

Encouraging cell voltage at the current density of interest,  $25 \text{ mA cm}^{-2}$ , has been attained for a reduction in the  $\text{H}_2\text{O}_2$  concentration to 0.075 M.

#### Acknowledgements

This work was supported by the Office of Naval Research (ONR) Electrochemical Science and Technology Program, Dr. Richard Carlin, Program Manager and by the Naval undersea warfare center (NUWC) In-House Laboratory Independent Research (ILIR) Program, Mr. Richard Philips, Director. The authors gratefully acknowledge the technical assistance with the flocking technique provided by Drs. Yong Ku Kim and Armand Lewis of the University of Massachusetts Dartmouth Textile Sciences Department. We thank the Mitsubishi Chemical Company for providing

the carbon fiber and Engineered Fibers Technology, LLC, for cutting the fiber to our specified length.

## References

- [1] D. Linden, Handbook of Batteries, 2nd Edition, McGraw-Hill, New York, 1995.
- [2] A.J. Bard, R. Parsons, J. Jordan, Standard Potentials in Aqueous Solution, IUPAC, Marcel Dekker, Inc. 1985.
- [3] G. Scamans, J. Hunter, C. Tuck, R. Hamlen, N. Fitzpatrick, in: Keily, Baxter (Eds.), Further Development of Aluminum Batteries, Power Sources XII, 1988, p. 363.
- [4] J. Hunter, et al., Aluminum Batteries, European Patent Application no. 0354752, Alcan International, Ltd., 1989.
- [5] R. Bessette, E. Dow, G. Seebach, C. Marsh-Orndorff, H. Meunier, J. Van Zee, M. Medeiros, Enhanced Electrochemical Performance in the Development of the Aluminum–Hydrogen Peroxide Semi-Fuel Cell, *J. Power Sources* 65 (1997) 207.
- [6] R. Bessette, J. Cichon, D. Dischert, Performance optimization of aluminum solution phase catholyte semi-fuel cell, in: Proceedings of the 38th Power Sources Conference, Cherry Hill, NJ, 1998.
- [7] M. Medeiros, E. Dow, R. Bessette, Magnesium-solution phase catholyte in an acid/seawater electrolyte semi fuel cell system, in: Proceedings of the Joint International Meeting of the Electrochemical Society and the Electrochemical Society of Japan, Honolulu, Hawaii, 1999, pp. 17–22.
- [8] M. Medeiros, E. Dow, Magnesium-solution phase catholyte seawater electrochemical system, *J. Power Sources* 80 (1999) 78–82.
- [9] M. Poirier, C. Perreault, L. Couture, C. Sapundzhiev, Evaluation of catalysts for the decomposition of methane to hydrogen for fuel cell applications, in: Proceedings of the First International Symposium on New Materials for Fuel Cell Systems, Montreal, Quebec, Canada, 1995, p. 258.
- [10] T. Okamoto, I. Baba, H. Kato, Japan Patent JP6-36784, Collector for Fuel Cell and Fuel Cell with the Collector, 1992.
- [11] J. Collman, K. Kim, Electrocatalytic four-electron reduction of dioxygen by iridium porphyrins adsorbed on graphite, *J. Am. Chem. Soc.* 108 (24) (1986) 7847.
- [12] J. Cox, R. Jaworski, Voltammetric reduction and determination of hydrogen peroxide at an electrode modified with a film containing palladium and iridium, *Anal. Chem.* 61 (1989) 2176.
- [13] J. Cichon, R. Bessette, D. Dischert, Electrode surface modification for cathode catalysis in semi-fuel cells, in: Proceedings of the 194th Electrochemical Society Meeting, Boston, MA, 1998.
- [14] O. Hasvold, K.H. Johansen, O. Mollestad, S. Forseth, N. Storkersen, The alkaline aluminum–hydrogen peroxide power source in the Hugin II unmanned underwater vehicle, *J. Power Sources* 80 (1999) 254.
- [15] M.G. Medeiros, R.R. Descheres, C.M. Deschenes, D.W. Atwater, Optimization of the Magnesium-Solution Phase Catholyte Semi-Fuel Cell for Long Duration Testing, in: Proceedings of the 22nd International Power Sources Symposium, Manchester, England, 2001.

Abstract

## Multivariate analysis for battery optimisation and testing

W. Paul Hagan<sup>\*</sup>

*Battstat, 22, Spencer Close, Gloucester GL3 3EA, UK*

---

### Abstract

A variety of multivariate techniques, available in specialist software packages are introduced and reviewed. The main techniques of use to battery manufacturers and researchers are:

- principal component analysis (PCA);
- cluster analysis;
- prediction using principal component regression (PCR) and partial least squares (PLS).

In addition to introducing each of the techniques, examples of their application are drawn from recent literature reports and from previously unpublished work by the author. © 2001 Published by Elsevier Science B.V.

*Keywords:* Mathematical modelling; State-of-charge determination

---

---

<sup>\*</sup> Tel.: +44-1452-612046.

E-mail address: [wphdym@yahoo.co.uk](mailto:wphdym@yahoo.co.uk) (W. Paul Hagan).

# Findings of the rechargeable battery study sponsored by NATIBO (North American technology and industrial base organization)

James A Gucinski<sup>a,\*</sup>, Michael Slack<sup>b</sup>

<sup>a</sup>*Power Systems Department, Naval Surface Warfare Center, Crane, IN 47522, USA*

<sup>b</sup>*Department of National Defense, 101 Colonel By Drive, Ottawa, Ont., Canada K1A 0K2*

Received 28 October 2000; accepted 28 November 2000

---

## Abstract

This paper summarizes and updates the findings of the North American technology and industrial base organization (NATIBO) study entitled “Rechargeable Battery/Systems for Communication/Electronic Application”. The mission of the NATIBO organization is to promote a cost effective and healthy technology and industrial base that is responsive to the national and economical security needs of the United States and Canada. © 2001 Elsevier Science B.V. All rights reserved.

**Keywords:** Standardization; Military batteries

---

## 1. Introduction

For the purpose of this paper, it is assumed that the reader is familiar with the rechargeable battery/charger technologies; therefore this paper will only skim the surface of this material. The main focus will be on the conclusions, recommendations and on the consequences to changing from primary to rechargeable technologies.

## 2. Objectives

The main objective of this study was to compare the current trends in the commercial rechargeable battery and battery charger markets and relate these to the requirements of the military. It also assessed which battery and battery charging technologies would be required/desired for military communications and electronics (C/E) equipment and to analyze the North American technology and industrial base capability to produce the type and quantities of rechargeable batteries required by the Department of Defense, USA (DoD) and Department of National Defense, Canada (DND).

## 3. Scope

The rechargeable batteries and battery chargers studied were only those used in the communications and electronics (C/E) industry and similar applications. Battery chemistries addressed were sealed lead-acid, Ni/Cd, Ni/MH, lithium-ion (Li-ion), and lithium polymer. Batteries used for starting, lighting or ignition, and propulsion were not studied. Types of chargers studied included integrated, stand-alone, and multi-port, and their charging methods. The study focused on those representative companies who currently provide, or are expected to provide in the near future, rechargeable batteries and chargers to the DoD/DND.

## 4. Methodology

The rechargeable battery/charger industrial base study required a clear, concise, and well-defined methodology to survey government, industry, and academia effectively and compile military, commercial, political, marketplace, and academic perspectives. The data collected and analyzed for this study were drawn from previously published reports, conference proceedings, journal articles, Internet home pages, and other on-line sources, as well as from discussions with US and Canadian representatives from industry, government, and academia.

---

\* Corresponding author.

E-mail address: gucinski\_j@crane.navy.mil (J.A. Gucinski).

The study group's goal was to meet with or contact a representative sample of rechargeable battery/charger researchers, rechargeable battery/charger suppliers, end users, proponents and policy makers. Factors taken into consideration in selecting sites to visit or contact included volume of production and business with DoD and DND, battery chemistries produced, chargers manufactured, state of the technology, applications, and new technology development. Site visits were conducted in the US and in Canada.

Data collection guidelines were developed and used to facilitate obtaining data from all points of contact either through telephone interviews and/or site visits.

## 5. Background

NATIBO completed a sector study assessment of the overall battery industrial base in August 1994. Since then the production base for non-rechargeable batteries unique to the military has eroded due to reduced peacetime demands and high operating and support (O&S) costs. These costs have driven the US Department of Defense (DoD) and Canadian Department of National Defense (DND) to increase significantly the use of rechargeable batteries, during operations other than war.

In Canada, the Canadian Forces have used rechargeable batteries for a number of years as a reliable, cost effective, source of power. The Canadian Forces have also determined that they will increase the use of rechargeable batteries to power their portable communications equipment for many of the same reasons outlined by DoD. At present, the Canadian Forces are using rechargeable Ni/Cd batteries to power their equipment. By contrast, the DoD is deploying the Ni/MH system and pursuing the rechargeable lithium technologies. The Canadian decision is based on concerns regarding the reliability and service life of Ni/MH batteries. In all likelihood, the Canadian Forces will wait to procure rechargeable lithium batteries and associated chargers as

these technologies mature, foregoing the use of Ni/MH batteries altogether.

## 6. A technology overview and comparison of battery systems

In the military, parameters other than cost — such as weight, capacity, and the number of batteries to complete a mission — have an impact on the battery technology selection process. Currently, the baseline to which all rechargeable batteries are compared is the BA-5590/U Li/SO<sub>2</sub> battery. The BA-5590/U battery is used in over 50 different pieces of US Army equipment, including the single channel ground and airborne radio system (SINCGARS) tactical radio. Table 1 compares the parameters of specific rechargeable batteries to the non-rechargeable BA-5590/U.

Table 2 is a comparison showing how the major rechargeable battery technologies compare to the baseline non-rechargeable Li/SO<sub>2</sub> technology. In all cases, the capacity is less and the weight is greater.

However, the cost per cycle of all the rechargeable batteries (in the order of US\$ 2 to US\$ 3, given that one may not get the total cycle life) is substantially less than the single-use baseline battery cost of approximately US\$ 68.00 per unit.

## 7. Technology overview of charging methods

### 7.1. Constant current charging

Constant current charging is the simplest method of charging, delivering a single-value low level current to the discharged battery. The current is set at a fixed rate that is usually selected at 10% of the maximum Ah rated capacity of the battery. Constant current charging is best suited for use on lead-acid and Ni/Cd batteries. The type of charger is usually small, lightweight, and relatively inexpensive.

Table 1  
Comparison of battery parameters<sup>a</sup>

Chemistry/military designation	Nominal voltage of cell V	Energy (Whbdm <sup>-3</sup> )	Operating temperature range (°C)	Cycle life <sup>b</sup>	Weight as compared to BA-5590/U	Capacity in Ah as compared to BA-5590/U <sup>c</sup>	Disposal
Li/SO <sub>2</sub> BA-5590/U	3.0	415	–55 to +70	1	1.0	1.0 (7.2 Ah) <sup>d</sup>	Hazard
Sealed lead-acid BB-490/U	2.0	90	–20 to +55	250–500	2.04	0.30	Hazard/recycle
Sealed Ni/Cd BB-590/U	1.2	80–105	–30 to +40	300–700	1.8	0.39	Hazard/recycle
Ni/MH BB-390/U	1.2	175	–20 to +40	1000	1.73	0.75	Non hazard
Li-ion BB-XX90/U	2.9	200	–30 to +55	>1000	1.32	0.78	Non hazard
Lithium polymer BB-XX90/U	3.2	350	–20 to +55	Unknown	1.45	0.89	Non hazard

<sup>a</sup> Specific energies, operating temperatures, and cycle lives were taken from: D. Linden (Ed.), Handbook of Batteries, 2nd Edition, McGraw-Hill, New York.

<sup>b</sup> The number of cycles (the discharge and subsequent or preceding charge) under specified conditions, which are available from a rechargeable battery before it fails to meet specified criteria as to performance.

<sup>c</sup> Capacities based on BA-5590/U Li/SO<sub>2</sub>.

<sup>d</sup> In series configuration to give nominal 30 V output.

Table 2

Comparison of mission requirements and cost

Chemistry/military designation	Weight in kg (lb.)	Batteries per mission <sup>a</sup>	Mission weight in kg (lb.)	Battery unit price (dollar) <sup>b</sup>	Cost/mission <sup>c,d</sup> (dollar)
Li/SO <sub>2</sub> BA-5590/U	1 (2.2)	1	1 (2.2)	68.00	68.00
Sealed lead-acid BB-490/U	2 (4.5)	4	8 (18.0)	155.00	2.76
Sealed Ni/Cd BB-590/U	1.8 (4.0)	4	7.2 (16.0)	153.00	2.73
Ni/MH BB-390/U	1.7 (3.8)	2	3.4 (7.6)	293.00	2.61
Li-ion BB-XX90/U	1.3 (2.9)	2	2.6 (5.8)	e	e
Lithium polymer/BB-XX90/U	1.4 (3.2)	1	1.4 (3.2)	e	e

<sup>a</sup> Based on a 24 h mission using the SINCGARS.<sup>b</sup> BB-490/U and BB-590/U prices from Mathews Associates; BB-390/U and BA-5590/U prices from US Army CECOM.<sup>c</sup> Based on price paid by user and 224 cycles.<sup>d</sup> Cost of charging equipment and charging not included in this estimate.<sup>e</sup> Not yet in military inventory.

## 7.2. Constant potential charging

Constant potential charging allows the charger's maximum current to flow into the battery until its voltage reaches a preset limit. This system allows for higher charging currents, thus returning the battery quicker to a full state of charge. This system works well with batteries that exhibit a voltage rise at the end of charge, such as the lead-acid battery. Constant potential charging is detrimental to Ni/Cd batteries, which exhibit a drop in voltage when the battery goes into overcharge and begins to heat up, causing the voltage to drop. Some other chemistries, especially Li-ion, are not able to absorb additional energy once fully charged and must be removed from the charging source. "Float charging" is not recommended for these latter chemistries.

## 7.3. Constant current/constant potential charging

Constant current/constant potential charging is a combination of the two methods above. The system is designed to limit the maximum charger current until the battery voltage reaches a set limit. Then, the voltage control takes over; allowing the current to taper to a minimum value as the battery voltage nears full charge. The combination of constant current and constant potential allows for fast charging without the problems of gassing and overheating due to charging at high rates. This method is especially useful for sealed lead-acid batteries. It is particularly detrimental to Ni/Cd batteries that begin to heat up near the end of charge, causing the voltage to drop. This results in an increase in charge current at a time when the battery does not need high currents for charging.

## 7.4. Pulse charging

Pulse charging applies a series of charge/discharge or charge/rest cycles until the battery is fully charged. The charge current pulse is larger than the normal charging value and may be followed by a rest period rather than a discharge

cycle. Using this method, a battery can be fully recharged, with less gassing and heating, over a shorter time period that could be realized by any of the above methods. This method of charging has been used on Ni/Cd batteries to restore capacity lost due to "memory effect".

## 7.5. Smart charging

Smart charging adjusts the voltage and current supplied to the battery based on the monitoring of critical battery parameters (temperature, cell balancing). Charger operation can be optimized by using a micro-controller to carefully monitor and adjust the charging rate, the time, and, in some cases, the voltage. This optimization is used to increase charging efficiency, reduce charging time, or extend cell life. Use of smart charging is critical to rechargeable lithium chemistries to prevent the activation of the battery's internal safety features, which, if activated, render the battery useless. The charge rates and times are optimized to the specific battery chemistry and internal conditions during charging. This system does require special circuitry. The chargers that utilize this method tend to be larger and more expensive. They usually require high levels of power to support the rapid recharge that the system may select based on the battery's state of charge.

# 8. Applications for rechargeable batteries and chargers

## 8.1. Commercial rechargeable batteries

Rechargeable batteries are normally found in one of three generic formats. The oldest format is individual standard-size commercial batteries (such as "AA", "C", and "D"-size batteries). These batteries were normally marketed independent of the charger, which itself was a basic version of the multi-port system. Many consumers find it cost effective to buy individual rechargeable batteries and their associated chargers to power common items like flashlights, radios, and electronic toys and games.

The second format is product-specific battery packs. This format is where standard cells are combined to form a battery pack that is removable from the using equipment. These applications normally have a separate, stand-alone, dedicated charger. Examples of this would be cellular phones and pagers.

The third format is those commercial devices where the rechargeable battery and charger are integrated into the actual device. For example, many laptop computers employ this technique, as did some of the older portable power tools. Another example is cordless telephones, which are constantly on charge when placed in their base-station receptacles. This is convenient when one component of the total system is normally connected to household or commercial electrical power outlets.

The commercial market for rechargeable batteries is vast and expanding. It includes portable communications such as cordless telephones, cellular telephones, pagers and two-way radios, portable computers. It also includes portable entertainment such as radios, tape players, CD players, televisions, toys, and games. Portable tools is another, which includes drills, screwdrivers, sanders, saws, personal grooming tools such as shavers and toothbrushes, kitchen tools like mixers, blenders, and carving knives. Another segment is portable lighting, which includes flashlights and lanterns, also portable medical devices including hearing aids, heart products (pacemakers and defibrillators), and a variety of portable scientific and testing devices.

The improvements in rechargeable battery technology are driven by this rapid growth of the portable electronics market. Virtually all portable electronic product developments seek increased functionality (marketing features) at reduced weight. As these electronic devices become more miniaturized, the battery becomes a larger fraction of the overall volume and weight of the item. Therefore, the incentive for future advances in battery technology is to provide greater stored power with reduced volume and weight.

## 8.2. Rechargeable batteries for defence

DoD and DND have very demanding requirements for rechargeable batteries when compared to those of the commercial market. In addition to mission critical applications, high current requirements and long hours of continuous operation, the military has temperature and environmental (such as vibration and shock) requirements that exceed those of most civilian applications.

The US and Canadian Militaries have many generic C/E applications including

- Communications, navigation, and identification.
- Computers.
- Remote sensors, range finders, and laser target designators.
- Night vision devices.
- Mine detectors.

When selecting a battery chemistry to meet the requirements of either commercial or military applications, certain engineering and logistics factors must be considered. These include

- Cost (the unit price for commercial applications and life-cycle cost for the military applications are the driving influences).
- Weight.
- Safety (especially overheating during recharging).
- Operational requirements.
- Shelf life (including loss of charge over time).
- Operating environment.
- Human factors engineering.
- Disposal.

Future defence challenges include

- Laser flash protection.
- Microclimate conditioning systems.
- Chemical detection.
- Mine detection.
- Medical sensors.
- Helmet mounted displays.
- Mobility sensors.
- Voice communications (individual).
- Combat identification.
- Image transfer systems.
- Individual positioning/navigation systems.
- Thermal weapons sights.
- Forward observer/forward air controller communications.
- Aiming lights.
- Small arms fire control.
- Data network connectivity for situation awareness, command and control, and target handover.

Providing power to all of these systems will place heavy demands upon the battery packs, and innovative solutions will be demanded.

## 9. Options for facilitating more widespread use of rechargeable battery technologies

### 9.1. Reduced operating and servicing costs

As the defence budgets of the US and Canada continue to decrease, DoD and DND must look for cost savings in all areas. The US Army has already shown that the use of rechargeable batteries can reduce operating cost for training exercises. The attraction of reducing costs should help increase the future use of rechargeable batteries in all types of military applications and equipment.

### 9.2. Usage of commercial batteries

By taking advantage of what the commercial sector has done with rechargeable batteries and chargers, DoD and

DND can avoid the expense of R&D for military-unique cells and cell technology. By using the commercial industrial base, the US and Canada can avoid the development of an industrial base for rechargeable batteries that would be unique to the military.

### 9.3. Increased battery cycle life

As shown in Table 2 (comparison of mission requirements and cost), rechargeable batteries can have enormous cost savings because they can be used and reused over several different missions because of their ability to be recharged.

### 9.4. Reduction of battery weight

C/E applications of rechargeable batteries will increase in the future as battery weight decreases. The Land Warrior/Soldier Systems programs depend on sources of power that the individual can carry easily. If the weight of the power supplies were less, effort would be better-utilized in carrying additional combat capability.

### 9.5. Smart technologies

The use smart technologies will enable a more efficient use of rechargeable batteries. Batteries will be charged faster and safer to the optimum level without degrading the battery or shortening its life. The increase in efficiency will lower life cycles cost and improve the effectiveness of the batteries.

### 9.6. Low power electronics and power management

The use of low power electronics and of power management will increase the mission time supported by batteries thus increasing the attractiveness of rechargeable batteries.

## 10. Barriers against more widespread use of rechargeable batteries

### 10.1. Power source logistics

As rechargeable batteries and chargers are introduced into military units, a new logistics tail will develop. Currently, non-rechargeable batteries are consumed—similar to ammunition. Rechargeable batteries will not be treated as consumables, but will require a back-up supply line that allows them to be continuously rotated for charging. Also required will be an area where the batteries can be recharged, a power source for the chargers, manpower for recharging, and transportation.

### 10.2. Applications unique to the military

The applicability and use of rechargeable batteries in high risk airborne and reconnaissance missions where support is low is both untested and unproven.

### 10.3. The commercial trend towards small cells

The military will substitute rechargeable batteries for the current non-rechargeable batteries. The use of large cells is more efficient than connecting many more small cells. Besides the complexity of connecting small cells, heat generated by the small cells becomes a problem, which can affect battery life and performance if not managed properly. As commercial products (cell phones, PDAs, etc.) becomes smaller, the need increases for smaller, lighter rechargeable batteries. Commercial producers will respond by facilitating production capabilities for small cells—not large cells. Any niche market that the military creates will cause the costs of these rechargeable batteries to increase.

### 10.4. High initial cost

As shown in Clause 6, the initial cost of a rechargeable battery is higher than the comparable non-rechargeable battery. However, the total life cycle cost of the rechargeable battery is lower than the non-rechargeable. With current resources scarce, the decision to expend them in anticipation of future savings is difficult.

### 10.5. Acceptance by the soldier

Some units within the US Army are reluctant to switch to rechargeable batteries due to perceived reduced performance when compared to non-rechargeables. Not only do these units have to deal with a new battery, but also with the charger that accompanies it. The logistics to assure that portable power is available is an additional task that must be performed with no increase in resources.

### 10.6. Performance at extremes of temperature

The military requirement for C/E equipment to operate at extreme temperature conditions (–40 to +65°C/150°F) eliminates the use of nearly all currently available rechargeable chemistries.

### 10.7. Shelf life

Rechargeable batteries may require charging during storage to compensate for their inherent self discharge.

## 11. Conclusions

### 11.1. There is a deterioration of the Li/SO<sub>2</sub> industrial base

The use of rechargeable batteries in most operational scenarios short of full combat will have the effect of reducing the consumption of non-rechargeable batteries in peacetime. This reduction could be rather large. The result could further erode an already weak military-unique



non-rechargeable battery production base for Li/SO<sub>2</sub> primary batteries.

*11.2. Power source logistics are not being thoroughly addressed*

There are a number of logistical considerations that need to be thoroughly examined such as movement of batteries, manpower dedicated to charging the batteries and the provision of power to the chargers. In addition, rechargeable batteries require charging during storage to compensate for their inherent self-discharge.

*11.3. The commercial trend to smaller cells is against the requirements for military applications*

Industry that is making for the commercial and consumer market is moving towards smaller cell sizes in response to the trend for smaller and more energy efficient commercial electronics (i.e. cellular phones and beepers). However, the battery configurations for existing military applications are predetermined. If the military services use these commercially available cell sizes, it will require putting more, smaller, cells into the battery configuration in order to achieve their capacity requirements. This would cause other design issues, such as increased internal heating (or heat management), increased weight and additional inter-cell wiring. There also would be a loss in the total available capacity that could be packaged into the battery.

*11.4. Batteries and chargers are not being considered as a single system*

In the past, the military procured rechargeable batteries and their chargers separately. This approach was considered feasible due to a relatively limited use of rechargeable batteries. However, as the use of rechargeable batteries increases and where the new technologies are sensitive to a specific charge algorithm, this approach is no longer valid.

*11.5. The specific capacities of batteries are approaching their realistic limits*

As highlighted in Clause 6, the rechargeable battery technology is beginning to level out in terms of the available capacity from the various chemistries. Although advances will still be made in improving the performance of rechargeable batteries — in the short term, in lithium polymer and in the longer term, in solid state batteries — no “silver bullets” are seen on the horizon. This necessitates the increased

emphasis on power management techniques and the use of low power electronics.

*11.6. The use of rechargeable batteries reduces the operating and servicing costs for military applications*

Rechargeable batteries offer significant reductions in battery-related O&S costs. Even after costs associated with the procurement of chargers and the additional resources required to operate and power the chargers are accounted for, the savings both in procurement dollars and disposal costs have the potential to be significant.

*11.7. DoD and DND are increasing the use of rechargeable batteries for combat electronics applications*

Faced with increasing costs associated with the use of non-rechargeable batteries and decreasing budgets, DoD and DND accelerated the use of rechargeable batteries in C/E applications. The Canadian Forces have used rechargeable batteries for a number of years as a reliable, cost effective, source of power. Within DoD, the US Army has been aggressively pursuing the use of rechargeable batteries to reduce battery-related O&S costs.

### Acknowledgements

The authors would like to express their appreciation to the many individuals whose co-operation in providing essential information made this effort possible. This study could not have been completed without the dedicated efforts of the North American Technology and Industrial Base Organization Rechargeable Battery/Battery Charger Industrial Base Study Working Group members, listed here in alphabetical order: Mr. L. Bradley, Marine Corp. Systems Command; Major D. Clark, Directorate Defense Research and Engineering; Ms. G. Cypret, US Army Material Systems Analysis Activity; Mr. M. Gietter, US Army Communications-Electronics Command; Ms. C. Gonsalves, Directorate Defense Research and Engineering; Mr. R. Green, Naval Surface Warfare Center, Crane; Mr. J. Gucinski, Naval Surface Warfare Center, Crane; Ms. N. Hoesly, US Army Material Systems Analysis Activity; Ms. J. Jacks, Marine Corps Systems Command; Mr. D. Mains, Naval Surface Warfare Center, Crane; Mr. Al Moore, US Air Force Research Laboratory; Mr. M. Slack, Canadian Department of National Defense; Mr. J. Speaker, Naval Surface Warfare Center, Crane; Mr. F. Stonestreet, US Army Material Systems Analysis Activity; Mr. R. White, US Army Material Systems Analysis Activity.

# Electrochemical power sources for unmanned underwater vehicles used in deep sea survey operations

Øistein Hasvold\*, Nils Størkersen

*Norwegian Defence Research Establishment, P.O. Box 25, NO-2027 Kjeller, Norway*

Received 30 November 2000; accepted 10 December 2000

---

## Abstract

A comparison of available energy from different power sources for unmanned underwater vehicles, discharged at atmospheric pressure or at ambient pressure, has been undertaken. The basis for the comparison has been a neutrally buoyant power source with a total volume of 300 l. For deep diving vehicles, the use of batteries that can operate at ambient pressure is advantageous. This advantage increases as the mean density of the battery decreases and as the mean density of the pressure hull increases. A fuel cell using spherical gas containers is also an attractive power source for deep diving survey underwater vehicles. © 2001 Elsevier Science B.V. All rights reserved.

**Keywords:** Applications/underwater vehicles; Semi-fuel cells; Comparisons/battery systems

---

## 1. Introduction

In the late 80s, a group at the Norwegian Defence Research Establishment (FFI) began looking at the possibility of demonstrating the use of the magnesium/seawater/dissolved oxygen system [1] as an energy source for an unmanned, untethered underwater vehicle (UUV). This system has a very high specific energy density, but the power output is very low, unless a forced flow of seawater through the battery is employed.

The idea was to use the velocity of the vehicle to force seawater through the battery [2]. Even so, the specific power density was low, forcing us to develop low power solutions for UUV propulsion, communication and manoeuvring. The project, to develop and test a technology demonstrator, was concluded in 1993 after a successful series of sea trials. Then the work began to look for application of this newly learned technology.

We soon found out that near term applications of UUV technology required much more power than available from the seawater battery technology. On the other hand, the very high energy density of the seawater battery was not necessarily required. An endurance in the range of 6 to 48 h was considered sufficient for most applications.

Mine counter measures (MCM) is one area where UUV technology is considered to be very attractive [4]. Effective

mine hunting operations with UUVs requires access to high-resolution topography data and the capability of forward detection, classification and precise localisation of manmade objects on the seabed or in the water column.

The submerged endurance should be as long as possible to allow for large area coverage and the turnaround time between missions should be as short as possible, i.e. large energy density and short recharge time from the battery. These technical requirements are very similar to the requirements for a UUV for high-resolution seabed mapping, which could be used by the offshore industry. Thus, a joint team was formed with participation from the Royal Norwegian Navy, Norwegian offshore industry (Statoil), Kongsberg Simrad AS (KS), Norwegian Underwater Interventions AS (NUI), Norwegian Industrial and Regional Development Fund (SND) and FFI for developing UUVs for high precision seabed mapping and military route surveys (HUGIN). The work reported here took place in the mid and late 90s.

## 2. Underwater vehicles for seabed mapping

Modern seabed mapping is usually done from a surface vessel carrying a multibeam echosounder and cruising at a known speed and course. A typical sounder may have 127 beams covering a swath of 120°. In this way, a three-dimensional picture of the seabed is created along the route of the vessel. Given that the vessel knows its orientation and position along the route, a map can be generated. In shallow

---

\* Corresponding author. Tel: +47-63-80-75-34; fax: +47-63-80-75-09.  
E-mail address: oistein.hasvold@ffi.no (Ø. Hasvold).

water, this map can have both a high resolution and a high accuracy, but as the water gets deeper, it is necessary to submerge the sensor to get it closer to the seabed in order to get a high resolution. Traditionally, this has been done with remotely operated vehicles (ROV), which are connected to the mother vessel by an umbilical or by using towed equipment. In all cases, the positioning of the submerged multibeam echosounder relative to the surface vessel is based on acoustic positioning. This positioning equipment is most accurate when the platform is located straight below the surface vessel. Thus, one problem with towed platforms is the uncertainty in global platform position caused by layback, whereas the main problem with ROVs is the drag of the umbilical, reducing the speed of operation to a fraction of a knot at large depths. Both systems suffer from mechanical disturbances caused by the umbilical or towing cable.

The obvious solution to these difficulties was to use a UUV as the platform for the multibeam echosounder. Because the power for propulsion increases with approximately the cube of the vehicle speed, a realistic target speed was 4 knots. Still, it was important to keep power consumption as low as possible on all subsystem of the vehicle. Due to size limitations, total volume of the UUV was set to  $1.2 \text{ m}^3$ .

The first phase of the HUGIN project was finalised through the commissioning of two UUV systems, the HUGIN I and II. In 1998, the HUGIN II vehicle was transferred to NUI, who has since then operated the system on a commercial basis for high-quality topographic seabed mapping on the Norwegian continental shelf under the name of 'NUI EXPLORER'. These services have provided documentation to be used by the oil companies in support to offshore site and pipeline developments [3]. The system is

also used for data acquisition in support to national fishery research and estimation activities and for marine science missions.

HUGIN I was constructed with Ni/Cd batteries in two cylindrical aluminium pressure containers to allow us time to develop vehicle subsystems and to decide on the high energy density battery chemistry for HUGIN II. The result of that process was the development of the pressure compensated alkaline aluminium hydrogen peroxide semi-fuel cell described at the 21st Power Sources Conference [5]. This paper describes the process ahead of this decision, but it also takes into consideration the more recent technology.

The alkaline aluminium–hydrogen peroxide semi-fuel cell is also used in HUGIN 3000; a UUV produced by KS and FFI and delivered to C&C Technology, Lafayette, USA in July 2000. This vehicle, shown in Figs. 1 and 2, has a displacement of  $2.4 \text{ m}^3$  compared to  $1.2 \text{ m}^3$  for HUGIN I and II. Depth rating is increased from 600 to 3000 m and the endurance at nominal load (900 W) is 48 h. The increase in performance compared to HUGIN II, is primarily due to an increase in cell numbers from 4 to 6, an increased efficiency of the dc/dc converter (94% at 900 W), an improved propulsion motor and increased size and instrumentation. Some of these improvements will also be implemented on HUGIN I and NUI EXPLORER.

### 3. Battery systems for UUVs

When designing a UUV, one has to take into consideration that the weight of the vehicle must equal the Archimedes buoyancy force for the vehicle to be neutrally buoyant. This is equivalent to saying that the mean density of the UUV

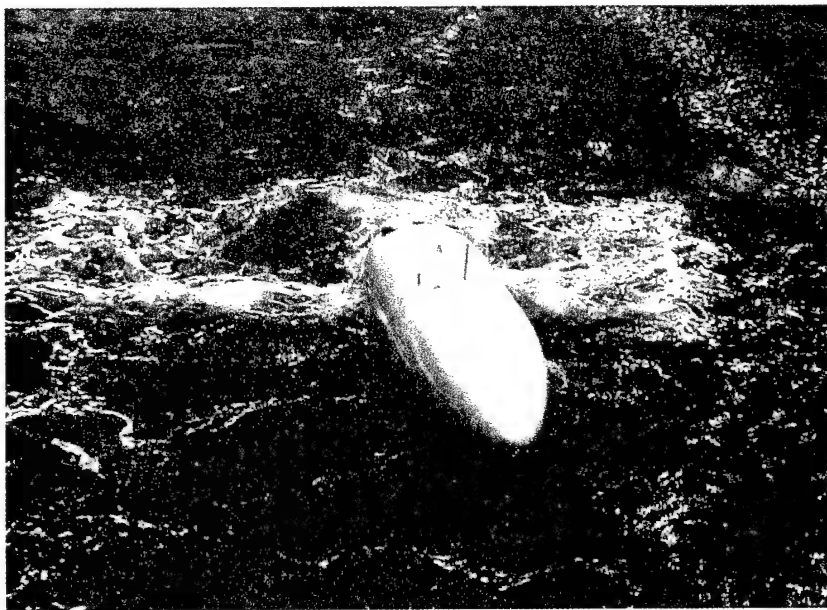


Fig. 1. HUGIN 3000 in the deployment phase.

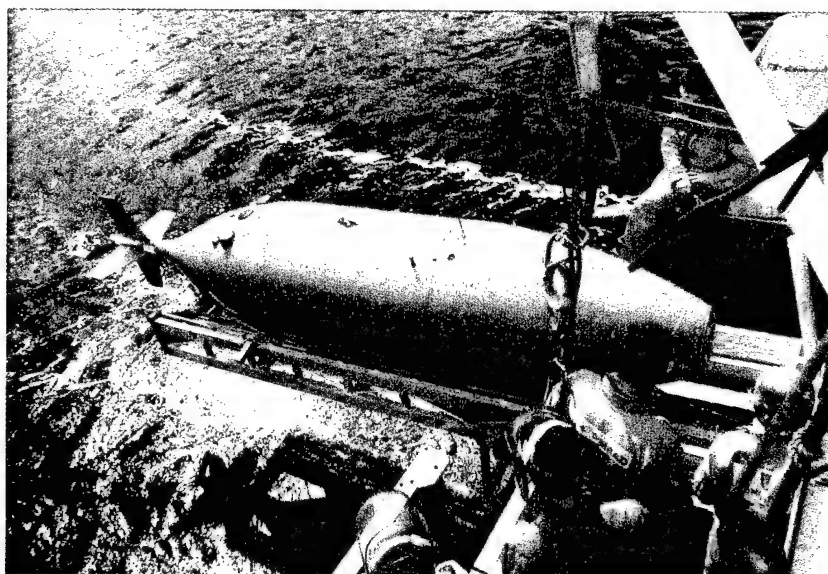


Fig. 2. HUGIN 3000 during retrieval.

must be equal to the density of the surrounding water. Small deviations from neutrality can be compensated as long as the vehicle is in motion by using dynamic lift, or when still, by using thrusters, but this is costly in terms of power consumption. As the design depth of the vehicle is increased, the mean density of the empty pressure containers (pressure hull) increases, decreasing the ability of the vehicle to carry useful weight such as batteries and instrumentation while remaining neutrally buoyant. A second design consideration is that the centre of gravity must be on the vertical line below the centre of buoyancy.

To compensate for excess weight, flotation materials such as syntactic foam (glass bubbles in a polymer matrix), have been developed. A typical foam material has a density of  $550 \text{ kg m}^{-3}$  and a working depth rating of 3000 m. The main advantage of using foam (as opposed to, for example, large hollow glass spheres) is that the foam can be machined into any shape and put where required, thus, exploiting the available void space to a maximum.

Pressure resistant containers are typically either spherical or cylindrical with semi-spherical end caps. The sphere is the best in terms of mean density as defined by empty weight divided by external volume, the cylinder is more convenient to use. Thus, shallow diving UUVs are mainly based on cylindrical pressure resistant containers, while deep diving UUVs often use spheres (the outer hull, giving the UUV its shape, is usually not pressure resistant and may be made of thin fibre reinforced plastic).

The selection of a power source for a specific UUV application with a defined energy requirement, is usually done by comparing the performances of completely neutrally buoyant battery sections, given a defined available volume and a design depth.

Electrochemical power sources for underwater applications are classified in four different groups:

1. standard batteries inside a pressure hull and working at normal pressure;
2. pressure compensated batteries working at ambient pressure, but electrically insulated from the seawater;
3. seawater batteries;
4. fuel cells.

Typical examples from the three battery groups are: lead/acid batteries operating at normal pressure in conventional submarines, pressure compensated batteries in the US Navy deep sea rescue vehicle (DSRV) and magnesium/silver chloride seawater batteries in torpedoes such as the UK Stingray lightweight torpedo. In the magnesium/silver chloride battery, seawater is used as the battery electrolyte and the internal pressure of the battery is equal to the external (ambient) pressure, given by the water depth and seawater density. In the DSRV, the battery is based on silver/zinc cells where the voids in the cell is filled with oil and the pressure of the electrolyte is kept equal to the external pressure via a flexible member between the oil and the seawater.

When comparing battery systems, a number of factors should be considered in addition to the specific energy content and power capability, typical factors being cost, battery life (both in terms of cycle and calendar life), maintenance requirements and safety. This also holds for UUV batteries. In addition, pressure compensated batteries may have variation in buoyancy with depth or with degree of discharge. Variation in buoyancy with depth of discharge is always the case for seawater batteries.

For shallow diving UUVs, the net mean density of the pressure vessel is low and the simplest and probably the most efficient battery solution is to use a battery system with a high energy density and put the battery and electronic systems together inside the pressure vessel. In this case, the only concern is to keep a safe atmosphere within the

pressure vessel at all times, safe meaning non-explosive, non-combustible and non-corrosive.

As the design depth of the UUV is increased, things get more complex. Below is a comparison of battery systems, given a design depth of 3000 m and an available volume of 0.300 m<sup>3</sup> with neutral buoyancy.

#### 4. Batteries discharged at atmospheric pressure

For this configuration, standard batteries can be used. Of special interest are the high energy density batteries presently being developed for the electric vehicle (EV) industry. In contrast to EV batteries, however, batteries for deep sea survey UUVs are typically discharged at a nearly constant power and over a time of typically 12–36 h. Thus, high rate capability is usually not required for this type of UUV. This simplifies both cell design and inter-cell connections, especially if high rate charging is not required. Thermal control under discharge is also comparatively easy since the seawater temperature is rarely outside the range of –2–26°C.

In the calculations, it has been assumed that the battery container has a depth rating of 3000 m and has the shape of a cylinder with a length of 1.6 m and with semi-spherical end-caps. Wall thickness is 20 mm and the internal diameter is 260 mm. Internal volume is 87 l. The battery container is made from an aluminium alloy with a density of 2700 kg m<sup>-3</sup>. The battery weight is calculated from cell weight plus an additional 8 kg for interconnections and hardware. During discharge, a diode voltage drop of 0.5 V is assumed. Syntactic foam with a density of 550 kg m<sup>-3</sup> is used to balance the weight and volume of the system.

Given the constraints above, the calculated battery weight is 125 kg (cell weight 117 kg), the weight of the empty container is 77 kg and the weight of syntactic foam is 103 kg.

Using typical battery data, Table 1 shows the performance to be expected.

For a HUGIN I type of UUV, the load is approximately 550 W. Thus, in the example above, from 8 to 127 h of continuous operation is possible, depending on the type of battery.

Low rate silver/zinc batteries have traditionally been the preferred rechargeable battery for UUV operation. They have energy densities ranging from 100 to 200 Wh kg<sup>-1</sup>

when new, but short wet life and declining capacity with cycle count have been major problems. However, the silver/zinc battery is still the yardstick to which other systems are compared. In Table 1, we have arbitrarily used the figure 120 Wh kg<sup>-1</sup> as a typical figure over the lifetime of a silver/zinc battery.

In the future, we expect that Li-ion will be the preferred chemistry over silver/zinc for rechargeable UUV batteries. In contrast to silver/zinc, the Li-ion cell is hermetically sealed and does not evolve gas during charge. Thus, the battery may be charged in the sealed container and may also be charged much faster than silver/zinc batteries. To obtain practical experiences in operation with Li-ion batteries, in 1998, we exchanged the Ni/Cd battery in HUGIN I with a Li-ion battery made from 360 Sony US26650 cells. This also allowed us to remove one of the two battery containers to allow space for a larger sensor suite. The battery was designed with eight blocks connected in series and with 40 cells in a parallel in each block, giving a nominal capacity of 108 Ah. A combination of hardware and software protects the battery at the cell level.

In the future, lithium-ion batteries developed and optimised for low rate, room temperature discharge, should be available with much higher energy density than indicated above. Not least the availability of large EV cells should decrease cost and increase the performance of the Li-ion UUV batteries. In terms of safety, however, the authors prefer many small cells, as it is our experience with lithium batteries that battery incidents mostly start with one cell only. Thus, even though increasing cell number increases the probability of an incident, keeping cell size small may reduce the severity of the incident.

At the present time, FFI do not consider the use of lithium primary batteries, partly due to the high cost of operation and partly due to the safety aspects of the use of multiples of large, high rate batteries. However, given the exceedingly high energy density of some lithium primary batteries, they should be very suitable for specialised operation requiring long range. Given a low rate design, safe use of large lithium batteries designed for UUV applications should be possible (Zolla et al. [6]), provided that special safety considerations are maintained. One measure to increase safety would be to use single cells paralleled via diodes or fuses and connected to a dc/dc converter. Such a design would completely remove failure modes related to serial connections such as over-discharge of failed cells, but at a cost of reduced energy.

Table 1  
Batteries operating at atmospheric pressure

Chemistry	Energy density of cell (Wh kg <sup>-1</sup> )	Energy density of neutrally buoyant system (Wh kg <sup>-1</sup> )	System energy (kWh)
Ni/Cd 4.5 Ah D-cell	36	14	4.2
Ni/MH 9 Ah D-cell	60	23	6.9
Ag/Zn	120	46	14
Li-ion MP176065	120	46	14
Li/SOCl <sub>2</sub>	400–600	153–230	47–70



Table 2  
Battery systems operating at ambient pressure

Chemistry	Energy density (Wh kg <sup>-1</sup> )	Energy density of neutrally buoyant system (Wh kg <sup>-1</sup> )	System energy (kWh)
Silver/zinc	90 <sup>a</sup>	47	14 <sup>b</sup>
Al/H <sub>2</sub> O <sub>2</sub> <sup>c</sup>	101	83	25
Future Li-ion	120	75	22

<sup>a</sup> Value for Yardney LR700DS single cell. Weight and volume of battery box and gas separation system are not included.

<sup>b</sup> Estimated system value. Value based on the weight of single cells is 16.4 kWh.

<sup>c</sup> Based on the HUGIN 3000 semi fuel-cell, but scaled down to fit within the 300 l neutral volume that is used for system comparisons.

## 5. Pressure compensated battery designs

Most battery chemistries can be used in pressure compensated designs. The main requirement is that the battery does not contain voids that may be compressed. Typically the cell is composed from solid or liquid phases, with a flexible member between the liquid electrolyte and the outside water. This flexible member compensates for differences in compressibility of the different materials allowing volume change with pressure and also allows for small amounts of compressible gas in the battery. If a larger amount of gas is expected, a gas separation system is mandatory.

Two examples of this technology which are in commercial use are the alkaline aluminium–hydrogen peroxide system (Al/H<sub>2</sub>O<sub>2</sub>) used in HUGIN II and HUGIN 3000 UV and the balanced silver/zinc battery used in DSRV.

As in Table 1, the performance data are calculated for a neutrally buoyant system with a volume of 300 l and syntactic foam as buoyancy material. The data for the Al battery is calculated from the performance in HUGIN 3000 on its second discharge of aluminium anodes (HUGIN II is equipped with aluminium for three discharges [5], HUGIN 3000 for two discharges. After each discharge, the electrolyte is exchanged and hydrogen peroxide refilled). The Wh kg<sup>-1</sup> system data is based on clear electrolyte. In a system designed for precipitation of aluminium hydroxide, the energy density can be approximately doubled, but at the expense of the ability of a rapid recharge.

A third battery system, called future Li-ion, is also included in the table. This battery is, for the calculation, assumed to be inside a sealed box made from 1 mm titanium and filled with oil, the volume of the battery box being 12% larger than the cell volume. Titanium weight is assumed to be 20% larger than that corresponding to the weight of the walls of the battery box in order to allow for stiffening

members. The oil is assumed to have a density of 870 kg m<sup>-3</sup>. The cell used for this calculation is the Ultralife UBC6034148 with a nominal capacity of 6.3 Wh and a nominal weight of 52 g. This is a polymer electrolyte, lithium ion — manganese oxide type, of a pouch cell construction. The cell is prismatic and the cell container is a thin metallised plastic foil envelope.

We did a discharge test of one cell under a pressure of 300 bar in an oil-filled container. The cell behaved normally during this discharge, in fact, we saw no measurable effect of the pressure on the cell voltage. After the test, however, the cell weight was increased by 3% and subsequent cycles at atmospheric pressure showed a decrease in capacity. Thus, this particular cell design is not suitable for this application, primarily because it contains voids, but it is an example of what can be achieved in the future, given cells that are designed for this application. One change in design may be to let the cell contain a small excess of liquid electrolyte, so that a pressure differential cannot develop over the cell container.

Table 2 gives some data on these three systems.

## 6. Seawater batteries

Because these batteries use seawater as electrolyte, a significant increase in energy density compared to other batteries is observed. A further increase is possible if the battery is using oxygen dissolved in the seawater as oxidant. Table 3 gives calculated figures on a low rate silver chloride battery and a magnesium-dissolved oxygen battery.

The figures in Table 3 are uncertain. The published nominal energy density for a silver chloride pile type of torpedo battery is 107 Wh kg<sup>-1</sup>, based on dry weight (Yardney MK 44/MK61 MOD 0). For the energy calculation, we used a cell voltage of 1.4 V and assumed nearly 100%

Table 3  
Battery systems with seawater as electrolyte

Chemistry	Energy density (Wh kg <sup>-1</sup> )	Energy density of neutrally buoyant system (Wh kg <sup>-1</sup> )	System energy (kWh)
Mg/AgCl	200	100	30
Mg/O <sub>2</sub>	600	167	50

Table 4  
Fuel cell system based on spherical aluminium containers

System weight (kg)	System volume (l)	System energy density (Wh kg <sup>-1</sup> )	System energy (kWh)
246	300	130	32

Faradaic efficiency for the silver chloride reduction and a Faradaic efficiency of the magnesium anode alloy of 50%. A further reduction in specific energy caused by the use of a dc/dc converter may be necessary for a battery based on discrete cells. In any case, this battery system is attractive as it is very compact, the battery volume being only 72 l, the rest being syntactic foam and buoyancy compensation hardware.

The figures for the magnesium/dissolved oxygen battery are based on a dc/dc converter efficiency of 80% and a power loss of 20% in order to pump the seawater through the battery [2]. Compared to the other battery chemistries, the low specific power for this system makes it less suitable for missions of short duration. Typical applications being missions with a duration of one or a few weeks. Thus, it is not directly comparable to the other systems.

Other seawater battery systems such as CuCl, PbCl<sub>2</sub> and MnO<sub>2</sub> with magnesium anodes have been evaluated, but found inferior to those described.

## 7. Fuel cells

Small fuel cells with kW outputs are interesting sources of power for UUVs. The energy density of the system based on the weight of the reactants, a cell voltage of 0.70 V and a Faradaic efficiency of 0.95 is approximately 2 kWh kg<sup>-1</sup>. Space application over many years has shown that the fuel cell technology is maturing. In spite of that the use of hydrogen/oxygen fuel cells in small UUVs has not yet been reported.

There may be two main reasons for this. One is the cost of the cell, the other is the problems associated with weight and space efficient storage of the reactants.

Traditionally, compressed gas has been the preferred method of storage. Thus, the energy density achievable is primarily determined by the performance of the gas containers in terms of wt.% of hydrogen or oxygen, keeping in mind that the containers should be rated for external pressure as well as internal pressure.

The figures in Table 4 have been calculated assuming spherical containers made from an aluminium alloy with an allowable working stress of 130 MPa. Two large containers, one for hydrogen and one for the fuel cell, and one smaller container for oxygen make up the system. The external volume of the three spheres is 300 l. Fill pressure is 300 bar and they contain 16 kg of reactants. The weight of the fuel cell and its auxiliary equipment has been set to 20 kg. The external diameter of the large spheres is 612 mm and the wall thickness is 30 mm, internal volume is 88 l. The

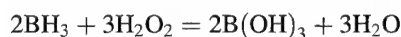
small sphere has an internal volume of 44 l, an external diameter of 485 mm and a wall thickness of 24 mm.

In contrast to the other systems described, this system has a net positive buoyancy of 55 kg. This is primarily because of the low weight of the spherical containers. A change to cylindrical containers would increase the gas container weight by a factor of two, but as cylindrical containers are easier to place within a hull, this may still be preferred.

In a real system, power used for auxiliary systems will reduce the figure for available system energy. An increase in weight caused by an auxiliary battery for start-up, inert gas system for flushing of the container etc. must also be taken into consideration. However, in spite of that the resulting figures should still be attractive.

An increase in gas pressure from 300 to 450 bar has been evaluated, but the large deviation from ideal gas behaviour [9], especially for hydrogen, makes higher pressure less attractive.

An alternative to the use of compressed gas is to produce hydrogen and oxygen chemically. For hydrogen, one of the more weight efficient method being the reaction of boron hydride with water, whereas oxygen can be produced by decomposition of hydrogen peroxide, 1 kg of pure hydrogen peroxide giving 0.471 kg of pure oxygen. Again, assuming a Faradaic efficiency of 0.95 and a cell voltage of 0.7, the specific energy based on the weight of water, boron hydride and hydrogen peroxide according to:



is 865 Wh kg<sup>-1</sup>. This figure is based on the use of pure hydrogen peroxide and that the water formed by decomposition of hydrogen peroxide can be used in the reaction with boron hydride, forming boric acid and hydrogen. Even after reduction of this figure by a factor of three–five, to allow for a practical system, the performance would still be quite good.

Given the high activity on fuel cell development [8], both for portable power and for electric vehicles (EV), one would expect to see fuel cells as a major power source for UUVs in the future.

## 8. Conclusion

From this work, we conclude that for a design depth of 3000 m, an increase in energy density by approximately 50% may be obtained through the use of pressure compensated batteries. This is especially advantageous for power

sources with a low mean density such as the  $\text{Al}/\text{H}_2\text{O}_2$  battery. At larger depths, the pressure compensated designs will be even more advantageous because the mean density of the pressure containers increases.

The numerical results are based on a certain set of assumptions, the most important being the shape of the pressure containers and the density, strength and stiffness of the materials used for its construction. If these assumptions are changed, different results will be obtained. Thus, the exact numbers are not the main point, but the method of selecting the power source, given that system energy is the main criterion.

Still, it is probably safe to say that for the deep diving survey UUV's, the  $\text{Al}/\text{H}_2\text{O}_2$  semi-fuel cell operating at ambient pressure is the rechargeable system that gives the user most endurance at present and in the near future. Compared to silver/zinc, it gives a nearly 50% improvement of the endurance.

For many applications, Li-ion batteries operating at atmospheric or ambient pressure may become the system of choice. Being electrically rechargeable, the logistics is simpler and in the future, comparable endurance to the  $\text{Al}/\text{H}_2\text{O}_2$  system may be achieved. We have used a value of  $120 \text{ Wh kg}^{-1}$  for the Li-ion cell in our calculations, whereas values as high as  $240 \text{ Wh kg}^{-1}$  [7] have been postulated with this chemistry.

The fuel cell is a very attractive future power source for UUVs for underwater survey operation. Based on compressed gas, it has light weight, is rapid to refill and the nearly constant load makes it possible to optimise

the system for maximum efficiency, allowing a long endurance.

## References

- [1] Ø. Hasvold, Seawater batteries for long term application, in: T. Keily, E.W. Baxter (Eds.), *Power Sources*, Vol. 13, International Power Sources Symposium Committee, 1991, pp. 307–318.
- [2] Ø. Hasvold, A magnesium–seawater power source for autonomous underwater vehicles, in: A. Attewell, T. Keily (Eds.), *Power Sources*, Vol. 14, International Power Sources Symposium, Leatherhead, UK, 1993, p. 243.
- [3] N. Størkersen, K. Kristensen, A. Indereide, J. Seim, T. Glancey, Hugin UUV for seabed surveying, *Sea Technol.* 39 (2) (1998) 99.
- [4] P.E. Hagen, Dual use development: the HUGIN untethered underwater vehicle, in: *Proceedings of the SMi conference on Naval Mines*, London, 27–28 November 2000.
- [5] Ø. Hasvold, K.H. Johansen, O. Mollestad, S. Forseth, N. Størkersen, The alkaline aluminium/hydrogen peroxide power source in the Hugin II unmanned underwater vehicle, *J. Power Sources* 80 (1999) 254–260.
- [6] A. Zolla, J. Westenberger, D. Noll, Development of a high power, high energy density lithium thionyl chloride battery for advanced unmanned underwater propulsion, in: *Proceedings of the 39th Power Sources Conference*, Cherry Hill, USA, 1999, pp. 64–68.
- [7] P.H. Smith, et al., High energy density lithium rechargeable batteries for underwater vehicle propulsion, in: A. Attewell, T. Keily (Eds.), *Power Sources*, Vol. 14, 1993, pp. 257–265 (target SDV sized cell with  $220 \text{ Wh/kg}$ ).
- [8] G.D. Lovering (Ed.), in: *Proceedings of the sixth Grove Fuel Cell Symposium*, 13–16 September, London 1999, *J. Power Sources* 86 (2000).
- [9] G.W. Castellan, The Beattie–Bridgeman equation, in: *Physical Chemistry*, Addison Wesley, Reading, MA, 1964, pp. 42–43.



Abstract

## The thermodynamics of battery safety

S. Mores<sup>\*</sup>, M.R. Ottaway, E. Price

*Thermal Hazard Technology, 1 North House, Bond Estates, Bond Avenue, Bletchley MK1 1SW, UK*

---

**Abstract**

Accelerating rate calorimetry is well suited to studying both the thermokinetics and thermodynamics of chemically reactive exothermic systems. Originally developed as a tool to aid the chemical and allied industries, the technique has gained considerable popularity within the battery manufacturing community.

The THT accelerating rate calorimeter has a number of options available, designed to study batteries during cycling (KSU) and abuse (BSU). The Gibbs free energy ( $\Delta G$ ) of a system may be determined and used as an indicator of hazard potential. Furthermore, changes in  $\Delta G$  based on calorimetric and electrometric data may be used to study the effects of cycling on battery efficiency. © 2001 Published by Elsevier Science B.V.

**Keywords:** Calorimetry; Battery safety

---

---

<sup>\*</sup> Corresponding author. Tel.: +44-1908-646-700;  
fax: +44-1908-625-209.  
E-mail address: stelios.mores@science.org.uk (S. Mores).

## Safety of lithium batteries in transportation

Michael D. Farrington\*

*Farrington, Lockwood Company Limited, 100 Terence Matthews Crescent, Kanata, Ont., Canada K2M 1P7*

Received 22 December 2000; accepted 5 January 2001

---

### Abstract

UN Document [“Recommendations on the Transport of Dangerous Goods Manual of Tests and Criteria”, 3rd Revised Edition, 1999] outlines a test plan that is fundamental to the classification for transport of lithium batteries with metallic lithium, lithium alloy or lithium-ion intercalation electrodes. The tests can be divided into two categories: safety tests (internal and external short circuit, forced-over-discharge, charge) and environmental tests (reduced pressure, thermal, vibration and shock). These safety tests are intended to assess known unsafe behavior in abusive circumstances.

This paper discusses the importance of environmental tests in the transport scenario and presents a discussion on how the existing safety tests provide only a false sense of security. Simple measures that prevent abuses in transport are suggested that would be more effective and ensure greater safety. A recent incident at Los Angeles International Airport (LAX), where lithium cells in transit were abused and caused to burn, is now cited by some regulators as proof that safety testing is required. This paper describes how that logic is flawed. Testing would not have prevented the LAX incident. Therefore, continued promotion of and focus on safety testing is working against the ultimate goal of improved safety in transport. This paper concludes that effective regulations should promote and maximize safe transportation of lithium batteries through environmental testing and the elimination of unsafe circumstances that enable lithium batteries to become a hazard in transport. © 2001 Elsevier Science B.V. All rights reserved.

**Keywords:** Specifications; Lithium batteries; Safety testing

---

### 1. Introduction

This paper continues on the theme of regulations for the transport of lithium batteries which began at the 21st International Power Sources Symposium with proposed amendments to UN ST/SG/AC.10/11: transport of dangerous goods — lithium batteries [2], presented in May 1999. It contained a brief history of the lithium battery transport regulations, many specific and general criticisms of the UN regulations, that have not substantially changed to-date, and many proposals for amending the regulations. Reference [2] holds up well after two more years of lithium battery safety debate and its contents will not be repeated here.

An amendment process is ongoing for a variety of reasons. The introduction of lithium-ion products as lithium batteries under the UN regulations is certainly a major factor. Our interest pre-dates that issue and concerns the value and appropriateness of specific tests and the overall test plan associated with the UN regulations. Writing about

the amendment process is challenging as the issues under debate change frequently when many draft proposals are flying around. Private sector interests have one additional limiting constraint. Only national government representatives, with little or no direct technical knowledge or experience, may officially propose amendments, attend and vote on the amendments at the UN.

A working committee made up of dangerous goods officials from Canada, the United States, Great Britain, France, Germany and Japan have been officially debating amendments.

Current regulations rely heavily on the tests in the UN test plan to determine the transportation classification of a lithium battery. The practical use of tests is something that can be assessed. Review of the UN test methodology has provided little assurance that meeting the requirements of some tests would equate to transportation safety. One event has brought attention to the question of what constitutes a hazard for transporting lithium batteries. A lithium battery incident at Los Angeles International Airport (LAX) provides us with a case that illustrates how the current regulations fail to assure confidence in safe transport.

---

\* Tel.: +1-613-591-0754; fax: +1-613-591-3580.  
E-mail address: flcl@igs.net (M.D. Farrington).

Why lithium batteries are potentially hazardous in transport is no great mystery. Assuring safety during the transport of these products is the goal of the regulations.

## 2. Regulations

There are many aspects of dangerous goods transport regulations. UN regulations are recommendations to national authorities. Each nation retains its own authority over transport regulations, however, it makes sense to minimize differences from one nation to another in order to facilitate international shipping. Most nations either accept the UN recommendations as is, or re-publish them with specific national modifications introduced. Canada is an example of the former. The USA is an example of a country that re-publishes the UN recommendations. The Code of Federal Regulations, known as CFRs, contain their modified version of the UN Special Provisions. The Special Provisions outline the basic rules such as what is regulated, allowed sizes, and general instructions for packaging.

Each mode of transport — air, marine, road or rail for example, have international organizations which also parrot the UN regulations. These organizations and their members have real power since they can ultimately refuse to carry a shipment, regardless of the UN recommendations. Conversely, shipping a lithium battery is only a practical problem if a carrier will not accept the shipment, regardless of UN classification for shipment.

Air transport is generally the most restrictive. International Civil Airlines Organization (ICAO) and International Air Transport Authority (IATA) must be convinced of safety of lithium batteries submitted for air transport. Representatives from ICAO and IATA are following the amendment process and participating where appropriate.

At issue is the logic behind current regulations. Every lithium cell or battery type within the scope of Special Provision 188 or 230 must be tested to the UN test plan before it can be classified and before it can be shipped. There are other conditions to be met, but this evaluation focuses on the tests in the test plan.

## 3. The limited value of testing

The data generated by any test are directly related to the design and specific parameters of the test. For example, a charge test at a given current informs us of the behavior of the sample under test at that one current. If the test is specified at a certain temperature, then we also learn about the behavior at that certain temperature. We are left with a number of uncertainties. We are not certain if the sample is representative of all similar products. Therefore, we perform multiple tests. But we are still uncertain if the group of cells tested is representative of all lots produced. We do not know if products produced earlier or later than the test lot are

identical to the test lot or if changes have been made to materials or procedures without a change to the model number. The UN tests allow a very broad scope of change to a product before requiring re-test. We do not know how minor changes might affect the test results.

Practical considerations such as cost, time and the destructive nature of the tests (which means all products cannot be tested) force us to ignore the uncertainties.

Chief among the uncertainties is how do these products behave at other charge currents? Most cell and battery tests and test plans are attempting to determine the safety of the products when operating normally in their application. The limits of performance within the application are defined by the limits of the product to operate safely and can be determined from the specifications published by the manufacturer of the cell. This could also mean that certain performance-limiting devices are incorporated into the cell, battery or equipment. It, therefore, makes better sense to design a test, for example the charge test, where the charging current is specified to be within the manufacturer's specified operating limit or below the operation of a fuse or positive temperature coefficient (PTC) device.

But how relevant is this to the transport scenario? If cells in shipment become loose and can operate in uncontrolled combinations with each other, it is possible that charging of a cell will occur, just as short circuits, forced discharges and crushing are likely to occur. It is likely that any such accidental charging current will exceed the tested limit and the manufacturer's specification. Any value of the limited testing regime has disappeared.

If the decision to ship these products was based upon such test results, then the test results have misled us.

Could a charge test be devised that would be all encompassing? No doubt an extreme test could be applied, however, with lithium cells and batteries the test results would likely be violent and appear to prove the point that lithium cells and batteries cannot be shipped safely. This would be incorrect logic.

There is a safe means to transport a lithium cell or battery with respect to the risk of charging. Simply stated, charging must be prevented from occurring during transport. Just as cells and batteries are equipped with current limiting devices to ensure they operate in their applications within manufacturer's specified limits, cells and batteries during transport must be effectively prevented from charging. The low cost solution to this puzzle is effective, not necessarily expensive. It is packaging. Packaging must be considered as a performance-limiting device. Exactly the same argument can be made for forced discharge testing of cells.

Unfortunately, the UN test plan contains certain tests that are designed for assessing safety within limits that do not correlate to the possibilities of an unlimited transport accident. These tests provide information that is limited by the design of each test. Most test conditions can be considered only as a single point on a multi-dimensional spectrum (combinations of voltage, current, temperature and pressure)

of possible transport accident conditions. What is proven regarding safe transportation from each test is dwarfed by what is ignored. When considering transport accident possibilities, the spectrum is nearly infinite.

If a potentially dangerous circumstance, such as charging, short circuit, forced discharging or crushing, can be prevented, then is that not preferable to limited testing that attempts to “prove” that the dangerous circumstance can be safely tolerated?

Some have argued that since existing tests are conducted at the extreme limits of allowed performance, the tests are, therefore, testing beyond what may reasonably be expected under normal conditions of transport [3]. This is an example of the incorrect logic that is applied to lithium battery transportation safety testing. In fact, the existing tests fall far short of simulating the spectrum of possible transport accident possibilities regardless of how harsh they are. They cannot possibly anticipate or simulate all possible accident conditions. Hence, such performance tests are more accurately referred to as limited tests throughout this document.

The environmental exposure tests make sense when determining transport safety. Finite limits are known for the temperature exposure that products in transport will see. The atmospheric pressure limits are known. Appropriate vibration and shock tests can be developed that accurately simulate the various modes of transportation. These tests must continue to be applied and require review to assure accurate simulations of real transport experience. Tests for vibration, shock and temperature currently in force are less than adequate simulations of the real transport environment extremes.

There is still great confusion about the internal short circuit test. The current edition of the UN test plan, ST/SG/AC.10/11/Revision 3 (1999), has amended this test to read: each cell is deformed until the open circuit voltage drops abruptly or is reduced to at least one third, or until a maximum force of  $1000 \times$  the weight of the cell, but not less than 10 kN, is applied. The choice of three optional test endpoints (OCV drop, voltage drops to  $1/3$  OCV or 10 kN applied force) shows clearly the confusion between an internal short circuit test or a crush test. The two OCV-related test endpoints define this as an internal short circuit test. The applied force endpoint redefines this as a crush test — albeit one entitled an internal short circuit test.

Regardless, the test proves almost nothing about the transport safety of a cell design if the test operator chooses to end the test when the OCV changes abruptly (and most do). Everything tested will likely pass, and yet the sample cell under test is potentially dangerous if crushed beyond the point of an abrupt change in voltage. The result is a product being transported that is still a potential hazard in a transport accident if it is crushed. If the test is conducted to the applied force rule and a fire or worse is the result, it may be ruled unsafe to transport. This would be equally twisted logic. The product would be entirely safe to transport so long as it is not crushed in the process.

The danger due to the development of an internal short circuit is real, and so is the danger due to crushing. Internal short circuits that, by design of the cell or battery pack, can pose a risk to safe transportation can be identified with appropriate vibration and shock testing. Artificially, crushing a cell can create an internal short circuit but it does not simulate the type of internal short circuit that has historically been a transportation problem. The existing UN test plan does evaluate the possibility of an internal short circuit for battery packs (a short circuit within the pack external to the cells). Once again we have a situation where the safety of a product in transport is based upon data from a poorly designed, limited test. Once again, would it not be superior to prevent cells and batteries from being crushed during transport? Attention to packaging would be all that is necessary to prevent crushing.

#### 4. The LAX incident

Two years ago, the motivation of some for amending the transport regulations was driven by the fact that the existing regulations did not allow for large batteries such as electric vehicle batteries. Regulators appeared to be ignorant of the poor quality of the existing regulations and, therefore, approached the amendment problem by dealing almost solely with the definitions of scope in the Special Provisions. Cosmetic changes to the test plan were suggested to accommodate the mass and size of the larger batteries and have now been incorporated into Revision 3 (1999) of the UN test plan [1].

Focus has now turned to more fundamental questions of transport safety. On 28 April, 1999, a fire destroyed freight, including lithium batteries, on two aircraft cargo pallets at the Northwest Airlines cargo facility at LAX. The pallets had been taken off an inbound passenger-carrying flight from Osaka, Japan. The aircraft was a Boeing 747, operated by northwest airlines as flight 0026. The US National Transportation Safety Board's (NTSB's) investigation of this incident revealed that lithium batteries likely present a serious fire hazard to air transportation required immediate attention. [4] This incident now commonly referred to as the LAX incident was investigated by the NTSB and resulted in the issuance of Safety Recommendations A-99-80 through 84 [4].

The events of that day are captured on an airport security video for all to see.<sup>1</sup> Essentially, two pallets, one containing 100 000 primary lithium cells (Sanyo CR2  $\text{Li/MnO}_2$ ), the other containing 20 000 more of these primary cells and some rechargeable cells as well, were abused many times by the fork-lift truck operators as they moved them around an outdoor cargo area of the airport. Abuse occurred over a period of hours resulting in a fire that could not initially be put out with the portable fire fighting equipment at hand and

<sup>1</sup> Both the RSPA and NTSB have copies of this airport security video.

was only extinguished when a fire truck arrived and doused the pallets with a large volume of water. Details are available online from the NTSB report [4] and the subsequent Advisory Notice put out by the Research and Special Programs Administration (RSPA), DOT [5].

The exact cause of the fire may never be known. Once the packaging integrity was destroyed, it could have started by any of the following mechanisms: crushing of cells, short circuiting of cells, charging or forced discharging. It really does not matter. It is clear that the fork-lift trucks sufficiently damaged the packaging allowing cells to move into contact with each other. Many fell out of the pallet altogether.

This incident caught the attention of regulators. The primary lithium cells that caught fire were not dangerous goods by definition of Special Provision 188 (and 49CFR173.185) due to the small amount of lithium per cell. They were not required to be tested to the UN test plan. As a result of the specific language of the regulations, there was no requirement for the shipment to be identified as lithium batteries and, therefore, handlers were unaware of the nature of their cargo. It was clearly demonstrated that lithium cells contain flammable materials and can burn. It was also demonstrated that it is very difficult to extinguish them. These and other serious issues have been raised by the NTSB. The RSPA, working with industry, ICAO and IATA are required to address the NTSB's concerns for safe lithium battery transportation by air.

In the meantime, several lessons learned from the incident can be described that relate to the UN test plan. It is our opinion that the Sanyo CR2 cell, had it been applied to the UN test plan, would have passed all of the tests. This opinion arises from experience with other similar products, not specifically the CR2 involved at LAX, which has not been tested by our laboratory. As suggested in the preceding discussion on the limited value of testing, the circumstances of those cells in the LAX transport accident were uncontrolled. Once packaging integrity was destroyed, cell combinations were possible which may have produced uncontrolled high voltages or high currents. There was a completely different thermal environment than the test laboratory. There were unknown mechanical pressures introduced from the shear mass of products on each pallet. Therefore, an individual cell may have been subjected to a crushing force once it was unprotected. The NTSB have recommended the DOT should consider the testing requirements for lithium batteries in the United Nations "Recommendations on the Transport of Dangerous Goods Manual of Tests and Criteria" [1]. Therefore, it is timely to note that the existing test plan would not have prevented the LAX incident. It is also important to note that the shipment had traversed the Pacific Ocean in the belly of a Boeing 747 without incident before the packaging was damaged. How far from safe transport was this shipment?

It is interesting to note that the fire at LAX was extinguished only when a fire truck arrived that could deliver a sufficiently large volume of water to cool the burning pallet.

This course of action was taken without fire-fighters knowing that the pallet contained lithium batteries. It was, purely by coincidence, the correct course of action. The success of applying large volumes of water to lithium battery fires was established in the UK over 10 years ago [6] and is generally known within the primary lithium battery industry. The UK study pointed out that the flammable electrolytes are the major contributor to a lithium battery fire and that lithium metal itself makes only a minor contribution. As such, speed is essential in stopping the fire, and the solvent fires would present no special problem to fire-fighters.

## 5. Safe transport of lithium batteries

Some regulators take the view that lithium batteries are inherently unsafe. For example, when referring to primary lithium batteries that power automated external defibrillators, the US Department of Transport's Federal Aviation Administration stated: safety of these batteries is stressed because extremely energetic materials are used in lithium cells and they are not intrinsically safe [7]. In time, this position will hopefully change to agree with the natural behavior of lithium batteries. With any battery, lithium or otherwise, it is safe to assume that under standard temperatures and pressures they are safe if not operating. To be viable as a commercial product, they must remain safe when operating within the design limits. It is in the manufacturers' interest to ensure this is true. It can be reasonably determined by applying such standard testing as outlined by UL, the IEC or others. Safety problems only arise when an unsafe circumstance occurs. Lithium batteries have existed long enough for us to understand these circumstances well. Lithium batteries must not be exposed to temperatures, pressures, mechanical shocks or vibrations beyond their design limits. Therefore, testing to environmental limits makes sense and must be continued as there is a safety benefit from continuing vigilance.

Safety behavior of lithium batteries when operating can be eliminated as a transportation issue if they are not operating during transport. This can be assured with effective packaging that isolates cells and batteries. Therefore, it becomes irrelevant how a cell or battery behaves when short circuited, forced discharged, or charged. Crushing can be eliminated by effective packaging and reasonable handling. Internal short circuiting, either within a cell or external to a cell but within a battery pack can be ruled out as a transport risk with appropriate vibration and shock testing of sufficient severity and duration. These issues were addressed in the last paper [2]. Tests within the UN test plan for short circuit, charge, forced discharge and internal short circuit fall far short of simulating the enormous range of possible accident circumstances. However, if the focus of regulators would change to address prevention of these unsafe circumstances during transport, then the "performance" tests are simply not necessary. If cells and batteries are prevented from

engaging in these operations during transport, assessing how they behave while operating is irrelevant. Eliminating these unsafe circumstances from the transport experience would provide far more assurance of safety to equipment and personnel.

The challenge for regulators should not be the design of new or improved tests. Regardless of effort or good intentions, performance tests can only provide limited information relevant to safety in transport. Such limited safety assurance does not compare well to effective prevention of operation and prevention of abuse. Defining the transportation environment accurately so that suitable performance-limiting packaging and handling requirements can be defined and stated clearly would yield greater assurance of safe transport. Using the LAX incident as an example, one lesson learned was that abuse inflicted on the pallets by forklifts must be taken into account as a possible experience the packaging must bear without losing its performance-limiting characteristics. This type of abusive handling is undesirable but difficult to eliminate and should be expected to occur [8].

How far from safe transport was the LAX shipment? It is difficult to say with certainty, but from descriptions of the packaging involved, which was clearly inadequate, it is likely that the very serious incident could have been prevented by only a very small, and possibly inexpensive, change to the packaging. Double boxing might have been enough. Stronger cell isolation in two directions instead of one might have been enough. A number of low cost, readily available solutions might have prevented the loss of packaging integrity and, therefore, prevented the cells from spilling freely and, therefore, preventing the fire.

The DOT is correct when it says that lithium batteries contain extremely energetic materials and, therefore, it is important that carriers and handlers know what they are carrying. When shipments of lithium batteries are so identified, handlers and carriers must then be sufficiently knowledgeable to act responsibly. International, national and modal regulations should provide more guidance to the shipper on the environment and other relevant circumstances of transport than they currently do, so that a shipper can select adequate packaging to survive the journey. Shippers have to understand that the packaging is more than a containment system, but also a cell or battery performance-limiting system that must remain intact during the entire trip. Shippers need more accurate guidance than is currently available to them in order to make their shipments safe.

It is obvious that lithium batteries should be identified as such, regardless of size. There is on-going debate as to how to accomplish this. Suggestions to consider:

1. include a warning on the packaging stating that the packaging integrity is critical to safety of the lithium batteries within; and
2. any damage to the packaging should disqualify the shipment from continued transport until repaired or

re-packed to the original condition. Such ideas are more easily suggested than implemented in this multi-lingual world of international transport. However, such warnings would serve to remind shippers, handlers, and carriers of the essential requirement for packaging integrity. If the LAX shipment had been attended to after the first forklift abuse, perhaps the fire would not have started. Unfortunately, the pallets were abused over and over by the forklift operators who were oblivious to the contents.

Cells and batteries shipped in equipment are covered under UN Special Provision 231. Normally, an installed battery is isolated by an "off" switch, but not always. The same principles of safety as stated above must apply to cells and batteries in equipment. The same requirements for environment tolerance including temperature, pressure, shock and vibration must all be evaluated through testing. There are many instances where cells and batteries installed in equipment are operating at micro-ampere current levels to power clocks or maintain memory. Historically, these levels of current have not presented a safety problem. There should be continued allowance for very low current operation. There are safety circuitry requirements in these instances, such as effective current limiting devices and diodes, that must be employed in these applications.

## 6. Conclusion

Regulators can assure safe lithium battery transport by introducing into regulations measures that prevent exposure to unsafe circumstances during transport. Effective packaging, not necessarily expensive packaging, that isolates cells and batteries and prevents operation, including abusive circumstances that can be encountered, is essential. Respectful, knowledgeable handling requires identification of package contents. Environmental testing should be continued and reviewed for accurate transport simulation. Regulations should include sufficient guidance for shippers to determine effective packaging for a particular shipment.

Ultimately, the lithium battery transport systems should operate based upon a respect for the highly energetic materials used in lithium batteries instead of a fear of them.

## Acknowledgements

The author would like to thank Laurie Farrington and George Donaldson for their time spent editing and proof reading this document.

## References

- [1] United Nations Document "Recommendations on the Transport of Dangerous Goods Manual of Tests and Criteria", 3rd Revised Edition, 1999.



- [2] M.D. Farrington, Proposed amendments to UN ST/SG/AC.10/11: transport of dangerous goods — lithium batteries, *J. Power Sources* 80 (1999) 278–285.
- [3] Draft information paper prepared by the expert from the United States proposing that the test methods for lithium batteries be revised, dated 25 July 2000 (to my knowledge, never submitted to the UN but circulated within the lithium battery working group for comments).
- [4] US National Transportation Safety Board, Safety Recommendation A-99-80 through 84, 16 November 1999.
- [5] Advisory Notice: Transportation of Lithium Batteries, *Federal Register*/Vol. 65, No. 174/Thursday, 7 September 2000/Notice NO. P 54336.
- [6] A. Attewell, The behavior of lithium batteries in a fire, *J. Power Sources* 26 (1989) 195–200.
- [7] Notice of Proposed Rulemaking (NPRM) Emergency Medical Equipment, US Department of Transportation, Federal Aviation Administration, 14CFR parts 121 and 135, Docket No. FAA-2000-7119, Notice No. 00-03 RIN 2120-AG89.
- [8] Neil McCulloch, Cargo Safety and Dangerous Goods, IATA, personal communication.

## Poster abstracts

### P1

#### Synthesis of $\text{Na}_x\text{V}_2\text{O}_5$ bronzes based on electrolytic $\text{V}_2\text{O}_5$ for use as the cathodes of lithium accumulators

E.M. Shembel\*, R. Apostolova, V. Nagirny

*Ukrainian State Chemical Technology University, 320005 Dnipropetrovsk, Ukraine*

D. Aurbach, B. Markovsky

*Bar-Ilan University, 52900 Ramat-Gan, Israel*

Miniaturization of electrochemical power sources for microelectronics requires us to use the technologies of thin films. Particularly, a rather simple method of an electrolytic metal oxide deposition enables the preparation of cathodes with a given thickness, beginning from a monolayer. Electrolysis allows us to design chemical composition, water content, size of crystallites, specific surface of the active mass deposited and, correspondingly, the electrochemical characteristics of the deposited products [1].

By anodic oxidation of vanadyl sulfate electrolytes, thin-layer deposits of electrolytic (e-)  $\text{V}_2\text{O}_5$  oxides [2] and  $\beta$ -bronze  $\text{Na}_x\text{V}_2\text{O}_5$  [3] were previously obtained as cathodes of lithium accumulators. The physico-chemical, structural and electrochemical properties of e- $\text{V}_2\text{O}_5$  are similar to those of  $\text{V}_2\text{O}_5$  gels. It is known that by using the ion exchange properties and other characteristics of  $\text{V}_2\text{O}_5$  gel layers, one can produce films of heterogeneous oxide compounds namely,  $\text{Me}_x\text{V}_2\text{O}_5$  (Me = Al, Fe, Na, and others) [4]. We have synthesized a number of vanadium oxide bronzes i- $\text{Me}_x\text{V}_2\text{O}_5$  ( $x = \text{Na}, \text{Ag}, \text{Cu}$ ) by ion-exchange (i) methods using e- $\text{V}_2\text{O}_5$  as the precursor.

Descriptions of the synthesis of  $\beta$ -bronze i- $\text{Na}_x\text{V}_2\text{O}_5$  and its investigation as a cathode material for lithium accumulators are presented. For the synthesis of i- $\text{Na}_x\text{V}_2\text{O}_5$ ,  $\text{V}_2\text{O}_5$  was deposited as a thin layer on conducting substrates or used as a dispersed powder by the method described in reference [5]. Then, the e- $\text{V}_2\text{O}_5$  samples produced, were kept in contact with a solution of  $\text{VOSO}_4$  (0.2 M), containing  $\text{Na}^+$  ions ( $10\text{--}20 \text{ g l}^{-1}$ ), at pH = 1.8 without passage of a current. The electrochemical characteristics of the washed and dried samples after exposure at  $20^\circ\text{C}$ , do not differ too much from those of regular e- $\text{V}_2\text{O}_5$ . The data from IR

spectroscopy, X-ray and thermal analysis as well as from electrochemical investigation indicate that by annealing at  $500^\circ\text{C}$  for 7 h, the e- $\text{V}_2\text{O}_5$  samples exposed to the  $\text{Na}^+$ -containing solutions, are transformed into the monoclinic bronze i- $\text{Na}_x\text{V}_2\text{O}_5$ . i- $\text{Na}_x\text{V}_2\text{O}_5$  bronze is identical to  $\beta$ -bronze which is a single phase in the range  $x = 0.22\text{--}0.40$ .

Cathodes made of  $\text{Na}_x\text{V}_2\text{O}_5$  bronze can be cycled efficiently within the range 3.70–2.40 V in commonly used electrolyte solutions such as PC, DME/1 M  $\text{LiClO}_4$  solution, yielding  $150\text{--}180 \text{ Ah kg}^{-1}$  at practical discharge currents such as  $100 \mu\text{A cm}^{-2}$ .

### References

- [1] E.M. Shembel, V.M. Nagirny, R.D. Apostolova, D. Aurbach, B. Markovsky, in: Proceedings of the 197th Meeting of the Electrochemical Society, Toronto, Vol. 2000-1, May 2000, Abstract 105.
- [2] E.M. Shembel, R.D. Apostolova, V.M. Nagirny, D. Aurbach, B. Markovsky, *J. Power Sources* 80 (1999) 90.
- [3] E.M. Shembel, R.D. Apostolova, V.M. Nagirny, D. Aurbach, B. Markovsky, *J. Power Sources* 80/82 (1999) 480.
- [4] J.P. Pereira-Ramos, *J. Power Sources* 54 (1995) 120.
- [5] R.D. Apostolova, E.M. Shembel, V.M. Nagirny, *Elektrokhimiya* 36 (2000) 41.

\* Corresponding author

E-mail address: shembel@onil.dp.ua (E.M. Shembel)

PII: S0378-7753(01)00572-9

### P2

#### A new cathode system for lithium-ion batteries

A.G. Ritchie\*, C.O. Giwa, P. Bowles, J.C. Lee

*Defence Evaluation Research Agency, Haslar, PO12 2A0, UK*

A. Gilmour

*Lexcel Technology Ltd., Henley-on-Thames1 R69 ILU, UK*

A.C.C. Tseung, J. Silver, D. Lapharri

*The University of Greenwich, Woolwich Campus, London SE18 6PF, UK*



A new cathode system for lithium-ion batteries was announced at the 1997 International Power Sources Symposium at Brighton [1]. It uses a mixture of lithium sulphite and a transition metal oxide [2]. This system has now been studied further, both in cycling studies at DERA and Lexcel and in electrochemical studies by cyclic voltammetry at the University of Greenwich.

Cycling studies have been carried out on lithium sulphite alone and also on lithium sulphite/transition metal oxide mixtures. The initial studies on this system [1] used a pressed pellet construction for the cathode. Further studies at DERA using this construction confirmed the cycling capability of this system. Cathode coatings using the doctor blade technique are in progress and are reported in the poster.

Electrochemical studies using cyclic voltammetry at the University of Greenwich showed that lithium sulphite would cycle on its own but that higher voltages were obtained when a metal oxide was present.

## References

- [1] A. Gilmour, A novel rechargeable lithium composite cathode system, in: Proceedings of the 20th International Power Sources Symposium, Brighton, April 1997. *J. Power Sources* 65 (1997) 241–245, Power Sources 16.
- [2] A. Gilmour, A rechargeable electrochemical cell, European Patent EP871986B1, 8th December 1999.

\* Corresponding author. Tel.: +44-2392-335429;  
fax: +44-2392-335102  
E-mail address: agritchie@dera.gov.uk (A.G. Ritchie)

PII: S0378-7753(01)00572-9

## P3

### Safety studies on lithium batteries using the accelerating rate calorimeter

Stelios Mores\*, Martyn Ottaway

*Thermal Hazard Technology, 1 North House, Bond Avenue, Bletchley MK1 1SW, UK*

A number of Accelerating Rate Calorimeter studies have been conducted on lithium chemistry based batteries. Temperature, pressure and self-heat rate data have been recorded as a function of time within an adiabatic environment. Focusing on the more common chemistries, a few examples are considered, taken under conditions such as shock discharge and thermal decomposition at elevated temperatures. Use is made of the data as a means of quantifying associated thermal stability hazards in storage and handling scenarios.

\* Corresponding author  
E-mail address: stelios.mores@science.org.uk (S. Mores)

PII: S0378-7753(01)00572-9

## P4

### A thermal battery using the Na/NiCl<sub>2</sub> couple

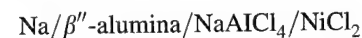
J.-Y. Poinso\*, A. Dubois, C. Barthet

*DMAT/SR2C, CEA Le Ripault, BP 16, 37260 Monts, France*

The sodium–nickel chloride cell couple is a very promising battery system, using  $\beta''$ -alumina as a solid electrolyte. The high cell voltage (2.58 V at 300°C), high theoretical specific energy (790 Wh kg<sup>-1</sup>), good cycling characteristics have made this system a good candidate for electric vehicle applications.

However, these features, the wide operating temperature range (250–570°C), and the lack of self-discharge even at elevated temperature, make this system attractive for use as a thermal battery, especially for long lifetimes and medium power applications.

The cell diagram of the sodium–nickel chloride cell couple is:



In the usual configuration, a  $\beta''$ -alumina tube separates the molten sodium (anode) and the molten sodium tetrachloroaluminate (secondary electrolyte). For thermal batteries, a bipolar configuration is required, and the first difficulties were technological obstacles.

We have begun to show that flat disc electrolyte membranes (thickness typically 0.9 mm) are thermally shock-proof even during the very rapid burning of the iron–potassium perchlorate heat pellets used to raise the temperature of thermal batteries.

We have made monopolar cells. Because sodium is liquid at the working temperature, we have used a mixture of carbon and sodium as the anode. The components for the cathode (NiCl<sub>2</sub>, NaAlCl<sub>4</sub>, C) are mixed and pressed to obtain a pellet. Carbon is used because it has a low weight and good conductive properties. The binding of the constituents is rather good, and a formation pressure of about 0.3 kg/cm<sup>2</sup> is used.

In this way, we made piles of up to five cells. The results are rather good at elevated temperatures (500–550°C). For a single cell with a diameter of 35 mm, the total resistance is about 0.1  $\Omega$  at 0.2  $\Omega$  and this does not depend on current. However, the results deteriorate when the temperature decreases (> 1  $\Omega$  at 350°C).  $\beta''$ -alumina as an electrolyte is not so good as we expected, but the resistances of the electrode–electrolyte interfaces contribute a very significant part of the overall resistance.

We are now trying to improve the performances of this system, especially by decreasing the percentage of the inactive materials — carbon, NaAlCl<sub>4</sub> — and by reducing the thickness of the electrolyte.

\* Corresponding author  
E-mail address: poinso@wanadoo.fr (J.-Y. Poinso)

PII: S0378-7753(01)00572-9

## P5

**Green thermal batteries**

C. Thaler\*, S. Schoeffert

*ASB-Aerospatiale Batteries, Allée Sainte Hélène, 18021 Bourges Cedex, France*

J. Sweeney

*MSB-Missiles and Space Batteries Ltd., East Shawhead, Coatbridge ML5 4UZ, Scotland, UK*

Thermal batteries have historically been dependent on the use of chromates as the oxidising agent in either their main heat source or in the fusetrain take-over heat source from the igniter to the main chromate-free heat source. Chromates are also present in the special cells used by ASB and MSB in thermal batteries that have to meet very fast activation time requirements. This calcium anode cell technology has potassium dichromate as the depolariser. Thermal batteries using these cells can be specified to have activation times of <100 milliseconds.

Because of the health concerns associated with the use of chromates, ASB and MSB have initiated a programme to remove chromates from all their battery designs.

Our poster will present both the work that has been carried out to develop a “green” battery for a specific fast activating application and the test results obtained. The new design comprises a fast activating starter section, an existing qualified Li/FeS<sub>2</sub> power section, and a new heat paper that has been formulated without chromates but has equivalent performance to the standard material. Because the design is based on well-established manufacturing processes, it offers a low risk solution for very fast activation specification requirements.

\*Corresponding author

E-mail address: c.thaler@asb-group.com (C. Thaler)

PII: S0378-7753(01)00572-9

## P6

**Electrode materials for power super-capacitors**

K. Jurewicz

*Institute of Chemistry and Electrochemistry, Poznan University of Technology, ul. Piotrowo 3, 60-963 Poznan, Poland*

Theoretically, very high peak power and extremely long cycle lives are the main attributes of supercapacitors as compared to electrochemical accumulators. Their

practical realisation needs the use of appropriate electrode materials.

Usefulness of the various materials can be determined from their galvanostatic, voltametric and impedance spectroscopy characteristics.

In the work presented, these techniques were used to examine carbon fibres obtained from various precursors, i.e. poly acrylonitrile, cellulose and phenol resin, also as carbon/carbon composite and carbon/conductive polymer with polyaniline or polypyrrole.

Miscellaneous conditions for pyrolysis and activation processes for obtaining of active carbon fibres were used.

The electrochemical investigations were carried out in aqueous KOH or H<sub>2</sub>SO<sub>4</sub> electrolytes. The results obtained were correlated with the electrolytic medium, the porous structure and chemical composition of the carbon materials and composites examined.

E-mail address: jurewicz@fct.put.poznan.pl (K. Jurewicz)

PII: S0378-7753(01)00572-9

## P7

**Survey of valve-regulated lead-acid battery reliability: information exchange**

Jennifer Dunleavy

*Energetics, Inc., 501 School St. SW, Suite 500, Washington, DC 20024, USA*

Paul Butler\*

*Sandia National Laboratories, MS0613, P.O. Box 5800, Albuquerque, NM 87185-0613 USA*

Results of an investigation on the reliability of valve-regulated lead-acid (VRLA) batteries will be presented. Surveys of VRLA end-users and manufacturers have provided detailed design, operation, and field failure information for tens of thousands of installations. These data will be presented and possible interpretations of the results will be discussed. The key areas of interest have been to characterize the relationships between VRLA technologies, service conditions, performance, and field failures. Preliminary correlations will be proposed for discussion, as will estimates of VRLA battery reliability. The ultimate goal of the study will be to suggest approaches to improving field performance and life.

\*Corresponding author. Tel.: +1-505-844-7874

E-mail address: pcbutle@sandia.gov (P. Butler)

PII: S0378-7753(01)00572-9

**P8****Advanced cellulosic membranes for silver–zinc rechargeable cells**

Harlan Lewis\*, Patricia Jackson

NAVSEA Crane, 300 Highway 361, Crane, IN 47522, USA

Colin Marshall

UCB Films plc, Wigton, Cumbria CA7 9BG, England, UK

UCB Films plc membrane materials are under evaluation as separation in model silver–zinc rechargeable cells. The cells are on a cycle life study at 100% depth-of-discharge where individual electrode voltage measurements are recorded every fifth cycle to monitor development of cell impedance and zinc shape change. Cells are withdrawn periodically for dissection to allow determination of rate of silver migration, of anode shedding and changes in membrane physical properties.

This poster will report the results of the cycle life study for both reinforced and unreinforced sausage casing with respect to the parameters under evaluation, with recommendations for their utilization in cells using rechargeable alkaline chemistry.

\* Corresponding author

E-mail address: lewis\_h@crane.navy.mil (H. Lewis)

PII: S0378-7753(01)00572-9

**P9****Advanced cellulosic sausage casing membranes for silver–zinc rechargeable cells**

Patricia Jackson, Harlan Lewis\*

NAVSEA Crane, 300 Highway 361, Crane, IN 47522, USA

Thomas Danko

Viskase Corporation 6855W, 65th Street, Chicago, IL 60638, USA

Viskase Corporation sausage casing membrane materials are under evaluation as separation, in conjunction with polyvinyl alcohol film, in model silver–zinc rechargeable cells. The cells are in a cycle life study at 100% depth-of-discharge where individual electrode voltage measurements are recorded every fifth cycle to monitor the development of cell impedance and zinc shape change. Cells are withdrawn

periodically for dissection to allow determination of the rate of silver migration, of anode shedding, and changes in membrane physical properties.

This poster reports the results of the cycle life study for both reinforced and unreinforced sausage casing with respect to the parameters under evaluation, with recommendations for their utilization in alkaline chemistry cells using rechargeable alkaline chemistry.

\* Corresponding author

E-mail address: lewis\_h@crane.navy.mil (H. Lewis)

PII: S0378-7753(01)00572-9

**P10****Perspectives on an ecological means of individual and public city transport by electric vehicles**

Miroslav Cenek

Institute of Electrotechnology, Electrical Engineering and Computer Science, Technical University, 602 00 Brno, Czech Republic

At the present time the application of electric vehicles both in individual and in public city transport is being developed, for ecological reasons.

First came the development of four-wheeled ecologically friendly vehicles for personal and pick-up uses. However, their application is significantly limited to use for business purposes in State administration and municipal enterprises, in spite of proven ecological benefits. Insufficient legislative support by State authorities is hindering any major expansion of this sort of city transport. Such support could eliminate the present significantly higher cost of electric vehicles when compared with vehicles using internal combustion engines (12 Euros per km after covering 120 000 km [1]).

A more significant improvement can be expected from two-wheeled electric vehicles, both for city and out-of-city operation. This concerns electric bicycles with auxiliary electric drive, folding electric scooters with two or three wheels and electric scooters of classical design.

During the last few years there has been significant development of electrobuses, ecologically friendly electric vehicles that can be purely electric or with hybrid drives. This fact is proven by the positive experiences obtained from an eight-year operation of electrobuses for city transportation in Santa Barbara, California, U.S.A. Problems associated with electrobuses with hybrid drives are being addressed by a European Union project in which the following cities are participating: Stavanger, Brugge, Luxembourg, Sintra, Alicante, Athens, Trento, Savona and Besançon.

There is a 32-year history of two and four-wheeled electric vehicles in the Czech Republic. During the eight

years since 1992, there has been intense activity both in University research, and by financial support from State Ministries in the production of electric vehicles, chargers (particularly fast-chargers) and monitoring devices for accumulators. Legislative support has started in some cities.

## References

- [1] G. Maggetto, P. Jacobs, P. Van den Bossche, S. Van den Bossche. Program for collaboration between CEC and National Programmes on Electric Vehicles in Europe, Task 4: Non Technical Aspects, Final Report, 51–65, Vrije Universiteit Brussel, Utrecht, The Netherlands 1996.

E-mail address: cenek@uete.fee.vutbr.cz (M. Cenek)

PII: S0378-7753(01)00572-9

## P11

### Microporous carbons for supercapacitors<sup>☆</sup>

K. Jurewicz\*, E. Frackowiak

*Institute of Chemistry and Technical Electrochemistry,  
Poznan University of Technology, ul. Piotrowo 3, 60-965  
Poznan, Poland*

F. Beguin

*CRMD-CNRS University, 1B rue de la Férollerie, 45071  
Orléans, France*

Due to the availability of various precursors and technologically well-developed methods of modification, materials based on carbon are especially adapted for application in electrochemical capacitors. They can be used with aqueous solutions (basic and acidic) as well as in aprotic media. During the preparation of carbon material it is possible, over a wide range, to affect the microtexture and chemical composition through the selection of precursor, conditions of carbonisation and the activation process.

The method used to prepare the carbon determines the electrochemical parameters of a capacitor. Generally, the most convenient is to use carbon materials in the fibrous form, however in our case the powdered carbon obtained from petroleum coke and then chemically activated supplied high capacitance values of over 200 F g<sup>-1</sup>. Specific surface area of this carbon, as measured by nitrogen gas adsorption at 77 K, was approximately 2800 m<sup>2</sup> g<sup>-1</sup>.

Electrochemical parameters of the investigated material, which was in the form of a pellet comprising 85% of C, 10% of PVDF and 5% of AB, were determined in the two electrode 'swagelok' cell as described elsewhere

[Frackowiak et al., Appl. Phys. Lett. 77 (2000) 2421–2423] using 6 M KOH and 1 M H<sub>2</sub>SO<sub>4</sub> electrolytes. Specific capacitance was calculated from voltammetry characteristics at scan rates from 1 to 10 mV s<sup>-1</sup>, galvanostatic cycling with current densities from 50 to 1000 mA g<sup>-1</sup> and impedance spectroscopy in the range from 1 mHz to 100 kHz. Electrochemical investigations were carried out using a multichannel potentiostat/galvanostat (VMP Biologic, France) and a Solartron SI 1260. All the techniques gave comparable results of specific capacitance of carbon (approximately 270 F g<sup>-1</sup> in alkaline solution and approximately 230 F g<sup>-1</sup> in acidic medium).

The results obtained show that alkaline electrolyte is preferable for this type of carbon when used as capacitor material. During voltammetry experiments from 0 to 0.8 V, the shape of the characteristics remains perfectly rectangular even at the fast scan rates (10 mV s<sup>-1</sup>). Only in the wider range of potential (from 0 to 1.0 V) does the shape of voltammograms change slightly, but the stored charge remains the same and galvanostatic characteristics are still linear. This means that carbon material allows quick charge propagation. This is also confirmed by impedance spectroscopy (material supplies a high capacitance of over 120 F g<sup>-1</sup> at 1 Hz). This is a proof that the carbon material, apart from having a well-developed surface area, possesses the required porosity from the presence of mesopores. In acidic solution, the capacitance values are lower by about 20%, however the frequency response is better. Further investigations are planned to correlate microtexture, pore size, distribution of pores and chemical composition of carbon with capacitance parameters for aqueous as well as aprotic electrolyte solutions.

<sup>☆</sup>This research was financially supported by NATO grant Sfp 973849

\*Corresponding author

E-mail address: jurewicz@fct.put.poznan.pl (K. Jurewicz)

PII: S0378-7753(01)00719-4

## P12

### Lead film electrodes as both negative and positive plates of a lead-acid battery

L.A. Yolshina\*, V.Ya. Kudyakov

*Institute of High-Temperature Electrochemistry, Urals Branch  
of the Russian Academy of Sciences, Ekaterinburg, Russia*

As has been shown previously, the electrochemical characteristics of lead film electrodes may be significantly influenced by the materials and shape of metallic substrates. Lead layers were deposited by the currentless, contact-exchange method from a molten salt electrolyte onto pure and technical grade smooth aluminium plates and grids 300–700 μm thick and onto copper grids 100–150 μm thick.

As lead and aluminium (or copper) are practically mutually insoluble at temperatures up to 1000 K, the covering thus obtained consists of pure continuous lead. The lead film varies much in thickness at a number of points over the specimen, but pores never reach through to the aluminium base. The minimum thickness of covering is no less than 80  $\mu\text{m}$ .

Because of the special features of this method of lead plating, the lead covering has a highly developed surface. Thus, the actual surface area of a lead film electrode can be 10 times as great as the apparent one. Lead coating of similar quality was also produced on coarse grids made from technical grade aluminium (99% Al) and aluminium alloys, which have much more prospects as constructive materials because of their better mechanical strength as compared to pure aluminium.

The electrochemical measurements of entirely immersed lead/aluminium electrodes were performed in a standard electrochemical cell under argon atmosphere. A silver chloride electrode (Ag/AgCl/saturated KCl solution) served as reference. 'Extra pure' grade 29 and 32 wt.%  $\text{H}_2\text{SO}_4$  was used as electrolyte. Cycling of lead film electrode over the range 0.7–2.0 V was carried out under potentiodynamic conditions with a linear scanning rate of 10  $\text{mV s}^{-1}$  and holding time of 200 s at the potential limits. The discharge current peak occurs at the potential of 1.5 V for the electrode on the aluminium plate. For an electrode on the aluminium substrate, the minimum value of the peak current density was observed during the first two cycles because of formation of a lead dioxide layer.

The peak discharge current increases up to the sixth cycle and then remains constant during the next 700 cycles. In some instances, the scanning voltammetry was stopped after 300 cycles and the working electrode was left to stand in sulphuric acid solution for 24–72 h. Only during the first cycle after this rest time was the magnitude of current discharge peak low. It then increased and attained its former value. Similar electrochemical behaviour was observed for the lead film electrode on the copper substrate.

It was shown that by exchanging the aluminium plate by a fine grid increases the value of current discharge peak by three–five times. In the case of lead plating onto a thin aluminium grid, we obtained a current density of 350–500  $\text{mA cm}^{-2}$ . This value is even higher than that obtained from an electrode on a fine copper grid. During prolonged testing, bulking and scaling of the lead coating was never observed.

\*Corresponding author. Tel.: +7-3432-488-153  
E-mail address: domnin@ihite.uran.ru (L.A. Yolshina)

## P13

### Effect of sulfur and oxygen on the corrosion of stainless steel when in a fuel cell carbonate electrolyte

E.V. Nikitina\*, V.Ya. Kudryakov, O.I. Klyushnikov

*Institute of High-Temperature Electrochemistry, Urals Branch of the Russian Academy of Sciences, Ekaterinburg, Russia*

We have investigated the effect of the corrosion on the steel, 12Cr18Ni10Ti by artificially injecting sulfur-, halogen- and oxygen-containing compounds of sodium into the high-temperature carbonate electrolyte of a fuel cell.

Corrosion resistance of the steel in a carbonate electrolyte has a significant role in the successful realisation of high-temperature devices.

At 873–1073 K, under an atmosphere of carbon dioxide and oxygen (2/1) or under atmospheric air, the interaction of the alkali carbonate melt (carbonates of lithium, sodium, potassium) with steel samples took place in a three-electrode cell with a special port for adding of salts, both when the cell was on open circuit and when it was under anodic potentiostatic polarization. The counter electrode was platinum wire, the reference one was the oxygen-carbonate electrode.

Addition of 2 mol% of sodium peroxide causes a significant shift of the corrosion potential into the electropositive region, with some growth of corrosion rate due to expansion of the thickness of the protective layers. There is a parabolic dependence of the corrosion rate during the steel sample's exposure in the melt.

At high temperature, the introduction of the peroxide into the salt phase resulted in the emergence of different oxygen ions and a layer with a higher oxygen content.

Under anodic polarization, the current density is lower than without excess oxygen, but the magnitude of the passive region does not change. Addition of 2 mol% of sodium halides causes a shift in the corrosion potential of about 0.1 V. Corrosion rate grows with increase of temperature.

Injection of sodium sulfide and sulfate has considerable effect on corrosion processes, both during polarization and on open circuit.

\*Corresponding author  
E-mail address: domnin@ihite.uran.ru (E.V. Nikitina)

## Author Index of Volume 96, issue 1

- Adcock, P.L. 233  
Agbossou, K. 168  
Amphlett, J.C. 204  
Anouar, A. 168  
Antonov, S.N. 52  
Atwater, D.W. 236  
Atwater, T. 151
- Bachhiesl, U. 200  
Bastian, M.J. 184  
Bell, R. 128  
Benczúr-Ürmösy, G. 76  
Bessette, R.R. 236, 240  
Bhattacharyya, A. 102  
Bose, T.K. 168  
Bowles, P.G. 180  
Brey, R.M. 184  
Brown, C. 121  
Burgess, J. 180  
Butler, P. 94
- Chacón, J. 68  
Chahine, R. 168  
Chervakov, O.V. 20  
Chu, D. 174  
Conway, B.E. 57  
Coowar, F. 199  
Crespi, A.M. 33  
Cuellar, E.A. 184  
Curran, T. 40
- Damodar, S. 151  
Danko, T. 128  
Dasgupta, D. 102  
Davies, D.P. 233  
De Doncker, R.W. 106  
DeMatteis, J. 184  
Deschenes, C.M. 236, 240  
Doughty, D. 29  
Dunleavy, J. 94
- Erbacher, J.K. 39  
Eweka, E. 180
- Farber-DeAnda, M. 94  
Farrington, M.D. 260  
Feng, F. 90
- Fennie Jr., C. 151
- Gamboa, S.A. 90  
Gardner, K. 174  
Gavrilov, A.B. 184  
Geng, M. 90  
Ghosh, S. 102  
Gilmour, A. 180  
Gitzendanner, R. 40  
Giwa, C.O. 180  
Gopukumar, S. 14  
Gucinski, J.A. 246  
Gupta, K. 214
- Hacker, V. 200  
Halliop, E. 204  
Hamelin, J. 168  
Hammond, M. 173  
Hammouche, A. 106  
Harmel, J. 76  
Hasvold, 252  
Hernández, J.C. 68  
Heydecke, J. 145  
Hodgson, D.R. 233  
Hong, K. 85  
Hossain, S. 5  
Huot, J.-Y. 133
- Ilic, D. 145
- Jackson, P. 128  
Jacobs, R. 174  
Jansen, T. 160  
Jarvis, C.R. 199  
Jena, A. 214  
Jiang, R. 174  
Jossen, A. 113
- Kalaiselvi, N. 14  
Karden, E. 106  
Karlsson, G. xv  
Kilb, M. 145  
Kniveton, M. 140  
Knop, I. 145  
Kohlhase, M. 76  
Kordesck, K. 200
- LaFratta, C.N. 240  
Laurencelle, F. 168  
Lee, M. 199  
Lewis, H. 128  
Loutfy, R. 5
- Macklin, W.J. 199  
Maksyuta, I.M. 20  
Malservisi, M. 133  
Maniguet, S. 226  
Manna, M.E. 184  
Manoharan, R. 220  
Marsh, C. 40  
Matchett, A.J. 90  
Mathew, R.J. 226  
Matty, T. 47  
May, B. 233  
Medeiros, M.G. 236, 240  
Meshri, D. 20  
Moore, Q. 167  
Moreno, D. 68  
Mores, S. 259  
Moseley, P. 94  
Muniyandi, N. 14
- Nagasubramanian, G. 29  
Neduzhko, L.I. 20  
Nelatury, S. 151  
Nikitina, E.V. 273  
Northwood, D.O. 90  
Novak, P. 20
- Ohms, D. 76  
Ojeda, A. 68  
Ostapenko, G.I. 52  
Ottaway, M.R. 259
- Patrissi, C.J. 240  
Paul Hagan, W. 245  
Pell, W.G. 57  
Peppley, B.A. 204  
Periyasamy, P. 14  
Perrin, M. 113  
Piller, S. 113  
Polischyk, Yu.V. 20  
Prabhuram, J. 220  
Premkumar, T. 14
- Price, E. 259  
Puglia, F. 40
- Quakenbush, T. 174
- Raadschelders, J.W. 160  
Raghavan, M. 14  
Ramesh babu, B. 14  
Reisner, D. 151  
Reisner, D.E. 20  
Renganathan, N.G. 14  
Ritchie, A.G. 1, 180  
Roberts, M.A. 226  
Russell, A.E. 226
- Sack, T. 47  
Sadiq, A. 204  
Saleh, Y. 5  
Salkind, A. 128, 151  
Schaedlich, G. 76  
Schmidt, C.L. 33  
Schmidt, J. 174  
Schulz, G. 145  
Sebastian, P.J. 90  
Shembel, E.M. 20  
Singh, P. 151  
Skarstad, P.M. 33  
Slack, M. 246  
Smith, D.F. 121  
Sondahl, S.K. 33  
Soria, M.L. 68  
St-Arnaud, J.-M. 168  
Stephens, J. 174  
Størkensen, N. 252
- Thirunakaran, R. 14  
Thompsett, D. 226
- Voss, H. 179
- Walter, J. 106  
Weaving, J.S. 199  
Wiesener, K. 76  
Wise, R.D. 184  
Yao, J. 226



## Subject Index of Volume 96, issue 1

- Applications
  - Fuel cells; Polymer electrolyte membrane; Portable communications (Chu, D. (96) 174)
- Applications/aircraft
  - Lithium ion batteries; Nickel/metal hydride batteries; Chargers/change control (Erbacher, J.K. (96) 39)
- Applications/automobiles
  - Lead-acid batteries; Testing/high-rate (Bhattacharyya, A. (96) 102)
- Applications/electric vehicles
  - Nickel/metal hydride batteries; Bipolar stack designs (Ohms, D. (96) 76)
- Applications/medical defibrillators
  - Lithium/silver vanadium oxide batteries (Crespi, A.M. (96) 33)
- Applications/military communications
  - Lithium-ion batteries (Moore, Q. (96) 167)
- Applications/portable military equipment
  - Energy sources/choosing; Fuel cells/direct methanol; Portable batteries (Raadschelders, J.W. (96) 160)
- Applications/portable power
  - Fuel cells/polymer electrolyte (Voss, H. (96) 179)
- Applications/standby power
  - Lead-acid batteries/valve regulated; Applications/telecommunications (Kniveton, M. (96) 140)
- Applications/telecommunications
  - Lead-acid batteries/valve regulated; Applications/standby power (Kniveton, M. (96) 140)
- Applications/underwater vehicles
  - Semi-fuel cells; Comparisons/battery systems (Hasvold, Ø. (96) 252)
- Aprotic solvents
  - Lithium batteries/polymer electrolyte; Gel polymer electrolytes; Iron pyrites (Shembel, E.M. (96) 20)
- Battery safety
  - Calorimetry (Mores, S. (96) 259)
- Battery separators
  - Capillary flow porometry; Pore structure; Fuel cell separators (Jena, A. (96) 214)
- Bipolar stack designs
  - Nickel/metal hydride batteries; Applications/electric vehicles (Ohms, D. (96) 76)
- Calorimetry
  - Battery safety (Mores, S. (96) 259)
- Capillary flow porometry
  - Pore structure; Fuel cell separators; Battery separators (Jena, A. (96) 214)
- Carbon electrodes
  - Semi-fuel cells; Carbon fibers (Bessette, R.R. (96) 240)
- Carbon fibers
  - Semi-fuel cells; Carbon electrodes (Bessette, R.R. (96) 240)
- Carbon-carbon composites
  - Lithium-ion batteries (Hossain, S. (96) 5)
- Catalysis
  - Fuel cells/polymer electrolyte membrane (Hodgson, D.R. (96) 233)
- Charge/discharge curves
  - Electrochemical capacitors; Internal resistance; Cyclic voltammetry (Pell, W.G. (96) 57)
- Chargers/change control
  - Applications/aircraft; Lithium ion batteries; Nickel/metal hydride batteries (Erbacher, J.K. (96) 39)
- Comparisons/battery systems
  - Applications/underwater vehicles; Semi-fuel cells (Hasvold, Ø. (96) 252)
- Computer simulation
  - Solid electrolyte batteries; Porous electrodes (Ostapenko, G.I. (96) 52)
- Cost effectiveness
  - Standby power supplies; Telecommunications; Lead-acid batteries; Reliability (Karlsson, G. (96) xv)
- Cyclic voltammetry
  - Electrochemical capacitors; Internal resistance; Charge/discharge curves (Pell, W.G. (96) 57)
- Cyclic voltammetry
  - Hydrogen-absorbing alloy; Metal hydride electrode; Hydrogen surface coverage (Geng, M. (96) 90)
- Defense applications
  - Li-ion batteries; High power (Sack, T. (96) 47)
- Electrical testing
  - Nickel metal hydride batteries; High rate applications; Hybrid vehicles (Soria, M. Luisa (96) 68)
- Electrochemical capacitors
  - Internal resistance; Cyclic voltammetry; Charge/discharge curves (Pell, W.G. (96) 57)
- Electrochemical impedance spectroscopy
  - Lead-acid batteries; Time-domain spectroscopy; Fourier analysis; VRLA batteries (Salkind, A. (96) 151)
- Electrolyte additives
  - Lithium-ion cells; Interfacial resistances (Nagasubramanian, G. (96) 29)
- Electrolytes/non-aqueous
  - Lithium-ion batteries (Puglia, F. (96) 40)
- Electrolytes/PVdF-PVC polymer
  - PVdF polymer; Ionic conductivity (Muniyandi, N. (96) 14)
- Electrolyzer
  - Hydrogen; Renewable energy; Wind turbine; Photovoltaic array; Fuel cells (Agbossou, K. (96) 168)
- Energy sources/choosing
  - Applications/portable military equipment; Fuel cells/direct methanol; Portable batteries (Raadschelders, J.W. (96) 160)
- Fourier analysis
  - Lead-acid batteries; Electrochemical impedance spectroscopy; Time-domain spectroscopy; VRLA batteries (Salkind, A. (96) 151)
- Fuel cell catalysts
  - X-ray absorption spectroscopy; X-ray diffraction (Russell, A.E. (96) 226)

- Fuel cell separators
  - Capillary flow porometry; Pore structure; Battery separators (Jena, A. (96) 214)
- Fuel cells
  - Hydrogen; Renewable energy; Wind turbine; Photovoltaic array; Electrolyzer (Agbossou, K. (96) 168)
- Fuel cells
  - Polymer electrolyte membrane; Applications; Portable communications (Chu, D. (96) 174)
- Fuel cells/acid electrolyte
  - Fuel cells/alkaline electrolyte; Noble metal catalysts; Methanol oxidation: formation of poisoning species (Manoharan, R. (96) 220)
- Fuel cells/acidic electrolytes
  - Fuel cells/direct methanol (Kordesch, K. (96) 200)
- Fuel cells/alkaline electrolyte
  - Fuel cells/acid electrolyte; Noble metal catalysts; Methanol oxidation: formation of poisoning species (Manoharan, R. (96) 220)
- Fuel cells/direct methanol
  - Applications/portable military equipment; Energy sources/choosing; Portable batteries (Raadschelders, J.W. (96) 160)
- Fuel cells/direct methanol
  - Fuel cells/acidic electrolytes (Kordesch, K. (96) 200)
- Fuel cells/direct methanol
  - Impedance spectroscopy (ac) (Amphlett, J.C. (96) 204)
- Fuel cells/polymer electrolyte membrane
  - Catalysis (Hodgson, D.R. (96) 233)
- Fuel cells/polymer electrolyte
  - Applications/portable power (Voss, H. (96) 179)
- Gas evolution reactions
  - Lead-acid batteries/flooded; Polarization (Hammouche, A. (96) 106)
- Gel polymer electrolytes
  - Lithium batteries/polymer electrolyte; Aprotic solvents; Iron pyrites (Shembel, E.M. (96) 20)
- High power
  - Li-ion batteries; Defense applications (Sack, T. (96) 47)
- High rate applications
  - Nickel metal hydride batteries; Hybrid vehicles; Electrical testing (Soria, M. Luisa (96) 68)
- Hybrid vehicles
  - Nickel metal hydride batteries; High rate applications; Electrical testing (Soria, M. Luisa (96) 68)
- Hydrogen peroxide
  - Magnesium anodes; Semi-fuel cells; Taguchi matrix (Medeiros, M.G. (96) 236)
- Hydrogen surface coverage
  - Hydrogen-absorbing alloy; Metal hydride electrode; Cyclic voltammetry (Geng, M. (96) 90)
- Hydrogen
  - Renewable energy; Wind turbine; Photovoltaic array; Electrolyzer; Fuel cells (Agbossou, K. (96) 168)
- Hydrogen-absorbing alloy
  - Metal hydride electrode; Hydrogen surface coverage; Cyclic voltammetry (Geng, M. (96) 90)
- Impedance spectroscopy (ac)
  - Fuel cells/direct methanol (Amphlett, J.C. (96) 204)
- Interfacial resistances
  - Lithium-ion cells; Electrolyte additives (Nagasubramanian, G. (96) 29)
- Internal resistance
  - Electrochemical capacitors; Cyclic voltammetry; Charge/discharge curves (Pell, W.G. (96) 57)
- Ionic conductivity
  - Electrolytes/PVdF-PVC polymer; PVdF polymer (Muniyandi, N. (96) 14)
- Iron pyrites
  - Lithium batteries/polymer electrolyte; Gel polymer electrolytes; Aprotic solvents (Shembel, E.M. (96) 20)
- Lead-acid batteries
  - Electrochemical impedance spectroscopy; Time-domain spectroscopy; Fourier analysis; VRLA batteries (Salkind, A. (96) 151)
- Lead-acid batteries
  - Standby power supplies; Telecommunications; Reliability; Cost effectiveness (Karlsson, G. (96) xv)
- Lead-acid batteries
  - State-of-charge (Piller, S. (96) 113)
- Lead-acid batteries
  - Testing/high-rate; Applications/automobiles (Bhattacharyya, A. (96) 102)
- Lead-acid batteries/flooded
  - Polarization; Gas evolution reactions (Hammouche, A. (96) 106)
- Lead-acid batteries/valve regulated
  - Applications/telecommunications; Applications/standby power (Kniveton, M. (96) 140)
- Lead-acid batteries/valve regulated
  - Performance surveys (Butler, P. (96) 94)
- Li-ion batteries
  - High power; Defense applications (Sack, T. (96) 47)
- Lithium batteries
  - Specifications; Safety testing (Farrington, M.D. (96) 260)
- Lithium batteries/polymer electrolyte
  - (Coowar, F. (96) 199)
- Lithium batteries/polymer electrolyte
  - Gel polymer electrolytes; Aprotic solvents; Iron pyrites (Shembel, E.M. (96) 20)
- Lithium ion batteries
  - Applications/aircraft; Nickel/metal hydride batteries; Chargers/change control (Erbacher, J.K. (96) 39)
- Lithium ion rechargeable batteries
  - Lithium oxides (Ritchie, A.G. (96) 1)
- Lithium oxides
  - Lithium ion rechargeable batteries (Ritchie, A.G. (96) 1)
- Lithium primary cells
  - Polycarbon monofluoride (Ritchie, A.G. (96) 180)
- Lithium-ion batteries
  - Applications/military communications (Moore, Q. (96) 167)
- Lithium-ion batteries
  - Carbon-carbon composites (Hossain, S. (96) 5)
- Lithium-ion batteries
  - Electrolytes/non-aqueous (Puglia, F. (96) 40)
- Lithium-ion batteries
  - Nickel-metal hydride batteries; Portable communications; Miniaturization (Ilic, D. (96) 145)
- Lithium-ion batteries
  - Polymer electrolytes; Mobile telephones (Cuellar, E.A. (96) 184)
- Lithium-ion cells
  - Electrolyte additives; Interfacial resistances (Nagasubramanian, G. (96) 29)
- Lithium/silver vanadium oxide batteries
  - Applications/medical defibrillators (Crespi, A.M. (96) 33)
- Magnesium anodes
  - Semi-fuel cells; Hydrogen peroxide; Taguchi matrix (Medeiros, M.G. (96) 236)
- Mathematical modelling
  - State-of-charge determination (Paul Hagan, W. (96) 245)
- Metal hydride electrode
  - Hydrogen-absorbing alloy; Hydrogen surface coverage; Cyclic voltammetry (Geng, M. (96) 90)
- Metal hydrides
  - Nickel/metal hydride batteries (Hong, K. (96) 85)



- Methanol oxidation: formation of poisoning species  
 Fuel cells/alkaline electrolyte; Fuel cells/acid electrolyte; Noble metal catalysts (Manoharan, R. (96) 220)
- Military batteries  
 Standardization (Gucinski, J.A. (96) 246)
- Miniaturization  
 Nickel-metal hydride batteries; Lithium-ion batteries; Portable communications (Ilic, D. (96) 145)
- Mobile telephones  
 Lithium-ion batteries; Polymer electrolytes (Cuellar, E.A. (96) 184)
- Nickel metal hydride batteries  
 High rate applications; Hybrid vehicles; Electrical testing (Soria, M. Luisa (96) 68)
- Nickel-metal hydride batteries  
 Lithium-ion batteries; Portable communications; Miniaturization (Ilic, D. (96) 145)
- Nickel/metal hydride batteries  
 Applications/aircraft; Lithium ion batteries; Chargers/change control (Erbacher, J.K. (96) 39)
- Nickel/metal hydride batteries  
 Bipolar stack designs; Applications/electric vehicles (Ohms, D. (96) 76)
- Nickel/metal hydride batteries  
 Metal hydrides (Hong, K. (96) 85)
- Noble metal catalysts  
 Fuel cells/alkaline electrolyte; Fuel cells/acid electrolyte; Methanol oxidation: formation of poisoning species (Manoharan, R. (96) 220)
- Performance surveys  
 Lead-acid batteries/valve regulated (Butler, P. (96) 94)
- Photovoltaic array  
 Hydrogen; Renewable energy; Wind turbine; Electrolyzer; Fuel cells (Agbossou, K. (96) 168)
- Polarization  
 Lead-acid batteries/flooded; Gas evolution reactions (Hammouche, A. (96) 106)
- Polycarbon monofluoride  
 Lithium primary cells (Ritchie, A.G. (96) 180)
- Polymer electrolyte membrane  
 Fuel cells; Applications; Portable communications (Chu, D. (96) 174)
- Polymer electrolytes  
 Lithium-ion batteries; Mobile telephones (Cuellar, E.A. (96) 184)
- Pore structure  
 Capillary flow porometry; Fuel cell separators; Battery separators (Jena, A. (96) 214)
- Porous electrodes  
 Solid electrolyte batteries; Computer simulation (Ostapenko, G.I. (96) 52)
- Portable batteries  
 Applications/portable military equipment; Energy sources/choosing; Fuel cells/direct methanol (Raadschelders, J.W. (96) 160)
- Portable communications  
 Fuel cells; Polymer electrolyte membrane; Applications (Chu, D. (96) 174)
- Portable communications  
 Nickel-metal hydride batteries; Lithium-ion batteries; Miniaturization (Ilic, D. (96) 145)
- PVdF polymer  
 Electrolytes/PVdF-PVC polymer; Ionic conductivity (Muniyandi, N. (96) 14)
- Reliability  
 Standby power supplies; Telecommunications; Lead-acid batteries; Cost effectiveness (Karlsson, G. (96) xv)
- Renewable energy  
 Hydrogen; Wind turbine; Photovoltaic array; Electrolyzer; Fuel cells (Agbossou, K. (96) 168)
- Safety testing  
 Specifications; Lithium batteries (Farrington, M.D. (96) 260)
- Semi-fuel cells  
 Applications/underwater vehicles; Comparisons/battery systems (Havold, Ø. (96) 252)
- Semi-fuel cells  
 Carbon fibers; Carbon electrodes (Besette, R.R. (96) 240)
- Semi-fuel cells  
 Magnesium anodes; Hydrogen peroxide; Taguchi matrix (Medeiros, M.G. (96) 236)
- Separators/cellulosic  
 Silver/zinc rechargeable cells; Separators/graft copolymer (Lewis, H. (96) 128)
- Separators/graft copolymer  
 Silver/zinc rechargeable cells; Separators/cellulosic (Lewis, H. (96) 128)
- Silver oxides  
 Silver/zinc reserve batteries (Smith, D.F. (96) 121)
- Silver/zinc rechargeable cells  
 Separators/cellulosic; Separators/graft copolymer (Lewis, H. (96) 128)
- Silver/zinc reserve batteries  
 Silver oxides (Smith, D.F. (96) 121)
- Solid electrolyte batteries  
 Porous electrodes; Computer simulation (Ostapenko, G.I. (96) 52)
- Specifications  
 Lithium batteries; Safety testing (Farrington, M.D. (96) 260)
- Standardization  
 Military batteries (Gucinski, J.A. (96) 246)
- Standby power supplies  
 Telecommunications; Lead-acid batteries; Reliability; Cost effectiveness (Karlsson, G. (96) xv)
- State-of-charge determination  
 Mathematical modelling (Paul Hagan, W. (96) 245)
- State-of-charge  
 Lead-acid batteries (Piller, S. (96) 113)
- Taguchi matrix  
 Magnesium anodes; Semi-fuel cells; Hydrogen peroxide (Medeiros, M.G. (96) 236)
- Telecommunications  
 Standby power supplies; Lead-acid batteries; Reliability; Cost effectiveness (Karlsson, G. (96) xv)
- Testing/high-rate  
 Lead-acid batteries; Applications/automobiles (Bhattacharyya, A. (96) 102)
- Time-domain spectroscopy  
 Lead-acid batteries; Electrochemical impedance spectroscopy; Fourier analysis; VRLA batteries (Salkind, A. (96) 151)
- VRLA batteries  
 Lead-acid batteries; Electrochemical impedance spectroscopy; Time-domain spectroscopy; Fourier analysis (Salkind, A. (96) 151)
- Wind turbine  
 Hydrogen; Renewable energy; Photovoltaic array; Electrolyzer; Fuel cells (Agbossou, K. (96) 168)
- X-ray absorption spectroscopy  
 Fuel cell catalysts; X-ray diffraction (Russell, A.E. (96) 226)
- X-ray diffraction  
 Fuel cell catalysts; X-ray absorption spectroscopy (Russell, A.E. (96) 226)
- Zinc anodes  
 Zinc-alkaline primary cells (Huot, J.-Y. (96) 133)
- Zinc-alkaline primary cells  
 Zinc anodes (Huot, J.-Y. (96) 133)